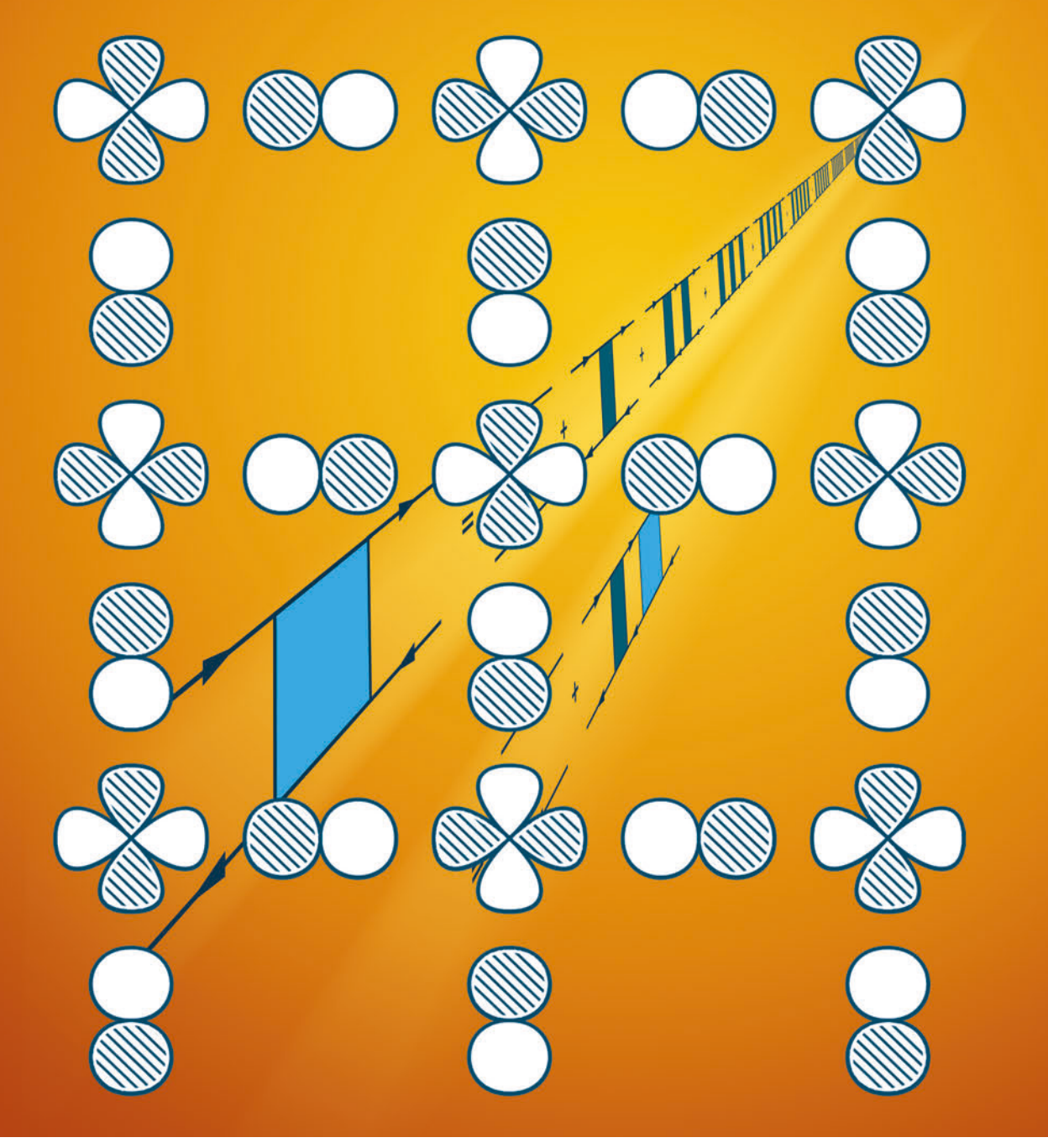

Quantum Materials: Experiments and Theory

Eva Pavarini, Erik Koch, Jeroen van den Brink, and George Sawatzky (Eds.)

German Research School
for Simulation Sciences

JÜLICH
FORSCHUNGSZENTRUM

Schriften des Forschungszentrums Jülich
Reihe Modeling and Simulation Band / Volume 6

Forschungszentrum Jülich GmbH
Institute for Advanced Simulation

German Research School for
Simulation Sciences GmbH

**Lecture Notes of the Autumn School on
Correlated Electrons 2016**

Eva Pavarini, Erik Koch, Jeroen van den Brink, and George Sawatzky (Eds.)

Quantum Materials: Experiments and Theory

Autumn School organized by
the Forschungszentrum Jülich
and the German Research School
for Simulation Sciences

at Forschungszentrum Jülich
12 – 16 September 2016

Schriften des Forschungszentrums Jülich
Reihe Modeling and Simulation

Band / Volume 6

ISSN 2192-8525

ISBN 978-3-95806-159-0

Bibliographic information published by the Deutsche Nationalbibliothek.
The Deutsche Nationalbibliothek lists this publication in the Deutsche
Nationalbibliografie; detailed bibliographic data are available in the
Internet at http://dnb.d-nb.de.

Publisher:	Forschungszentrum Jülich GmbH Institute for Advanced Simulation
Cover Design:	Grafische Medien, Forschungszentrum Jülich GmbH
Printer:	Druckerei Schloemer, Düren
Copyright:	Forschungszentrum Jülich 2016
Distributor:	Forschungszentrum Jülich Zentralbibliothek, Verlag D-52425 Jülich Phone +49 (0)2461 61-5368 · Fax +49 (0)2461 61-6103 e-mail: zb-publikation@fz-juelich.de Internet: http://www.fz-juelich.de

Schriften des Forschungszentrums Jülich
Reihe Modeling and Simulation, Band / Volume 6

ISSN 2192-8525
ISBN 978-3-95806-159-0

The complete volume ist freely available on the Internet on the Jülicher Open Access Server (JUWEL)
at http://www.fz-juelich.de/zb/juwel

Contents

Preface

Quantum materials exhibit a spectacular variety of unusual emergent behavior that is practically impossible to predict from first-principles. Experiment is crucial for discovering phenomena such as the metal-insulator-transition, the Kondo effect, or superconductivity. Theory provides the paradigm for understanding these states of matter. Developing such understanding relies on the close interplay between theory and experiment, with experiments constantly putting theoretical ideas to a test. This year's school covers experimental techniques such as optics, photoemission, NMR, and tunneling spectroscopy. Understanding these experiments requires the realistic modeling of materials as well as approaches to solving them. Lectures ranging from the model building schemes to advanced many-body techniques provide the foundation to unraveling the mystery of these materials. Introductions to theoretical approaches for calculating spin, charge, and orbital structure as well as response functions provide direct contact to the experimental probes. The aim of the school is to introduce advanced graduate students and up to the essence of emergence and modern approaches for modeling strongly correlated matter.

A school of this size and scope requires support and help from many sources. We are very grateful for all the financial and practical support we have received. The Institute for Advanced Simulation and the German Research School for Simulation Sciences at the Forschungszentrum Jülich provided the major part of the funding and were vital for the organization of the school and the production of this book. The DFG Research Unit FOR 1346 generously supported many of the speakers. The Institute for Complex Adaptive Matter (ICAM) offered travel grants for selected international participants.

The nature of a school makes it desirable to have the lecture notes available when the lectures are given. This way students get the chance to work through the lectures thoroughly while their memory is still fresh. We are therefore extremely grateful to the lecturers that, despite tight deadlines, provided their manuscripts in time for the production of this book. We are confident that the lecture notes collected here will not only serve the participants of the school but will also be useful for other students entering the exciting field of strongly correlated materials.

We are grateful to Mrs. H. Lexis of the Verlag des Forschungszentrum Jülich and to Mrs. D. Mans of the Graphische Betriebe for providing their expert support in producing the present volume on a tight schedule. We heartily thank our students and postdocs who helped with proofreading the manuscripts, often on quite short notice: Michael Baumgärtel, Khaldoon Ghanem, Julian Mußhoff, Esmaeel Sarvestani, Amin Kiani Sheikhabadi, Guoren Zhang, and Qian Zhang.

Finally, our special thanks go to Dipl.-Ing. R. Hölzle for his invaluable advice on the innumerable questions concerning the organization of such an endeavor, and to Mrs. L. Snyders for expertly handling all practical issues.

Eva Pavarini, Erik Koch, Jeroen van den Brink, and George Sawatzky

August 2016

1 The Explicit Role of Anion States in High-Valence Metal Oxides

George Sawatzky and Robert Green
Stuart Blusson Quantum Matter Institute and
Max Planck/UBC Centre for Quantum Materials
University of British Columbia
2355 East Mall, Vancouver BC, Canada V6T 1Z4

Contents

E. Pavarini, E. Koch, J. van den Brink, and G. Sawatzky (eds.)
Quantum Materials: Experiments and Theory
Modeling and Simulation Vol. 6
Forschungszentrum Jülich, 2016, ISBN 978-3-95806-159-0
http://www.cond-mat.de/events/correl16

1 Introduction

Correlated metal-oxide compounds exhibit a wide range of interesting properties, including for example high-temperature superconductivity, metal-insulator transitions, and various forms of orbital and magnetic ordering. Many of these metal-oxide compounds with especially interesting properties contain cations which have exceptionally high oxidation states, when one assigns those oxidation states using the usual formal valence-counting methodologies. transition-metal elements from the $3d$, $4d$, and $5d$ series can usually attain several different oxidation states in compounds, ranging for example from 2+ to 5+ for vanadium in oxides. Given this flexibility of the cations, one usually assumes a closed valence shell structure for the anions, meaning that the chalcogens (O, S, Se, Te) would have a 2- valence and the halides (F, Cl, Br, I) would have 1-. Similarly, fixed cation valences according to closed shells are usually assumed for certain columns of the periodic table, including 1+ for the alkali elements under Li, 2+ for the alkaline earth elements under Be, and 3+ for those under Sc and B.

In these standard valence-counting formalisms where anion and the above cation valences are fixed, the remaining cations then adopt the compensating valence to end up with a charge neutral unit cell or formula unit. Following this approach, Fe in FeS_2 would be 4+, Ni in the rare-earth (R) nickelates $R NiO_3$ would be 3+, and there would be Cu^{3+} present in the hole-doped cuprate $La_{2-x}Sr_xCuO_4$. However, there are many examples where this classification is not valid—Fe in FeS_2 for example is actually 2+ and there are accordingly missing sulfur $3p$ electrons. This leads to the formation of sulfur pairs having a net pair valence of 2- rather than 4-. In this case the antibonding S $3p$ states in the pairs are empty and therefore form rather narrow bands just above the chemical potential which form the conduction band (depending on where the transition-metal electron addition d states are, as we will discuss below). Similarly, in superoxides such as KO_2 the O atoms form pairs, but now with each pair having a 1- charge and spin of $1/2$, leading to an O $2p$ hole-based ferromagnetic ground state. In the hole-doped cuprates, convention would predict the introduction of Cu^{3+} into the mainly Cu^{2+} lattice, leading to a mixed valent state. However, it is known that the holes actually reside mainly in O $2p$ orbitals, leaving the Cu with a 2+ valence and a spin of $1/2$. In some pictures (like that of the Zhang-Rice singlets) these O holes tend to form molecules of 4 oxygen atoms in a square around a particular Cu, forming a singlet spin state due to the very strong Cu-O exchange interaction which is of order 0.5 eV. Similarly, we will argue that also Ni does not really like to be 3+ and so in the perovskite structure rare-earth nickelates the Ni behaves like Ni^{2+} in a normal high-spin state of $S = 1$ and there is one hole per 3 oxygens in the O $2p$ band of states. Realizing that each Ni is at the center of an octahedron of O ions we would have on average 2 holes per O octahedron and again these are found to condense into octahedral molecules of O around every second Ni^{2+} ion.

In this lecture we will look at the consequences for the electronic structure and the corresponding physical properties of oxides involving unconventionally high cation oxidation states which accordingly may better be viewed as having unfilled anion valence bands. In solid state physics we are mostly interested in the low-energy scale possible excitations from the ground state which determine the physical properties in a temperature range of perhaps 0 to 500 K, thus we

will focus our considerations on those states which are at most several eV above and/or below the chemical potential. Further, in the study of transition-metal oxides or rare-earth compounds we mostly start from a viewpoint of what the valences of the elements are in the limit of zero interatomic hybridization (i.e., in the ionic limit). The hybridization, which of course plays a crucial role, is then introduced and band structures and interatomic interactions result. As we know, in transition-metal based ionic solids the valence state of an ion determines the number of d electrons involved and this in turn determines the spin, orbital, and total angular momentum via Hund's rules in the lowest energy states. The excited states, or multiplets, important in describing various forms of spectroscopy are also determined to first order in this ionic starting point. Thus, this starting knowledge is the first guess as to what the spin and the d occupation numbers really are in the material. However, if indeed the anion valence states are not fully occupied and the cations accordingly have unexpected valences in the ionic limit, the lowest energy states could be very different from this formal oxidation state based picture, and the model Hamiltonians which should be used could differ strongly from the typical ionic ansatz. This is especially important for the analysis of materials using x-ray based spectroscopies such as resonant x-ray reflectometry and resonant elastic and inelastic x-ray scattering.
In the following we will start with a brief motivation of the importance of anion states by looking at divalent late $3d$ transition-metal (i.e. Ni or Cu) oxides. We will discuss how studies of the first ionization states found that doped holes were more likely to occupy the ligand (oxygen) states. From this introduction we will then look at higher valence oxides where holes can be *self-doped* into the ligand band. We will show how this affects the usual crystal field and Hund's rule based starting points of a typical theoretical model. In Section 3, we will then progress to the very basic classification scheme referred to as the ZSA scheme, which did not focus on the case of very high oxidation states for which the so called charge-transfer gap could be negative. We will discuss the various classes possible in an extended ZSA scheme, showing the transition from Mott-Hubbard to charge-transfer to mixed-valence and then to the strong negative charge-transfer gap systems. In each case we look at the ground state and the electron removal and addition states (i.e., the one-electron Green functions). In Section 4, we will look at examples of very interesting negative charge transfer compounds, including the perovskite nickelates and also the related non-correlated bismuthates. Here we will also show how a significant amount of information concerning the ground state local electronic structure can be obtained from resonant x-ray absorption and scattering experiments, and will introduce the model Hamiltonians which can be used in this regard. Lastly, in Section 5 we will look at materials in the fascinating mixed-valence class, focusing primarily on the highly studied samarium hexaboride.

2 The importance of anion states

In this section, we will provide some generally accepted examples which exemplify the importance of anion states in high-valence oxides. First we will give a brief review of the studies of hole-doped states in divalent copper and nickel oxides which led to the concept of Zhang-Rice singlets in the high-T_c cuprates. Following that we will show that similar effects can be

present in undoped compounds with high formal oxidation states, such as Ni^{3+} in the perovskite rare-earth nickelates.

2.1 Hole doped states in divalent Cu and Ni oxides

The common feature among all high-T_c cuprate compounds are the CuO_2 planes (containing Cu^{2+} in the parent compounds) which are doped with holes or electrons to induce superconductivity. Of critical importance then, when trying to understand the nature of high-T_c, is to understand the nature of the doped carriers. Early spectroscopic studies, particularly x-ray absorption spectroscopy (XAS) at the oxygen K edge, found strong evidence that the holes doped into CuO_2 planes primarily resided in the oxygen $2p$ band [1–3]. This showed that the doping did not yield Cu^{3+} in the lattice, and accordingly that the Cu was still 2+ with $S = 1/2$.

Theoretical studies were undertaken to understand the character of the doped holes. In particular, an Anderson impurity model was employed by Eskes *et al.* to examine the one-electron removal spectrum of a Cu^{2+} impurity which hybridized with an oxygen $2p$ band, as this spectrum relates directly to the states achievable through hole doping [4]. It was found that since the Cu d^8 states were below the top of the O $2p$ band (i.e., the parent compound is a charge-transfer insulator) the first ionization state is a singlet $^1A_{1g}$ state which is pushed out of the O $2p$ continuum. Around the same time, the similar Zhang-Rice (ZR) singlet picture was developed [5], which is also based on the fact that the doped holes occupy linear combinations of oxygen $2p$ orbitals in a square coordinated around the Cu site.

These early studies of the cuprate superconductors showed the importance of the anion states, especially upon doping. However, even with this importance established, there are very different ways in which the anion states can be treated. On one hand, the ZR singlet picture was rather quickly adopted by many working on the theory of high-T_c cuprates, in part because it simplifies the problem to that of an effective single-band Hubbard model where the charge-transfer energy plays the role of U. Due to the extended nature of the "atomic" wave function, which includes the linear combination of O $2p$ orbitals of $x^2 - y^2$ symmetry, longer-range hoppings beyond nearest neighbors have to be included. A large number of theoretical studies have been carried out and still use this single-band approach. On the other hand, also at the very beginning of the field in 1988, Emery and Reiter [6] introduced a somewhat different model also based on doped holes being mainly on O but placing the importance of the holes on the very large antiferromagnetic exchange interaction of the O $2p$ hole with its *two* neighboring Cu spins. This leads to the description of the quasiparticle as being a three-spin polaron. Recently, this model has gained considerable support from a very large scale exact diagonalization study by Lau *et al.*, who found that the ground state and k dependence of the single hole in the full 3-band model is in close agreement with the 3-spin polaron model in which a strong Cu-Cu ferromagnetic correlation is found for the Cu atoms sandwiching the O $2p$ hole [7–9]. Another interesting part of this calculation is also that, without introducing longer-range hoppings, it yields basically the same dispersion relation for the quasiparticle as the extended single-band Hubbard model, although the spectral weights differ considerably. The ferromagnetic correlation of the neigh-

boring Cu spins to the O hole is something that seems difficult to reconcile within a single band Hubbard model based on ZR singlets. It is also interesting to note that in recent work it has been shown that different models giving basically the same single particle dispersion can yield very different two particle spectral functions as are relevant for superconductivity [10]. Thus, debate remains regarding the importance of the explicit inclusion of the anion states in models describing the cuprates.

In addition to the identification of doped holes in cuprates occupying O $2p$ orbitals, similar studies showed that when NiO is hole-doped with Li, the holes also occupy the oxygen $2p$ orbitals [11]. For Li-doped CoO, the holes have a strongly mixed Co $3d$ and O $2p$ character [12]. Given that all of these parent compounds are divalent, one should expect the anion states to become even more important in higher valence oxides, where charge-transfer energies are generally smaller due to increased electron affinities of the metal ions.

2.2 Similar effects in undoped negative charge transfer compounds

The previous section detailed the importance of oxygen $2p$ holes in hole-doped divalent late $3d$ transition-metal oxides. In this section we will introduce how such oxygen holes may be present in *undoped* high-valence oxides due to the presence of a so-called negative charge transfer energy. To accomplish this, we first provide a brief example in Figure 1(a) of how crystal field and Hund's rule energetics determine the ground state configuration of a correlated transition-metal ion in a compound. For this example of a Ni^{3+} ion, first one accounts for multiplet interactions. According to Hund's first rule, we assume our lowest energy configuration is the one with maximum spin. The next highest state we consider has one spin flipped, which in this case costs energy $2J$, where $J = \frac{1}{14}(F^2 + F^4)$, and F^2 and F^4 are the multipole Coulomb (Slater) integrals [13,14]. Next, we account for an octahedral crystal field potential, which splits the $3d$ orbitals into an e_g group and a t_{2g} group. Evident from this picture is that depending on the relative sizes of J and $10Dq$ (where $10Dq$ is a measure of the point charge crystal field [15]), one can have either a high-spin or low-spin ground state.

In Fig. 1(b), we now extend our example to a configuration interaction (CI) model. Now we explicitly account for hybridization with nearest neighbors. Assuming the neighbors are fully occupied ligands, with CI one constructs a wavefunction out of a linear combination of configurations of the form $d^{n+i}\underline{L}^i$, where $i = \{0, 1, 2, ...\}$ and $\underline{L}$ is a hole in the ligand shell left behind when an electron hops to the $3d$ shell. Note that the ligand hole orbital must have the same symmetry as the central d ion. The energy cost of a ligand electron transferring to the d shell is the charge-transfer energy Δ, and one must also account for additional Coulomb energies when extra electrons hop to the d shell. If we set the energy of the $d^n\underline{L}^0$ (i.e. $i = 0$) configuration to 0, then the energies of the $i = 1, 2, 3, ...$ configurations are given by Δ, $2\Delta + U$, $3\Delta + 3U$, and so on.

Returning to Fig. 1(b), here we analyze possible positive and negative charge-transfer cases for formally trivalent Ni^{3+} oxides using a simplified configuration interaction model. Starting with $3d^7$ and $3d^8\underline{L}$ configurations (where $\underline{L}$ denotes a ligand hole), we show the configuration

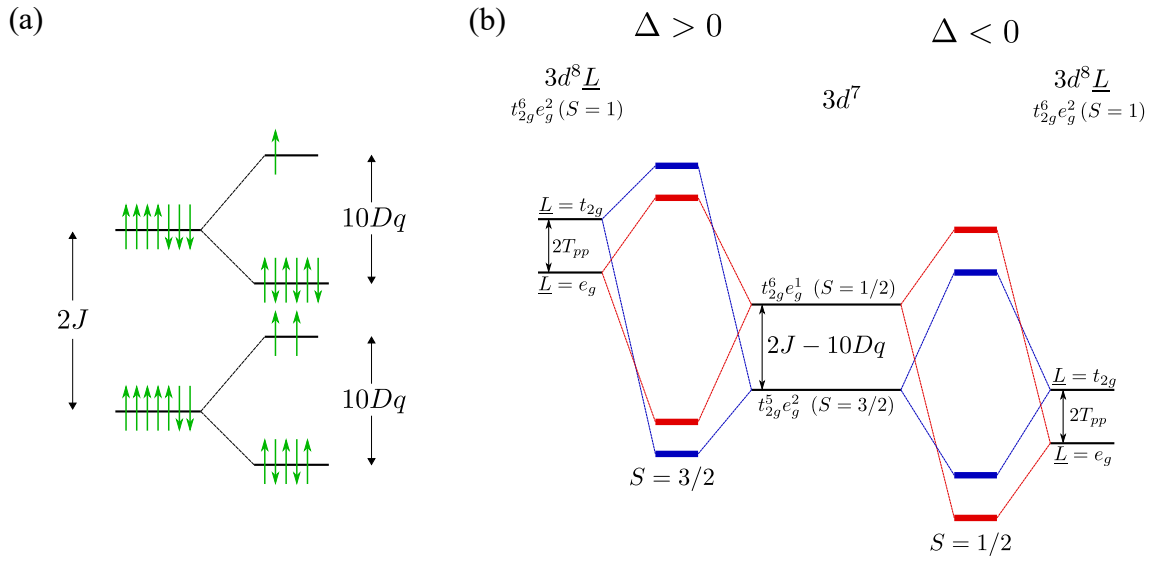

Fig. 1: *(a) The Hund's rule and crystal field energetics are introduced for a Ni^{3+} (d^7) system. (b) A configuration interaction model demonstration why low-spin Ni^{3+} compounds must be negative charge transfer systems. For $\Delta > 0$ (left), typical hopping integrals are not strong enough to push the low-spin bonding state below the high-spin bonding state. For $\Delta < 0$ (right), however, the low-spin state is easily stabilized as the ground state.*

interaction bonding and antibonding states for positive (left) and negative (right) charge transfer situations. The $3d^7$ configuration has two states in this simplified picture which are the high-spin ($S = 3/2$, $t_{2g}^5 e_g^2$) and low-spin ($S = 1/2$, $t_{2g}^6 e_g^1$) states. The energy separation between the states before hybridization is considered is given by $2J - 10Dq$ where J is approximately 1.25 eV (according to atomic Hartree-Fock calculations [14], rescaled by 80% to account for intra-atomic configuration interaction as usual) and the point-charge crystal-field contribution $10Dq$ is roughly 0.75 eV (slightly larger than the ~0.5 eV usually used for divalent compounds, to account for the shorter bond lengths in formally trivalent compounds). Each of these states hybridizes with the $3d^8\underline{L}$ configuration, where the d electrons have a high-spin ($S = 1$, $t_{2g}^6 e_g^2$) arrangement. The ligand hole consists of a linear combination of O $2p$ orbitals of π or σ bonding symmetry with the transition-metal $3d$ orbitals. Thus, the hole can be of e_g or t_{2g} symmetry, yielding two states separated by $2T_{pp} = (pp\sigma - pp\pi) \approx 1.5$ eV [16].

When hybridization is gradually introduced for this positive charge transfer case, a bonding $S = 3/2$ ground state is attained, illustrated by the lower blue line in the figure. Given that the e_g hopping integral is generally about twice as large as the t_{2g} for octahedrally coordinated transition-metal compounds, one would expect that for increased hybridization strength the low-spin (red, $S = 1/2$) bonding state would eventually become the ground state. However, such a situation would require significantly larger hopping integrals than are present in the $3d$ oxides.

If instead we consider the negative charge transfer arrangement of our configurations as shown on the right of Fig. 1(a), a low-spin state arises much more naturally. Now the $d^8\underline{L}$ states are below the d^7, and when hybridization is introduced the bonding state having the symmetry of

the $t_{2g}^6 e_g^1$ configuration and thus with ($S = 1/2$)—but with mainly $d^8\underline{L}$ character—is stabilized as the ground state. Thus by having a negative charge-transfer energy and accordingly a strong ligand-hole contribution to the ground state, a low-spin Ni compound is realized with typical hopping integrals. One can consider this as a competition between the Hund's rule J, which wants to maximize the spin, and the O $2p$ – TM $3d$ exchange interaction which is antiferromagnetic. If the hole is mainly on the oxygen rather than in a t_{2g} orbital of the (d^7) Ni, then it would rather be in an e_g symmetry state and would have a strong antiferromagnetic coupling with the d^8 spin-1 state, leading to a $S = 1/2$ state. Note that with a negative charge transfer energy, the stronger e_g hybridization leads to a unique inverted contribution to ligand-field splitting from covalence [17].

In Fig. 2(a), we test this simplified picture using a full configuration interaction calculation for a NiO_6 cluster having Coulomb interactions, crystal-field, spin-orbit, and ligand-ligand hopping energies characteristic of the perovskite rare-earth nickelates, RNiO$_3$. The black solid line shows the low-spin/high-spin transition as a function of the effective charge-transfer energy Δ_{eff} and the hybridization strength V_{e_g} (with $V_{t_{2g}}$ fixed at $0.58\,V_{e_g}$). Here, Δ_{eff} accounts for the various energy shifts of the multiplet Coulomb interactions, ionic crystal-field contribution, spin-orbit interaction, and T_{pp}, such that with no hybridization the lowest-energy $d^8\underline{L}$ state crosses below the lowest-energy d^7 state when Δ_{eff} becomes negative. The color of the plot indicates the contributions of the d^7 and $d^8\underline{L}$ configurations to the ground state (note the basis also contains $d^9\underline{L}^2$ and $d^{10}\underline{L}^3$ configurations, so we plot the *relative* weights of the d^7 and $d^8\underline{L}$ for clarity).

A key observation from Figure 2(a) is that the low-spin regime is always characterized by a dominant $d^8\underline{L}$ contribution to the ground state. This includes a sharp jump in $d^8\underline{L}$ weight at the spin-state transition, originating from the fact that the hybridization is stronger for the low-spin states which have more e_g holes. The phase diagram confirms the discussion of Figure 1(b)—that a low-spin state can be achieved with realistic hybridization parameters if the ground state is mainly $d^8\underline{L}$—and actually shows that even for very large hopping integrals the low-spin state is still mainly $d^8\underline{L}$. Note that the ground state can have more $d^8\underline{L}$ than d^7 character even for $\Delta_{\text{eff}} > 0$ as the $d^9\underline{L}^2$ and $d^{10}\underline{L}^3$ configurations push the $d^8\underline{L}$ lower in energy than the bare charge-transfer value Δ_{eff}. We also indicate with the star in Fig. 2(a) the location of the rare-earth nickelates in this phase diagram. For these parameters [18], the nickelates are indeed best described as negative charge transfer compounds. We will discuss the nickelates further in Section 4.

For clarity, in Fig. 2(b) we demonstrate the relationship between the typically used Δ, and Δ_{eff} which is more relevant for small and negative charge transfer energy systems. Within our configuration interaction scheme, Δ defines the central energies of the various configurations. As displayed in the figure and explained in the caption, configurations with n ligand holes have energy $n\Delta$, with an additional energy-offset due to the Coulomb repulsion U. However, within each configuration are multiplet, crystal-field, spin-orbit, and ligand-ligand hopping (T_{pp}) energies, which mean that the lowest state within each configuration will be shifted from the central energy by different amounts. One should then define the energy Δ_{eff}, which is the energy be-

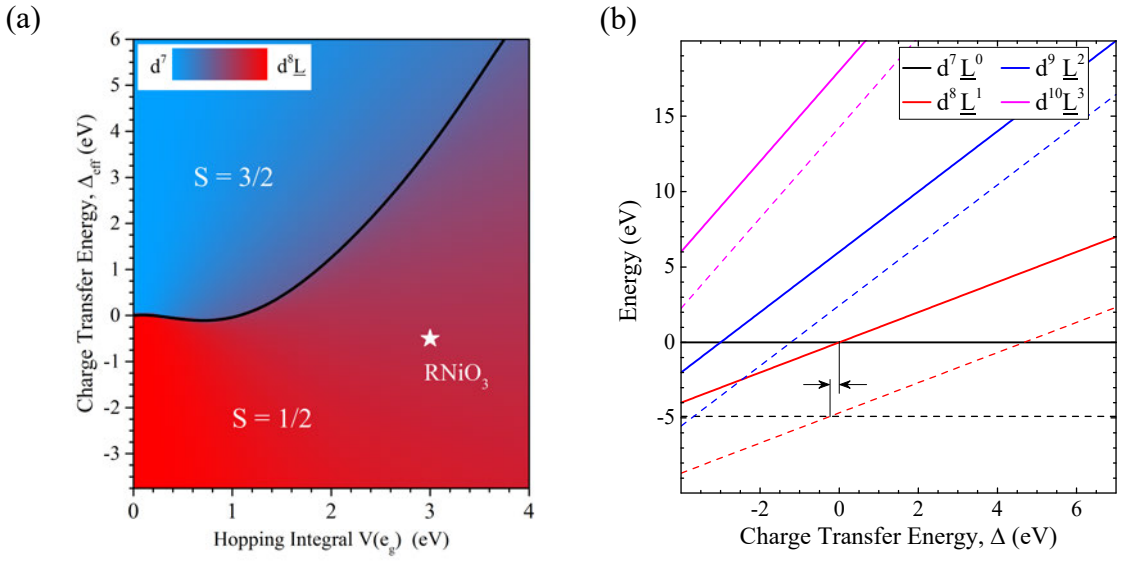

Fig. 2: *Results of a full configuration interaction calculation. (a) The low-spin phase space is always characterized by a dominant $d^8\underline{L}$ component in the ground state wavefunction. (b) Solid lines show the shell average energies, given by 0, Δ, $2\Delta + U$, and $3\Delta + 3U$ for the d^7 to $d^{10}\underline{L}^3$ configurations, respectively. The dashed lines are the lowest multiplet for each configuration, which account for higher multipole Coulomb interactions, crystal fields, spin-orbit interactions, and T_{pp}. The arrows show the difference between the configuration averaged Δ (used for the x axis), and the effective charge-transfer energy Δ_{eff}, which becomes negative when the lowest energy $d^8\underline{L}$ multiplet is lower than the lowest d^7 multiplet.*

tween the lowest energy d^7 state and the lowest energy $d^8\underline{L}$ state. For the case of Fig. 2(b), the difference between Δ and Δ_{eff} is relatively small, but for other elements and d shell fillings, the difference can be significantly larger.

3 Classification of correlated compounds

3.1 Mott-Hubbard and charge-transfer insulators

It has been known for many years that often correlated transition-metal compounds such as NiO or CoO have substantial electronic band gaps of a few eV, whereas band theory predicts much smaller gaps or no gaps at all [19]. The explanation for this discrepancy came from the ideas of Mott and Peierls [20, 21], and relies on the fact that the $3d$ electrons forming states near the Fermi level are relatively localized, and therefore have large Coulomb repulsion energies, denoted by U. This U then suppresses charge fluctuations of the form $d^n d^n \rightarrow d^{n-1} d^{n+1}$ which would describe the conduction in such a material. Formalizing these ideas into a suitable model led to the development of the Hubbard model [22, 23] and such materials are accordingly often termed Mott-Hubbard insulators. A simplified illustration of the effect of the Coulomb repulsion U on an otherwise metallic $3d$ density of states is shown in Fig. 3(a), where a broad metallic band splits into a full lower band and empty upper band with an insulating gap determined by

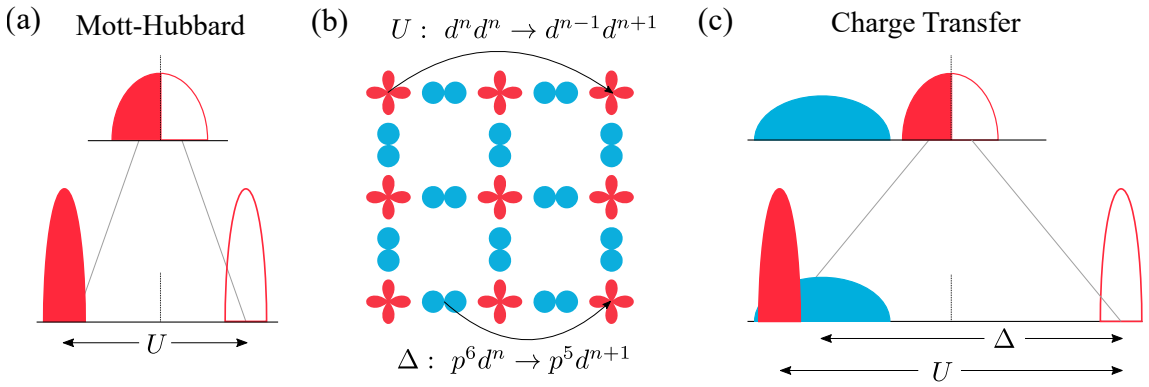

Fig. 3: *Distinction between Mott-Hubbard and charge-transfer insulators introduced by the ZSA work. (a) A broad, metallic band is split into full and empty electron removal and addition bands by Coulomb repulsion, and leads to an insulating gap of size U. (b) The low-energy charge fluctuations of energies U and Δ are illustrated. The red orbitals correspond to correlated transition-metal sites while the blue are those of the ligands. (c) The concept of a charge-transfer insulator, where the gap now involves the ligand states and is determined by Δ, which can be much smaller than U.*

the size of U. Figure 3(b) demonstrates the type of charge fluctuation in a correlated compound which costs energy U.

While this Mott-Hubbard understanding of correlated insulators was enormously successful, some new issues arose when applying it to various materials. It was found, for example, that the size of U in materials like NiO (~7 eV) is actually quite a bit larger than the electronic band gap (~4 eV), and thus it was evident that something else must be at play to determine the gap. Additionally, among series of such materials, the size of the gap often correlates more directly to the anion electronegativity than to the cation U. In fact, many sulfides which should have comparable U values to oxides are actually conductors. Further, new experiments and configuration interaction based interpretations in the mid 1980s found that the first ionization state of NiO had largely oxygen $2p$ character, and not the expected lower Hubbard band ($d^8 \rightarrow d^7$) character [24, 25].

As a solution to these discrepancies, the Zaanen-Sawatzky-Allen (ZSA) theory of correlated compounds was developed [26]. By using an Anderson impurity model applicable to such insulating compounds, the ZSA study found that in many compounds U is not the important energy scale for the band gap, but rather the charge-transfer energy Δ. The charge-transfer energy is defined as the energy cost of removing a ligand (i.e. oxygen, sulfur, etc.) $2p$ electron and placing it in a transition-metal $3d$ orbital. A schematic density of states (in the limit of no metal-ligand hybridization) is shown for a charge-transfer compound in Fig. 3(c). Again the upper part of the Figure shows the DOS without Coulomb interactions considered, this time now with the $3d$ band in red and a fully occupied ligand $2p$ band in blue. In the lower part, the Coulomb repulsion is included, leading to the formation of upper and lower Hubbard bands. Now one can see that if Δ is smaller than U, the lower-energy charge fluctuations which determine the energy gap of the compound will be of the form $p^6 d^n \rightarrow p^5 d^{n+1}$, where p refers

to the ligand $2p$ orbitals as shown in Fig. 3(b). The ZSA scheme led to a very comprehensive understanding of the conductivity behavior of many classes of transition-metal compounds [26]. In particular it is the early transition-metal oxides, such as V_2O_3, Ti_2O_3, Cr_2O_3, etc., which can be described as Mott-Hubbard insulators, while the later $3d$ oxides like CoO, NiO, and CuO are charge-transfer insulators.

3.2 Mixed valence and negative charge transfer insulators

While the original ZSA theory provided a sound qualitative understanding of many transition-metal compounds, it did not focus much on compounds with high oxidation state cations. Generally, for increased cation oxidation states while keeping the anions fixed, one expects a decrease in the charge-transfer energy as the electron affinities of the higher valence states are larger. In Fig. 4, we show schematic electron addition and removal spectra, in the limit of vanishing metal-ligand hybridization, as the charge-transfer energy is gradually reduced from the Mott-Hubbard regime to the charge-transfer regime and further. We have a broad band (shown in blue) due to the light electrons (ligand $2p$) and narrow Hubbard bands (red) for the correlated electrons (metal $3d$). The Hubbard bands are again separated by the Coulomb repulsion energy U, and the energy separation between the center of the upper Hubbard band and the center of the light-electron band is again defined as the charge-transfer energy, Δ. This definition of Δ is the most common [26], but we also define an effective charge-transfer energy Δ_{eff} between the top of the broad band and the bottom of the upper Hubbard band. This effective charge-transfer energy is more relevant when describing high oxidation state compounds. When higher multipole Coulomb interactions (multiplets) are included, Δ_{eff} would also account for these, and would be the energy difference between the lowest (i.e. Hund's rule) d^n state and the lowest $d^{n+1}\underline{L}$ state. In our simple schematic, which neglects multiplet effects, we can relate Δ and Δ_{eff} as

$$\Delta_{\text{eff}} = \Delta - \frac{w_d + w_p}{2} \tag{1}$$

where w_d and w_p are the widths of the metal and ligand ($3d$ and $2p$) bands. If multiplets are included, one should use the strict definition of Δ_{eff} as the energy difference between the lowest d^n and $d^{n+1}\underline{L}$ multiplets.

As the charge-transfer energy is reduced moving downward in Fig. 4, four distinct regimes are encountered. The first two are the Mott-Hubbard and charge-transfer regimes, as discussed above in relation to the ZSA work. However, if one continues to reduce the charge-transfer energy, the mixed-valence phase is reached. Here the d^{n+1} original upper Hubbard band has now crossed into the top of the valence band. As indicated, the ground state becomes more difficult to represent, with some atoms in a d^n and some in a d^{n+1} configuration, leading to lower and upper Hubbard bands of d^{n-1} and d^{n+2}, respectively, which are separated by a total energy of $2U$. The now very complicated ground state wavefunction depends on details of longer-range interatomic interactions, which may lead to a kind of ordering of the transition-metal valence states. An example is the case of magnetite (Fe_3O_4), where in the spinel structure the tetrahedral

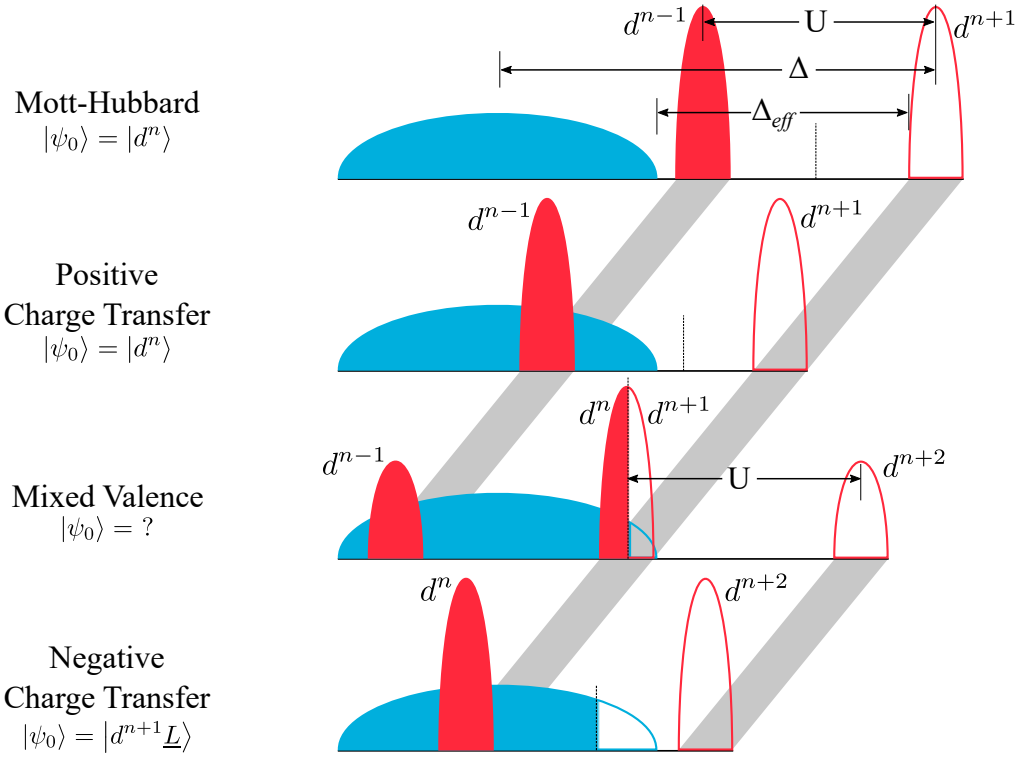

Fig. 4: *The energetics of correlated compounds depicted with schematic electron removal and addition spectra. A broad band, nominally full, is shown in blue and narrow, correlated (d) bands are shown in red. A very small hybridization is assumed between the broad and narrow bands. A constant Coulomb repulsion U separates lower and upper Hubbard bands throughout the figure, whereas the charge-transfer energy Δ is varied. The Fermi level is shown with a dashed vertical line and electron removal spectra are shaded in, while electron addition spectra are only outlined. Moving from the top to bottom, the energy of the correlated bands is shifted lower, leading to a reduction of the charge-transfer energy and the four distinct regimes. The nature of the ground state wavefunction $|\psi_0\rangle$ is given for each case.*

sites contain Fe^{3+} but the octahedral sites are mixed valent (though not due to a negative charge-transfer gap), and below the so-called Verwey transition some kind of charge ordering occurs which is not yet clearly resolved [27, 28]. Such charge density wave like situations can indeed involve multiple $\boldsymbol{q}$ vectors and form complicated structures. Additional examples are doped $LaMnO_3$ and other doped transition-metal compounds. In Section 5 we will consider a case of very small hybridization in SmB_6 where a unique, new form of ordering of the valence in momentum space rather than real space is suggested.

Moving beyond the mixed valence regime in Fig. 4, by decreasing the charge-transfer energy further we enter the negative charge transfer phase. Here the ground state is described as $|d^{n+1}\underline{L}\rangle$ meaning that the upper and lower Hubbard bands are now d^{n+2} and d^n states, respectively, where again n is the filling which corresponds to the formal valence. The ligand band has now been accordingly *self-doped* [29, 30] with holes. In other words, this regime corresponds to the case where a transition-metal cation does not adopt its formal oxidation state, instead keeping one extra electron which leaves the anion with one fewer. Generally electron affinities

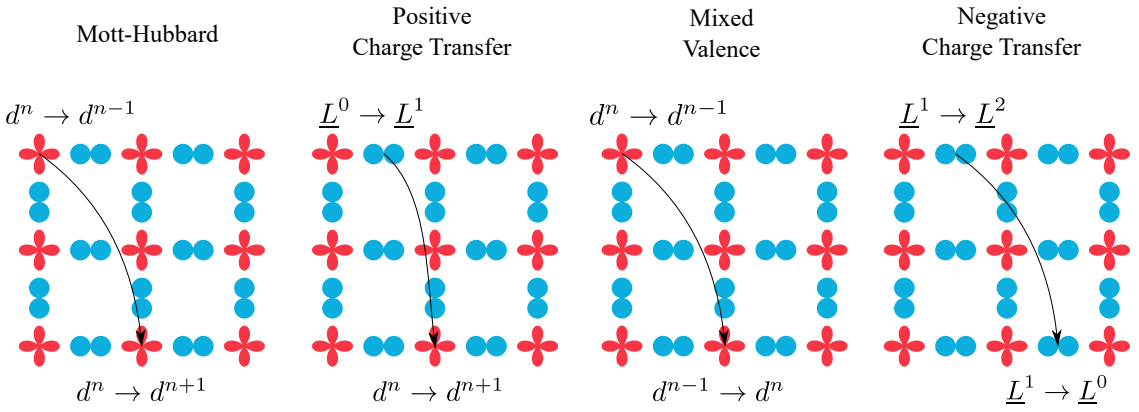

Fig. 5: *Lowest energy charge fluctuations in the different classes of correlated compounds.*

increase moving toward the end of the $3d$ series and, as mentioned above, with increasing cation valence. Thus it is expected that formally trivalent Ni^{3+} and Cu^{3+} oxides, as well as formally tetravalent oxides of Co^{4+} and Fe^{4+}, will be in the negative charge-transfer regime, or at least mixed valent. One can also move toward the negative charge-transfer regime via ligands with weaker electronegativities. Thus going from oxides to sulfides or selenides (or from fluorides down to iodides) will generally move one closer to, or into, the negative charge-transfer regime. In Fig. 5, we extend the schematic charge fluctuations of Fig. 3(b) to now include the mixed valent and negative charge-transfer classes. As before, the Mott-Hubbard and positive charge-transfer classes are characterized by lowest energy charge fluctuations determined by U and Δ, respectively. Mixed valent compounds are typically metals or have very small gaps, with charge fluctuations that can involve both the cation and anion states. In the limit of very small hybridization, however, very interesting charge fluctuation behavior can occur, as we will discuss in the context of SmB_6 in Section 5. Negative charge-transfer compounds have a metallic ligand $2p$ DOS before the inclusion of hybridization, and so may be (bad) metals, or may have many different behaviors, including metal-insulator transitions as in the rare-earth nickelates.

4 Negative charge transfer compounds

As alluded to in the previous section, in general the conditions favorable for negative charge-transfer energies are large electron affinities on the cations, achievable through high formal valences and cations near the end of the $3d$ series, and low ligand electronegativities, achievable by going from halides to chalcogenides to pnictides, or moving down the respective columns of anions in the periodic table. In this section, we will look at some example materials in detail.

4.1 Perovskite rare-earth nickelates

The perovskite rare-earth (R) nickelate compounds, $RNiO_3$, exhibit many fascinating properties including a metal-insulator transition, with temperatures tunable via the size of the rare-earth

ion [31]. In the insulating phase, the nickelates undergo a structural distortion where alternating NiO_6 octahedra expand and compress in a rocksalt pattern breathing distortion. Additionally, within this insulating phase the nickelates also order antiferromagnetically with an unusual $\boldsymbol{q} = (1/4, 1/4, 1/4)$ propagation vector. First synthesized in the 1970s [32], the nickelates rose in popularity through the early 1990s [33–35], and are extremely popular today as they are a prime example of how emergent properties can be tuned through heterostructured growth [36–40].

The nickelates have a formal Ni^{3+} oxidation state, suggesting a $3d^7$ occupation of the nickel. Various studies have indicated that the nickelates possess a low-spin state, so early interpretations were that the ground state had a $t_{2g}^6 e_g^1$ occupation, with $S = 1/2$. However, such a state should have a strong Jahn-Teller effect similar in strength to that observed in Mn^{3+} perovskite oxides like $LaMnO_3$, but one is not observed experimentally. Additionally, one has the arguments laid out in Section 2, which showed that low-spin Ni^{3+} oxides should be very rare if not impossible. With these key observations established, it has become clear in recent years that the nickelates are actually negative charge-transfer compounds with a ground state better described as $3d^8\underline{L}$ (though with a certain d^7 contribution to the wavefunction due to strong hybridization) and with a $S = 1/2$ spin that emerges from antiferromagnetic coupling between a $t_{2g}^6 e_g^2$ ($S = 1$) configuration and a self-doped ($S = 1/2$) ligand hole.

When viewed as negative charge transfer materials, the metal-insulator transition and unique magnetic ordering of the nickelates can be understood on a theoretical basis. As shown by Mizokawa *et al.* [41], and later by others [42,43], when the negative charge-transfer $d^8\underline{L}$ ($S = 1/2$) ground state undergoes the breathing distortion, a traditional $3d$-based charge disproportionation does not occur. Instead, a *bond* disproportionation occurs, and the distinct expanded and compressed NiO_6 octahedra take on respective configurations tending toward $d^8\underline{L}^0$ ($S = 1$) and $d^8\underline{L}^2$ ($S = 0$). The situation then appears to instead resemble Peierls type of physics, involving strong electron-phonon interactions.

Recently we have adapted these negative charge-transfer theories to models which can be applied to the analysis of resonant x-ray spectroscopy experiments. Conventional approaches to the analysis of various core-level absorption, photoemission, and scattering data include multiplet ligand-field theory and the multiplet Anderson impurity model. In the former, a MO_6 cluster is analyzed using configuration interaction theory, including all Coulomb interactions of the $3d$ and relevant core shells, and hybridization with the nearest neighbor ligands is included. In the impurity approximation, hybridization with a bath of ligands is included, instead of just the nearest neighbors, to account for the ligand bandwidth. These two techniques have had great success in the analysis of core level spectra for the $3d$ oxides (see, e.g. [44–46]). However, these approaches were never successful in modelling the various spectra measured on rare-earth nickelates.

Key x-ray spectroscopy experiments on the nickelates include x-ray absorption spectroscopy (XAS), resonant magnetic diffraction (RMD), and resonant inelastic x-ray scattering (RIXS). First, the oxygen K-edge XAS spectra show a strong pre-edge feature [47], indicative of a large hole character in the oxygen $2p$ orbitals, which can be viewed as evidence for negative charge-transfer energetics. The XAS spectra at the Ni $L_{2,3}$ edge are characterized by a strong, sharp first

peak, followed by a broader continuum-like feature [48, 49]. Earlier studies using a multiplet ligand-field theory (MLFT) approach to interpret these XAS lineshapes showed some success with interpreting the primary features as different multiplet peaks arising from a highly mixed final state spectrum [50]. However, such an interpretation has now been found to be inconsistent with the lineshapes of RMD spectra, where the magnetic response is heavily concentrated at the energy of the first sharp XAS peak. In fact, most models to date could obtain a certain degree of agreement with the lineshapes of either XAS or RMD, but not both.
The conventional ligand-field theory (or cluster model) used for $L_{2,3}$ edge spectroscopy, and employed for most previous studies on the nickelates, has the Hamiltonian:

$$H_{LF} = H_U^{dd} + H_U^{pd} + H_{\boldsymbol{l\cdot s}}^{d} + H_{\boldsymbol{l\cdot s}}^{p} + H_o^p + H_o^d + H_o^L + H_{hyb}^{dL}, \tag{2}$$

with,

H_U^{dd}	the Coulomb repulsion between two $3d$ electrons including all multiplet effects,
H_U^{pd}	the Coulomb repulsion between a $2p$ core and $3d$ valence electron including all multiplet effects,
$H_{\boldsymbol{l\cdot s}}^{d}$	the $3d$ spin-orbit interaction,
$H_{\boldsymbol{l\cdot s}}^{p}$	the $2p$ core level spin-orbit interaction,
H_o^p	the onsite energy of the $2p$ core orbitals,
H_o^d	the orbital dependent onsite energy of the $3d$ valence orbitals,
H_o^L	the orbital dependent onsite energy of the Ligand orbitals, and
H_{hyb}^{dL}	the hybridization strength between the $3d$ and Ligand orbitals.

The onsite energies account for the specific charge-transfer energetics of the system. Detailed expressions for each term can be found elsewhere [18]. This model can be adapted to the breathing-distorted nickelates by moving to a double cluster model, where two Ni-O octahedra represent the expanded and compressed octahedral sites of the nickelate lattice. One then has the Hamiltonian

$$H = H_{LF_A} + H_{LF_B} + H_{mix} \tag{3}$$

where H_{LF_A} and H_{LF_B} are complete ligand field theory Hamiltonians of the compressed and expanded sites, and H_{mix} adds hybridization between them. Realizing that the rocksalt distortion means the two octahedra types are arranged in an O_h symmetric manner, H_{mix} consists of hybridization operators having e_g and t_{2g} symmetry [18].
With this model for the local electronic structure, a two site arrangement is created which does not break the O_h point group symmetry, and both the negative charge transfer self doping and the bond disproportionation physics can be captured. Importantly, with such a model all of the $3d$ orbitals are in the basis (as opposed to the earlier restricted orbital studies [41–43]) and the core orbitals are also in the basis, so accurate spectroscopy simulations can be performed. The effects of negative charge transfer and bond disproportionation can then be compared against experiment.

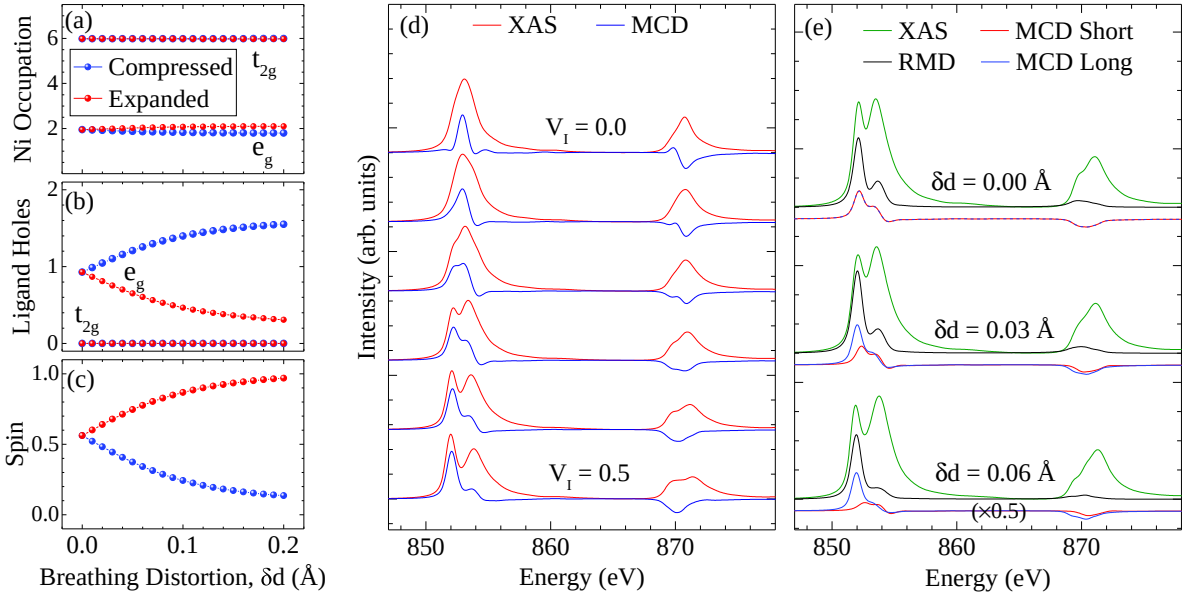

Fig. 6: *Ground state characteristics and spectral responses of perovskite nickelates from a double cluster model. (a-c) The Ni (a) and ligand (b) occupations show that the breathing distortion involves primarily the oxygen $2p$ holes rather than the Ni $3d$ electrons. (c) The spins on the long and short bond Ni tend toward $S = 1$ and $S = 0$, respectively. (d) The single cluster limit ($V_I = 0$) cannot reproduce the two-peaked structure at each edge with MCD focused on the first peak, but with $V_I > 0.3$ these features are captured by the double cluster. (e) A breathing distortion splits the XAS peaks further, and the magnetic diffraction signal is focused at the energy of the first XAS peak, both in agreement with experiment.*

In Fig. 6(a-c), we detail the ground state properties of the double cluster model, as a function of the size of the breathing distortion. The results confirm those of the previous restricted orbital studies—under the breathing distortion, very little charge disproportionation occurs via the $3d$ electrons, whereas the ligand holes are rather active. With no breathing distortion each octahedron has a $3d^8\underline{L}$ configuration, but as shown in Fig. 6(b) in the presence of the breathing distortion the holes bond more strongly with the short bond Ni than the long bond. This leads to a reduction of the spin moment on the compressed octahedron, such that it tends toward $S = 0$ while the expanded octahedron tends toward $S = 1$ (Fig. 6(c)).

In Fig. 6(d), we show calculated Ni $L_{2,3}$ XAS spectra for different values of intercluster hopping V_I [18], starting from the conventional single cluster limit ($V_I = 0$). In the single cluster limit, the spectrum looks very different from experiment [48,49], as the characteristic two peak structure for the L_3 resonance near 853 eV is completely missing. However, for increasing V_I to 0.3 and higher, a pronounced first peak is pushed out of the resonance, and the spectra strongly resemble experiment. Thus it is evident for such a highly covalent, negative charge-transfer energy compound that intersite interactions not captured in single cluster models are very important in the spectral response. Additionally, one can see that the fundamental magnetic circular dichroism (MCD) response is strongly concentrated at the first sharp peak, which is a crucial requirement for agreement with magnetic scattering experiments.

In Fig. 6(e) we show the XAS, MCD, and resonant magnetic diffraction (RMD) responses for three different sizes of lattice breathing distortions, δd. First, we see that for increasing breathing distortion, the total XAS spectral shape (summed over the two sites) only changes a minor amount, with the two L_3 peaks moving apart with increased breathing distortion. This trend is in good agreement with the rare-earth series, where smaller rare earths lead to larger breathing distortion and slightly more separated XAS peaks [48, 49]. Next, we note that the MCD spectra of the two sites become inequivalent when the breathing distortion is introduced. In accordance with the different spin moments for the two Ni, the long bond MCD spectrum becomes stronger and the short bond becomes weaker. However, the strongest response is always at the energy of the first XAS peak. This leads to the distinct RMD spectral shapes as shown, which again are strongly peaked at the first XAS resonance. This characteristic agrees very well with all experiments on various nickelate bulk and heterostructure materials.

The double cluster model thus bridges the gap between the recent theories of bond disproportionation in the nickelates [41–43], and experimental observations made through spectroscopy. The key aspect of the model is the inclusion of the full $3d$ orbital degeneracy, as well as the $2p$ core shell, which allows the simulation of core level spectroscopy. The excellent agreement between the calculated and experimental XAS and RMD provides validation for both the negative charge-transfer energy and bond disproportionation theory of the nickelates.

4.2 Perovskite bismuthates

Up until this point, our focus has been on correlated transition-metal compounds. However, it has recently been shown that the non-correlated perovskite bismuthates $SrBiO_3$ and $BaBiO_3$ exhibit characteristics very similar to the negative charge transfer picture discussed above [51]. These compounds, when doped, are high-T_c superconductors and have accordingly attracted significant attention. Interestingly, at low temperatures they exhibit the same breathing type of lattice distortion that was introduced above for the nickelates. Every other octahedron expands or compresses in a rocksalt-pattern distortion. Earlier studies suggested that the breathing distortion was concomitant with a charge disproportionation, where the formally tetravalent Bi cations disproportionate into Bi^{3+} and Bi^{5+} for the expanded and compressed octahedra, respectively [52–56]. However, Foyevtsova *et al.* recently showed, using density-functional theory calculations, that the oxygen $2p$ states are very important for the bismuthates in a very similar manner to negative charge-transfer transition-metal compounds [51]. In particular, strong hybridization between O $2p$ and Bi $6s$ states pushes antibonding states of mainly O $2p$ character with A_{1g} symmetry above the Fermi level. Under the breathing distortion, pairs of these oxygen holes then condense into A_{1g} molecular orbitals around the short bond Bi sites, in a similar nature to the E_g symmetry oxygen hole action of the nickelates.

We first show this analogy between the bismuthates and nickelates schematically in Fig. 7. For the nickelates, the E_g symmetry $d^8 \rightarrow d^7$ electron removal states are below the top of the oxygen band, and mix strongly with the E_g symmetry oxygen states near the top of the oxygen band. This leads to the distinct, antibonding E_g symmetry oxygen hole states present in the

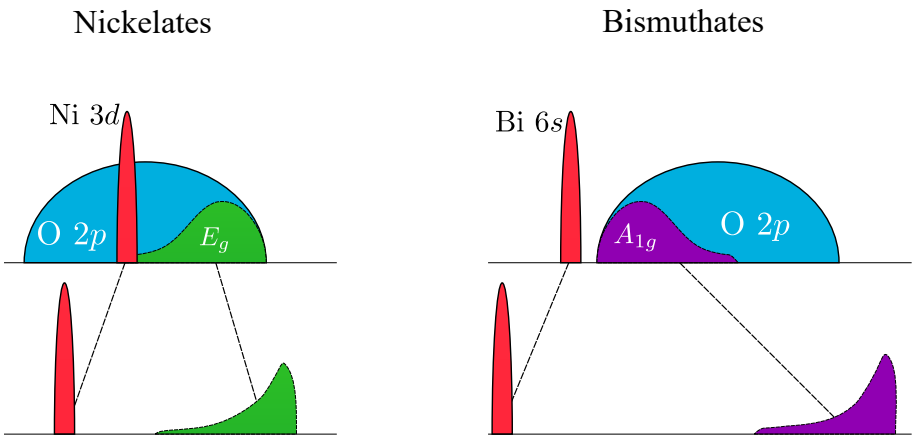

Fig. 7: *Schematic showing the similarities of the perovskite nickelate and bismuthate electronic structure. In the nickelates, the Ni* $3d$ *states which have* E_g *symmetry mix with the oxygen* $2p$ *states of the same symmetry, which are located near the top of the valence band. Consequently, the oxygen hole states pushed out of the top of the valence band have* E_g *symmetry. In the bismuthates, the situation is similar, but now the relevant cation states are the Bi* $6s$*, which are very deep. They mix strongly with the oxygen* $2p$ *states having* A_{1g} *symmetry which are located at the bottom of the oxygen DOS. The hybridization is very strong, leading to states of primarily oxygen* $2p$ *character and* A_{1g} *symmetry being pushed out of the top of the valence band. Note the cation bands are drawn with narrow widths before and after hybridization for simplicity.*

nickelates, which then form molecular orbitals around short-bond Ni sites in the presence of the breathing distortion. For bismuthates the situation is very similar to the nickelates, except now the Bi $6s$ states are the important cation states and therefore it is states of A_{1g} rather than E_g symmetry which are important. The very deep $6s$ states mix very strongly with the A_{1g} oxygen $2p$ states, which are actually near the bottom of the oxygen band. The hybridization is strong enough, however, to push antibonding states of primarily oxygen character above the Fermi level. Again, these oxygen hole states then disproportionate under the breathing distortion, leading to the formation of A_{1g} oxygen hole molecular orbitals around the short bond Bi sites. Thus, even though the magnetic and correlation physics of the nickelates and bismuthates are drastically different, strong similarities exist regarding the importance of the oxygen $2p$ states in the electronic structure.

In Fig. 8, we show the actual density-functional results of Foyevtsova *et al.* [51], where the upper and lower panels contain the projected densities of states for the compressed and expanded octahedra, respectively, in the low-temperature, breathing-distorted phase of $SrBiO_3$. Of particular significance is the strong, narrow conduction band of the compressed octahedron. Here the DOS projection shows that these states are of primarily O $2p$ character, having A_{1g} symmetry. These states are accordingly suppressed for the expanded octahedron, demonstrating the bond disproportionation that involves action of the oxygen $2p$ holes, rather than the typically assumed Bi charge disproportionation. It is important to note that this is a pure DFT calculation for a non-correlated material, and thus demonstrates clearly the extremely important role of the O $2p$ based molecular orbitals in forming the low-energy scale states, which in the end are also responsible for the superconductivity in the potassium doped materials.

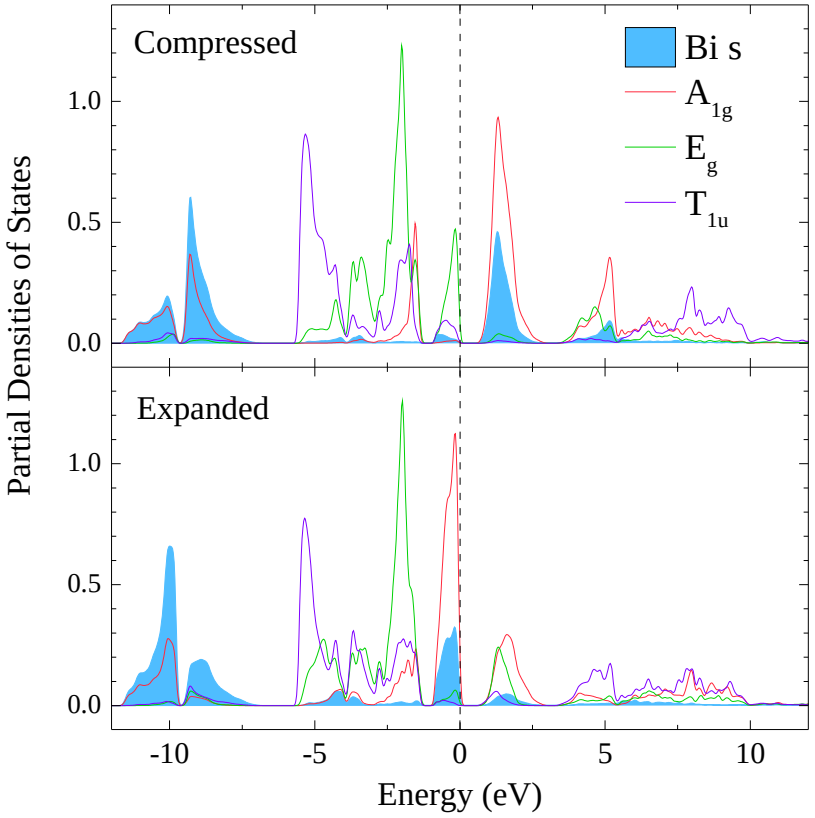

Fig. 8: *Projected densities of states for the compressed (upper) and expanded (lower) octahedra in the low temperature, breathing distorted phase of $SrBiO_3$.*

4.3 Other negative or small charge transfer compounds

The nickelates are arguably one of the most highly studied negative charge transfer compounds at present. However, there are many other compounds which are known to be or might be negative charge transfer systems that have been studied in recent years. In fact, one of the first studies to use the term "negative charge transfer energy" was carried out by Mizokawa *et al.*, and investigated the compound $NaCuO_2$ [57]. As this is a sort of reference compound for the high-T_c cuprates, several groups studied the electronic structure of this material around the same time [58, 59]. Indeed, through an analysis of x-ray photoelectron spectroscopy (XPS), Mizokawa *et al.* showed that the ground state does not contain Cu^{3+} ($3d^8$) as the formal valence counting would suggest, but rather it is better described as $3d^9\underline{L}$, where again oxygen holes are present due to a negative charge transfer energy.

Other negative charge transfer compounds include the disulfide pyrites FeS_2, CoS_2, and NiS_2. Here one expects that the S_2 would have a 4- valence and the cations accordingly 4+, but in fact it is found that the cations are divalent and there are accordingly missing sulfur $3p$ electrons. This leads to the formation of sulfur pairs with a net pair valence of 2- rather than 4-. In this case the antibonding S $3p$ states in the pairs are empty and therefore form rather narrow bands just above the chemical potential [60]. Accordingly, the pyrites exhibit very interesting and diverse properties: FeS_2 is a diamagnetic semiconductor, CoS_2 is a ferromagnetic metal, and

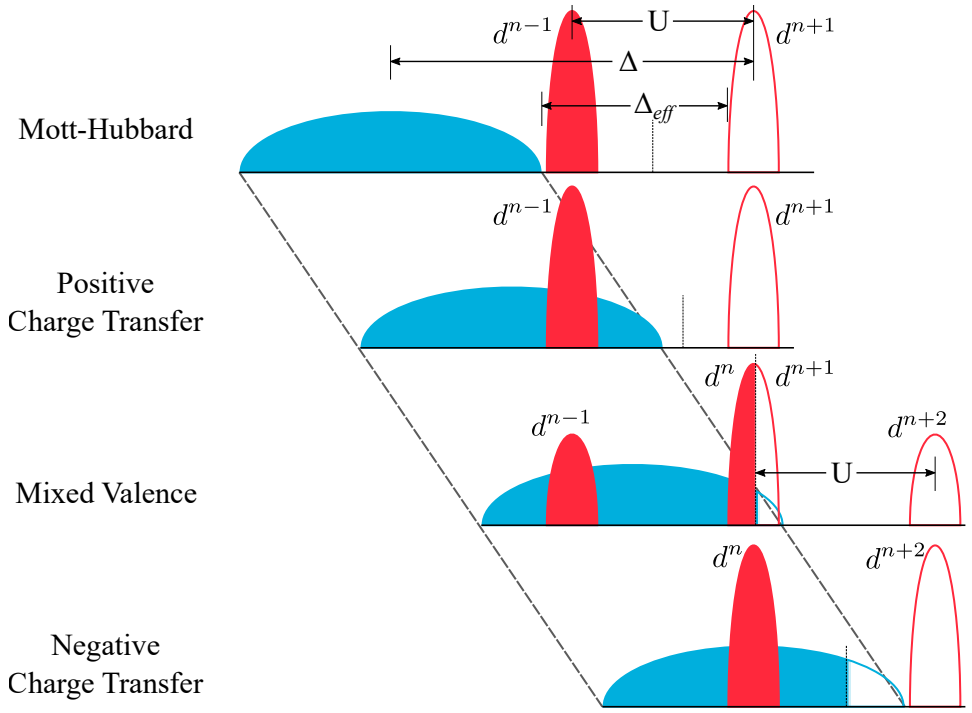

Fig. 9: *The energetics of correlated compounds depicted with schematic electron removal and addition spectra in a similar nature to Fig. 4. A broad band, nominally full, is shown in blue and narrow, correlated (d) bands are shown in red. A very small hybridization is assumed between the broad and narrow bands. A constant Coulomb repulsion U separates lower and upper Hubbard bands throughout the figure. From the top to bottom, the ligand electronegativity is decreased, which can lead to different classes of compounds for the same transition-metal cations, even having the same formal valence.*

NiS_2 is a Mott insulator which orders antiferromagnetically [61,62]. The electronic structures of these pyrites have been studied by various x-ray spectroscopies [60, 63–66]. Further interesting properties emerge when some or all of the sulfur is substituted by Se. In particular, $Ni(S_{1-x}Se_x)_2$ is highly studied, as it exhibits a metal-insulator transition for $x = 0.23$ at $T = 0$, which changes to $x = 0.4$ at room temperature [60, 67–69].

An additional highly studied negative charge transfer compound is NiS [70–72] and the related $NiS_{1-x}Se_x$ [73, 74]. Here the 2+ formal valence of the Ni is not abnormally high. However, the anions S and Se have increasingly low electronegativities compared to oxygen, which also can lead to a mixed valence or a negative charge transfer energy. We show this effect schematically in Fig. 9, which is similar in nature to Fig. 4, but now we span the four classes of correlated compounds by shifting the ligand band, rather than the transition-metal bands. In this sense, moving from the positive to negative charge transfer regime in Fig. 9 would represent moving from NiO to $NiS_{1-x}Se_x$, where the formal Ni valence does not change but the ligand electronegativity does. Recent studies classify NiS as a self-doped, nearly compensated, antiferromagnetic metal [70]. It is interesting to note that researchers have been searching for Ni^{1+} oxides (although in 2D structures) in order to simulate the high-T_c cuprate electronic structure. For example, recently $La_4Ni_3O_8$ has been studied in this regard [75]. In fact, in a negative charge

transfer scenario, the Ni in NiS would be 1+ with holes in the sulfur band. In this sense it would indeed share similarities with very heavily hole-doped cuprates, having a d^9 transition-metal configuration and also a presence of ligand holes.
Moving toward the center of the $3d$ elements, the formally tetravalent Fe perovskites $AFeO_3$ with A = Ca, Sr, or Ba are known to have negative charge transfer energies [76–81]. This class of materials possesses a wide range of interesting properties. $CaFeO_3$ was found to exhibit a charge-ordered state [81], which might actually be similar to the bond-disproportionation states in the nickelates and bismuthates. $SrFe_{1-x}Co_xO_3$ is ferromagnetic and exhibits a large negative magnetoresistance [78]. $La_{1-x}Sr_xFeO_3$ with $x \approx 2/3$ also exhibits a charge disproportionation, accompanied by an order of magnitude resistivity jump and antiferromagnetic ordering [77,82]. Lastly, an example of an early $3d$ transition-metal compound with a negative charge transfer energy is CrO_2 [29]. This material has attracted significant interest as a half-metallic ferromagnet [83], and was industrially very relevant in the past as the main active component in many (now all but obsolete) magnetic recording tapes [84]. A combination of LSDA+U calculations [29] and spectroscopy [83] have verified that, even though the $3d$ electrons of the Cr have large Coulomb interactions, the material is metallic due to the negative charge transfer energy, with charge carriers at the Fermi energy having a large O $2p$ component.

5 Mixed valent rare-earth compounds

In this section, we will look at existing mixed valent compounds in detail. As mentioned earlier, the combination of correlated and band like states crossing the Fermi level in a mixed valent compound leads to a very complicated electronic structure. However, the mixed valent rare-earth compounds, such as SmB_6 and SmS have a slightly simplified description due to the very weak hybridization between the correlated $4f$ states and the broad band states. The full electronic structure is no doubt very complicated, but the weak hybridization leads to some very clear and interesting phenomena in these materials.
Samarium hexaboride was first heavily studied from the late 1960s to early 1980s. Early experimental studies of x-ray absorption [85] and susceptibility [86] measurements showed evidence that the Sm was present in both divalent and trivalent states, corresponding to f^6 and f^5 orbital occupations, respectively. Later experiments showed several interesting features, including a resistivity saturation at low temperatures and a lack of magnetic ordering down to 0.35 K [87, 88]. A similar lack of magnetism was found for SmS, which was also known to be a mixed valent compound [89]. The unique characteristics of such mixed valent compounds were analyzed with various theories, the most popular being the Anderson impurity and lattice models [90–102].
SmB_6 is now under intense study again, as recent theory work has predicted that it could be a so-called topological Kondo insulator [103, 104]. The low-temperature resistivity saturation could then be an indication of topologically protected surface states. Many experimental studies have been undertaken to test the topological insulator hypothesis (see, e.g. [105–108]), but a clear answer has yet to emerge.

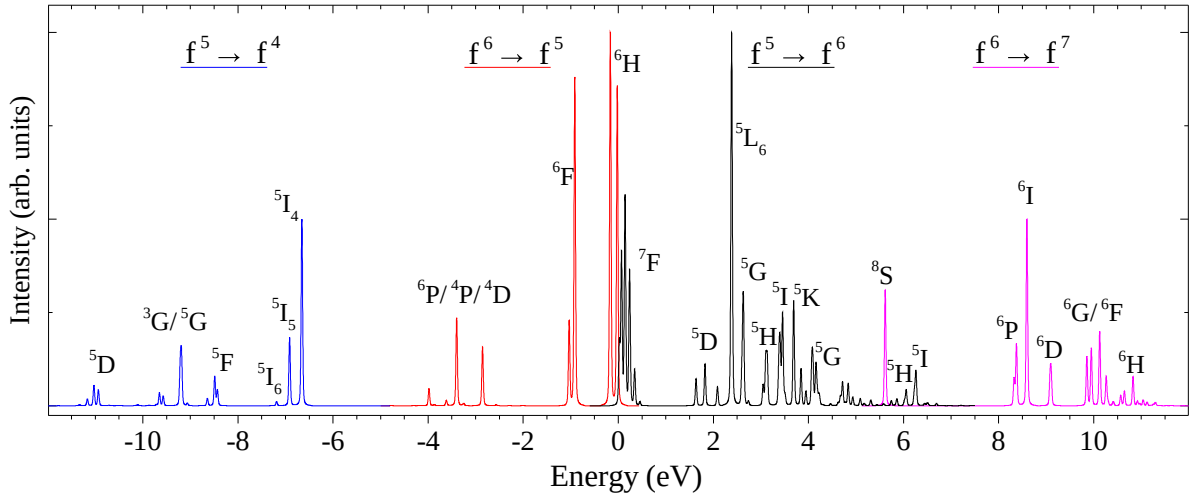

Fig. 10: *Calculated f electron addition and removal spectra of mixed-valent SmB_6. All f orbital degeneracies are included, as well as the local multiplet Coulomb interactions, which lead to the large number of excitations spread over ~20 eV.*

The tightly contracted and highly correlated $4f$ shells of the Sm ions in SmB_6 lead to very strong multiplet effects in the electron addition and removal spectra. Further, since the complicated mixed valent ground state has components of both the f^n and f^{n+1} atomic fillings (with the lowest energy states being the Hund's rule ground states in each case), the one-electron excitation spectrum will contain four sets of features corresponding to electron addition and removal from each of the fillings (this effect was also shown schematically for the mixed-valence class in Fig. 4). In Fig. 10, we show a calculation of the multiplet rich, one-electron excitation spectrum in the atomic limit of a mixed valent Sm system. The four regions of the spectrum are indicated, and the term symbols denote the dominant contribution of each main peak (the usual ${}^{2S+1}L_J$ notation is used, but J is omitted in cases where different J peaks are too close to discern at this scale). There are a set of low energy excitations present near the Fermi level—since the lowest-energy f^5 and f^6 multiplets are nearly degenerate in such a mixed valent material, the one-electron removal from f^6 reaches the very low energy f^5 states, and the one-electron addition to f^5 reaches the very low energy f^6 states. However, we cannot add an electron to f^6 or remove one from f^5 at the low energy scale.

Further away from the Fermi level are the high-energy lower and upper Hubbard bands composed of $f^5 \rightarrow f^4$ and $f^6 \rightarrow f^7$ excitations, respectively. Each set of excitations is separated from the Fermi level by the Coulomb energy U, leading to a total energy separation of $2U$, as was also shown schematically in Fig. 4. An important observation from this plot are the very different intensities of the various multiplet peaks. This is of course not surprising, but the intensities of these peaks are related to the coefficients of fractional parentage (CFPs) for adding and removing electrons to/from the Hund's rule lowest energy states of the f^5 and f^6 configurations. These CFPs also play an important role in the intersite hopping of the compound, so we will investigate them in some detail in the following.

It was shown in the early work of Racah [109] that one could construct antisymmetrized eigenfunctions for a general many-electron atomic configuration l^n by using a suitable linear combination of the states obtained by angular-momentum coupling one additional electron to the eigenfunctions for the l^{n-1} configuration. The CFPs are then the coefficients of these linear combinations. One can quickly realize, then, that the required transition amplitudes between f^n and f^{n-1} configurations for calculating one-electron Green functions or hopping matrix elements will also be defined by these CFPs. An extensive tabulation of these coefficients is given by Nielson and Koster [110].

For a given f^{n-1} configuration of the correlated $4f$ shell, if we assume for now the validity of Russell-Saunders LS-coupling, we have a many-body wavefunction $|\Psi^{n-1}_{LSJ}\rangle$. The electron addition amplitude to reach a final state $|\Psi^{n}_{L'S'J'}\rangle$, which as stated above relates to the CFP for particular configurations, is then given by

$$\langle \Psi^{n}_{L'S'J'} | \boldsymbol{f}^{\dagger}_{lsj} | \Psi^{n-1}_{LSJ} \rangle \tag{4}$$

where $\boldsymbol{f}^{\dagger}_{lsj}$ creates an f electron with the given quantum numbers. As shown for example by Hirst [111], this quantity can be written in terms of 3-j and 9-j symbols as

$$\langle \Psi^{n}_{L'S'J'} | \boldsymbol{f}^{\dagger}_{lsj} | \Psi^{n-1}_{LSJ} \rangle = \left[\begin{pmatrix} L & l & L' \\ -L & L-L' & L' \end{pmatrix} \begin{pmatrix} S & s & S' \\ -S & S-S' & S' \end{pmatrix} \right]^{-1} \begin{Bmatrix} L & L' & l \\ S & S' & s \\ J & J' & j \end{Bmatrix} C_{J,J',j} \tag{5}$$

where

$$C_{J,J',j} = \sqrt{(2J+1)\,(2J'+1)\,(2j+1)}\,. \tag{6}$$

For one-electron addition and removal spectra of a mixed valent compound, the transition rates are computed starting from the Hund's rule ground states of the f^n and f^{n-1} configurations, into all possible states that can be reached by removing or adding an electron. For the specific example of SmB_6, as shown in Fig. 10, the starting configurations are f^5 and f^6, and thus one can reach electron removal states of f^4 and f^5, and electron addition states of f^6 and f^7.

Closely related to the one-electron addition and removal spectra in a mixed valent compound are the intersite hopping integrals which couple the f^n and f^{n-1} configurations. If we define our f^n Hund's rule ground state as $|\Psi^{n}_{H}\rangle$, then it can transition to the f^{n-1} states $|\Psi^{n-1}_{i}\rangle$, with a total intensity of

$$I^{-}_{T} = \sum_{i} \left| \langle \Psi^{n-1}_{i} | \boldsymbol{f} | \Psi^{n}_{H} \rangle \right|^2 = n\,, \tag{7}$$

where sum rules and the degeneracy of the f shell dictate that $I^{-}_{T} = n$. In other words, the total intensity is given by the number of electrons which can be removed from the f^n configuration (for the actual hopping processes this is then scaled by the one-electron overlap integral). Similarly, the total one-electron addition intensity for the $|\Psi^{n-1}_{H}\rangle$ Hund's rule ground state is

$$I^{+}_{T} = \sum_{i} \left| \langle \Psi^{n}_{i} | \boldsymbol{f}^{\dagger} | \Psi^{n-1}_{H} \rangle \right|^2 = 15 - n\,, \tag{8}$$

where now the sum rule depends on the number of holes available in the shell ($14 - [n-1]$).

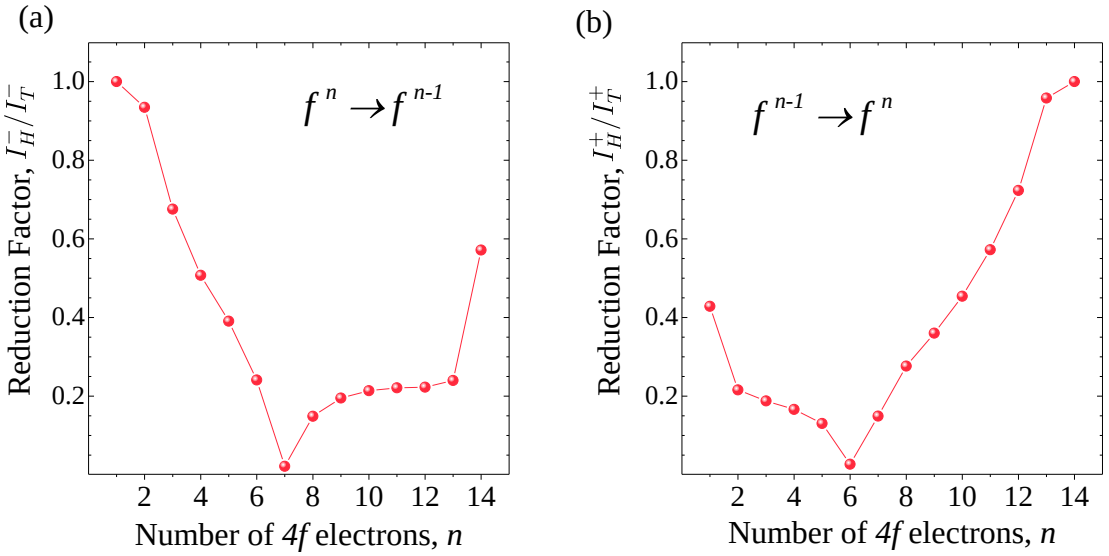

Fig. 11: *Reduction factors when transition rates are restricted to Hund's rule ground states for final state. (a) Electron removal from a f^n Hund's rule ground state into a f^{n-1} Hund's rule ground state. (b) Electron addition from a f^{n-1} into a f^n state. The asymmetry between (a) and (b) arises from the degeneracy of the states.*

For the mixed valent rare-earth compounds, the one-electron overlap integrals are generally very weak due to the contracted $4f$ radial wavefunctions. This weak hopping means that often the only important interactions to consider for the ground state are between the Hund's rule ground states of each configuration (all other higher-energy states can be neglected for the low-energy scale physics). For the case of SmB_6 these important lowest energy states are the $^6H_{5/2}$ and $^7F_0$ states of the f^5 and f^6 configurations, respectively. Thus the intensity integrals of Eqns. (7) and (8) can be restricted to final states corresponding to the Hund's rule ground states. We then have diminished angular matrix elements for this Hund-Hund hopping, now with a total intensity given by

$$I_H^- = \sum_{m_j'} \left| \langle \Psi_{H,m_j'}^{n-1} | \boldsymbol{f} | \Psi_{H,m_j}^{n} \rangle \right|^2 \tag{9}$$

and

$$I_H^+ = \sum_{m_j'} \left| \langle \Psi_{H,m_j'}^{n} | \boldsymbol{f}^\dagger | \Psi_{H,m_j}^{n-1} \rangle \right|^2 \tag{10}$$

where $|\Psi_{H,m_j}^n\rangle$ denotes a particular m_j Hund's rule ground state of the n electron configuration. We demonstrate the strong reduction in hopping strength that can take place in such a situation by plotting I_H^-/I_T^- and I_H^+/I_T^+ in Figs. 11(a) and 11(b), respectively. This effect was demonstrated by Hirst [111] using Eqn. (5) within the LS-coupling approximation. In Fig. 11, we show comparable results to Hirst, but now via slightly more precise exact diagonalization calculations in intermediate coupling using the code *Quanty* [45, 112–114]. From Fig. 11(a), we see there is no reduction factor for the electron removal from a f^1 configuration. This of course makes sense, since the f^0 final state is non-degenerate, so no transition intensity is lost by restricting the final state to be a Hund's rule ground state. However, one finds a very strong

reduction for both electron removal and electron addition which ends in a f^6 configuration, for example. The reason for the very strong reduction in this case is that the f^6 Hund's rule ground state is a $^7F_0$ singlet. This will be important for our further discussion of SmB_6 below. Finally, note that the asymmetry between the plots arises from the degeneracies of the states: a singlet $^7F_0$ f^6 state can hop to any of the 6 degenerate states of the $^6H_{5/2}$ f^5 configuration, but a particular one of those 6 only hops to the one singlet $^7F_0$ state. This observation is similar in nature to the "$1/N$" scaling arguments used to avoid infrared divergences and solve the Anderson impurity model in earlier studies of rare-earth compounds [98–101].

As evident from Fig. 11, the hopping for such a mixed valent compound (e.g. SmB_6) can be very weak, even on top of the effect of contracted $4f$ radial wavefunctions. The importance of these angular matrix element effects is also evident from the overestimated dispersion widths in DFT calculations, which capture the contracted radial wavefunction effect, but not the CFP effect. Dispersional widths of the f bands for SmB_6 are more than an order of magnitude larger in DFT calculations compared to those found in ARPES experiments (~200 vs. 7 meV) [115–117].

Within the above approximations, the only f-f hopping allowed at low energy scales occurs via removing an electron from an f^6 atom and adding it to an f^5 atom, both in their Hund's rule ground states. More specifically, the f^6 atom will transition from a $^7F_0$ state to a $^6H_{5/2}$ state, and the f^5 atom will transition from a $^6H_{5/2}$ to a $^7F_0$ state. From the coefficients of fractional parentage, the transition amplitude between the $^7F_0$ singlet and a single m_j state of the 6-fold degenerate $^6H_{5/2}$ term is 0.200 times the total $f^6 \rightarrow f^5$ amplitude (where we account for the degeneracy by dividing by $\sqrt{1/6}$). Similarly, the amplitude from one of the $^6H_{5/2}$ states to the $^7F_0$ state is 0.164 times the total $f^5 \rightarrow f^6$ amplitude. Multiplying these two amplitudes for the total f-f hopping process gives a reduction factor of 0.033 for the f bandwidth compared to the one-electron bandwidth that one would obtain from DFT or LDA+U. This is in very good agreement with the discrepancy between DFT and experimental bandwidths pointed out above (200 meV vs. 7 meV, respectively).

This very strong reduction factor coming from the coefficients of fractional parentage suggests that in a first approximation we can neglect the direct f-f hopping. The d-f hopping is also reduced by the CFP effect, but only by the amplitude and not the square, so the hybridization is still important, relatively speaking. It is interesting to note that a full DMFT calculation taking into account all the multiplet structure [117] gives a bandwidth reduction of the f bands, and a reduction of the d-f hopping, consistent with the above discussion of the coefficients of fractional parentage. Note also that the phases of the coefficients of fractional parentage (which we neglected above for simplicity) could be very important. For example in manganites, similar hopping considerations which included phases found that a Berry phase is accumulated when electrons hop in loops [118].

For systems with a large U, or ones in which the splitting between the ground state and higher energy f^n configurations is large (compared to the energy scale we are considering as important), we can neglect all of the hoppings involving higher energy states when considering the lowest energy scale physics. So even the spin-orbit splitting of the f^6 manifold with $J = 0$ as the lowest energy state is large enough to neglect in zeroth order when dealing with the

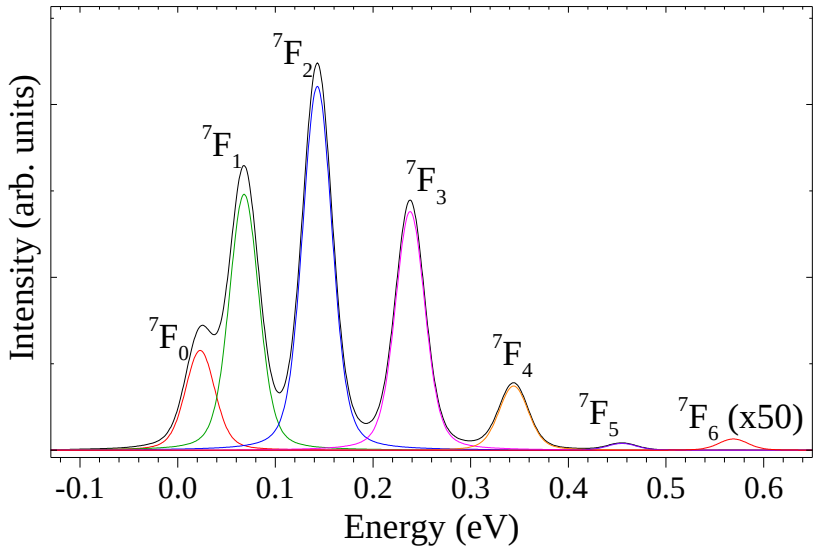

Fig. 12: *The f^5 to f^6 electron addition spectrum of Fig. 10, now zoomed in to low energy scales.*

low-temperature properties below 100 K. The splitting of these J states for f^6 is shown in Fig. 12, and is about 45 meV (or 520 K) for the lowest $J = 1$ excitation relative to the $J = 0$. In what follows we also neglect the crystal-field splitting within the multiplets, although this may be a bit of a stretch and a rigorous treatment should include them. Considering only the lowest-energy crystal-field states (which would likely be one of the doublets) would reduce the degeneracy to that of a Kramers doublet.

Having established the very weak hybridization present in compounds such as SmB_6 (due to both contracted radial wavefunctions and fractional-parentage matrix element effects), and that subsequently only the lowest energy f^5 and f^6 states need to be considered in a first approximation, we can now consider the band structure of the broad d band with which the f shells hybridize. Again, due to the very weak hybridization, there will only be appreciable mixing at k points near where the band crosses the f levels. We show this effect in Fig. 13, where a general light-electron band (blue) crosses the localized f level and a small hybridization is present. A small gap opens near the crossing points, and at these points the wavefunction has a true mixed character as indicated by the color of the plot. Far away from these crossing points, there is very little mixing between the f and d bands.

The schematic band structure of Fig. 13 reveals a very interesting characteristic of such materials: they are best described as mixed valent *in momentum space*. For regions of Fig. 13(a) where $|k| > 0.5\pi/a$, there are f electron removal states very close to the Fermi level. If our mixed valent compound has the valences f^{n-1} and f^n, then in these regions of momentum space the ground state is almost purely f^n. In this way, it costs very little energy to remove an electron and reach the f^{n-1} state, which is nearly degenerate with the f^n state, but we cannot add an electron within the low energy scale. As was shown in Figs. 4 and 10, to add an electron to the f^n state would cost energy U, and accordingly no such f electron addition states are present for $|k| > 0.5\pi/a$ in Fig. 13(a) (they are too high in energy to be seen).

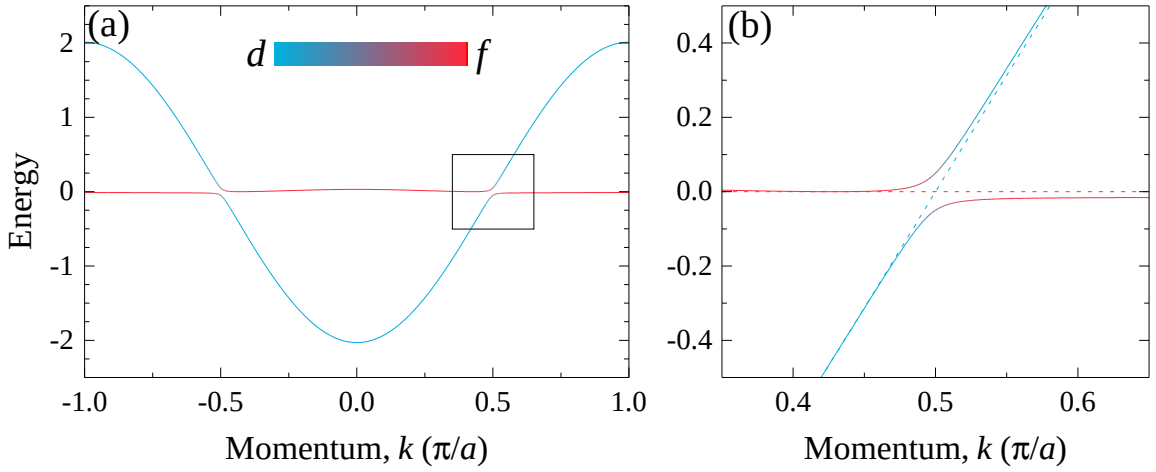

Fig. 13: *Paradigmatic bandstructure of a mixed-valent rare-earth compound. A very narrow f band crosses the broad conduction band at the Fermi level. Weak hybridization opens a small gap at the band crossing points. Panel (b) shows an enlargement of the band crossing region. The color scale indicates the f and d weight in the band.*

Just as the regions of momentum space where $|k| > 0.5\pi/a$ have an almost pure f^n ground state, the regions where $|k| < 0.5\pi/a$ have an almost pure f^{n-1} ground state. In this region there is an f electron addition state just above the Fermi level, as it costs essentially no energy to reach the f^n from the f^{n-1} state, but there are no f electron removal states shown as they would cost energy U and are thus far away in energy. In this sense it becomes clear that the mixed valent compound has well defined regions in momentum space with integral valences, but in fact each valence state is delocalized in real space. The many-body wave function in this situation becomes very complicated. This simple picture also indicates that a DMFT calculation which does very well in many aspects must include a strong k-dependent self energy, and in fact if a gap occurs as indicated in Figure 13, the self energy would be discontinuous or at least very strongly varying as one moves through the k region of the crossing.

In the case of SmB_6 the broad band is actually an almost equal mixture of B $2p$ states and Sm d states, as clearly shown from DFT calculations [119]. The minimum in the dispersion is at the X point in the Brillouin zone. In order to conserve charge, this band would be empty if the Sm was purely 2+ (f^6) and would contain on average one electron per formula unit if the Sm is 3+ (f^5). In a mixed valent situation there will be an exact compensation of f and d electrons depending on the $Sm^{2+/3+}$ ratio. If the d-f hybridization were zero then the crossing surface of the d band and the f states in momentum space would describe a Fermi surface consistent with Luttinger's theorem, as also argued by Richard Martin some time ago [120, 121]. So the surface describing the crossing point at which a gap has its largest value has the same topology as the Fermi surface one would obtain in a band theory calculation. It is an interesting question as to whether this "pseudo" Fermi surface is something that can be seen via the de Haas–van Alphen effect in high-field quantum oscillation experiments [122–125].

The above discussion provides a unique picture of the electronic structure of the low energy states of SmB_6. This is quite different from a description in which the basic physics involves an impurity-like Kondo singlet low-energy scale state and these Kondo impurities forming a lattice which then could develop a gap and become insulating. Whether or not our above description could also be termed a "Kondo insulator" is perhaps debatable. It is also interesting to go back and have another look if perhaps other so-called heavy Fermion systems may actually fall into this category in which we rather should study things in momentum space to start with, in place of considering a lattice of Kondo impurities.

This example of the rare earths is an extreme case and can be treated in this way because of the weak hybridization. In other mixed valent systems like the actinides or the transition-metal compounds, things become very complicated because the effect of the strong hybridization between the local strongly correlated states and the broad bands crossing the Fermi energy can be very large and comparable to the band width of the broad bands. In the extreme limit of that case we would somehow be back to a DFT-based band description in which the local correlations are suppressed because of the strong hybridization with the broad bands, forming rather extended Wannier functions and diluting the effective on-site Coulomb interactions. The most interesting cases, however, are the intermediate cases which very likely involve the $3d$ transition-metal compounds such as the rare earth TM perovskite structure oxides, the ion battery materials such as $LiNiO_2$, as well as the sulfides, selenides, tellurides, bromides, and iodides of the late $3d$ transition metals.

6 Summary

The central theme of this lecture is that often anion states can be much more important in correlated compounds than one would initially expect. In transition-metal compounds which have large formal oxidation states, it is often the case that the formal rules are broken. The transition metals are then better described as having more typical valences, and the anion bands are self-doped to compensate this different charge on the cations. We presented these effects through an extension of the Zaanen-Sawatzky-Allen classification scheme for transition-metal compounds. In addition to the two original classes of Mott-Hubbard and (positive) charge transfer insulators, we showed how mixed valent and negative charge transfer insulators can naturally arise. The perovskite rare-earth nickelates are a paradigmatic example of negative charge transfer compounds, where the self-doped oxygen holes make very important contributions to the conductivity and magnetism in the compounds. We also showed how similar effects can be found in non-correlated compounds such as perovskite bismuthates. Finally, we explored the interesting mixed-valence regime through the example of rare-earth compounds such as SmB_6. Weak hybridization and mixed-valent energetics lead to the unique phenomenon of ordered valences in momentum space. A key lesson to take away from these discussions is that one might need to choose a non-conventional starting point when constructing a model to describe the electronic structure of high-valence compounds.

Acknowledgments

We thank Ilya Elfimov, Mona Berciu, Kateryna Foyevtsova, Alfred Cheung, Arash Khazraie, and Maurits Haverkort for input and helpful discussions. This article was written with the support of the Natural Sciences and Engineering Research Council of Canada, the Canadian Institute for Advanced Research, and the Max Planck–UBC Centre for Quantum Materials.

References

[1] J.A. Yarmoff, D.R. Clarke, W. Drube, U.O. Karlsson, A. Taleb-Ibrahimi, and F.J. Himpsel, Phys. Rev. B **36**, 3967 (1987)

[2] N. Nücker, J. Fink, J.C. Fuggle, P.J. Durham, and W.M. Temmerman, Phys. Rev. B **37**, 5158 (1988)

[3] C.T. Chen, F. Sette, Y. Ma, M.S. Hybertsen, E.B. Stechel, W.M.C. Foulkes, M. Schulter, S.-W. Cheong, A.S. Cooper, L.W. Rupp, B. Batlogg, Y.L. Soo, Z.H. Ming, A. Krol, and Y.H. Kao, Phys. Rev. Lett. **66**, 104 (1991)

[4] H. Eskes and G.A. Sawatzky, Phys. Rev. Lett. **61**, 1415 (1988)

[5] F.C. Zhang and T.M. Rice, Phys. Rev. B **37**, 3759 (1988)

[6] V.J. Emery and G. Reiter, Phys. Rev. B **38**, 4547 (1988)

[7] B. Lau, M. Berciu, and G.A. Sawatzky, Phys. Rev. B **81**, 172401 (2010)

[8] B. Lau, M. Berciu, and G.A. Sawatzky, Phys. Rev. Lett. **106**, 036401 (2011)

[9] B. Lau, M. Berciu, and G.A. Sawatzky, Phys. Rev. B **84**, 165102 (2011)

[10] M. Möller, G.A. Sawatzky, and M. Berciu, Phys. Rev. B **86**, 075128 (2012)

[11] P. Kuiper, G. Kruizinga, J. Ghijsen, G.A. Sawatzky, and H. Verweij, Phys. Rev. Lett. **62**, 221 (1989)

[12] J. van Elp, J.L. Wieland, H. Eskes, P. Kuiper, G.A. Sawatzky, F.M.F. de Groot, and T.S. Turner, Phys. Rev. B **44**, 6090 (1991)

[13] J. Slater: *Quantum Theory of Atomic Structure* (McGraw-Hill, 1960)

[14] R.D. Cowan: *The Theory of Atomic Structure and Spectra* (University of California Press, 1981)

[15] C.J. Ballhausen: *Introduction to Ligand Field Theory* (McGraw-Hill, 1962)

[16] I.S. Elfimov, S. Yunoki, and G.A. Sawatzky, Phys. Rev. Lett. **89**, 216403 (2002)

[17] A.V. Ushakov, S.V. Streltsov, and D.I. Khomskii, J. Phys.: Condens. Matter **23**, 445601 (2011)

[18] R.J. Green, M.W. Haverkort, and G.A. Sawatzky, (to be published) (2016)

[19] J.H. de Boer and E.J.W. Verwey, Proc. Phys. Soc. **49**, 59 (1937)

[20] N.F. Mott and R. Peierls, Proc. Phys. Soc. **49**, 72 (1937)

[21] N.F. Mott, Proc. Phys. Soc. A **62**, 416 (1949)

[22] J. Hubbard, Proc. R. Soc. A **277**, 237 (1964)

[23] J. Hubbard, Proc. R. Soc. A **281**, 401 (1964)

[24] A. Fujimori and F. Minami, Phys. Rev. B **30**, 957 (1984)

[25] G.A. Sawatzky and J.W. Allen, Phys. Rev. Lett. **53**, 2339 (1984)

[26] J. Zaanen, G.A. Sawatzky, and J.W. Allen, Phys. Rev. Lett. **55**, 418 (1985)

[27] E.J.W. Verwey, Nature **144**, 327 (1939)

[28] M.S. Senn, J.P. Wright, and J.P. Attfield, Nature **481**, 173 (2012)

[29] M.A. Korotin, V.I. Anisimov, D.I. Khomskii, and G.A. Sawatzky, Phys. Rev. Lett. **80**, 4305 (1998)

[30] D.I. Khomskii, Lith. J. Phys. **37**, 65 (1997)

[31] M.L. Medarde, Journal of Physics: Condensed Matter **9**, 1679 (1997)

[32] G. Demazeau, A. Marbeuf, M. Pouchard, and P. Hagenmuller, J. Solid State Chem. **3**, 582 (1971)

[33] P. Lacorre, J.B. Torrance, J. Pannetier, A.I. Nazzal, P.W. Wang, and T.C. Huang, J. Solid State Chem. **91**, 225 (1991)

[34] J.L. Garcia-Munoz, J. Rodriguez-Carvajal, P. Lacorre, and J.B. Torrance, Phys. Rev. B **46**, 4414 (1992)

[35] J.B. Torrance, P. Lacorre, A.I. Nazzal, E.J. Ansaldo, and C. Niedermayer, Phys. Rev. B **45**, 8209 (1992)

[36] A. Frano, E. Schierle, M.W. Haverkort, Y. Lu, M. Wu, S. Blanco-Canosa, U. Nwankwo, A.V. Boris, P. Wochner, G. Cristiani, H.U. Habermeier, G. Logvenov, V. Hinkov, E. Benckiser, E. Weschke, and B. Keimer, Phys. Rev. Lett. **111**, 106804 (2013)

[37] A.V. Boris, Y. Matiks, E. Benckiser, A. Frano, P. Popovich, V. Hinkov, P. Wochner, M. Castro-Colin, E. Detemple, V.K. Malik, C. Bernhard, T. Prokscha, A. Suter, Z. Salman, E. Morenzoni, G. Cristiani, H.U. Habermeier, and B. Keimer, Science **332**, 937 (2011)

[38] E. Benckiser, M.W. Haverkort, S. Brueck, E. Goering, S. Macke, A. Frano, X. Yang, O.K. Andersen, G. Cristiani, H.-U. Habermeier, A.V. Boris, I. Zegkinoglou, P. Wochner, H.-J. Kim, V. Hinkov, and B. Keimer, Nat. Mater. **10**, 189 (2011)

[39] J. Liu, M. Kargarian, M. Kareev, B. Gray, P.J. Ryan, A. Cruz, N. Tahir, Y.-D. Chuang, J. Guo, J.M. Rondinelli, J.W. Freeland, G.A. Fiete, and J. Chakhalian, Nat. Commun. **4**, 2714 (2013)

[40] S. Catalano, M. Gibert, V. Bisogni, O.E. Peil, F. He, R. Sutarto, M. Viret, P. Zubko, R. Scherwitzl, A. Georges, G.A. Sawatzky, T. Schmitt, and J.-M. Triscone, APL Mater. **2**, 116110 (2014)

[41] T. Mizokawa, D.I. Khomskii, and G.A. Sawatzky, Phys. Rev. B **61**, 11263 (2000)

[42] H. Park, A.J. Millis, and C.A. Marianetti, Phys. Rev. Lett. **109**, 156402 (2012)

[43] S. Johnston, A. Mukherjee, I. Elfimov, M. Berciu, and G.A. Sawatzky, Phys. Rev. Lett. **112**, 106404 (2014)

[44] F.M.F. de Groot and A. Kotani: *Core Level Spectroscopy of Solids* (CRC Press, Taylor & Francis Group, 2008)

[45] M.W. Haverkort, M. Zwierzycki, and O.K. Andersen, Phys. Rev. B **85**, 165113 (2012)

[46] J. Zaanen, C. Westra, and G.A. Sawatzky, Phy. Rev. B **33**, 8060 (1986)

[47] M. Medarde, A. Fontaine, J.L. García-Muñoz, J. Rodríguez-Carvajal, M. de Santis, M. Sacchi, G. Rossi, and P. Lacorre, Phys. Rev. B **46**, 14975 (1992)

[48] C. Piamonteze, F.M.F. de Groot, H.C.N. Tolentino, A.Y. Ramos, N.E. Massa, J.A. Alonso, and M.J. Martínez-Lope, Phys. Rev. B **71**, 020406 (2005)

[49] J.W. Freeland, M. van Veenendaal, and J. Chakhalian, Journal of Electron Spectroscopy and Related Phenomena **208**, 56 (2015)

[50] T. Mizokawa, A. Fujimori, T. Arima, Y. Tokura, N. Mōri, and J. Akimitsu, Phys. Rev. B **52**, 13865 (1995)

[51] K. Foyevtsova, A. Khazraie, I. Elfimov, and G.A. Sawatzky, Phys. Rev. B **91**, 121114 (2015)

[52] T.M. Rice and L. Sneddon, Phys. Rev. Lett. **47**, 689 (1981)

[53] D. Cox and A. Sleight, Solid State Commun. **19**, 969 (1976)

[54] D.E. Cox and A.W. Sleight, Acta Crystallographica B **35**, 1 (1979)

[55] C.M. Varma, Phys. Rev. Lett. **61**, 2713 (1988)

[56] I. Hase and T. Yanagisawa, Phys. Rev. B **76**, 174103 (2007)

[57] T. Mizokawa, H. Namatame, A. Fujimori, K. Akeyama, H. Kondoh, H. Kuroda, and N. Kosugi, Phys. Rev. Lett. **67**, 1638 (1991)

[58] D.D. Sarma, O. Strebel, C.T. Simmons, U. Neukirch, G. Kaindl, R. Hoppe, and H.P. Müller, Phys. Rev. B **37**, 9784 (1988)

[59] K. Karlsson, O. Gunnarsson, and O. Jepsen, J. Phys.: Condens. Matter **4**, 2801 (1992)

[60] W. Folkerts, G.A. Sawatzky, C. Haas, R.A. de Groot, and F.U. Hillebrecht, J. Phys. C: Solid State Physics **20**, 4135 (1987)

[61] K. Adachi, K. Sato, and M. Takeda, J. Phys. Soc. Japan **26**, 631 (1969)

[62] S. Ogawa, J. Appl. Phys. **50**, 2308 (1979)

[63] A.E. Bocquet, K. Mamiya, T. Mizokawa, A. Fujimori, T. Miyadai, H. Takahashi, M. Mōri, and S. Suga, J. Phys.: Condens. Matter **8**, 2389 (1996)

[64] A. Fujimori, K. Mamiya, T. Mizokawa, T. Miyadai, T. Sekiguchi, H. Takahashi, N. Môri, and S. Suga, Phys. Rev. B **54**, 16329 (1996)

[65] J. Kanamori, A. Okiji, H. Shiba, K. Terakura, K. Mamiya, T. Mizokawa, A. Fujimori, H. Takahashi, N. Mori, T. Miyadai, S. Suga, N. Chandrasekharan, S. Krishnakumar, and D. Sarma, Physica B **237**, 390 (1997)

[66] K. Mamiya, T. Mizokawa, A. Fujimori, T. Miyadai, N. Chandrasekharan, S.R. Krishnakumar, D.D. Sarma, H. Takahashi, N. Môri, and S. Suga, Phys. Rev. B **58**, 9611 (1998)

[67] J. Mazzaferro, H. Ceva, and B. Alascio, Phys. Rev. B **22**, 353 (1980)

[68] J.A. Wilson: *The Metallic and Non-Metallic States of Matter* (London: Taylor and Francis, 1985) p. 215

[69] A. Ferraz, R. Chapman, N. March, B. Alascio, and C. Sayers, Solid State Commun. **57**, 937 (1986)

[70] S.K. Panda, I. Dasgupta, E. Sasioglu, S. Blügel, and D.D. Sarma, Sci. Rep. (2013)

[71] S.K. Panda, P. Thunström, I.D. Marco, J. Schött, A. Delin, I. Dasgupta, O. Eriksson, and D.D. Sarma, New J. Phys. **16**, 093049 (2014)

[72] M. Nakamura, A. Fujimori, M. Sacchi, J.C. Fuggle, A. Misu, T. Mamori, H. Tamura, M. Matoba, and S. Anzai, Phys. Rev. B **48**, 16942 (1993)

[73] D.D. Sarma, S.R. Krishnakumar, N. Chandrasekharan, E. Weschke, C. Schüßler-Langeheine, L. Kilian, and G. Kaindl, Phys. Rev. Lett. **80**, 1284 (1998)

[74] S.R. Krishnakumar, N. Shanthi, P. Mahadevan, and D.D. Sarma, Phys. Rev. B **61**, 16370 (2000)

[75] V.V. Poltavets, K.A. Lokshin, A.H. Nevidomskyy, M. Croft, T.A. Tyson, J. Hadermann, G. Van Tendeloo, T. Egami, G. Kotliar, N. ApRoberts-Warren, A.P. Dioguardi, N.J. Curro, and M. Greenblatt, Phys. Rev. Lett. **104**, 206403 (2010)

[76] A.E. Bocquet, A. Fujimori, T. Mizokawa, T. Saitoh, H. Namatame, S. Suga, N. Kimizuka, Y. Takeda, and M. Takano, Phys. Rev. B **45**, 1561 (1992)

[77] A. Chainani, M. Mathew, and D.D. Sarma, Phys. Rev. B **48**, 14818 (1993)

[78] M. Abbate, G. Zampieri, J. Okamoto, A. Fujimori, S. Kawasaki, and M. Takano, Phys. Rev. B **65**, 165120 (2002)

[79] N. Hayashi, T. Yamamoto, H. Kageyama, M. Nishi, Y. Watanabe, T. Kawakami, Y. Matsushita, A. Fujimori, and M. Takano, Angewandte Chemie **123**, 12755 (2011)

[80] T. Tsuyama, T. Matsuda, S. Chakraverty, J. Okamoto, E. Ikenaga, A. Tanaka, T. Mizokawa, H.Y. Hwang, Y. Tokura, and H. Wadati, Phys. Rev. B **91**, 115101 (2015)

[81] T. Akao, Y. Azuma, M. Usuda, Y. Nishihata, J. Mizuki, N. Hamada, N. Hayashi, T. Terashima, and M. Takano, Phys. Rev. Lett. **91**, 156405 (2003)

[82] H. Wadati, A. Chikamatsu, R. Hashimoto, M. Takizawa, H. Kumigashira, A. Fujimori, M. Oshima, M. Lippmaa, M. Kawasaki, and H. Koinuma, J. Phys. Soc. Jpn **75**, 054704 (2006)

[83] D.J. Huang, L.H. Tjeng, J. Chen, C.F. Chang, W.P. Wu, S.C. Chung, A. Tanaka, G.Y. Guo, H.-J. Lin, S.G. Shyu, C.C. Wu, and C.T. Chen, Phys. Rev. B **67**, 214419 (2003)

[84] G. Bate, IEEE Transactions on Magnetics **14**, 136 (1978)

[85] E.E. Vainshtein, S.M. Vlokhin, and Y.B. Paderno, Fiz. Tverd. Tela **6**, 2909 (1964)

[86] Y.B. Paderno, S. Pokrzywnicki, and B. Stalinski, Phys. Status Solidi **24**, K73 (1967)

[87] A. Menth, E. Buehler, and T.H. Geballe, Phys. Rev. Lett. **22**, 295 (1969)

[88] J.W. Allen, B. Batlogg, and P. Wachter, Phys. Rev. B **20**, 4807 (1979)

[89] M.B. Maple and D. Wohlleben, Phys. Rev. Lett. **27**, 511 (1971)

[90] L.L. Hirst, Physik der kondensierten Materie **11**, 255 (1970)

[91] C.M. Varma and Y. Yafet, Phys. Rev. B **13**, 2950 (1976)

[92] D. Khomskii and A. Kocharjan, Solid State Commun. **18**, 985 (1976)

[93] A.N. Kockaryan and D.I. Khomskii, JETP **44**, 404 (1976)

[94] C.M. Varma, Rev. Mod. Phys. **48**, 219 (1976)

[95] L.L. Hirst, Phys. Rev. B **15**, 1 (1977)

[96] F.D.M. Haldane, Phys. Rev. B **15**, 2477 (1977)

[97] R.M. Martin and J.W. Allen, J. Appl. Phys. **50**, 7561 (1979)

[98] H.R. Krishna-murthy, J.W. Wilkins, and K.G. Wilson, Phys. Rev. B **21**, 1003 (1980)

[99] H.R. Krishna-murthy, J.W. Wilkins, and K.G. Wilson, Phys. Rev. B **21**, 1044 (1980)

[100] O. Gunnarsson and K. Schönhammer, Phys. Rev. B **28**, 4315 (1983)

[101] O. Gunnarsson and K. Schönhammer, Phys. Rev. Lett. **50**, 604 (1983)

[102] P. Coleman, Phys. Rev. B **29**, 3035 (1984)

[103] M. Dzero, K. Sun, V. Galitski, and P. Coleman, Phys. Rev. Lett. **104**, 106408 (2010)

[104] V. Alexandrov, M. Dzero, and P. Coleman, Phys. Rev. Lett. **111**, 226403 (2013)

[105] D.J. Kim, S. Thomas, T. Grant, J. Botimer, Z. Fisk, and J. Xia, Scientific Reports **3**, 3150 (2013)

[106] S. Wolgast, C. Kurdak, K. Sun, J.W. Allen, D.-J. Kim, and Z. Fisk, Phys. Rev. B **88**, 180405 (2013)

[107] X. Zhang, N.P. Butch, P. Syers, S. Ziemak, R.L. Greene, and J. Paglione, Phys. Rev. X **3**, 011011 (2013)

[108] Z.-H. Zhu, A. Nicolaou, G. Levy, N.P. Butch, P. Syers, X.F. Wang, J. Paglione, G.A. Sawatzky, I.S. Elfimov, and A. Damascelli, Phys. Rev. Lett. **111**, 216402 (2013)

[109] G. Racah, Phys. Rev. **63**, 367 (1943)

[110] C.W. Nielson and G.F. Koster: *Spectroscopic coefficients for the p^n, d^n, and f^n configurations* (MIT Press, 1963)

[111] L.L. Hirst, Phys. Rev. B **15**, 1 (1977)

[112] M.W. Haverkort et al.: `http://www.quanty.org`

[113] Y. Lu, M. Höppner, O. Gunnarsson, and M.W. Haverkort, Phys. Rev. B **90**, 085102 (2014)

[114] M.W. Haverkort, G. Sangiovanni, P. Hansmann, A. Toschi, Y. Lu, and S. Macke, Europhys. Lett. **108**, 57004 (2014)

[115] J. Kim, K. Kim, C.-J. Kang, S. Kim, H.C. Choi, J.-S. Kang, J.D. Denlinger, and B.I. Min, Phys. Rev. B **90**, 075131 (2014)

[116] J.D. Denlinger, J.W. Allen, J.-S. Kang, K. Sun, B.I. Min, D.J. Kim, and Z. Fisk, JPS Conf. Proc. **3**, 017038 (2014)

[117] J.D. Denlinger, J.W. Allen, J.-S. Kang, K. Sun, J.-W. Kim, J.H. Shim, B.I. Min, D.-J. Kim, and Z. Fisk, arXiv:1312.6637

[118] E. Müller-Hartmann and E. Dagotto, Phys. Rev. B **54**, R6819 (1996)

[119] I. Elfimov, Private Communication

[120] R.M. Martin, Phys. Rev. Lett. **48**, 362 (1982)

[121] R.M. Martin, Journal of Applied Physics **53**, 2134 (1982)

[122] B.S. Tan, Y.-T. Hsu, B. Zeng, M.C. Hatnean, N. Harrison, Z. Zhu, M. Hartstein, M. Kiourlappou, A. Srivastava, M.D. Johannes, T.P. Murphy, J.-H. Park, L. Balicas, G.G. Lonzarich, G. Balakrishnan, and S.E. Sebastian, Science **349**, 287 (2015)

[123] J. Knolle and N.R. Cooper, Phys. Rev. Lett. **115**, 146401 (2015)

[124] O. Erten, P. Ghaemi, and P. Coleman, Phys. Rev. Lett. **116**, 046403 (2016)

[125] L. Zhang, X.-Y. Song, and F. Wang, Phys. Rev. Lett. **116**, 046404 (2016)

2 Mean-Field Theory: Hartree-Fock and BCS

Erik Koch
Institute for Advanced Simulation
Forschungszentrum Jülich

Contents

E. Pavarini, E. Koch, J. van den Brink, and G. Sawatzky (eds.)
Quantum Materials: Experiments and Theory
Modeling and Simulation Vol. 6
Forschungszentrum Jülich, 2016, ISBN 978-3-95806-159-0
http://www.cond-mat.de/events/correl16

1 Many-electron states

One of the deepest mysteries of physics is that all the different objects that surround us are built from a small set of indistinguishable particles. The very existence of such elementary particles that have all their properties in common is a direct consequence of quantum physics. Classical objects can always be distinguished by their location in space. This lead Leibniz to formulate his Principle of the Identity of Indiscernibles [1]. For quantum objects, however, the uncertainty principle makes the distinction of particles by their position impossible. Indistinguishability of quantum objects then means that there is no measurement that would let us tell them apart, i.e., all expectation values $\langle\Psi|M|\Psi\rangle$ must remain the same when we change the labeling of the distinct but indistinguishable the particles.

The consequences for observables are straightforward: An observable $M(x)$ acting on a single-particle degree of freedom x must operate on all indistinguishable particles in the same way, i.e., $\sum_i M(x_i)$. A two-body observable $M(x,x')$ must operate on all pairs in the same way, $\sum_{i,j} M(x_i,x_j)$ with $M(x,x') = M(x',x)$. We can thus write any observable in the form

$$M(\mathbf{x}) = M^{(0)} + \sum_i M^{(1)}(x_i) + \frac{1}{2!}\sum_{i\neq j} M^{(2)}(x_i,x_j) + \frac{1}{3!}\sum_{i\neq j\neq k} M^{(3)}(x_i,x_j,x_k) + \cdots \tag{1}$$

$$= M^{(0)} + \sum_i M^{(1)}(x_i) + \sum_{i<j} M^{(2)}(x_i,x_j) + \sum_{i<j<k} M^{(3)}(x_i,x_j,x_k) + \cdots , \tag{2}$$

where the summations can be restricted since the operators must be symmetric in their arguments, e.g. $M^{(2)}(x_i,x_j) = M^{(2)}(x_j,x_i)$, while for two or more identical coordinates the operator is really one of lower order: $M^{(2)}(x_i,x_i)$, e.g., only acts on a single coordinate and should be included in $M^{(1)}$.

For the many-body wave functions $\Psi(x_1,x_2,\cdots)$ the situation is slightly more complex. Since the probability density $|\Psi(x_1,x_2,\cdots)|^2$ is an observable, they should transform as one-dimensional (irreducible) representations, i.e., either be symmetric or antisymmetric under particle permutations. Which of the two options applies to a given elementary particle is determined by the spin-statistics theorem [2, 3]: The wave functions of particles with integer spin are symmetric, those of particles with half-integer spin change sign wen arguments are exchanged. From an arbitrary N-particle wave function we thus obtain a many-electron wavefunction by antisymmetrizing

$$\mathcal{S}_-\,\Psi(x_1,\ldots,x_N) := \frac{1}{\sqrt{N!}}\sum_P (-1)^P \Psi\left(x_{p(1)},\ldots,x_{p(N)}\right) , \tag{3}$$

where $(-1)^P$ is the parity of the permutation P that maps $n \to p(n)$. Since there are $N!$ different permutations, this can easily become an extremely costly operation. Remarkably, a product of N single-electron states φ_α can be antisymmetrized much more efficiently (in $\mathcal{O}(N^3)$ steps) by

writing it in the form of a determinant

$$\Phi_{\alpha_1,\ldots,\alpha_N}(x_1,\ldots,x_N) := \frac{1}{\sqrt{N!}} \begin{vmatrix} \varphi_{\alpha_1}(x_1) & \varphi_{\alpha_2}(x_1) & \cdots & \varphi_{\alpha_N}(x_1) \\ \varphi_{\alpha_1}(x_2) & \varphi_{\alpha_2}(x_2) & \cdots & \varphi_{\alpha_N}(x_2) \\ \vdots & \vdots & \ddots & \vdots \\ \varphi_{\alpha_1}(x_N) & \varphi_{\alpha_2}(x_N) & \cdots & \varphi_{\alpha_N}(x_N) \end{vmatrix} . \tag{4}$$

For $N = 1$ the Slater determinant is simply the one-electron orbital $\Phi_\alpha(x) = \varphi_\alpha(x)$ and for $N = 2$ we get the familiar two-electron Slater determinant $\Phi_{\alpha,\alpha'}(x,x') = (\varphi_\alpha(x)\varphi_{\alpha'}(x') - \varphi_{\alpha'}(x)\varphi_\alpha(x'))/\sqrt{2}$.

Slater determinants are important because they can be used to build a basis of the many-electron Hilbert space. To see how, we consider a complete set of orthonormal single-electron states

$$\int dx\, \overline{\varphi_n(x)}\, \varphi_m(x) = \delta_{n,m} \text{ (orthonormal)} \quad \sum_n \overline{\varphi_n(x)}\, \varphi_n(x') = \delta(x - x') \text{ (complete)} . \tag{5}$$

To expand an arbitrary N-particle function $a(x_1,\ldots,x_N)$, we start by considering it as a function of x_1 with $x_2,\ldots,x_N$ kept fixed. We can then expand it in the complete set $\{\varphi_n\}$ as

$$a(x_1,\ldots,x_N) = \sum_{n_1} a_{n_1}(x_2,\ldots,x_N)\, \varphi_{n_1}(x_1)$$

with expansion coefficients

$$a_{n_1}(x_2,\ldots,x_N) = \int dx\, \overline{\varphi_{n_1}(x_1)}\, a(x_1,x_2,\ldots,x_N) .$$

These, in turn, can be expanded as a functions of x_2

$$a_{n_1}(x_2,\ldots,x_N) = \sum_{n_2} a_{n_1,n_2}(x_3,\ldots,x_N)\, \varphi_{n_2}(x_2) .$$

Repeating this, we obtain the expansion of a in product states

$$a(x_1,\ldots,x_N) = \sum_{n_1,\ldots,n_N} a_{n_1,\ldots,n_N}\, \varphi_{n_1}(x_1)\cdots\varphi_{n_N}(x_N) .$$

When the N-particle function Ψ is antisymmetric, the expansion coefficients will be antisymmetric under permutation of the indices $a_{n_{p(1)},\ldots,n_{p(N)}} = (-1)^P a_{n_1,\ldots,n_N}$. Fixing an order of the indices, e.g., $n_1 < n_2 < \ldots < n_N$, we thus get an expansion in Slater determinants

$$\Psi(x_1,\ldots,x_N) = \sum_{n_1<\ldots<n_N} \sqrt{N!}\, a_{n_1,\ldots,n_N}\, \Phi_{n_1,\ldots,n_N}(x_1,\ldots,x_N) .$$

Since we can write any antisymmetric function as such a configuration-interaction expansion, the set of Slater determinants

$$\left\{ \Phi_{n_1,\ldots,n_N}(x_1,\ldots,x_N) \,\middle|\, n_1 < n_2 < \cdots < n_N \right\} \tag{6}$$

forms a basis of the N-electron Hilbert space. Since the overlap of two Slater determinants

$$\int d\boldsymbol{x}\, \overline{\Phi_{\alpha_1,\ldots,\alpha_N}(\boldsymbol{x})}\, \Phi_{\beta_1,\ldots,\beta_N}(\boldsymbol{x}) = \frac{1}{N!}\sum_{P,P'}(-1)^{P+P'}\prod_n \int dx_n\, \overline{\varphi_{\alpha_{p(n)}}(x_n)}\, \varphi_{\alpha_{p'(n)}}(x_n)$$

$$= \langle \Phi_{\alpha_1,\ldots,\alpha_N} | \Phi_{\beta_1,\ldots,\beta_N}\rangle = \begin{vmatrix} \langle\varphi_{\alpha_1}|\varphi_{\beta_1}\rangle & \cdots & \langle\varphi_{\alpha_1}|\varphi_{\beta_N}\rangle \\ \vdots & \ddots & \vdots \\ \langle\varphi_{\alpha_N}|\varphi_{\beta_1}\rangle & \cdots & \langle\varphi_{\alpha_N}|\varphi_{\beta_N}\rangle \end{vmatrix} \tag{7}$$

is the determinant of the overlap of the constituent orbitals, the Slater determinants (6) form a complete orthonormal basis of the N-electron Hilbert space when the orbitals $\varphi_n(x)$ are a complete orthonormal basis of the one-electron Hilbert space.

While we use a set of N one-electron orbitals $\varphi_n(x)$ to define an N-electron Slater determinant $\Phi_{\alpha_1,\ldots,\alpha_N}(\boldsymbol{x})$ (4), this representation is not unique: Any unitary transformation among the N occupied orbitals will not change the determinant. Thus, strictly, a Slater determinant is not determined by the set of indices we usually give, but, up to a phase, by the N-dimensional subspace spanned by the orbitals $\varphi_1, \ldots, \varphi_N$ in the single-electron Hilbert space. The projector to this space is the one-body density matrix

$$\Gamma^{(1)}(x,x') = N\int dx_2\cdots dx_N\, \overline{\Phi(x,x_2,\ldots,x_N)}\,\Phi(x',x_2,\ldots,x_N)\,. \tag{8}$$

To see this, we expand the Slater determinant along its first row

$$\Phi_{\alpha_1\cdots\alpha_N}(x_1,\ldots,x_N) = \frac{1}{\sqrt{N}}\sum_{n=1}^{N}(-1)^{1+n}\,\varphi_{\alpha_n}(x_1)\,\Phi_{\alpha_{i\neq n}}(x_2,\ldots,x_N)\,, \tag{9}$$

where $\Phi_{\alpha_{i\neq n}}(x_2,\ldots,x_N)$ is the determinant with the first row and the n-th column removed, which can be written as $N-1$-electron Slater determinants with orbital α_n removed. Inserting this into (8) we find

$$\Gamma^{(1)}_{\Phi}(x,x') = \sum_{n=1}^{N}\overline{\varphi_{\alpha_n}(x)}\,\varphi_{\alpha_n}(x')\,, \tag{10}$$

which is the expansion of the one-body density matrix in eigenfunctions (natural orbitals) showing that its eigenvalues (natural occupation numbers) are one. Any many-electron wave function $\Psi(\boldsymbol{x})$ with the same one-body density matrix $\Gamma^{(1)}_{\Phi}$ equals $\Phi(\boldsymbol{x})$ up to a phase, i.e., $|\langle\Psi|\Phi\rangle| = 1$.

We can generalize this procedure and calculate higher order density matrices by introducing the generalized Laplace expansion

$$\Phi_{\alpha_1\cdots\alpha_N}(\mathbf{x}) = \frac{1}{\sqrt{\binom{N}{p}}}\sum_{n_1<\cdots<n_p}(-1)^{1+\sum_i n_i}\,\Phi_{\alpha_{n_1}\cdots\alpha_{n_p}}(x_1,\ldots,x_p)\Phi_{\alpha_{i\notin\{n_1,\ldots,n_p\}}}(x_{p+1},\ldots,x_N),$$

which is obtained by writing the permutation of all N indices as a permutation of $N-p$ indices and the remaining p indices separately summing over all distinct sets of p indices. This allows us to evaluate arbitrary matrix elements and higher order density matrices [4]. But as can be seen from the above expansion, the expressions very quickly get quite cumbersome. Fortunately there is a representation that is much better suited to handling antisymmetric wave functions. It is called second quantization.

2 Second quantization

While originally introduced for quantizing the electromagnetic field, we can use the formalism of second quantization just as a convenient way of handling antisymmetric wave functions [5,6]. The idea behind this approach is remarkably simple: When writing Slater determinants in the form (4) we are working in a real-space basis. It is, however, often better not to work in a specific basis but to consider abstract states: Instead of a wave function $\varphi_\alpha(x)$, we write a Dirac state $|\alpha\rangle$. Second quantization allows us to do the same for Slater determinants.
Let us consider a Slater determinant for two electrons, one in state $\varphi_\alpha(x)$, the other in state $\varphi_\beta(x)$. It is simply the antisymmetrized product of the two states

$$\Phi_{\alpha\beta}(x_1, x_2) = \frac{1}{\sqrt{2}} \big(\varphi_\alpha(x_1)\varphi_\beta(x_2) - \varphi_\beta(x_1)\varphi_\alpha(x_2)\big) . \tag{11}$$

This expression is quite cumbersome because we explicitly specify the coordinates. We can get rid of the coordinates by defining a two-particle Dirac state

$$|\alpha, \beta\rangle := \frac{1}{\sqrt{2}} \big(|\alpha\rangle|\beta\rangle - |\beta\rangle|\alpha\rangle\big) .$$

While the expression is already simpler, we still have to keep track of the order of the particles by specifying the position of the kets. The idea of second quantization is to specify the states using operators

$$c_\beta^\dagger c_\alpha^\dagger |0\rangle = |\alpha, \beta\rangle . \tag{12}$$

Now the order of the particles is specified by the order of the operators. To ensure the antisymmetry of the wave function the operators have to change sign when they are reordered

$$|\alpha, \beta\rangle = c_\beta^\dagger c_\alpha^\dagger |0\rangle = -c_\alpha^\dagger c_\beta^\dagger |0\rangle = -|\beta, \alpha\rangle . \tag{13}$$

Naturally, this also implies the Pauli principle for the special case $\beta = \alpha$.

2.1 Creation and annihilation operators

To arrive at the formalism of second quantization we postulate a set of operators that have certain reasonable properties. We then verify that we can use these operators to represent Slater determinants. But first we consider a few simple states to motivate what properties the new operators should have.
To be able to construct many-electron states we start from the simplest such state: $|0\rangle$ the *vacuum state* with no electron, which we assume to be normalized $\langle 0|0\rangle = 1$. Next we introduce for each single-electron state $|\alpha\rangle$ an operator $c_\alpha^\dagger$ such that $c_\alpha^\dagger|0\rangle = |\alpha\rangle$. These operators are called *creation operators* since they add an electron (in state α) to the state that they act on: in $c_\alpha^\dagger|0\rangle$ the creation operator adds an electron to the vacuum state ($N = 0$), resulting in a single-electron state. Applying another creation operator produces a two-electron state $c_\beta^\dagger c_\alpha^\dagger|0\rangle$. As we have seen above, to ensure the antisymmetry of the two electron state, the product of

creation operators has to change sign when they are reordered: $c^\dagger_\alpha c^\dagger_\beta = -c^\dagger_\beta c^\dagger_\alpha$. This is more conveniently written as $\{c^\dagger_\alpha,\, c^\dagger_\beta\} = 0$ by introducing the *anti-commutator*

$$\{A,\, B\} := A\,B + B\,A\,. \tag{14}$$

As we have seen, the simplest state we can produce with the creation operators is the single-electron state $|\alpha\rangle = c^\dagger_\alpha|0\rangle$. When we want to calculate its norm, we have to consider the adjoint of $c^\dagger_\alpha|0\rangle$, formally obtaining $\langle\alpha|\alpha\rangle = \langle 0|c_\alpha c^\dagger_\alpha|0\rangle$, or, more generally, $\langle\alpha|\beta\rangle = \langle 0|c_\alpha c^\dagger_\beta|0\rangle$. This must mean that c_α, the adjoint of a creation operator, must remove an electron from the state, otherwise the overlap of $c_\alpha c^\dagger_\beta|0\rangle$ with the vacuum state $\langle 0|$ would vanish. We therefore call the adjoint of the creation operator an *annihilation operator*. We certainly cannot take an electron out of the vacuum state, so $c_\alpha|0\rangle = 0$. To obtain the correct overlap of one-electron states as $\langle\alpha|\beta\rangle = \langle 0|c_\alpha c^\dagger_\beta|0\rangle$ we postulate the anticommutation relation $\{c_\alpha, c^\dagger_\beta\} = \langle\alpha|\beta\rangle$. For completeness, taking the adjoint of the anticommutation relation for the creation operators, we obtain the corresponding anticommutator of the annihilators: $\{c_\alpha,\, c_\beta\} = 0$.
Thus, we define the vacuum state $|0\rangle$ and the set of operators c_α related to single-electron states $|\alpha\rangle$ with the properties

$$\boxed{\begin{array}{ll} c_\alpha|0\rangle = 0 & \big\{c_\alpha,\, c_\beta\big\} = 0 = \big\{c^\dagger_\alpha,\, c^\dagger_\beta\big\} \\ \langle 0|0\rangle = 1 & \big\{c_\alpha,\, c^\dagger_\beta\big\} = \langle\alpha|\beta\rangle \end{array}} \tag{15}$$

We note that the creators and annihilators are not ordinary operators in a Hilbert space, but transfer states from an N-electron to a $N \pm 1$-electron Hilbert space, i.e., they are operators defined on *Fock space*. It is also remarkable that the mixed anti-commutator is the only place where the orbitals that distinguish different operators enter. Moreover, despite being operators, the creators transform in the same way as the single-electron states they represent while the vacuum state is invariant:

$$|\tilde\alpha_i\rangle = \sum_\mu |\alpha_\mu\rangle\, U_{\mu i} \qquad \rightsquigarrow \quad \tilde c^\dagger_{\tilde\alpha_i}|0\rangle = \sum_\mu c^\dagger_{\alpha_\mu}|0\rangle\, U_{\mu i} = \left(\sum_\mu c^\dagger_{\alpha_\mu} U_{\mu i}\right)|0\rangle. \tag{16}$$

A set of operators that allows us to make contact with the notation of first quantization are the *field operators* $\hat\Psi^\dagger(x)$, with $x = (r,\sigma)$, that create an electron of spin σ at position r, i.e., in state $|x\rangle = |r,\sigma\rangle$. Given a complete, orthonormal set of orbitals $\{\varphi_n\}$, we can expand $|x\rangle$

$$\hat\Psi^\dagger(x)|0\rangle = |x\rangle = \sum_n |\varphi_n\rangle\langle\varphi_n|x\rangle = \sum_n \langle\varphi_n|x\rangle\, c^\dagger_{\varphi_n}|0\rangle \tag{17}$$

from which we obtain

$$\hat\Psi^\dagger(x) = \sum_n \overline{\langle x|\varphi_n\rangle}\, c^\dagger_{\varphi_n} = \sum_n \overline{\varphi_n(x)}\, c^\dagger_{\varphi_n}. \tag{18}$$

The anticommutators then follow from (15) for an orthonormal and complete set, e.g.,

$$\big\{\hat\Psi(x),\, \hat\Psi^\dagger(x')\big\} = \sum_{n,m}\langle x|\varphi_n\rangle \underbrace{\big\{c_{\varphi_n},\, c^\dagger_{\varphi_m}\big\}}_{=\delta_{n,m}} \langle\varphi_m|x'\rangle = \sum_n \langle x|\varphi_n\rangle\langle\varphi_n|x'\rangle = \langle x|x'\rangle = \delta(x-x'),$$

resulting in the anticommutation relations for the field operators

$$\left\{\hat{\Psi}(x),\, \hat{\Psi}(x')\right\} = 0 = \left\{\hat{\Psi}^\dagger(x),\, \hat{\Psi}^\dagger(x')\right\} \quad \text{and} \quad \left\{\hat{\Psi}(x),\, \hat{\Psi}^\dagger(x')\right\} = \langle x|x'\rangle. \tag{19}$$

We can, of course, expand the field operators also in a non-orthogonal set of orbitals $\{|\chi_i\rangle\}$, as long as it is complete, $\sum_{i,j} |\chi_i\rangle (S^{-1})_{ij} \langle\chi_j| = \mathbb{1}$, where $S_{ij} = \langle\chi_i|\chi_j\rangle$ is the overlap matrix

$$\hat{\Psi}^\dagger(x) = \sum_{i,j} c_i^\dagger \, (S^{-1})_{ij} \, \langle\chi_j|x\rangle. \tag{20}$$

Conversely, given any single-electron wave functions in real space $\varphi(x)$, we can express the corresponding creation operator in terms of the field operators

$$c_\varphi^\dagger = \int dx \, \varphi(x) \, \hat{\Psi}^\dagger(x). \tag{21}$$

Its anticommutator with the field operators just gives back the single-electron wave function

$$\left\{\hat{\Psi}(x),\, c_\varphi^\dagger\right\} = \int dx' \, \varphi(x') \left\{\hat{\Psi}(x),\, \hat{\Psi}^\dagger(x')\right\} = \varphi(x)\,. \tag{22}$$

2.2 Representation of Slater determinants

We have now all the tools in place to write the Slater determinant (4) in second quantization, using the creation operators to specify the occupied orbitals and the field operators to define the coordinates for the real-space representation

$$\Phi_{\alpha_1\alpha_2\ldots\alpha_N}(x_1, x_2, \ldots, x_N) = \frac{1}{\sqrt{N!}} \left\langle 0 \,\middle|\, \hat{\Psi}(x_1)\hat{\Psi}(x_2)\ldots\hat{\Psi}(x_N)\, c_{\alpha_N}^\dagger \ldots c_{\alpha_2}^\dagger c_{\alpha_1}^\dagger \,\middle|\, 0 \right\rangle. \tag{23}$$

Not surprisingly, the proof is by induction. As a warm-up we consider the case of a single-electron wave function ($N = 1$). Using the anticommutation relation (22), we see that

$$\left\langle 0 \,\middle|\, \hat{\Psi}(x_1)\, c_{\alpha_1}^\dagger \,\middle|\, 0 \right\rangle = \left\langle 0 \,\middle|\, \varphi_{\alpha_1}(x_1) - c_{\alpha_1}^\dagger \hat{\Psi}(x_1) \,\middle|\, 0 \right\rangle = \varphi_{\alpha_1}(x_1)\,. \tag{24}$$

For the two-electron state $N = 2$, we anticommute $\hat{\Psi}(x_2)$ in two steps to the right

$$\begin{aligned}
\left\langle 0 \,\middle|\, \hat{\Psi}(x_1)\hat{\Psi}(x_2)\, c_{\alpha_2}^\dagger c_{\alpha_1}^\dagger \,\middle|\, 0 \right\rangle &= \left\langle 0 \,\middle|\, \hat{\Psi}(x_1) \left(\varphi_{\alpha_2}(x_2) - c_{\alpha_2}^\dagger \hat{\Psi}(x_2)\right) c_{\alpha_1}^\dagger \,\middle|\, 0 \right\rangle \\
&= \left\langle 0 \,\middle|\, \hat{\Psi}(x_1) c_{\alpha_1}^\dagger \,\middle|\, 0 \right\rangle \, \varphi_{\alpha_2}(x_2) - \left\langle 0 \,\middle|\, \hat{\Psi}(x_1) c_{\alpha_2}^\dagger \hat{\Psi}(x_2) c_{\alpha_1}^\dagger \,\middle|\, 0 \right\rangle \\
&= \varphi_{\alpha_1}(x_1)\varphi_{\alpha_2}(x_2) - \varphi_{\alpha_2}(x_1)\varphi_{\alpha_1}(x_2)\,.
\end{aligned} \tag{25}$$

We see how anticommuting automatically produces the appropriate signs for the antisymmetric wave function. Dividing by $\sqrt{2}$, we obtain the desired two-electron Slater determinant.

The general case of an N-electron state works just the same. Anti-commuting $\hat\Psi(x_N)$ all the way to the right produces $N-1$ terms with alternating sign

$$\begin{aligned}
\Big\langle 0 \Big| \hat\Psi(x_1)\dots\hat\Psi(x_{N-1})\hat\Psi(x_N)\, c^\dagger_{\alpha_N} c^\dagger_{\alpha_{N-1}}\dots c^\dagger_{\alpha_1} \Big| 0\Big\rangle \;=& \\
+ \quad \Big\langle 0 \Big| \hat\Psi(x_1)\dots\hat\Psi(x_{N-1})\, c^\dagger_{\alpha_{N-1}}\dots c^\dagger_{\alpha_1} \Big| 0\Big\rangle \;& \varphi_{\alpha_N}(x_N) \\
- \quad \Big\langle 0 \Big| \hat\Psi(x_1)\dots\hat\Psi(x_{N-1})\textstyle\prod_{n\neq N-1} c^\dagger_{\alpha_n} \Big| 0\Big\rangle \;& \varphi_{\alpha_{N-1}}(x_N) \\
\vdots& \\
(-1)^N \Big\langle 0 \Big| \hat\Psi(x_1)\dots\hat\Psi(x_{N-1})\, c^\dagger_{\alpha_N} \;\dots\; c^\dagger_{\alpha_2} \Big| 0\Big\rangle \;& \varphi_{\alpha_1}(x_N)\,.
\end{aligned}$$

Using (23) for the $N-1$-electron states, this is nothing but the Laplace expansion of

$$D = \begin{vmatrix} \varphi_{\alpha_1}(x_1) & \varphi_{\alpha_2}(x_1) & \cdots & \varphi_{\alpha_N}(x_1) \\ \varphi_{\alpha_1}(x_2) & \varphi_{\alpha_2}(x_2) & \cdots & \varphi_{\alpha_N}(x_2) \\ \vdots & \vdots & \ddots & \vdots \\ \varphi_{\alpha_1}(x_N) & \varphi_{\alpha_2}(x_N) & \cdots & \varphi_{\alpha_N}(x_N) \end{vmatrix}$$

along the Nth row. Dividing by $\sqrt{N!}$ we see that we have shown (23) for N-electron states, completing the proof by induction.
Thus, as we can write the representation of a single-electron state $|\varphi\rangle$ in real-space as the matrix element $\langle x|\varphi\rangle = \varphi(x)$, we can obtain the representation of the N-electron $\prod c^\dagger_{\alpha_n}|0\rangle$ as the matrix element with the field operators $\langle 0|\prod\hat\Psi(x_n)$. Thus, we can rewrite the basis (6) for the N-electron states in a form independent of the real-space representation

$$\left\{ c^\dagger_{n_N}\cdots c^\dagger_{n_1}|0\rangle \;\middle|\; n_1<\cdots<n_N \right\}, \tag{26}$$

which allows us to write any N-electron state as

$$|\Psi\rangle = \sum_{n_1<\cdots<n_N} a_{n_1,\dots,n_N}\, c^\dagger_{n_N}\cdots c^\dagger_{n_1}|0\rangle. \tag{27}$$

From this we see that, for an orthonormal basis, the expectation value of the *occupation number operator* $\hat n_i = c_i^\dagger c_i$ is the probability that state φ_{n_i} is occupied

$$\langle\Psi|\hat n_i|\Psi\rangle = \sum_{n_i\in\{n1<\cdots<n_N\}} |a_{n_1,\dots,n_N}|^2, \tag{28}$$

since only determinants that contain φ_{n_i} contribute. The sum of all these operators $\hat N = \sum_i \hat n_i$ is the number operator, since now each determinant contributes N times

$$\langle\Psi|\sum_i \hat n_i|\Psi\rangle = \sum_i \sum_{n_i\in\{n1<\cdots<n_N\}} |a_{n_1,\dots,n_N}|^2 = N\,. \tag{29}$$

For the special case of the field operators we obtain the density operator $\hat n(x) = \hat\Psi^\dagger(x)\hat\Psi(x)$ and $\hat N = \int dx\,\hat\Psi^\dagger(x)\hat\Psi(x)$.

2.3 Representation of n-body operators

Having established the relation between product states and Slater determinants, it is straightforward to express the matrix elements of a general n-body operator (2)

$$M(\mathbf{x}) = M^{(0)} + \sum_i M^{(1)}(x_i) + \sum_{i<j} M^{(2)}(x_i, x_j) + \sum_{i<j<k} M^{(3)}(x_i, x_j, x_k) + \cdots \tag{30}$$

with N-electron Slater determinants:

$$\begin{aligned}
&\int dx_1 \cdots dx_N \, \overline{\Phi_{\beta_1 \cdots \beta_N}(x_1, \cdots, x_N)} \, M(x_1, \ldots, x_N) \, \Phi_{\alpha_1 \cdots \alpha_N}(x_1, \cdots, x_N) \\
= &\int dx_1 \cdots dx_N \, \langle 0 | c_{\beta_1} \cdots c_{\beta_N} \hat{\Psi}^\dagger(x_N) \cdots \hat{\Psi}^\dagger(x_1) | 0 \rangle M(x_1, \ldots, x_N) \langle 0 | \hat{\Psi}(x_1) \cdots \hat{\Psi}(x_N) c^\dagger_{\alpha_N} \cdots c^\dagger_{\alpha_1} | 0 \rangle \\
&= \left\langle 0 \,\middle|\, c_{\beta_1} \cdots c_{\beta_N} \, \hat{M} \, c^\dagger_{\alpha_N} \cdots c^\dagger_{\alpha_1} \,\middle|\, 0 \right\rangle
\end{aligned}$$

with the representation of the n-body operator in terms of field operators

$$\hat{M} = \frac{1}{N!} \int dx_1 \cdots x_N \, \hat{\Psi}^\dagger(x_N) \cdots \hat{\Psi}^\dagger(x_1) \, M(x_1, \cdots, x_N) \, \hat{\Psi}(x_1) \cdots \hat{\Psi}(x_N) \, . \tag{31}$$

Note that this particular form of the operator is only valid when applied to N-electron states, since we have used that the N annihilation operators bring us to the zero-electron space, where $|0\rangle\langle 0| = \mathbb{1}$. Keeping this in mind, we can work entirely in terms of our algebra (15).
To see what (31) means we look at its parts (30). We start with the simplest case, the zero-body operator, which, up to a trivial prefactor, is $M^{(0)}(x_1, \cdots, x_N) = 1$. Operating on an N-electron wave function, it gives

$$\begin{aligned}
\hat{M}^{(0)} &= \frac{1}{N!} \int dx_1 dx_2 \cdots x_N \, \hat{\Psi}^\dagger(x_N) \cdots \hat{\Psi}^\dagger(x_2) \hat{\Psi}^\dagger(x_1) \, \hat{\Psi}(x_1) \hat{\Psi}(x_2) \cdots \hat{\Psi}(x_N) \\
&= \frac{1}{N!} \int \quad dx_2 \cdots x_N \, \hat{\Psi}^\dagger(x_N) \cdots \hat{\Psi}^\dagger(x_2) \qquad \hat{N} \qquad \hat{\Psi}(x_2) \cdots \hat{\Psi}(x_N) \\
&= \frac{1}{N!} \int \quad dx_2 \cdots x_N \, \hat{\Psi}^\dagger(x_N) \cdots \hat{\Psi}^\dagger(x_2) \qquad 1 \qquad \hat{\Psi}(x_2) \cdots \hat{\Psi}(x_N) \\
&\;\;\vdots \\
&= \frac{1}{N!} \, 1 \cdot 2 \, \cdots \, N = 1 \, ,
\end{aligned} \tag{32}$$

where we have used that

$$\int dx \, \hat{\Psi}^\dagger(x) \hat{\Psi}(x) = \hat{N}$$

is the number operator and that applying n annihilation operators $\hat{\Psi}(x_j)$ to an N-electron state gives a state with $N - n$ electrons. We note that we obtain a form of $\hat{M}^{(0)} = 1$ that, contrary to (31), no longer depend on the number of electrons in the wave function that it is applied to.

2.3.1 One-body operators

Next we consider one-body operators $M(x_1,\ldots,x_N)=\sum_j M^{(1)}(x_j)$

$$\begin{aligned}\hat{M}^{(1)} &= \frac{1}{N!}\int dx_1\cdots dx_N\,\hat\Psi^\dagger(x_N)\cdots\hat\Psi^\dagger(x_1)\sum_j M^{(1)}(x_j)\;\hat\Psi(x_1)\cdots\hat\Psi(x_N)\\ &= \frac{1}{N!}\sum_j\int dx_j\,\hat\Psi^\dagger(x_j)\,M^{(1)}(x_j)\,(N-1)!\,\hat\Psi(x_j)\\ &= \frac{1}{N}\sum_j\int dx_j\,\hat\Psi^\dagger(x_j)\,M^{(1)}(x_j)\,\hat\Psi(x_j)\\ &= \int dx\quad\hat\Psi^\dagger(x)\;\;M^{(1)}(x)\;\;\hat\Psi(x)\end{aligned}$$

Here we have first anticommuted $\hat\Psi^\dagger(x_j)$ all the way to the left and $\hat\Psi(x_j)$ to the right. Since these take the same numbers of anticommutations, there is no sign involved. The operation leaves the integrals over the variables except x_i, a zero-body operator for $N-1$ electron states, operating on $\hat\Psi(x_j)|N\text{-electron state}\rangle$. Again we notice that we obtain an operator that no longer depends on the number of electrons, i.e., that is valid in the entire Fock space.
Expanding the field-operators in a complete orthonormal set $\hat\Psi(x)=\sum_n\varphi_n(x)\,c_n$ gives

$$\hat{M}^{(1)}=\sum_{n,m}\int dx\,\overline{\varphi_n(x)}\,M(x)\,\varphi_m(x)\;c_n^\dagger c_m=\sum_{n,m}\langle\varphi_n|M^{(1)}|\varphi_m\rangle\;c_n^\dagger c_m=\sum_{n,m}c_n^\dagger\,M^{(1)}_{nm}\,c_m.\quad(33)$$

The matrix elements $M^{(1)}_{nm}=\langle\varphi_n|M^{(1)}|\varphi_m\rangle$ transforms like a single-electron matrix $\boldsymbol{M}^{(1)}$: From (16) and writing the annihilation operators as a column vector $\boldsymbol{c}$ we see that

$$\hat{M}^{(1)}=\boldsymbol{c}^\dagger\,\boldsymbol{M}^{(1)}\,\boldsymbol{c}\;=\boldsymbol{c}^\dagger\boldsymbol{U}^\dagger\,\boldsymbol{U}\boldsymbol{M}^{(1)}\boldsymbol{U}^\dagger\,\boldsymbol{U}\boldsymbol{c}=\tilde{\boldsymbol{c}}^\dagger\,\tilde{\boldsymbol{M}}^{(1)}\,\tilde{\boldsymbol{c}}\,.\quad(34)$$

Once we have arrived at the representation in terms of orbitals, we can restrict the orbital basis to a non-complete set. This simply gives the operator in the variational (Fock) subspace spanned by the orbitals.

2.3.2 Two-body operators

For the two-body operators $M(x_1,\ldots,x_N)=\sum_{i<j}M^{(2)}(x_i,x_j)$ we proceed in the familiar way, anti-commuting first the operators with the coordinates involved in $M^{(2)}$ all the way to the left and right, respectively. This time we are left with a zero-body operator for $N-2$ electrons:

$$\begin{aligned}\hat{M}^{(2)} &= \frac{1}{N!}\int dx_1\cdots dx_N\,\hat\Psi^\dagger(x_N)\cdots\hat\Psi^\dagger(x_1)\sum_{i<j}M^{(2)}(x_i,x_j)\;\hat\Psi(x_1)\cdots\hat\Psi(x_N)\\ &= \frac{1}{N!}\sum_{i<j}\int dx_i dx_j\,\hat\Psi^\dagger(x_j)\hat\Psi^\dagger(x_i)\,M^{(2)}(x_i,x_j)\,(N-2)!\,\hat\Psi(x_i)\hat\Psi(x_j)\\ &= \frac{1}{N(N-1)}\sum_{i<j}\int dx_i dx_j\,\hat\Psi^\dagger(x_j)\hat\Psi^\dagger(x_i)\,M^{(2)}(x_i,x_j)\,\hat\Psi(x_i)\hat\Psi(x_j)\\ &= \frac{1}{2}\int dx\,dx'\,\hat\Psi^\dagger(x')\,\hat\Psi^\dagger(x)\;\;M^{(2)}(x,x')\;\;\hat\Psi(x)\,\hat\Psi(x')\end{aligned}$$

Expanding in an orthonormal basis, we get

$$\begin{aligned}\hat{M}^{(2)} &= \frac{1}{2}\sum_{n,n',m,m'} \int dx dx' \, \overline{\varphi_{n'}(x')\varphi_n(x)}\, M^{(2)}(x,x')\, \varphi_m(x)\varphi_{m'}(x') \quad c^\dagger_{n'}c^\dagger_n c_m c_{m'} \\ &= \frac{1}{2}\sum_{n,n',m,m'} \langle \varphi_n\varphi_{n'}|M^{(2)}|\varphi_m\varphi_{m'}\rangle \qquad\qquad c^\dagger_{n'}c^\dagger_n c_m c_{m'} \end{aligned} \tag{35}$$

where the exchange of the indices in the second line is a consequence of the way the Dirac state for two electrons is usually written: first index for the first coordinate, second index for the second, while taking the adjoint of the operators changes their order. $M_{nn',\,mm'} = \langle \varphi_n\varphi_{n'}|M^{(2)}|\varphi_m\varphi_{m'}\rangle$ transforms like a fourth-order tensor: Transforming to a different basis (16) gives

$$\tilde{M}^{(2)}_{\nu\nu',\mu\mu'} = \sum_{n,n',m,m'} U^\dagger_{\nu n} U^\dagger_{\nu' n'} M_{nn',mm'} U_{m\mu} U_{m'\mu'} \,. \tag{36}$$

Form the symmetry of the two-body operator $M^{(2)}(x,x') = M^{(2)}(x',x)$ follows $M_{nn',\,mm'} = M_{n'n,\,m'm}$. Moreover, $M_{nn,\,mm'}$ will not contribute to $\hat{M}^{(2)}$ since $c^\dagger_n c^\dagger_n = \{c^\dagger_n,\, c^\dagger_n\}/2 = 0$, and likewise for $M_{nn',\,mm}$.

Note that the representation (35) is not quite as efficient as it could be: The terms with n and n' and/or m and m' exchanged connect the same basis states. Collecting these terms by introducing an ordering of the operators and using the symmetry of the matrix elements we obtain

$$\hat{M}^{(2)} = \sum_{n'>n,m'>m} c^\dagger_{n'}c^\dagger_n \underbrace{\left(M^{(2)}_{nn',\,mm'} - M^{(2)}_{n'n,\,mm'}\right)}_{=:\breve{M}^{(2)}_{nn',\,mm'}} c_m c_{m'} \,. \tag{37}$$

Since the states $\{c^\dagger_{n'}c^\dagger_n|0\rangle \mid n'>n\}$ form a basis of the two-electron Hilbert space, considering nn' as the index of a basis state, the $\breve{M}^{(2)}_{nn',\,mm'}$ form a two-electron matrix $\breve{\boldsymbol{M}}^{(2)}$.

The procedure of rewriting operators in second quantization obviously generalizes to operators acting on more than two electrons in the natural way. We note that, while we started from a form of the operators (30) that was explicitly formulated in an N-electron Hilbert space, the results (32), (33), and (35) are of the same form no matter what value N takes. Thus these operators are valid not just on some N-electron Hilbert space, but on the entire Fock space. This is a particular strength of the second-quantized formulation.

2.4 Reduced density matrices and Wick's theorem

Introducing reduced density matrices it is straightforward to evaluate expectation values for general many-electron states. From the representation of single-electron operators (33) we find

$$\langle\Psi|M^{(1)}|\Psi\rangle = \sum_{n,m} M^{(1)}_{nm} \underbrace{\langle\Psi|c^\dagger_n c_m|\Psi\rangle}_{=:\Gamma^{(1)}_{nm}} = \operatorname{Tr} \boldsymbol{\Gamma}^{(1)}\boldsymbol{M}^{(1)}, \tag{38}$$

where the trace is over the one-electron basis and we use that observables are hermitian. For two-electron operators (37) we find

$$\langle\Psi|M^{(2)}|\Psi\rangle = \sum_{n'>n,\,m'>m} \breve{M}^{(2)}_{nn',\,mm'} \underbrace{\langle\Psi|c^\dagger_{n'}c^\dagger_n c_m c_{m'}|\Psi\rangle}_{=:\breve{\Gamma}^{(2)}_{nn',\,mm'}} = \operatorname{Tr}\breve{\boldsymbol{\Gamma}}^{(2)}\breve{\boldsymbol{M}}^{(2)}, \tag{39}$$

where now the trace in over the two-electron basis. In general, if we know the p-body density matrix $\breve{\boldsymbol{\Gamma}}^{(p)}$ for a given many-electron state $|\Psi\rangle$, we can calculate the expectation value of any operator of order up to p. We can obtain lower-order density matrices by taking partial traces over higher-order matrices, e.g.,

$$\sum_k \Gamma^{(2)}_{nk,\,mk} = \sum_k \langle\Psi|c^\dagger_n c^\dagger_k c_k c_m|\Psi\rangle = \langle\Psi|c^\dagger_n\,\hat{N}\,c_m|\Psi\rangle = (N-1)\,\Gamma^{(1)}_{nm}\,. \tag{40}$$

Note the similarity to (32). In terms of the two-electron matrix $\breve{\boldsymbol{\Gamma}}^{(2)}$ we trace (keeping track of the Fermion sign) over all two-electron states with orbital n or m occupied.
For Slater determinants $|\Phi\rangle = c^\dagger_{\alpha_N}\cdots c^\dagger_{\alpha_1}|0\rangle$ the density matrices have a particularly simple form. To see this we introduce the projection onto the space of occupied orbitals assuming, for simplicity, that the orbitals $|\alpha_n\rangle$ are orthonormal

$$P = \sum_n |\alpha_n\rangle\langle\alpha_n|\,. \tag{41}$$

We can then split any orbital into its components in the occupied and the virtual space: $|\varphi\rangle = P|\varphi\rangle + (\mathbb{1}-P)|\varphi\rangle$. Applying an annihilation operator to the Slater determinant we then find that only the component in the virtual space gives a zero contribution, similarly for a creation operator:

$$c_{|\varphi\rangle}|\Phi\rangle = c_{P|\varphi\rangle}|\Phi\rangle \qquad \text{and} \quad c^\dagger_{|\varphi\rangle}|\Phi\rangle = c^\dagger_{(\mathbb{1}-P)|\varphi\rangle}|\Phi\rangle. \tag{42}$$

The one-body density matrix of a Slater determinant is thus given by

$$\begin{aligned}\Gamma^{(1)}_{nm} &= \langle\Phi|c^\dagger_n c_m|\Phi\rangle = \langle\Phi|c^\dagger_{P|\varphi_n\rangle}c_{P|\varphi_m\rangle}|\Phi\rangle = \langle P\varphi_m|P\varphi_n\rangle\langle\Phi|\Phi\rangle - \langle\Phi|c_{P|\varphi_m\rangle}c^\dagger_{P|\varphi_n\rangle}|\Phi\rangle \\ &= \langle\varphi_m|P|\varphi_n\rangle.\end{aligned} \tag{43}$$

As an operator in the one-electron Hilbert space $\mathcal{H}^{(1)}$, the one-body density matrix of a Slater determinant is thus the projector onto the occupied subspace. Up to a phase factor it defines the Slater determinant uniquely. All higher-order density matrices of a Slater determinant can thus be written in terms of the one-body density matrix. For the two-body density matrix we find, simply commuting $c^\dagger_{P|n_1\rangle}$ to the right (note the similarity to the derivation in Sec. 2.2)

$$\begin{aligned}\langle\Phi|c^\dagger_{n_2}c^\dagger_{n_1}c_{m_1}c_{m_2}|\Phi\rangle &= \langle\Phi|c^\dagger_{Pn_2}c^\dagger_{Pn_1}c_{Pm_1}c_{Pm_2}|\Phi\rangle \\ &= \langle Pm_1|Pn_1\rangle\langle\Phi|c^\dagger_{Pn_2}c_{Pm_2}|\Phi\rangle - \langle\Phi|c^\dagger_{Pn_2}c_{Pm_1}c^\dagger_{Pn_1}c_{Pm_2}|\Phi\rangle \\ &= \Gamma^{(1)}_{n_1m_1}\Gamma^{(1)}_{n_2m_2} - \langle Pm_2|Pn_1\rangle\langle\Phi|c^\dagger_{Pn_2}c_{Pm_1}|\Phi\rangle + \langle\Phi|c^\dagger_{Pn_2}c_{Pm_1}c_{Pm_2}c^\dagger_{Pn_1}|\Phi\rangle \\ &= \det\begin{pmatrix}\Gamma^{(1)}_{n_1m_1} & \Gamma^{(1)}_{n_1m_2}\\ \Gamma^{(1)}_{n_2m_1} & \Gamma^{(1)}_{n_2m_2}\end{pmatrix}.\end{aligned} \tag{44}$$

Using the same procedure together with the Laplace expansion we find the higher-order density matrices

$$\langle \Phi | c^\dagger_{n_p} \cdots c^\dagger_{n_1} c_{m_1} \cdots c_{m_p} | \Phi \rangle = \det \begin{pmatrix} \Gamma^{(1)}_{n_1 m_1} & \cdots & \Gamma^{(1)}_{n_1 m_p} \\ \vdots & \ddots & \vdots \\ \Gamma^{(1)}_{n_p m_1} & \cdots & \Gamma^{(1)}_{n_p m_p} \end{pmatrix}. \tag{45}$$

Matrix elements between different Slater determinants are not quite as simple, as the terms with the creation operator anticommuted to the right need no longer vanish. Still, we can express expectation values as determinants using (7)

$$\langle \Phi_{\boldsymbol{\alpha}} | \Phi_{\boldsymbol{\beta}} \rangle = \det \begin{pmatrix} \langle \alpha_1 | \beta_1 \rangle & \cdots & \langle \alpha_1 | \beta_N \rangle \\ \vdots & \ddots & \vdots \\ \langle \alpha_N | \beta_1 \rangle & \cdots & \langle \alpha_N | \beta_N \rangle \end{pmatrix}. \tag{46}$$

The overlap is non-zero if each vector in the occupied space of $|\Phi_{\boldsymbol{\alpha}}\rangle$ has a component in the occupied space of $|\Phi_{\boldsymbol{\beta}}\rangle$, i.e., $P_{\boldsymbol{\beta}} |\alpha_n\rangle \neq 0$, or, more symmetrically, $\dim(P_{\boldsymbol{\beta}} P_{\boldsymbol{\alpha}} \mathcal{H}^{(1)}) = N$. Note that the combination of the two projectors $P_{\boldsymbol{\alpha}} P_{\boldsymbol{\beta}}$ is, in general, no longer a projection.
To evaluate the matrix element for a one-electron operator we simply change the order of the operators to obtain an expression that is given by a determinant

$$\begin{aligned}
\langle \Phi_{\boldsymbol{\alpha}} | c^\dagger_n c_m | \Phi_{\boldsymbol{\beta}} \rangle &= \langle \Phi_{\boldsymbol{\alpha}} | c^\dagger_{P_{\boldsymbol{\alpha}} n} c_{P_{\boldsymbol{\beta}} m} | \Phi_{\boldsymbol{\beta}} \rangle \\
&= \langle \varphi_m | P_{\boldsymbol{\beta}} P_{\boldsymbol{\alpha}} | \varphi_n \rangle \langle \Phi_{\boldsymbol{\alpha}} | \Phi_{\boldsymbol{\beta}} \rangle - \langle \Phi_{\boldsymbol{\alpha}} | c_{P_{\boldsymbol{\beta}} m} c^\dagger_{P_{\boldsymbol{\alpha}} n} | \Phi_{\boldsymbol{\beta}} \rangle \\
&= \langle \varphi_m | P_{\boldsymbol{\beta}} P_{\boldsymbol{\alpha}} | \varphi_n \rangle \langle \Phi_{\boldsymbol{\alpha}} | \Phi_{\boldsymbol{\beta}} \rangle - \det \begin{pmatrix} \langle \alpha_1 | \varphi_n \rangle & \langle \alpha_1 | \beta_1 \rangle & \cdots & \langle \alpha_1 | \beta_N \rangle \\ \vdots & \vdots & & \vdots \\ \langle \alpha_N | \varphi_n \rangle & \langle \alpha_N | \beta_1 \rangle & \cdots & \langle \alpha_N | \beta_N \rangle \\ \langle \varphi_m | P_{\boldsymbol{\beta}} P_{\boldsymbol{\alpha}} | \varphi_n \rangle & \langle \varphi_m | \beta_1 \rangle & \cdots & \langle \varphi_m | \beta_N \rangle \end{pmatrix} \\
&= \langle \varphi_m | P_{\boldsymbol{\beta}} P_{\boldsymbol{\alpha}} | \varphi_n \rangle \langle \Phi_{\boldsymbol{\alpha}} | \Phi_{\boldsymbol{\beta}} \rangle - \langle \Phi_{\boldsymbol{\alpha}, P_{\boldsymbol{\beta}} \varphi_m} | \Phi_{\boldsymbol{\beta}, P_{\boldsymbol{\alpha}} \varphi_n} \rangle.
\end{aligned} \tag{47}$$

For $|\Phi_{\boldsymbol{\alpha}}\rangle = |\Phi_{\boldsymbol{\beta}}\rangle$ we recover (43). Higher-order expectation values are calculated in a similar way, moving the creation operators successively to the right, giving, e.g.,

$$\begin{aligned}
&\langle \Phi_{\boldsymbol{\alpha}} | c^\dagger_{n_2} c^\dagger_{n_1} c_{m_1} c_{m_2} | \Phi_{\boldsymbol{\beta}} \rangle = \langle \Phi_{\boldsymbol{\alpha}} | c^\dagger_{P_{\boldsymbol{\alpha}} n_2} c^\dagger_{P_{\boldsymbol{\alpha}} n_1} c_{P_{\boldsymbol{\beta}} m_1} c_{P_{\boldsymbol{\beta}} m_2} | \Phi_{\boldsymbol{\beta}} \rangle \\
&= \begin{vmatrix} \langle \Phi_{\boldsymbol{\alpha}} | c^\dagger_{n_1} c_{m_1} | \Phi_{\boldsymbol{\beta}} \rangle & \langle \Phi_{\boldsymbol{\alpha}} | c^\dagger_{n_1} c_{m_2} | \Phi_{\boldsymbol{\beta}} \rangle \\ \langle \Phi_{\boldsymbol{\alpha}} | c^\dagger_{n_2} c_{m_1} | \Phi_{\boldsymbol{\beta}} \rangle & \langle \Phi_{\boldsymbol{\alpha}} | c^\dagger_{n_2} c_{m_2} | \Phi_{\boldsymbol{\beta}} \rangle \end{vmatrix} - \begin{vmatrix} \Delta_{n_1 m_1} & \Delta_{n_1 m_2} \\ \Delta_{n_2 m_1} & \Delta_{n_2 m_2} \end{vmatrix} \\
&\quad + (1 - \langle \Phi_{\boldsymbol{\alpha}} | \Phi_{\boldsymbol{\beta}} \rangle) \begin{vmatrix} \langle \varphi_{m_1} | P_{\boldsymbol{\beta}} P_{\boldsymbol{\alpha}} | \varphi_{n_1} \rangle & \langle \varphi_{m_2} | P_{\boldsymbol{\beta}} P_{\boldsymbol{\alpha}} | \varphi_{n_1} \rangle \\ \langle \varphi_{m_1} | P_{\boldsymbol{\beta}} P_{\boldsymbol{\alpha}} | \varphi_{n_2} \rangle & \langle \varphi_{m_2} | P_{\boldsymbol{\beta}} P_{\boldsymbol{\alpha}} | \varphi_{n_2} \rangle \end{vmatrix} + \langle \Phi_{\boldsymbol{\alpha}, P_{\boldsymbol{\beta}} \varphi_{m_1}, P_{\boldsymbol{\beta}} \varphi_{m_2}} | \Phi_{\boldsymbol{\beta}, P_{\boldsymbol{\alpha}} \varphi_{n_1}, P_{\boldsymbol{\alpha}} \varphi_{n_2}} \rangle,
\end{aligned}$$

where $\Delta_{n,m} = \langle \Phi_{\boldsymbol{\alpha}} | c^\dagger_n c_m | \Phi_{\boldsymbol{\beta}} \rangle - \langle \varphi_m | P_{\boldsymbol{\beta}} P_{\boldsymbol{\alpha}} | \varphi_n \rangle$. For $|\Phi_{\boldsymbol{\alpha}}\rangle = |\Phi_{\boldsymbol{\beta}}\rangle$ this reduces to (44). While these expressions can be efficiently evaluated expanding the $N + p$-order determinant, the expressions quickly get quite involved.
The situation simplifies dramatically when we only consider operators c_n and $c^\dagger_n$ corresponding to an orthonormal basis $\{|\varphi_n\rangle | \, n\}$ of $\mathcal{H}^{(1)}$. The Slater determinants are then orthonormal and of

the form $|\Phi_{\boldsymbol{n}}\rangle = |\Phi_{n_1,\ldots,n_N}\rangle = c^\dagger_{n_N}\cdots c^\dagger_{n_1}|0\rangle$. Diagonal matrix elements are then

$$\begin{aligned}
\langle\Phi_{\boldsymbol{n}}|c^\dagger_n c_m|\Phi_{\boldsymbol{n}}\rangle &= \delta_{n,m}\delta_{n\in\{n_1,\ldots,n_N\}}\\
\langle\Phi_{\boldsymbol{n}}|c^\dagger_n c^\dagger_{n'} c_{m'} c_m|\Phi_{\boldsymbol{n}}\rangle &= \left(\delta_{n,m}\delta_{m',m'} - \delta_{n,m'}\delta_{n',m}\right)\delta_{n,n',m,m'\in\{n_1,\ldots,n_N\}}\\
\langle\Phi_{\boldsymbol{n}}|c^\dagger_{k_p}\cdots c^\dagger_{k_1} c_{m_1}\cdots c_{m_p}|\Phi_{\boldsymbol{n}}\rangle &= \det(\delta_{k_i,m_j})\,\delta_{k_1,\ldots,k_p,m_1,\ldots,m_p\in\{n_1,\ldots,n_N\}}.
\end{aligned}$$

Off-diagonal matrix elements vanish unless the determinants differ in exactly the operators inside the matrix element:

$$\begin{aligned}
\langle\Phi_{\boldsymbol{n}}|c^\dagger_n c_m|\Phi_{\boldsymbol{m}}\rangle &= \pm\delta_{m=m_i}\delta_{n=n_j}\,\delta_{\{m_1,\ldots,m_N\}\setminus\{m_i\}=\{n_1,\ldots,n_N\}\setminus\{n_j\}}\\
\langle\Phi_{\boldsymbol{n}}|c^\dagger_n c^\dagger_{n'} c_{m'} c_m|\Phi_{\boldsymbol{m}}\rangle &= \pm\delta_{\{m,m'\}=\{m_i,m_{i'}\}}\delta_{\{n,n'\}=\{n_j,n_{j'}\}}\delta_{\{\boldsymbol{m}\}\setminus\{m_i,m_{i'}\}=\{\boldsymbol{n}\}\setminus\{n_j,n_{j'}\}}.
\end{aligned}$$

Thus, when we transform an operator $\hat{M}^{(p)}$ to the basis in which the Slater determinants are written, all matrix elements between determinants that differ by more than p operators vanish. These are the Slater-Condon rules.

3 Variational methods

The variational principle and the Schrödinger equation are equivalent. Consider the energy expectation value as a wave-function functional

$$E[\Psi] = \frac{\langle\Psi|H|\Psi\rangle}{\langle\Psi|\Psi\rangle}\,. \tag{48}$$

Its variation is

$$E[\Psi+\delta\Psi] = E[\Psi] + \frac{\langle\delta\Psi|H|\Psi\rangle + \langle\Psi|H|\delta\Psi\rangle}{\langle\Psi|\Psi\rangle} - \langle\Psi|H|\Psi\rangle\,\frac{\langle\delta\Psi|\Psi\rangle + \langle\Psi|\delta\Psi\rangle}{\langle\Psi|\Psi\rangle^2} + \mathcal{O}^2. \tag{49}$$

The first-order term vanishes for

$$H|\Psi\rangle = E[\Psi]\,|\Psi\rangle\,, \tag{50}$$

which is the Schrödinger equation. The general approach to solving it for many-electron systems is configuration interaction (CI): We choose an orthonormal set of orbitals $\{\varphi_n \,|\, n\}$ from which we construct an orthonormal basis $\{\Phi_{n_1,\ldots,n_N} \,|\, n_1 < \cdots < n_N\}$ of N-electron Slater determinants. Expanding $|\Psi\rangle$ in this basis

$$|\Psi\rangle = \sum_{n_1<\cdots<n_N} a_{n_1,\ldots,n_N}\,|\Phi_{n_1,\ldots,n_N}\rangle = \sum_{\boldsymbol{n}_i} a_{\boldsymbol{n}_i}\,|\Phi_{\boldsymbol{n}_i}\rangle\,, \tag{51}$$

the Schrödinger equation (50) becomes a matrix eigenvalue problem

$$\begin{pmatrix}
\langle\Phi_{\boldsymbol{n}_1}|H|\Phi_{\boldsymbol{n}_1}\rangle & \langle\Phi_{\boldsymbol{n}_1}|H|\Phi_{\boldsymbol{n}_2}\rangle\cdots\\
\langle\Phi_{\boldsymbol{n}_2}|H|\Phi_{\boldsymbol{n}_1}\rangle & \langle\Phi_{\boldsymbol{n}_2}|H|\Phi_{\boldsymbol{n}_2}\rangle\cdots\\
\vdots & \vdots\quad\ddots
\end{pmatrix}
\begin{pmatrix} a_{\boldsymbol{n}_1}\\ a_{\boldsymbol{n}_2}\\ \vdots \end{pmatrix}
= E
\begin{pmatrix} a_{\boldsymbol{n}_1}\\ a_{\boldsymbol{n}_2}\\ \vdots \end{pmatrix}. \tag{52}$$

Note that the indices $\boldsymbol{n}_i$ of the determinants are ordered sets of single-electron indices.
For a complete basis set the matrix dimension is, of course, infinite, but even for finite basis sets of K single-electron functions the dimension for an N-electron problem increase extremely rapidly. There are $K \cdot (K-1) \cdot (K-2) \cdots (K-(N-1))$ ways of picking N indices out of K. Since we only use one specific ordering of these indices, we still have to divide by $N!$ to obtain the number of such determinants:

$$\dim \mathcal{H}_K^{(N)} = \frac{K!}{N!(K-N)!} = \binom{K}{N} . \tag{53}$$

For $N = 25$ electrons and $K = 100$ orbitals the dimension already exceeds 10^{23}. And still, being a non-complete basis set, diagonalizing (52) still would only give a variational energy, meaning that, for example, the ground state of (52) is the state that minimizes the energy wave-function functional (48) on the $\binom{K}{N}$-dimensional subspace of the N-electron Hilbert space.

3.1 Non-interacting electrons

Even when considering a system of N non-interacting electrons we have to solve the large matrix eigenvalue problem (52). Writing the non-interacting Hamiltonian in the basis used for the CI expansion (51) we obtain

$$\hat{H} = \sum_{n,m} H_{nm}\, c_n^\dagger c_m \,,$$

which, in general, has non-vanishing matrix elements between Slater determinants that differ in at most one operator. But we can simplify things drastically by realizing that we can choose any basis for the CI expansion. If we choose the eigenstates of the single-electron matrix H_{nm} as basis, second-quantized Hamiltonian is

$$\hat{H} = \sum_{n,m} \varepsilon_n \delta_{n,m}\, c_n^\dagger c_m = \sum_n \varepsilon_n\, c_n^\dagger c_n \,.$$

In this basis all off-diagonal matrix elements vanish and the CI Hamiltonian (52) is diagonal. Thus all $\binom{K}{N}$ eigenstates are Slater determinants

$$|\Phi_{\boldsymbol{n}}\rangle = c_{n_N}^\dagger \cdots c_{n_1}^\dagger |0\rangle \qquad \text{with eigenenergy} \quad E_{\boldsymbol{n}} = \sum_i \varepsilon_{n_i} \,. \tag{54}$$

This shows that choosing an appropriate basis for a CI expansion is crucial. A good general strategy should thus be to solve the matrix problem (52) and at the same time look for the basis set (of given size) that minimizes the variational energy. This is the idea of the multi-configurational self-consistent field method (MCSCF) [7]. In the following we will restrict ourselves to the simplest case where the many-body basis consists of a single Slater determinant. This is the Hartree-Fock method.

3.2 Hartree-Fock theory

The idea of the Hartree-Fock approach is to find an approximation to the ground-state of the N-electron problem by minimizing the total-energy wave-function functional (48) allowing only N-electron Slater determinants as variational functions. Since expectation values of Slater determinants are determined by their one-body density matrix, remember (45), this means that we want to find the occupied subspace for which (48) is minimized.
To perform these variations we introduce unitary transformations in Fock-space (related to the Thouless representation of Slater determinants [8])

$$\hat{U}(\lambda) = e^{i\lambda\hat{M}} \qquad \text{with} \quad \hat{M} = \sum_{\alpha,\beta} M_{\alpha\beta}\, c^\dagger_\alpha c_\beta \quad \text{hermitian} . \tag{55}$$

To see that $\hat{U}$ is a transformation among Slater determinants, we apply it to a product state

$$e^{i\lambda\hat{M}}\, c^\dagger_{\alpha_N} \cdots c_{\alpha_1}|0\rangle = e^{i\lambda\hat{M}} c^\dagger_{\alpha_N} e^{-i\lambda\hat{M}}\; e^{i\lambda\hat{M}} \cdots e^{-i\lambda\hat{M}} e^{i\lambda\hat{M}} c^\dagger_{\alpha_1} e^{-i\lambda\hat{M}}\; e^{i\lambda\hat{M}}|0\rangle . \tag{56}$$

Since the annihilators produce zero when applied to the vacuum state, we have

$$e^{i\lambda\hat{M}}|0\rangle = |0\rangle . \tag{57}$$

To evaluate $e^{i\lambda\hat{M}}\, c^\dagger_\gamma\, e^{-i\lambda\hat{M}}$, we use that the commutator of the product of a creator and an annihilator with a creation operator is again a creation operator (see App. B)

$$[c^\dagger_\alpha c_\beta,\, c^\dagger_\gamma] = c^\dagger_\alpha \{c_\beta,\, c^\dagger_\gamma\} - \{c^\dagger_\alpha,\, c^\dagger_\gamma\} c_\beta = c^\dagger_\alpha\, \delta_{\beta,\gamma} \tag{58}$$

to calculate the coefficients of its power-series expansion in λ:

$$\begin{aligned}
\left.\frac{d}{d\lambda}\right|_{\lambda=0} e^{i\lambda\hat{M}}\, c^\dagger_\gamma\, e^{-i\lambda\hat{M}} &= \left. e^{i\lambda\hat{M}}\; i\,[\hat{M},\, c^\dagger_\alpha]\, e^{-i\lambda\hat{M}}\right|_{\lambda=0} &&= i\sum_\alpha c^\dagger_\alpha\, M_{\alpha\gamma} \\
\left.\frac{d^2}{d\lambda^2}\right|_{\lambda=0} e^{i\lambda\hat{M}}\, c^\dagger_\gamma\, e^{-i\lambda\hat{M}} &= \left.\frac{d}{d\lambda}\right|_{\lambda=0} e^{i\lambda\hat{M}} \left(i\sum_{\alpha'} c^\dagger_{\alpha'}\, M_{\alpha'\gamma} \right) e^{-i\lambda\hat{M}} &&= i^2 \sum_\alpha c^\dagger_\alpha \underbrace{\sum_{\alpha'} M_{\alpha\alpha'} M_{\alpha'\gamma}}_{(\boldsymbol{M}^2)_{\alpha\gamma}} \\
&\;\;\vdots \\
\left.\frac{d^n}{d\lambda^n}\right|_{\lambda=0} e^{i\lambda\hat{M}}\, c^\dagger_\gamma\, e^{-i\lambda\hat{M}} &= &&\; i^n \sum_\alpha c^\dagger_\alpha\, (\boldsymbol{M}^n)_{\alpha\gamma}
\end{aligned}$$

from which we find that

$$e^{i\lambda\hat{M}}\, c^\dagger_\gamma\, e^{-i\lambda\hat{M}} = \sum_\alpha \sum_{n=0}^{\infty} \frac{(i\lambda\boldsymbol{M})^n_{\alpha\gamma}}{n!} = \sum_\alpha c^\dagger_\alpha \left(e^{i\lambda\boldsymbol{M}}\right)_{\alpha\gamma} \tag{59}$$

the creation operators are transformed by the unitary matrix single-electron unitary $e^{i\lambda\boldsymbol{M}}$, i.e., $\hat{U}$ corresponds to a basis transformation in all operators, cf. (16). Thus, the right-hand-side of

(56) is again a Slater determinant formed from creation operators in the transformed basis. The annihilation operators transform accordingly as

$$e^{i\lambda\hat{M}}\, c_\gamma\, e^{-i\lambda\hat{M}} = \sum_\alpha \left(e^{i\lambda \boldsymbol{M}}\right)_{\gamma\alpha} c_\alpha\,. \tag{60}$$

Using this transformation, the variation of the energy expectation value can be written as

$$\begin{aligned} E(\lambda) &= \langle\Phi|e^{i\lambda\hat{M}}\,\hat{H}\,e^{-i\lambda\hat{M}}|\Phi\rangle \\ &= \langle\Phi|\hat{H}|\Phi\rangle + i\lambda\langle\Phi|[\hat{H},\,\hat{M}]|\Phi\rangle + \frac{(i\lambda)^2}{2}\langle\Phi|\big[[\hat{H},\,\hat{M}],\,\hat{M}\big]|\Phi\rangle + \cdots \end{aligned} \tag{61}$$

where each successive derivative in the power series expansion produces a commutator $[\,\cdot\,,\,\hat{M}]$ around those that were already present. The energy functional is stationary for Φ^{HF} when

$$\langle\Phi^{\mathrm{HF}}|[\hat{H},\,\hat{M}]|\Phi^{\mathrm{HF}}\rangle = 0 \tag{62}$$

for every hermitian single-electron operator $\hat{M}$. This condition is most easily understood when we work with orthonormal orbitals $\{|\varphi\rangle|\,n\}$ from which the Slater determinant can be constructed: $|\Phi^{\mathrm{HF}}\rangle = c_N^\dagger\cdots c_1^\dagger|0\rangle$. Then (62) is equivalent to

$$\langle\Phi^{\mathrm{HF}}|[\hat{H},\,c_n^\dagger c_m + c_m^\dagger c_n]|\Phi^{\mathrm{HF}}\rangle = 0 \quad \forall\, n,\, m$$

(actually $n \geq m$ suffices). Since

$$c_n^\dagger c_m|\Phi^{\mathrm{HF}}\rangle = \begin{cases} \delta_{n,m}|\Phi^{\mathrm{HF}}\rangle & \text{if } n,\, m \in \{1,\ldots,N\} \\ 0 & \text{if } m \quad \notin \{1,\ldots,N\} \end{cases},$$

i.e., (62) is automatically fulfilled if both n and m are either occupied or unoccupied (virtual). This is not unexpected since transformations among the occupied or virtual orbitals, respectively, do not change the Slater determinant. The condition thus reduces to

$$\langle\Phi^{\mathrm{HF}}|c_m^\dagger c_n\hat{H}|\Phi^{\mathrm{HF}}\rangle = 0 \quad \forall\, m \in \{1,\ldots,N\},\, n \notin \{1,\ldots,N\}\,. \tag{63}$$

In other words, for the Hamiltonian there are no matrix elements between the stationary Slater determinant and determinants that differ from it in one orbital. The condition that for the Hartree-Fock determinant the Hamiltonian does not produce single excitations is called the Brillouin theorem.

Let us consider a Hamiltonian with one- and two-body terms

$$\hat{H} = \sum_{n,m} c_n^\dagger\, T_{nm}\, c_m + \sum_{n>n',m>m'} c_n^\dagger c_{n'}^\dagger \left(U_{nn',mm'} - U_{nn',m'm}\right) c_{m'} c_m$$

Then for each $n > N \geq m$ the singly-excited term

$$\left(T_{nm} + \sum_{m'\leq N}\left(U_{nm',mm'} - U_{nm',m'm}\right)\right) c_n^\dagger c_m|\Phi^{\mathrm{HF}}\rangle = 0$$

must vanish. This is the same condition as for a non-interacting Hamiltonian with matrix elements

$$F_{nm} = T_{nm} + \sum_{m' \le N} (U_{nm',mm'} - U_{nm',m'm}) \,. \tag{64}$$

$\boldsymbol{F}$ is called the Fock matrix. It depends, via the summation over occupied states, i.e., the density matrix, on the Slater determinant it is acting on. So we cannot simply diagonalize the single-electron matrix $\boldsymbol{F}$ since this will, in general, give a different determinant. Instead we need to find a Slater determinant for which $\boldsymbol{F}$ is diagonal (in fact, it is sufficient if it is block-diagonal in the occupied and virtual spaces). This is typically done by constructing a new Slater determinant from the N lowest eigenstates of $\boldsymbol{F}$ and iterating. Alternatively, we can use, e.g., steepest descent methods to minimize the expectation value directly or optimizing the one-body density matrix [9, 10]. At self-consistency the Fock matrix is diagonal with eigenvalues

$$\varepsilon_m^{\mathrm{HF}} = \left(T_{mm} + \sum_{m' \le N} \underbrace{(U_{mm',mm'} - U_{mm',m'm})}_{=:\Delta_{mm'}} \right) = \left(T_{mm} + \sum_{m' \le N} \Delta_{mm'} \right) \tag{65}$$

and the Hartree-Fock energy is given by

$$\langle \Phi^{\mathrm{HF}} | \hat{H} | \Phi^{\mathrm{HF}} \rangle = \sum_{m \le N} \left(T_{mm} + \sum_{m'<m} \Delta_{mm'} \right) = \sum_{m \le N} \left(T_{mm} + \frac{1}{2} \sum_{m' \le N} \Delta_{mm'} \right) .$$

Removing an electron from the occupied orbital φ_a changes the energy expectation value by

$$\langle \Phi^{\mathrm{HF}}_{a\ \mathrm{rem}} | \hat{H} | \Phi^{\mathrm{HF}}_{a\ \mathrm{rem}} \rangle - \langle \Phi^{\mathrm{HF}} | \hat{H} | \Phi^{\mathrm{HF}} \rangle = - \left(T_{aa} + \frac{1}{2} \sum_{m' \le N} \Delta_{am'} \right) - \frac{1}{2} \sum_{m \ne a \le N} \Delta_{ma} = -\varepsilon_a^{\mathrm{HF}}. \tag{66}$$

When we assume that removing an electron does not change the orbitals much, which should be a good approximation in the limit of many electrons $N \gg 1$, this gives the ionization energy (Koopmans' theorem). Likewise, the energy expectation value of an excited Slater determinant $\Phi^{\mathrm{HF}}_{a\to b}$ with an electron moved from orbital $a \le N$ to orbital $b > N$ is

$$\varepsilon^{\mathrm{HF}}_{a\to b} = \langle \Phi^{\mathrm{HF}}_{a\to b} | \hat{H} | \Phi^{\mathrm{HF}}_{a\to b} \rangle - \langle \Phi^{\mathrm{HF}} | \hat{H} | \Phi^{\mathrm{HF}} \rangle = \varepsilon_b^{\mathrm{HF}} - \varepsilon_a^{\mathrm{HF}} - \Delta_{ab} \tag{67}$$

It can be interpreted as the energy of a state with an electron-hole excitation, again neglecting relaxation effects. For the Coulomb interaction

$$\begin{aligned} \Delta_{ab} = \frac{1}{2}(\Delta_{ab} + \Delta_{ba}) &= \frac{1}{2} \left(\left\langle \varphi_a\varphi_b \left| \frac{1}{r-r'} \right| \varphi_a\varphi_b - \varphi_b\varphi_a \right\rangle + \left\langle \varphi_b\varphi_a \left| \frac{1}{r-r'} \right| \varphi_b\varphi_a - \varphi_a\varphi_b \right\rangle \right) \\ &= \frac{1}{2} \left\langle \varphi_a\varphi_b - \varphi_b\varphi_a \left| \frac{1}{r-r'} \right| \varphi_a\varphi_b - \varphi_b\varphi_a \right\rangle > 0 \end{aligned}$$

so that the third term in (67) describes the attraction between the excited electron and the hole.

3.2.1 Homogeneous electron gas

Since the homogeneous electron gas is translation invariant it is natural to write the Hamiltonian (for states with homogeneous charge density) in the basis of plane waves $\langle r,\sigma|\boldsymbol{k},\sigma\rangle = \frac{1}{(2\pi)^{3/2}} e^{i\boldsymbol{k}\cdot\boldsymbol{r}}$

$$\hat{H} = \sum_\sigma \int d\boldsymbol{k}\, \frac{|\boldsymbol{k}^2|}{2} c^\dagger_{\boldsymbol{k},\sigma} c_{\boldsymbol{k},\sigma} + \frac{1}{2(2\pi)^3} \sum_{\sigma,\sigma'} \int d\boldsymbol{k} \int d\boldsymbol{k}' \int' d\boldsymbol{q}\, \frac{4\pi}{|\boldsymbol{q}|^2} c^\dagger_{\boldsymbol{k}-\boldsymbol{q},\sigma} c^\dagger_{\boldsymbol{k}'+\boldsymbol{q},\sigma'} c_{\boldsymbol{k}',\sigma'} c_{\boldsymbol{k},\sigma}\,, \quad (68)$$

where the prime on the $\boldsymbol{q}$ integral means that $\boldsymbol{q} = 0$ is excluded since the homogeneous contribution to the Coulomb repulsion of the electrons is cancelled by its attraction with the homogeneous neutralizing background charge density. It seems reasonable to consider as an ansatz a Slater determinant $|\Phi_{k_F}\rangle$ of all plane wave states with momentum some Fermi momentum $|\boldsymbol{k}| < k_F$. The charge density for such a determinant follows, using the anticommutator of the field operator

$$\{\hat{\Psi}^\dagger_\sigma(\boldsymbol{r}),\, c_{\boldsymbol{k},\sigma}\} = \int d\boldsymbol{r}' \frac{e^{-i\boldsymbol{k}\cdot\boldsymbol{r}}}{(2\pi)^{3/2}} \{\hat{\Psi}^\dagger_\sigma(\boldsymbol{r}),\, \hat{\Psi}_\sigma(\boldsymbol{r}')\} = \frac{e^{-i\boldsymbol{k}\cdot\boldsymbol{r}}}{(2\pi)^{3/2}}\,,$$

from the diagonal of the density matrix

$$n_\sigma(\boldsymbol{r}) = \langle \Phi^{\mathrm{HF}}|\hat{\Psi}^\dagger_\sigma(\boldsymbol{r})\hat{\Psi}_\sigma(\boldsymbol{r})|\Phi^{\mathrm{HF}}\rangle = \int_{|\boldsymbol{k}|<k_F} d\boldsymbol{k}\, \left|\frac{e^{i\boldsymbol{k}\cdot\boldsymbol{r}}}{(2\pi)^{3/2}}\right|^2 = \frac{k_F^3}{6\pi^2}\,. \quad (69)$$

It is independent of position, so $|\Phi_{k_F}\rangle$ looks like an appropriate ansatz for a homogeneous system. Moreover, it fulfills the stationarity condition (63): To create just a single excitation one of the creation operators in the Coulomb term of (68) must fill one of the annihilated states, i.e., $\boldsymbol{q} = 0$ or $\boldsymbol{q} = \boldsymbol{k} - \boldsymbol{k}'$. But this implies that the term is diagonal with $\boldsymbol{q} = 0$ giving the direct and $\boldsymbol{q} = \boldsymbol{k} - \boldsymbol{k}'$ the exchange contribution. Since the $\boldsymbol{q} = 0$ term is not present in the Hamiltonian, the eigenenergies of the Fock matrix are just the sum of the kinetic and the exchange terms

$$\varepsilon^{\mathrm{HF}}_{k,\sigma} = \frac{|\boldsymbol{k}|^2}{2} - \frac{1}{4\pi^2} \int_{|\boldsymbol{k}'|<k_F} d\boldsymbol{k}'\, \frac{1}{|\boldsymbol{k}-\boldsymbol{k}'|^2} = \frac{k^2}{2} - \frac{k_F}{\pi}\left(1 + \frac{k_F^2 - k^2}{2k_F k} \ln\left|\frac{k_F + k}{k_F - k}\right|\right) \quad (70)$$

It depends only on $k = |\boldsymbol{k}|$. Interestingly the slope of $\varepsilon^{\mathrm{HF}}_{\boldsymbol{k},\sigma}$ becomes infinite for $k \to k_F$. Thus, the density of states $D(\varepsilon_k)d\varepsilon = 4\pi k^2\, dk$, given by

$$D^{\mathrm{HF}}_\sigma(\varepsilon) = 4\pi k^2 \left(\frac{d\varepsilon^{\mathrm{HF}}_{k,\sigma}}{dk}\right)^{-1} = 4\pi k^2 \left(k - \frac{k_F}{\pi k}\left(1 - \frac{k_F^2 + k^2}{2k_F k} \ln\left|\frac{k_F + k}{k_F - k}\right|\right)\right)^{-1} \quad (71)$$

vanishes at the Fermi level (see Fig. 1). This is not quite what we expect from a respectable electron gas... It is clearly a defect of the Hartree-Fock approximation.

Instead of calculating the energy expectation value also directly in k-space, it is instructive to look at the exchange term in real space. To evaluate the electron-electron repulsion we need the

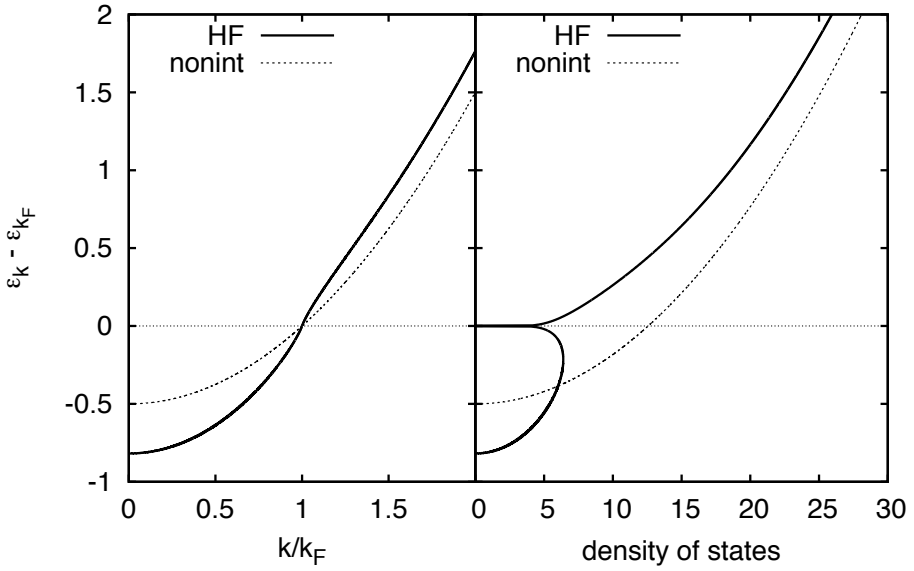

Fig. 1: *Hartree-Fock eigenvalues and density of states for the homogeneous solution $|\Psi_{k_F}\rangle$ of the homogeneous electron gas compared to non-interacting values.*

diagonal of the 2-body density matrix, which is given by (44) in terms of the one-body density matrix

$$\langle\Phi_{k_F}|\hat\Psi^\dagger_{\sigma'}(\boldsymbol{r}')\hat\Psi^\dagger_\sigma(\boldsymbol{r})\hat\Psi_\sigma(\boldsymbol{r})\hat\Psi_{\sigma'}(\boldsymbol{r}')|\Phi_{k_F}\rangle = \det\begin{pmatrix} \Gamma^{(1)}_{\sigma\sigma}(\boldsymbol{r},\boldsymbol{r}) & \Gamma^{(1)}_{\sigma\sigma'}(\boldsymbol{r},\boldsymbol{r}') \\ \Gamma^{(1)}_{\sigma'\sigma}(\boldsymbol{r}',\boldsymbol{r}) & \Gamma^{(1)}_{\sigma'\sigma'}(\boldsymbol{r}',\boldsymbol{r}') \end{pmatrix},$$

where the one-body density matrix vanishes unless $\sigma' = \sigma$ where it is evaluated as in (69)

$$\begin{aligned}\Gamma_{\sigma\sigma}(\boldsymbol{r},\boldsymbol{r}') &= \langle\Phi_{k_F}|\hat\Psi^\dagger_\sigma(\boldsymbol{r})\hat\Psi_\sigma(\boldsymbol{r}')|\Phi_{k_F}\rangle \\ &= \int_{|\boldsymbol{k}|<k_F} d\boldsymbol{k}\,\frac{e^{-i\boldsymbol{k}\cdot(\boldsymbol{r}-\boldsymbol{r}')}}{(2\pi)^3} = \frac{1}{4\pi^2}\int_0^{k_F} dk\,k^2\int_{-1}^{1} d\cos\theta\, e^{ik|\boldsymbol{r}-\boldsymbol{r}'|\cos\theta} \\ &= \frac{k_F^3}{2\pi^2}\underbrace{\frac{\sin x - x\cos x}{x^3}}_{\overset{x\to0}{\longrightarrow}1/3} = 3n_\sigma\,\frac{\sin x - x\cos x}{x^3}\end{aligned} \tag{72}$$

with $x = k_F|\boldsymbol{r}-\boldsymbol{r}'|$. Dividing the 2-body density matrix by n_σ^2 and subtracting the direct term (which is canceled by the contribution of the background charge) we obtain the exchange hole [10]

$$g_x(r,0) - 1 = -9\left(\frac{\sin k_F r - k_F r\cos k_F r}{(k_F r)^3}\right)^2. \tag{73}$$

It is shown in Fig. 2. The exchange energy per spin is then the Coulomb interaction of the charge density with its exchange hole

$$E_x = \frac{1}{2}\int d\boldsymbol{r}\,n_\sigma\int d\boldsymbol{r}' n_\sigma\frac{g_x(r,r')-1}{|\boldsymbol{r}-\boldsymbol{r}'|} = \frac{1}{2}\underbrace{\int d\boldsymbol{r}\,n_\sigma}_{=N}\int d\tilde{\boldsymbol{r}}\,n_\sigma\,\frac{g_x(\tilde r,0)-1}{\tilde r}\,.$$

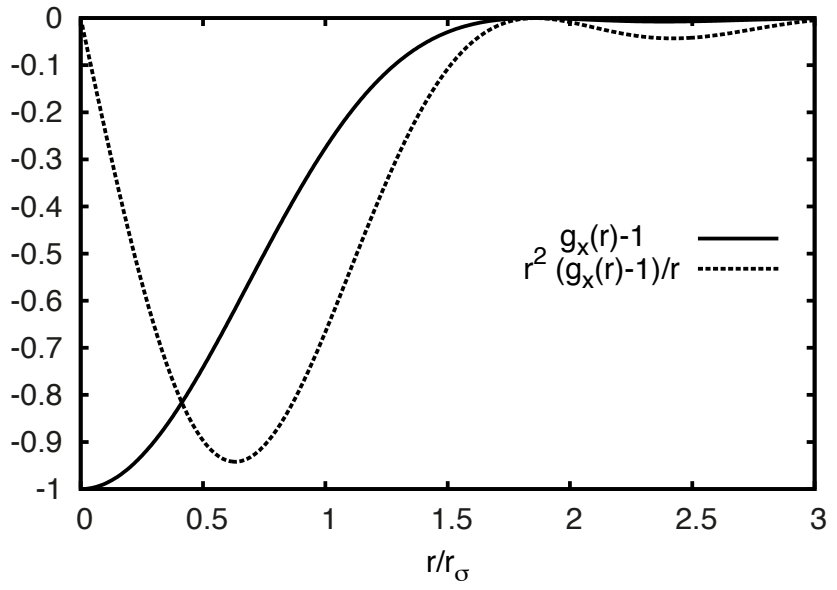

Fig. 2: *Exchange hole for a paramagnetic homogeneous electron gas in units of the spin Wigner-Seitz radius $k_F\, r_\sigma = (9\pi/2)^{1/3}$. In addition, the dotted line shows the contribution of the exchange hole to the Coulomb repulsion energy of Eq. (74).*

The exchange energy per electron of spin σ is thus

$$\varepsilon_x^\sigma = \frac{4\pi n_\sigma}{2}\int_0^\infty dr\, r^2\, \frac{g(r,0)-1}{r} = -\frac{9\cdot 4\pi n_\sigma}{2k_F^2}\underbrace{\int_0^\infty dx\, \frac{(\sin x - x\cos x)^2}{x^5}}_{=1/4} = -\frac{3k_F}{4\pi}\,. \tag{74}$$

Together with the kinetic energy per electron of spin σ

$$\varepsilon_{\rm kin}^\sigma = 4\pi\int_0^{k_F} dk\, k^2\, \frac{k^2}{2}\Bigg/ 4\pi\int_0^{k_F} dk\, k^2 = \frac{3k_F^2}{10} \tag{75}$$

we obtain the total energy per electron

$$\varepsilon_{\rm HF} = \frac{n_\uparrow(\varepsilon_{\rm kin}^\uparrow + \varepsilon_x^\uparrow) + n_\downarrow(\varepsilon_{\rm kin}^\downarrow + \varepsilon_x^\downarrow)}{n_\uparrow + n_\downarrow} = \frac{3(6\pi^2)^{2/3}}{10}\,\frac{n_\uparrow^{5/3} + n_\downarrow^{5/3}}{n} - \frac{3}{4}\left(\frac{6}{\pi}\right)^{1/3}\frac{n_\uparrow^{4/3} + n_\downarrow^{4/3}}{n}\,.$$

While the kinetic energy is lowest when $n_\uparrow = n_\downarrow$, exchange favors spin polarization. For reasonable electron densities the kinetic energy dominates, only at extremely low densities exchange dominates and the solution would be ferromagnetic.

A ferromagnetic Slater determinant would, of course, have two different Fermi momenta, $k_F^\uparrow \neq k_F^\downarrow$. It also would break the symmetry of the Hamiltonian under spin rotations. This is an example of how we can lower the energy expectation value by allowing Slater determinants that break a symmetry of the system. When we do not restrict the symmetry of the Slater determinant, the approach is called unrestricted Hartree-Fock. For the electron gas this approach actually gives Hartree-Fock states that even break translational symmetry, see, e.g., [11]

3.2.2 Hubbard model

As a simple example to illustrate the difference between restricted and unrestricted Hartree-Fock we consider the Hubbard model with two sites, $i = 1, 2$, between which the electrons can hop with matrix element $-t$ and with an on-site Coulomb repulsion U

$$\hat{H} = -t \sum_{\sigma} \left(c^\dagger_{2\sigma} c_{1\sigma} + c^\dagger_{1\sigma} c_{2\sigma} \right) + U \sum_{i \in \{1,2\}} n_{i\uparrow} n_{i\downarrow} \,. \tag{76}$$

The number of electrons N and the total spin projection S_z are conserved, so the Fock space Hamiltonian is block-diagonal in the Hilbert spaces with fixed number of up- and down-spin electrons $N_\uparrow$ and $N_\downarrow$ with dimensions

N	0	1		2			3		4	
$N_\uparrow$	0	1	0	2	1	0	2	1	2	
$N_\downarrow$	0	0	1	0	1	2	1	2	2	
dim	1	2	2	1	4	1	2	2	1	16

Exact solutions: The Hamiltonian for $N = N_\uparrow = 1$ is easily constructed. By introducing the basis states $c^\dagger_{1\uparrow}|0\rangle$ and $c^\dagger_{2\uparrow}|0\rangle$, we obtain the Hamiltonian matrix

$$\left\langle 0 \right| \begin{pmatrix} c_{1\uparrow} \\ c_{2\uparrow} \end{pmatrix} \hat{H} \begin{pmatrix} c^\dagger_{1\uparrow} & c^\dagger_{2\uparrow} \end{pmatrix} \left| 0 \right\rangle = \begin{pmatrix} 0 & -t \langle 0 | c_{1\uparrow}\, c^\dagger_{1\uparrow} c_{2\uparrow}\, c^\dagger_{2\uparrow} | 0 \rangle \\ -t \langle 0 | c_{2\uparrow}\, c^\dagger_{2\uparrow} c_{1\uparrow}\, c^\dagger_{1\uparrow} | 0 \rangle & 0 \end{pmatrix} = \begin{pmatrix} 0 & -t \\ -t & 0 \end{pmatrix}.$$

This is easily diagonalized giving the familiar bonding and antibonding solution

$$|\varphi_\pm\rangle = \frac{1}{\sqrt{2}} \left(c^\dagger_{1\uparrow} \pm c^\dagger_{2\uparrow} \right) |0\rangle = c^\dagger_{\pm\uparrow} |0\rangle \,. \tag{77}$$

For $N_\uparrow = 1 = N_\downarrow$, we obtain a non-trivial interacting system

$$\left\langle 0 \right| \begin{pmatrix} c_{1\uparrow}c_{2\downarrow} \\ c_{2\uparrow}c_{1\downarrow} \\ c_{1\uparrow}c_{1\downarrow} \\ c_{2\uparrow}c_{2\downarrow} \end{pmatrix} \hat{H} \begin{pmatrix} c^\dagger_{2\downarrow}c^\dagger_{1\uparrow} & c^\dagger_{1\downarrow}c^\dagger_{2\uparrow} & c^\dagger_{1\downarrow}c^\dagger_{1\uparrow} & c^\dagger_{2\downarrow}c^\dagger_{2\uparrow} \end{pmatrix} \left| 0 \right\rangle = \begin{pmatrix} 0 & 0 & -t & -t \\ 0 & 0 & -t & -t \\ -t & -t & U & 0 \\ -t & -t & 0 & U \end{pmatrix}. \tag{78}$$

To diagonalize the matrix, we transform the basis into linear combinations of covalent and ionic states

$$|\mathrm{cov}_\pm\rangle = \frac{1}{\sqrt{2}} \left(c^\dagger_{2\downarrow} c^\dagger_{1\uparrow} \pm c^\dagger_{1\downarrow} c^\dagger_{2\uparrow} \right) |0\rangle \tag{79}$$

$$|\mathrm{ion}_\pm\rangle = \frac{1}{\sqrt{2}} \left(c^\dagger_{1\downarrow} c^\dagger_{1\uparrow} \pm c^\dagger_{2\downarrow} c^\dagger_{2\uparrow} \right) |0\rangle \tag{80}$$

It is then easy to verify that $|\mathrm{cov}_-\rangle$ is an eigenstate with eigenvalue $\varepsilon_{\mathrm{cov}_-} = 0$ and that $|\mathrm{ion}_-\rangle$ has eigenenergy $\varepsilon_{\mathrm{ion}_-} = U$. The remaining two states mix

$$\begin{pmatrix} \langle \mathrm{cov}_+| \\ \langle \mathrm{ion}_+| \end{pmatrix} \hat{H} \begin{pmatrix} |\mathrm{cov}_+\rangle & |\mathrm{ion}_+\rangle \end{pmatrix} = \frac{1}{2} \left\{ U - \begin{pmatrix} U & 4t \\ 4t & -U \end{pmatrix} \right\}. \tag{81}$$

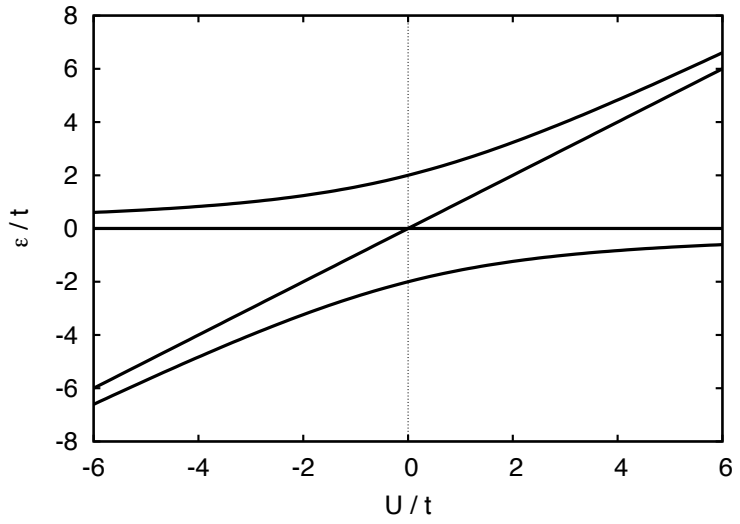

Fig. 3: *Spectrum of the two-site Hubbard model as a function of U/t.*

Rewriting the matrix

$$\begin{pmatrix} U & 4t \\ 4t & -U \end{pmatrix} = \sqrt{U^2+16t^2} \begin{pmatrix} \cos\Theta & \sin\Theta \\ \sin\Theta & -\cos\Theta \end{pmatrix} , \tag{82}$$

we find the ground state of the half-filled two-site Hubbard model

$$\begin{aligned} |\mathrm{gs}\rangle &= \cos\Theta/2\,|\mathrm{cov}_+\rangle + \sin\Theta/2\,|\mathrm{ion}_+\rangle & (83)\\ &= \frac{1}{\sqrt{2}}\left(\cos\tfrac{\Theta}{2}\,c^\dagger_{2\downarrow}c^\dagger_{1\uparrow} + \cos\tfrac{\Theta}{2}\,c^\dagger_{1\downarrow}c^\dagger_{2\uparrow} + \sin\tfrac{\Theta}{2}\,c^\dagger_{1\downarrow}c^\dagger_{1\uparrow} + \sin\tfrac{\Theta}{2}\,c^\dagger_{2\downarrow}c^\dagger_{2\uparrow}\right)|0\rangle & (84)\end{aligned}$$

with an energy of $\varepsilon_{\mathrm{gs}} = (U - \sqrt{U^2+16t^2})/2$. Without correlations ($U = 0 \rightsquigarrow \Theta = \pi/2$), all basis states have the same prefactor, so we can factorize the ground state, writing it as a product $c^\dagger_{+\downarrow}c^\dagger_{+\uparrow}|0\rangle$ of the operators defined in (77). For finite U this is no longer possible. In the strongly correlated limit $U \gg t$ ($\Theta \searrow 0$) the ground state becomes the maximally entangled state $|\mathrm{cov}_+\rangle$ and can not even approximately be expressed as a two-electron Slater determinant.

Hartree-Fock: We now want to see what Hartree-Fock can do in such a situation. Since the Hamiltonian is so simple, we can directly minimize the energy expectation value. The most general ansatz is a Slater determinant of an orbital $\varphi(\theta_\uparrow) = \sin(\theta_\uparrow)\,\varphi_1 + \cos(\theta_\uparrow)\,\varphi_2$ for the spin-up, and $\varphi(\theta_\downarrow) = \sin(\theta_\downarrow)\,\varphi_1 + \cos(\theta_\downarrow)\,\phi_2$ for the spin-down electron:

$$|\Phi(\theta_\uparrow,\theta_\downarrow)\rangle = \left(\sin(\theta_\downarrow)\,c^\dagger_{1\downarrow} + \cos(\theta_\downarrow)\,c^\dagger_{2\downarrow}\right)\,\left(\sin(\theta_\uparrow)\,c^\dagger_{1\uparrow} + \cos(\theta_\uparrow)\,c^\dagger_{2\uparrow}\right)\,|0\rangle\ . \tag{85}$$

The energy expectation value as a function of the parameters θ_σ is then

$$\begin{aligned}\langle\Phi(\theta_\uparrow,\theta_\downarrow)|\hat{H}|\Phi(\theta_\uparrow,\theta_\downarrow)\rangle &= -2t\,(\sin\theta_\uparrow\sin\theta_\downarrow + \cos\theta_\uparrow\cos\theta_\downarrow)\,(\cos\theta_\uparrow\sin\theta_\downarrow + \sin\theta_\uparrow\cos\theta_\downarrow)\\ &\quad + U\left(\sin^2\theta_\uparrow\sin^2\theta_\downarrow + \cos^2\theta_\uparrow\cos^2\theta_\downarrow\right)\ . \end{aligned}\tag{86}$$

If the Slater determinant respects the symmetry of the molecule under the exchange of sites (mirror symmetry of the H_2 molecule), it follows that the Hartree-Fock orbitals for both spins

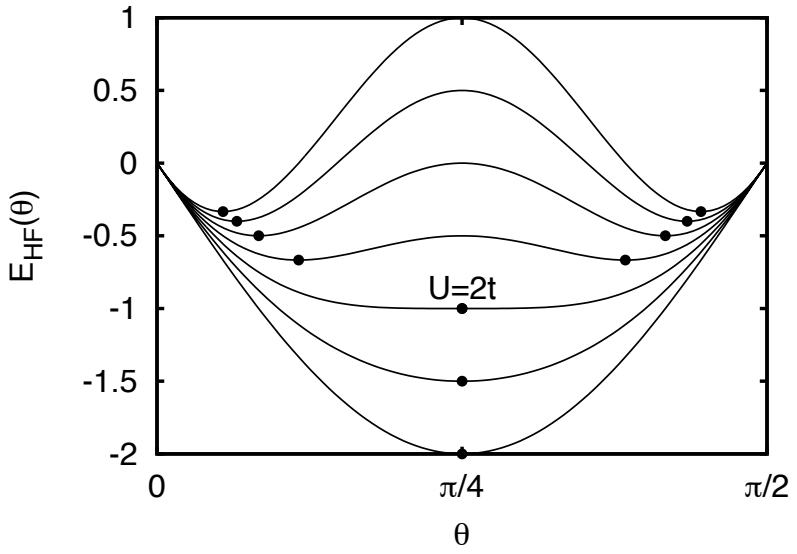

Fig. 4: *Energy expectation value for a Slater determinant $\Phi(\theta, \pi/2-\theta)$ for $U=0,\ t,\ 2t,\ \ldots,\ 6t$. When $U \leq 2t$ the minimum is at $\theta = \pi/4$. This is the Hartree-Fock solution with the bonding orbitals φ_+ occupied. For $U \geq 2t$, $\theta = \pi/4$ is still an extremal point (restricted Hartree-Fock solution), but an energy minimum is only attained when the symmetry is broken (unrestricted Hartree-Fock solution).*

are the bonding state φ_+ ($\theta = \pi/4$). This is the *restricted Hartree-Fock* solution. The corresponding energy is $E(\pi/4, \pi/4) = -2t+U/2$. The unrelaxed excited determinants are obtained by replacing occupied orbitals φ_+ with φ_-. Altogether we obtain the restricted Hartree-Fock spectrum

$$\begin{aligned} E(\ \ \pi/4,\ \ \pi/4) &= \ -2t + U/2 \\ E(\ \ \pi/4, -\pi/4) &= \ \ \ \ U/2 \\ E(-\pi/4,\ \ \pi/4) &= \ \ \ \ U/2 \\ E(-\pi/4, -\pi/4) &= \ \ 2t + U/2 \end{aligned} \tag{87}$$

Comparing to the energy for a state with both electrons of the same spin ($E = 0$), we see that there is no spin-triplet, i.e., Hartree-Fock breaks the spin symmetry [12]. The states (87) are *spin-contaminated* [13]. Even worse, the Hartree-Fock ground state, and consequently all the states, are independent of U. The weight of the ionic states is always $1/2$, leading to an increase of the energy with $U/2$.

To avoid this, we can allow the Hartree-Fock solution to break the symmetry of the molecule (*unrestricted Hartree-Fock*), putting, e.g., more of the up-spin electron in the orbital on site 1 and more of the down-spin electron in orbital 2. In an extended system this corresponds to an antiferromagnetic spin-density wave. For $U < 2t$ this does not lead to a state of lower energy. For larger U, however, there is a symmetry-broken ground state

$$\Phi_{\mathrm{UHF}} = \Phi(\theta, \pi/2-\theta) \ \text{ with } \ \theta(U) = \frac{\pi}{4} \pm \frac{1}{2} \arccos\left(\frac{2t}{U}\right). \tag{88}$$

Its energy is $E_{\mathrm{UHF}} = -2t^2/U$. Still there is no triplet state (spin contamination) and, for $U \to \infty$, the overlap with the true singlet ground state goes to $|\langle \Phi_{\mathrm{UHF}} | \Psi_- \rangle|^2 = 1/2$.

From Fig. 4 it might appear that there are just two degenerate unrestricted Hartree-Fock determinants. But, remembering that we can chose the spin quantization axis at will, we see that by rotating the spins by an angle α about the axis $\hat{n}$ (see App. C)

$$R_{\hat{n}}(\alpha) = e^{-i\hat{n}\cdot\vec{\sigma}\,\alpha/2} = \cos(\alpha/2) - i\sin(\alpha/2)\,\hat{n}\cdot\vec{\sigma}$$

we can produce a continuum of degenerate solutions $\hat{R}_{\hat{n}}(\alpha)|\Phi_{\mathrm{UHF}}\rangle$. As an example we consider the state we obtain when we rotate the spin quantization axis from the $\hat{z}$ into the $\hat{x}$ direction

$$R_{\hat{y}}(-\pi/2) = \frac{1}{\sqrt{2}}\begin{pmatrix} 1 & 1 \\ -1 & 1 \end{pmatrix}$$

which transforms the creation operators according to (16) as

$$\left(c_{i\uparrow}^\dagger,\, c_{i\downarrow}^\dagger\right) R_{\hat{y}}(-\pi/2) = \left(\frac{1}{\sqrt{2}}\left(c_{i\uparrow}^\dagger - c_{i\downarrow}^\dagger\right),\, \frac{1}{\sqrt{2}}\left(c_{i\uparrow}^\dagger + c_{i\downarrow}^\dagger\right)\right).$$

The determinant (85) thus transforms to

$$\hat{R}_{\hat{y}}(-\pi/2)|\Phi(\theta_\uparrow,\theta_\downarrow)\rangle = \frac{1}{2}\Big(s_\downarrow(c_{1\uparrow}^\dagger + c_{1\downarrow}^\dagger) + c_\downarrow(c_{2\uparrow}^\dagger + c_{2\downarrow}^\dagger)\Big)\Big(s_\uparrow(c_{1\uparrow}^\dagger - c_{1\downarrow}^\dagger) + c_\uparrow(c_{2\uparrow}^\dagger - c_{2\downarrow}^\dagger)\Big)|0\rangle \tag{89}$$

where we introduced the abbreviations $s_\sigma = \sin\theta_\sigma$ and $c_\sigma = \cos\theta_\sigma$. Since the Hamiltonian (76) is invariant under spin rotations, $\hat{R}_{\hat{y}}(-\pi/2)\,\hat{H}\,\hat{R}_{\hat{y}}^\dagger(-\pi/2) = \hat{H}$, the energy expectation value of the rotated state is still given by (86).

Attractive Hubbard model For negative U allowing the spin orbitals to differ, $\Phi(\theta,\,\pi/2-\theta)$, does lower the energy expectation value. The minimum is always obtained for the restricted Hartree-Fock determinant $\Phi(\pi/4,\,\pi/4)$. In fact, for the attractive Hubbard model rather than breaking spin symmetry, we should try to break the charge symmetry: For $U < -2t$ the ansatz $\Phi(\theta,\theta)$ minimizes the energy for the two states $\theta(U) = \pi/4 \pm \arccos(-2t/U)$ with energy $E(U) = 2t^2/U + U$. Thus, the unrestricted Hartree-Fock ground state breaks the charge symmetry, i.e., is a charge-density wave state. On the other hand, looking back to (89) we see that $\Phi(\theta,\theta)$ is invariant under the spin rotation. This is actually true for any $\hat{R}_{\hat{n}}(\alpha)$ so that the unrestricted Hartree-Fock ground state of the attractive Hubbard model does not break spin symmetry.

It seems strange that for the attractive model we only find two unrestricted Hartree-Fock states, while for the repulsive model we have a continuum of states. To find the 'missing' states we consider a new kind of transformation that mixes creation and annihilation operators: When we exchange the role of the creation and annihilation operators for the up spins only, i.e.,

$$\tilde{c}_{i\uparrow}^\dagger = (-1)^i c_{i\uparrow} \quad \text{and} \quad \tilde{c}_{i\downarrow}^\dagger \to c_{i\downarrow}^\dagger, \tag{90}$$

the Hamiltonian (76) transforms into a two-site Hubbard model with the sign of U changed

$$\hat{H} = -t\sum_\sigma\left(\tilde{c}_{2\sigma}^\dagger\tilde{c}_{1\sigma} + \tilde{c}_{1\sigma}^\dagger\tilde{c}_{2\sigma}\right) - U\sum_{i\in\{1,2\}}\tilde{n}_{i\uparrow}\tilde{n}_{i\downarrow} + U(\tilde{n}_{1\downarrow} + \tilde{n}_{2\downarrow}). \tag{91}$$

Let us see what happens to the Slater determinant (85) when we apply the same transformation. In doing this, we have to remember that the vacuum state must vanish when acted on with an annihilator. For $|0\rangle$ this is no longer true for the transformed operators, but we can easily write down a state

$$|\tilde{0}\rangle = c^\dagger_{2\uparrow} c^\dagger_{1\uparrow} |0\rangle \tag{92}$$

that behaves as a suitable vacuum state: $\tilde{c}_{i\sigma}|\tilde{0}\rangle = 0$ and $\langle\tilde{0}|\tilde{0}\rangle$. We can then rewrite the transformed Slater determinant (85) as

$$\begin{aligned}
|\tilde{\Phi}(\theta_\uparrow,\theta_\downarrow)\rangle &= \Big(\sin(\theta_\downarrow)\,\tilde{c}^\dagger_{1\downarrow} + \cos(\theta_\downarrow)\,\tilde{c}^\dagger_{2\downarrow}\Big)\Big(\sin(\theta_\uparrow)\,\tilde{c}^\dagger_{1\uparrow} + \cos(\theta_\uparrow)\,\tilde{c}^\dagger_{2\uparrow}\Big)\,|\tilde{0}\rangle \\
&= \Big(\sin(\theta_\downarrow)\,c^\dagger_{1\downarrow} + \cos(\theta_\downarrow)\,c^\dagger_{2\downarrow}\Big)\Big(-\sin(\theta_\uparrow)\,c_{1\uparrow} + \cos(\theta_\uparrow)\,c_{2\uparrow}\Big)\,c^\dagger_{2\uparrow}c^\dagger_{1\uparrow}|0\rangle \\
&= \Big(\sin(\theta_\downarrow)\,c^\dagger_{1\downarrow} + \cos(\theta_\downarrow)\,c^\dagger_{2\downarrow}\Big)\Big(+\sin(\theta_\uparrow)\,c^\dagger_{2\uparrow} + \cos(\theta_\uparrow)\,c^\dagger_{1\uparrow}\Big)\,|0\rangle\ .
\end{aligned}$$

Thus, the transformation takes the unrestricted state $|\Phi(\theta,\pi/2-\theta)\rangle$ for the repulsive Hubbard model into the unrestricted state $|\Phi(\theta,\theta)\rangle$ for the attractive Hubbard model. Transforming the rotated state (89) in the same way, we find something remarkable:

$$\begin{aligned}
&\frac{1}{2}\Big(s_\downarrow(\tilde{c}^\dagger_{1\uparrow}+\tilde{c}^\dagger_{1\downarrow}) + c_\downarrow(\tilde{c}^\dagger_{2\uparrow}+\tilde{c}^\dagger_{2\downarrow})\Big)\Big(s_\uparrow(\tilde{c}^\dagger_{1\uparrow}-\tilde{c}^\dagger_{1\downarrow}) + c_\uparrow(\tilde{c}^\dagger_{2\uparrow}-\tilde{c}^\dagger_{2\downarrow})\Big)\,|\tilde{0}\rangle \\
&= \frac{1}{2}\Big(s_\downarrow(-c_{1\uparrow}+c^\dagger_{1\downarrow}) + c_\downarrow(c_{2\uparrow}+c^\dagger_{2\downarrow})\Big)\Big(s_\uparrow(-c_{1\uparrow}-c^\dagger_{1\downarrow}) + c_\uparrow(c_{2\uparrow}-c^\dagger_{2\downarrow})\Big)\,c^\dagger_{2\uparrow}c^\dagger_{1\uparrow}|0\rangle \\
&= \frac{1}{2}\Big((s_\downarrow c_\uparrow + c_\downarrow s_\uparrow)\big(c^\dagger_{1\downarrow}c^\dagger_{1\uparrow} + c^\dagger_{2\downarrow}c^\dagger_{2\uparrow}\big)|0\rangle + 2\big(s_\downarrow s_\uparrow c^\dagger_{1\downarrow}c^\dagger_{2\uparrow} + c_\downarrow c_\uparrow c^\dagger_{2\downarrow}c^\dagger_{2\uparrow}\big)|0\rangle \\
&\qquad + (s_\downarrow c_\uparrow - c_\downarrow s_\uparrow)\big(c^\dagger_{2\downarrow}c^\dagger_{1\downarrow}c^\dagger_{2\uparrow}c^\dagger_{1\uparrow} - 1\big)|0\rangle \qquad\qquad \Big).
\end{aligned}$$

The energy expectation value of this state is by construction the same as for the charge-density state. For $\theta_\downarrow = \pi/2-\theta_\uparrow$ the new state has a uniform density, but the wave function no longer has a well-defined particle number, i.e., it breaks particle number conservation. It is still a product state in the transformed operators and vacuum, but it is a state in Fock space. States of this type are crucial for describing superconductivity.

3.3 BCS theory

Next we consider the BCS Hamiltonian

$$\hat{H}_{\mathrm{BCS}} = \sum_{\boldsymbol{k}\sigma} \varepsilon_{\boldsymbol{k}}\, c^\dagger_{\boldsymbol{k}\sigma} c_{\boldsymbol{k}\sigma} - \sum_{\boldsymbol{k}\boldsymbol{k}'} G_{\boldsymbol{k}\boldsymbol{k}'}\, c^\dagger_{\boldsymbol{k}\uparrow} c^\dagger_{-\boldsymbol{k}\downarrow} c_{-\boldsymbol{k}'\downarrow} c_{\boldsymbol{k}'\uparrow} \tag{93}$$

with an attractive interaction between pairs of electrons of opposite spin and momentum (Cooper pairs). We now want to see if we can use the idea of product states in Fock space that we encountered for the attractive Hubbard model. To start, let us consider the determinant of plane wave states that we used for the homogeneous electron gas $|\Phi_{k_F}\rangle$. Since all states with momentum below k_F are occupied, we have

$$c^\dagger_{\boldsymbol{k}\sigma}|\Phi_{k_F}\rangle = 0 \ \text{ for } |\boldsymbol{k}| < k_F \text{ and } \quad c_{\boldsymbol{k}\sigma}|\Phi_{k_F}\rangle = 0 \ \text{ otherwise.}$$

Thus $|\Phi_{k_F}\rangle$ behaves like a vacuum state for the transformed operators

$$\tilde{c}_{\boldsymbol{k}\sigma} = \Theta(k_F - |\boldsymbol{k}|)\, c^\dagger_{\boldsymbol{k}\sigma} + \Theta(|\boldsymbol{k}| - k_F)\, c_{\boldsymbol{k}\sigma} = \begin{cases} c^\dagger_{\boldsymbol{k}\sigma} & \text{for } |\boldsymbol{k}| < k_F \\ c_{\boldsymbol{k}\sigma} & \text{for } |\boldsymbol{k}| > k_F \end{cases}$$

Allowing the operators to mix, we can generalize this transformation to

$$\begin{aligned} b_{\boldsymbol{k}\uparrow} &= u_k c_{\boldsymbol{k}\uparrow} - v_k c^\dagger_{-\boldsymbol{k}\downarrow} \\ b_{\boldsymbol{k}\downarrow} &= u_k c_{\boldsymbol{k}\downarrow} + v_k c^\dagger_{-\boldsymbol{k}\uparrow} \end{aligned}$$

The corresponding creation operators are obtained, of course, by taking the adjoint. Notice how states with $\boldsymbol{k}$ and $-\boldsymbol{k}$ are mixed. These Bogoliubov-Valatin operators fulfill the canonical anticommutation relations

$$\{b_{\boldsymbol{k}\sigma},\, b_{\boldsymbol{k}'\sigma'}\} = 0 = \{b^\dagger_{\boldsymbol{k}\sigma},\, b^\dagger_{\boldsymbol{k}'\sigma'}\} \quad \text{and} \quad \{b_{\boldsymbol{k}\sigma},\, b_{\boldsymbol{k}'\sigma'}\} = \delta(\boldsymbol{k} - \boldsymbol{k}')\, \delta_{\sigma,\sigma'}$$

when (the non-trivial anticommutators are $\{b_{\boldsymbol{k}\uparrow},\, b_{-\boldsymbol{k}\downarrow}\}$ and $\{b_{\boldsymbol{k}\sigma},\, b^\dagger_{\boldsymbol{k}\sigma}\}$)

$$u_k^2 + v_k^2 = 1\,. \tag{94}$$

A vacuum state for the new operators can be constructed from the generalized product state $\prod_{\boldsymbol{k}\sigma} b_{\boldsymbol{k}\sigma}|0\rangle$. Expanding the operators

$$b_{-\boldsymbol{k}\uparrow} b_{\boldsymbol{k}\downarrow} b_{\boldsymbol{k}\uparrow} b_{-\boldsymbol{k}\downarrow}|0\rangle = v_k(u_k + v_k\, c^\dagger_{-\boldsymbol{k}\uparrow} c^\dagger_{\boldsymbol{k}\downarrow})\, v_k(u_k + v_k\, c^\dagger_{\boldsymbol{k}\uparrow} c^\dagger_{-\boldsymbol{k}\downarrow})\, |0\rangle$$

and calculating the norm

$$\langle 0|(u_k + v_k\, c_{-\boldsymbol{k}\downarrow} c_{\boldsymbol{k}\uparrow})(u_k + v_k\, c^\dagger_{\boldsymbol{k}\downarrow} c^\dagger_{-\boldsymbol{k}\uparrow})(u_k + v_k\, c^\dagger_{-\boldsymbol{k}\uparrow} c^\dagger_{\boldsymbol{k}\downarrow})(u_k + v_k\, c^\dagger_{\boldsymbol{k}\uparrow} c^\dagger_{-\boldsymbol{k}\downarrow})|0\rangle = u_k^4 + 2u_k^2 v_k^2 + v_k^4$$

we see from (94) that the BCS wavefunction

$$|\mathrm{BCS}\rangle = \prod_{\boldsymbol{k}} (u_k + v_k\, c^\dagger_{\boldsymbol{k}\uparrow} c^\dagger_{-\boldsymbol{k}\downarrow})\, |0\rangle \tag{95}$$

is the (normalized) vacuum for the Bogoliubov-Valatin operators.
To calculate physical expectation values we express the electron operators as

$$\begin{aligned} c_{\boldsymbol{k}\uparrow} &= u_k b_{\boldsymbol{k}\uparrow} + v_k b^\dagger_{-\boldsymbol{k}\downarrow} \\ c_{\boldsymbol{k}\downarrow} &= u_k b_{\boldsymbol{k}\downarrow} - v_k b^\dagger_{-\boldsymbol{k}\uparrow} \end{aligned}$$

The expectation value for the occupation of a plane wave state, e.g., is

$$\langle \mathrm{BCS}|\hat{n}_{\boldsymbol{k}\uparrow}|\mathrm{BCS}\rangle = \langle \mathrm{BCS}|(u_k b^\dagger_{\boldsymbol{k}\uparrow} + v_k b_{-\boldsymbol{k}\downarrow})(u_k b_{\boldsymbol{k}\uparrow} + v_k b^\dagger_{-\boldsymbol{k}\downarrow})|\mathrm{BCS}\rangle = v_k^2 = \langle \mathrm{BCS}|\hat{n}_{-\boldsymbol{k}\downarrow}|\mathrm{BCS}\rangle\,.$$

Unlike the electron gas Slater determinant $|\Phi_{k_F}\rangle$, where $n_{\boldsymbol{k}\sigma}$ is 1 below k_F and vanishes above, varying the parameter v_k in the BCS wave function allows us to get arbitrary momentum distributions $\langle n_{\boldsymbol{k}\sigma}\rangle$. Since the BCS wave function has contributions in all particle sectors with an even number of electrons, there are also less-conventional expectation values, e.g.,

$$\langle \mathrm{BCS}|c^\dagger_{\boldsymbol{k}\uparrow} c^\dagger_{-\boldsymbol{k}\downarrow}|\mathrm{BCS}\rangle = \langle \mathrm{BCS}|(u_k b^\dagger_{\boldsymbol{k}\uparrow} + v_k b_{-\boldsymbol{k}\downarrow})(u_k b^\dagger_{-\boldsymbol{k}\downarrow} - v_k b_{\boldsymbol{k},\uparrow})|\mathrm{BCS}\rangle = u_k v_k = \langle c_{-\boldsymbol{k}\downarrow} c_{\boldsymbol{k}\uparrow}\rangle.$$

When minimizing the energy expectation value, we have to introduce a chemical potential μ that is chosen to give the desired number of particles $N = \sum_{\boldsymbol{k}\sigma} v_k^2$. We get

$$\langle \mathrm{BCS}|\hat{H} - \mu\hat{N}|\mathrm{BCS}\rangle = \sum_{\boldsymbol{k}\sigma}(\varepsilon_{\boldsymbol{k}} - \mu)\, v_k^2 - \sum_{\boldsymbol{k},\boldsymbol{k}'} G_{\boldsymbol{k}\boldsymbol{k}'}\, u_k v_k u_{k'} v_{k'}\,. \tag{96}$$

Minimizing with respect to v_k (and remembering that $u_k = \sqrt{1 - v_k^2}$) we find the variational equations

$$4(\varepsilon_{\boldsymbol{k}} - \mu)\, v_k = 2\sum_{\boldsymbol{k}'} G_{\boldsymbol{k}\boldsymbol{k}'} \left(u_k - \frac{v_k}{u_k} v_k\right) u_{k'} v_{k'}\,. \tag{97}$$

For simplicity we assume that $G_{\boldsymbol{k}\boldsymbol{k}'}$ is constant over a small range of $\boldsymbol{k}$ values around the Fermi surface and vanishes outside. We define

$$\Delta := \sum_{\boldsymbol{k}'} G_{\boldsymbol{k}\boldsymbol{k}'}\, u_{k'} v_{k'} = G \sum_{\boldsymbol{k}:\text{close to FS}} u_k v_k \tag{98}$$

and obtain, squaring the variational equation and remembering that $1 - (u_k^2 + v_k^2)^2 = 0$,

$$4(\varepsilon_{\boldsymbol{k}} - \mu)^2 u_k^2 v_k^2 = (\varepsilon_{\boldsymbol{k}} - \mu)^2\big(1 - (u_k^2 - v_k^2)^2\big) = \Delta^2(u_k^2 - v_k^2)$$

from which we get the momentum distribution

$$v_k^2 = \frac{1}{2}\left(1 - \frac{\varepsilon_{\boldsymbol{k}} - \mu}{\sqrt{(\varepsilon_{\boldsymbol{k}} - \mu)^2 + \Delta^2}}\right). \tag{99}$$

For $\Delta = 0$ this is just the step function of a Fermi gas, for finite Δ the transition is more smooth. We still have to determine the parameters μ and Δ. The chemical potential is fixed by

$$N = \sum_{\boldsymbol{k}} 2v_k^2 = \sum_{\boldsymbol{k}} \left(1 - \frac{\varepsilon_{\boldsymbol{k}} - \mu}{\sqrt{(\varepsilon_{\boldsymbol{k}} - \mu)^2 + \Delta^2}}\right) \tag{100}$$

while for Δ we obtain from (98), solving (97) for $u_k v_k$ and summing over k, and using $u_k^2 - v_k^2 = 1 - 2v_k^2$

$$\Delta = G\sum_{\boldsymbol{k}} u_k v_k = \frac{G}{2}\sum_{\boldsymbol{k}} \frac{\Delta(u_k^2 - v_k^2)}{\varepsilon_{\boldsymbol{k}} - \mu} = \Delta\frac{G}{2}\sum_{\boldsymbol{k}} \frac{1}{\sqrt{(\varepsilon_k - \mu)^2 + \Delta^2}} \tag{101}$$

the self-consistent gap equation for Δ.

To see that Δ is indeed a gap, consider the (unrelaxed) quasi-electron states

$$|\boldsymbol{k}\uparrow\rangle = \frac{1}{u_k} c^\dagger_{\boldsymbol{k}\uparrow}|\mathrm{BCS}\rangle = b^\dagger_{\boldsymbol{k}\uparrow}|\mathrm{BCS}\rangle. \tag{102}$$

Adding an electron of momentum $\boldsymbol{k}$ destroys its Cooper pair, changing $\langle n_{\boldsymbol{k}\uparrow} + n_{\boldsymbol{k}\downarrow}\rangle$ from $2v_k^2$ to 1 and removing the interaction of the pair with all others:

$$\begin{aligned}\langle \boldsymbol{k}\uparrow|\hat{H} - \mu\hat{N}|\boldsymbol{k}\uparrow\rangle - \langle \mathrm{BCS}|\hat{H} - \mu\hat{N}|\mathrm{BCS}\rangle &= (\varepsilon_{\boldsymbol{k}} - \mu)\,(1 - 2v_k^2) + 2\Delta\, u_k v_k \\ = (\varepsilon_{\boldsymbol{k}} - \mu)\,(1 - 2v_k^2) + \frac{\Delta^2}{\varepsilon_{\boldsymbol{k}} - \mu}(u_k^2 - v_k^2) &= \mathrm{sgn}(\varepsilon_{\boldsymbol{k}} - \mu)\,\sqrt{(\varepsilon_{\boldsymbol{k}} - \mu)^2 + \Delta^2}.\end{aligned}$$

For $\Delta =$ we recover Koopmans' Hartree-Fock result, while for $\Delta > 0$ a gap opens around the Fermi level. Fig. 5 compares the quasi-electron dispersion and the corresponding density of states for the two cases.

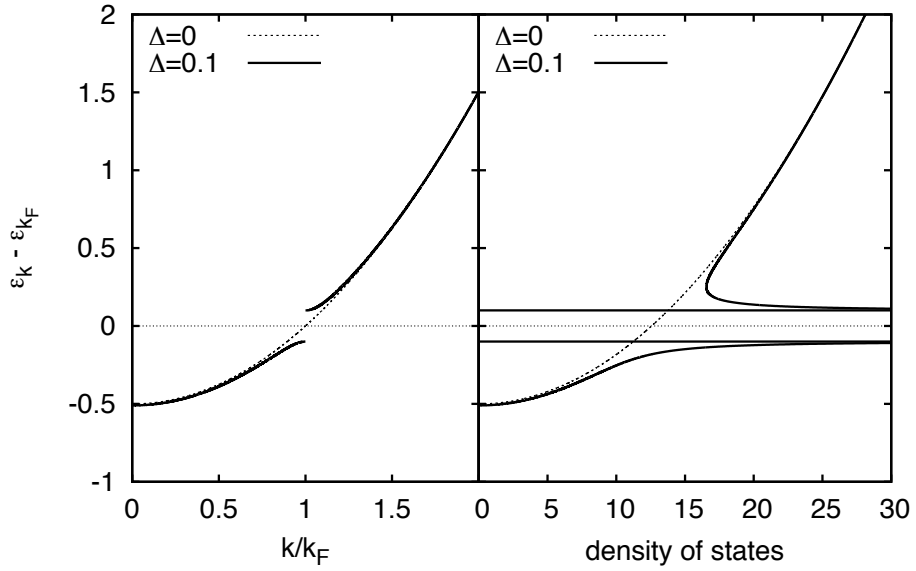

Fig. 5: *Quasi-electron energy and density of states for the BCS state with and without gap.*

4 Conclusion

We have seen that second quantization is an remarkable useful formalism. With just a few simple rules for the creation and annihilation operators and the corresponding vacuum, it converts dealing with many-electron states to straightforward algebraic manipulations. Moreover it is naturally suited for performing calculations in variational spaces spanned by a finite basis of orbitals. But its advantages go beyond a mere simplification. By abstracting from the coordinate representation, it allows us to express many-body operators in a way that is independent of the number of electrons. Because of this it becomes possible to consider Fock-space wave functions which do not have a definite number of electrons. This allows us to consider unrestricted mean-field states that not only break spatial or spin symmetries but also particle conservation. This additional freedom allows us to extend the concept of a Slater determinant to product states in Fock space, an example of which is the BCS wave function.

Acknowledgment

Support of the Deutsche Forschungsgemeinschaft through FOR1346 is gratefully acknowledged.

A Basis orthonormalization

A general one-electron basis spanned by functions $|\chi_n\rangle$ will have an overlap matrix

$$S_{nm} = \langle\chi_n|\chi_m\rangle$$

that is positive definite (and hence invertible) and hermitian. The completeness relation is

$$\mathbb{1} = \sum_{k,l} |\chi_k\rangle (S^{-1})_{kl} \langle\chi_l| \,.$$

While we can work directly with such a basis, it is often more convenient to have an orthonormal basis, so that we do not have to deal with the overlap matrices in the definition of the second quantized operators and in the generalized eigenvalue problem.
To orthonormalize the basis $\{|\chi_n\rangle\}$, we need to find a basis transformation $\boldsymbol{T}$ such that

$$|\varphi_n\rangle := \sum_m |\chi_m\rangle\, T_{mn} \qquad \text{with} \quad \langle\varphi_n|\varphi_m\rangle = \delta_{mn} \,.$$

This implies that $\boldsymbol{T}^\dagger \boldsymbol{S} \boldsymbol{T} = \mathbb{1}$, or equivalently $\boldsymbol{S}^{-1} = \boldsymbol{T}\boldsymbol{T}^\dagger$. This condition does not uniquely determine $\boldsymbol{T}$. In fact there are many orthonormalization techniques, e.g., Gram-Schmidt orthonormalization or Cholesky decomposition.
Usually we will have chosen the basis functions $|\chi_n\rangle$ for a physical reason, e.g., atomic orbitals, so that we would like the orthonormal basis functions to be as close to the original basis as possible, i.e, we ask for the basis transformation $\boldsymbol{T}$ that minimizes

$$\begin{aligned}
\sum_n \big\| \,|\varphi_n\rangle - |\chi_n\rangle\, \big\|^2 &= \sum_n \Big\| \sum_m |\chi_m\rangle (T_{mn} - \delta_{mn}) \Big\|^2 \\
&= \operatorname{Tr} \left(\boldsymbol{T}^\dagger - \mathbb{1}\right) \boldsymbol{S} \left(\boldsymbol{T} - \mathbb{1}\right) \\
&= \operatorname{Tr} \big(\underbrace{\boldsymbol{T}^\dagger \boldsymbol{S} \boldsymbol{T}}_{=\mathbb{1}} - \boldsymbol{T}^\dagger \boldsymbol{S} - \boldsymbol{S}\boldsymbol{T} + \boldsymbol{S}\big) \,.
\end{aligned}$$

Given an orthonormalization $\boldsymbol{T}$, we can obtain any other orthonormalization $\tilde{\boldsymbol{T}}$ by performing a unitary transformation, i.e., $\tilde{\boldsymbol{T}} = \boldsymbol{T}\boldsymbol{U}$. Writing $\boldsymbol{U} = \exp(i\lambda \boldsymbol{M})$, we obtain the variational condition

$$0 \stackrel{!}{=} \operatorname{Tr} \left(+i\boldsymbol{M}\boldsymbol{T}^\dagger \boldsymbol{S} - i\boldsymbol{S}\boldsymbol{T}\boldsymbol{M}\right) = i \operatorname{Tr} \left(\boldsymbol{T}^\dagger \boldsymbol{S} - \boldsymbol{S}\boldsymbol{T}\right)\boldsymbol{M},$$

which is fulfilled for $\boldsymbol{S}\boldsymbol{T} = \boldsymbol{T}^\dagger \boldsymbol{S}$, i.e., $\boldsymbol{S}\boldsymbol{T}^2 = \boldsymbol{T}^\dagger \boldsymbol{S}\boldsymbol{T} = \mathbb{1}$. The second variation at $\boldsymbol{T} = \boldsymbol{S}^{-1/2}$

$$\frac{1}{2} \operatorname{Tr} \left(\boldsymbol{M}^2 \boldsymbol{S}^{1/2} + \boldsymbol{S}^{1/2} \boldsymbol{M}^2\right) > 0$$

is positive, since $\boldsymbol{S}$ and the square of the hermitian matrix $\boldsymbol{M}$ are both positive definite. Hence the Löwdin symmetric orthogonalization [14]

$$\boldsymbol{T}_{\text{Löwdin}} = \boldsymbol{S}^{-1/2}$$

minimizes the modification of the basis vectors.

B Some useful commutation relations

Expression of commutators of products of operators can be derived by adding and subtracting terms that differ only in the position of one operator, e.g.,

$$\begin{aligned}
[A_1 A_2 \cdots A_N,\, B] = &\quad A_1 A_2 \cdots A_N B - B A_1 A_2 \cdots A_N \\
= &\quad A_1 A_2 \cdots A_N B - A_1 A_2 \cdots B A_N \\
&+ A_1 A_2 \cdots B A_N - A_1 \cdots B A_{N-1} A_N \\
&+ \qquad\qquad \cdots \\
&+ A_1 B A_2 \cdots A_N - B A_1 A_2 \cdots A_N \\
= &\sum_i A_1 \cdots A_{i-1}\, [A_i,\, B]\, A_{i+1} \cdots A_N
\end{aligned}$$

The following special cases are particularly useful

$$\begin{aligned}
[AB,\, C] &= A\,[B,\, C] \,+\, [A,\, C]\,B \\
&= A\{B,\, C\} - \{A,\, C\}B \\
[A,\, BC] &= B\,[A,\, C] \,+\, [A,\, B]\,C \\
&= [A,\, B]\,C \,+\, B\,[A,\, C] \\
&= \{A,\, B\}C - B\{A,\, C\} \\
[AB,\, CD] &= A\,[B,\, C]\,D + AC\,[B,\, D] \,+\, [A,C]\,DB + C\,[A,\, D]\,B \\
&= A\{B,\, C\}D - AC\{B,\, D\} + \{A,C\}DB - C\{A,\, D\}B
\end{aligned}$$

Important examples are

$$\begin{aligned}
\left[c_i^\dagger c_j,\, c_\gamma^\dagger\right] &= \quad c_i^\dagger \delta_{j,\gamma} \\
\left[c_i^\dagger c_j,\, c_\gamma\right] &= -c_j \delta_{i,\gamma}
\end{aligned}$$

For the commutator of products of creation and annihilation operators appearing in one- and two-body operators we find

$$\left[c_i^\dagger c_j,\, c_\alpha^\dagger c_\beta\right] = \left[c_i^\dagger c_j,\, c_\alpha^\dagger\right] c_\beta + c_\alpha^\dagger \left[c_i^\dagger c_j,\, c_\beta\right] = \langle j|\alpha\rangle\, c_i^\dagger c_\beta - \langle \beta|i\rangle\, c_\alpha^\dagger c_j$$

and

$$\left[c_i^\dagger c_j^\dagger c_k c_l,\, c_\alpha^\dagger c_\beta\right] = \langle l|\alpha\rangle\, c_i^\dagger c_j^\dagger c_k c_\beta + \langle k|\alpha\rangle\, c_i^\dagger c_j^\dagger c_\beta c_l - \langle \beta|j\rangle\, c_i^\dagger c_\alpha^\dagger c_k c_l - \langle \beta|i\rangle\, c_\alpha^\dagger c_j^\dagger c_k c_l$$

C Pauli matrices and spin rotations

The Pauli or spin matrices are defined as

$$\sigma_x = \begin{pmatrix} 0 & 1 \\ 1 & 0 \end{pmatrix} \quad \sigma_y = \begin{pmatrix} 0 & -i \\ i & 0 \end{pmatrix} \quad \sigma_z = \begin{pmatrix} 1 & 0 \\ 0 & -1 \end{pmatrix}$$

They are hermitian, i.e. $\sigma_i^\dagger = \sigma_i$, and $\sigma_i^2 = 1$. Therefore their eigenvalues are ± 1. The eigenvectors of σ_z are $|m_z\rangle$, $m_z = \pm 1$:

$$|+1\rangle = \begin{pmatrix} 1 \\ 0 \end{pmatrix} \quad \text{and} \quad |-1\rangle = \begin{pmatrix} 0 \\ 1 \end{pmatrix}.$$

For these vectors we find

$$\sigma_x|\,m_z\rangle = |\,-m_z\rangle \quad \sigma_y|\,m_z\rangle = i m_z|\,-m_z\rangle \quad \sigma_z|\,m_z\rangle = m_z|\,m_z\rangle.$$

The products of the Pauli matrices are $\sigma_x\,\sigma_y = i\sigma_z$, where the indices can be permuted cyclically. From this follows for the commutator

$$[\sigma_x, \sigma_y] = 2i\sigma_z$$

while the anticommutator vanishes:

$$\{\sigma_x, \sigma_y\} = 0$$

Finally a rotation by an angle α about the axis $\hat{n}$ changes the spin matrices

$$R_{\hat{n}}(\alpha) = e^{-i\hat{n}\cdot\vec{\sigma}\,\alpha/2} = \cos(\alpha/2) - i\sin(\alpha/2)\,\hat{n}\cdot\vec{\sigma}\,.$$

References

[1] P. Forrest: *The Identity of Indiscernibles*, in The Stanford Encyclopedia of Philosophy (Winter 2012 Ed.), E.N. Zalta (ed.)
http://plato.stanford.edu/entries/identity-indiscernible/

[2] W. Pauli: *The connection between spin and statistics*, Phys. Rev. **58**, 715 (1940)

[3] R.F. Streater and A.S. Wightman: *PCT, Spin and Statistics, and All That* (Benjamin, New York, 1964)

[4] P.-O. Löwdin: *Quantum Theory of Many-Particle Systems I*, Phys. Rev. **97**, 1474 (1955)

[5] P. Jordan and O. Klein: *Zum Mehrkörperproblem in der Quantenmechanik*, Z. Physik **45**, 751 (1927)

[6] P. Jordan and E. Wigner: *Über das Paulische Äquivalenzverbot*, Z. Physik **47**, 631 (1928)

[7] P. Jorgensen and J. Simons: *Second Quantization-Based Methods in Quantum Chemistry* (Academic Press, New York, 1981)

[8] D.J. Thouless: *Stability conditions and nuclear rotations in the Hartree-Fock theory*, Nucl. Phys. **21**, 225 (1960)

[9] Le Thi Hoai: *Product wave-functions in Fock-space* (MSc Thesis, German Research School for Simulation Sciences, 2015)

[10] E. Koch: *Many-Electron States* in [15]

[11] S. Zhang and D.M. Ceperley: *Hartree-Fock Ground State of the Three-Dimensional Electron Gas*, Phys. Rev. Lett. **100**, 236404 (2008)

[12] E. Koch: *Exchange Mechanisms* in [16]

[13] A. Szabo and N.S. Ostlund: *Modern Quantum Chemistry* (McGraw Hill, New York, 1989)

[14] P.-O. Löwdin: *On the Non-Orthogonality Problem Connected with the Use of Atomic Wave Functions in the Theory of Molecules and Crystals*, J. Chem. Phys. **18**, 365 (1950)

[15] E. Pavarini, E. Koch, and U. Schollwöck (Eds.): *Emergent Phenomena in Correlated Matter*, Reihe Modeling and Simulation, Vol. 3 (Forschungszentrum Jülich, 2013)
http://www.cond-mat.de/events/correl13

[16] E. Pavarini, E. Koch, F. Anders, and M. Jarrell (Eds.): *From Models to Materials*, Reihe Modeling and Simulation, Vol. 2 (Forschungszentrum Jülich, 2012)
http://www.cond-mat.de/events/correl12

3 Tight-Binding Models and Coulomb Interactions for s, p, and d Electrons

W.M.C. Foulkes
Department of Physics, Imperial College London
South Kensington Campus, London SW7 2AZ
United Kingdom

Contents

E. Pavarini, E. Koch, J. van den Brink, and G. Sawatzky (eds.)
Quantum Materials: Experiments and Theory
Modeling and Simulation Vol. 6
Forschungszentrum Jülich, 2016, ISBN 978-3-95806-159-0
http://www.cond-mat.de/events/correl16

1 Introduction

The tight-binding method is the simplest fully quantum mechanical approach to the electronic structure of molecules and solids. Although less accurate than density functional calculations done with a good basis set, tight-binding calculations provide an appealingly direct and transparent picture of chemical bonding [1–10]. Easily interpreted quantities such as local densities of states and bond orders can be obtained from density-functional codes too, but emerge much more naturally in a tight-binding picture. Another advantage of tight-binding calculations is that they require much less computer time than more sophisticated electronic structure calculations, whilst still producing qualitatively and often quantitatively correct results. Chemists also value the efficiency and intuitive simplicity of the tight-binding method, although they usually refer to it as Hückel theory.

In non-interacting systems, tight-binding calculations are so simple that analytic results are often attainable — a rare occurrence in the study of electrons in molecules and solids. Interacting systems are much more difficult to deal with and the scope for analytic work is correspondingly smaller, but the multi-band Hubbard model, which may be viewed as an interacting generalization of a tight-binding model, forms the starting point of much of the work in the field.

Section 2 provides a simple introduction to tight-binding methods for non-interacting systems, showing how to obtain the Hamiltonian matrix by choosing a basis of localized atomic-like basis functions and using the variational principle. The distinction between the semi-empirical and ab-initio tight-binding methods is clarified and a few example semi-empirical tight-binding calculations are discussed.

Section 3 addresses the relationship between non-selfconsistent tight-binding models and density-functional theory, which was not fully understood until the late eighties [11, 12].

Section 4 introduces the multi-band Hubbard generalization of the tight-binding approximation and explains how it may be used to describe systems of interacting electrons. The rotational symmetry of the Coulomb interaction places strong restrictions on the form of the electron-electron interaction part of the multi-band Hubbard Hamiltonian: for an s shell the interaction Hamiltonian has only one free parameter; for a p shell there are two free parameters; and for a d shell there are three free parameters. It turns out that some of the most widely used Hubbard- and Stoner-like models of interacting electrons are missing terms that must be present by symmetry and are not necessarily small [13].

2 Tight-binding models

All electronic structure methods require the calculation of sets of one-electron orbitals $\psi_i(\boldsymbol{r})$. In most cases, these are solutions of a non-interacting or mean-field Schrödinger equation of the form[1]

[1]This chapter uses dimensionless equations involving only the numerical values of physical quantities. The numerical values are as measured in Hartree atomic units, where the Dirac constant $\hbar = h/2\pi$, the mass of an electron m_e, and the elementary charge e are all equal to unity, and the permittivity of free space

$$\left(-\frac{1}{2}\nabla^2 + V_{\text{eff}}(\boldsymbol{r})\right)\psi_i(\boldsymbol{r}) = \epsilon_i\psi_i(\boldsymbol{r})\,. \tag{1}$$

The effective potential V_{eff} is a simple multiplicative function of position in density-functional theory (DFT), but in Hartree-Fock theory it becomes a non-local integral operator, and in quasiparticle theory it is both non-local and energy dependent.

Differential equations such as Eq. (1) are often solved by introducing a spatial grid and discretizing, but this approach is not much used in electronic structure theory. Instead, most electronic structure methods represent the orbitals as linear combinations of basis functions and recast the Schrödinger equation in matrix form. The finite-element approach so prevalent in engineering also uses a basis set, although the basis functions in that case are polynomials defined within polyhedral volume elements, patched together at the interfaces between elements. The clearest way to explain the basis-set approach is via the variational principle.

2.1 Variational formulation of the Schrödinger equation

The problem of finding the eigenfunctions of a Hamiltonian $\hat{H}$ is equivalent to the problem of finding the stationary points (by which, of course, I mean the stationary wave functions) of the functional

$$E[\psi] = \langle\psi|\hat{H}|\psi\rangle \tag{2}$$

subject to the normalization constraint

$$N[\psi] = \langle\psi|\psi\rangle = 1\,. \tag{3}$$

The constrained minimum value of $E[\psi]$ is the ground-state eigenvalue; the values of $E[\psi]$ at other stationary points are excited-state eigenvalues.

Suppose we make a guess, $\tilde{\psi}_i$, at the i'th energy eigenfunction ψ_i. We can then write

$$\tilde{\psi}_i = \frac{\psi_i + \Delta\psi_i}{\langle\psi_i + \Delta\psi_i|\psi_i + \Delta\psi_i\rangle^{1/2}},$$

where $\Delta\psi_i$ is small if the guess is good. Since $E[\psi]$ is stationary with respect to normalization-conserving variations about ψ_i, the energy estimate

$$E[\tilde{\psi}_i] = \epsilon_i + \mathcal{O}[(\Delta\psi_i)^2]$$

has a second-order error. If $\Delta\psi_i$ is small, the error in ϵ_i is even smaller.

The practical importance of this simple observation is hard to exaggerate. It explains why variational approaches often yield reliable energies even when the approximate eigenfunctions are quite poor.

ε_0 is equal to $1/(4\pi)$. Distances are made dimensionless by dividing by the Hartree atomic unit of length, $a_0 = 4\pi\varepsilon_0\hbar^2/(m_e e^2) \approx 0.529 \times 10^{-10}$ m, also known as the Bohr radius. Energies are made dimensionless by dividing by the Hartree atomic unit of energy, $\hbar^2/(ma_0^2) = e^2/(4\pi\varepsilon_0 a_0) \approx 27.2$ eV.

A convenient way to guess a wave function is to choose a finite set of M basis functions, $\{\phi_1(\boldsymbol{r}),\, \phi_2(\boldsymbol{r}),\, \ldots,\, \phi_M(\boldsymbol{r})\}$, and express $\tilde{\psi}(\boldsymbol{r})$ as a linear combination:

$$\tilde{\psi}(\boldsymbol{c}, \boldsymbol{r}) = \sum_{\alpha=1}^{M} c_\alpha\, \phi_\alpha(\boldsymbol{r})\,. \tag{4}$$

Basis sets commonly used to approximate the energy eigenfunctions of atoms, molecules and solids include atom-centered Gaussians, plane waves, and atomic orbitals. The values of the expansion coefficients can be chosen by seeking the stationary points of

$$E[\tilde{\psi}] = E(\boldsymbol{c}) = \int \left(\sum_{\alpha=1}^{M} c_\alpha \phi_\alpha\right)^* \hat{H} \left(\sum_{\beta=1}^{M} c_\beta \phi_\beta\right) d^3r = \sum_{\alpha,\beta}^{M} c_\alpha^*\, H_{\alpha\beta}\, c_\beta\,, \tag{5}$$

subject to the normalization constraint

$$N[\tilde{\psi}] = N(\boldsymbol{c}) = \int \left(\sum_{\alpha=1}^{M} c_\alpha \phi_\alpha\right)^* \left(\sum_{\beta=1}^{M} c_\beta \phi_\beta\right) d^3r = \sum_{\alpha,\beta}^{M} c_\alpha^*\, S_{\alpha\beta}\, c_\beta = 1\,, \tag{6}$$

where

$$H_{\alpha\beta} \equiv \int \phi_\alpha^* \hat{H} \phi_\beta = \text{Hamiltonian matrix}, \tag{7}$$

$$S_{\alpha\beta} \equiv \int \phi_\alpha^* \phi_\beta \quad = \text{overlap matrix}. \tag{8}$$

Given a basis set, the Hamiltonian and overlap matrix elements must be obtained by integration. The integrals can be evaluated analytically in some cases, but usually have to be estimated numerically, perhaps using a grid-based quadrature method. Some basis sets (such as plane waves) are orthonormal, in which case $S_{\alpha\beta} = \delta_{\alpha\beta}$ is the identity matrix. The Hamiltonian and overlap matrices are always Hermitian.

By choosing a finite basis set, we have replaced the problem of finding the stationary points of a functional $E[\tilde{\psi}]$ by the problem of finding the stationary points of a function of many variables $E(c_1, c_2, \ldots, c_M)$. This is a great simplification. If the basis set is poor, the functions $\tilde{\psi}(\boldsymbol{r}) = \sum_{\alpha=1}^{M} c_\alpha\, \phi_\alpha(\boldsymbol{r})$ that make $E(c_1, c_2, \ldots, c_M)$ stationary subject to the normalization constraint $\sum_{\alpha,\beta} c_\alpha^*\, S_{\alpha\beta}\, c_\beta = 1$ may not be very similar to the exact eigenfunctions, but at least we will have the variational principle in our favor when evaluating energies.

It is straightforward to show that $E(\boldsymbol{c})$ is stationary subject to $N(\boldsymbol{c}) = 1$ when

$$\sum_{\beta=1}^{M} H_{\alpha\beta}\, c_\beta = \tilde{\epsilon} \sum_{\beta=1}^{M} S_{\alpha\beta}\, c_\beta\,, \tag{9}$$

where $\tilde{\epsilon}$ is a Lagrange multiplier for the normalization constraint. This *generalized Hermitian matrix eigenproblem* ("generalized" because of the presence of a positive-definite Hermitian overlap matrix $\boldsymbol{S}$) yields M real eigenvalues $\tilde{\epsilon}_i$ and M eigenvectors $\boldsymbol{c}_i$ with components $c_{i\alpha}$, $\alpha = 1, 2, \ldots, M$. The corresponding approximate eigenfunctions are

$$\tilde{\psi}_i(\boldsymbol{r}) = \sum_{\alpha=1}^{M} c_{i\alpha} \phi_\alpha(\boldsymbol{r})\,. \tag{10}$$

Standard computational libraries such as LAPACK contain robust and well-tested subroutines for solving generalized eigenvalue problems.

Another way to think about the linear variational method is in terms of projection operators. The generalized matrix eigenproblem of Eq. (9) may be derived by seeking the stationary points of $\langle\psi|\hat{P}\hat{H}\hat{P}|\psi\rangle$ subject to the normalization constraint $\langle\psi|\hat{P}|\psi\rangle = 1$, where $\hat{P}$ is the projector onto the space spanned by the basis functions. The linear variational method produces *exact* eigenfunctions of the *projected* Hamiltonian $\hat{H}^P \equiv \hat{P}\hat{H}\hat{P}$.

The Rayleigh-Ritz variational principle tells us that M approximate eigenvalues, $\tilde{\epsilon}_1$, $\tilde{\epsilon}_2$, ..., $\tilde{\epsilon}_M$, obtained by solving a linear variational problem with a basis set of M functions are upper bounds for the corresponding exact eigenvalues:

$$\tilde{\epsilon}_1 \geq \epsilon_1, \quad \tilde{\epsilon}_2 \geq \epsilon_2, \quad \ldots, \quad \tilde{\epsilon}_M \geq \epsilon_M.$$

Improving or extending the basis set can only lower these bounds. This convenient systematic convergence underlies the success of the linear variational approach and explains why it is so frequently used to solve the Schrödinger equation.

2.2 The tight-binding Hamiltonian matrix

If the basis functions used in the linear variational method are atomic or atomic-like orbitals, the generalized matrix eigenvalue problem is called a tight-binding model. The phrase "atomic-like" refers to orbitals that resemble atomic orbitals in form but have been modified in some way. Atomic orbitals centered on different atoms are not automatically orthogonal, so one common modification is to replace them by orthogonalized linear combinations. More generally, since there is no guarantee that atomic orbitals are a good basis for the strongly delocalized energy eigenfunctions found in many molecules and solids, one can often gain accuracy by changing the atomic orbitals in simple ways, using the variational principle as a guide. A more extreme approach is to replace the atomic orbitals by localized linear combinations of exact energy eigenfunctions for the solid, guaranteeing that the basis set is able to represent those eigenfunctions exactly.

2.2.1 *Ab initio* tight binding

The most straightforward way to construct a tight-binding model is to choose an atomic-like basis set and evaluate the Hamiltonian and overlap matrix elements defined in Eqs. (7) and (8). If the basis functions and (pseudo-)potential are represented as linear combinations of Gaussians, the necessary integrals can be evaluated analytically, but in most other cases they must be found using numerical quadrature methods. If one is willing to evaluate the matrix elements repeatedly as the charge density iterates to self-consistency and the effective potential changes (see Sec. 3 for a fuller discussion), this *ab initio* tight-binding approach [14–16, 7] can be used to solve the full DFT or Hartree-Fock equations.

When used in this manner, the tight-binding method differs little from the atom-centered Gaussian methods used by quantum chemists. There is, however, a difference of emphasis: scientists who label their approach as tight binding use minimal basis sets, often consisting of just a few

basis functions on each atom. They view the loss of accuracy caused by the limitations of the basis as a price worth paying for the sake of simplicity. Most quantum chemists prefer to increase the number of Gaussians until the results of their calculations converge.

Using a minimal basis set of atomic-like functions is most successful when the distances between atoms are reasonably large compared with the ranges of the basis functions. This is known as the tight-binding limit. In nearly-free-electron sp-bonded metals such as aluminium, where the valence wave functions look more like plane waves than atomic orbitals, minimal tight-binding basis sets are not very effective. This does not prevent the use of *ab initio* tight binding, but means that more basis functions are required to obtain accurate results. In d- and f-electron metals, the tight-binding description works better for the d and f bands than for the more delocalized s and p bands.

It is tempting to avoid the complication of dealing with an overlap matrix by orthogonalizing the basis functions. This is easily accomplished using the modified Gram-Schmidt algorithm or by multiplication with the inverse square root of the overlap matrix (which always exists because $\boldsymbol{S}$ is Hermitian and positive definite). In most cases, however, orthonormalizing the atomic-like basis functions is a bad idea. Generalized eigenvalue problems are not much harder to solve than ordinary eigenvalue problems, so little computer time is saved, but the complexity of the method is increased because the orthonormalized basis functions include contributions from atomic-like orbitals centered on several different atoms and lack the simple rotational symmetries of atomic-like orbitals. The complicated dependence of the orthonormalized orbitals on the local crystal structure also makes it harder to find simple parametrizations of the Hamiltonian matrix.

2.2.2 Wannier tight binding

A more sophisticated approach to *ab initio* tight binding is to use a basis of localized linear combinations of exact eigenfunctions; these are called Wannier functions by physicists and Foster-Boys orbitals by chemists [17,18]. Since there is one Wannier function for every energy eigenfunction, the Wannier functions span the band(s) from which they were created. Solving the tight-binding matrix eigenvalue problem in the Wannier function basis therefore reproduces those energy bands and eigenfunctions exactly. This means that using the Wannier basis for, say, electronic transport calculations, ought to give accurate results. The "maximally localized" [18] Wannier bonding orbitals for Si and GaAs are illustrated in Fig. 1.

Wannier-based tight-binding methods preserve many of the advantages of simpler tight-binding approaches without the inaccuracy, but Wannier functions are complicated in form and hard to calculate without solving the Schrödinger equation. Furthermore, although carefully constructed Wannier functions decay exponentially with distance away from the atom or bond on which they are centered [18], they may not decay rapidly. The Hamiltonian and overlap matrices can be quite long-ranged and may have non-zero matrix elements between Wannier functions on distant atoms, making them inconvenient to use. Finally, if an atom moves, the Wannier functions and all matrix elements involving them have to be recalculated from scratch, which is inefficient.

Fig. 1: *Maximally-localized Wannier functions constructed from the four valence bands of Si (left) and GaAs (right; Ga at upper right, As at lower left). The Wannier functions are real and have opposite sign on the blue and red isosurfaces. Not surprisingly, the functions look like σ-bonded combinations of sp^3 hybrid orbitals. (Reprinted figure with permission from Ref. [18], Copyright 2012 by the American Physical Society.)*

2.2.3 Semi-empirical tight binding

A much simpler approach is semi-empirical tight-binding [2, 3], in which the Hamiltonian and overlap matrix elements are treated as adjustable parameters and fitted to the results of experiments or more sophisticated calculations. The basis functions never appear explicitly and are used only to help justify the chosen forms of the Hamiltonian and overlap matrices. To limit the number of fitting parameters, it is normally assumed that the inter-atomic matrix elements extend to first or second neighbors only. Many semi-empirical tight-binding models also set the overlap matrix to the identity, assuming implicitly that the underlying basis set has been orthonormalized.

The drawbacks of this approach are obvious: it is approximate and may or may not give accurate results; but it does incorporate the essential wave-like physics described by the Schrödinger equation. To the best of my knowledge, it is the least computationally intensive fully quantum mechanical method available. To show what can be done using relatively modest computational resources, Fig. 2 is a snapshot from a 95 fs semi-empirical tight-binding molecular-dynamics simulation of a radiation damage cascade in a box of 13,440 Cu atoms subject to periodic boundary conditions.

2.2.4 One-, two- and three-center integrals

In an attempt to simplify the construction of semi-empirical tight-binding models, various approximations are made. The tight-binding description of the electronic structure of a given crystal structure then requires only a handful of fitting parameters. If the tight-binding model is to be used in a molecular-dynamics simulation, where the atoms are moving and the structure is changing, these parameters become functions of the local structure of the solid. For example, a Hamiltonian or overlap matrix element involving atomic-like basis functions on two different atoms is a function of the separation between those atoms and perhaps also of the positions of other neighboring atoms.

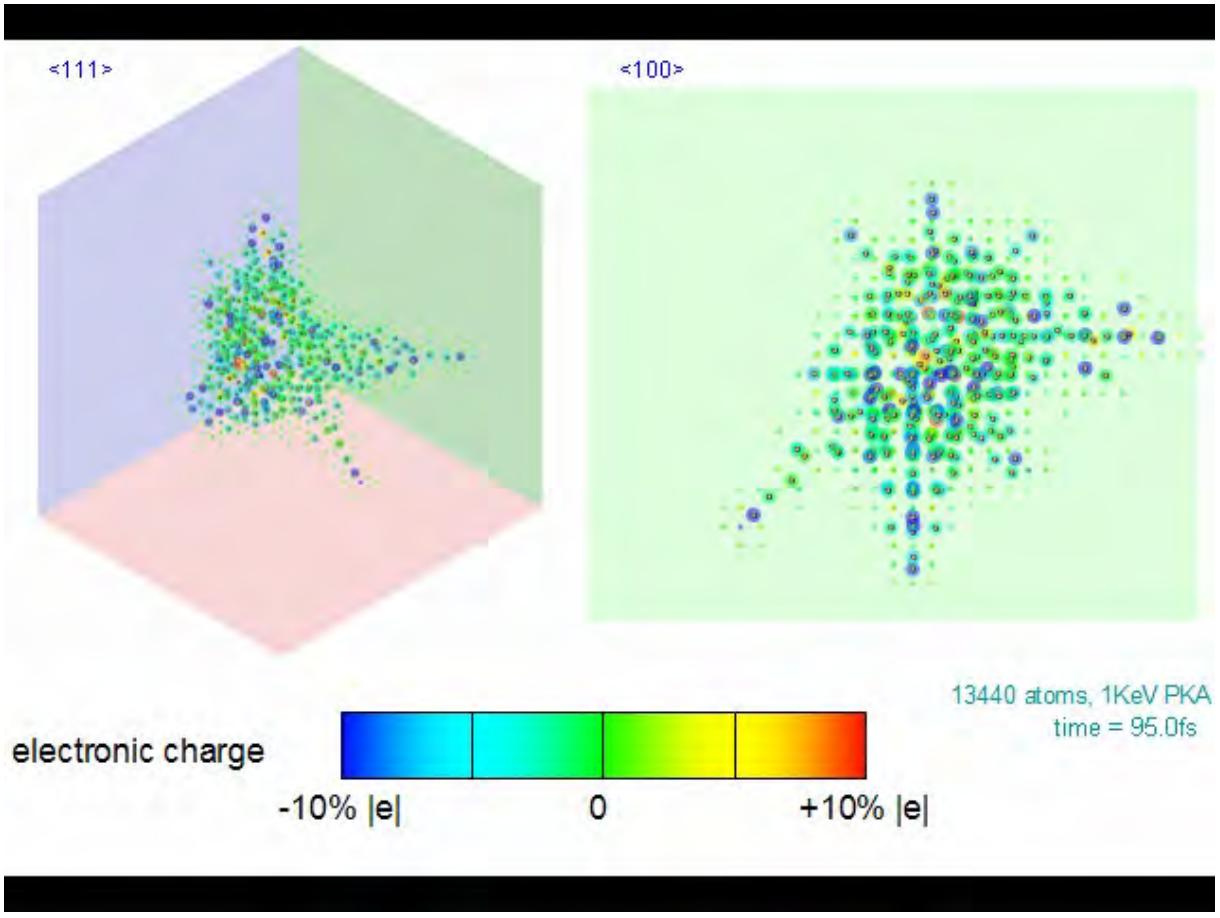

Fig. 2: *The final configuration of a 95 fs tight-binding molecular dynamics simulation of a radiation damage cascade in Cu. The cascade was initiated by giving 1 keV of kinetic energy to a single atom in the middle of a simulation cell of 13,440 atoms. Only atoms that have moved significantly are shown. One of the advantages of the tight-binding method relative to classical force-field methods is that it has access to electronic properties. Here we show the instantaneous atomic charges.*

The most useful approximation concerns the form of the potential $V_{\rm eff}(\boldsymbol{r})$, which is often assumed to be a superposition of short-ranged spherical contributions, one centered on each atom:

$$V_{\rm eff}(\boldsymbol{r}) \approx \sum_I V_{{\rm eff},I}(|\boldsymbol{r}-\boldsymbol{d}_I|)\,, \tag{11}$$

where $\boldsymbol{d}_I$ is the position of the nucleus of atom I (or the ionic core of atom I if, as is usual, the tight-binding model describes the valence electrons only). DFT calculations for many molecules and solids have shown that Eq. (11) is often quite a good approximation.
A general Hamiltonian matrix element between basis function α on atom I and basis function β on atom J then takes the form:

$$H_{I\alpha,J\beta} = \langle\phi_{I\alpha}|\hat{H}|\phi_{J\beta}\rangle = \langle\phi_{I\alpha}|\Big(-\frac{1}{2}\nabla^2 + \sum_K V_{{\rm eff},K}(|\boldsymbol{r}-\boldsymbol{d}_K|)\Big)|\phi_{J\beta}\rangle\,. \tag{12}$$

If I and J happen to be the same, $I = J$, the matrix element includes one- and two-center

contributions:

$$\langle\phi_{I\alpha}|\hat{H}|\phi_{I\beta}\rangle = \underbrace{\langle\phi_{I\alpha}|\left(-\frac{1}{2}\nabla^2 + V_{\text{eff},I}\right)|\phi_{I\beta}\rangle}_{\text{one-center}} + \sum_{K\ (\neq I)} \underbrace{\langle\phi_{I\alpha}|V_{\text{eff},K}|\phi_{I\beta}\rangle}_{\text{two-center crystal field}}. \tag{13}$$

The one-center term can be calculated considering a single spherical atom in isolation. The two-center crystal-field terms, which are often ignored, depend on the relative positions of two different atoms and describe how the Hamiltonian matrix elements between orbitals centered on atom I are affected by the potential of atom K.

If I and J differ, the Hamiltonian matrix elements include two- and three-center contributions:

$$\langle\phi_{I\alpha}|\hat{H}|\phi_{J\beta}\rangle = \underbrace{\langle\phi_{I\alpha}|\left(-\frac{1}{2}\nabla^2 + V_{\text{eff},I} + V_{\text{eff},J}\right)|\phi_{J\beta}\rangle}_{\text{two-center electron hopping}} + \sum_{K\ (\neq I,J)} \underbrace{\langle\phi_{I\alpha}|V_{\text{eff},K}|\phi_{J\beta}\rangle}_{\text{three-center}}. \tag{14}$$

The two-center electron hopping contributions are the same as in a dimer involving atoms I and J only and can be calculated without considering the rest of the solid. The three-center contributions are typically small and, like the crystal-field terms, are often ignored. (Both crystal-field and three-center terms are normally retained in *ab initio* tight-binding calculations.) The overlap matrix elements can be decomposed in an analogous manner, but include one- and two-center contributions only.

If we make the two-center approximation (ignore all three-center integrals) and neglect crystal-field terms, the Hamiltonian matrix for a solid or molecule becomes very simple. It contains one-center terms, which can be calculated by considering an isolated "atom" with a spherical Hamiltonian, and two-center electron hopping terms, which can be calculated by considering an isolated "dimer" with a cylindrical Hamiltonian. The words "atom" and "dimer" are in quotation marks because the potential $V_{\text{eff},I}$ associated with atom I may not resemble the potential of an isolated atom and may depend on the environment in which atom I is located.

2.2.5 Slater-Koster parameters

Most tight-binding models use atomic-like basis functions of the form $R_{nl}(r)\tilde{Y}_l^m(\theta,\phi)$, where $R_{nl}(r)$ is a radial function, $\tilde{Y}_l^m(\theta,\phi)$ is a real spherical harmonic defined by

$$\tilde{Y}_l^m = \frac{1}{i\sqrt{2}}\left[(-1)^m Y_l^{-m} - Y_l^m\right], \qquad m < 0, \tag{15}$$

$$\tilde{Y}_l^m = Y_l^m, \qquad m = 0, \tag{16}$$

$$\tilde{Y}_l^m = \frac{1}{\sqrt{2}}\left[(-1)^m Y_l^m + Y_l^{-m}\right], \qquad m > 0, \tag{17}$$

and Y_l^m is a conventional complex spherical harmonic. The real spherical harmonics are the Cartesian s, p and d orbitals familiar from high-school chemistry lessons and are illustrated in Figs. 3 and 4.

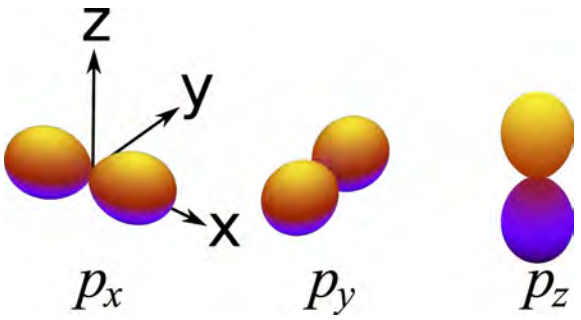

Fig. 3: *The real spherical harmonics* $\tilde{Y}_1^1 = p_x$, $\tilde{Y}_1^{-1} = p_y$ *and* $\tilde{Y}_0^0 = p_z$. *The distance from the origin to the surface in direction* (θ,ϕ) *is proportional to* $|\tilde{Y}_l^m(\theta,\phi)|^2$

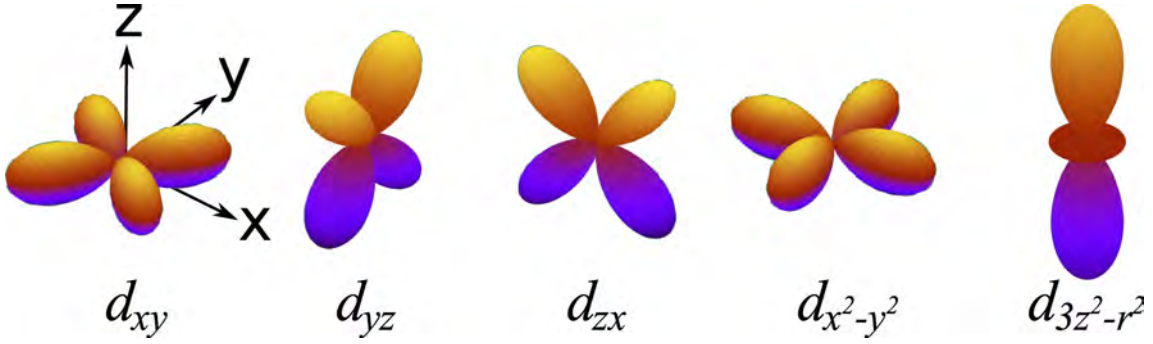

Fig. 4: *The* $l = 2$ *real spherical harmonics* $\tilde{Y}_2^{-2} = d_{xy}$, $\tilde{Y}_2^{-1} = d_{yz}$, $\tilde{Y}_2^1 = d_{zx}$, $\tilde{Y}_2^2 = d_{x^2-y^2}$, *and* $\tilde{Y}_2^0 = d_{3z^2-r^2}$. *The distance from the origin to the surface in direction* (θ,ϕ) *is proportional to* $|\tilde{Y}_l^m(\theta,\phi)|^2$

Because the effective potential $V_{\text{eff},I}$ of an atom is assumed to be spherically symmetric, there is only one non-zero one-center matrix element for every distinct choice of the compound index nl. Two-center matrix elements may be calculated by considering an isolated dimer with effective potential $V_{\text{eff},I} + V_{\text{eff},J}$. If this dimer is aligned with the z axis, the z-component of angular momentum is a good quantum number and matrix elements between basis functions with different values of the azimuthal quantum number m are zero. This reduces the number of non-zero two-center matrix elements substantially.

As an example, consider a dimer oriented along the z axis. One of the two atoms has a valence shell of p orbitals and the other a valence shell of d orbitals. For simplicity, we assume that the basis set is orthonormal, implying that the orbitals on the two atoms have been orthogonalized in some way. The non-zero one-center matrix elements involving orbitals on the first atom all have the same value, which we call V_p; the one-center matrix elements involving orbitals on the second atom are all equal to V_d. The non-zero hopping matrix elements linking the two atoms have only two possible values, $h_{pd\sigma}$ and $h_{pd\pi}$, corresponding to pairs of orbitals with $m = 0$ or $m = 1$. Since no p orbital has $m = \pm 2$, there are no non-zero hopping matrix elements with $m = \pm 2$, even though there are d orbitals with $m = \pm 2$ on the second atom. Thus, the electronic structure of the dimer is defined by just four numbers. Quantities such as V_p, V_d, $h_{pd\sigma}$, and $h_{pd\pi}$ are called Slater-Koster parameters [1].

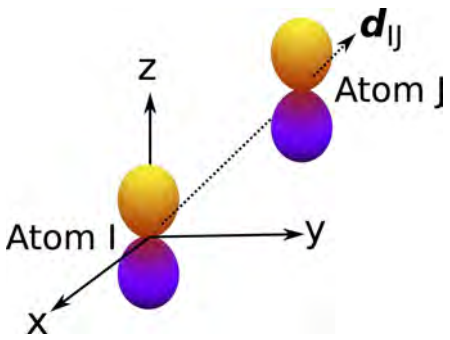

Fig. 5: *A two-center matrix element between p_z orbitals on atoms I and J separated by the vector $\boldsymbol{d}_{IJ} = \boldsymbol{d}_J - \boldsymbol{d}_I$. Each p_z orbital may be expressed as a linear combination of p_x, p_y and p_z orbitals quantized relative to the $\boldsymbol{d}_{IJ}$ axis, so the matrix element is a linear combination of the Slater-Koster parameters $h_{pp\pi}$ and $h_{pp\sigma}$.*

We have not yet worked out how to evaluate two-center Hamiltonian matrix elements for dimers not aligned with the global z axis. An example of this problem is shown in Fig. 5. The two p_z orbitals are neither parallel nor perpendicular to the dimer axis $\boldsymbol{d}_{IJ}$, so the two-center hopping matrix element between them is neither $h_{pp\sigma}$ (the value for two p orbitals pointing along $\boldsymbol{d}_{IJ}$) nor $h_{pp\pi}$ (the value for two p orbitals pointing perpendicular to $\boldsymbol{d}_{IJ}$). Fortunately, rotating a real spherical harmonic $\tilde{Y}_l^m$ always produces a linear combination of real spherical harmonics with the same value of l but different values of m. More precisely, if the operator $\hat{R}^{\boldsymbol{\omega}}$ rotates the function to which it is applied by ω radians about an axis parallel to the unit vector $\hat{\boldsymbol{\omega}}$, the rotated real spherical harmonic $\hat{R}^{\boldsymbol{\omega}}\tilde{Y}_l^m$ can be expressed as a linear combination of the $2l+1$ unrotated real spherical harmonics with the same value of l:

$$\hat{R}^{\boldsymbol{\omega}}\tilde{Y}_l^m = \sum_{m'=-l}^{l} \tilde{D}^l_{m',m}(\boldsymbol{\omega})\,\tilde{Y}_l^{m'}. \tag{18}$$

This allows us to express the orbitals pictured in Fig. 5 as linear combinations of orbitals aligned with the dimer axis, and hence to express the two-center Hamiltonian and overlap matrix elements for the tilted dimer in terms of the Slater-Koster parameters. Slater and Koster [1] provide a convenient table expressing the two-center matrix elements of the rotated dimer in terms of the Slater-Koster parameters and the direction cosines of the dimer axis. Given the one-center Slater-Koster parameters for all atom types and the two-center Slater-Koster parameters for all pairs of atom types at all inter-atomic separations, one can use this table to write down the two-center tight-binding Hamiltonian for any molecule or solid built of those atoms.

2.2.6 Fitting and transferability

Semi-empirical tight-binding Hamiltonian and overlap matrix elements (if the model is non-orthogonal) are often fitted to bandstructures. This makes sense if individual electronic eigenvalues and eigenfunctions are the quantities of interest, as is the case, for example, in electronic transport calculations, but is not appropriate if the tight-binding model is to be used to calculate total energies or inter-atomic forces. In that case it is better to fit to total energies and/or forces

calculated for a variety of structures using a more accurate method such as DFT with a good basis set. The wider the range of local atomic environments included in the data set, the better the results. Large tabulations of fitted tight-binding parameters are available [19].
It would be impractical to refit the parameters of a tight-binding model for every different arrangement of the ions in a molecular dynamics simulation, so assumptions have to be made about how the matrix elements between nearby orbitals depend on ionic positions. The short range of the atomic-like basis functions, and the observation that the form of the potential in one region of a solid or molecule does not normally depend strongly on the positions of distant atoms, suggest that only the local ionic arrangement is important. It does not, however, imply that the mapping from ionic positions to matrix elements is simple. If the assumptions made in parametrizing a tight-binding model are wrong or inaccurate, it is likely to produce poor results whenever the local ionic arrangement is far from any of the arrangements included in the training set. In such cases we say that the tight-binding model is not "transferable".
In general, despite all the work that has been done, parametrizing and fitting semi-empirical tight-binding models remains a dark art. Some of the most successful attempts [20] are among the simplest and were constructed using very little data, while highly-fitted models often prove brittle and show poor transferability. The problem of constructing a transferable semi-empirical tight-binding model is similar in nature to the problem of constructing a transferable classical force field and leads to similar frustrations. Tight-binding models are better than force fields because they are properly quantum mechanical — but they are only an approximation. As we illustrate with a few examples below, semi-empirical tight-binding is at its best when used to build a qualitative understanding of chemical bonding.

2.3 Example semi-empirical tight-binding calculations

2.3.1 The hydrogen molecule

Two hydrogen atoms are held a distance d apart and approximated using a tight-binding model with a single atomic-like s orbital on each atom. The Hamiltonian and overlap matrices are

$$\boldsymbol{H} = \begin{pmatrix} V & h \\ h & V \end{pmatrix} \quad \text{and} \quad \boldsymbol{S} = \begin{pmatrix} 1 & s \\ s & 1 \end{pmatrix}. \tag{19}$$

The eigenvectors are

$$\boldsymbol{e}_+ = \frac{1}{\sqrt{2(1+s)}} \begin{pmatrix} 1 \\ 1 \end{pmatrix} \qquad \text{and} \qquad \boldsymbol{e}_- = \frac{1}{\sqrt{2(1-s)}} \begin{pmatrix} 1 \\ -1 \end{pmatrix}, \tag{20}$$

normalized such that

$$\boldsymbol{e}_i^\dagger \, \boldsymbol{S} \, \boldsymbol{e}_j = \delta_{ij}, \tag{21}$$

as is appropriate for a generalized eigenvalue problem. The corresponding eigenvalues are

$$\epsilon_\pm = \frac{V \pm h}{1 \pm s}. \tag{22}$$

It is reassuring to see the bonding and anti-bonding linear combinations of basis functions emerge naturally from the analysis.

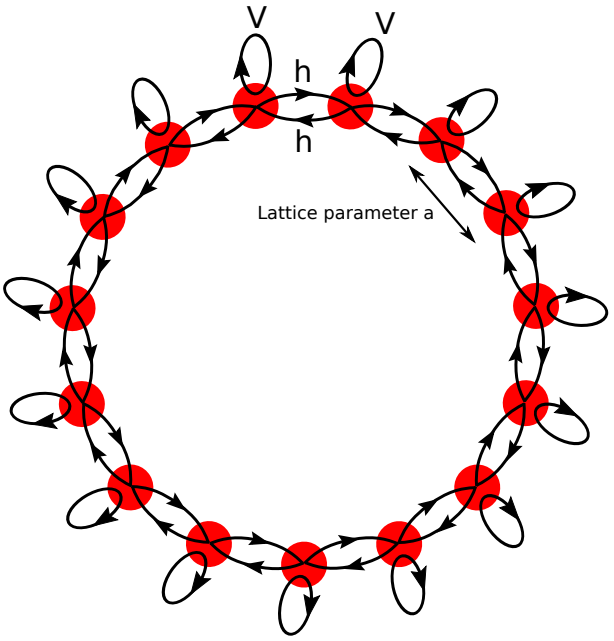

Fig. 6: *A schematic representation of the tight-binding Hamiltonian matrix of a ring of hydrogen atoms subject to periodic boundary conditions.*

2.3.2 Bandstructure of a ring of hydrogen atoms

Consider a chain of N hydrogen atoms subject to periodic boundary conditions (i.e., with the ends joined together to form a ring). A schematic representation of the Hamiltonian matrix is shown in the Fig. 6. As in the case of the H_2 molecule, there are on-site (diagonal) Hamiltonian matrix elements V and nearest-neighbor hopping matrix elements h. This time, however, we assume for simplicity that the basis set is orthonormal. We shall also assume, as usually turns out to be the case, that h is negative. The Hamiltonian is an $N \times N$ matrix with N large, so it looks as if it will be difficult to find the eigenvalues and eigenvectors. If we remember to use Bloch's theorem, however, the problem becomes simple.

A normalized Bloch-like linear combination of basis functions takes the form

$$|\psi_{k_p}\rangle = \frac{1}{\sqrt{N}} \sum_{n=0}^{N-1} |\phi_n\rangle \, e^{ik_p na} \,, \tag{23}$$

where

$$k_p = \frac{2\pi p}{Na} \quad \text{with} \quad p = 0, 1, 2, \ldots, N-1, \tag{24}$$

and a is the bond length. The values of k_p are chosen such that $|\psi_{k_p}\rangle$ satisfies the periodic boundary conditions: $\langle\phi_0|\psi_{k_p}\rangle = \langle\phi_N|\psi_{k_p}\rangle$. Since $\exp(ik_{p+N}na) = \exp(ik_pna)$ for any integer n, we lose nothing by restricting p to the range $0 \leq p < N$.

Applying the projected Hamiltonian $\hat{H}^P = \sum_{m,n} |\phi_m\rangle H_{mn} \langle\phi_n|$ to the Bloch function $|\psi_{k_p}\rangle$

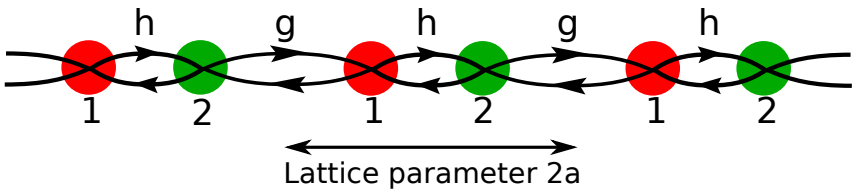

Fig. 7: *A schematic representation of the tight-binding Hamiltonian matrix of part of a large ring of diatomic molecules subject to periodic boundary conditions.*

gives

$$\begin{aligned}\hat{H}^P|\psi_{k_p}\rangle &= \frac{1}{\sqrt{N}}\sum_{n=0}^{N-1}\hat{H}^P|\phi_n\rangle \\ &= \frac{1}{\sqrt{N}}\sum_{n=0}^{N-1}\Big(V|\phi_n\rangle + h|\phi_{n-1}\rangle + h|\phi_{n+1}\rangle\Big)e^{ik_pna} \\ &= V\left(\frac{1}{\sqrt{N}}\sum_{n=0}^{N-1}|\phi_n\rangle e^{ik_pna}\right) + he^{ik_pa}\left(\frac{1}{\sqrt{N}}\sum_{n=0}^{N-1}|\phi_{n-1}\rangle e^{ik_p(n-1)a}\right) \\ &\qquad + he^{-ik_pa}\left(\frac{1}{\sqrt{N}}\sum_{n=0}^{N-1}|\phi_{n+1}\rangle e^{ik_p(n+1)a}\right). \qquad (25)\end{aligned}$$

Noting that $|\phi_{-1}\rangle \equiv |\phi_{n-1}\rangle$ and $|\phi_N\rangle \equiv |\phi_0\rangle$ because of the periodic boundary conditions, this simplifies to

$$\hat{H}^P|\psi_{k_p}\rangle = \left[V + h(e^{ik_pa} + e^{-ik_pa})\right]|\psi_{k_p}\rangle, \qquad (26)$$

showing that $|\psi_{k_p}\rangle$ is an eigenfunction of $\hat{H}^P$ with eigenvalue

$$\epsilon(k_p) = V + 2h\cos(k_pa)\,. \qquad (27)$$

As the size N of the ring increases, the allowed values of k_p get closer and closer together and the cosinusoidal bandstructure of the infinite tight-binding ring is sampled more and more densely.

2.3.3 Bandstructure of a ring of diatomic molecules

The tight-binding model pictured in Fig. 7 has two orbitals per unit cell and produces two energy bands. There are N unit cells ($2N$ atoms) altogether and N inequivalent values of k consistent with the periodic boundary conditions. For simplicity we set the diagonal Hamiltonian matrix elements V_1 and V_2 to zero; the nearest-neighbor off-diagonal Hamiltonian matrix elements h and g (both of which are < 0) alternate along the chain.
Since we have two basis functions per unit cell, we can construct two Bloch functions at each allowed value of k:

$$|\psi^{(1)}\rangle = \frac{1}{\sqrt{N}}\sum_n e^{ikn2a}|\phi_{n,1}\rangle, \qquad |\psi^{(2)}\rangle = \frac{1}{\sqrt{N}}\sum_n e^{ikn2a}|\phi_{n,2}\rangle,$$

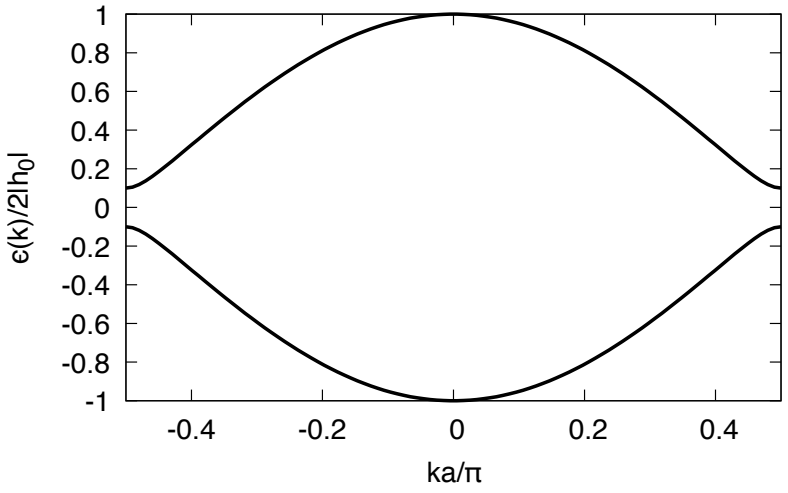

Fig. 8: *The bandstructure of the tight-binding ring of dimers in the limit as the number N of two-atom unit cells tends to infinity. There are two bands because there are two basis functions per unit cell.*

where $|\phi_{n,1}\rangle$ and $|\phi_{n,2}\rangle$ are the two basis functions in unit cell n. The unit cell now has length $2a$, so the Brillouin zone is $-\pi/(2a) \leq k < \pi/(2a)$. The corresponding vectors of orbital coefficients, $\boldsymbol{c}^{(1)}$ and $\boldsymbol{c}^{(2)}$, with components

$$c^{(1)}_{n,1} = \frac{1}{\sqrt{N}} e^{ikn2a}, \qquad c^{(1)}_{n,2} = 0,$$

and

$$c^{(2)}_{n,1} = 0, \qquad c^{(2)}_{n,2} = \frac{1}{\sqrt{N}} e^{ikn2a},$$

satisfy

$$\begin{aligned} \boldsymbol{H}\boldsymbol{c}^{(1)} &= h\boldsymbol{c}^{(2)} + ge^{+ik2a}\boldsymbol{c}^{(2)}, \\ \boldsymbol{H}\boldsymbol{c}^{(2)} &= h\boldsymbol{c}^{(1)} + ge^{-ik2a}\boldsymbol{c}^{(1)}, \end{aligned}$$

where $\boldsymbol{H}$ is the $2N \times 2N$ Hamiltonian matrix. It follows that the linear combination $\boldsymbol{v} = \alpha_1\boldsymbol{c}^{(1)} + \alpha_2\boldsymbol{c}^{(2)}$ is an eigenvector of $\boldsymbol{H}$ if

$$\begin{pmatrix} 0 & h + ge^{-ik2a} \\ h + ge^{ik2a} & 0 \end{pmatrix} \begin{pmatrix} \alpha_1 \\ \alpha_2 \end{pmatrix} = \lambda \begin{pmatrix} \alpha_1 \\ \alpha_2 \end{pmatrix}.$$

The two energy eigenvalues $\epsilon_\pm(k)$ at wavevector k are the eigenvalues of this 2×2 matrix. Writing $h = (1 + \Delta)h_0$ and $g = (1 - \Delta)h_0$, some algebra shows that

$$\epsilon_\pm(k) = \pm 2|h_0|\sqrt{1 - (1 - \Delta^2)\sin^2(ka)}\,.$$

Fig. 8 shows the bandstructure in the case when $\Delta = 0.1$.

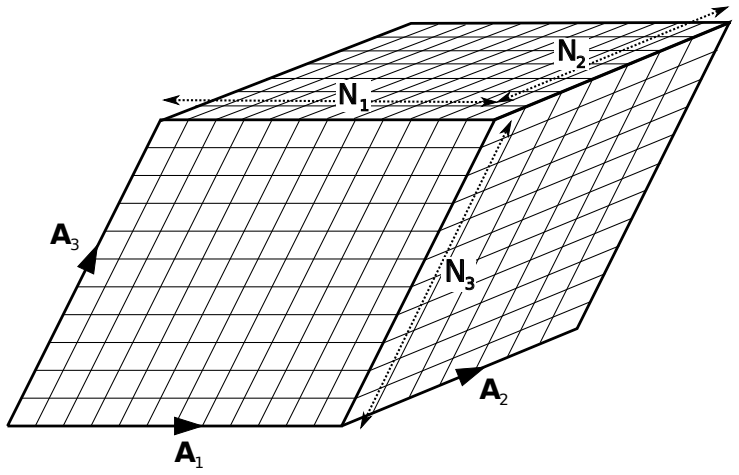

Fig. 9: *The $N_1 \times N_2 \times N_3$ parallelepiped supercell to which periodic boundary conditions are applied.*

2.3.4 Bandstructure of a face-centered-cubic solid

Consider a large but finite face-centered-cubic crystal consisting of a block of $N_1 \times N_2 \times N_3$ parallelepiped unit cells, as illustrated in Fig. 9. Apply periodic (*not* Bloch) boundary conditions, so that an electron leaving one face of the block immediately reappears at the equivalent point on the opposite face. The primitive Bravais lattice vectors are

$$\boldsymbol{A}_1 = \frac{a}{2}(0,1,1)\,, \qquad \boldsymbol{A}_2 = \frac{a}{2}(1,0,1)\,, \qquad \boldsymbol{A}_3 = \frac{a}{2}(1,1,0)\,, \tag{28}$$

and the corresponding reciprocal vectors are

$$\boldsymbol{B}_1 = \frac{2\pi}{a}(-1,1,1)\,, \qquad \boldsymbol{B}_2 = \frac{2\pi}{a}(1,-1,1)\,, \qquad \boldsymbol{B}_3 = \frac{2\pi}{a}(1,1,-1)\,. \tag{29}$$

The $N_1N_2N_3$ distinct $\boldsymbol{k}$ vectors consistent with the periodic boundary conditions are

$$\boldsymbol{k} = \frac{m_1}{N_1}\boldsymbol{B}_1 + \frac{m_2}{N_2}\boldsymbol{B}_2 + \frac{m_3}{N_3}\boldsymbol{B}_3 \quad \text{with} \quad 0 \le m_1 < N_1,\ \ 0 \le m_2 < N_2,\ \ 0 \le m_3 < N_3. \tag{30}$$

As in the previous examples, we approximate the system as an orthogonal tight-binding model with one atomic-like s orbital per atom. The diagonal matrix elements V_s are set to zero (defining the zero of energy) and the nearest-neighbor hopping matrix elements are equal to h. Matrix elements linking orbitals on more distant neighbors are assumed to be zero. The Bloch linear combinations of basis functions are

$$|\psi_{\boldsymbol{k}}\rangle = \frac{1}{\sqrt{N_1N_2N_3}} \sum_{\boldsymbol{d}} |\phi_{\boldsymbol{d}}\rangle\, e^{i\boldsymbol{k}\cdot\boldsymbol{d}}\,, \tag{31}$$

where the sum is over the positions $\boldsymbol{d}$ of all $N_1N_2N_3$ atoms in the block and $|\phi_{\boldsymbol{d}}\rangle$ is the basis function on the atom at $\boldsymbol{d}$. Eq. (31) is a three-dimensional analogue of the one-dimensional Bloch linear combination used in Sec. 2.3.2.

Applying the projected Hamiltonian $\hat{H}^P = \sum_{\boldsymbol{d},\boldsymbol{d}'} |\phi_{\boldsymbol{d}}\rangle\, H_{\boldsymbol{d},\boldsymbol{d}'}\, \langle\phi_{\boldsymbol{d}'}|$ to the Bloch linear combination gives

$$\begin{aligned}\hat{H}^P|\psi_{\boldsymbol{k}}\rangle &= \frac{1}{\sqrt{N_1N_2N_3}} \sum_{\boldsymbol{d}} \hat{H}^P|\phi_{\boldsymbol{d}}\rangle e^{i\boldsymbol{k}\cdot\boldsymbol{d}} \\ &= \frac{1}{\sqrt{N_1N_2N_3}} \sum_{\boldsymbol{d}'} \sum_{\boldsymbol{d}} |\phi_{\boldsymbol{d}'}\rangle\langle\phi_{\boldsymbol{d}'}|\hat{H}^P|\phi_{\boldsymbol{d}}\rangle e^{i\boldsymbol{k}\cdot\boldsymbol{d}} \\ &= \frac{1}{\sqrt{N_1N_2N_3}} \sum_{\boldsymbol{d}'} |\phi_{\boldsymbol{d}'}\rangle e^{i\boldsymbol{k}\cdot\boldsymbol{d}'} \sum_{\boldsymbol{d}} \langle\phi_{\boldsymbol{d}'}|\hat{H}^P|\phi_{\boldsymbol{d}}\rangle e^{i\boldsymbol{k}\cdot(\boldsymbol{d}-\boldsymbol{d}')}. \end{aligned} \tag{32}$$

The only non-zero contributions to the inner summation are those for which $\boldsymbol{d}$ is a nearest neighbor of $\boldsymbol{d}'$, in which case the matrix element is equal to h. The summation over all lattice vectors $\boldsymbol{d}$ may therefore be replaced by a summation over the positions of the 12 nearest neighbors of the atom at $\boldsymbol{d}'$. Denoting the vectors from the atom at $\boldsymbol{d}'$ (or any other lattice site) to its 12 nearest neighbors by $\boldsymbol{n}$, we obtain

$$\hat{H}^P|\psi_{\boldsymbol{k}}\rangle = \frac{1}{\sqrt{N_1N_2N_3}} \sum_{\boldsymbol{d}'} |\phi_{\boldsymbol{d}'}\rangle e^{i\boldsymbol{k}\cdot\boldsymbol{d}'} \sum_{\boldsymbol{n}} h e^{i\boldsymbol{k}\cdot\boldsymbol{n}} = \left(h \sum_{\boldsymbol{n}} e^{i\boldsymbol{k}\cdot\boldsymbol{n}}\right) |\psi_{\boldsymbol{k}}\rangle \tag{33}$$

Just as for a ring of hydrogen atoms, the Bloch functions are automatically eigenvalues of the tight-binding Hamiltonian. This is generally the case when there is only one basis function per unit cell, since the translational symmetry is then sufficient to determine the energy eigenfunctions completely. The sum over the 12 nearest neighbors is easily evaluated to obtain

$$\epsilon(\boldsymbol{k}) = 4h\left[\cos\left(\frac{k_y a}{2}\right)\cos\left(\frac{k_z a}{2}\right) + \cos\left(\frac{k_z a}{2}\right)\cos\left(\frac{k_x a}{2}\right) + \cos\left(\frac{k_x a}{2}\right)\cos\left(\frac{k_y a}{2}\right)\right].$$

This simple expression provides an accurate description of the bandstructure of any face-centered-cubic crystal of weakly-interacting atoms with outermost s shells. All of the Noble gases except helium crystallize into face-centered cubic structures under sufficient pressure, and all have bandstructures of this form.

3 Tight-binding models and density-functional theory

3.1 Introduction

Section 2 showed how the tight-binding approximation can be used to find approximate solutions of one-particle Schrödinger equations of the form

$$\left[-\frac{1}{2}\nabla^2 + V_{\text{eff}}(\boldsymbol{r})\right]\psi_i(\boldsymbol{r}) = \epsilon_i\psi_i(\boldsymbol{r}). \tag{34}$$

This is useful but by no means the end of the story, since tight-binding models are also used to describe how the total energy of a solid or molecule varies as the atoms move around [2, 3, 7, 9, 11, 12, 14, 15]. Any tight-binding model capable of providing a reliable account of the

structure-dependent total energy can be used as an engine for the calculation of the inter-atomic forces (gradients of the total energy with respect to atomic positions) required for quantum molecular dynamics simulations. Tight-binding quantum molecular dynamics simulations are less accurate than their DFT equivalents but require much less computer power.
If one wishes to describe total energies, calculating the electronic eigenvalues ϵ_i of the occupied valence states is not sufficient [21]. The total energy also includes another term that represents, roughly, the repulsive interaction between the ionic cores:

$$E_{\text{total}}^{\text{TB}}(\boldsymbol{d}) = \sum_{i \text{ occ}} \epsilon_i(\boldsymbol{d}) + E_{\text{ion-ion}}(\boldsymbol{d}), \tag{35}$$

where $\boldsymbol{d} \equiv \{\boldsymbol{d}_1, \boldsymbol{d}_2, \ldots, \boldsymbol{d}_{N_I}\}$ is shorthand for the set of all ionic positions. (The dependence of the electronic eigenvalues ϵ_i on $\boldsymbol{d}$ arises via the position dependence of the Hamiltonian and overlap matrix elements.) The ion-ion interaction energy $E_{\text{ion-ion}}(\boldsymbol{d})$ must also be parametrized and/or fitted and is often but not always assumed to be pairwise in form:

$$E_{\text{ion-ion}}(\boldsymbol{d}) = \sum_{I>J} V_{\text{ion-ion}}^{\text{pair}}(\boldsymbol{d}_I - \boldsymbol{d}_J), \tag{36}$$

where the sum is over all pairs I and J of ions and $\boldsymbol{d}_I$ and $\boldsymbol{d}_J$ are the corresponding ionic positions.
The form of Eq. (35) is reminiscent of the expression for the total energy in Hohenberg-Kohn-Sham DFT,

$$E = \sum_{i \text{ occ}} \epsilon_i - \int V_{\text{KS}}([n], \boldsymbol{r}) n(\boldsymbol{r})\, d^3r + \int V_{\text{nuc}}(\boldsymbol{r}) n(\boldsymbol{r})\, d^3r + \frac{1}{2} \iint \frac{n(\boldsymbol{r}) n(\boldsymbol{r}')}{|\boldsymbol{r} - \boldsymbol{r}'|}\, d^3r' d^3r + E_{xc}[n] + E_{nn}, \tag{37}$$

where $n(\boldsymbol{r})$ is the electron number density and the eigenvalues are solutions of the Kohn-Sham equation, which looks like Eq. (34) with a density-dependent effective potential of the form:

$$V_{\text{KS}}([n], \boldsymbol{r}) = V_{\text{nuc}}(\boldsymbol{r}) + \int \frac{n(\boldsymbol{r}')}{|\boldsymbol{r} - \boldsymbol{r}'|} d^3r' + V_{xc}([n], \boldsymbol{r}). \tag{38}$$

The first term on the right-hand side of Eq. (38) is the potential exerted on the electrons by the classical, point-like nuclei; the second, known as the Hartree term, is the Coulomb potential of the electron charge cloud; and the third is the exchange-correlation potential, which is discussed below. The second term on the right-hand side of Eq. (37) cancels the potential energy contribution to the sum of energy eigenvalues, leaving only the kinetic energy contribution; the third, fourth and fifth terms add the energy of interaction between the electrons and nuclei, the Coulomb interaction energy of the electronic charge cloud, and the exchange-correlation energy. The final term is the classical Coulomb interaction energy of the nuclei with each other. A recap of the basics of DFT is given in Sec. 3.2 below. For the time being, we note only that the DFT total-energy expression, which experience has shown is usually very accurate, consists of a sum of eigenvalues and additional "ion-ion repulsion" terms. This looks quite like the tight-binding total energy expression, except that: (i) the DFT ion-ion repulsion terms

are density dependent and not obviously simple or pairwise; and (ii) the Kohn-Sham effective potential depends on the electron density $n(\boldsymbol{r})$, which in turn depends on the eigenfunctions via $n(\boldsymbol{r}) = \sum_{i \text{ occ}} |\psi_i(\boldsymbol{r})|^2$.

The dependence of the Kohn-Sham potential on the wavefunctions obtained by solving the Kohn-Sham equation means that an iterative method of solution is required. The first step is to guess an input electron density $n^{\text{in}}(\boldsymbol{r})$, which might perhaps be a superposition of atomic densities. The corresponding Kohn-Sham potential $V_{\text{KS}}([n^{\text{in}}], \boldsymbol{r})$ can then be calculated and the Kohn-Sham equation solved to find the output wavefunctions and hence the output density $n^{\text{out}}(\boldsymbol{r}) = \sum_{i \text{ occ}} |\psi_i^{\text{out}}(\boldsymbol{r})|^2$. The input and output densities differ in general, so the next step is to adjust the input density to try to reduce the difference between the input and output densities. After an iterative series of adjustments, a "self-consistent" electron density $n_0(\boldsymbol{r})$ is obtained, for which the wavefunctions $\psi_{0i}(\boldsymbol{r})$ obtained by solving the Kohn-Sham equation with input potential $V_{\text{KS}}([n_0], \boldsymbol{r})$ regenerate $n_0(\boldsymbol{r})$ exactly. In tight-binding total energy calculations, by contrast, the Schrödinger equation only has to be solved once and no self-consistency is required.

The aim of the rest of this section is to explain the link between DFT and tight-binding theory. Can we derive a non-selfconsistent tight-binding model with a simple ion-ion repulsion term from the much more complicated self-consistent formalism of DFT?

3.2 Review of density-functional theory

Density-functional theory [22, 23] looks like a mean-field theory, but is remarkable because it provides an exact mapping from a system of interacting electrons to a system of non-interacting electrons moving in an effective potential that depends on the electron density. Solving the self-consistent non-interacting problem gives, in principle, the *exact* interacting ground-state energy E_0 and electron density $n_0(\boldsymbol{r})$ for any given arrangement of the nuclei. The success of DFT, which appears to be a theory of non-interacting electrons but in fact describes a system of interacting electrons, in part explains the success of the "standard model" of a solid as an assembly of non-interacting electrons moving in a fixed external potential.

3.2.1 Preliminaries

The N-electron eigenfunctions $\Psi(\boldsymbol{r}_1, \boldsymbol{r}_2, \ldots, \boldsymbol{r}_N)$ of any finite collection of atoms satisfy the many-electron Schrödinger equation:

$$\left(-\frac{1}{2} \sum_i \nabla_i^2 + \sum_{i>j} \frac{1}{|\boldsymbol{r}_i - \boldsymbol{r}_j|} - \sum_i \sum_I \frac{Z_I}{|\boldsymbol{r}_i - \boldsymbol{d}_I|} + \sum_{I>J} \frac{Z_I Z_J}{|\boldsymbol{d}_I - \boldsymbol{d}_J|} \right) \Psi = E\Psi, \tag{39}$$

where $\boldsymbol{r}_i$ is the position of electron i and Z_I is the atomic number of atom I at position $\boldsymbol{d}_I$. For simplicity, we shorten this to

$$\left(\hat{T} + \hat{V}_{\text{ee}} + \hat{V}_{\text{en}} + E_{\text{nn}} \right) \Psi = E\Psi. \tag{40}$$

We are working within the Born-Oppenheimer approximation and treating the nuclei as stationary and classical, so the nuclear positions $\boldsymbol{d}_I$ and nuclear-nuclear Coulomb interaction energy E_{nn} are regarded as constants when solving the electronic problem.
The central quantity in DFT is the electron (number) density $n(\boldsymbol{r})$, the operator for which is

$$\hat{n}(\boldsymbol{r}) = \sum_i^N \delta(\boldsymbol{r} - \boldsymbol{r}_i). \tag{41}$$

Since

$$\hat{V}_{\text{en}} = \sum_i^N V_{\text{nuc}}(\boldsymbol{r}_i) = \int V_{\text{nuc}}(\boldsymbol{r}) \sum_i^N \delta(\boldsymbol{r} - \boldsymbol{r}_i)\, d^3r, \tag{42}$$

the electron-nucleus interaction operator (or any other one-electron potential energy term) can be written in terms of the electron density operator:

$$\hat{V}_{\text{en}} = \int V_{\text{nuc}}(\boldsymbol{r})\, \hat{n}(\boldsymbol{r})\, d^3r. \tag{43}$$

Note that $\boldsymbol{r}$ in this equation is a simple vector, not an operator; the electron position operators $\boldsymbol{r}_1, \boldsymbol{r}_2, \ldots, \boldsymbol{r}_N$ are buried in the definition of $\hat{n}(\boldsymbol{r})$. Taking an expectation value of Eq. (43) gives the obvious result:

$$\langle\Psi|\hat{V}_{\text{en}}|\Psi\rangle = \int V_{\text{nuc}}(\boldsymbol{r})\, \langle\Psi|\hat{n}(\boldsymbol{r})|\Psi\rangle\, d^3r = \int V_{\text{nuc}}(\boldsymbol{r}) n(\boldsymbol{r})\, d^3r. \tag{44}$$

3.2.2 The energy functional

The first step in any derivation of DFT is to show that there exists a functional, $E[n]$, of the electron number density $n(\boldsymbol{r})$, which takes its minimum value, equal to the ground-state energy E_0, when the density is the ground-state density $n_0(\boldsymbol{r})$. Levy [24] manages this by giving an explicit construction of such a functional:

$$E[n] = \min_{\Psi\to n} \langle\Psi|\hat{H}|\Psi\rangle = \min_{\Psi\to n} \langle\Psi|\hat{T} + \hat{V}_{\text{ee}} + \hat{V}_{\text{en}} + E_{\text{nn}}|\Psi\rangle. \tag{45}$$

In words: given an electron density $n(\boldsymbol{r})$, the functional $E[n]$ is evaluated by checking all possible normalized antisymmetric N-electron wavefunctions which give that density to find the one that minimizes $\langle\Psi|\hat{H}|\Psi\rangle$. This minimum value is the value assigned to the functional at the density $n(\boldsymbol{r})$. It can be shown that it is possible to find at least one N-electron wavefunction corresponding to any reasonable density $n(\boldsymbol{r})$, so the constrained search always produces a value.
The variational principle guarantees that the minimum value of $E[n]$ occurs when $n(\boldsymbol{r})$ is equal to the ground-state density $n_0(\boldsymbol{r})$. The optimal wavefunction Ψ is then the ground state Ψ_0, and the value of the functional is the ground-state energy:

$$E[n_0] = \min_{\Psi\to n_0} \langle\Psi|\hat{H}|\Psi\rangle = \langle\Psi_0|\hat{H}|\Psi_0\rangle = E_0\,. \tag{46}$$

Since E_{nn} is a constant, and since the expectation value of $\hat{V}_{\text{en}}$ gives the same result,

$$\langle\Psi|\hat{V}_{\text{en}}|\Psi\rangle = \int V_{\text{en}}(\boldsymbol{r})n(\boldsymbol{r})\,d^3r, \tag{47}$$

for *all* wavefunctions Ψ yielding the density $n(\boldsymbol{r})$, the total-energy functional may be written in the form

$$E[n] = \min_{\Psi\to n}\langle\Psi|\hat{T}+\hat{V}_{\text{ee}}|\Psi\rangle + \int V_{\text{en}}(\boldsymbol{r})n(\boldsymbol{r})\,d^3r + E_{\text{nn}} = F[n] + \int V_{\text{en}}(\boldsymbol{r})n(\boldsymbol{r})\,d^3r + E_{\text{nn}}, \tag{48}$$

where the second equality defines $F[n]$.
The definition of $F[n]$ makes no reference to the positions of the nuclei, so its value depends on the electron density $n(\boldsymbol{r})$ only. It is thus a *universal* functional: given an input density $n(\boldsymbol{r})$, the value of $F[n]$ is fixed regardless of the nuclear charges or positions. (Remember that functionals such as $E[n]$ and $F[n]$ are defined for *all* reasonable input densities $n(\boldsymbol{r})$; the density that minimizes $E[n]$ depends on the arrangement of the ions, but that is a separate issue.) Since the functional $F[n]$ is the same in all solids, atoms and molecules, it could in principle be calculated once and for all.

3.2.3 Contributions to the energy functional

If, given a density $n(\boldsymbol{r})$, we could easily evaluate $E[n]$, the many-electron problem would be solved: all that we would have to do to find the ground-state density and energy would be to vary $n(\boldsymbol{r})$ until the functional reached a minimum. Unfortunately, but not unexpectedly, evaluating the functional is equivalent to solving the full N-body problem and is out of the question. We therefore have to approximate.
To make approximating the energy functional easier, it helps to identify some of the contributions to $F[n]$. Since the definition of $F[n]$ involves an expectation value of the electron-electron interaction, one obvious contribution is the Hartree energy:

$$E_{\text{H}}[n] = \frac{1}{2}\iint \frac{n(\boldsymbol{r})n(\boldsymbol{r}')}{|\boldsymbol{r}-\boldsymbol{r}'|}d^3r\,d^3r'. \tag{49}$$

Another large and easily recognizable contribution is the kinetic energy of the interacting electrons. Although this is hard to evaluate, we can work out the kinetic energy $T_s[n]$ of a system of non-interacting electrons with ground-state density $n(\boldsymbol{r})$. There is no reason to think that $T_s[n]$ is the same as the kinetic energy of the interacting electrons, but it is of the same order of magnitude and relatively easy to calculate.
One way to work out $T_s[n]$ is to choose a non-interacting Hamiltonian, $-\frac{1}{2}\nabla^2 + V_{\text{eff}}(\boldsymbol{r})$, solve the Schrödinger equation

$$\left[-\frac{1}{2}\nabla^2 + V_{\text{eff}}(\boldsymbol{r})\right]\psi_i(\boldsymbol{r}) = \epsilon_i\psi_i(\boldsymbol{r}), \tag{50}$$

and occupy first N eigenfunctions to obtain the corresponding electron density

$$n(\boldsymbol{r}) = \sum_{i \text{ occ}} |\psi_i(\boldsymbol{r})|^2. \tag{51}$$

$T_s[n]$ is then given by:

$$T_s[n] = \sum_{i \text{ occ}} \int \psi_i^*(\boldsymbol{r}) \left(-\frac{1}{2}\nabla^2\right) \psi_i(\boldsymbol{r})\, d^3r = \sum_{i \text{ occ}} \epsilon_i - \int V_{\text{eff}}(\boldsymbol{r}) n(\boldsymbol{r})\, d^3r\,. \tag{52}$$

The drawback of this technique is that it produces the value of $T_s[n]$ at the density $n(\boldsymbol{r})$ obtained by solving the Schrödinger equation. If you require $T_s[n]$ at a given density $n(\boldsymbol{r})$, it is necessary to vary the input potential $V_{\text{eff}}(\boldsymbol{r})$ until the output density $\sum_{i \text{ occ}} |\psi_i(\boldsymbol{r})|^2$ is equal to $n(\boldsymbol{r})$. This may not even be possible — not every density $n(\boldsymbol{r})$ is the ground-state density of a non-interacting system — although it rarely if ever poses a problem in practice.
So far, then, we have identified two contributions that we believe should make up a large part of $F[n]$. The next step is to write

$$F[n] = T_s[n] + E_{\text{H}}[n] + E_{\text{xc}}[n], \tag{53}$$

or, equivalently,

$$E[n] = T_s[n] + \int V_{\text{nuc}}(\boldsymbol{r}) n(\boldsymbol{r})\, d^3r + E_{\text{H}}[n] + E_{\text{xc}}[n] + E_{\text{nn}}. \tag{54}$$

The terms we have identified have been written explicitly, and $E_{\text{xc}}[n]$, known as the exchange and correlation energy, is a "rubbish" term to take care of the rest of $F[n]$. Like $F[n]$, the Hartree energy $E_{\text{H}}[n]$ and the non-interacting kinetic energy $T_s[n]$ are universal functionals of the electron density and could, in principle, be calculated once and for all. Since

$$E_{\text{xc}}[n] = F[n] - T_s[n] - E_{\text{H}}[n], \tag{55}$$

it follows that the exchange-correlation functional $E_{\text{xc}}[n]$ is also universal.
Given an electron density $n(\boldsymbol{r})$, the non-interacting kinetic energy, the Hartree energy, the electron-nuclear interaction energy, and the nuclear-nuclear interaction energy are all easily obtained. The only difficult term is the unknown universal functional $E_{\text{xc}}[n]$. This includes all of the complicated parts of the many-body problem and has to be approximated. The surprising accuracy of simple approximations to $E_{xc}[n]$ is the reason DFT is so useful. The question of how to construct good approximate exchange-correlation functionals is fascinating but too complicated to discuss here. For our purposes, it is sufficient to assume that good approximations exist and can be evaluated easily.

3.2.4 Minimization of the energy functional

We now know how to evaluate all the terms in the energy functional

$$E[n] = T_s[n] + E_{\text{en}}[n] + E_{\text{H}}[n] + E_{\text{nn}} + E_{\text{xc}}[n]. \tag{56}$$

To calculate the exact interacting ground-state density $n_0(\boldsymbol{r})$ (and hence the exact ground-state energy E_0), we have to find the density that minimizes $E[n]$ subject to the normalization constraint $\int n(\boldsymbol{r})\, d^3r = N$. Mathematically, the ground-state density is determined by the stationarity condition,

$$\delta E = \int \frac{\delta E[n]}{\delta n(\boldsymbol{r})}\, \delta n(\boldsymbol{r})\, d^3r = 0, \tag{57}$$

which must hold for all density variations $\delta n(\boldsymbol{r})$ that integrate to zero.
The variations of the electron-nuclear and Hartree terms are easy to find:

$$\delta E_{\text{en}} = \delta \left(\int V_{\text{nuc}}(\boldsymbol{r}) n(\boldsymbol{r})\, d^3r \right) = \int V_{\text{nuc}}(\boldsymbol{r})\, \delta n(\boldsymbol{r})\, d^3r, \tag{58}$$

$$\delta E_{\text{H}} = \int \left(\int \frac{n(\boldsymbol{r}')}{|\boldsymbol{r} - \boldsymbol{r}'|}\, d^3r' \right) \delta n(\boldsymbol{r})\, d^3r = \int V_H([n], \boldsymbol{r})\, \delta n(\boldsymbol{r})\, d^3r, \tag{59}$$

where $V_{\text{H}}([n], \boldsymbol{r})$ is the Hartree potential mentioned earlier. The variation of the exchange-correlation energy,

$$\delta E_{\text{xc}} = \int \frac{\delta E_{\text{xc}}}{\delta n(\boldsymbol{r})}\, \delta n(\boldsymbol{r})\, d^3r = \int V_{\text{xc}}([n], \boldsymbol{r})\, \delta n(\boldsymbol{r})\, d^3r \tag{60}$$

defines the exchange-correlation potential $V_{\text{xc}}([n], \boldsymbol{r})$, which is easy enough to work out given a simple approximate exchange-correlation functional.
The variation of the kinetic energy functional can be found by returning to Eqs. (50), (51), and (52). Suppose that the input potential changes from V_{eff} to $V_{\text{eff}} + \delta V_{\text{eff}}$, causing the output density — the density at which T_s is calculated — to change from n to $n + \delta n$. Using first-order perturbation theory, the sum of the occupied one-electron eigenvalues changes by

$$\sum_{i \text{ occ}} \delta\epsilon_i = \sum_{i \text{ occ}} \int \psi_i^*(\boldsymbol{r})\, \delta V_{\text{eff}}(\boldsymbol{r})\, \psi_i(\boldsymbol{r})\, d^3r = \int n(\boldsymbol{r})\, \delta V_{\text{eff}}(\boldsymbol{r})\, d^3r. \tag{61}$$

Hence

$$\begin{aligned} \delta T_s = \quad & \delta \left[\sum_{i \text{ occ}} \epsilon_i - \int V_{\text{eff}}(\boldsymbol{r}) n(\boldsymbol{r})\, d^3r \right] \\ = \quad & \int n(\boldsymbol{r})\, \delta V_{\text{eff}}(\boldsymbol{r})\, d^3r - \int \left[n(\boldsymbol{r})\, \delta V_{\text{eff}}(\boldsymbol{r}) + V_{\text{eff}}(\boldsymbol{r})\, \delta n(\boldsymbol{r}) \right] d^3r \\ = & - \int V_{\text{eff}}(\boldsymbol{r})\, \delta n(\boldsymbol{r})\, d^3r\,. \end{aligned} \tag{62}$$

By combining the variations of each term, we can now write down the Euler-Lagrange equation that determines the minimum of the total energy functional:

$$\begin{aligned} \delta E &= \delta T_s + \delta E_{\text{en}} + \delta E_{\text{H}} + \delta E_{\text{xc}} \\ &= \int \Big(- V_{\text{eff}}(\boldsymbol{r}) + V_{\text{nuc}}(\boldsymbol{r}) + V_H([n], \boldsymbol{r}) + V_{\text{xc}}([n], \boldsymbol{r}) \Big) \delta n(\boldsymbol{r})\, d^3r = 0. \end{aligned} \tag{63}$$

Because of the constraint of normalization conservation,

$$\int \delta n(\boldsymbol{r})\, d^3r = 0, \tag{64}$$

the $\boldsymbol{k} = \boldsymbol{0}$ Fourier component of $-V_{\text{eff}} + V_{\text{nuc}} + V_{\text{H}} + V_{\text{xc}}$ is not fixed by Eq. (63). All other Fourier components must be zero, however, and hence

$$V_{\text{eff}}(\boldsymbol{r}) = V_{\text{nuc}}(\boldsymbol{r}) + V_{\text{H}}([n], \boldsymbol{r}) + V_{\text{xc}}([n], \boldsymbol{r}) + \text{const.} = V_{\text{KS}}([n], \boldsymbol{r}) + \text{const.} \tag{65}$$

The value of the constant has no effect on the calculation of $T_s[n]$ (which is the only purpose of V_{eff}), so we set it to zero.

Let us think about the meaning of Eq. (65). The total energy functional is minimized when the potential $V_{\text{eff}}(\boldsymbol{r})$ appearing in the non-interacting Schrödinger equation with ground-state density $n(\boldsymbol{r})$ is exactly equal to $V_{\text{KS}}([n], \boldsymbol{r}) = V_{\text{nuc}}(\boldsymbol{r}) + V_{\text{H}}([n], \boldsymbol{r}) + V_{\text{xc}}(]n], \boldsymbol{r})$. Since V_{H} and V_{xc} depend on the electron density, this is the self-consistency condition discussed in Sec. 3.1: the potential occurring in the non-interacting Schrödinger equation is determined by the ground-state electron density obtained by solving that equation.

3.2.5 Expressions for the DFT total energy

Once the ground-state density $n_0(\boldsymbol{r})$ and the corresponding effective potential $V_{\text{KS}}([n_0], \boldsymbol{r})$ and one-electron wavefunctions $\psi_{0i}(\boldsymbol{r})$ have been found, the total ground-state energy is given by

$$E[n_0] = T_s[n_0] + E_{\text{en}}[n_0] + E_H[n_0] + E_{\text{xc}}[n_0] + E_{\text{nn}}. \tag{66}$$

Since

$$T_s[n_0] = \sum_{i \text{ occ}} \epsilon_{0i} - \int V_{\text{KS}}([n_0], \boldsymbol{r}) n_0(\boldsymbol{r})\, d^3r, \tag{67}$$

the ground-state energy may also be written as

$$E = \sum_{i \text{ occ}} \epsilon_{0i} - \int V_{\text{KS}}([n_0], \boldsymbol{r}) n_0(\boldsymbol{r})\, d^3r + E_{\text{en}}[n_0] + E_H[n_0] + E_{\text{xc}}[n_0] + E_{\text{nn}}. \tag{68}$$

The total ground-state energy is not just the sum of the one-electron eigenvalues, as might be expected, but includes additional density-dependent terms. These we referred to earlier as the ion-ion interaction terms, but they are more often called the double-counting-correction terms. This name is appropriate because $V_{\text{KS}}([n_0], \boldsymbol{r})$ includes the Hartree potential,

$$V_{\text{H}}([n_0], \boldsymbol{r}) = \int \frac{n_0(\boldsymbol{r}')}{|\boldsymbol{r} - \boldsymbol{r}'|} d^3r', \tag{69}$$

so the sum of self-consistent eigenvalues includes the Hartree energy twice:

$$\int V_{\text{H}}([n_0], \boldsymbol{r}) n_0(\boldsymbol{r}) d^3r = \iint \frac{n_0(\boldsymbol{r}) n_0(\boldsymbol{r}')}{|\boldsymbol{r} - \boldsymbol{r}'|} = 2E_H[n_0]. \tag{70}$$

The double-counting corrections remedy this problem.

3.3 Density-functional theory without self-consistency

Although DFT calculations require iteration to self-consistency, most tight-binding total energy calculations do not. To help relate the tight-binding approximation to DFT, we now ask whether DFT calculations can also be made non-selfconsistent. The idea is to guess the ground-state density $n_0(\boldsymbol{r})$ and perhaps also the ground-state Kohn-Sham potential $V_{\text{KS}}([n_0], \boldsymbol{r})$, and evaluate the total energy functional using these guesses. Since the guesses are inputs to the non-selfconsistent calculation, we call then $n^{\text{in}}(\boldsymbol{r})$ and $V_{\text{eff}}^{\text{in}}(\boldsymbol{r})$ from now on. To improve the accuracy of the approximate energies obtained, we insist that the expression evaluated to obtain the approximate total energy must be exact when the input density and potential are exact and stationary with respect to small variations of the input density and/or potential about the exact ground state. The errors in energies evaluated are then of second or higher order in $n^{\text{in}}(\boldsymbol{r}) - n_0(\boldsymbol{r})$ and $V_{\text{eff}}^{\text{in}}(\boldsymbol{r}) - V_{\text{KS}}([n_0], \boldsymbol{r})$, which we hope are small.

DFT is already a variational theory, in that the total energy functional $E[n]$ is minimized at the ground-state density: if the guessed density is $n^{\text{in}}(\boldsymbol{r}) = n_0(\boldsymbol{r}) + \Delta n(\boldsymbol{r})$, the error in the total energy is positive and of order $(\Delta n)^2$. The standard DFT functional is difficult to work with, however, because the evaluation of $T_s[n^{\text{in}}]$ requires the potential $V_{\text{eff}}(\boldsymbol{r})$ for which n^{in} is the non-interacting ground-state density. Finding this potential requires a self-consistency cycle no easier than that appearing in an ordinary self-consistent DFT calculation.

Another option is to guess the input potential $V_{\text{eff}}^{\text{in}}(\boldsymbol{r})$, solve the Kohn-Sham equation once non-selfconsistently to obtain the corresponding one-electron eigenfunctions and output density, and call the output density $n^{\text{out}}(\boldsymbol{r})$. At that point we have all of the information required to evaluate

$$E[n^{\text{out}}] = T_s[n^{\text{out}}] + E_{en}[n^{\text{out}}] + E_H[n^{\text{out}}] + E_{\text{xc}}[n^{\text{out}}] + E_{nn} \tag{71}$$

without self-consistent cycling. The drawback of this approach is that, even though $V_{\text{eff}}^{\text{in}}(\boldsymbol{r})$ may have a simple form — it could, for example, be a superposition of spherical atomic-like potentials as assumed in many tight-binding models — the output density $n^{\text{out}}(\boldsymbol{r})$ will not normally be simple and the double-counting correction terms will be far from pairwise. The link between DFT and tight binding remains elusive.

3.3.1 General variational formulation of density-functional theory

The derivation of density functionals better adapted for use in non-selfconsistent calculations is made easier by starting from a very general variational formulation of DFT first described in the form used here by Haydock in 1998 [21].

Consider the following functional of $n(\boldsymbol{r})$, $V_{\text{eff}}(\boldsymbol{r})$, and $\Psi(\boldsymbol{r}_1, \boldsymbol{r}_2, \ldots, \boldsymbol{r}_N)$, regarded as independent functions:

$$E[n, V_{\text{eff}}, \Psi] = \langle\Psi| \left(\hat{T} + \int V_{\text{eff}}(\boldsymbol{r}) \hat{n}(\boldsymbol{r})\, d^3r \right) |\Psi\rangle - \int V_{\text{eff}}(\boldsymbol{r}) n(\boldsymbol{r})\, d^3r + G[n], \tag{72}$$

where

$$G[n] = \int V_{\text{nuc}}(\boldsymbol{r}) n(\boldsymbol{r})\, d^3r + E_{\text{H}}[n] + E_{\text{xc}}[n] + E_{nn} \tag{73}$$

is shorthand for the sum of all Coulomb and exchange-correlation contributions to the total energy functional. The Kohn-Sham potential $V_{\rm KS}([n],\boldsymbol{r})$ corresponding to density $n(\boldsymbol{r})$ is the functional derivative of $G[n]$:

$$V_{\rm KS}([n],\boldsymbol{r}) = \frac{\delta G}{\delta n(\boldsymbol{r})}. \tag{74}$$

We seek the stationary points of $E[n, V_{\rm eff}, \Psi]$ subject to the normalization constraints $\langle\Psi|\Psi\rangle = 1$ and $\int n(\boldsymbol{r})d^3r = N$. Since $\Psi(\boldsymbol{r}_1, \boldsymbol{r}_2, \ldots, \boldsymbol{r}_N)$ and $n(\boldsymbol{r})$ are independent functions in this approach, the two constraints are also independent.

The problem of finding the stationary points of $\langle\Psi|\hat{H}|\Psi\rangle$ subject to $\langle\Psi|\Psi\rangle = 1$ is equivalent to solving the Schrödinger equation $\hat{H}\Psi = E\Psi$, where E is a Lagrange multiplier for the constraint. The variations of $E[n, V_{\rm eff}, \Psi]$ with respect to $n(\boldsymbol{r})$ and $V_{\rm eff}(\boldsymbol{r})$ are easy to work out [note that varying the function $n(\boldsymbol{r})$ has no effect on the operator $\hat{n}(\boldsymbol{r})$], leading to the three Euler-Lagrange equations:

$$-V_{\rm eff}(\boldsymbol{r}) + V_{\rm KS}([n],\boldsymbol{r}) = \mu, \tag{75}$$

$$\langle\Psi|\hat{n}(\boldsymbol{r})|\Psi\rangle - n(\boldsymbol{r}) = 0, \tag{76}$$

$$\left(\hat{T} + \int V_{\rm eff}(\boldsymbol{r})\hat{n}(\boldsymbol{r})\right)|\Psi\rangle = E_{\text{non-int}}|\Psi\rangle, \tag{77}$$

where μ is a Lagrange multiplier for the density normalization constraint. The Lagrange multiplier for the wavefunction normalization constraint has been called $E_{\text{non-int}}$ to avoid confusion with the energy functional itself. All three Euler-Lagrange equations must be satisfied at any stationary point of $E[n, V_{\rm eff}, \Psi]$.

The remarkable feature of these three equations is that they are fully equivalent to the equations of self-consistent DFT. The first says that the effective one-electron potential must equal the Kohn-Sham potential to within an arbitrary constant μ; this is the DFT self-consistency condition. The second says that $\Psi(\boldsymbol{r}_1, \boldsymbol{r}_2, \ldots, \boldsymbol{r}_N)$ must generate the one-electron density $n(\boldsymbol{r})$, just as in the Levy definition of the total energy functional. The third and final Euler-Lagrange equation says that the wavefunction Ψ must be an eigenfunction of the non-interacting Schrödinger equation

$$\sum_{i=1}^{N}\left(-\frac{1}{2}\nabla_i^2 + V_{\rm eff}(\boldsymbol{r}_i)\right)\Psi = E_{\text{non-int}}\Psi, \tag{78}$$

which separates into N one-electron equations:

$$\left(-\frac{1}{2}\nabla^2 + V_{\rm eff}(\boldsymbol{r})\right)\psi_i(\boldsymbol{r}) = \epsilon_i[V_{\rm eff}]\,\psi_i(\boldsymbol{r}). \tag{79}$$

If follows that the wavefunction Ψ appearing in the definition of the general density functional is single Slater determinant of the one-electron eigenfunctions used to calculate the non-interacting kinetic energy; it is not the physical many-electron wavefunction. If $E[n, V_{\rm eff}, \Psi]$ is stationary with respect to variations of n and $V_{\rm eff}$ and minimized with respect to Ψ, the equations of DFT are fully satisfied and $E[n, V_{\rm eff}, \Psi]$ is the ground-state energy of the interacting system.

Since $E[n, V_{\text{eff}}, \Psi]$ is stationary about the self-consistent DFT solution, we can replace n, V_{eff}, and Ψ by three *independent* guesses, n^{in}, $V_{\text{eff}}^{\text{in}}$ and Ψ^{in}, safe in the knowledge that $\Delta E = E[n^{\text{in}}, V_{\text{eff}}^{\text{in}}, \Psi^{\text{in}}] - E[n_0, V_{\text{KS}}[n_0], \Psi_0)$ is a quadratic form in the quantities $n^{\text{in}} - n_0$, $V_{\text{eff}}^{\text{in}} - V_{\text{KS}}[n_0]$, and $\Psi^{\text{in}} - \Psi_0$. If these are all small, the error in the calculated energy should be even smaller.

3.3.2 The Harris functional

The general variational formulation of DFT is a little too general to be useful in practice, but serves as a good starting point for deriving simpler density functionals. If we start by carrying out the constrained minimization with respect to Ψ to find the one-electron eigenvalues and eigenfunctions corresponding to the input potential V_{eff}, we obtain a functional of n and V_{eff} only:

$$E_{\text{GHF}}[n, V_{\text{eff}}] = \sum_{i \text{ occ}} \epsilon_i[V_{\text{eff}}] - \int V_{\text{eff}}(\boldsymbol{r}) n(\boldsymbol{r})\, d^3r + G[n]. \tag{80}$$

This functional was first discussed by Foulkes and Haydock [12] and is sometimes called the generalized Harris or generalized Harris-Foulkes functional [8]. The one-electron eigenvalues $\epsilon_i[V_{\text{eff}}]$ are obtained by solving

$$\left(-\frac{1}{2}\nabla^2 + V_{\text{eff}}(\boldsymbol{r})\right) \psi_i(\boldsymbol{r}) = \epsilon_i[V_{\text{eff}}]\, \psi_i(\boldsymbol{r}). \tag{81}$$

Note that the evaluation of $E_{\text{GHF}}[n, V_{\text{eff}}]$ for given inputs $n(\boldsymbol{r})$ and $V_{\text{eff}}(\boldsymbol{r})$ requires the one-electron Schrödinger equation to be solved once only; no self-consistent looping is required.
A further simplification is to set $V_{\text{eff}}(\boldsymbol{r})$ equal to $V_{\text{KS}}([n], \boldsymbol{r})$. Since $V_{\text{eff}}(\boldsymbol{r})$ and $V_{\text{KS}}([n], \boldsymbol{r})$ are the same in the ground state, this does not affect the location of the stationary point. The resulting functional of $n(\boldsymbol{r})$ only is called the Harris or Harris-Foulkes functional [25, 12, 8]:

$$E_{\text{HF}}[n] = \sum_{i \text{ occ}} \epsilon_i[n] - \int V_{\text{KS}}([n], \boldsymbol{r}) n(\boldsymbol{r})\, d^3r + G[n]. \tag{82}$$

The energy eigenvalues $\epsilon_i[n]$ are now obtained by solving

$$\left(-\frac{1}{2}\nabla^2 + V_{\text{KS}}([n], \boldsymbol{r})\right) \psi_i(\boldsymbol{r}) = \epsilon_i[n]\, \psi_i(\boldsymbol{r}). \tag{83}$$

As in the case of $E_{\text{GHF}}[n, V_{\text{eff}}]$, no-selfconsistent looping is required to evaluate $E_{\text{HF}}[n]$ for a given $n(\boldsymbol{r})$.
Both $E_{\text{GHF}}[n, V_{\text{eff}}]$ and $E_{\text{HF}}[n]$ are stationary about the ground state, a property that could in principle be used to guide an iterative, self-consistent algorithm towards the exact ground-state energy and density. In most cases, however, this has no advantages over the standard approach using the Hohenberg-Kohn-Sham functional. The main uses of $E_{\text{GHF}}[n, V_{\text{eff}}]$ and $E_{\text{HF}}[n]$ are in non-selfconsistent DFT calculations.

3.4 The tight-binding total energy method as a stationary approximation to density-functional theory

Let us return to the generalized Harris functional, Eq. (80), and the corresponding one-electron problem, Eq. (81). The functional is stationary about the exact ground state, so evaluating it for input densities and potentials close to the ground state produces total energies with second-order errors. With this in mind, we choose an input density in the form of a superposition of spherical densities,

$$n^{\text{in}}(\boldsymbol{r}) = \sum_I n_I(|\boldsymbol{r} - \boldsymbol{d}_I|), \tag{84}$$

and an input potential in the form of a superposition of spherical atomic-like potentials,

$$V_{\text{eff}}^{\text{in}}(\boldsymbol{r}) = \sum_I V_{\text{eff},I}(|\boldsymbol{r} - \boldsymbol{d}_I|). \tag{85}$$

For most solids, it is possible to construct superpositions of spherical atomic-like densities and potentials that match the exact ground-state density and Kohn-Sham potential rather well. The spherical densities required to describe a highly ionic solid might, of course, be ionic, integrating to produce a net atomic charge. Once the approximate potential and density have been constructed, we solve Eq. (81) non-selfconsistently to find the one-electron eigenvalues $\epsilon_i[V_{\text{eff}}^{\text{in}}]$. The energy functional $E_{\text{GHF}}[n^{\text{in}}, V_{\text{eff}}^{\text{in}}]$ is then evaluated using Eq. (80).

Because $V_{\text{eff}}^{\text{in}}(\boldsymbol{r})$ is a superposition of spherical atomic-like potentials, the one-electron Hamiltonian has exactly the form assumed in Sec. 2.2.4. We can therefore find the one-electron eigenvalues by choosing a basis set of atomic-like orbitals, constructing the one-, two- and three-center contributions to the tight-binding Hamiltonian and overlap matrices, and solving the generalized tight-binding eigenvalue problem. Furthermore, since both $V_{\text{eff}}^{\text{in}}$ and n^{in} are superpositions of spherical functions, almost all of the double-counting corrections appearing in Eq. (80) are strictly pairwise. The only exceptions are the exchange-correlation terms, which retain some weak non-pairwise character because $E_{\text{xc}}[n]$ is not a simple quadratic functional of n. In the exchange-only version of the local density approximation, for example, $E_{\text{xc}}[n]$ is proportional to the integral of $n^{4/3}(\boldsymbol{r})$ over the system.

If we ignore the small three- and higher-center contributions to the exchange-correlation double-counting terms, we have succeeded in deriving something very close to a tight-binding total energy model [11, 12]. The potential of the solid is approximated as a superposition of spherical atomic-like contributions, and the corresponding one-electron Schrödinger equation is solved once, non-selfconsistently, using a basis set of localized atomic-like functions. The total energy is the sum of the occupied eigenvalues and an (almost) pairwise ion-ion repulsion. The variational principle ensures that the calculated total energy decreases systematically towards $E[n^{\text{in}}, V_{\text{eff}}^{\text{in}}]$ as the basis set is improved; and the stationarity of the GHF functional ensures that $E[n^{\text{in}}, V_{\text{eff}}^{\text{in}}] - E_0$ is quadratic in $n^{\text{in}}(\boldsymbol{r}) - n_0(\boldsymbol{r})$ and $V_{\text{eff}}^{\text{in}}(\boldsymbol{r}) - V_{\text{KS}}([n_0], \boldsymbol{r})$.

The first derivation of the tight-binding total energy method [11, 12] from DFT was based on the Harris functional of the density only, with an input density in the form of a superposition of spherical atomic-like densities. The exchange-correlation contributions to the effective potential

$V_{\rm KS}([n^{\rm in}],\boldsymbol{r})$ appearing in Eq. (83) cannot then be written as a sum of spherical atomic-like contributions, which complicates the argument somewhat, but the conclusions are similar.
The accuracy of the Harris functional used with a superposition of spherical atomic-like densities has been tested for a wide range of solids [26–28] with surprising success. It is often capable of producing quantitatively accurate results, especially if the spherical atomic-like densities are optimized in some way [**?**, 28]. It does not work so well in transition metals, where the electronic configuration of an atom in the solid may be very different from that of an isolated atom, and often fails in ionic solids with significant charge transfer. In cases like these self-consistent tight-binding calculations are required [30–33].

4 Coulomb interactions for s, p, and d electrons

Although DFT is exact in principle, real DFT calculations require approximate exchange-correlation functionals. These are hard to improve systematically and do not always work as well as one might hope. Furthermore, the version of DFT described here yields ground-state properties only (time-dependent DFT [34] gives some excited-state properties). What can we do if the exchange-correlation functional proves inaccurate or we wish to calculate quantities DFT cannot provide? The most natural option is to return to the many-electron Schrödinger equation, Eq. (39), and attempt to solve that directly. Are there tight-binding-like models for many-particle problems?

4.1 The tight-binding full-configuration-interaction method

The main feature of the tight-binding approach is the choice of a basis of atomic-like orbitals, $\phi_\alpha(\boldsymbol{r})$, with $\alpha = 1, 2, \ldots, M$. The many-electron wavefunction $\Psi(\boldsymbol{r}_1, \boldsymbol{r}_2, \ldots, \boldsymbol{r}_N)$, which is a totally antisymmetric function of N different electron positions, can be approximated as a linear combination of Slater determinants of these orbitals:

$$D_{\boldsymbol{\alpha}}(\boldsymbol{r}_1, \boldsymbol{r}_2, \ldots, \boldsymbol{r}_N) = \frac{1}{\sqrt{N!}} \begin{vmatrix} \phi_{\alpha_1}(\boldsymbol{r}_1) & \phi_{\alpha_2}(\boldsymbol{r}_1) & \ldots & \ldots & \phi_{\alpha_N}(\boldsymbol{r}_1) \\ \phi_{\alpha_1}(\boldsymbol{r}_2) & \phi_{\alpha_2}(\boldsymbol{r}_2) & \ldots & \ldots & \phi_{\alpha_N}(\boldsymbol{r}_2) \\ & & & & \\ & & & & \\ \phi_{\alpha_1}(\boldsymbol{r}_N) & \phi_{\alpha_2}(\boldsymbol{r}_N) & \ldots & \ldots & \phi_{\alpha_N}(\boldsymbol{r}_N) \end{vmatrix}, \tag{86}$$

where $\boldsymbol{\alpha} = (\alpha_1, \alpha_2, \ldots, \alpha_N)$ lists the indices of the orbitals appearing in $D_{\boldsymbol{\alpha}}$. A Slater determinant containing the same orbital twice vanishes because it has two identical columns, so we can assume that all of the indices are different. The order in which the indices appear affects the sign of the determinant only, so it is often convenient to insist that $\alpha_1 < \alpha_2 < \ldots < \alpha_N$. Given a determinant for which this is not the case, one can always permute the indices into ascending order. Every pair interchange swaps two columns and changes the sign of the determinant, but nothing else is affected. We assume from now on that the one-electron basis set is

orthonormal, $\langle\phi_\alpha|\phi_\beta\rangle = \delta_{\alpha\beta}$, in which case the N-electron basis set of Slater determinants is also orthonormal:

$$\langle D_{\boldsymbol{\alpha}}|D_{\boldsymbol{\beta}}\rangle = \int D^*_{\boldsymbol{\alpha}}(\boldsymbol{r}_1,\boldsymbol{r}_2,\ldots,\boldsymbol{r}_N)D_{\boldsymbol{\beta}}(\boldsymbol{r}_1,\boldsymbol{r}_2,\ldots,\boldsymbol{r}_N)\,d^3r_1d^3r_2\ldots d^3r_N = \delta_{\boldsymbol{\alpha\beta}}, \tag{87}$$

where $\delta_{\boldsymbol{\alpha\beta}} = \delta_{\alpha_1\beta_1}\delta_{\alpha_2\beta_2}\ldots\delta_{\alpha_N\beta_N}$ and the lists $(\alpha_1,\alpha_2,\ldots,\alpha_N)$ and $(\beta_1,\beta_2,\ldots,\beta_N)$ are in ascending order.

Because the one-electron basis set is finite, the N-electron basis of Slater determinants is far from complete. It is, however, huge. Consider, for example, a system of $N = 10$ electrons described using a basis set of $M = 20$ one-electron orbitals. The number of possible Slater determinants is the number of ways of picking N orbitals from a set of M possibilities. This is ${}^MC_N = {}^{20}C_{10} = 184,756$.

The next step is to approximate the eigenstates of the many-electron Hamiltonian as linear combinations of Slater determinants,

$$\Psi = \sum_{\boldsymbol{\alpha}} c_{\boldsymbol{\alpha}} D_{\boldsymbol{\alpha}}, \tag{88}$$

and determine the optimal expansion coefficients using the linear variational method described in Sec. 2.1. The resulting matrix eigenvalue problem takes the form

$$\sum_{\boldsymbol{\beta}} H_{\boldsymbol{\alpha\beta}} c_{\boldsymbol{\beta}} = E c_{\boldsymbol{\alpha}}, \tag{89}$$

where $H_{\boldsymbol{\alpha\beta}} = \langle D_{\boldsymbol{\alpha}}|\hat{H}|D_{\boldsymbol{\beta}}\rangle$. Note that $\hat{H}$ is the full N-electron Hamiltonian operator and $H_{\boldsymbol{\alpha\beta}} = \langle D_{\boldsymbol{\alpha}}|\hat{H}|D_{\boldsymbol{\beta}}\rangle$ is a $3N$-dimensional integral. Fortunately, because $\hat{H}$ only contains one- and two-electron operators, all non-zero Hamiltonian matrix elements can be expressed in terms of three- and six-dimensional integrals. Solving the eigenvalue problem in Eq. (89) yields ${}^MC_N$ approximate eigenvalues and eigenfunctions of the exact many-electron Hamiltonian. These may also be viewed as exact eigenvalues and eigenfunctions of the projected Hamiltonian $\hat{P}\hat{H}\hat{P}$, where $\hat{P}$ is the projector onto the space spanned by the ${}^MC_N$ Slater determinants in the basis.

This approach is very difficult to use because of the enormous size of the many-electron Hilbert space, but is useful for small atoms and molecules. Chemists call it the full configuration interaction method. Seen from the point of view of this article, it is the many-electron equivalent of the tight-binding method.

4.1.1 Second-quantized notation

The projected Hamiltonian $\hat{P}\hat{H}\hat{P}$ corresponding to the real-space Hamiltonian

$$\hat{H} = \sum_i \left(-\frac{1}{2}\nabla_i^2 + V_{\text{nuc}}(\boldsymbol{r}_i)\right) + \sum_{i>j}\frac{1}{|\boldsymbol{r}_i-\boldsymbol{r}_j|} \tag{90}$$

may be written in second-quantized notation as

$$\hat{H} = \sum_{\alpha,\beta} h_{\alpha\beta}\,\hat{c}^\dagger_\alpha\hat{c}_\beta + \frac{1}{2}\sum_{\alpha,\beta,\chi,\gamma} V_{\alpha\beta,\chi\gamma}\,\hat{c}^\dagger_\alpha\hat{c}^\dagger_\beta\hat{c}_\gamma\hat{c}_\chi, \tag{91}$$

where $\hat{c}_\alpha^\dagger$ and $\hat{c}_\alpha$ are creation and annihilation operators for electrons in the one-electron orbital $\phi_\alpha(\boldsymbol{r})$ and

$$h_{\alpha\beta} = \int \phi_\alpha^*(\boldsymbol{r}) \left(-\frac{1}{2}\nabla_i^2 + V_{\text{nuc}}(\boldsymbol{r}) \right) \phi_\beta(\boldsymbol{r})\, d^3r, \tag{92}$$

$$V_{\alpha\beta,\chi\gamma} = \iint \phi_\alpha^*(\boldsymbol{r})\phi_\beta^*(\boldsymbol{r}') \frac{1}{|\boldsymbol{r}-\boldsymbol{r}'|} \phi_\chi(\boldsymbol{r})\phi_\gamma(\boldsymbol{r}')\, d^3r d^3r', \tag{93}$$

are the one- and two-particle Hamiltonian matrix elements. The creation and annihilation operators satisfy the anticommutation relations:

$$\left\{ \hat{c}_\alpha, \hat{c}_\beta^\dagger \right\} = \hat{c}_\alpha \hat{c}_\beta^\dagger + \hat{c}_\beta^\dagger \hat{c}_\alpha = \delta_{\alpha\beta}. \tag{94}$$

Second-quantized notation is explained in the first chapter of almost every book on many-body theory; the dense but precise explanation given by Negele and Orland [35] is a good one. It is important to understand that "second quantization" is a misnomer: the second-quantized notation brings nothing new except algebraic convenience; the second-quantized Hamiltonian is exactly the same as the original N-electron Hamiltonian; and the basis set of Slater determinants has not changed.

The systems for which DFT fails and many-body tight-binding methods are most useful are often magnetic, so we can no longer ignore the electron spin. The spin-dependent tight-binding basis functions take the form

$$\phi_{\alpha,\zeta}(\boldsymbol{r}, s) = \phi_\alpha(\boldsymbol{r})\chi_\zeta(s), \tag{95}$$

where $s = \uparrow, \downarrow$ and χ_ζ is either $\chi_\uparrow$ or $\chi_\downarrow$, with $\chi_\uparrow(s) = \delta_{s,\uparrow}$ and $\chi_\downarrow(s) = \delta_{s,\downarrow}$. Note that the spatial parts of the basis functions are independent of spin; this is by choice. The spin-dependent Hamiltonian is

$$\hat{H} = \sum_\zeta \sum_{\alpha,\beta} h_{\alpha\beta}\, \hat{c}_{\alpha,\zeta}^\dagger \hat{c}_{\beta,\zeta} + \frac{1}{2} \sum_{\zeta,\zeta'} \sum_{\alpha,\beta,\chi,\gamma} V_{\alpha\beta,\chi\gamma}\, \hat{c}_{\alpha,\zeta}^\dagger \hat{c}_{\beta,\zeta'}^\dagger \hat{c}_{\gamma,\zeta'} \hat{c}_{\chi,\zeta}, \tag{96}$$

where $\hat{c}_{\alpha,\zeta}^\dagger$ and $\hat{c}_{\alpha,\zeta}$ are the creation and annihilation operators for the basis function $\phi_{\alpha,\zeta}(\boldsymbol{r}, s)$ and satisfy the commutation relations

$$\left\{ \hat{c}_{\alpha,\zeta}, \hat{c}_{\beta,\zeta'}^\dagger \right\} = \delta_{\alpha\beta}\delta_{\zeta\zeta'}. \tag{97}$$

Because the spatial parts of the basis functions were chosen to be independent of spin, the matrix elements $h_{\alpha\beta}$ and $V_{\alpha\beta,\chi\gamma}$ are still as given in Eqs. (92) and (93). Relativistic spin-dependent interactions such as the spin-orbit term have not been included but can easily be added.

The Hamiltonian as expressed in Eq. (96) is closely related to the tight-binding Hamiltonian considered earlier. The one-electron matrix elements $h_{\alpha\beta}$ are analogous to the tight-binding matrix elements $H_{\alpha\beta} = \langle\phi_\alpha|(-\frac{1}{2}\nabla^2 + V_{\text{eff}}(\boldsymbol{r})|\phi_\beta\rangle$, except that the nuclear potential appears in place of the effective potential. These matrix elements can be parametrized in terms of a small number of Slater-Koster parameters, just as in tight-binding theory. The two-particle Coulomb interaction matrix elements $V_{\alpha\beta,\chi\gamma}$ are more complicated. In DFT-based tight-binding

methods they are replaced by the density-dependent Hartree and exchange-correlation potentials incorporated into V_{eff}.

Switching to a second-quantized formalism has improved the notation but has not made the many-electron problem any easier to solve. The complicated form of Eq. (91) is also an impediment to pencil-and-paper work. Even if we consider only the three p orbitals on a single atom, the interaction matrix $V_{\alpha\beta,\chi\gamma}$ has $3^4 = 81$ elements. For the five d orbitals this rises to $5^4 = 625$ elements. Such large collections of numbers are not easy to deal with analytically, so simplifications are required.

The first simplification, often made in the many-body community, is to neglect all Coulomb integrals involving orbitals on more than one atom. Given the long range of the Coulomb interaction this seems unintuitive at first, and quantum chemists, who like to get things *right*, normally prefer to evaluate all of the matrix elements for all of the orbitals. Most of the many-body problems studied by condensed matter physicists, however, concern atoms in solids, often metals, where the interactions between atoms are strongly screened by mobile valence electrons. In many cases this screening is so efficient that electrons occupying localized d of f orbitals on one atom interact only weakly with electrons in d or f orbitals on other atoms and the screened inter-atomic Coulomb matrix elements really can be ignored. The mobile valence electrons are not included in the tight-binding model explicitly, but their effect is to renormalize the matrix elements between the localized orbitals that are included.

4.1.2 Coulomb interactions on a single atom

The rest of this article discusses what we know about the symmetries of the matrix $V_{\alpha\beta,\chi\gamma}$ that describes the (screened) Coulomb interactions on a single atom. Can we carry out an equivalent of the Slater-Koster analysis, allowing us to express the elements of $V_{\alpha\beta,\chi\gamma}$ in terms of a minimal set of basic parameters? How many parameters do we need?

These are questions with a long history, but they still cause a great deal of confusion. The forms of $V_{\alpha\beta,\chi\gamma}$ for shells of s and p electrons are well established, but many different d-shell Hamiltonians have been proposed and most of them are wrong in one way or another. Some are missing essential symmetries, failing to remain invariant under rotations in real and/or spin space; others are missing terms no smaller than the terms kept; and even the best are missing terms thought to be small. Many otherwise sophisticated papers on many-body physics start with an incorrect model Hamiltonian and may reach false conclusions as a result. The history of the subject and the failings of some of the most widely used Hamiltonians are summarized in Ref. [13], which also clears up the confusion for shells of s, p and d electrons. Here we explain the results derived in that paper.

Before going on, we remark that the correct form of the on-site Coulomb operator has been known for more than 50 years and that quantum chemists use it as a matter of course. If we assume that the $2l + 1$ basis functions in a shell of angular momentum l have the same angular dependence as the spherical harmonics Y_l^m, with $m = -l, -l + 1, \ldots, l$, the theory of angular momentum [36] may be used to derive formulae for $V_{\alpha\beta,\chi\gamma}$. See Ref. [37] for a clear explanation.

The drawback of this approach is that the formulae are complicated and expressed in terms of quantities such as Gaunt or Racah coefficients, which are inconvenient for analytic work. The formulae derived here are less general, in that they apply to s, p and d shells only, but simpler. The most important symmetry of $V_{\alpha\beta,\chi\gamma}$ is rotational invariance. If the basis functions used to describe a shell of angular momentum l have the same angular dependence as spherical harmonics Y_l^m, the orbital label α may be identified with the m index. Such basis functions transform into linear combinations of each other under rotations:

$$\hat{R}^{\boldsymbol{\omega}}\phi_\alpha = \sum_{\alpha'=-l}^{l} D^l_{\alpha',\alpha}(\boldsymbol{\omega})\phi_{\alpha'}. \tag{98}$$

The operator $\hat{R}^{\boldsymbol{\omega}}$ rotates the function to which it is applied by ω radians about an axis parallel to the unit vector $\hat{\boldsymbol{\omega}}$, and $D^l(\boldsymbol{\omega})$ is the $(2l+1)\times(2l+1)$ matrix corresponding to $\hat{R}^{\boldsymbol{\omega}}$ in the irreducible representation of the rotation group of angular momentum l. The Coulomb interaction $1/|\boldsymbol{r}-\boldsymbol{r}'|$ is unchanged if $\boldsymbol{r}$ and $\boldsymbol{r}'$ are rotated simultaneously, so $V_{\alpha\beta,\chi\gamma}$ does not change if every orbital is replaced by a rotated version:

$$\begin{aligned} V_{\alpha\beta,\chi\gamma} &= \iint \phi^*_\alpha(\boldsymbol{r})\phi^*_\beta(\boldsymbol{r}')\,\frac{1}{|\boldsymbol{r}-\boldsymbol{r}'|}\,\phi_\chi(\boldsymbol{r})\phi_\gamma(\boldsymbol{r}')\,d^3r d^3r' \\ &= \iint \left(\hat{R}^{\boldsymbol{\omega}}\phi_\alpha(\boldsymbol{r})\right)^* \left(\hat{R}^{\boldsymbol{\omega}}\phi_\beta(\boldsymbol{r}')\right)^* \frac{1}{|\boldsymbol{r}-\boldsymbol{r}'|} \left(\hat{R}^{\boldsymbol{\omega}}\phi_\chi(\boldsymbol{r})\right)\left(\hat{R}^{\boldsymbol{\omega}}\phi_\gamma(\boldsymbol{r}')\right) d^3r d^3r' \\ &= \sum_{\alpha'\beta'\chi'\gamma'} \left(D^l_{\alpha',\alpha}(\boldsymbol{\omega})\right)^* \left(D^l_{\beta',\beta}(\boldsymbol{\omega})\right)^* V_{\alpha'\beta',\chi'\gamma'} D^l_{\chi',\chi}(\boldsymbol{\omega}) D^l_{\gamma',\gamma}(\boldsymbol{\omega}). \end{aligned} \tag{99}$$

This shows that $V_{\alpha\beta,\chi\gamma}$ is a rotationally invariant fourth-rank tensor. If the basis functions are defined using the real spherical harmonics $\tilde{Y}^l_m$ introduced in Sec. 2.2.5, the D^l matrices, which are complex and unitary, are replaced by the $\tilde{D}^l$ matrices from Eq. (18), which are real and orthogonal. Since most Hubbard-like models use real spherical harmonics, we are primarily interested in this case.

4.2 Hubbard-like Hamiltonians for atoms

4.2.1 The one-band Hubbard model: s-orbital symmetry

If the outermost shell is an s shell and all other shells are ignored, the model Hamiltonian for an atom has only one spatial orbital ϕ_α and one non-zero Coulomb matrix element $V_{\alpha\alpha,\alpha\alpha}$, which is called the Hubbard parameter and denoted U_0. The interaction Hamiltonian takes the form

$$\hat{V} = \frac{1}{2}U_0 \sum_{\zeta,\zeta'} \hat{c}^\dagger_{\alpha,\zeta}\hat{c}^\dagger_{\alpha,\zeta'}\hat{c}_{\alpha,\zeta'}\hat{c}_{\alpha,\zeta} = \frac{1}{2}U_0\left(\hat{c}^\dagger_{\alpha,\uparrow}\hat{c}^\dagger_{\alpha,\downarrow}\hat{c}_{\alpha,\downarrow}\hat{c}_{\alpha,\uparrow} + \hat{c}^\dagger_{\alpha,\downarrow}\hat{c}^\dagger_{\alpha,\uparrow}\hat{c}_{\alpha,\uparrow}\hat{c}_{\alpha,\downarrow}\right) = U_0\,\hat{n}_{\alpha,\uparrow}\hat{n}_{\alpha,\downarrow}, \tag{100}$$

where I have noted that $\hat{c}_{\alpha,\zeta}\hat{c}_{\alpha,\zeta} = 0$, reordered the creation and annihilation operators using the anticommutation relations, and introduced the number operator $\hat{n}_{\alpha,\zeta} = \hat{c}^\dagger_{\alpha,\zeta}\hat{c}_{\alpha,\zeta}$, which counts

how many electrons are in basis state $\phi_{\alpha,\zeta}$. Equation (100) is the famous Hubbard interaction and is the starting point for much of the analytic work on strongly interacting systems.
It is often convenient to rewrite the atomic interaction Hamiltonian in terms of the operators for the total number of electrons on the atom,

$$\hat{n} = \sum_{\alpha,\zeta} \hat{n}_{\alpha,\zeta}, \tag{101}$$

and the electronic spin moment of the atom,

$$\hat{\boldsymbol{m}} = \sum_{\alpha,\zeta,\zeta'} \hat{c}^\dagger_{\alpha,\zeta} \boldsymbol{\sigma}_{\zeta,\zeta'} \hat{c}_{\alpha,\zeta'}, \tag{102}$$

where $\boldsymbol{\sigma}_{\zeta,\zeta'} = (\sigma^x_{\zeta,\zeta'}, \sigma^y_{\zeta,\zeta'}, \sigma^z_{\zeta,\zeta'})$ is the vector of Paul spin matrices

$$\sigma^x = \begin{pmatrix} 0 & 1 \\ 1 & 0 \end{pmatrix}, \qquad \sigma^y = \begin{pmatrix} 0 & -i \\ i & 0 \end{pmatrix}, \quad \text{and} \quad \sigma^z = \begin{pmatrix} 1 & 0 \\ 0 & -1 \end{pmatrix}.$$

In the case of an s shell there is only one spatial orbital and the sums over α in Eqs. (101) and (102) have only one term each.
The square of the number operator for an s shell is

$$\hat{n}^2 = (\hat{n}_{\alpha,\uparrow} + \hat{n}_{\alpha,\downarrow})(\hat{n}_{\alpha,\uparrow} + \hat{n}_{\alpha,\downarrow}) = 2\hat{n}_{\alpha,\uparrow}\hat{n}_{\alpha,\downarrow} + \hat{n}_{\alpha,\uparrow} + \hat{n}_{\alpha,\downarrow} = 2\hat{n}_{\alpha,\uparrow}\hat{n}_{\alpha,\downarrow} + \hat{n}, \tag{103}$$

where we have noted that $\hat{n}_{\alpha,\sigma}\hat{n}_{\alpha,\sigma} = \hat{n}_{\alpha,\sigma}$. The Hubbard interaction for an s shell may therefore be rewritten in terms of the operator for the total number of electrons as

$$\hat{V} = \frac{1}{2} U_0 \left(\hat{n}^2 - \hat{n}\right). \tag{104}$$

The one-electron $-\hat{n}$ term on the right-hand side of Eq. (103) arises because the creation operators in $\hat{n}^2$ are not all to the left of the annihilation operators; if we attempt to reorder the creation and annihilation operators to ensure that this is the case, the anticommutators produce additional one-electron terms. This mixing of one- and two-electron terms is awkward, so we define $:\hat{n}^2:$, the "normal ordered" version of $\hat{n}^2$, by permuting the creation and annihilation operators until all of the creation operators are on the left, *without* adding the anticommutator terms that would be required to leave the product of operators unaltered. If the rearrangement requires an odd number of flips, the normal ordering also introduces a sign change. It is easy to show quite generally (not just for an s shell) that

$$:\hat{n}^2: \; = \hat{n}^2 - \hat{n}, \tag{105}$$

so we can write the s-shell Hubbard interaction as

$$\hat{V} = \frac{1}{2} U_0 :\hat{n}^2: . \tag{106}$$

The s-band Hubbard interaction can also be written in terms of $:\hat{m}^2: \;=:\hat{\boldsymbol{m}}\cdot\hat{\boldsymbol{m}}:$. Using the identity $\boldsymbol{\sigma}_{\zeta\zeta'}\cdot\boldsymbol{\sigma}_{\xi\xi'} = 2\delta_{\zeta'\xi}\delta_{\zeta\xi'} - \delta_{\zeta\zeta'}\delta_{\xi\xi'}$, one finds that

$$:\hat{m}^2: \;= -\sum_{\alpha\beta}\sum_{\zeta\xi}\left(2\hat{c}^{\dagger}_{\alpha,\zeta}\hat{c}^{\dagger}_{\beta,\xi}\hat{c}_{\alpha,\xi}\hat{c}_{\beta,\zeta} + \hat{c}^{\dagger}_{\alpha,\zeta}\hat{c}^{\dagger}_{\beta,\xi}\hat{c}_{\beta,\xi}\hat{c}_{\alpha,\zeta}\right) = \hat{m}^2 - 3\hat{n}. \tag{107}$$

For an s shell this is equivalent to

$$:\hat{m}^2: \;= -6\hat{n}_{\alpha,\uparrow}\hat{n}_{\alpha,\downarrow} = -3:\hat{n}^2: \tag{108}$$

and we obtain

$$\hat{V} = -\frac{1}{6}U_0:\hat{m}^2:. \tag{109}$$

4.2.2 The three-band Hubbard model: p-orbital symmetry

Suppose that the orbitals α, β, χ, and γ are real spherical harmonic p orbitals with angular dependence x/r, y/r and z/r. The rotation matrix $D^{l}_{\alpha'\alpha}(\boldsymbol{\omega})$ is then a familiar Cartesian 3×3 rotation matrix $\boldsymbol{R}_{\boldsymbol{\omega}}$, and $V_{\alpha\beta,\chi\gamma}$ is a rotationally invariant fourth-rank Cartesian tensor. The general form of such a tensor is well known [38]:

$$V_{\alpha\beta,\chi\gamma} = U\delta_{\alpha\chi}\delta_{\beta\gamma} + J\delta_{\alpha\gamma}\delta_{\beta\chi} + J'\delta_{\alpha\beta}\delta_{\chi\gamma}, \tag{110}$$

where $U = V_{\alpha\beta,\alpha\beta}$, $J = V_{\alpha\beta,\beta\alpha}$, and $J' = V_{\alpha\alpha,\beta\beta}$, all with $\alpha\neq\beta$.
Bearing in mind that the Cartesian p orbitals are real, a brief inspection of the form of the matrix element, Eq. (93), shows that $V_{\alpha\beta,\chi\gamma} = V_{\chi\beta,\alpha\gamma} = V_{\alpha\gamma,\chi\beta}$, implying that $J = J'$. Hence we find

$$V_{\alpha\beta,\chi\gamma} = U\delta_{\alpha\chi}\delta_{\beta\gamma} + J(\delta_{\alpha\gamma}\delta_{\beta\chi} + \delta_{\alpha\beta}\delta_{\chi\gamma}). \tag{111}$$

This shows that the most general p-shell on-site Coulomb interaction Hamiltonian is defined by just two independent parameters; the interaction matrix $V_{\alpha\beta,\chi\gamma}$ still has 81 elements, but only two are independent. Setting $\alpha=\beta=\chi=\gamma$ recovers the well-known equation $U_0 = U + 2J$, where $U_0 = V_{\alpha\alpha,\alpha\alpha}$.
Starting from Eq. (111) and wading through lots of algebra, it is straightforward but tedious to show that the Coulomb interaction Hamiltonian may be written:

$$\hat{V} = \frac{1}{2}\left[(U-J):\hat{n}^2: \;- J:\hat{m}^2: \;- J:\hat{L}^2:\right], \tag{112}$$

where

$$\hat{\boldsymbol{L}} = i\sum_{\alpha\beta\zeta}\left(\epsilon_{1\beta\alpha},\epsilon_{2\beta\alpha},\epsilon_{3\beta\alpha}\right)\hat{c}^{\dagger}_{\alpha,\zeta}\hat{c}_{\beta,\zeta} \tag{113}$$

is the vector angular momentum operator, $\epsilon_{\alpha\beta\gamma}$ is the three-dimensional Levi-Civita symbol, and $\hat{L}^2 = \hat{\boldsymbol{L}}\cdot\hat{\boldsymbol{L}}$. An equivalent expression is

$$\hat{V} = \frac{1}{2}\left[\left(U-\frac{1}{2}J\right):\hat{n}^2: \;-\frac{1}{2}J:\hat{m}^2: \;+ J\sum_{\alpha\beta}:(\hat{n}_{\alpha\beta})^2:\right], \tag{114}$$

where the operator $\hat{n}_{\alpha\beta} = \sum_\zeta \hat{c}^\dagger_{\alpha,\zeta}\hat{c}_{\beta,\zeta}$ transfers an electron of either spin from orbital β to orbital α. The normal-ordered square of this operator,

$$:(\hat{n}_{\alpha\beta})^2: \;= \sum_{\zeta,\zeta'} :\hat{c}^\dagger_{\alpha,\zeta}\hat{c}_{\beta,\zeta}\hat{c}^\dagger_{\alpha,\zeta'}\hat{c}_{\beta,\zeta'}: \;= 2\left(\hat{c}_{\alpha,\uparrow}\hat{c}_{\alpha,\downarrow}\right)^\dagger\left(\hat{c}_{\beta,\uparrow}\hat{c}_{\beta,\downarrow}\right), \tag{115}$$

describes the hopping of singlet pairs of electrons from spatial orbital β to spatial orbital α. Equation (112) exemplifies Hund's first and second rules for the atom. Noting that $\hat{\boldsymbol{m}} = 2\hat{\boldsymbol{S}}$, where $\hat{\boldsymbol{S}}$ is the electron spin operator, we see that the energy is minimized by first maximizing the spin (prefactor $-2J$) and then maximizing the orbital angular momentum (prefactor $-\frac{1}{2}J$).

4.2.3 The five-band Hubbard model: d-orbital symmetry

If we consider Eq. (99) for a shell of d orbitals, the matrices D^l belong to the five-dimensional $l = 2$ irreducible representation of the rotation group; they are no longer the familiar 3×3 Cartesian rotation matrices. One way to determine the number of independent parameters required to specify $V_{\alpha\beta,\chi\gamma}$ completely is to use the theory of angular momentum [36], but we find it easier to use the theory of irreducible Cartesian tensors [39]. This allows us to re-express the behavior of $V_{\alpha\beta,\chi\gamma}$ under rotations using 3×3 rotation matrices only.

A Cartesian tensor of rank n transforms under rotation in the standard way:

$$(\hat{R}^{\boldsymbol{\omega}}T)_{ij\ldots k} = \sum_{i'j'\ldots k'} R^{\boldsymbol{\omega}}_{ii'}R^{\boldsymbol{\omega}}_{jj'}\ldots R^{\boldsymbol{\omega}}_{kk'}T_{i'j'\ldots k'}, \tag{116}$$

with $R^{\boldsymbol{\omega}}$ the 3×3 matrix for a rotation of ω radians about an axis parallel to $\hat{\boldsymbol{\omega}}$. This mapping transforms the 3^n elements of T into linear combinations of each other, so the elements form a basis for a 3^n-dimensional representation of the rotation group. In general, however, this representation is reducible. An *irreducible* Cartesian tensor of rank n and angular momentum l transforms in the same way as a general Cartesian tensor, but only has $2l + 1$ independent components. The rule for rotating the tensor, Eq. (116), transforms these $2l + 1$ independent components into linear combinations of each other, so they form a basis for a $2l + 1$ dimensional representation of the rotation group. The Cartesian tensor is said to be irreducible if this representation is irreducible.

We can illustrate these ideas by considering the tensor product of two vectors:

$$T = \boldsymbol{a} \otimes \boldsymbol{b} = \begin{pmatrix} a_1b_1 & a_1b_2 & a_1b_3 \\ a_2b_1 & a_2b_2 & a_2b_3 \\ a_3b_1 & a_3b_2 & a_3b_3 \end{pmatrix}. \tag{117}$$

The nine elements of this tensor transform into linear combinations of each other under rotations, so they are a basis for a nine-dimensional representation of the rotation group. If we wanted to, we could construct the 9×9 matrix corresponding to the action of any given rotation directly from the tensorial transformation rule. We would find, however, that the 9×9 representation is not irreducible. In fact, as we already know from the theory of the addition of angular momentum,

$$1 \otimes 1 = 0 \oplus 1 \oplus 2. \tag{118}$$

This implies that it must be possible to create from the set of nine independent elements a single rotationally invariant s function, a set of three p functions, and a set of five d functions.
We can accomplish this explicitly by writing $\boldsymbol{a} \otimes \boldsymbol{b}$ as the sum of three tensors:

$$T_{ij} = (\boldsymbol{a} \otimes \boldsymbol{b})_{ij} = \frac{1}{3}(a_k b_k)\delta_{ij} + T_{\{ij\}} + \left[T_{(ij)} - \frac{1}{3}(a_k b_k)\delta_{ij}\right] \tag{119}$$

where $T_{(ij)} \equiv \frac{1}{2}(T_{ij} + T_{ji})$, $T_{\{ij\}} \equiv \frac{1}{2}(T_{ij} - T_{ji})$, and the summation convention is in force for repeated suffices. The first term is a multiple of the unit tensor and hence transforms like an s function; the three non-zero independent elements of the antisymmetric tensor $T_{\{ij\}}$ are the components of the vector product $\boldsymbol{a} \times \boldsymbol{b}$ and transform under rotations like the three p functions; and the five independent elements of the traceless symmetric tensor $T_{(ij)} - \frac{1}{2}(a_k b_k)\delta_{ij}$ transform under rotations like the five Cartesian d orbitals. Note that antisymmetric matrices remain antisymmetric and traceless symmetric matrices remain traceless symmetric matrices when rotated.
If we choose $\boldsymbol{a} = \boldsymbol{b} = \boldsymbol{r} = (x, y, z)$, the d-like nature of the traceless symmetric part of $\boldsymbol{a} \otimes \boldsymbol{b}$ becomes obvious:

$$(\boldsymbol{r} \otimes \boldsymbol{r})_{(ij)} - \frac{1}{3}r^2\delta_{ij} = \begin{pmatrix} x^2 - \frac{1}{3}r^2 & xy & xz \\ xy & y^2 - \frac{1}{3}r^2 & yz \\ xz & yz & z^2 - \frac{1}{3}r^2 \end{pmatrix}. \tag{120}$$

The off-diagonal elements xy, yz and zx are the three t_{2g} functions; and the two independent diagonal elements, which we can take to be $3z^2 - r^2$ and $x^2 - y^2$, are the two e_g functions. We call this traceless symmetric tensor B from now on:

$$B_{ij} = (\boldsymbol{r} \otimes \boldsymbol{r})_{(ij)} - \frac{1}{3}r^2\delta_{ij}. \tag{121}$$

The link between the traceless symmetric tensor B and the d orbitals is a special case of a general result, which states that the $2l + 1$ independent elements of a totally symmetric l^{th} rank Cartesian tensor with all traces removed are a basis for the angular momentum l representation of the rotation group.
If we view every d orbital as an element (or linear combination of elements) of B, each d orbital may be labelled using two Cartesian indices i and j. The isotropic fourth-rank five-dimensional tensor $V_{\alpha\beta,\chi\gamma}$ from Eq. (93) then becomes an isotropic eighth-rank three-dimensional tensor $V_{ij,kl,mn,op}$, which transforms like $B_{ij}B_{kl}B_{mn}B_{op}$.
It is a theorem due to Weyl [40] that any isotropic Cartesian tensor of even rank can be expressed as a linear combination of products of Kronecker deltas, so the remaining task is to determine the number of independent products of four Kronecker deltas consistent with the symmetries of the eighth-rank tensor, bearing in mind that the second-rank tensors B of which it is composed are traceless and symmetric. The details of this calculation are explained in Ref. [13].
The result, translated back into the notation where each of the five d orbitals is labelled by a

single index with five possible values, is

$$V_{\alpha\beta,\chi\gamma} = \frac{1}{2}\left(U\delta_{\alpha\chi}\delta_{\beta\gamma} + \left[J + \frac{5}{2}\Delta J\right](\delta_{\alpha\gamma}\delta_{\beta\chi} + \delta_{\alpha\beta}\delta_{\gamma\chi}) - 48\Delta J\sum_{ijkl}\xi_{\alpha ij}\xi_{\beta jk}\xi_{\chi kl}\xi_{\gamma li}\right), \tag{122}$$

where $\boldsymbol{\xi}$ is a five-component vector of the traceless symmetric 3×3 transformation matrices used to convert from the two-index notation to the one-index notation:

$$\xi_1 = \begin{pmatrix} -\frac{1}{2\sqrt{3}} & 0 & 0 \\ 0 & -\frac{1}{2\sqrt{3}} & 0 \\ 0 & 0 & \frac{1}{\sqrt{3}} \end{pmatrix},\ \xi_2 = \begin{pmatrix} 0 & 0 & \frac{1}{2} \\ 0 & 0 & 0 \\ \frac{1}{2} & 0 & 0 \end{pmatrix},\ \xi_3 = \begin{pmatrix} 0 & 0 & 0 \\ 0 & 0 & \frac{1}{2} \\ 0 & \frac{1}{2} & 0 \end{pmatrix},\ \xi_4 = \begin{pmatrix} 0 & \frac{1}{2} & 0 \\ \frac{1}{2} & 0 & 0 \\ 0 & 0 & 0 \end{pmatrix},\ \xi_5 = \begin{pmatrix} \frac{1}{2} & 0 & 0 \\ 0 & -\frac{1}{2} & 0 \\ 0 & 0 & 0 \end{pmatrix}.$$

The indices $(1,2,3,4,5)$ correspond to the d orbitals $(3z^2-r^2, zx, yz, xy, x^2-y^2)$. The three independent parameters U, J and ΔJ are defined as follows:

$$U = V_{(zx)(yz),(zx)(yz)}, \tag{123}$$

$$J = \frac{1}{2}\left(V_{(zx)(yz),(yz)(zx)} + V_{(3z^2-r^2)(x^2-y^2),(x^2-y^2)(3z^2-r^2)}\right), \tag{124}$$

$$\Delta J = V_{(3z^2-r^2)(x^2-y^2),(x^2-y^2)(3z^2-r^2)} - V_{(zx)(yz),(yz)(zx)}. \tag{125}$$

U is the Hartree term between pairs of t_{2g} orbitals, J is the average of the e_g and t_{2g} exchange integrals, and ΔJ is the difference between the e_g and t_{2g} exchange integrals. These definitions are the same as those used by Oleś and Stollhoff [41], but our Hamiltonian, unlike theirs, is rotationally invariant in orbital space.

Rewriting Eq. (122) in terms of rotationally invariant operators gives

$$\hat{V} = \frac{1}{2}\left[\left(U - \frac{1}{2}J + 5\Delta J\right){:}\,\hat{n}^2{:} - \frac{1}{2}(J-6\Delta J){:}\,\hat{m}^2{:} + (J-6\Delta J)\sum_{\alpha\beta}{:}\,(\hat{n}_{\alpha\beta})^2{:} + \frac{2}{3}\Delta J{:}\,\hat{Q}^2{:}\right]. \tag{126}$$

where $\hat{Q}^2 = \sum_{\mu\nu}\hat{Q}_{\mu\nu}\hat{Q}_{\nu\mu}$ is the square of the on-site quadrupole operator defined and discussed in Ref. [13]. The mean-field versions of the s, p, and d Hamiltonians may also be found in that paper.

4.2.4 Comparison with the Stoner Hamiltonian

The interaction part of the Stoner Hamiltonian for shells of p and d orbitals is usually defined as

$$\hat{V}_{\text{Stoner}} = \frac{1}{2}(U - \frac{1}{2}J){:}\ \hat{n}^2{:}\ -\frac{1}{4}J{:}\ \hat{m}_z^2{:}\ . \tag{127}$$

The $\hat{m}_z^2$ term breaks rotational symmetry in spin space, so this is a collinear Stoner Hamiltonian, appropriate only in cases when the ground state breaks the rotational spin symmetry and chooses a z axis. We can, however, restore the spin-rotation invariance by replacing $\hat{m}_z^2$ by $\hat{m}^2$. This produces the vector Stoner Hamiltonian,

$$\hat{V}_{\hat{m}^2\text{Stoner}} = \frac{1}{2}(U - \frac{1}{2}J){:}\ \hat{n}^2{:}\ -\frac{1}{4}J{:}\ \hat{m}^2{:}\ , \tag{128}$$

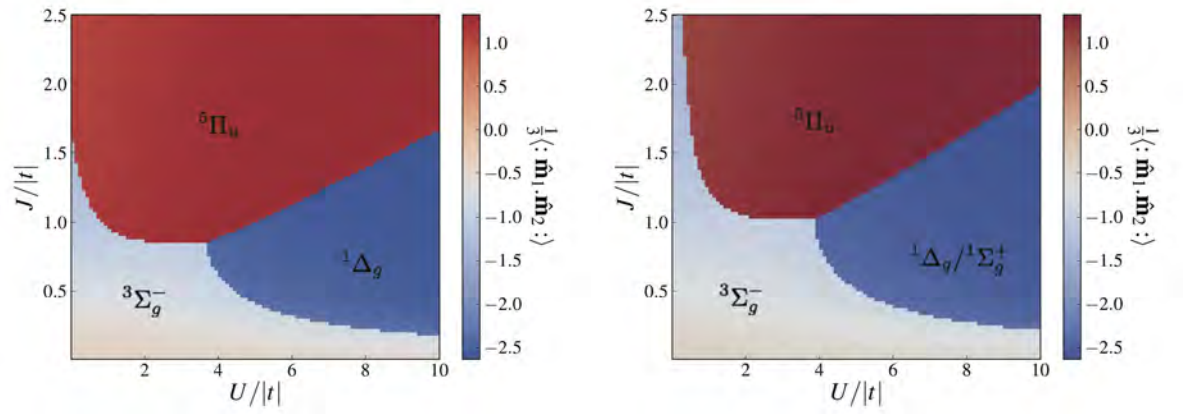

Fig. 10: *The magnetic correlation between two p-shell atoms, each with two electrons, as a function of the Hubbard parameters $U/|t|$ and $J/|t|$, where t is the $pp\sigma$ Slater-Koster parameter that describes the rate of electron hopping between atoms; the $pp\pi$ hopping parameter is $-t/2$. The regions of the graph are labelled by the symmetry of the ground state. The left-hand graph is generated using the full p-electron Hamiltonian from Sec. 4.2.2; the right-hand graph is generated using the vector Stoner Hamiltonian of Eq. (128). The Stoner phase diagram has a region with symmetry $^3\Sigma_g^-$ extending a long way up the J axis, which is not present when the full Hamiltonian is used. It also has a region with two degenerate ground states with symmetries $^1\Delta_g$ and $^1\Sigma_g^+$; this degeneracy is broken when the full p-electron Hamiltonian is used. From Ref. [13].*

which turns out to be identical to the Hamiltonian proposed by Dworin and Narath [42]. Working backwards from this Hamiltonian to the general form of the matrix element $V_{\alpha\beta,\chi\gamma}$ gives

$$V_{\alpha\beta,\chi\gamma}^{\hat{m}^2\text{Stoner}} = U\delta_{\alpha\chi}\delta_{\beta\gamma} + J\delta_{\alpha\gamma}\delta_{\beta\chi}, \tag{129}$$

which looks like the general p-shell result, Eq. (111), except that it is missing the $J\delta_{\alpha\beta}\delta_{\chi\gamma}$ term. Consequently, the vector Stoner Hamiltonian does not respect the invariance of the matrix element on interchange of α with χ or β with γ apparent from the form of Eq. (93) when the orbitals are real. As can be seen from Fig. 10, this omission affects the computed results significantly.

4.2.5 Conclusion

We have shown how to derive multi-band Hubbard-like Hamiltonians to describe shells of s, p, and d orbitals. There are important differences [13] between results obtained using the Hamiltonians derived here, which respect the symmetries of the problem, and the Stoner Hamiltonian, which does not. The vector version of the Stoner Hamiltonian misses the pair-hopping term present in our p- and d-shell Hamiltonians and the quadrupole term present in our d-shell Hamiltonian. The collinear version of the Stoner Hamiltonian breaks rotational symmetry in spin space, which makes it inappropriate for describing spin dynamics.

References

[1] J.C. Slater and G.F. Koster, Phys. Rev. **94**, 1498 (1954)

[2] V. Heine: in H. Ehrenreich, F. Seitz, and D. Turnbull (Eds.)
Solid State Physics, Vol. 35, pp. 1–127 (Academic Press, New York, 1980)

[3] R. Haydock: in H. Ehrenreich, F. Seitz, and D. Turnbull (Eds.)
Solid State Physics, Vol. 35, pp. 215–294 (Academic Press, New York, 1980)

[4] W.A. Harrison: *Electronic Structure and the Properties of Solids: The Physics of the Chemical Bond* (Dover Publications, New York, 1989)

[5] A.P. Sutton: *Electronic Structure of Materials* (Oxford University Press, 1995)

[6] C.M. Goringe, D.R. Bowler, and E. Hernández, Rep. Prog. Phys. **60**, 1447 (1997)

[7] A.P. Horsfield and A.M. Bratkovsky, J. Phys.: Condens. Matter **12**, R1 (2000)

[8] M. Finnis: *Interatomic Forces in Condensed Matter* (Oxford University Press, 2003)

[9] A.T. Paxton: In J. Grotendorst, N. Attig, S. Blügel, and D. Marx (Eds.) *Multiscale Simulation Methods in Molecular Sciences - Lecture Notes* (NIC Series, Institute for Advanced Simulation, Forschungszentrum Jülich, 2009), Vol. 42, pp. 145–176

[10] L.A. Agapito, S. Ismail-Beigi, S. Curtarolo, M. Fornari, and M.B. Nardelli, Phys. Rev. B **93**, 035104 (2016)

[11] A.P. Sutton, M.W. Finnis, D.G. Pettifor, and Y. Ohta, J. Phys. C: Solid State Phys. **21**, 35 (1988)

[12] W.M.C. Foulkes and R. Haydock, Phys. Rev. B **39**, 12520 (1989)

[13] M.E.A. Coury, S.L. Dudarev, W.M.C. Foulkes, A.P. Horsfield, P.-W. Ma, and J.S. Spencer, Phys. Rev. B **93**, 075101 (2016)

[14] O.F. Sankey and D.J. Niklewski, Phys. Rev. B **40**, 3979 (1989)

[15] D. Porezag, T. Frauenheim, T. Köhler, G. Seifert, and R. Kaschner, Phys. Rev. B **51**, 12947 (1995)

[16] A.P. Horsfield, Phys. Rev. B **56**, 6594 (1997)

[17] G.H. Wannier, Phys. Rev. **52**, 191 (1937)

[18] N. Marzari, A.A. Mostofi, J.R. Yates, I. Souza, and D. Vanderbilt, Rev. Mod. Phys. **84**, 1419 (2012)

[19] D.A. Papaconstantopoulos: *Handbook of the Band Structure of Elemental Solids: From Z=1 to Z=112* (Springer, New York, 2015), 2 ed.

[20] A.P. Sutton, T.N. Todorov, M.J. Cawkwell, and J. Hoekstra, Phil. Mag. A **81**, 1833 (2001)

[21] R. Haydock: In P.E.A. Turchi, A. Gonis, and L. Colombo (Eds.) *Tight-Binding Approach to Computational Materials Science* (Materials Research Society, Warrendale, 1998), *Materials Research Society Symposium Proceedings*, Vol. 491, pp. 35–43

[22] P. Hohenberg and W. Kohn, Phys. Rev. **136**, B864 (1964)

[23] W. Kohn and L.J. Sham, Phys. Rev. **140**, A1133 (1965)

[24] U. von Barth: in D. Langreth and H. Suhl (Eds.) *Many-Body Phenomena at Surfaces* (Academic Press, Orlando, 1984), pp. 3–49

[25] J. Harris, Phys. Rev. B **31**, 1770 (1985)

[26] H.M. Polatoglou and M. Methfessel, Phys. Rev. B **37**, 10403 (1988)

[27] A.J. Read and R.J. Needs, J. Phys.: Condens. Matter **1**, 7565 (1989)

[28] J. Hartford, L.B. Hansen, and B.I. Lundqvist, J. Phys.: Condens. Matter **8**, 7379 (1996)

[29] M.W. Finnis, J. Phys.: Condens. Matter **2**, 331 (1990)

[30] M. Elstner, D. Porezag, G. Jungnickel, J. Elsner, M. Haugk, T. Frauenheim, S. Suhai, and G. Seifert, Phys. Rev. B **58**, 7260 (1998)

[31] M.W. Finnis, A.T. Paxton, M. Methfessel, and M. van Schilfgaarde, Phys. Rev. Lett. **81**, 5149 (1998)

[32] K. Esfarjani and Y. Kawazoe, J. Phys.: Condens. Matter **10**, 8257 (1998)

[33] P.K. Schelling, N. Yu, and J.W. Halley, Phys. Rev. B **58**, 1279 (1998)

[34] M.A.L. Marques, C.A. Ullrich, F. Nogueira, A. Rubio, K. Burke, and E.K.U. Gross (Eds.): *Time-Dependent Density Functional Theory*, *Lecture Notes in Physics*, Vol. 706 (Springer, Berlin, Heidelberg, 2006)

[35] J.W. Negele and H. Orland: *Quantum Many-Particle Systems* (Perseus Books, Boulder, 1998)

[36] A.R. Edmonds: *Angular Momentum in Quantum Mechanics* (Princeton University Press, Princeton, 1996)

[37] R.C. Powell: *Physics of Solid-State Laser Materials*, Vol. 1 (Springer Science, New York, 1998)

[38] P.C. Matthews: *Vector Calculus* (Springer, London, 2000)

[39] J.A.R. Coope, R.F. Snider, and F.R. McCourt, J. Chem. Phys. **43**, 2269 (1965)

[40] E.A. Kearsley and J.T. Fong, J. Res. Nat. Bur. Stand. B **79**, 49 (1975)

[41] A.M. Oleś and G. Stollhoff, Phys. Rev. B **29**, 314 (1984)

[42] L. Dworin and A. Narath, Phys. Rev. Lett. **25**, 1287 (1970)

4 An Introduction to the Hubbard Hamiltonian

Richard T. Scalettar
Department of Physics
University of California, Davis

Contents

E. Pavarini, E. Koch, J. van den Brink, and G. Sawatzky (eds.)
Quantum Materials: Experiments and Theory
Modeling and Simulation Vol. 6
Forschungszentrum Jülich, 2016, ISBN 978-3-95806-159-0
http://www.cond-mat.de/events/correl16

1 Introduction

The Hubbard Hamiltonian (HH) offers one of the most simple ways to get insight into how the interactions between electrons give rise to insulating, magnetic, and even novel superconducting effects in a solid. It was written down [1–4] in the early 1960's and initially applied to the behavior of the transition-metal monoxides (FeO, NiO, CoO), compounds which are antiferromagnetic insulators, yet had been predicted to be metallic by methods which treat strong interactions less carefully.

Over the intervening years, the HH has been applied to many systems, from 'heavy fermions' and the Cerium volume collapse transition in the 1980's, to high temperature superconductors in the 1990's. Indeed, it is an amazing feature of the HH that, despite its simplicity, its exhibits behavior relevant to many of the most subtle and beautiful properties of solid state systems. We focus here for the most part on the single-band HH. Multi-band variants like the Periodic Anderson Model (PAM) allow one to introduce other fundamental concepts in many-body physics, such as the competition between magnetic order and singlet formation. Randomness can be simply introduced into the HH, so it can be used as a starting point for investigations of the interplay of interactions and disorder in metal-insulator transitions and, recently, many-body localization. 'Textbook' discussions of the HH can be found in Refs. [5–8] and a recent celebration of its 50th anniversary [9] emphasizes the resurgence of interest due to optical lattice emulation experiments.

The HH has been studied by the full range of analytic techniques developed by the condensed-matter community, from static mean-field approaches (which we will outline here) and the much richer dynamical mean-field theory, to diagrammatic approaches of various degrees of sophistication (the random phase approximation and parquet approach), as well as expansions in the degeneracy of the number of 'flavors' (spin, orbital angular momentum). It has also been extensively attacked with numerical methods like exact diagonalization (ED) and quantum Monte Carlo (QMC).

The objective of these notes is to provide an introduction to the HH and to a few of the most simple ways in which it is solved. Along the way we will discover that these basic calculations lend initial insight to concepts like the Mott gap, moment formation, the mapping of the HH to the Heisenberg model, and magnetism. We begin with a discussion of the second quantized operators with which the HH is written.

2 Creation and destruction operators

Creation and destruction operators $a^\dagger, a$ are familiar from the treatment of the harmonic oscillator. We briefly review their properties, which parallel those of the operators in the HH.

The harmonic oscillator creation and destruction operators are defined in terms of the position and momentum operators,

$$\hat{a} \ = \sqrt{\frac{m\omega}{2\hbar}}\ \hat{x} + i\sqrt{\frac{1}{2m\omega\hbar}}\ \hat{p} \quad \text{and} \quad \hat{a}^\dagger = \sqrt{\frac{m\omega}{2\hbar}}\ \hat{x} - i\sqrt{\frac{1}{2m\omega\hbar}}\ \hat{p}\ . \tag{1}$$

From $[\hat{p}, \hat{x}] = -i\hbar$, one shows that these operators obey the commutation relations,

$$[\hat{a}, \hat{a}^\dagger] = 1 \tag{2}$$

and that the Hamiltonian is,

$$\hat{H} = \frac{1}{2m}\,\hat{p}^2 + \frac{1}{2}m\omega^2\,\hat{x}^2 = \hbar\omega\left(\hat{a}^\dagger\hat{a} + \frac{1}{2}\right). \tag{3}$$

The 'number operator' is defined to be $\hat{n} = \hat{a}^\dagger\,\hat{a}$, so that $\hat{H} = \hbar\omega\,(\,\hat{n} + \frac{1}{2}\,)$.
The ground state of the quantum oscillator is written as $|\,0\,\rangle$ and has the properties that,

$$\hat{a}|\,0\,\rangle = 0 \quad \text{and} \quad \hat{H}|\,0\,\rangle = \frac{\hbar\omega}{2}\,|\,0\,\rangle. \tag{4}$$

The excited states are built up by applying the creation operator repeatedly to the ground state.

$$\hat{a}^\dagger|\,n\,\rangle = \sqrt{n+1}\;|\,n+1\,\rangle \tag{5}$$

and obey the formula,

$$\hat{H}|\,n\,\rangle = \hbar\omega\left(n + \frac{1}{2}\right)\;|\,n\,\rangle. \tag{6}$$

The finite temperature expectation value of any quantum mechanical operator $\hat{A}$ is determined by the Hamiltonian, $\langle\,\hat{A}\,\rangle = Z^{-1}\,\mathrm{Tr}[\,\hat{A}\,e^{-\beta\hat{H}}\,]$. It is simple to verify that $\langle\,\hat{n}\,\rangle = 1/(e^{\beta\hbar\omega} - 1)$, the Bose-Einstein distribution function. For this reason, one often refers to $\hat{a}^\dagger$ and $\hat{a}$ as 'boson' creation and destruction operators. Note that henceforth I will be setting $\hbar = 1$. I will also choose Boltzmann's constant $k_{\rm B} = 1$.
The HH is written in terms of 'fermion' creation and destruction operators. These operators differ in several respects from the operators $\hat{a}^\dagger, \hat{a}$ for a single harmonic oscillator. Perhaps most confusing is a conceptual difference: the fermion operators in the HH are not introduced in terms of familiar position and momentum operators. Rather they stand on their own. Feynman, in his Nobel Prize acceptance speech [10] alludes to this abstractness, *"I didn't have the knowledge to understand the way these were defined in the conventional papers because they were expressed at that time in terms of creation and annihilation operators, and so on, which, I had not successfully learned. I remember that when someone had started to teach me about creation and annihilation operators, that this operator creates an electron, I said, 'how do you create an electron? It disagrees with the conservation of charge', and in that way, I blocked my mind from learning a very practical scheme of calculation"* As in many cases, the passage of time has led to contemptuous familiarity, so that we forget these were once mysterious objects. In addition to the fact they are not written in terms of $\hat{x}$ and $\hat{p}$, another new feature is that in the HH there is a set of creation and destruction operators, which are distinguished by attaching a site index $\mathbf{j}$ and a spin index σ. Thus $\hat{c}^\dagger_{\mathbf{j}\sigma}$ ($\hat{c}_{\mathbf{j}\sigma}$) create (destroy) fermions of spin σ on site $\mathbf{j}$.
As a consequence, the occupation number states are no longer characterized by a single number n, as for a single harmonic oscillator, but instead by a collection of occupation numbers $n_{\mathbf{j}\sigma}$. One writes such states as $|\,n_{\mathbf{1}\uparrow}\,n_{\mathbf{2}\uparrow}\,n_{\mathbf{3}\uparrow}\,n_{\mathbf{1}\downarrow}\,n_{\mathbf{2}\downarrow}\,n_{\mathbf{3}\downarrow}\,\ldots\,\rangle$.

Because these operators are meant to describe fermions, in contrast to Eq. (2), they are defined to have certain *anticommutation* relations. (the anticommutator of two operators $\{\hat{A}, \hat{B}\} = \hat{A}\hat{B} + \hat{B}\hat{A}$)

$$\{\hat{c}_{\mathbf{j}\sigma}, \hat{c}^\dagger_{\mathbf{l}\sigma'}\} = \delta_{\mathbf{j},\mathbf{l}}\,\delta_{\sigma,\sigma'} \qquad \{\hat{c}^\dagger_{\mathbf{j}\sigma}, \hat{c}^\dagger_{\mathbf{l}\sigma'}\} = 0 \qquad \{\hat{c}_{\mathbf{j}\sigma}, \hat{c}_{\mathbf{l}\sigma'}\} = 0\,. \tag{7}$$

Like its bosonic counterpart, $c^\dagger_{j\sigma}|\,0\,\rangle = |\,1\,\rangle$ creates a fermion when acting on the vacuum. However, as a consequence of the anticommutation relations, $\hat{c}^\dagger_{\mathbf{j}\sigma}|\,1\,\rangle = \hat{c}^\dagger_{\mathbf{j}\sigma}\hat{c}^\dagger_{\mathbf{j}\sigma}|\,0\rangle = 0$. This is of course the Pauli principle. The maximum occupation of a particular site with a given spin is 1. Besides the Pauli principle, the anticommutation relations also ensure that the particles are fermions, that is, their wave function changes sign when two fermions with different labels are exchanged, $\hat{c}^\dagger_{\mathbf{j}\sigma}\,\hat{c}^\dagger_{\mathbf{l}\sigma} = -\hat{c}^\dagger_{\mathbf{l}\sigma}\,\hat{c}^\dagger_{\mathbf{j}\sigma}$.

These anticommutation relation require we specify a convention for the relation between a state like $|\,1\,0\,1\,0\,0\,\ldots\,\rangle$ and the vacuum state $|\mathrm{vac}\rangle = |\,0\,0\,0\,0\,0\,\ldots\,\rangle$. The two possibilities, $|\,1\,0\,1\,0\,0\,\ldots\rangle = \hat{c}^\dagger_{\mathbf{1}}\,\hat{c}^\dagger_{\mathbf{3}}\,|\mathrm{vac}\rangle$ and $|\,1\,0\,1\,0\,0\,\ldots\rangle = \hat{c}^\dagger_{\mathbf{3}}\,\hat{c}^\dagger_{\mathbf{1}}\,|\mathrm{vac}\rangle$ differ by a sign. Either definition is fine, but in all subsequent manipulations whatever convention was chosen must be followed consistently. We'll see some examples of the importance of this later.

3 The Hubbard Hamiltonian

Having introduced creation and annihilation operators, we can now write down the HH. Its form arises quite naturally from considering how we might simply describe the motion and interactions of electrons in a solid.

First, we need to account for the fact that there is a regular array of nuclear positions, which for simplicity we consider to be fixed. This suggests that we begin with a lattice of atoms (sites) on which the fermions move. Of course, a single *real* atom is already a very complex structure, with *many* different energy levels (orbitals). The HH simplifies the atoms in a solid to a collection of sites each with a single level (orbital). This is a good picture for a solid with just one energy band at the Fermi surface, so that, indeed, only one orbital is relevant.

With this (big!) simplification, the sites of the HH are constrained by the Pauli principle to four configurations: empty, a single up fermion, a single down fermion, or double occupation by a pair of up and down fermions. (Note that in the relatively new field of optical lattice emulation, the two fermionic types are not electrons of spin up and down, but rather fermionic atoms like ^{6}Li with two possible hyperfine states. I will, however, continue to use 'up' and 'down' to refer to the two fermionic types.)

In a solid where electrons can move around, the electrons interact via a screened Coulomb interaction. The biggest interaction will be for two electrons on the same site. The HH stops just there: interactions are modeled by a term which is zero if the site is empty of fermions or has only a single fermion, but has the value U if the site is doubly occupied (necessarily, by the Pauli principle, by fermions of opposite spin). The expression $U n_{\mathbf{j}\uparrow}\, n_{\mathbf{j}\downarrow}$ captures this property. In the simplest HH, there is no interaction $V n_{\mathbf{l}\sigma}\, n_{\mathbf{j}\sigma'}$ between fermions on different sites $\mathbf{l}$ and $\mathbf{j}$, although such terms are included in the 'extended' HH.

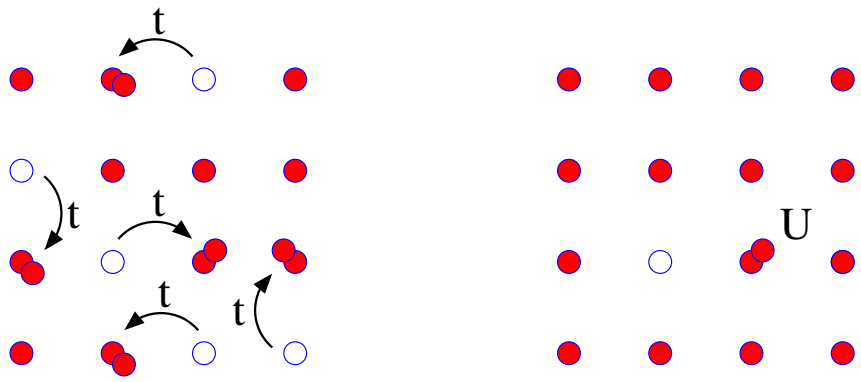

Fig. 1: *Pictorial representation of the terms in the Hubbard Hamiltonian. Left: The kinetic energy t. Right: The on-site repulsion U.*

A reasonable thought for the kinetic energy is an expression which destroys a fermion on one site and creates it on a neighbor. The energy scale t which governs this 'hopping' will be determined by the overlap of two wavefunctions on the pair of atoms. Since wavefunctions die off exponentially, it is reasonable to begin by allowing hopping only between the closest atoms in our lattice.

Formalizing this reasoning, the HH is then, dropping all the 'hats' which had been used to emphasize c , $c^\dagger$ are operators,

$$\hat{H} = -t \sum_{\langle \mathbf{j},\mathbf{l}\rangle\sigma} \left(c^\dagger_{\mathbf{j}\sigma} c_{\mathbf{l}\sigma} + c^\dagger_{\mathbf{l}\sigma} c_{\mathbf{j}\sigma} \right) + U \sum_{\mathbf{j}} n_{\mathbf{j}\uparrow} n_{\mathbf{j}\downarrow} - \mu \sum_{\mathbf{j}} (n_{\mathbf{j}\uparrow} + n_{\mathbf{j}\downarrow}) \,. \tag{8}$$

The first term is the kinetic energy: It describes the destruction of an fermion of spin σ on site $\mathbf{l}$ and its creation on site $\mathbf{j}$ (or *vice-versa*). The symbol $\langle \mathbf{j}, \mathbf{l} \rangle$ emphasizes that hopping is allowed only between two sites which are adjacent. The second term is the interaction energy. It goes through all the sites and adds an energy U if it finds the site is doubly occupied. The final term is a chemical potential which controls the filling. We refer to the situation where there is one fermion per site as 'half-filling' since the lattice contains half as many fermions as the maximum number (two per site). Studies of the HH often focus on the half-filled case because, as we shall see, it exhibits a lot of interesting phenomena (Mott insulating behavior, anti-ferromagnetic order, etc.) The HH is illustrated in Fig. 1.

Before starting to solve the HH in various limits, it is useful to discuss the idea of particle-hole symmetry.

4 Particle-hole symmetry

The Hubbard Hamiltonian has a fascinating 'particle-hole' symmetry (PHS) which allows us to relate its properties for different values of the parameters. PHS is also important because it is the basis of very useful mappings between the attractive and repulsive HH (see Sec. 10), and because it plays a crucial role in QMC simulations.

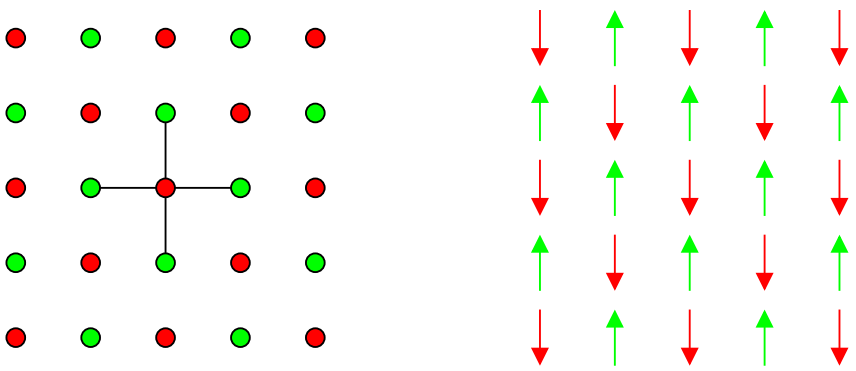

Fig. 2: *Left: The square lattice is bipartite lattice. The near-neighbors of red sites are all green and vice-versa. Right: A bipartite lattice naturally supports antiferromagnetic order in which fermions of one spin are adjacent only to those of opposite spin.*

We first introduce the notion of a bipartite lattice. This is a geometry in which the set of sites can be divided into two *sublattices* $\mathcal{A}$ and $\mathcal{B}$ such that a site in $\mathcal{A}$ has neighbors which are only members of $\mathcal{B}$ and *vice-versa*. See Fig. 2. The square and honeycomb lattices are bipartite, but the triangular lattice is not. Physically, bipartite lattices are highly conducive to antiferromagnetic order, since up and down spin fermions can occupy the two separate sublattices and each spin is always surrounded by neighbors of the opposite spin. Antiferromagnetic order on the triangular lattice is, in contrast, *frustrated*. If each site has a fermion, all conceivable ways to occupy the lattice must possess some bonds connecting sites with spins in the same direction. Bipartite lattices in which the cardinalities of the $\mathcal{A}$ and $\mathcal{B}$ sublattices are different are possible, and, indeed, Lieb has proven some profound theorems concerning ferromagnetism on such lattices. We will encounter these later.

Consider, now, the introduction into the HH of new operators which exchange the role of creation and destruction:

$$d^\dagger_{\mathbf{l}\sigma} = (-1)^{\mathbf{l}} c_{\mathbf{l}\sigma} \, . \tag{9}$$

The $(-1)^{\mathbf{l}}$ factor takes the value -1 on one sublattice and $+1$ on the other. This is aptly named a particle-hole transformation (PHT) because $d^\dagger_{\mathbf{l}\sigma} d_{\mathbf{l}\sigma} = 1 - c^\dagger_{\mathbf{l}\sigma} c_{\mathbf{l}\sigma}$. The occupations (eigenstates of the number operators) $n = 0, 1$ are interchanged.

The key observation is that the kinetic energy in the HH, on a bipartite lattice, is unchanged under a PHT. That is, it takes exactly the same form in terms of the d operators as it did in terms of the c operators:

$$c^\dagger_{\mathbf{l}\sigma} c_{\mathbf{j}\sigma} \quad \rightarrow \quad (-1)^{\mathbf{j}+\mathbf{l}} d_{\mathbf{l}\sigma} d^\dagger_{\mathbf{j}\sigma} \quad = \quad d^\dagger_{\mathbf{l}\sigma} d_{\mathbf{j}\sigma} \, . \tag{10}$$

In obtaining the last equality we used the fact that one minus sign arises from the anticommutation of the two operators, and that a second minus sign arises from the bipartite nature of the lattice, which guarantees that $(-1)^{\mathbf{l}+\mathbf{j}} = -1$.

It is useful to rewrite the HH in a way in which this PHS of the kinetic energy term is present in the interaction term. The expression $U(n_{\mathbf{j}\uparrow} - \frac{1}{2})(n_{\mathbf{j}\downarrow} - \frac{1}{2})$ is also unchanged under the particle-hole transformation. Since $U(n_{\mathbf{j}\uparrow} - \frac{1}{2})(n_{\mathbf{j}\downarrow} - \frac{1}{2}) = U n_{\mathbf{j}\uparrow} n_{\mathbf{j}\downarrow} - \frac{U}{2}(n_{\mathbf{j}\downarrow} + n_{\mathbf{j}\uparrow}) + \frac{U}{4}$, this new form

of the interaction differs from the original only by a trivial shift in the chemical potential and an overall additive constant to the energy.
The upshot is that the PHS form of the HH,

$$H = -t \sum_{\langle \mathbf{j},\mathbf{l}\rangle\sigma} \left(c^\dagger_{\mathbf{j}\sigma} c_{\mathbf{l}\sigma} + c^\dagger_{\mathbf{l}\sigma} c_{\mathbf{j}\sigma} \right) + U \sum_{\mathbf{j}} \left(n_{\mathbf{j}\uparrow} - \frac{1}{2} \right) \left(n_{\mathbf{j}\downarrow} - \frac{1}{2} \right) - \mu \sum_{\mathbf{j}} (n_{\mathbf{j}\uparrow} + n_{\mathbf{j}\downarrow}) \qquad (11)$$

is completely equivalent to the original HH.
The utility of this rewriting is fully appreciated by considering how observables transform. Under a PHT, the density ρ transforms to $1-\rho$, and the HH transforms to the HH with the sign of μ reversed. (The chemical potential term is the only piece of the re-written HH which is not PHS.) As a consequence, $\rho(\mu) = 2 - \rho(-\mu)$ and, in particular, at $\mu = 0$ we have half-filling $\rho = 1$. These statements are true for any value of t, T, or U!
In fact, PHS implies that the whole phase diagram of the HH on a bipartite lattice is symmetric about half-filling. When the square lattice HH is used to model cuprate superconductors, one often includes a next near neighbor hopping t' which connects sites across the diagonal of a square, i.e., sites on the same sublattice. This breaks PHS and the properties of the HH are *not* the same above and below half-filling ($\mu > 0$ and $\mu < 0$), correctly capturing the fact that the hole- and electron-doped cuprates have rather different properties.

5 The single-site limit

Having dealt with this important symmetry, we can get a first insight into the physics of the HH by considering just a single site. Alternately phrased, we can set $t = 0$ in the HH. In this case, $[\hat{H}, n_{\mathbf{j}\sigma}] = 0$ for each $\mathbf{j}$, so that the eigenstates of $\hat{H}$ are also eigenstates of all the *individual* number operators. The number operators also commute with each other, so basic principles of quantum and statistical mechanics tell us we can consider each term in $\hat{H}$ on its own. We thus arrive at a single site model which is very easily solved. (Since all sites are independent, we drop the site index in this limit.)
We have four possibilities corresponding to the site being empty $|\,0\,\rangle$ having a up fermion or down spin fermion $|\uparrow\rangle, |\downarrow\rangle$, or being doubly occupied. $|\uparrow\downarrow\rangle$. Each of these is an eigenstate of $\hat{H}$ with eigenvalues $U/4, -U/4-\mu, -U/4-\mu, U/4-2\mu$, respectively. The partition function,

$$Z = \mathrm{Tr}\left[e^{-\beta \hat{H}} \right] = e^{-\beta U/4} + 2\, e^{-\beta\,(-U/4-\mu)} + e^{-\beta\,(U/4-2\mu)}, \qquad (12)$$

and the occupation is given by,

$$\rho = \langle n_\uparrow + n_\downarrow \rangle = Z^{-1}\, \mathrm{Tr}\left[(n_\uparrow + n_\downarrow)\, e^{-\beta \hat{H}} \right] = Z^{-1} \left(2\, e^{-\beta(-U/4-\mu)} + 2\, e^{-\beta(U/4-2\mu)} \right) \qquad (13)$$

Clearly, $\rho = 1$ at $\mu = 0$ in this expression. But, as emphasized earlier, this is true even at $t \neq 0$. It is instructive to make a plot of ρ vs. μ. Figure 3 shows the result for $U = 4$ and decreasing temperatures $T = 2.0$, 0.5, and 0.25. For $T = 0.25$, *thermal* fluctuations are small and one observes a step-like structure in the density. ρ is small until the chemical potential exceeds

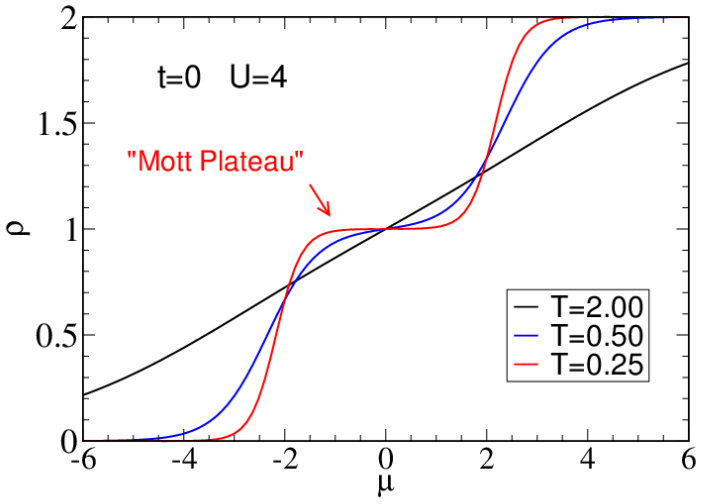

Fig. 3: *Density ρ as a function of chemical potential μ for the single site ($t = 0$) HH. As the temperature decreases, a 'Mott Plateau' develops: Increasing μ initially adds a fermion to the site, but ρ gets frozen at $\rho = 1$. The chemical potential must jump by $\Delta\mu = U$ to add a second fermion. The compressibility $\kappa = \partial\rho/\partial\mu = 0$ in the Mott gap.*

$-U/2$. At this point it rises to $\rho = 1$. However we do not fill the site with a second particle, $\rho = 2$ until μ jumps by U. This is our first encounter with one of the fundamental features of the HH, the 'Mott insulating gap'. This will be discussed in more detail later, but for now we just notice that the presence of one fermion on a site blocks the addition of a second (until a sufficiently large chemical potential overcomes the repulsion). The flat region of $\rho = 1$ extending from $\mu = -U/2$ to $\mu = U/2$ is sometimes referred to as the 'Mott plateau'. The compressibility $\kappa = \partial\rho/\partial\mu = 0$ in the Mott gap.

As seen in Fig. 3, finite temperature T washes out the sharp jumps in ρ. One of the key questions encountered in the HH is to determine the conditions under which *quantum* fluctuations induced by the hopping t destroy the Mott plateau.

A fundamental physical quantity in the HH is the 'local moment'.

$$\langle m^2 \rangle = \langle (n_\uparrow - n_\downarrow)^2 \rangle = \langle n_\uparrow + n_\downarrow \rangle - 2\langle n_\uparrow n_\downarrow \rangle = \rho - 2D \tag{14}$$

where D is the 'double occupancy'. The local moment is zero if the site is either empty ($|\,0\,\rangle$) or has two oppositely pointed spins ($|\uparrow\downarrow\rangle$), but takes the value one if the site has a single fermion ($|\uparrow\rangle$ or $|\downarrow\rangle$).

Figure 4 shows $\langle m^2 \rangle$ as a function of U for fixed $T = 2$ (left), and as a function of T for fixed $U = 4$ (right). The plot shows half-filling $\rho = 1$ ($\mu = 0$). At large U or small T the local moment $\langle m^2 \rangle \to 1$ can become perfectly formed. There is no double occupancy, and hence no empty sites either, if $\rho = 1$. As with the Mott plateau, turning on quantum fluctuations $t \neq 0$ changes the behavior of $\langle m^2 \rangle$. Perfect moments no longer form at $T = 0$ for finite U.

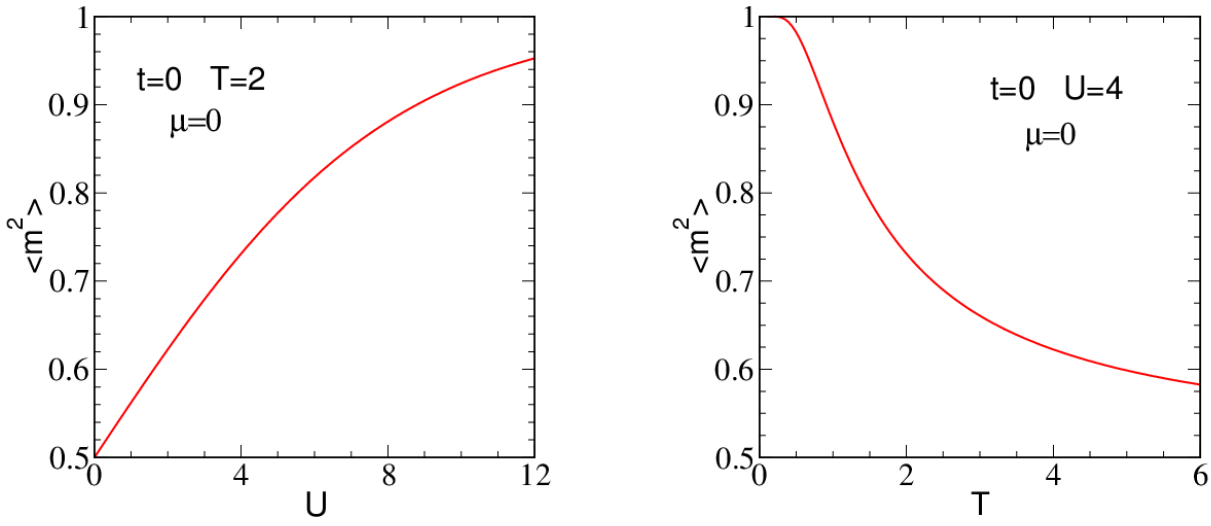

Fig. 4: *Left: The local moment $\langle m^2 \rangle$ as a function of U at fixed temperature $T = 2$. Right: The local moment $\langle m^2 \rangle$ as a function of T at fixed $U = 4$. Local moments develop as either T is reduced or U is increased. Chemical potential $\mu = 0$ in both panels, so the site is half-filled.*

6 The non-interacting Hubbard Hamiltonian

There are two alternate, but equivalent, ways of looking at the $U = 0$ HH. One involves working in real space. The other in momentum space. Let's start with the real space analysis.

We first note that the HH commutes with the operators $N_\uparrow = \sum_{\mathbf{j}} n_{\mathbf{j}\uparrow}$ and $N_\downarrow = \sum_{\mathbf{j}} n_{\mathbf{j}\downarrow}$ which count the *total* number of up and down fermions on the lattice. (There is no commutation with the *individual* number operators as we had for $t = 0$.) You can show this by considering the commutator of the kinetic energy on a single 'link' of the lattice connecting sites $\mathbf{i}$ and $\mathbf{j}$ with the total number of fermions on those two sites, and proving $[c^\dagger_{\mathbf{i}\sigma} c_{\mathbf{j}\sigma} + c^\dagger_{\mathbf{j}\sigma} c_{\mathbf{i}\sigma}, n_{\mathbf{i}\sigma} + n_{\mathbf{j}\sigma}] = 0$. A handy identity in working through the algebra relates commutators and anticommutators, $[AB, C] = A\{B, C\} - \{A, C\}B$. Actually, one can almost guess that this hopping term must conserve particle number, since it contains one creation and one annihilation operator for the relevant sites.

The implication of this commutation is that in finding the eigenstates of the HH, we can consider different sectors of total $N_\uparrow$ and $N_\downarrow$ separately. (This is true even if U is nonzero.) So let's think about the sector where $N_\uparrow = 1$ and $N_\downarrow = 0$. A basis consists of occupation number states $|1\,0\,0\,0\,0\,0\cdots\rangle$, $|0\,1\,0\,0\,0\,0\cdots\rangle$, $|0\,0\,1\,0\,0\,0\cdots\rangle$, ... There are N of these basis vectors, where N equals the number of sites in the lattice. Obviously, we only need to track the up-spin fermion location. Let's imagine for simplicity that we are in one dimension. Applying $\hat{H}$ to these states moves the occupied site to the left or right. As an explicit example for how $\hat{H}$ acts,

$$\hat{H}\,|0\,1\,0\,0\,0\,0\cdots\rangle = -\mu\,|0\,1\,0\,0\,0\,0\cdots\rangle - t\,|1\,0\,0\,0\,0\,0\cdots\rangle - t\,|0\,0\,1\,0\,0\,0\cdots\rangle\,. \qquad (15)$$

Consequentially, the matrix for $\hat{H}$ in this basis is just

$$H = \begin{pmatrix} -\mu & -t & 0 & 0 & \cdots & 0 & -t \\ -t & -\mu & -t & 0 & \cdots & 0 & 0 \\ 0 & -t & -\mu & -t & \cdots & 0 & 0 \\ 0 & 0 & -t & -\mu & \cdots & 0 & 0 \\ \vdots & \vdots & \vdots & \vdots & & \vdots & \vdots \\ -t & 0 & 0 & 0 & \cdots & -t & -\mu \end{pmatrix} . \tag{16}$$

If we impose periodic boundary conditions (pbc) then the first row of the matrix has a $-t$ in its final column, and the last row of the matrix has a $-t$ in its first column, representing a hopping between the first and last sites in the chain.

The eigenvalues of an $N \times N$ tridiagonal matrix with 'a' along the diagonal and 'b' above and below the diagonal, with pbc, are $\lambda_n = a + 2b\cos k_n$ where $k_n = 2\pi n/N$ and $n = 1, 2, 3, \ldots N$. To see this, insert the *ansatz* $v_l = e^{ikl}$ in the eigenvalue equation $a\, v_l + b\, v_{l-1} + b\, v_{l+1} = \lambda\, v_l$. The discretization of k arises from the requirement $v_0 = v_N$ and $v_{N+1} = v_1$, which must be used for the equations with $l = 1$ and $l = N$ to have the above form.

This property of tridiagonal matrices solves the noninteracting HH in the one particle sector for a one dimensional chain. The eigenvalues are $\epsilon(k) = -\mu - 2t\cos k$ and the eigenvector $\vec{v}_k$ has components $(\vec{v}_k)_l = e^{ikl}$. It is interesting to note that, mathematically, this problem is identical to the calculation of the modes of a one dimensional mass-spring system, where the analogous calculation yields the normal modes and (squares of) the normal mode frequencies.

What about the two particle sector? The basis vectors now are the $N(N-1)/2$ occupation number states, $|1\,1\,0\,0\,0\,0\cdots\rangle$, $|1\,0\,1\,0\,0\,0\cdots\rangle$, $|1\,0\,0\,1\,0\,0\cdots\rangle$, $\cdots$. One can take these states and follow the same construction as with $N_\uparrow = 1$: Act with $\hat{H}$ on each one and get the matrix for the HH in this basis. Diagonalizing yields $N(N-1)/2$ eigenvalues and eigenvectors. If you do this, you will find the eigenvalues are just composed of sums of pairs of the eigenvalues of the $N_\uparrow = 1$ matrix, with the 'Pauli Principle' restriction that you choose distinct eigenvalues! This is pretty amazing since, at first glance, the matrices appear completely unrelated to each other. For example, the rows of the matrix for $N_\uparrow = 2$ associated with states in which the occupied sites are not adjacent have four columns with $-t$, while those for states with adjacent occupation have only two columns with $-t$. The matrix looks far less symmetric than for $N_\uparrow = 1$.

Important Note: When you do the calculation you *must* keep very careful track of the signs in returning sequences of creation operators into the order you selected for your convention! Otherwise the eigenvalues for $N_\uparrow = 2$ will *not* be related to those of $N_\uparrow = 1$. See Sec. 2.

The message here is that, in the absence of the interaction term U, all the information about the eigenstates of the HH are contained by solving the single particle sector. However, when $U \neq 0$, the eigenvalues absolutely cannot be obtained in this way. (In fact, you will have to consider the up and down spin fermion occupations together.) Interactions turn the HH into a *many-body problem*.

A second, and much better, way to analyze the $U = 0$ HH is to do a canonical transformation on the creation and destruction operators. Just as in classical mechanics where a canonical

transformation preserves the Poisson brackets, here we seek to preserve the fermion operator anticommutation relations. (The PHT of Sec. 4 has this property.) We define

$$c^\dagger_{\mathbf{k}\sigma} = \frac{1}{\sqrt{N}} \sum_{\mathbf{l}} e^{i\mathbf{k}\cdot\mathbf{l}}\, c^\dagger_{\mathbf{l}\sigma}\,. \tag{17}$$

As already noted above, the momentum $\mathbf{k}$ has discretized values so that there is the same number of momentum creation operators as creation operators in real space.
The following 'orthogonality' identities are very useful

$$\frac{1}{N}\sum_l e^{i(k_n-k_m)l} = \delta_{n,m} \quad \text{and} \quad \frac{1}{N}\sum_n e^{ik_n(l-j)} = \delta_{l,j}\,. \tag{18}$$

They allow you to invert Eq. (17) and prove

$$c^\dagger_{\mathbf{l}\sigma} = \frac{1}{\sqrt{N}} \sum_{\mathbf{k}} e^{-i\mathbf{k}\cdot\mathbf{l}}\, c^\dagger_{\mathbf{k}\sigma}. \tag{19}$$

and also to verify that the anticommutation relations

$$\{c_{\mathbf{k}\sigma}, c^\dagger_{\mathbf{p}\sigma'}\} = \delta_{\mathbf{k},\mathbf{p}}\delta_{\sigma,\sigma'} \qquad \{c^\dagger_{\mathbf{k}\sigma}, c^\dagger_{\mathbf{p}\sigma'}\} = 0 \qquad \{c_{\mathbf{k}\sigma}, c_{\mathbf{p}\sigma'}\} = 0 \tag{20}$$

are indeed preserved by this canonical transformation. The total number operator takes the same form in either basis $\hat{N} = \sum_{\mathbf{j}}(n_{\mathbf{j}\uparrow} + n_{\mathbf{j}\downarrow}) = \sum_{\mathbf{k}}(n_{\mathbf{k}\uparrow} + n_{\mathbf{k}\downarrow})$.
We can also write down the $U = 0$ HH in terms of these momentum space operators.

$$H = \sum_{\mathbf{k}\sigma}(\epsilon_{\mathbf{k}} - \mu)\, c^\dagger_{\mathbf{k}\sigma} c_{\mathbf{k}\sigma} = \sum_{\mathbf{k}\sigma}(\epsilon_{\mathbf{k}} - \mu)\, n_{\mathbf{k}\sigma} \quad \text{with} \quad \epsilon_{\mathbf{k}} = \sum_l e^{i\vec{k}\cdot\vec{a}_l}\,. \tag{21}$$

Here $\vec{a}_l$ are the real space vectors pointing to the nearest neighbors of a given site. (We are assuming t connects only those nearest neighbors.) In one dimension, $\vec{a}_l = \pm\hat{x}$ so that $\epsilon_k = -2t\cos k$, as we have previously observed working in real space. (I have set the lattice constant equal to one.)
This Hamiltonian looks like the one arising in the quantum oscillator in Sec. 2 in the sense that it is expressed in terms of a sum of independent number operators which are all mutually commuting. It is now even more evident that the list of single-particle levels $\epsilon_{\mathbf{k}}$ tells us everything about all the particle sectors: At $U = 0$, even if one has many particles, they just occupy the one particle states in accordance with the Pauli principle.
It is important to realize that the result that an analysis of the one-particle sector gives us full information about the model for any particle number rests only on the fact that the interactions are turned off. It is not necessary that the hopping t between different sites be the same for all pairs of sites, or that it be limited to near neighbors, or that the chemical potential be the same on all sites. All that matters is that $\hat{H}$ be a quadratic form in the fermion creation and destruction operators. To emphasize: To solve any Hamiltonian $\hat{H}$ which takes the form $H = \sum_{\mathbf{l},\mathbf{j}} c^\dagger_{\mathbf{l}}\, h_{\mathbf{l},\mathbf{j}}\, c_{\mathbf{j}}$ with h a (symmetric) matrix of real numbers, simply diagonalize h and allow the resulting energy levels to be filled in a way which satisfies the exclusion principle.

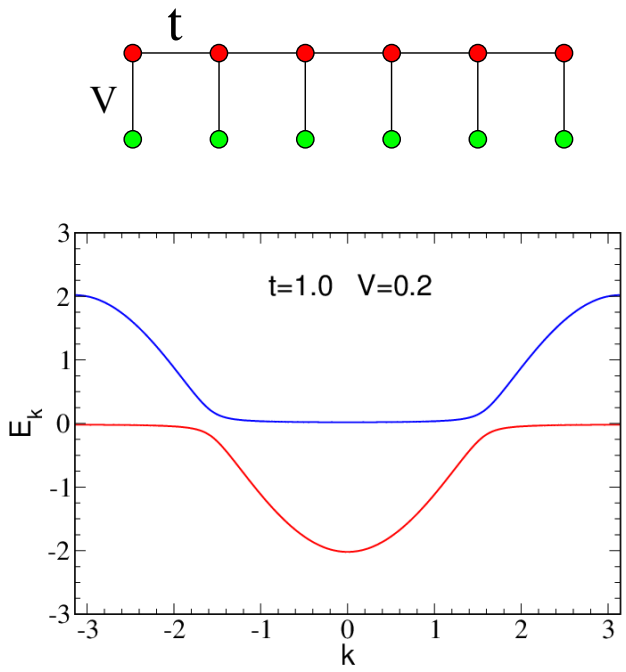

Fig. 5: *Top: The geometry of the PAM in one dimension. Bottom: The dispersion relation.*

We will consider two further examples of computing dispersion relations which illustrate how to handle lattices with a basis ('multiband HH') and also show often encountered geometries. The first adds a 'staggered potential' $\Delta \sum_{\rm l} (-1)^{\rm l} \, n_{\rm l}$ to the HH on a bipartite lattice. Considering, again, a one dimensional chain for simplicity, we write $(-1)^l = e^{il\pi}$. Going to momentum space one encounters,

$$\Delta \sum_l (-1)^l \, c_l^\dagger c_l = \Delta \frac{1}{N} \sum_l e^{i\pi l} \sum_k e^{-ikl} \, c_k^\dagger \sum_p e^{+ipl} \, c_p = \Delta \sum_k c_k^\dagger c_{k+\pi} \tag{22}$$

Going to momentum space has not fully diagonalized the Hamiltonian: the wavevectors k and $k+\pi$ mix. Using the forms already written down for the hopping terms in the HH,

$$H = \sum_k \begin{pmatrix} c_k^\dagger & c_{k+\pi}^\dagger \end{pmatrix} \begin{pmatrix} -2t\cos k & \Delta \\ \Delta & -2t\cos(k+\pi) \end{pmatrix} \begin{pmatrix} c_k \\ c_{k+\pi} \end{pmatrix} \tag{23}$$

where the k sum is over the reduced Brillouin zone $-\pi/2 < k < \pi/2$.

One must still do a final diagonalization of the 2×2 matrices in Eq. (23), which yields the two bands $E_k = \pm\sqrt{(-2t\cos k)^2 + \Delta^2}$. The staggered potential has opened up a band gap at the reduced Brillouin zone boundaries $k = \pm\pi/2$. Understanding the energy bands in a staggered potential is important to doing mean-field theory for the HH. See Sec. 9.

A second example is that of the Periodic Anderson Model (PAM). The PAM is a multi-orbital variant of the HH in which there is a 'conduction' band with creation operators $c_{\rm l}^\dagger$ and a 'localized' band with creation operators $d_{\rm l}^\dagger$. There is no Hubbard U for the conduction band, while

the fermions in the localized band hop only to the conduction band. The Hamiltonian is

$$H = -t \sum_{\langle \mathbf{j},\mathbf{l}\rangle\sigma} \left(c^\dagger_{\mathbf{j}\sigma} c_{\mathbf{l}\sigma} + c^\dagger_{\mathbf{l}\sigma} c_{\mathbf{j}\sigma} \right) + V \sum_{\langle \mathbf{j},\mathbf{l}\rangle\sigma} \left(c^\dagger_{\mathbf{j}\sigma} d_{\mathbf{l}\sigma} + d^\dagger_{\mathbf{l}\sigma} c_{\mathbf{j}\sigma} \right)$$
$$+ U \sum_{\mathbf{j}} \left(n_{d\mathbf{j}\uparrow} - \frac{1}{2} \right) \left(n_{d\mathbf{j}\downarrow} - \frac{1}{2} \right) - \mu \sum_{\mathbf{j}} (n_{c\mathbf{j}\uparrow} + n_{c\mathbf{j}\downarrow} + n_{d\mathbf{j}\uparrow} + n_{d\mathbf{j}\downarrow}) \,. \qquad (24)$$

This geometry is illustrated in one dimension in Fig. 5(top).

Going to momentum space for the non-interacting PAM at $\mu = 0$ yields 2×2 matrices similar in structure to the staggered potential example. We again simplify to one dimension,

$$H = \sum_k \begin{pmatrix} c^\dagger_k & d^\dagger_k \end{pmatrix} \begin{pmatrix} -2t\cos k & V \\ V & 0 \end{pmatrix} \begin{pmatrix} c_k \\ d_k \end{pmatrix} . \qquad (25)$$

A final diagonalization is required to yield the band structure $E_k = \frac{1}{2}\left(\epsilon_k \pm \sqrt{\epsilon_k^2 + 4V^2}\right)$. These two bands exhibit a 'hybridization gap'. Where the dispersionless d-band crosses the c-band at $k = \pm\pi/2$ the hybridization V repels the two curves.

Having computed the dispersion relation $\epsilon_{\mathbf{k}}$, it is valuable to obtain the density of states (DOS)

$$N(E) = \frac{1}{N} \sum_{\mathbf{k}} \delta(E - \epsilon_{\mathbf{k}}) \,. \qquad (26)$$

As its formula makes apparent, the DOS counts the number of energy levels having a particular value E. In the continuum limit (large number of sites), the sum over discrete momenta is replaced by an integral according to the rule $\frac{1}{N}\sum_{\mathbf{k}} \to (2\pi)^{-d} \int d\mathbf{k}$, where d is the spatial dimension. For the one-dimensional HH with $\epsilon_k = -2t\cos k$, $N(E) = 1/(\pi\sqrt{4t^2 - E^2})$. We will use this result in Sec. 9. This DOS diverges at $E = \pm 2t$ where the bands are flat, as we are told should be the case by Ashcroft and Mermin.

A particularly important example of the dispersion relation of the $U = 0$ HH is that of the square lattice, where $\epsilon_{\mathbf{k}} = -2t\,(\cos k_x + \cos k_y)$ according to Eq. (21). One of the reasons this is an interesting geometry is that it forms the simplest picture of the cuprate superconductors: the copper atoms of the CuO_2 sheets reside on a square lattice. Early theories of superconductivity in the cuprates relied on the special van-Hove singularity of the DOS of the square lattice. See Fig. 6(left). One can see the basic idea of the possible role of this divergence from the BCS formula for the superconducting transition temperature $T_c \sim \omega\, e^{-1/VN(E_F)}$. Here V is some coupling constant and ω is an energy scale (a phonon frequency in conventional superconductivity). A large value of the DOS, $N(E_F)$, reduces the size of the negative number in the exponential, boosting T_c. When we discuss Stoner theory we will see another example of how an understanding of the DOS is useful.

Amazingly, the full picture of pairing in the cuprates remains a mystery. The HH is unsolved on the 2D square lattice, and, in particular, whether the ground state away from half-filling has long range d-wave pairing correlations is still open.

As in an electronic structure calculation, the Fermi Surface (FS) of the HH is constructed from the dispersion relation $\epsilon_{\mathbf{k}}$ as the locus of momentum space points that separates filled and empty

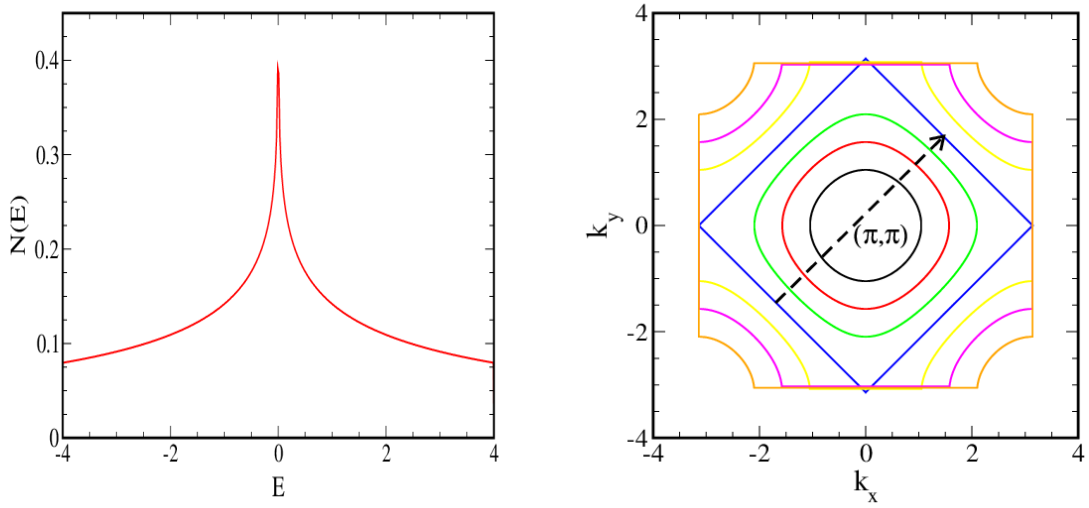

Fig. 6: *Left: The density of states of the square lattice HH. It has a singularity at $\mu = 0$ (half-filling). Right: The Fermi Surface of the square lattice HH for different values of the filling. It evolves from circles about the Γ point at low filling to a rotated square at half-filling $\rho = 1$.*

states at $T = 0$ in the absence of interactions. The FS of the square lattice HH is shown for various values of μ in Fig. 6(right). Like the DOS, the FS of the square lattice has a unique feature at half-filling: perfect nesting. What this means is that the same wave vector $\mathbf{k} = (\pi, \pi)$ maps large segments of the FS onto itself. Since the properties of a fermionic system are dominated by the FS, this suggests that this momentum vector might play a crucial role in the physics of the square lattice. Sure enough, antiferromagnetic order, a large magnetic structure factor at $\mathbf{k} = (\pi, \pi)$, is a feature of the HH at $\rho = 1$ all the way down to $U = 0$.

With $\epsilon_{\mathbf{k}}$ in hand, one can compute all the standard statistical mechanics properties: The partition function, density, internal energy, free energy, and entropy of the $U = 0$ HH are

$$
\begin{aligned}
Z &= \mathrm{Tr}\left[e^{-\beta \hat{H}} \right] = \prod_{\mathbf{k}} \sum_{n_{\mathbf{k}}=0,1} e^{-\beta(n_{\mathbf{k}}-\mu)} = \prod_{\mathbf{k}} \left(1 + e^{-\beta(\epsilon_{\mathbf{k}}-\mu)}\right) \\
\rho &= Z^{-1}\, \mathrm{Tr}\left[\sum_{\mathbf{k}} n_{\mathbf{k}} e^{-\beta \hat{H}} \right] = \sum_{\mathbf{k}} \left(1 + e^{+\beta(\epsilon_{\mathbf{k}}-\mu)}\right)^{-1} = \sum_{\mathbf{k}} f_{\mathbf{k}} \\
E &= Z^{-1}\, \mathrm{Tr}\left[\hat{H}\, e^{-\beta \hat{H}} \right] = \sum_{\mathbf{k}} \epsilon_{\mathbf{k}} \left(1 + e^{+\beta(\epsilon_{\mathbf{k}}-\mu)}\right)^{-1} = \sum_{\mathbf{k}} \epsilon_{\mathbf{k}} f_{\mathbf{k}} \\
S &= \beta\,(E - F) = \beta\, E - \ln Z\ .
\end{aligned}
\tag{27}
$$

Here we introduced the usual definition of the Fermi function $f_{\mathbf{k}}$.

There are several other lattice structures on which the HH is commonly studied and hence whose dispersion relations and DOS are worth knowing. The DOS of the triangular and honeycomb lattices are shown in Fig. 7. The honeycomb lattice is notable for its linearly vanishing DOS at half-filling. Comparison of the DOS of the triangular lattice with that of the square and honeycomb lattices emphasizes the fact that $N(E) = N(-E)$ for bipartite lattices, but not for non-bipartite ones.

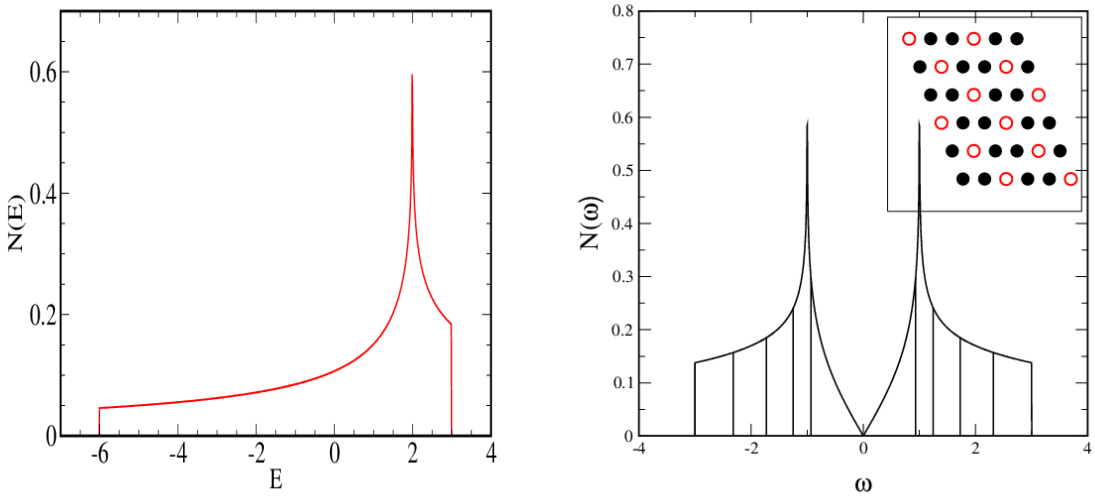

Fig. 7: *Left: The DOS of the $U = 0$ triangular lattice HH. This non-bipartite lattice does not have the property $N(E) = N(-E)$ of the square and honeycomb lattices. Right: The DOS of the $U = 0$ honeycomb lattice HH. Vertical lines demark the chemical potentials of fillings $\rho = 0.1, 0.2, 0.3, \cdots$. Filling $\rho = 0.5$ is at $E = 0$. Inset emphasizes the honeycomb lattice can be viewed as a depleted triangular lattice.*

Our final example is the 'Lieb lattice'. This geometry consists of a square array of sites to which are added additional sites at the midpoint of each bond. See Fig. 8. This structure is of fundamental importance to the cuprate superconductors since it provides a more refined picture of the CuO_2 planes which includes the bridging oxygen sites in addition to the square lattice copper ones. In that application, the parent compounds like La_2CuO_4 have one fermion per CuO_2 unit cell, and there is an additional site energy on the oxygens such that the fermion resides mostly on the coppers.

In the absence of such a site energy, however, something amazing happens. Despite the fact that all the sites are connected and so, seemingly, a fermion placed locally on the lattice would inevitable spread out to occupy the whole structure, instead there are perfectly localized states in real space! Consider Fig. 8 and the state $|\,\psi\,\rangle = (\,c_1^\dagger - c_2^\dagger + c_3^\dagger - c_4^\dagger\,)\,|\,0\,0\,0\,0\,\cdots 0\,\rangle$. When the $U = \mu = 0$ HH for the Lieb lattice acts on $|\,\psi\,\rangle$ one obtains $\hat{H}|\,\psi\,\rangle = 0$! That is, $|\,\psi\,\rangle$ is an eigenstate of $\hat{H}$ of eigenvalue zero. A fermion created onto this cluster of four sites will remain localized there forever. This is quite a surprise since $\hat{H}$ is translationally invariant and we expect the eigenstates to be spread out.

One can reconcile this expectation by noting that this same construction can be done on any equivalent set of four sites on the lattice, so there is a huge set of states all with the same energy $E = 0$. One can form linear combinations of such states which are extended as in Eq. (17). The resulting momentum space states have an energy bands which is completely dispersionless: $\epsilon_{\mathbf{k}} = 0$ independent of $\mathbf{k}$.

This same result can of course be obtained from the procedure we have outlined earlier. Going

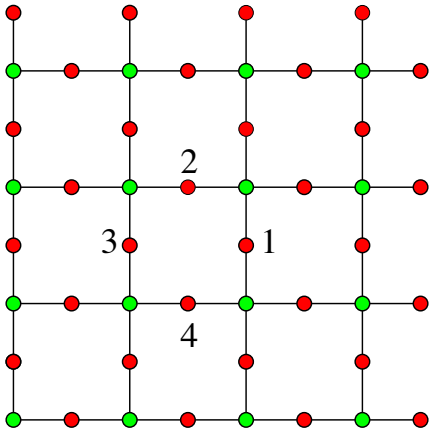

Fig. 8: *The geometry of the 'Lieb lattice'. Creation of a fermion with the appropriate phases on the four labeled sites results in a localized mode. See text.*

to momentum space results in a 3×3 matrix

$$\begin{pmatrix} 0 & -t\,(1+e^{ik_x}) & -t\,(1+e^{ik_y}) \\ -t\,(1+e^{-ik_x}) & 0 & 0 \\ -t\,(1+e^{-ik_y}) & 0 & 0 \end{pmatrix} \tag{28}$$

one of whose energy bands is $E_{\mathbf{k}} = 0$.
Lieb has shown [11] that the presence of such flat bands is a generic feature of bipartite lattices for which the numbers of $\mathcal{A}$ and $\mathcal{B}$ sites are *unequal*. More importantly, ferrimagnetic order can be rigorously proven to occur in the ground state. This is one of the few things known exactly about the HH. We briefly discuss some further interesting interaction-driven physics of the Lieb lattice in Sec. 11.

7 Introduction to exact diagonalization: the two-site HH

The single site HH gave us some insight into the role of U in such phenomena as moment formation and the development of the Mott plateau, but the absence of t precluded any consideration of the interplay between kinetic and potential energy, and the formation of intersite magnetic correlations. These can, however, be captured by examining the HH on two spatial sites. This is the simplest non-trivial example of a powerful method to solve model Hamiltonians: exact diagonalization (ED).
We begin by using the occupation number basis $|\, n_{1\uparrow}\, n_{1\downarrow}\, n_{2\uparrow}\, n_{2\downarrow}\,\rangle$ to enumerate the states in the Hilbert space. The commutation relations $[\hat{H}, n_{1\uparrow} + n_{2\uparrow}] = [\hat{H}, n_{1\downarrow} + n_{2\downarrow}] = 0$ reflect the conservation of the number of up and down fermions, and divide the $2^4 = 16$ states into nine sectors, $(n_{1\uparrow} + n_{2\uparrow}, n_{1\downarrow} + n_{2\downarrow}) = (0,0), (1,0), (2,0), (0,1), (1,1), (2,1), (0,2), (1,2), (2,2)$ of dimensions $1, 2, 1, 2, 4, 2, 1, 2, 1$, respectively. The sectors of dimension 1 immediately identify four eigenstates of the HH on two sites: The completely empty lattice, the lattice completely packed with four fermions, and the states with two like-spin fermions. All these have zero kinetic energy because there are either no fermions present to hop, or else there are two of the

same species and the Pauli principle blocks hopping. The $(2,0)$ and $(0,2)$ energies are $-U/2$ and the $(0,0)$ and $(2,2)$ energies are $+U/2$.

The four sectors of dimension two are almost equally simple. They each have eigenenergies $\pm t$. In the case when there is a single fermion, it can hop between sites. With three fermions, the two which are of like spin are frozen by the Pauli principle and again one has a single fermion which can hop. The fact that the one and three particle sectors have the same spectrum is a reflection of our use of the PHS version of the HH.

The $(1,1)$ sector has dimension four and is the only slightly complicated one. We are rewarded for enduring its diagonalization by some interesting physics. If we denote by $\#$ a site which is doubly occupied, and by 0 a site that is empty, then the action of $\hat{H}$ on the four states $|\uparrow\ \downarrow\rangle, |\downarrow\ \uparrow\rangle, |\#\ 0\rangle, |0\ \#\rangle$, is given by the 4×4 matrix

$$\begin{pmatrix} -U/2 & 0 & -t & -t \\ 0 & -U/2 & -t & -t \\ -t & -t & U/2 & 0 \\ -t & -t & 0 & U/2 \end{pmatrix} . \tag{29}$$

The eigenvalues of this matrix are $-U/2$, $U/2$, $\pm\sqrt{4t^2+U^2/4}$.

We have now discovered the complete spectrum of the two-site Hubbard Hamiltonian. We emphasize again that, in contrast to the noninteracting case $U=0$, we cannot infer all the eigenenergies from consideration of the single particle sector.

The low temperature properties of the two-site HH are determined by the lowest energy eigenstates. These are four of the six states in the half-filled sectors $(2,0),(0,2)$ and $(1,1)$ with energies $-U/2$ (threefold degenerate), $U/2$, and $\pm\sqrt{4t^2+U^2/4}$. If we think about $U \gg t$ we can rewrite $\pm\sqrt{4t^2+U^2/4} = \pm(U/2)\sqrt{1+16t^2/U^2} \approx \pm U/2\,(1+8t^2/U^2) = -U/2 - 4t^2/U,\ \ +U/2+4t^2/U$.

We have four states with energies roughly $-U/2$ and two with energy roughly $+U/2$. In the thermodynamic limit, these two groupings of states, separated by energy U, are referred to as the 'upper and lower Hubbard bands' (UHB, LHB).

Besides illustrating the UHB and LHB, a particularly nice outcome of this two-site ED analysis is that it also provides a clear illustration of the mapping of the HH to the spin-1/2 Heisenberg model in the large-U limit. It is natural to imagine some such relation between the models because at large U the HH favors single occupation of each site with either an up or a down spin fermion, paralleling the situation of the spin-1/2 Heisenberg model on which each site can have $S_z = \pm 1/2$.

Our solution of the two-site HH allows us to make this mapping more quantitative. Consider two spin-1/2 objects with a Hamiltonian $\hat{H} = J\,\vec{S}_1\cdot\vec{S}_2$. The spectrum is obtained by a trick: $J\vec{S}_1\cdot\vec{S}_2 = J/2\left((\vec{S}_1+\vec{S}_2)^2 - \vec{S}_1^2 - \vec{S}_2^2\right)$. We know $\vec{S}_1^2 = \vec{S}_2^2 = 3/4$ and that, by the rules of adding angular momentum two spin-1/2 combine to spin-0 (non-degenerate 'singlet') or spin-1 (three-fold degenerate 'triplet'). The square of the total spin therefore takes the two values $(\vec{S}_1+\vec{S}_2)^2 = 0, 2$.

This observation allows us to solve the two-site Heisenberg model: $J\vec{S}_1 \cdot \vec{S}_2 = J\,(0 - 3/4 - 3/4) = -3J/4$ or $J\vec{S}_1 \cdot \vec{S}_2 = J\,(2 - 3/4 - 3/4) = +J/4$: The spectrum of the two-site Heisenberg model consists of one state of energy $-3J/4$ and three states of energy $+J/4$.
In the large-U limit, the LHB of the two-site HH has precisely the same structure: a single state of energy $-U/2 - 4t^2/U$ beneath a triplet of states of energy $-U/2$. This makes more precise the qualitative picture discussed above: the eigenspectra are rigorously identical. It also identifies the exchange energy scale $J = 4t^2/U$.
It should be clear that, with the aid of a computer, the ED method can be easily extended to larger numbers of sites [12, 13]. Three functions are at the core of an ED code: The first assigns a basis state number α to each collection of occupation numbers. The second inverts this process, yielding the occupations associated with any basis state number. Finally, a function computes the action of $\hat{H}$ on each basis state $|\alpha\rangle$, using the first function to get the occupations, rearranging the occupations based on the kinetic energy operator, and using the second function to get from these rearranged occupations the states $|\beta\rangle$. For each of these β one sets $H_{\alpha\beta} = \pm t$, where the sign is determined by considering how many interchanges are required to get the operators into their conventional order (as discussed in Sec. 2). The action of the potential energy is easily computed since it does not alter the occupations. Its value is assigned to $H_{\alpha\alpha}$.
More detailed descriptions of the ED method are available in [12,13]. The basic principle really is no more complex than that described above, but as with most simple methods, many clever ideas are involved in pushing them to their limits, such as the use of symmetries to partition $\hat{H}$ into the smallest possible blocks, and, especially, to extract experimentally useful quantities. ED really comes into its own in the computation of dynamical properties, which are very difficult to obtain with competing methods like QMC. For this reason it has been extremely valuable in recent work on thermalization and many-body localization.

8 Green functions: Mott gap and spectral function

As mentioned in the introduction, much of the initial work on the HH involved the use of perturbative, diagrammatic techniques whose central quantities are Green functions G. These approaches, and the important role of G, closely connect with more recently developed QMC methods. For that reason, we will now examine the one-particle Green function in the noninteracting $(U = 0)$ and single site $(t = 0)$ limits. The discussion will also reinforce some of our earlier observations. Much of our discussion will work in real space, since several QMC techniques are formulated there, and our results provide useful context for those methods [14].

8.1 Green functions at $U = 0$

We begin with the definition

$$G_{\mathbf{jn}}(\tau) = \left\langle c_{\mathbf{j}}(\tau) c^{\dagger}_{\mathbf{n}}(0) \right\rangle \quad \text{with} \quad c_{\mathbf{j}}(\tau) = e^{\hat{H}\tau} c_{\mathbf{j}}(0) e^{-\hat{H}\tau}\,. \tag{30}$$

In the limit of no interactions, $G_{\mathbf{jn}}(\tau)$ can be computed analytically. We first note that the imaginary time evolution in momentum space is

$$c_{\mathbf{k}}(\tau) = e^{\hat{H}\tau} c_{\mathbf{k}}(0) e^{-\hat{H}\tau} = e^{-\epsilon_{\mathbf{k}}\tau} c_{\mathbf{k}}(0) \tag{31}$$

This can be verified either by showing that both expressions give the same result on the two states $|\,0\,\rangle$ and $|\,1\,\rangle$, or by using the general theorem that $\partial\hat{A}(\tau)/\partial\tau = [\hat{H}, \hat{A}(\tau)]$.
Transforming the operators in G to momentum space, and using $\langle c_{\mathbf{k}} c_{\mathbf{k}}^\dagger \rangle = 1 - f_{\mathbf{k}}$ we see

$$G_{\mathbf{jn}}(\tau) = \frac{1}{N} \sum_{\mathbf{k}} e^{i\mathbf{k}\cdot(\mathbf{n}-\mathbf{j})} (1 - f_{\mathbf{k}}) e^{-\epsilon_{\mathbf{k}}\tau}. \tag{32}$$

Notice that G is just a function of the difference $\mathbf{n} - \mathbf{j}$, as you would expect for a translationally invariant Hamiltonian.
We have been a little bit careless in defining G. Usually in many-body theory one defines the so-called 'time ordered' Green's function, $G_{\mathbf{k}}(\tau) = -\langle \mathcal{T} c_{\mathbf{k}}(\tau) c_{\mathbf{k}}^\dagger(0) \rangle$ where the time ordering operator T is given by

$$\begin{aligned} \mathcal{T} c_{\mathbf{k}}(\tau) c_{\mathbf{k}}^\dagger(0) &= \quad c_{\mathbf{k}}(\tau) c_{\mathbf{k}}^\dagger(0) \quad \text{for } \tau > 0 \\ \mathcal{T} c_{\mathbf{k}}(\tau) c_{\mathbf{k}}^\dagger(0) &= -c_{\mathbf{k}}^\dagger(0) c_{\mathbf{k}}(\tau) \quad \text{for } \tau < 0\,. \end{aligned} \tag{33}$$

This more precise definition of G leads to the property that $G(\tau+\beta) = -G(\tau)$ for $-\beta < \tau < 0$. Hence the Fourier transform of G

$$G(\tau) = \sum_n G(i\,\omega_n) e^{-i\omega_n\tau} \qquad\qquad G(i\,\omega_n) = \int_0^\beta \frac{d\tau}{\beta} G(\tau) e^{i\,\omega_n\tau} \tag{34}$$

involves the 'Matsubara frequencies' $\omega_n = \pi(2n+1)/\beta$. In momentum space and imaginary time the Green function is given by

$$\begin{aligned} G_{\mathbf{k}}(\tau) &= -e^{-\epsilon_{\mathbf{k}}\tau}(1 - f_{\mathbf{k}}) \quad \text{for} \quad 0 < \tau < \beta \\ G_{\mathbf{k}}(\tau) &= \quad e^{-\epsilon_{\mathbf{k}}\tau} f_{\mathbf{k}} \qquad\quad \text{for} \; -\beta < \tau < 0 \end{aligned} \tag{35}$$

and in momentum space and frequency

$$G_{\mathbf{k}}(i\,\omega_n) = \frac{1}{i\,\omega_n - \epsilon_{\mathbf{k}}}\,. \tag{36}$$

Another way to get this last result is to take $\partial/\partial\tau$ of the definition of the time-ordered Green function written in the form

$$G_{\mathbf{k}}(\tau) = \langle c_{\mathbf{k}}(\tau) c_{\mathbf{k}}(0) \rangle\, \theta(\tau) - \langle c_{\mathbf{k}}(0) c_{\mathbf{k}}(\tau) \rangle\, \theta(-\tau)\,. \tag{37}$$

and then Fourier transform both sides to solve for $G_{\mathbf{k}}(i\,\omega_n)$. This approach is the basis of the 'equation of motion' method for computing G. One starts with the definition of G, takes a time derivative, evaluates the resulting commutators of $\hat{H}$ with the creation operators, and then Fourier transforms. If the Hamiltonian is quadratic in the fermion operators, then the set of equations so obtained closes, even if the different fermion operators mix. Of course, we already knew quadratic Hamiltonians are soluble!

8.2 Green functions at $t = 0$

It is instructive to look at the Green function for a single site, that is, the $t = 0$ HH. We have previously written down the Hilbert space for this problem and obtained the partition function and various equal time quantities. Now consider the calculation of

$$G_\uparrow(\tau) = \langle c_\uparrow(\tau) c_\uparrow^\dagger(0) \rangle. \tag{38}$$

Only the states $|\,0\,0\,\rangle$ and $|\,0\,1\,\rangle$ contribute to the expectation value since the creation operator for up fermions needs to see an empty up state. We compute the action of the sequence of operators on $|\,0\,0\,\rangle$:

$$\begin{aligned} c_\uparrow(\tau) c_\uparrow^\dagger(0)\ |\,0\,0\,\rangle &= e^{H\tau} c_\uparrow(0) e^{-H\tau} c_\uparrow^\dagger(0)\ |\,0\,0\,\rangle = e^{H\tau} c_\uparrow(0) e^{-H\tau}\ |\,1\,0\,\rangle \\ &= e^{H\tau} c_\uparrow(0) e^{+U\tau/4}\ |\,1\,0\,\rangle = e^{H\tau} e^{+U\tau/4}\ |\,0\,0\,\rangle = e^{+U\tau/2}\ |\,0\,0\,\rangle \end{aligned} \tag{39}$$

and similarly for $|\,0\,1\,\rangle$.
Completing the calculation yields

$$G_\uparrow(\tau) = \frac{e^{+\beta U/4} e^{-\tau U/2} + e^{-\beta U/4} e^{\tau U/2}}{2\, e^{\beta U/4} + 2\, e^{-\beta U/4}}. \tag{40}$$

The Green's function is related to the 'spectral density' $A(\omega)$ by

$$G(\tau) = \int_{-\infty}^{+\infty} A(\omega)\, \frac{e^{-\omega\tau}}{e^{-\beta\omega} + 1}\, d\omega\,. \tag{41}$$

One can show that when

$$A(\omega) = \frac{1}{2}\, \big(\, \delta(\omega - U/2) + \delta(\omega + U/2) \,\big) \tag{42}$$

is inserted into Eq. (41), the result of Eq. (40) follows. The spectral function of the one-site HH consists of two delta-function peaks separated by U, a result closely connected to our earlier discussion of the Mott gap. Just as the Mott gap is softened (and perhaps even eliminated) by the introduction of t, the computation of $A(\omega)$ for the full HH is one of the central pursuits of the field.

9 A peek at magnetism

In this section we will discuss three common pictures of magnetism in the HH in order of increasing level of mathematical detail: a perturbation picture of the relative favorability of neighboring fermions being of the same or opposite spin; the Stoner criterion for ferromagnetism; and static mean-field theory (MFT). In the latter case we will only outline the calculation to be done, pointing to the connections with our discussion of the $U = 0$ HH.

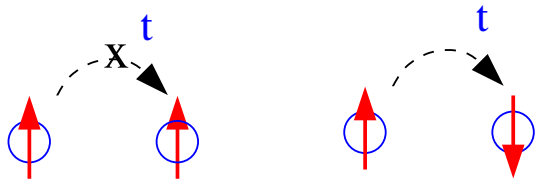

Fig. 9: *The Pauli principle prevents fermions of like spin on adjacent sites from hopping (left), a process which is allowed if the fermions have opposite spin (right).*

9.1 Perturbation theory

We already encountered the 'exchange energy' $J = 4t^2/U$ as the separation between the ground state and the three excited states in the lowest energies of the half-filled sector of the two-site HH. This scale can also be arrived at by doing perturbation theory in t. At $t = 0$, the half-filled HH will have exactly one fermion on every site. Because the sites are independent, the relative orientations are irrelevant to the energy.

Now consider perturbation theory in the hopping. There is no first order shift because the kinetic energy does not connect a state of fixed occupation number with itself. However, there is a second order contribution if the adjacent spins are antiparallel. The kinetic energy $\hat{K}$ can transport a fermion to its neighboring site, resulting in an intermediate state whose doubly occupied site has higher energy $+U$. Then a second action of $\hat{K}$ returns to the original state. The standard perturbation theory formula yields $E^{(2)} \sim -t^2/U$, and a careful counting gives the correct factor of four and $J = -4t^2/U$. This process is forbidden if the two spins are parallel. These two situations are illustrated in Fig. 9.

It is interesting that antiferromagnetism arises both from this strong coupling (perturbation theory in t) argument and also from weak coupling (small U) where we saw the nesting of the Fermi Surface select out the antiferromagnetic wavevector $\vec{k} = (\pi, \pi)$. Indeed, more sophisticated weak coupling approaches like the 'Random Phase Approximation' reinforce the notion that the magnetic susceptibility is largest at (π, π).

9.2 The Stoner criterion

Stoner developed a picture of ferromagnetism based on the competition between the increase in kinetic energy when making the up- and down-spin fermion numbers different and the associated decrease in potential energy. The basic idea is the following: Because of the Pauli principle, the way to occupy a given set of energy levels with the lowest energy is to start filling from the bottom and put two fermions, one of each spin, in each level. Otherwise, if you make the numbers of up and down fermions unequal, and don't fill each level with two fermions, you will have to occupy higher energies.

However, if you make the number of up and down fermions unequal, you can reduce the potential energy: Consider the limit of complete spin polarization where there are no fermions of one spin species. Then, obviously, the potential energy is zero. Very generally, polarization of the spin decreases the likelihood of double occupation and hence lowers the potential energy.

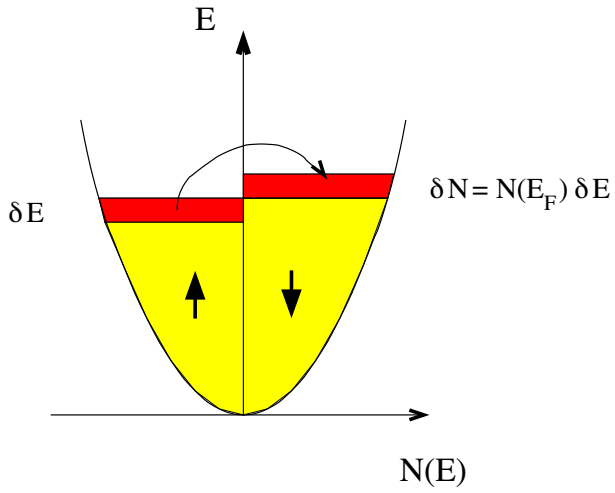

Fig. 10: *Polarizing the fermions increases the kinetic energy, since the levels which must be occupied by the majority species, according to the Pauli principle, are higher than those which could be filled by the minority species.*

Let's now make this argument more precise: Consider a system with density of states $N(E)$ and both up- and down-spin fermions filling the energy levels up to the same maximum Fermi level E_F. The density of up and down fermions is equal. We'll call it n.
We now compute the change in energy which results from a reduction in the density of up-spin fermions by δn and at the same time an increase the number of down-spin fermions by δn. The potential energy is lowered by

$$\delta P = U(n+\delta n)(n-\delta n) - Un^2 = -U(\delta n)^2. \tag{43}$$

If we shift an extra δn fermions into the down group, we will occupy energy levels above the original E_F. Recalling the definition of the density of states as the number of levels at an energy E (see Eq. (26)), we have that $N(E) = \delta N/\delta E$, whence $\delta n = N(E_F)\,\delta E$. This tells us how big the range of energies is above E_F we are filling in terms of δn. Likewise, we are emptying levels below E_F that used to be occupied by up spin fermions. See Fig. 10. The net result of this process is to shift δn fermions up in energy by an amount δE. The change in the kinetic energy is then

$$\delta K = +\delta n \delta E = +\frac{1}{N(E_F)}(\delta n)^2. \tag{44}$$

Putting these two expressions together

$$\delta E = \delta P + \delta K = \left(-U + \frac{1}{N(E_F)}\right)(\delta n)^2 = (-UN(E_F)+1)\,\frac{(\delta n)^2}{N(E_F)}\,. \tag{45}$$

We see that if $UN(E_F) > 1$ the total energy change $\delta E < 0$, so it is favorable to have the up and down fermion densities different and hence favorable to have ferromagnetism. This is called the Stoner criterion. It tells us that magnetism is favored by large fermion interactions and also by large DOS.

9.3 Mean-field theory: the idea and procedure

We have considered the HH in the limits of no hopping ($t = 0$), no interactions ($U = 0$), and small system sizes (one and two sites). We now describe how to use mean-field theory (MFT) to study magnetism.

What is MFT? We commented in an earlier section that a Hamiltonian which is quadratic in the fermion creation and destruction operators, $H = \sum_{\mathbf{l},\mathbf{j}} c^\dagger_{\mathbf{l}}\, h_{\mathbf{l},\mathbf{j}}\, c_{\mathbf{j}}$, can be solved by diagonalizing the matrix h. MFT is a method which produces such a quadratic Hamiltonian from a model like the HH which has quartic terms $U c^\dagger_\uparrow c_\uparrow c^\dagger_\downarrow c_\downarrow$ involving four fermion creation and destruction operators. The approach begins by expressing the number operators as an average value plus a deviation from the average:

$$\begin{aligned} n_{\mathbf{i}\uparrow} &= \langle n_{\mathbf{i}\uparrow}\rangle + (n_{\mathbf{i}\uparrow} - \langle n_{\mathbf{i}\uparrow}\rangle) \\ n_{\mathbf{i}\downarrow} &= \langle n_{\mathbf{i}\downarrow}\rangle + (n_{\mathbf{i}\downarrow} - \langle n_{\mathbf{i}\downarrow}\rangle)\,. \end{aligned} \tag{46}$$

Substituting these expressions into the Hubbard interaction term, and dropping the 'small' term (it's not really small!!) which is the product of the two deviations from the average yields

$$\begin{aligned} n_{\mathbf{i}\uparrow} n_{\mathbf{i}\downarrow} &= [\,\langle n_{\mathbf{i}\uparrow}\rangle + (n_{\mathbf{i}\uparrow} - \langle n_{\mathbf{i}\uparrow}\rangle)\,]\,[\,\langle n_{\mathbf{i}\downarrow}\rangle + (n_{\mathbf{i}\downarrow} - \langle n_{\mathbf{i}\downarrow}\rangle)\,] \\ &\approx \langle n_{\mathbf{i}\uparrow}\rangle\langle n_{\mathbf{i}\downarrow}\rangle + \langle n_{\mathbf{i}\downarrow}\rangle(n_{\mathbf{i}\uparrow} - \langle n_{\mathbf{i}\uparrow}\rangle) + \langle n_{\mathbf{i}\uparrow}\rangle(n_{\mathbf{i}\downarrow} - \langle n_{\mathbf{i}\downarrow}\rangle) \\ &= n_{\mathbf{i}\uparrow}\langle n_{\mathbf{i}\downarrow}\rangle + n_{\mathbf{i}\downarrow}\langle n_{\mathbf{i}\uparrow}\rangle - \langle n_{\mathbf{i}\uparrow}\rangle\langle n_{\mathbf{i}\downarrow}\rangle\,. \end{aligned} \tag{47}$$

The interpretation of this expression is clear. The up-spin fermions interact with the average density of the down-spin fermions, and similarly the down-spin fermions interact with the average density of the up-spin fermions. These two terms overcount the original single interaction term, so the product of the average densities is subtracted off.

Within this mean-field replacement, the Hubbard Hamiltonian is now quadratic, and takes the form (in one dimension)

$$H = -t\sum_{l\sigma}\left(c^\dagger_{l\sigma}c_{l+1\sigma} + c^\dagger_{l+1\sigma}c_{l\sigma}\right) + U\left(\, n_{l\uparrow}\langle n_{l\downarrow}\rangle + n_{l\downarrow}\langle n_{l\uparrow}\rangle) - \langle n_{l\uparrow}\rangle\langle n_{l\downarrow}\rangle\,\right). \tag{48}$$

Since H is quadratic, its solution is a matter of diagonalizing an appropriate matrix. Specifically, for the case of ferromagnetism, one imagines that the average occupation is independent of spatial site $\mathbf{l}$ but allowed to be different for the two spin species. That is, $\langle n_{\mathbf{l}\uparrow}\rangle = n + m$ and $\langle n_{\mathbf{l}\downarrow}\rangle = n - m$. Our goal is to calculate the energy E for fixed n as a function of m and see whether the minimum is at $m = 0$ (paramagnetic state, no ferromagnetism) or $m \neq 0$ (ferromagnetism). Because the expectation values $\langle n_{\mathbf{l}\uparrow}\rangle$ and $\langle n_{\mathbf{l}\downarrow}\rangle$ have a site independent form, the energy levels can easily be written down. (By now we are experts at this!) They are,

$$\epsilon_{\uparrow k} = U(n-m) - 2t\cos k \quad \text{and} \quad \epsilon_{\downarrow k} = U(n+m) - 2t\cos k\,. \tag{49}$$

Again, I have assumed we are in one dimension.

One merely has to take the various possible fillings of the lattice with up and down fermions and add these levels up. That is, we proceed as follows (if doing MFT computationally):

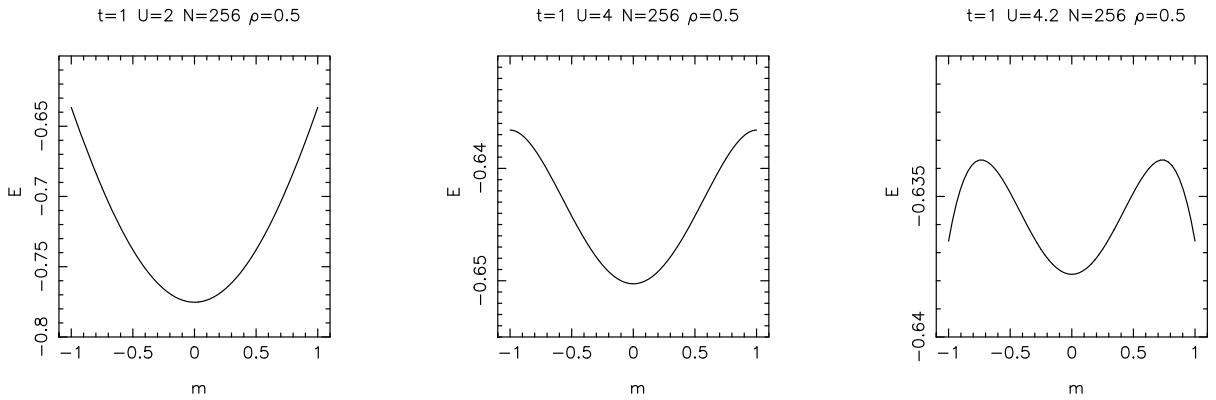

Fig. 11: *Energy versus magnetization of the $d = 1$ HH at $U/t = 2$ and $\rho = \frac{1}{2}$ (quarter filling, 128 fermions on an $N = 256$ site lattice). Left to Right: $U/t = 2.0, 4.0, 4.2$. The minimum energy is always in the paramagnetic phase, $m = 0$. But there is a hint at approaching possibility of ferromagnetism for $U/t = 4.2$ where local minima have begun to develop at $m = \pm 1$.*

(1) Fix the lattice size, N, to some fairly large value, for example $N = 128$ or greater.

(2) Choose a total particle number $N_{\rm tot}$ and on-site repulsion U.

(3) Loop over $N_\uparrow = 0, 1, 2, \ldots, N_{\rm tot}$. For each choice, set $N_\downarrow = N_{\rm tot} - N_\uparrow$. (Actually, your answers should be symmetric on interchange of $N_\uparrow$ and $N_\downarrow$, so you really only need do half the values $N_\uparrow = 0, 1, 2, \ldots, N_{\rm tot}/2$.) Define the densities, $n_\uparrow = N_\uparrow/N$ and $n_\downarrow = N_\downarrow/N$.

(4) Loop over the N allowed momentum values $k = 2\pi/N\{-N/2+1, -N/2+2, \ldots, N/2\}$. Fill up the lowest $N_\uparrow$ and $N_\downarrow$ of the energy levels. Recall that the levels are given by $\epsilon_\uparrow(k) = -2\,t\cos k + U\langle n_\downarrow\rangle$ and $\epsilon_\downarrow(k) = -2\,t\cos k + U\langle n_\uparrow\rangle$.

(5) Finally, normalize the energy to the number of sites and add in the term $-U\langle n_\uparrow\rangle\langle n_\downarrow\rangle$. This gives the energy for the given $N_\uparrow$ and $N_\downarrow = N_{\rm tot} - N_\uparrow$. Make a list of them and see which is lowest.

(6) Repeat the calculation for different U and $N_{\rm tot}$ to get the phase diagram.

9.4 MFT: some results

Figures 11 and 12 give representative results for one quarter filling, that is, a density $\rho = \rho_\uparrow + \rho_\downarrow = \frac{1}{2}$ fermions per site. (This is one quarter of the maximal density of two fermions per site.) The magnetization m is defined such that $m = (\rho_\uparrow - \rho_\downarrow)/(\rho_\uparrow + \rho_\downarrow)$.
At $U/t = 2$ the optimal energy is paramagnetic: the energy E is minimized at $m = 0$. This is still the case at $U/t = 4$, but the energy of the spin polarized solutions (m nonzero) are getting much closer to $m = 0$. (Note the energy scale.) When $U/t = 4.2$ the energies for large $|m|$ have started to turn down and are lower than intermediate m, though $E(m = 0)$ is still lowest. $U/t = 4.4$ has just gone ferromagnetic.

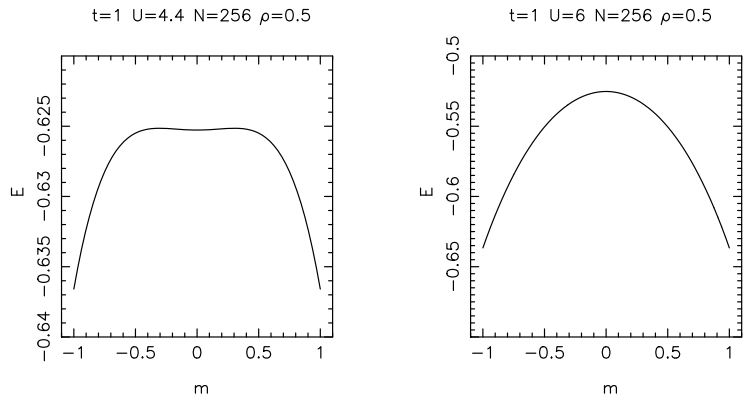

Fig. 12: *Same as Fig. 11 except $U/t = 4.4, 6.0$. The energy minima are now at $m = \pm 1$. The HH has undergone a ferromagnetic phase transition.*

Earlier in this section we derived the Stoner criterion for ferromagnetism, $UN(E_{\rm F}) > 1$. In addition, in Sec. 6, we computed the DOS for the $d = 1$ HH, $N(E) = 1/(\pi\sqrt{4t^2 - E^2})$. (This is the density of states for a single spin species, which is what was used in the Stoner criterion.) To compare with MFT, we need the relation between density ρ and Fermi energy $E_{\rm F}$

$$\rho(E_{\rm F}) = 2\int_{-2t}^{E_{\rm F}} dE\, N(E) \quad \rightsquigarrow \quad \rho_{d=1}(E_{\rm F}) = \frac{2}{\pi}\cos^{-1}\left(\frac{-E_{\rm F}}{2t}\right). \tag{50}$$

We include a factor of two for spin here, so that when we get ρ we use the total density (including both spin species). One can check this latter relation obeys the expected limits: $\rho = 0$ when $E_{\rm F} = -2t$, $\rho = 1$ when $E_{\rm F} = 0$, and $\rho = 2$ when $E_{\rm F} = +2t$.
Putting these equations together, we can get the density of states at $E_{\rm F}$ for a given filling:

$$N(\rho) = \frac{1}{2\pi t}\,\frac{1}{\sin(\pi\rho/2)}\,. \tag{51}$$

For half-filling, $\rho = 1$ we see that $N(\rho = 1) = 1/2\pi t$ and hence $U_{\rm crit} = 2\pi t$. For quarter-filling, $\rho = \frac{1}{2}$ we see that $N(\rho = 1) = 1/\sqrt{2}\pi t$ and hence $U_{\rm crit} = \sqrt{2}\pi t = 4.44t$. This is in pretty good agreement with Figs. 11 and 12 which showed us that $U_{\rm crit}$ was around $4.4t$. The slight disagreement (Fig. 12 suggests $U_{\rm crit}$ a bit less than $4.4t$ while Stoner gives $U_{\rm crit}$ a bit larger than $4.4t$) is a finite size effect. (The calculations were done on an $N = 256$ site lattice.)
One can also do MFT in the grand-canonical ensemble (GCE). That is, rather than computing the energy for fixed occupations, one uses a chemical potential μ and then *computes* $N_\downarrow$ and $N_\uparrow$ by filling those levels which are below μ. The density then comes out of the choice of μ, and, indeed, one needs to tune μ to get the desired density.
One advantage of working in the GCE is that one can frame the calculation in a self-consistent manner, so that starting at some densities $n_\uparrow, n_\downarrow$, the energies are computed and the new values for the densities are inferred, which are fed back into the calculation. The process is iterated until convergence is reached. (There is a danger of getting stuck in metastable configurations, however.)
MFT is an incredibly useful method, and should probably be used as a starting point for understanding almost any new model Hamiltonian. It is, in fact, the technique which was used to

solve the BCS theory of superconductivity: quadratic Hamiltonians can be solved even if they contain 'anomalous' terms consisting of pairs of creation and destruction operators. MFT can also be applied to inhomogeneous problems, for example in a HH with disorder or in situations where inhomogeneities arise spontaneously. It is merely a matter of replacing the analytic forms for the energy bands with a matrix diagonalization. In the former case, some beautiful work has been done on disordered superconductivity. In the latter case, striped phases of the HH were discovered early on via MFT, and seem to play a role in cuprate superconductivity.

9.5 MFT: antiferromagnetism

It should be clear that the basic idea to look for antiferromagnetism in the HH within MFT is the same as for ferromagnetism. Indeed, our earlier solution for the energy bands of the non-interacting HH serves us well here. We simply replace the ferromagnetic ansatz $\langle n_{\mathrm{l}\uparrow}\rangle = n+m$, $\langle n_{\mathrm{l}\downarrow}\rangle = n-m$. by an antiferromagnetic one, $\langle n_{\mathrm{l}\uparrow}\rangle = n+(-1)^{\mathrm{l}}m$, $\langle n_{\mathrm{l}\downarrow}\rangle = n-(-1)^{\mathrm{l}}m$, giving rise to a staggered potential. A bipartite lattice is assumed here.

The process for computing the energy of an antiferromagnetic configuration is the same as the steps (1–5) above, with the replacement of the ferromagnetic eigenvalues by the antiferromagnetic ones. Since we are assuming the total up and down densities over the whole lattice are identical, one no longer loops over different $N_\uparrow$. However, one does have to loop over different m. More precisely, one fixes $n = N_{\mathrm{tot}}/2$ and then tries $m = 1/N, 2/N \ldots$, One also needs to be careful to work in the reduced Brillouin zone.

In concluding this discussion of MFT, it should be emphasized that, while very useful in yielding insight into the possible phases of the system, is a completely uncontrolled approximation. MFT overestimates the tendency for ordered phases, and can (and does) predict magnetic order where none occurs. Even if a particular phase transition is correctly predicted by MFT, the details of the transition (critical temperature, critical exponents, etc) are usually incorrect.

10 The attractive Hubbard Hamiltonian

In Sec. 4 we considered PHTs, which we performed on both spin species. A PHT on only one spin species yields a connection between the HH with $U > 0$ and $U < 0$. In this case, $n_\downarrow \to 1 - n_\downarrow$, but $n_\uparrow \to n_\uparrow$ is unchanged. The kinetic energy term is invariant, but the sign of the interaction term is reversed, $U(n_\uparrow - \frac{1}{2})(n_\downarrow - \frac{1}{2}) \to -U(n_\uparrow - \frac{1}{2})(n_\downarrow - \frac{1}{2})$, and the chemical potential μ maps into a Zeeman field term $-\mu(n_\uparrow - n_\downarrow)$. Conversely, a Zeeman term in the original $U > 0$ model maps into a chemical potential term in the $U < 0$ model.

The HH with $-U$ is called the *attractive* HH because a negative value of U represents an attraction between spin up and spin down fermions on the same site. By considering how this

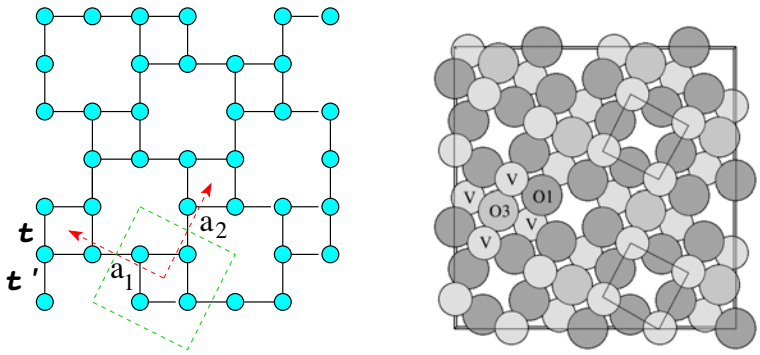

Fig. 13: *The magnetic vanadium atoms of CaV_4O_9 occupy a 1/5 depleted square lattice.*

partial PHT affects various operators, like the components of magnetization,

$$\begin{aligned} S^z_{\mathbf{i}} &= n_{\mathbf{i}\uparrow} - n_{\mathbf{i}\downarrow} \leftrightarrow n_{\mathbf{i}} = n_{\mathbf{i}\uparrow} + n_{\mathbf{i}\downarrow} \\ S^+_{\mathbf{i}} &= c^\dagger_{\mathbf{i}\uparrow} c_{\mathbf{i}\downarrow} \leftrightarrow c^\dagger_{\mathbf{i}\uparrow} c^\dagger_{\mathbf{i}\downarrow} \\ S^-_{\mathbf{i}} &= c^\dagger_{\mathbf{i}\downarrow} c_{\mathbf{i}\uparrow} \leftrightarrow c_{\mathbf{i}\downarrow} c_{\mathbf{i}\uparrow} \end{aligned} \tag{52}$$

one can show that magnetic order in the $+U$ HH is related to superconducting and charge order in the $-U$ HH, so that an understanding of the phases of one model immediately implies considerable information about the other.

For example, imagine starting with the 2D square lattice repulsive HH at half-filling. Its continuous xyz spin rotational invariance precludes long range magnetic order at finite temperature owing to the Mermin-Wagner theorem. (One of the key achievements of QMC was showing that the *ground* state does have order [15].) However, if a Zeeman field is added, this symmetry is reduced to xy, allowing for a Kosterlitz-Thouless transition at $T \neq 0$. Performing the partial PHT we infer that the doped attractive 2D HH (recall the Zeeman field for $U > 0$ maps onto a chemical potential for $U < 0$) has a finite temperature superconducting phase transition. This is a highly non-trivial assertion, made 'obvious' by the PHT. These sorts of considerations can be extended to various exotic sorts of pairing [16].

11 A peek at research: CaV_4O_9

Some of the current research on the HH takes a look at the properties of the HH on 'depleted lattices'. We already encountered one such geometry: the Lieb lattice has a regular array of 1/4 missing sites. As we noted, its band structure possesses a perfectly flat band, and it is interesting to try to understand how this affects magnetism (for $U > 0$) and superconductivity (for $U < 0$) [17]. Lieb [11] has given us some theorems about the former case, although quantitative calculations are still of interest. In the latter case, an intriguing question is the following: Consider the large (attractive) U limit of the HH. Tightly bound fermion pairs can be thought of as bosons, and superconductivity as Bose Einstein Condensation. However, if the band in which the bosons reside is perfectly flat, into which momentum state will they choose to condense?

A second depleted lattice that has been investigated [18] is a model of CaV_4O_9. See Fig. 13. The appropriate HH, or Heisenberg model in the large U limit, has distinct hoppings t and t' within four site plaquettes and between them. It turns out there is a window of $t'/t \approx 1$ (or $J'/J \approx 1$) where long range antiferromagnetic order forms at low temperature. Outside of that window, the ground state is a spin liquid.

12 Conclusions

In these notes we have tried to provide an introduction to the Hubbard Hamiltonian and some of its elementary physics. We have seen how to write the model down and understand its behavior in the limit of no interactions, no kinetic energy, small clusters (ED), and, finally, mean-field theory. We have not discussed the many sophisticated analytic and numerical methods that have been thrown at this simple, but remarkably stubborn, model.

One key piece of physics not addressed here, which arises prominently in the HH, and in its multiband variants like the PAM, is the idea of a 'Kondo resonance'. It turns out that as one progresses from weak to strong coupling, the spectral function does not smoothly evolve from a single blob to two (upper and lower) Hubbard bands. Instead, somewhere in the course of changing the interaction strength a three peak structure is in evidence: The beginning of the formation of upper and lower Hubbard bands, but also a sharp peak at the Fermi energy. This very important idea is at the heart of much of the research into the HH and its experimental realizations, and its successful capture was one of the key achievements of dynamical mean-field theory.

References

[1] M.C. Gutzwiller, Phys. Rev. Lett. **10**, 159 (1963)

[2] J. Kanamori, Prog. Theor. Phys. **30**, 275 (1963)

[3] J. Hubbard, Proc. R. Soc. A **276**, 237 (1963)

[4] J. Hubbard, Proc. R. Soc. A **281**, 401 (1964)

[5] P. Fazekas: *Lecture Notes on Electron Correlation and Magnetism* (World Scientific, Singapore, 1999)

[6] M. Rasetti (ed.): *The Hubbard Model – Recent Results* (World Scientific, Singapore, 1991)

[7] A. Montorsi (ed): *The Hubbard Model – A Reprint Volume* (World Scientific, Singapore, 1992)

[8] F. Gebhard: *The Mott Metal-Insulator Transition, Models and Methods* (Springer, Heidelberg, 1997)

[9] Editorial: *The Hubbard model at half a century*, Nature Physics **9**, 523 (2013)

[10] `http://www.nobelprize.org/nobel_prizes/physics/laureates/1965/feynman-lecture.html`

[11] E.H. Lieb, Phys. Rev. Lett. **62**, 1201 (1989)

[12] N. Laflorencie and D. Poilblanc: *Simulations of pure and doped low-dimensional spin-1/2 gapped systems*, Lecture Notes in Physics **645**, 227 (2004)

[13] `http://wiki.phys.ethz.ch/quantumsimulations/_media/quantumsimulation_ed_part_2.pdf`

[14] R. Blankenbecler, D.J. Scalapino, and R.L. Sugar, Phys. Rev. D **24**, 2278 (1981)

[15] J.E. Hirsch and S. Tang, Phys. Rev. Lett. **62**, 591 (1989)

[16] R.R.P. Singh and R.T. Scalettar, Phys. Rev. Lett. **66**, 3203 (1991)

[17] V.I. Iglovikov, F. Hébert, B. Grémaud, G.G. Batrouni, and R.T. Scalettar, Phys. Rev. B **90**, 094506 (2014)

[18] E. Khatami, R.R.P. Singh, W.E. Pickett, and R.T. Scalettar, Phys. Rev. Lett. **113**, 106402 (2014)

5 Multiplets in Transition-Metal Ions and Introduction to Multiband Hubbard Models

Robert Eder
Institut für Festkörperphysik
Karlsruhe Institute of Technology

Contents

E. Pavarini, E. Koch, J. van den Brink, and G. Sawatzky (eds.)
Quantum Materials: Experiments and Theory
Modeling and Simulation Vol. 6
Forschungszentrum Jülich, 2016, ISBN 978-3-95806-159-0
http://www.cond-mat.de/events/correl16

1 Introduction

Compounds containing $3d$ transition-metal ions have been intriguing solid state physicists ever since the appearance of solid state physics as a field of research. In fact, already in the 1930's NiO became the first known example of a correlated insulator in that it was cited by deBoer and Verwey as a counterexample to the then newly invented Bloch theory of electron bands in solids [1]. During the last 25 years $3d$ transition-metal compounds have become one of the central fields of solid state physics following the discovery of the cuprate superconductors, the colossal magnetoresistance phenomenon in the manganites and, most recently, the iron-pnictide superconductors.

It was conjectured early on that the reason for the special behavior of these compounds is the strong Coulomb interaction between electrons in their partially filled $3d$-shells. The $3d$ wave functions are orthogonal to those of the inner-shells — such as $1s$, $2s$, $2p$, $3s$ and $3p$ — solely due to their angular part $Y_{2,m}(\vartheta, \varphi)$. Their radial part $R_{3,2}(r)$ therefore is not pushed out to regions far from the nucleus by the requirement to be orthogonal to the inner shell wave functions and therefore is concentrated close to the nucleus (the situation is exactly the same for the $4f$ wave functions). Any two electrons in the $3d$-shell thus are forced to be close to each other on average so that their mutual Coulomb repulsion is strong (the Coulomb repulsion between two $3d$ electrons is small, however, when compared to the Coulomb force due to the nucleus and the inner shells so that the electrons *have to* stay close to one another!). For clarity we also mention that the Coulomb repulsion between two electrons in the inner shells of most heavier elements is of course much stronger than between $3d$ electrons. This, however, is irrelevant because these inner shells are several 100–1000 eV below the Fermi energy so that they are simply completely filled and inert. On the other hand, the $3d$-orbitals in transition-metal compounds or the $4f$-orbitals in materials containing the Rare Earth elements participate in the bands at the Fermi level so that the strong Coulomb interaction in these orbitals directly influences the conduction electrons. The conduction bands in such compounds therefore form dense many-body-systems of strongly interacting electrons and the energy from the Coulomb repulsion is large compared to the average kinetic energy. This dominance of the interaction energy in turn implies a propensity to show ordering phenomena and the ensuing phase transitions. It is therefore ultimately the Coulomb repulsion in the partially filled $3d$-shells of the transition-metals and the $4f$-shells of the rare earths which gives rise to the wide variety of spectacular phenomena observed in these compounds. Let us therefore discuss this Coulomb interaction in more detail.

2 Multiplets of a free ion

2.1 General considerations

As an example let us consider an Ni^{2+} ion in vacuum which has the electron configuration [Ar] $3d^8$. It is a standard exercise in textbooks of atomic physics to show that the d^8 configuration, which is equivalent to d^2, has the following multiplets or terms: ${}^3F$, ${}^3P$, ${}^1G$, ${}^1D$ and ${}^1S$,

Term	J	E (eV)
^3F	4	0.000
	3	0.169
	2	0.281
^1D	2	1.740
^3P	2	2.066
	1	2.105
	0	2.137
^1G	4	2.865
^1S	0	6.514

Table 1: *Energies of the multiplets of Ni^{2+} (taken from Ref. [2]. J is the total angular momentum quantum number and the $J = 4$ member of ^3F has been taken as the zero of energy.*

whereby according to the first two Hund's rules ^3F is the ground state. 'Multiplets' thereby is simply another word for 'eigenstates of the system of 26 electrons in the electric field of the Ni nucleus' (the nuclear charge of Ni is 28). Actually, the electrons in the shells below the $3d$-shell may be considered as inert due to the large binding energies of these shells so that to very good accuracy one can consider only the 8 electrons in the $3d$-shell. The energies of the multiplets can be deduced experimentally by analyzing the optical spectrum of Ni vapor and are listed in Table 1. They span a range of several eV whereby multiplets with nonzero spin are in addition split by spin-orbit coupling which results in intervals of order 0.1 eV. All of these eigenstates correspond to the same electron configuration, namely [Ar] $3d^8$, so that the fact that, say, ^3P has a higher energy than ^3F is not due to an electron having been promoted from a state with low energy to one with high energy as in an optical transition. Rather, the excited multiplets – ^3P, ^1G, ^1D and ^1S – should be viewed as collective excitations of the 8-electron system, similar in nature to a plasmon in an electron gas. And just as a plasmon can exist only due to the Coulomb interaction between electrons, the multiplet splitting in atomic shells also originates from the Coulomb interaction between electrons. To understand it we therefore need to discuss the Coulomb interaction between electrons in a partially filled atomic shell.

As a first step we introduce Fermionic creation and annihilation operators $c^\dagger_{n,l,m,\sigma}$ which create an electron with z-component of spin σ in the orbital with principal quantum number n, orbital angular momentum l, and z-component of orbital angular momentum m. In the case of a partly filled $3d$-shell all $n_i = 3$ and all $l_i = 2$ identically, so that these two indices could be omitted, but we will keep them for the sake of later generalizations. In the following we will often contract (n, l, m, σ) to the compound index ν for brevity, so that, e.g., $c^\dagger_{\nu_i} = c^\dagger_{n_i,l_i,m_i,\sigma_i}$.

The procedure we will follow is degenerate first-order perturbation theory as discussed in practically any textbook of quantum mechanics. The unperturbed Hamiltonian H_0 thereby corresponds to the energies of the different atomic shells

$$H_0 = \sum_{n,l} \epsilon_{n,l} \sum_{m,\sigma} c^\dagger_{n,l,m,\sigma} c_{n,l,m,\sigma}$$

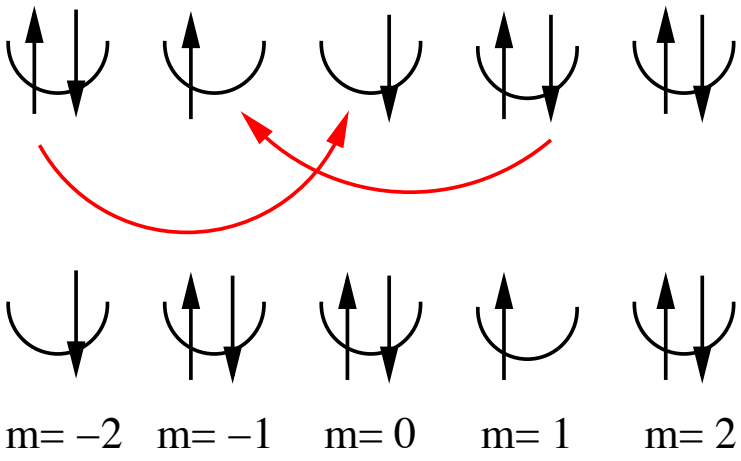

Fig. 1: *Coulomb scattering of two electrons in the d-shell. In the initial state $|\nu\rangle$ (top) the electrons are distributed over the five d-orbitals which are labeled by their m-values. Due to their Coulomb interaction two electrons scatter from each other and are simultaneously transferred to different orbitals, resulting in the state $|\mu\rangle$ (bottom).*

whereas the Coulomb interaction is considered as the perturbation H_1. The d^n configuration comprises all states which are obtained by distributing the n electrons over the $2 \cdot 5 = 10$ spin-orbitals:

$$|\nu\rangle = |\nu_1, \nu_2 \dots \nu_n\rangle = c^\dagger_{\nu_1} c^\dagger_{\nu_2} \dots c^\dagger_{\nu_n} |0\rangle \ . \tag{1}$$

and the number of these states obviously is $n_c = 10!/(n!\,(10-n)!)$. In writing the basis states as in (1) we need to specify an ordering convention for the creation operators on the right hand side. For example, only states are taken into account where $m_1 \leq m_2 \leq m_3 \cdots \leq m_n$. Moreover, if two m_i are equal the $c^\dagger_{m_i\downarrow}$-operator is assumed to be to the left of the $c^\dagger_{m_i\uparrow}$-operator. If we adopt this convention, every possible state obtained by distributing the n electrons over the 10 spin-orbitals is included exactly once in the basis. If the n_i and l_i were to take different values we could generalize this by demanding that the (n_i, l_i, m_i)-triples be ordered lexicographically. As will be seen below, strict application of an ordering convention for the Fermi operators is necessary to determine the correct Fermi signs for the matrix elements.

If only H_0 were present all the states (1) would be degenerate. The Coulomb interaction H_1 between the electrons then (partially) lifts this degeneracy and this is the physical reason for the multiplet splitting. The standard procedure in this a situation is to set up the matrix $h_{\mu,\nu} = \langle\mu|H_1|\nu\rangle$ and diagonalize it to obtain the first order energies and wave functions [3]. Thereby H_1 has both diagonal matrix elements such as $\langle\nu|H_1|\nu\rangle$ but also off-diagonal matrix elements $\langle\mu|H_1|\nu\rangle$. The diagonal matrix elements describe the fact that the Coulomb repulsion between two electrons in different orbitals depends on the spatial character of these orbitals whereas the off-diagonal matrix elements describe the scattering of two electrons from each other as shown in Figure 1.

In second quantization the Coulomb Hamiltonian H_1 takes the form

$$\begin{aligned} H_1 &= \frac{1}{2} \sum_{i,j,k,l} V(\nu_i, \nu_j, \nu_k, \nu_l)\; c^\dagger_{\nu_i} c^\dagger_{\nu_j} c_{\nu_k} c_{\nu_l}\;, \\ V(\nu_1, \nu_2, \nu_3, \nu_4) &= \int dx \int dx'\; \psi^*_{\nu_1}(x)\; \psi^*_{\nu_2}(x')\; V_c(x, x')\; \psi_{\nu_3}(x')\; \psi_{\nu_4}(x)\;, \\ V_c(x, x') &= \frac{1}{|\boldsymbol{r} - \boldsymbol{r}'|}\;. \end{aligned} \tag{2}$$

Here $x = (\boldsymbol{r}, \sigma)$ is the combined position and spin coordinate with $\int dx \cdots = \sum_\sigma \int d\boldsymbol{r} \ldots$ and V_c is the Coulomb interaction between electrons. Note the factor of $1/2$ in front of H_1 and the correspondence of indices and integration variables $\nu_3 \leftrightarrow x'$ and $\nu_4 \leftrightarrow x$ in the Coulomb matrix element, see textbooks of many-particle physics such as Fetter-Walecka [4].

2.2 The Coulomb matrix elements

Our single-particle basis consists of atomic spin-orbitals so if we switch to polar coordinates (r, ϑ, φ) for $\boldsymbol{r}$ the wave functions in (2) are

$$\psi_{\nu_i}(x) = R_{n_i, l_i}(r)\; Y_{l_i, m_i}(\vartheta, \varphi)\; \delta_{\sigma, \sigma_i}. \tag{3}$$

The radial wave functions R_{n_i, l_i} are assumed to be real, as is the case for the true radial wave function of bound states in a central potential. Apart from that we do not really specify them. In fact, it would be rather difficult to give a rigorous prescription for their determination. It will turn out, however, that these radial wave functions enter the Coulomb matrix elements only via a discrete and rather limited set of real numbers which are often obtained by a fit to experiment. In addition to (3), we use the familiar multipole expansion of the Coulomb interaction

$$\frac{1}{|\boldsymbol{r} - \boldsymbol{r}'|} = \sum_{k=0}^{\infty} \sum_{m=-k}^{k} Y^*_{k,m}(\vartheta', \varphi')\; \frac{4\pi}{2k+1}\; \frac{r_<^k}{r_>^{k+1}}\; Y_{k,m}(\vartheta, \varphi)\,. \tag{4}$$

We now insert (3) and (4) into (2). We recall that $\int dx \cdots = \sum_\sigma \int d\boldsymbol{r} \ldots$ and first carry out the sum over spin variables which gives a factor of $\delta_{\sigma_1, \sigma_4}\; \delta_{\sigma_2, \sigma_3}$. Next we pick one term with given k and m from the multipole expansion (4) and proceed to the integration over the spatial variables (r, ϑ, φ) and $(r', \vartheta', \varphi')$. Let us first consider the angular variables (ϑ, φ). Obviously these always come as arguments of spherical harmonics and there is one from $\psi^*_{\nu_1}(x)$, one from the multipole expansion (4), and one from $\psi_{\nu_4}(x)$. We thus obtain a factor of

$$\int_0^{2\pi} d\varphi \int_{-1}^{1} d\cos(\vartheta)\; Y^*_{l_1, m_1}(\vartheta, \varphi)\; Y_{k,m}(\vartheta, \varphi)\; Y_{l_4, m_4}(\vartheta, \varphi)\;. \tag{5}$$

Such a dimensionless integral over three spherical harmonics is called a Gaunt coefficient and can be shown to be proportional to a Clebsch-Gordan coefficient [5, 6]. This property is an immediate consequence of the Wigner-Eckart theorem.

Another interesting property can be seen if we recall the φ-dependence of the spherical harmonics: $Y_{l,m}(\vartheta,\varphi) = P_{l,m}(\vartheta)\, e^{im\varphi}$. It follows that the Gaunt coefficient (5) is different from zero only if $m_1 = m_4 + m$. Moreover, since the ϑ-dependent factors $P_{l,m}(\vartheta)$ are real [5, 6] all nonvanishing Gaunt coefficients are real as well. In the same way the integration over (ϑ', φ') gives

$$\int_0^{2\pi} d\varphi' \int_{-1}^{1} dcos(\vartheta')\; Y^*_{l_2,m_2}(\vartheta',\varphi')\; Y^*_{k,m}(\vartheta',\varphi')\; Y_{l_3,m_3}(\vartheta',\varphi'), \tag{6}$$

which by analogous reasoning is different from zero only if $m_2 + m = m_3$. Since both (5) *and* (6) must be different from zero for the *same* m in order to obtain a nonvanishing contribution, we must have $m_1 + m_2 = m_3 + m_4$. This is simply the condition that L^z be conserved in the Coulomb scattering of the two electrons.

It remains to do the integral over the two radial variables r and r'. These two integrations cannot be disentangled so we find a factor of

$$R^k(n_1l_1, n_2l_2, n_3l_3, n_4l_4) = \int_0^\infty dr\, r^2 \int_0^\infty dr'\, r'^2\, R_{n_1l_1}(r)\, R_{n_2l_2}(r')\, \frac{r_<^k}{r_>^{k+1}}\, R_{n_3l_3}(r')\, R_{n_4l_4}(r)\,. \tag{7}$$

These integrals, which have the dimension of energy, are labeled by the multipole index k, and the number of relevant multipole orders is severely limited by the properties of the Gaunt coefficients: First, since the latter are proportional to Clebsch-Gordan coefficients the three l-values appearing in them have to obey the so-called *triangular condition* [3] whence $k \leq \min(|l_1 + l_4|, |l_2 + l_3|)$. For a d-shell where $l_i = 2$ it follows that $k \leq 4$. Second, the parity of the spherical harmonic Y_{lm} is $(-1)^l$, i.e. even for the case $l_i = 2$. For integrals such as (5) or (6) to be different from zero the spherical harmonic $Y_{k,m}$ from the multipole expansion must have even parity, too, so that for Coulomb scattering within a d-shell only R^0, R^2 and R^4 are relevant. This shows that the sloppy definition of the wave function $R_{n_i,l_i}(r)$ is not a real problem because details of this wave function are irrelevant anyway. In a way, these three parameters may be viewed as a generalization of the Hubbard-U in that R^k is something like the 'the Hubbard-U for k-pole interaction'.

We introduce the following notation for the nonvanishing Gaunt coefficients

$$c^k(lm; l'm') = \sqrt{\frac{4\pi}{2k+1}} \int_0^{2\pi} d\varphi \int_{-1}^{1} d\cos(\vartheta)\, Y^*_{lm}(\vartheta,\varphi)\, Y_{k,m-m'}(\vartheta,\varphi)\, Y_{l',m'}(\vartheta,\varphi)\,. \tag{8}$$

These coefficients are tabulated in Appendix 20a of the textbook by Slater [5] or Table 4.4 of the textbook by Griffith [6], and also in the Appendix of this chapter. Using this notation and the fact that the Gaunt coefficients are real we can finally write the Coulomb matrix element as

$$\begin{aligned} V(\nu_1,\nu_2,\nu_3,\nu_4) = {} & \delta_{\sigma_1,\sigma_4}\, \delta_{\sigma_2,\sigma_3}\, \delta_{m_1+m_2,m_3+m_4} \\ & \times \sum_{k=0}^{\infty} c^k(l_1m_1; l_4m_4)\, c^k(l_3m_3; l_2m_2)\, R^k(n_1l_1, n_2l_2, n_3l_3, n_4l_4)\,. \end{aligned} \tag{9}$$

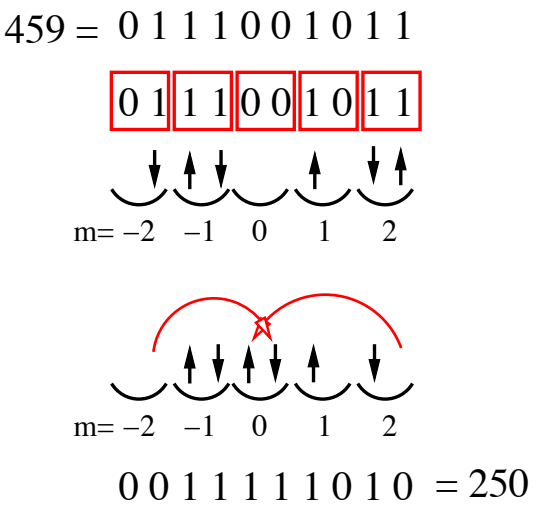

Fig. 2: *The coding of basis states by integers and a scattering process.*

2.3 Solution of the Coulomb problem by exact diagonalization

We now describe how the problem of the partly filled $3d$-shell can be solved numerically, using the method of exact diagonalization. The basis states (1) correspond to all possible ways of distributing n electrons over the 10 spin-orbitals of the $3d$-shell (two spin directions for each $m \in \{-2, -1 \ldots 2\}$). As illustrated in Figure 2 we can code each of these basis states by an integer $0 \leq i \leq 2^{10}$. If we really use all of these integers we are actually treating all states with $0 \leq n \leq 10$ simultaneously but this will be convenient for later generalizations. Next, for a given initial state $|\nu_1, \nu_2, \ldots \nu_n\rangle$ we can let the computer search for all possible transitions of the type shown in Figure 1 and compute the corresponding matrix elements from (9) using, say, the $c^k(lm; l'm')$ copied from Slater's textbook and some given R^0, R^2 and R^4. Let us consider the following matrix element

$$\langle 0|c_{\mu_n} \ldots c_{\mu_1}\, V(\lambda_1, \lambda_2, \lambda_3, \lambda_4)\, c^\dagger_{\lambda_1} c^\dagger_{\lambda_2} c_{\lambda_3} c_{\lambda_4}\, c^\dagger_{\nu_1} c^\dagger_{\nu_2} \ldots c^\dagger_{\mu_n} |0\rangle\,.$$

For this to be nonzero, the operators $c^\dagger_{\lambda_3}$ and $c^\dagger_{\lambda_4}$ must be amongst the $c^\dagger_{\nu_i}$, otherwise the annihilation operators in the Hamiltonian could be commuted to the right where they annihilate $|0\rangle$. In order for these pairs of operators to cancel each other, c_{λ_4} must first be commuted to the position right in front of $c^\dagger_{\lambda_4}$. If this takes n_4 interchanges of Fermion operators we get a Fermi sign of $(-1)^{n_4}$. Bringing next c_{λ_3} right in front of $c^\dagger_{\lambda_3}$ by n_3 interchanges of Fermion operators gives a sign of $(-1)^{n_3}$. Analogously, the creation operators $c^\dagger_{\lambda_1}$ and $c^\dagger_{\lambda_2}$ have to be commuted to the left to stand to the immediate right of their 'partner annihilation operators' so as to cancel them. If this requires an additional number of Fermion interchanges n_2 for $c^\dagger_{\lambda_2}$ and n_1 for $c^\dagger_{\lambda_1}$ there is an additional Fermi sign of $(-1)^{n_1+n_2}$. The total matrix element then is $(-1)^{n_1+n_2+n_3+n_4} V(\lambda_1, \lambda_2, \lambda_3, \lambda_4)$. The correct Fermi sign is crucial for obtaining correct results and must be evaluated by keeping track of all necessary interchanges of Fermion operators. This is perhaps the trickiest part in implementing the generation of the Hamilton matrix or any other operator in a computer program.

E	S	L	n	Term	E	S	L	n	Term
0.0000	1	3	21	^3F	0.0000	3/2	3	28	^4F
1.8420	0	2	5	^1D	1.8000	3/2	1	12	^4P
1.9200	1	1	9	^3P	2.1540	1/2	4	18	^2G
2.7380	0	4	9	^1G	2.7540	1/2	5	22	^2H
13.2440	0	0	1	^1S	2.7540	1/2	1	8	^2P
					3.0545	1/2	2	10	^2D
					4.5540	1/2	3	14	^2F
					9.9774	1/2	2	10	^2D

Table 2: *Energies of the d^8 multiplets calculated with $R^2 = 10.479$ eV, $R^4 = 7.5726$ eV (Left), and energies of the d^7 multiplets calculated with $R^2 = 9.7860$ eV, $R^4 = 7.0308$ eV (Right).*

Once the matrix has been set up it can be diagonalized numerically. Table 2 gives the resulting multiplet energies for d^8 and d^7, the values of L and S for each multiplet and the degeneracy n. The values of the R^k parameters have been calculated by using Hartree-Fock wave functions $R_{3,2}$ for Ni^{2+} and Co^{2+} in (7). The energy of the lowest multiplet is taken as the zero of energy and it turns out that all *energy differences* depend only on R^2 and R^4. Note the increasing complexity of the level schemes with increasing number of holes in the d-shell. Comparing the energies of the multiplets for d^8 with the experimental values in Table 1 one can see good agreement with deviations of order 0.1 eV. The only exception is ^1S. This is hardly a surprise because here the theoretical energy is 13 eV which is comparable to the difference in energy between the $3d$ and the $4s$-shell in Ni (which is ≈ 10 eV). It follows that the basic assumption of the calculation, namely that the separation between atomic shells is large compared to the multiplet energies, is not fulfilled for this particular multiplet. To treat ^1S more quantitatively it would likely be necessary to include basis states with configurations like $3d^7\,4s^1$, or, put another way, to consider the screening of the Coulomb interaction by particle-hole excitations from the $3d$- into the $4s$-shell. Finally, the Table shows that the ground states indeed comply with the first two of Hund's rules: They have maximum spin and maximum orbital angular momentum for this spin. It can be shown that this is indeed always the case as long as one uses Coulomb and exchange integrals with the correct, i.e. positive, sign [5, 6].

2.4 Diagonal matrix elements

The expression (9) is exact but looks somewhat complicated so let us try to elucidate its physical content and thereby also make contact with various approximate ways to describe the Coulomb interaction which can be found in the literature. We first consider those matrix elements where either $\nu_4 = \nu_1$ and $\nu_3 = \nu_2$ (case 1) or $\nu_3 = \nu_1$ and $\nu_4 = \nu_2$ (case 2). In both cases the four Fermion operators in the corresponding terms of H_1 can be permuted to give the product of number operators $n_{\nu_1} n_{\nu_2}$ (with $n_\nu = c_\nu^\dagger c_\nu$) whereby in case 2 an odd number of interchanges of Fermion operators is necessary so that an additional factor of (-1) appears. Whereas for case 1 the product $\delta_{\sigma_1,\sigma_4}\ \delta_{\sigma_2,\sigma_3}$ in (9) always is 1, it vanishes for case 2 unless $\sigma_1 = \sigma_2$. The Pauli

principle requires that $\nu_1 \neq \nu_2$ (otherwise one has the product $c^\dagger_{\nu_1} c^\dagger_{\nu_1} = 0$) so that for case 1 the two orbitals may have the same orbital quantum numbers n, l, m but then must differ in their spin, whereas in case 2 the spins have to be equal so that the orbital quantum numbers definitely must be different. Using (9) the respective matrix elements are

$$\begin{aligned} V(\nu_1,\nu_2,\nu_2,\nu_1) &= \sum_{k=0}^{\infty} c^k(l_1m_1;l_1,m_1)\, c^k(l_2m_2;l_2,m_2)\, R^k(n_1l_1,n_2l_2,n_2l_2,n_1l_1), \\ V(\nu_1,\nu_2,\nu_1,\nu_2) &= \delta_{\sigma_1\sigma_2} \sum_{k=0}^{\infty} c^k(l_1m_1;l_2,m_2)\, c^k(l_1m_1;l_2,m_2)\, R^k(n_1l_1,n_2l_2,n_1l_1,n_2l_2). \end{aligned} \tag{10}$$

It is customary to introduce the following abbreviations

$$\begin{aligned} a^k(lm;l'm') &= c^k(lm;lm)\;\; c^k(l'm';l'm') \\ b^k(lm;l'm') &= c^k(lm;l'm')\, c^k(lm;l'm') \\ F^k(nl;n'l') &= R^k(nl,n'l',n'l',nl) \\ G^k(nl;n'l') &= R^k(nl,n'l',nl,n'l') \end{aligned}$$

The F^k and G^k are called Slater-Condon parameters. The a^k and b^k are listed in Appendix 20a of Slater's textbook [5] and also the Appendix of the this chapter.
We now want to bring these diagonal matrix elements to a more familiar form and thereby specialize to a partly filled $3d$-shell. In this case all $n_i = 3$ and $l_i = 2$ so that for each k there is only one F^k and one G^k and, in fact, $G^k = F^k$. For brevity we omit the n and l quantum numbers in the rest of the paragraph so that, e.g., the electron operators become $c^\dagger_{m,\sigma}$ with m the z-component of $\boldsymbol{L}$. The sum of all diagonal matrix elements then becomes

$$\begin{aligned} H_{1,diag} &= \sum_m U_{m,m}\, n_{m,\uparrow} n_{m,\downarrow} + \frac{1}{2} \sum_{m\neq m'} \left(U_{m,m'} \sum_{\sigma,\sigma'} n_{m,\sigma} n_{m',\sigma'} - J_{m,m'} \sum_{\sigma} n_{m,\sigma} n_{m',\sigma} \right), \\ U_{m,m'} &= \sum_{k\,\in\{0,2,4\}} a^k(m,m')\, F^k, \qquad J_{m,m'} = \sum_{k\,\in\{0,2,4\}} b^k(m,m')\, F^k. \end{aligned}$$

The first term on the right-hand side originates from case 1 with $m_1 = m_2$ and the factor of $1/2$ in front of this term is cancelled because there are two identical terms of this type with either $\nu_1 = (m,\uparrow)$ and $\nu_2 = (m,\downarrow)$ or $\nu_1 = (m,\downarrow)$ and $\nu_2 = (m,\uparrow)$. Defining $n_m = n_{m,\uparrow} + n_{m,\downarrow}$ and $S^z_m = (n_{m,\uparrow} - n_{m,\downarrow})/2$ we have

$$\sum_{\sigma,\sigma'} n_{m,\sigma}\, n_{m',\sigma'} = n_m\, n_{m'} \qquad\qquad \sum_{\sigma} n_{m,\sigma}\, n_{m',\sigma} = 2\left(S^z_m\, S^z_{m'} + \frac{n_m n_{m'}}{4} \right),$$

so that

$$H_{1,diag} = \sum_m U_{m,m}\, n_{m,\uparrow}\, n_{m,\downarrow} + \frac{1}{2} \sum_{m\neq m'} \left((U_{m,m'} - \frac{1}{2} J_{m,m'})\, n_m n_{m'} - 2 J_{m,m'}\, S^z_m S^z_{m'} \right).$$

This is the sum of a Hubbard-like density interaction $\propto U_{m,m'}$ and an Ising-like spin interaction $\propto J_{m,m'}$. The interaction parameters thereby depend on the orbitals and can be expressed in terms of the Slater Condon parameters F^k and the products of Gaunt coefficients a^k and b^k. It is obvious that $J_{m,m'} > 0$ so that the Ising-like interaction describes ferromagnetic coupling — as one would expect on the basis of the first Hund's rule. A truncated Coulomb Hamiltonian like $H_{1,diag}$ is used in some LDA+U schemes [7] and also in many Dynamical Mean-Field calculations for $3d$ transition-metal compounds [8].
To complete the Hund's rule term we consider in addition those terms in H_1 where $\nu_1 = (m, \sigma)$, $\nu_2 = (m', \bar{\sigma})$, $\nu_3 = (m, \bar{\sigma})$ and $\nu_4 = (m', \sigma)$. In these terms the product $\delta_{\sigma_1,\sigma_4}\,\delta_{\sigma_2,\sigma_3}$ is nonvanishing as well and for both values of σ the matrix element (2) is

$$\sum_{k\,\in\{0,2,4\}} c^k(m,m')\,c^k(m,m')\,F^k \;\;=\;\; \sum_{k\,\in\{0,2,4\}} b^k(m,m')\,F^k = J_{m,m'}$$

The Fermion operators are $c^\dagger_{m,\uparrow}c^\dagger_{m',\downarrow}c_{m,\downarrow}c_{m',\uparrow} + c^\dagger_{m,\downarrow}c^\dagger_{m',\uparrow}c_{m,\uparrow}c_{m',\downarrow} = -(S^+_m\,S^-_{m'} + S^-_m\,S^+_{m'})$, i.e., the transverse part of the Heisenberg exchange. Combining these terms with the Ising-like spin exchange term we obtain

$$H_{1,H} = \sum_m U_{m,m}\,n_{m,\uparrow}\,n_{m,\downarrow} + \frac{1}{2}\sum_{m\neq m'}\left((U_{m,m'} - \frac{1}{2}J_{m,m'})\,n_m n_{m'} - 2J_{m,m'}\,\boldsymbol{S}_m\cdot\boldsymbol{S}_{m'}\right).$$

This is now the sum of a density interaction and a spin-rotation invariant ferromagnetic spin exchange. It has to be kept in mind that this Hamiltonian has been obtained by retaining only a relatively small subset of matrix elements in the original Coulomb Hamiltonian. A further simplification which is often used is to replace $U_{m,m'}$ and $J_{m,m'}$ by their averages over all corresponding pairs (m, m'). Using the a^k and b^k in the Appendix one readily obtains

$$\begin{aligned} U &= \frac{1}{25}\sum_{m,m'} U_{m,m'} = F^0, \\ U - J &= \frac{1}{20}\sum_{m\neq m'} (U_{m,m'} - J_{m,m'}) = F^0 - \frac{1}{14}(F^2 + F^4), \end{aligned}$$

so that $J = (F^2 + F^4)/14$.
To conclude the discussion, we consider the diagonal matrix elements $\langle\nu|H_1|\nu\rangle$ in the basis of n-electron states $|\nu\rangle$ defined in (1). Since ν_1 and ν_2 in (10) can be any two out of the n occupied orbitals in $|\nu\rangle$ the total diagonal matrix element of H_1 is obtained by summing over all $\frac{n(n-1)}{2}$ pairs (i, j) formed from the occupied orbitals

$$\langle\nu|H_1|\nu\rangle = \sum_{i<j}\sum_k \left(a^k(l_im_i, l_j, m_j)\,F^k(n_il_i, n_jl_j) - \delta_{\sigma_i\sigma_j}\,b^k(l_im_i, l_j, m_j)\,G^k(n_il_i, n_jl_j)\right). \tag{11}$$

As will be seen in the next paragraph, this formula is sufficient for the analytical calculation of the multiplet energies.

2.5 Analytical calculation of multiplet energies by the diagonal sum-rule

The exact diagonalization procedure outlined in Sec. 2.3. can be used to obtain all eigenenergies and the corresponding eigenstates of the Coulomb problem. It is a flexible numerical method of solution into which crystalline electric field, hybridization with ligand orbitals, spin-orbit coupling, and Coulomb interaction with holes in core shells, which is important for the discussion of X-ray absorption spectra, can be incorporated easily. On the other hand, multiplet theory was invented during the 1920's to explain the spectra of free atoms or ions, and at that time computers were not available. It turns out, however, that despite the apparent complexity of the problem the energies of the multiplets can be obtained analytically and this will be described in the following.

The first ingredient is the so-called diagonal sum-rule. This is simply the well-known theorem that the sum of the eigenvalues of a Hermitian matrix H is equal to its trace $\mathrm{Tr}(H) = \sum_i H_{ii}$. It follows immediately by noting that the trace of a matrix is invariant under basis transformations, i.e., $\mathrm{Tr}(H) = \mathrm{Tr}(UHU^{-1})$ for any unitary matrix U. By choosing U to be the matrix which transforms to the basis of eigenvectors of H the diagonal sum-rule follows immediately.

Next, one uses the fact that the Hamilton matrix is block-diagonal, with blocks defined by their values of L^z and S^z. The diagonal sum-rule then can be applied separately for each of these blocks. In addition, the dimension of the blocks decreases as L^z and S^z approach their maximum possible values so that the number of multiplets contained in a given block increases.

As an example for the procedure let us consider a p^2 configuration (by particle-hole symmetry this is equivalent to a p^4 configuration). We write the Fermion operators in the form $c_{l,m,\sigma}$, i.e., we suppress the principal quantum number n. Since we have 6 possible states for a single p-electron (three m-values and two spin directions per m-value) we have 15 states for two electrons. The triangular condition implicit in the Gaunt coefficients now restricts the multipole order k to be ≤ 2. Again, only even k contribute, so that we have two Slater-Condon parameters, F^0 and F^2 (and $F^k = G^k$). The following Table which is taken from Slater's textbook [5] gives the values of the coefficients $a^k(1, m; 1, m')$ and $b^k(1, m; 1, m')$: We first consider the sector with $S^z = 1$. The highest possible L^z is $L^z = 1$ which is realized only for a single state, $|1\rangle = c^\dagger_{1,0,\uparrow} c^\dagger_{1,1,\uparrow}|0\rangle$. We can conclude that one of the multiplets is ${}^3P$ and its energy is equal to

Table 3: *The coefficients a^k and b^k for two p-electrons.*

m	m'	a^0	$25a^2$	b^0	$25b^2$
±1	±1	1	1	1	1
±1	0	1	-2	0	3
0	0	1	4	1	4
±1	∓1	1	1	0	6

the diagonal matrix element of $|1\rangle$ which by (11) is

$$E(^3P) = \sum_{k\in\{0,2\}} \left(a^k(1,1;1,0) - b^k(1,1;1,0)\right) F^k = F^0 - \frac{5}{25}\, F^2.$$

We proceed to the sector $S^z = 0$. Here the highest possible L^z is $L^z = 2$ again obtained for only single state namely $c^\dagger_{1,1,\downarrow} c^\dagger_{1,1,\uparrow}|0\rangle$. We conclude that we also have ^1D with energy

$$E(^1D) = \sum_{k\in\{0,2\}} a^k(1,1;1,1)\, F^k = F^0 + \frac{1}{25}\, F^2.$$

The two multiplets that we found so far, ^1D and ^3P, comprise $5 + 9 = 14$ states – we thus have just one state missing, which can only be ^1S. To find its energy, we need to consider the sector $S^z = 0$ and $L^z = 0$. There are three states in this sector: $c^\dagger_{1,0,\downarrow} c^\dagger_{1,0,\uparrow}|0\rangle$, $c^\dagger_{1,-1,\uparrow} c^\dagger_{1,1,\downarrow}|0\rangle$ and $c^\dagger_{1,-1,\downarrow} c^\dagger_{1,1,\uparrow}|0\rangle$. Two out of the three eigenvalues of the 3×3 Hamiltonian in the basis spanned by these states must be $E(^3P)$ and $E(^1D)$, because these multiplets also have members with $S^z = 0$ and $L^z = 0$. To obtain $E(^1S)$ we accordingly compute the sum of the diagonal elements of the 3×3 matrix and set

$$\begin{aligned} E(^3P) + E(^1D) + E(^1S) &= \sum_{k\in\{0,2\}} \left(a^k(1,0;1,0) + 2\, a^k(1,-1;1,1)\right) F^k \\ \rightarrow\ E(^1S) &= F^0 + \frac{10}{25}\, F^2. \end{aligned}$$

This example shows the way of approach for multiplet calculations using the diagonal sum-rule: one starts out with a state with maximum L^z or S^z for which there is usually only a single basis state. This basis state belongs to some multiplet whose energy simply equals the 'diagonal element' of the 1×1 Hamiltonian. Then one proceeds to lower S^z and/or L^z and obtains energies of additional multiplets by calculating the trace of the respective block of the Hamilton matrix and using the known energies of multiplets with higher L^z or S^z. It turns out that in this way the energies of *all* multiplets involving s, p, d or f electrons can be expressed in terms of the Slater-Condon parameters by analytical formulas. A rather complete list can be found for example in the Appendices 21a and 21b of the textbook by Slater [5].

One point which may be helpful when reading the literature is the following: for the special case of a partly filled d-shell many authors use the so-called Racah parameters A, B, and C instead of the 3 Slater-Condon parameters F^0, F^2, and F^4. The rule for conversion is simple:

$$A = F^0 - \frac{49}{441} F^4 \qquad B = \frac{1}{49} F^2 - \frac{5}{441} F^4 \qquad C = \frac{35}{441} F^4\,.$$

The Racah-parameters have been introduced because the analytical formulas for the energies of the multiplets of d^n as derived by the diagonal sum-rule look nicer when they are expressed in terms of them. For example Griffith [6] gives multiplet energies in terms of the Racah-parameters in his Table 4.6.

As stated above, multiplet theory was originally developed to discuss the spectra of atoms or

p^2	C	N^+	O^{2+}	Si	P^+	S^{2+}
	1.124	1.134	1.130	1.444	1.430	1.399
p^4	O	F^+		S	Cl^+	
	1.130	1.152		1.401	1.392	

Table 4: *The ratio (12) for various Atoms and Ions with p^2 and p^4 configurations outside a closed shell.*

ions in the gas phase. The question then arises, as to what are the values of the Slater-Condon parameters. Of course one might attempt to compute these parameters using, e.g., Hartree-Fock wave functions in the expression (7). It turns out, however, that very frequently the number of multiplets considerably exceeds the number of relevant Slater-Condon parameters. In the case of the p^2 configuration we had three multiplets, ${}^3P$, ${}^1D$, and ${}^1S$, but only two Slater-Condon parameters F^0 and F^2. This would suggest to obtain the values of the Slater-Condon parameters by fit to the spectroscopic data and the textbook by Slater [5] contains a vast amount of experimental data which are analyzed in this way. For the p^2 configuration we restrict ourselves to a simple cross check. Using the above formulae and eliminating the F's we find:

$$r = \frac{E({}^1S) - E({}^1D)}{E({}^1D) - E({}^3P)} = \frac{3}{2}. \tag{12}$$

This relation should be obeyed by all ions with two p-electrons outside filled shells, e.g., the series C, N^{1+} and O^{2+} or two holes in a filled p-shell such as the series O and F^+. The energies of these multiplets have been measured with high precision and are available in databases [2] and Table 4 shows the resulting values of r. For the first-row elements the deviation is about 25%, for the second row only about 5%. We recall that multiplet theory corresponds to first order degenerate perturbation theory, where H_0 contains the orbital energies and H_1 the Coulomb interaction between electrons in one shell. It therefore will work the better the larger the separation between different atomic shells and this is indeed larger in the second row elements.

2.6 Spin-orbit coupling

As the last problem in this section on free atoms or ions we briefly discuss spin-orbit coupling. The corresponding Hamiltonian is

$$H_{SO} = \lambda_{SO} \sum_{i=1}^{n} \boldsymbol{l}_i \cdot \boldsymbol{S}_i = \lambda_{SO} \sum_{i=1}^{n} \left(l_i^z S_i^z + \frac{1}{2}(l_i^+ S_i^- + l_i^- S_i^+) \right).$$

where $\boldsymbol{l}_i$ ($\boldsymbol{S}_i$) are the operator of orbital (spin) angular momentum of the i^{th} electron. The spin-orbit coupling constant λ_{SO} can be written as [3]

$$\lambda_{SO} = \frac{\hbar^2}{2m_e^2 c^2 r_{orb}} \left. \frac{dV_{at}}{dr} \right|_{r=r_{orb}}$$

where m_e is the electron mass, c the speed of light, V_{at} is the atomic potential acting on the electron, and r_{orb} the spatial extent of the radial wave function.
The first term on the right hand side can be translated into second quantized form easily:

$$H_{SO}^{\parallel} = \lambda_{SO} \sum_{m=-l}^{l} \frac{m}{2} \left(c_{l,m,\uparrow}^{\dagger} c_{l,m,\uparrow} - c_{l,m,\downarrow}^{\dagger} c_{l,m,\downarrow} \right). \tag{13}$$

As regards the transverse part, we note [3] that the only nonvanishing matrix elements of the orbital angular momentum raising/lowering operator are $\langle l, m \pm 1 | l^{\pm} | l, m \rangle = \sqrt{(l \mp m)(l \pm m + 1)}$ whence

$$H_{SO}^{\perp} = \frac{\lambda_{SO}}{2} \sum_{m=-l}^{l-1} \sqrt{(l-m)(l+m+1)} \left(c_{l,m+1,\downarrow}^{\dagger} c_{l,m,\uparrow} + c_{l,m,\uparrow}^{\dagger} c_{l,m+1,\downarrow} \right). \tag{14}$$

Spin-orbit coupling can be implemented rather easily into the numerical procedure, the main difficulty again is keeping track of the Fermi sign. Due to the fact that neither L^z nor S^z are conserved anymore the corresponding reduction of the Hilbert space is no longer possible. In transition-metal compounds the spin-orbit coupling constant λ_{SO} for the $3d$-shell is rather small, of order $\lambda_{SO} \approx 0.05$ eV. Still, if the ground state of a given ion has a non-vanishing spin, spin-orbit coupling will determine how this spin orients itself in an ordered phase giving rise to a *magnetic anisotropy*. In the rare-earth elements spin-orbit coupling in the $4f$-shell is of comparable magnitude as the Coulomb repulsion. There, taking spin-orbit coupling into account is mandatory.

3 Effects of the environment in the crystal

So far we have considered a single ion in vacuum. Clearly, one might ask if the results obtained in this limit retain any relevance once the ion is embedded into a solid and this will be discussed in the following. One may expect, however, that the small spatial extent of the $3d$ radial wave function $R_{3,2}(r)$ suppresses any effect of the environment in a solid, so that in many cases the main effect of embedding the ion into a solid is the partial splitting of the multiplets of the free ion.
In many transition-metal compounds the $3d$ ions are surrounded by an approximately octahedral or tetrahedral 'cage' of nonmetal ions such as Oxygen, Sulphur, Arsenic. These nearest neighbor ions, which will be called 'ligands' in the following, have a two-fold effect: first, they produce a static electric field, the so-called *crystalline electric field* or CEF, and second there may be *charge transfer*, that means electrons from a filled ligand orbital may tunnel into a $3d$-orbital of the transition-metal ion and back due to the overlap of the respective wave functions.

3.1 Crystalline electric field

The electric field that acts on a given ion in a solid may to simplest approximation be obtained by representing the other ions in the solid as point charges. The electrostatic potential $V_{CEF}(\boldsymbol{r})$

produced by these point charges around the nucleus in question then in principle can be obtained by using the multipole expansion (4). This results in an expression of the type

$$V_{CEF}(\boldsymbol{r}) \;=\; \sum_{l=0}^{\infty} \sum_{m=-l}^{l} C_{l,m}\, r^l\, Y_{l,m}(\vartheta,\varphi)$$

where the coefficients $C_{l,m}$ depend on the geometry of the crystal. Matrix elements of $V_{CEF}(\boldsymbol{r})$ between atomic eigenfunctions of the type (3) can be calculated by applying similar procedures as in the computation of the Coulomb matrix elements (and in particular again involve Gaunt coefficients).

However, such calculations often do not give very accurate numbers. For example, there will always be some charge transfer between the ions in the solid so that it is difficult to decide which charge should be assigned to a given ion. Moreover, the calculation of matrix elements involves a radial integral over the wave function $R_{n,l}(r)$ which is not really well known. Therefore, we give a qualitative discussion based on symmetry.

Let α be some symmetry operation, i.e. a coordinate transformation represented by a unitary 3×3 matrix m_α, that leaves the environment of the ion in question invariant. In other words, the transition-metal ion itself must be transformed into itself whereas every other ion must be transformed into an ion of the same species. Then we define for any function of the coordinates $f(\boldsymbol{r})$ the operator $T_\alpha f(\boldsymbol{r}) = f(m_\alpha^{-1}\boldsymbol{r})$. Thus, if we want to know the value of $T_\alpha f(\boldsymbol{r})$ at some given point $\boldsymbol{r}$, we can look it up by evaluating the original function $f(\boldsymbol{r})$ at the point $\boldsymbol{r}' = m_\alpha^{-1}\boldsymbol{r}$ which is transformed into $\boldsymbol{r}$ by the operation α. In other words, if we imagine functions of $\boldsymbol{r}$ to be represented by color maps in real space, the map of $T_\alpha f(\boldsymbol{r})$ is that of $f(\boldsymbol{r})$ but subject to the transformation α. Since the charge density of the environment is invariant under the allowed symmetry operations, the same holds true for its electrostatic potential $V_{CEF}(\boldsymbol{r})$ so that $T_\alpha\; V_{CEF}(\boldsymbol{r}) = V_{CEF}(\boldsymbol{r})$. It follows that the Hamiltonian $\tilde{H} = H_{ion} + V_{CEF}(\boldsymbol{r})$ (where H_{ion} is the sum of the nuclear potential of the transition-metal ion, the kinetic energy of the electrons and their Coulomb interaction) commutes with T_α. It is then straightforward to show that if $\psi(\boldsymbol{r})$ is an eigenstate of $\tilde{H}$ with energy E, $\tilde{H}\;\psi(\boldsymbol{r}) = E\;\psi(\boldsymbol{r})$, the transformed function $T_\alpha\;\psi(\boldsymbol{r})$ is an eigenstate to the same energy:

$$[\tilde{H}, T_\alpha]\psi(\boldsymbol{r}) = 0 \quad \Rightarrow \quad \tilde{H}\;(T_\alpha\psi(\boldsymbol{r})) = T_\alpha E\;\psi(\boldsymbol{r}) = E\;(T_\alpha\psi(\boldsymbol{r})).$$

We can thus investigate to what degree the degeneracy of the five $3d$-orbitals is lifted in a given environment by systematically studying which (combinations of) $3d$-orbitals are transformed into each other by the symmetry operations which leave the environment invariant. For the general case this can be done by invoking the very elegant mathematical formalism of group theory [6, 9]. On the other hand, for an environment with cubic symmetry a simple shortcut is possible. Namely all 48 cubic symmetry operations can be expressed as the product of one of the 6 permutations of the 3 coordinate axis and one of the $2^3 = 8$ transformations which change the signs of an arbitrary subset of the 3 coordinates. Moreover the d-like spherical harmonics $Y_{2,m}$ can be expressed as linear combinations of products of two of the three components of the

unit vector $\boldsymbol{r}/|\boldsymbol{r}|$, such as xy/r^2 or z^2/r^2. For example

$$Y_{2,2}(\vartheta,\varphi) \;=\; \frac{1}{\sqrt{4\pi}}\sqrt{\frac{15}{8}}\,\sin^2\vartheta\; e^{\,2i\varphi} = \frac{1}{\sqrt{4\pi}}\sqrt{\frac{15}{8}}\,\left(\frac{x^2-y^2}{r^2}+2i\,\frac{xy}{r^2}\right).$$

It is then obvious that under cubic operations mixed products such as xy/r^2 will be transformed into mixed products, whereas squares such as z^2/r^2 will be transformed into squares. Thus, if we form linear combinations of the spherical harmonics which consist exclusively of either mixed products or squares, we know that these two groups of linear combinations will remain degenerate in the cubic environment. In fact, the mixed products are precisely the three t_{2g}-orbitals

$$\begin{aligned} d_{xy} &= \frac{i}{\sqrt{2}}\,(Y_{2,-2}-Y_{2,2}) = \sqrt{\frac{15}{4\pi}}\,\frac{xy}{r^2}\,,\\ d_{yz} &= \frac{i}{\sqrt{2}}\,(Y_{2,-1}+Y_{2,1}) = \sqrt{\frac{15}{4\pi}}\,\frac{yz}{r^2}\,,\\ d_{xz} &= \frac{1}{\sqrt{2}}\,(Y_{2,-1}-Y_{2,1}) = \sqrt{\frac{15}{4\pi}}\,\frac{xz}{r^2}\,, \end{aligned} \tag{15}$$

whereas from the squares the two e_g-orbitals can be formed:

$$\begin{aligned} d_{x^2-y^2} &= \frac{1}{\sqrt{2}}\,(Y_{2,-2}+Y_{2,2}) = \sqrt{\frac{15}{16\pi}}\,\frac{x^2-y^2}{r^2}\,,\\ d_{3z^2-r^2} &= Y_{2,0} = \sqrt{\frac{5}{16\pi}}\,\frac{3z^2-r^2}{r^2}\,. \end{aligned} \tag{16}$$

There are only two e_g-orbitals because one special combination of the squares, namely r^2, is transformed into itself under all symmetry operations. In a cubic environment, the 5-fold degenerate d-level therefore *always* splits into the 3-fold degenerate t_{2g}-level and the 2-fold degenerate e_g-level. The energy difference between the two e_g- and the three t_{2g}-orbitals is called $10Dq$ for historical reasons. The above discussion can be summarized in the operator for the electrostatic potential of an environment with cubic symmetry:

$$H_{CEF} = C - 4Dq\sum_{\alpha\in t_{2g},\sigma} c^\dagger_{\alpha,\sigma}c_{\alpha,\sigma} + 6Dq\sum_{\alpha\in e_g,\sigma} c^\dagger_{\alpha,\sigma}c_{\alpha,\sigma}\,.$$

The constant C, which gives the center of gravity of the energies of the five orbitals, is largely irrelevant. By expressing the e_g and t_{2g} harmonics d_α in terms of the original $Y_{l=2,m}$ via (15) and (16) we can thus represent H_{CEF} as a quadratic form in the original $c^\dagger_\nu$-operators. This quadratic form involves the splitting $10Dq$ as a parameter, so that this way of dealing with the crystalline electric field is very similar in spirit to our treatment of the Coulomb interaction in that details of the radial wave functions $R_{n,l}(r)$ are absorbed into a parameter which may be adjusted to experiment. Alternatively, the numerical value of $10Dq$ for a given solid may also be obtained from a fit to an LDA band structure. By adding H_{CEF} to the Hamiltonian for the intra-atomic Coulomb interaction we can now discuss the splitting of the original multiplets of the free ion

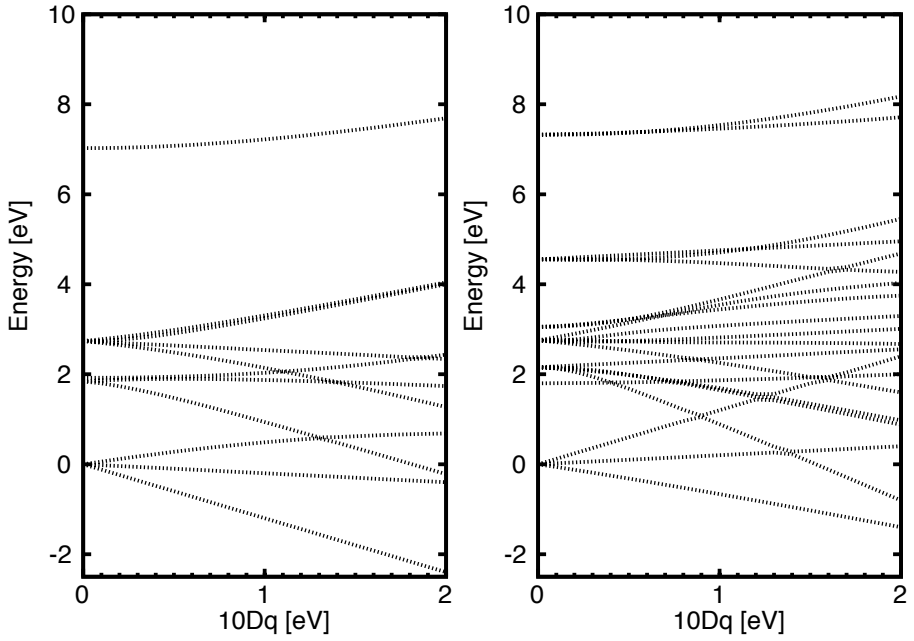

Fig. 3: *Examples for Tanabe-Sugano diagrams: the splitting of multiplets of d^8 (left) and d^7 (right) for increasing $10Dq$. The Slater-Condon parameters have the values given in Table 3.*

under the influence of the electrostatic potential of the environment. The following should be noted: the above discussion refers to the wave function of a *single electron*. The multiplets, however, are collective eigenstates of all n electrons in an atomic shell which are created by the Coulomb interaction between electrons. The question of how these collective states split in a cubic environment is not at all easy to answer. One way would be exact diagonalization including the term H_{CEF}. Plots of the energies of the resulting crystal-field multiplets versus $10Dq$ are called Tanabe-Sugano diagrams [10]. An example is shown in Figure 3.1 which shows the eigenenergies of the d^8 and d^7 configuration with Coulomb interaction and cubic CEF as $10Dq$ is increasing. One realizes that the highly degenerate multiplets of the free ion are split into several levels of lower degeneracy by the CEF, which is to be expected for a perturbation that lowers the symmetry. Note that the components into which a given multiplet splits up all have the same spin as the multiplet itself. This is because the spin of an electron does not feel an electrostatic potential — or, more precisely, because the operator of total spin commutes with any operator which acts only on the real-space coordinates $\boldsymbol{r}_i$ of the electrons.

An interesting example for the application of the Tanabe-Sugano diagrams are transition-metal ions in aqueous solution. In fact, the preference of transition-metal ions for an environment with cubic symmetry is so strong that such immersed ions often surround themselves with an octahedron of water molecules. Thereby the dipole moments of these six molecules all point away from the ion and thus create an electric field which cubic symmetry which again gives rise to the e_g-t_{2g} splitting. Optical transitions between the CEF-split multiplets, which are possible only due to slight distortions of the octahedron or the generation/annihilation of vibrational quanta during the transition, correspond to frequencies in the visible range and result in the charac-

teristic colors of such solutions. The Tanabe-Sugano diagrams have proved to be a powerful tool to understand the absorption spectra of such solutions [6]. By matching the energies of the observed transitions to energy differences in the Tanabe-Sugano diagrams one can extract estimates for the Slater-Condon parameters and for $10Dq$. The values of the Slater-Condon parameters are somewhat smaller than those for ions in vacuum due to dielectric screening in the solution. An independent estimate for $10Dq$ can also be extracted from measured heats of hydration (this is because both $10Dq$ and the electrostatic energy of the system 'ion plus octahedron' depend on the distance between the transition-metal ion and the water molecules) and compared to the estimate from the absorption spectrum whereby reasonable agreement is usually obtained [9].

3.2 Charge transfer

We proceed to a discussion of charge transfer. This means that electrons can tunnel from ligand orbitals into $3d$-orbitals, so that the number of electrons in the d-shell fluctuates. To deal with this we need to enlarge our set of Fermion operators $c^\dagger_\nu/c_\nu$ by operators $l^\dagger_\mu/l_\mu$ which create/annihilate electrons in orbitals centered on ligands. The compound index μ for the ligand operators also must include the index i of the ligand: $\mu = (i, n, l, m, \sigma)$. The Hamiltonian describing the charge transfer then would read

$$H_{kin} = \sum_{i,j} \Big(t_{\nu_i,\mu_j}\, c^\dagger_{\nu_i}\, l_{\mu_j} + H.c. \Big) + \sum_j \epsilon_{\mu_j}\, l^\dagger_{\mu_j}\, l_{\mu_j} + \sum_i \epsilon_{\nu_i}\, c^\dagger_{\nu_i}\, c_{\nu_i}\,. \tag{17}$$

The *hybridization integrals* t_{ν_i,μ_j,ν_j} may be expressed in terms of relatively few parameters by using the famous *Slater-Koster tables*, see the lecture by M. Foulkes [11] at this school. For example, if only the p-orbitals of the ligands are taken into account there are just two relevant parameters, $V_{pd\sigma}$ and $V_{pd\pi}$. Estimates for these may be obtained from fits to LDA band structures. If electrons are allowed to tunnel between d-shell and ligand orbitals the orbital energies ϵ_{μ_j} become relevant as well. Estimating the d-shell orbital energies from LDA calculations is tricky due to the *double counting problem*: the energies of the d-orbitals extracted from band structure calculations include the Hartree-potential, which is also included in the diagonal matrix elements of the Coulomb interaction and thus must be subtracted in some way.

We now specialize to the case where the ligands are oxygen ions which form an ideal octahedron with the transition-metal ion in the center of gravity of the octahedron. Retaining only the three oxygen $2p$-orbitals per ligand the total number of orbitals in this cluster would be $5 + 6 \cdot 3 = 23$ per spin direction which is far too big to be treated by exact diagonalization. However, the number of ligand orbitals can be reduced drastically if we note that for each of the real-valued transition-metal $3d$-orbitals $Y_\alpha(\vartheta, \varphi)$ there is precisely one linear combination of O $2p$-orbitals on the ligands, L_α, which hybridizes with it. The first term on the right-hand side of (17) then simplifies to

$$H_{hyb} = 2\, V_{pd\pi} \sum_{\alpha \in t_{2g}} \sum_\sigma \left(c^\dagger_{\alpha,\sigma}\, l_{\alpha\sigma} + H.c. \right) + \sqrt{3}\, V_{pd\sigma} \sum_{\alpha \in e_g} \sum_\sigma \left(c^\dagger_{\alpha,\sigma}\, l_{\alpha\sigma} + H.c. \right).$$

By inserting the unitary transformation (15) and (16) to transform to the original complex spherical harmonics this is easily included into the formalism. In the exact diagonalization program this means that the number of orbitals has to be doubled, because we have the five linear combinations L_α, each of which can accommodate an electron of either spin direction. This leads to a quite drastic increase in the dimension of the Hilbert space but using, e.g., the Lanczos algorithm, see e.g. Ref. [12], the problem still is tractable.

In constructing model-Hamiltonian-like descriptions of transition-metal compounds for which clusters containing several unit cells can be studied by exact diagonalization or quantum Monte Carlo, one can often find (approximate) analytical solutions by taking the limit of large $10Dq$. Then, one may restrict the basis to states where the numbers of electrons in the t_{2g} and e_g-orbitals are fixed. For example, for Ni^{2+} (i.e. d^8) in cubic symmetry one may assume that the six t_{2g}-orbitals always are completely filled. Then, one need to consider only the two electrons in the partially filled e_g level, resulting in a significant reduction of the number of possible basis states. Similarly, for early transition-metal compounds one often assumes that the e_g-orbitals are so high in energy that only the t_{2g}-orbitals need to be taken into account. Since it is the Coulomb interaction which reshuffles electrons between the five d-orbitals, the errors in these simplified models obviously are of order $F^2/10Dq$ or $F^4/10Dq$. In making such approximations it is advantageous to transform the Coulomb matrix elements (9) to real spherical harmonics. This is trivial, although tedious, because they are related by the unitary transformation (15), (16).

4 Cluster calculation of photoemission and X-ray absorption spectra

In the preceding section we have discussed the general formalism for exact diagonalization of a cluster consisting of a transition-metal ion and its nearest neighbor ions (ligands). Thereby the following terms were included into the Hamiltonian: the Coulomb repulsion between the electrons in the $3d$-shell, the electrostatic field produced by the other ions in the crystal, charge transfer between the ligands and the transition metal $3d$-orbitals and (possibly) the spin-orbit coupling in the $3d$-shell. By diagonalizing the resulting Hamilton matrix we can obtain the eigenfunctions $|\Psi_\nu\rangle$ and their energies E_ν and these can be used to simulate various experiments on transition-metal compounds such as electron spectroscopy, optical spectroscopy, electron spin resonance or inelastic neutron scattering. It has turned out that these simulations are in fact spectacularly successful. In many cases calculated spectra can be overlaid with experimental ones and agree peak by peak. Nowadays complete packages for such cluster simulations are available, and these are used routinely for the interpretation of, e.g., electron spectroscopy [13]. This shows in particular that the multiplets of the free ion, suitably modified by the effects of crystalline electric field and charge transfer, persist in the solid and thus are essential for a correct description of transition-metal compounds. In the following we want to explain this in more detail and consider photoelectron spectroscopy and X-ray absorption. In this lecture only a very cursory introduction can be given, there are however several excellent reviews on the

application of multiplet theory to the simulation of such experiments [14–16].
In a valence-band photoemission experiment electromagnetic radiation impinges on the sample which then emits electrons. This is nothing but the well-known photoeffect. Valence band photoemission means that the photoelectrons are ejected from states near the Fermi level so that to simplest approximation an ion in the solid undergoes the transition $d^n \rightarrow d^{n-1}$ (note that this ignores charge transfer, which in fact is quite essential!). What is measured is the current I of photoelectrons as a function of their kinetic energy E_{kin} and possibly the polar angles (ϑ, φ) relative to the crystallographic axes of the sample. Frequently one measures the angle-integrated spectrum, obtained by averaging over (ϑ, φ) or rather by measuring a polycrystalline sample. A further parameter, which strongly influences the shape of the spectrum $I(E_{kin})$, is the energy $h\nu$ of the incident photons. At sufficiently high $h\nu$ the photoionization cross-section for the transition-metal $3d$-orbitals is significantly larger than for the other orbitals in the solid so that the photoelectrons in fact are emitted almost exclusively from the $3d$-orbitals. This is often called XPS for X-ray photoemission spectroscopy.
The theory of the photoemission process is complicated [17, 18] but with a number of simplifying assumptions one can show that the photocurrent $I(E_{kin})$ measured in angle-integrated photoemission at high photon energy is proportional to the so-called single-particle spectral function

$$\begin{aligned} A(\omega) &= -\frac{1}{\pi Z}\Im \sum_{m=-2}^{2}\sum_{\mu} e^{-\beta E_\mu} \left\langle \Psi_\mu \left| c^\dagger_{3,2,m,\sigma} \, \frac{1}{\omega + (H - E_\mu) + i0^+} \, c_{3,2,m,\sigma} \right| \Psi_\mu \right\rangle \\ &= \frac{1}{Z} \sum_{m=-2}^{2}\sum_{\mu,\nu} e^{-\beta E_\mu} \left| \langle \Psi_\nu | c_{3,2,m,\sigma} | \Psi_\mu \rangle \right|^2 \delta(\omega + (E_\nu - E_\mu)). \end{aligned} \tag{18}$$

Here H is the Hamiltonian describing the solid, $|\Psi_\mu\rangle$ and E_μ denote the eigenstates and eigenenergies of H with a fixed electron number N_e. Moreover, $\beta = (k_B T)^{-1}$ with k_B the Boltzmann constant and T the temperature, and $Z = \sum_\mu \exp(-\beta E_\mu)$. The operator $c_{3,2,m,\sigma}$ removes an electron from a $3d$-orbital. In the thermodynamical limit the results will not depend on the position of the ion in the sample and accordingly we have suppressed the site index on $c_{3,2,m,\sigma}$. After removal of the electron the sample then remains in an eigenstate $|\Psi_\nu\rangle$ with $N_e - 1$ electrons and energy E_ν. The relation between E_{kin} and ω follows from energy conservation:

$$h\nu + E_\mu = E_{kin} + \Phi + E_\nu$$

The left- and right-hand sides of this equation are the energies of the system before (solid + photon) and after (solid + photoelectron) the photoemission process. Thereby Φ is the so-called work function, i.e., the energy needed to transverse the potential barrier at the surface of the solid (this needs to be introduced because the measured kinetic energy E_{kin} is the one *in vacuo*). It follows from the δ-function in the second line of (18) that we have to put $I(E_{kin}) \propto A(E_{kin} + \Phi - h\nu)$.
We now make an approximation, introduced by Fujimori and Minami [19], and evaluate $A(\omega)$ by replacing the energies and wave functions of the solid by those of the octahedral cluster. If

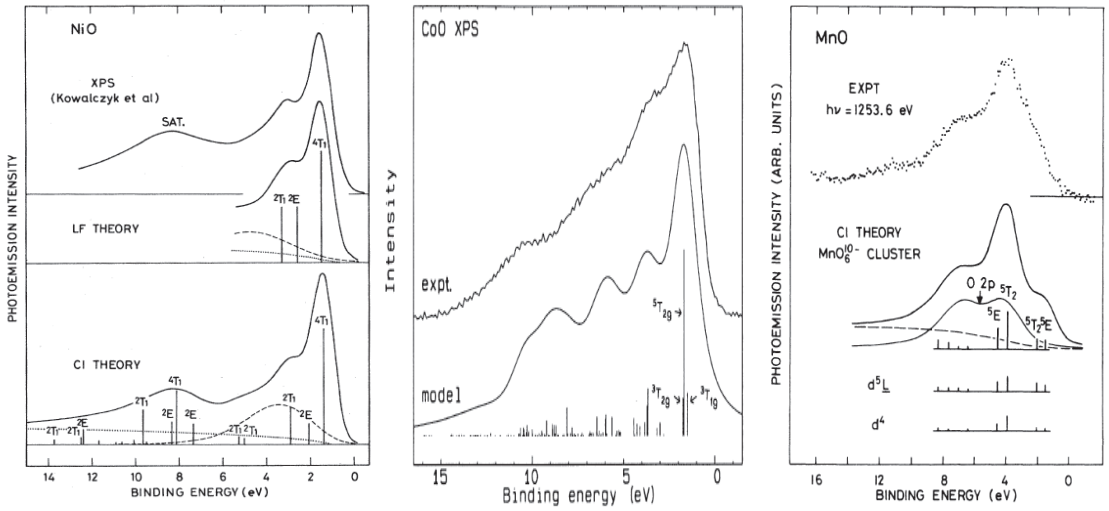

Fig. 4: *Comparison of experimental valence band photoemission spectra and results from cluster calculations: NiO (left), CoO(center), MnO(right). Reprinted with permission from [19], Copyright 1984 by the American Physical society, from [20], Copyright 1991 by the American Physical society, and from [21], Copyright 1990 by the American Physical society.*

we moreover let $T \to 0$ the sum over μ becomes a sum over the m degenerate ground states of the cluster and $e^{-\beta E_\mu}/Z \to 1/m$. The underlying assumption is that the coupling of the clusters to its environment in the solid will predominantly broaden the ionization states of the cluster into bands of not too large bandwidth. This broadening is usually simulated by replacing the δ-functions by Lorentzians. To compare to a measured spectrum, the calculated spectrum often is convoluted with a Gaussian to simulate the finite energy resolution of the photoelectron detector.

Figure 4 shows various examples from the literature where measured XPS-spectra are compared to spectra calculated by the procedure outlined above. The sticks in some of the theoretical spectra mark the final state energies E_ν and are labeled by the symbols of the irreducible representation of the octahedral group to which the corresponding final state wave function $|\Psi_\nu\rangle$ belongs. The figure shows that the agreement between the theoretical spectra and experiment is usually rather good. It is interesting to note that the three oxides shown in the figure all have the same crystal structure, namely the rocksalt structure. Since moreover Ni, Co and Mn are close neighbors in the periodic table, LDA predicts almost identical band structures with the main difference being an upward shift of the chemical potential with increasing nuclear charge of the transition metal. Despite this, the XPS spectra differ considerably and this change is reproduced very well by the theoretical spectra. This is clear evidence that the shape of the spectra is determined not so much by the single particle band structure, but by the multiplet structure of the transition-metal ion, which in turn depends on its valence and spin state.

How then does the multiplet structure determine the photoelectron spectrum? As mentioned above, if we neglect charge transfer, photoemission corresponds to the transition from the ground state of d^n, i.e. the lowest state in the Tanabe-Sugano diagram for the respective n, to some eigenstate of d^{n-1}. This final state, however, is nothing but some state in the Tanabe-

Sugano diagram for d^{n-1}. Moreover, if the ground state of d^n has spin S, the final state must have spin $S \pm \frac{1}{2}$ so that the number of possible final states is significantly restricted. In this way, the photoemission spectrum will contain relatively few sharp lines whose positions are determined by the energies of the multiplets.

Next, we discuss X-ray absorption. In an X-ray absorption experiment an electron from either the $2p$- or the $3p$-shell absorbs an incoming X-ray photon and is promoted to the $3d$-shell via a dipole transition. In terms of electron configurations, the transition thus is $2p^6 3d^n \to 2p^5 3d^{n+1}$ (for definiteness we will always talk about the $2p$-shell from now on). Of particular interest here is the range of photon energies just above the threshold were the energy of the photon is sufficient to lift the core electron to an unoccupied state. Above this threshold the X-ray absorption coefficient $\kappa(\omega)$ rises sharply, which is called an absorption edge. The energy of the edge thereby is characteristic for a given element so that one can determine unambiguously which atom in a complex solid or molecule is probed. The ω-dependence of $\kappa(\omega)$ in an energy range of a few eV above the absorption edge, called NEXAFS for Near Edge X-ray Absorption Fine Structure, contains information about the initial state of the $3d$-shell, i.e., its valence and spin state, and this information can be extracted by using cluster calculations. The measured quantity in this case is

$$\begin{aligned}\kappa(\omega) &= -\frac{1}{\pi Z}\,\Im \sum_{m=-2}^{2}\sum_{\mu} e^{-\beta E_\mu} \left\langle \Psi_\mu \middle| D(\boldsymbol{n})\, \frac{1}{\omega - (H - E_\mu) + i0^+} D(\boldsymbol{n}) \middle| \Psi_\mu \right\rangle \\ &= \frac{1}{Z} \sum_{m=-2}^{2}\sum_{\mu,\nu} e^{-\beta E_\mu} \left|\langle \Psi_\nu | D(\boldsymbol{n}) | \Psi_\mu \rangle\right|^2 \delta(\omega - (E_\nu - E_\mu)). \end{aligned} \tag{19}$$

This is very similar to the single-particle spectral function (18), the only difference is that now the dipole operator $D(\boldsymbol{n})$ appears in place of the electron annihilation operator $c_{3,2,m,\sigma}$. This also implies that the number of electrons in the final states $|\Psi_\nu\rangle$ now is equal to that in the initial states $|\Psi_\mu\rangle$.

We again make the approximation to use the octahedral cluster to simulate this experiment. The initial state for this experiment, $2p^6 3d^n$, is simply the ground state of the cluster. More difficult is the final state, $2p^5 3d^{n+1}$. This has a hole in the $2p$-shell so that the single-particle basis has to be enlarged once more to comprise also the 6 spin-orbitals available for $2p$ electrons. We may restrict the basis, however, to include only states with 5 electrons (or 1 hole) in these 6 spin-orbitals, so that the dimension of the Hilbert space increases only by a moderate factor of 6. The spin-orbit coupling constant $J_{SO,2p}$ in the $2p$-shell of $3d$ transition-metals is of order 10 eV so we definitely need to include spin-orbit coupling in the $2p$-shell. Here the forms (13) and (14) with $l = 1$ can be used. The orbital angular momentum $l = 1$ and the spin of $\frac{1}{2}$ can be coupled to a total angular momentum of either $J = \frac{3}{2}$ or $J = \frac{1}{2}$. Using the identity

$$\langle \boldsymbol{L} \cdot \boldsymbol{S} \rangle = \frac{1}{2}\Big(J(J+1) - L(L+1) - S(S+1) \Big)$$

we expect a splitting of $E_{\frac{3}{2}} - E_{\frac{1}{2}} = \frac{\lambda_{SO}}{2}(\frac{15}{4} - \frac{3}{4}) = \frac{3\lambda_{SO}}{2}$. This means that we actually have two edges, separated by $\frac{3\lambda_{SO}}{2} \approx 10 - 15$ eV for $2p$ core levels. The one for lower photon energy,

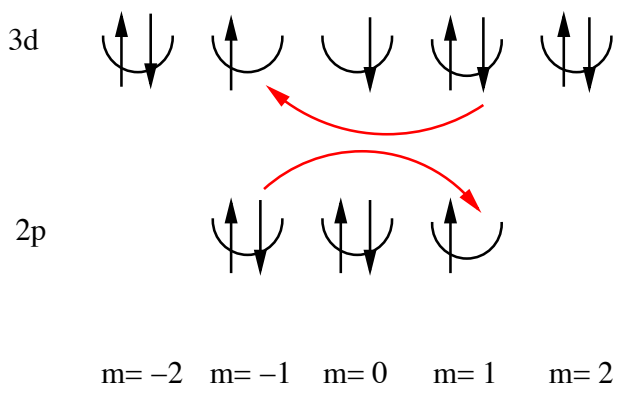

Fig. 5: *An electron in the $3d$-shell and an electron in the $2p$-shell scatter from one another.*

called the L_3 edge, is due to electrons coming from $^2P_{3/2}$, the one for higher photon energy (L_2-edge) due to electrons from $^2P_{1/2}$. Since there are 4 $^2P_{3/2}$ states but only 2 $^2P_{1/2}$ states the L_3 edge has roughly twice the intensity of the L_2 edge.
Next, there is the Coulomb interaction between the core-hole and the electrons in the d-shell. For example, there may now be Coulomb scattering between a $2p$ and a $3d$ electron as shown in Figure 5.
This, however, is again described by the corresponding Coulomb matrix element (9). Here now one of the indices ν_1 and ν_2 and one of the indices ν_3 and ν_4 must refer to the $2p$-orbital and there are two possible combinations. If ν_2 and ν_3 refer to the $2p$-orbital we have

$$\sum_k c^k(2, m_1; 2, m_4)\, c^k(1, m_3; 1, m_2)\; F^k(3, 2; 2, 1)\,.$$

The triangular condition for $c^k(1, m_3; 1, m_2)$ requires $k \leq 2$. Since only Y_{lm} with equal l and hence with equal parity are combined in one c^k only even k give nonvanishing contributions and we have two relevant Coulomb integrals, $F^0(2, 3; 2, 1)$ and $F^2(2, 3; 2, 1)$.
If ν_2 and ν_4 refer to the $2p$-orbital we have

$$\sum_k\; c^k(2, m_1; 1, m_4)\; c^k(2, m_3; 1, m_2) G^k(3, 2; 2, 1).$$

The triangular condition for both c^k requires $k \leq 3$. Since now Y_{1m} and Y_{2m} are combined in one Gaunt coefficient only odd k contribute, so that we have two relevant exchange integrals, $G^1(3, 2; 2, 1)$ and $G^3(3, 2; 2, 1)$. Apart from these minor changes, the implementation of the d-p Coulomb interaction is exactly the same as for the d-d interaction.
The Coulomb interaction between electrons in the $2p$-shell is definitely very strong, but it is irrelevant because we are considering only states with a *single hole* in this shell. Since this hole has no second hole to scatter from, the only effect of the Coulomb repulsion between electrons in the $2p$-shell is via the diagonal matrix elements which give a shift of the orbitals energy ϵ_{2p}. On the other hand ϵ_{2p} merely enters the position of the absorption edge, which would be $\approx \epsilon_{3d} - \epsilon_{2p}$, but not its spectral shape. Since we are not really interested in computing the onset of the edge, the precise value of ϵ_{2p} and hence the Coulomb interaction between $2p$ electrons is not important. The CEF effect on the inner shell electrons is usually neglected.

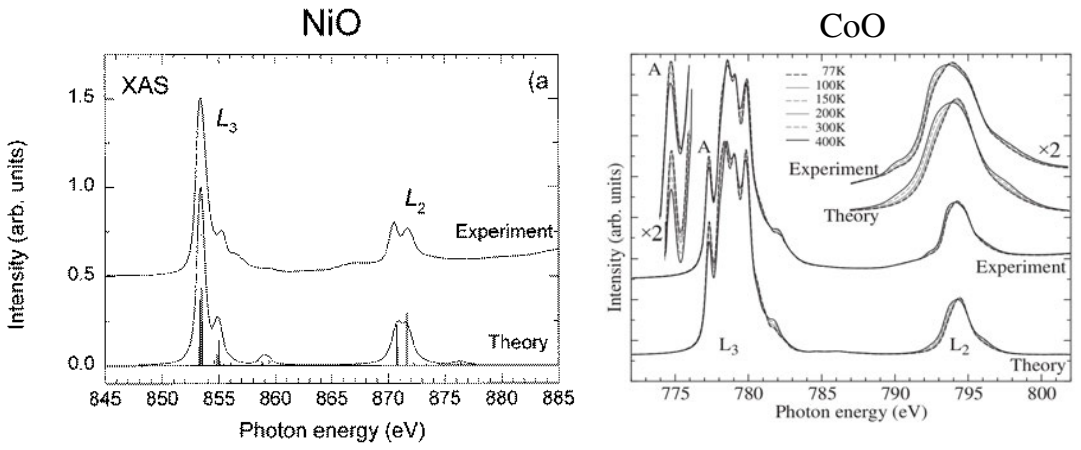

Fig. 6: *Comparison of experimental $2p$ XAS-spectra and results from cluster calculations: NiO (left) and CoO (right). Reprinted with permission from [22], Copyright 1999 by the American Physical society, and with permission from [23].*

Lastly, we discuss the dipole operator $D(\boldsymbol{n})$. This involves the matrix element of $\boldsymbol{n} \cdot \boldsymbol{r}$, where $\boldsymbol{n}$ is the vector which gives the polarization of the X-rays. This can be rewritten as

$$\boldsymbol{n} \cdot \boldsymbol{r} \;=\; r \sqrt{\frac{4\pi}{3}} \sum_{m=-1}^{1} \tilde{n}_m \, Y_{1,m}(\vartheta, \varphi) \,,$$

where $\tilde{n}_1 = (-n_x + i n_y)/\sqrt{2}$, $\tilde{n}_0 = n_z$ and $\tilde{n}_{-1} = (n_x + i n_y)/\sqrt{2}$. It follows that

$$\begin{aligned} O(\boldsymbol{n}) &= \sum_{m,m'} \sum_{\sigma} d_{m,m'} \; c^{\dagger}_{3,2,m,\sigma} \, c_{2,1,m',\sigma} \\ d_{m,m'}(\boldsymbol{n}) &= d \; \tilde{n}_{m-m'} \; c^1(2,m;1,m') \\ d &= \int_0^{\infty} dr \, r^3 \, R_{3,2}(r) \, R_{2,1}(r) \,. \end{aligned}$$

The factor of d merely scales the overall intensity of the spectrum and is largely irrelevant. Combining all of the above one can compute X-ray absorption spectra. Figure 6 shows examples from the literature where experimental $2p$-XAS spectra for NiO and CoO are compared to spectra obtained from the cluster model described above. In both cases one can see the splitting of approximately 15 eV between the L_3 and L_2 edges. The edges have an appreciable fine structure, however, which is reproduced well by theory. The spectrum for CoO is shown at different temperatures and indeed has a significant temperature dependence. The origin of the temperature dependence is as follows: Cobalt is Co^{2+} or d^7 in CoO and the ground state of d^7 in cubic symmetry is a spin quartet and is orbitally three-fold degenerate so that the total degeneracy is $n = 12$. In this situation, the weak spin-orbit interaction in the $3d$-shell can lift the 12-fold degeneracy and produce several closely spaced eigenstates. The splitting between these 12 eigenstates is of the order of the spin-orbit coupling constant in the $3d$-shell, $\lambda_{SO} \approx 50$ meV, and the higher lying states therefore may be thermally populated with increasing temperature (see the Boltzmann factors in (19)). This leads to the temperature dependence of the spectra which obviously is reproduced at least qualitatively by the cluster calculation.

XPS and XAS experiments are often performed because for example the valence or the spin state of the transition-metal ion in a given solid or molecule is unknown. Let us assume that we have two possible states of the ion, $|\Psi_0\rangle$ and $|\Psi_0'\rangle$, with energies E_0 and E_0' (for simplicity we assume that these are nondegenerate). Then we may ask: how will the spectrum change if we go from one ground state to the another? We note first that the final states $|\Psi_\nu\rangle$ and their energies E_ν in (18) and (19) are unchanged. What differs is first the energy differences $E_\nu - E_0$. However, since we do not know E_0 and E_0', otherwise we would know which one of them is lower in energy and hence the ground state, the absolute position of the peaks in the spectrum is of no significance. What is really relevant is the *intensity* of the peaks which involves the matrix elements $|\langle\Psi_\nu|c|\Psi_0\rangle|^2$ or $|\langle\Psi_\nu|D(\boldsymbol{n})|\Psi_0\rangle|^2$. These matrix elements may change drastically when the ground state wave function $|\Psi_0\rangle$ changes and by comparing with cluster simulations the shape of the spectrum can give information about the valence and spin state of the transition-metal ion.
To summarize this section: multiplet theory is of considerable importance in the interpretation of photoelectron spectroscopy and X-ray absorption. The simulated spectra usually show very good agreement with experimental ones. All of this shows that the multiplets of the free ion persist in the solid and that the proper description of the Coulomb interaction is crucial for the description of these compounds.

5 Conclusion

We have seen that the Coulomb repulsion between electrons in partially filled atomic shells leads to multiplet splitting. The multiplets may be viewed as collective excitations of the 'not-so-many-body-system' formed by the electrons in a partially filled atomic shell. We have seen that a relatively simple theory, essentially degenerate first order perturbation theory, describes the energies of the multiplets quite well and gives a good description of the line spectra of free atoms. When transition-metal atoms are embedded into a solid, the collective excitations of the electrons in their partly filled $3d$-shells are modified by the crystalline electric field of their environment and by hybridization with orbitals on neighboring atoms. If these effects are taken into account, which is relatively easy if one uses exact diagonalization, the resulting 'extended multiplet theory' turns out to be spectacularly successful in reproducing a wide variety of experimental results for transition-metal compounds. Photoemission spectra, X-ray absorption spectra, optical absorption spectra, electron spin resonance, and inelastic neutron scattering can be interpreted in terms of multiplet theory. The often excellent agreement between theory and experiment which can be thereby obtained is clear evidence that the multiplets of the free ion are a reality also in solids, with the only modification being some additional splitting due to the lowering of the symmetry and the modification of spectral intensities due to charge transfer. It has to be kept in mind, however, that in order to obtain agreement with experiment it is crucial to use the full Coulomb Hamiltonian, with its matrix elements expressed in terms of Slater-Condon parameters and Gaunt coefficients. Put another way, we may summarize the present lecture in three words: Multiplets do matter!

A Gaunt coefficients

m	m'	c^0	$7\,c^2$	$21\,c^4$	a^0	$49\,a^2$	$441\,a^4$	b^0	$49\,b^2$	$441\,b^4$
±2	±2	1	-2	1	1	4	1	1	4	1
±2	±1	0	$\sqrt{6}$	$-\sqrt{5}$	1	-2	-4	0	6	5
±2	0	0	-2	$\sqrt{15}$	1	-4	6	0	4	15
±1	±1	1	1	-4	1	1	16	1	1	16
±1	0	0	1	$\sqrt{30}$	1	2	-24	0	1	30
0	0	1	2	6	1	4	26	1	4	36
±2	∓2	0	0	$\sqrt{70}$	1	4	1	0	0	70
±2	∓1	0	0	$-\sqrt{35}$	1	-2	-4	0	0	35
±1	∓1	0	$-\sqrt{6}$	$-\sqrt{40}$	1	1	16	0	6	40

Table 5: *The Gaunt coefficients* $c^k(2,m;2,m')$ *and the products* $a^k(2,m;2,m')$ *and* $b^k(2,m;2,m')$

References

[1] J.H. de Boer and E.J.W. Verwey, Proc. Phys. Soc. London 49, 59 (1937)

[2] Yu. Ralchenko, A.E. Kramida, J. Reader, and NIST ASD Team (2011)
NIST Atomic Spectra Database (ver. 4.1.0): `http://physics.nist.gov/asd`

[3] L.D. Landau and E.M. Lifshitz: *Course of Theoretical Physics*
(Pergamon Press, Oxford New York, 1977)

[4] A.L. Fetter and J.D. Walecka: *Quantum Theory of Many Particle Systems*
(McGraw-Hill, San Francisco, 1971)

[5] J.C. Slater: *Quantum Theory of Atomic Structure*
(McGraw-Hill, New York, 1960)

[6] J.S. Griffith: *The Theory of Transition Metal Ions*
(Cambridge University Press, Cambridge, 1961)

[7] V.I. Anisimov, I.V. Solovyev, M.A. Korotin, M.T. Czyzyk, and G.A. Sawatzky,
Phys. Rev. B **48** (1993)

[8] J. Kunes, V.I. Anisimov, A.V. Lukoyanov, and D. Vollhardt
Phys. Rev. B **75**, 165115 (2007)

[9] B.N. Figgis: *Introduction to Ligand Fields*
(Interscience Publishers, New York London Sydney, 1966)

[10] S. Sugano, Y. Tanabe, and H. Kitamura: *Multiplets of Transition Metal Ions*
(Academic Press, New York 1970)

[11] M. Foulkes, lecture at this school

[12] E. Koch in *Many-Body Physics: From Kondo to Hubbard*
Reihe Modeling and Simulation, Vol. 5 (Forschungszentrum Jülich, 2015)
`http://www.cond-mat.de/events/correl15`

[13] See e.g. the CTM4XAS package:
`http://www.anorg.chem.uu.nl/CTM4XAS/index.html`

[14] F.M.F. de Groot, Journal of Electron Spectroscopy and Related Phenomena, **67** 525 (1994)

[15] F.M.F. de Groot, Coordination Chemistry Reviews, **249** 31 (2005)

[16] F.M.F. de Groot and A. Kotani: *Core Level Spectroscopy of Solids*
(Taylor And Francis, Abingdon on Thames, 2008)

[17] C. Caroli, D. Lederer-Rozenblatt, B. Roulet, and D. Saint-James, Phys. Rev. B **8**, 4552 (1973)

[18] P.J. Feibelman and D.E. Eastman, Phys. Rev. B **10**, 4932 (1974)

[19] A. Fujimori and F. Minami, Phys. Rev. B **30**, 957 (1984)

[20] J. van Elp, J.L. Wieland, H. Eskes, P. Kuiper, G.A. Sawatzky, F.M.F. de Groot, and T.S. Turner, Phys. Rev. B **44**, 6090 (1991)

[21] A. Fujimori, N. Kimizuka, T. Akahane, T. Chiba, S. Kimura, F. Minami, K. Siratori, M. Taniguchi, S. Ogawa, and S. Suga, Phys. Rev. B **42**, 7580 (1990)

[22] M. Finazzi, N.B. Brookes, and F.M.F. de Groot, Phys. Rev. B **59**, 9933 (1999)

[23] M. Haverkort, PhD Thesis (Universität zu Köln, 2005, see also arXiv:cond-mat/0505214)

6 Multi-Orbital Cluster Perturbation Theory for Transition-Metal Oxides

Franca Manghi
Dipartimento di Fisica, Informatica e Matematica
University of Modena and Reggio Emilia, Italy

Contents

E. Pavarini, E. Koch, J. van den Brink, and G. Sawatzky (eds.)
Quantum Materials: Experiments and Theory
Modeling and Simulation Vol. 6
Forschungszentrum Jülich, 2016, ISBN 978-3-95806-159-0
http://www.cond-mat.de/events/correl16

1 Introduction

Electrons in solids behave in most cases like independent particles, and that in spite of the strong interactions between them. The explanation of this apparent paradox relies on the concept of the Landau quasi-particle: the multiple forces acting on one electron dress it up with an interaction cloud and these new dressed particles (quasi-particles) are effectively independent one from the other. The time evolution of the system with one electron removed is what is measured in experiments and when this state evolves as a coherent superposition of oscillations of approximately the same frequency it corresponds to the propagation of a quasi-particle with a reasonably well defined energy and a sufficiently long life-time. In this situation the low-energy excitations of the interacting electrons can be put into a one-to-one correspondence with those of non-interacting electrons with renormalized properties (energy and mass) and the measured spectra can be reduced to a quasi-particle band structure.

From a theoretical point of view, the simplest way to account for the electron-electron interaction is to include it as a mean field, where each electron moves independently under the influence of the average charge distribution of all the others. Materials for which this rudimentary mean-field description is sufficient have broad energy bands associated with large values of the electron kinetic energy. This implies that the electrons are highly itinerant and therefore it is reasonable to describe them using a picture in which interactions become smooth and can be averaged over. On the contrary when bands are narrower and the associated kinetic energy smaller, namely when electrons tend to localize around lattice ions, they see each other as individual point charges and the correlation between their motion becomes important. For these systems the single-particle picture is inadequate and their electronic properties have to be described including the multiple pair-wise e-e interaction as a true many-body term.

Strongly correlated electron systems have been one of the most important topics in theoretical solid state research for more than half a century. The major challenge is that the interesting physics occurs in the regime of intermediate coupling strength, where perturbation theory does not apply. The search for non perturbative approaches has been intense in the last decades, leading to some widely accepted results, the most prominent one being the choice of the Hubbard model as the general framework to describe strong e-e correlation.

A variety of non-perturbative techniques have been proposed during the years to tackle this problem, ranging from Dynamical Mean Field Theory (DMFT) [1] to 3-Body Scattering (3BS) theory [2, 3]. However the agreement between experiments and many-body calculations is still far from being fully quantitative [4–6] and different theoretical methods are constantly explored.

Recently schemes based on cluster formalisms have been developed. These so-called Quantum Cluster (QC) theories [7] share the basic idea to solve the problem of many interacting electrons in an extended lattice by a *divide-and-conquer* strategy, namely solving first the many-body problem in a subsystem of finite size and then embedding it within the infinite medium. The embedding procedure can be variationally optimized as in the Dynamical Cluster Approach (DCA) [8] and Cellular Dynamical Mean Field Theory (CDMFT) [9]. Even neglecting optimization in the embedding procedure the method, that in this case has been called Cluster

Perturbation Theory (CPT) [10], gives access to non trivial many-body effects, reproducing exactly both the non-interacting band limit and the atomic limit when on-site repulsion exceeds intersite hopping; for intermediate values of on-site e-e repulsion CPT opens a gap in metallic systems at half occupation. QC approaches account for the momentum dependence of many-body corrections more appropriately than other schemes, and for this reason they should provide a more accurate description of the quasi-particle dispersion. However QC approaches have been mostly applied to model systems and only few quasi-particle calculations for realistic systems have been reported up to now [11, 12]. The application of CPT to multi-orbital solids and to transition-metal oxides in particular will be our focus.

2 CPT for multiorbital systems

In CPT the lattice is seen as a periodic repetition of identical clusters and the Hubbard Hamiltonian can be partitioned in two terms, an intra-cluster ($\hat{H}_c$) and an inter-cluster one ($\hat{V}$)

$$\hat{H} = \hat{H}_c + \hat{V}\,, \tag{1}$$

where

$$\begin{aligned} \hat{H}_c &= \sum_{il\alpha} \varepsilon_{il\alpha}\, \hat{n}_{il\alpha} + \sum_{\alpha\beta}\sum_{ijl} t_{il\alpha,jl\beta}\, \hat{c}^{\dagger}_{il\alpha}\hat{c}_{jl\beta} + \sum_{il\alpha\beta} U^{i}_{\alpha\beta}\, \hat{n}_{il\alpha\uparrow}\hat{n}_{il\beta\downarrow} \\ \hat{V} &= \sum_{\alpha\beta}\sum_{ij,l\neq l'} t_{il\alpha,jl'\beta}\, \hat{c}^{\dagger}_{il\alpha}\hat{c}_{jl'\beta}\,. \end{aligned} \tag{2}$$

Here α, β are orbital indices, $\varepsilon_{il\alpha}$ are intra-atomic orbital parameters and $t_{il\alpha,jl'\beta}$ hopping terms connecting orbitals centered on different sites. Each atom is identified by the cluster it belongs to (index l) and by its position inside the cluster (index i). The lattice is a collection of $L \to \infty$ clusters each of them containing M atoms whose position is identified by the vector $\mathbf{R}_l$+$\mathbf{r}_i$. Each atom in the cluster is characterized by a set of orbitals $n_i^{\rm orb}$ per site and $K = \sum_{i=1}^{M} n_i^{\rm orb}$ is the total number of orbitals per cluster.

Since in the Hubbard model the e-e Coulomb interaction is on-site, the inter-cluster Hamiltonian $\hat{V}$ contains only single-particle terms and the many-body part is present in the intra-cluster Hamiltonian $\hat{H}_c$ only. Of course the complexity of the problem resides in the coexistence of the two contributions, while in the two limits $t \gg U$ or $U \gg t$ the Hamiltonian can be easily solved: in the first case the many-body term is negligible and $\hat{H}$ is reduced to a trivial one-body Hamiltonian; the second case, the atomic limit, corresponds to $\hat{H} \simeq \hat{H}_c$, namely to a Hamiltonian that does not mix the coordinates of electrons belonging to different clusters. In this case the eigenstates $|\Psi_n^N\rangle$ of the full Hamiltonian for N electrons ($N =\to \infty$) becomes

$$|\Psi_n^N\rangle = |\Phi_n^N\rangle = \prod_{l=1}^{L\to\infty} |\phi_n^K(l)\rangle \tag{3}$$

where $|\phi_n^K(l)\rangle$ are the few-body eigenstates of the l-th isolated cluster that can be calculated numerically by exact diagonalization.

The partition of the Hamiltonian into intra-cluster and inter-cluster terms gives rise to some exact expressions and suggests some relevant approximations. Let us consider the resolvent operator $\hat{G}$

$$\hat{G}^{-1}(z) \equiv z - \hat{H}_c - \hat{V} = \hat{G^c}^{-1} - \hat{V} \quad \text{with} \quad \hat{G^c}^{-1} \equiv z - \hat{H}_c \tag{4}$$

and the Dyson-like equation that is deduced from it $\hat{G} = \hat{G^c} + \hat{G^c}\,\hat{V}\,\hat{G}$, where the lattice Green function and the cluster one are connected by the inter-cluster interaction. The expectation value of the resolvent operator over the interacting ground state with one removed/added particle, $\hat{c}_{\mathbf{k}n}|\Psi_0^N\rangle$ / $\hat{c}^\dagger_{\mathbf{k}n}|\Psi_0^N\rangle$, gives the one-particle propagator for the extended lattice

$$\mathcal{G}(\mathbf{k}n\omega) = \mathcal{G}^+(\mathbf{k}n\omega) + \mathcal{G}^-(\mathbf{k}n\omega) \tag{5}$$

with $\mathcal{G}^\pm(\mathbf{k}n\omega)$, the particle and hole propagators, given by

$$\begin{aligned} \mathcal{G}^-(\mathbf{k}n\omega) &= \langle\Psi_0^N|\,\hat{c}^\dagger_{\mathbf{k}n}\,\hat{G}(-\omega + E_0^N + i\eta)\,\hat{c}_{\mathbf{k}n}\,|\Psi_0^N\rangle \\ \mathcal{G}^+(\mathbf{k}n\omega) &= \langle\Psi_0^N|\,\hat{c}_{\mathbf{k}n}\,\hat{G}(\ \ \omega + E_0^N + i\eta)\,\hat{c}^\dagger_{\mathbf{k}n}\,|\Psi_0^N\rangle\,. \end{aligned} \tag{6}$$

Since we are looking for a relationship between the lattice and cluster Green function, it is useful to introduce a transformation from the localized to the Bloch basis

$$\hat{c}_{\mathbf{k}n} = \frac{1}{\sqrt{K\times L}}\sum_{il\alpha}\mathcal{C}^n_{i\alpha}(\mathbf{k})e^{i\mathbf{k}\cdot(\mathbf{R}_l+\mathbf{r}_i)}\,\hat{c}_{il\alpha} \quad \text{and} \quad \hat{c}^\dagger_{\mathbf{k}n} = \frac{1}{\sqrt{K\times L}}\sum_{il\alpha}\mathcal{C}^n_{i\alpha}(\mathbf{k})^* e^{-i\mathbf{k}\cdot(\mathbf{R}_l+\mathbf{r}_i)}\,\hat{c}^\dagger_{il\alpha},$$

where n is a band index and $\mathcal{C}^n_{i\alpha}(\mathbf{k})$ are the eigenstate coefficients obtained by a band calculation for a superlattice of L identical clusters. By straightforward substitutions we get

$$\mathcal{G}(\mathbf{k}n\omega) = \frac{1}{K}\sum_{ii'\alpha\beta} e^{-i\mathbf{k}\cdot(\mathbf{r}_i-\mathbf{r}_{i'})}\,\mathcal{C}^n_{i\alpha}(\mathbf{k})^*\mathcal{C}^n_{i'\beta}(\mathbf{k})\,\mathcal{G}_{i\alpha i'\beta}(\mathbf{k}\omega)\,, \tag{7}$$

where $\mathcal{G}_{i\alpha i'\beta}(\mathbf{k}\omega)$ is the superlattice Green function, namely the Fourier transform of the Green function in the local basis

$$\mathcal{G}_{i\alpha i'\beta}(\mathbf{k}\omega) = \frac{1}{L}\sum_{ll'} e^{-i\mathbf{k}\cdot(\mathbf{R}_l-\mathbf{R}_{l'})}\,\mathcal{G}_{\substack{i\alpha i'\beta\\ ll'}}(\omega) \tag{8}$$

and

$$\begin{aligned} \mathcal{G}_{\substack{i\alpha i'\beta\\ ll'}}(\omega) &= \left\langle\Psi_0^N\left|\hat{c}^\dagger_{il\alpha}\left(\hat{G^c}(\omega) + \hat{G^c}(\omega)\hat{V}\hat{G}(\omega)\right)\hat{c}_{i'l'\beta}\right|\Psi_0^N\right\rangle \\ &\quad + \left\langle\Psi_0^N\left|\hat{c}_{il\alpha}\left(\hat{G^c}(\omega) + \hat{G^c}(\omega)\hat{V}\hat{G}(\omega)\right)\hat{c}^\dagger_{i'l'\beta}\right|\Psi_0^N\right\rangle. \end{aligned} \tag{9}$$

All the equations written up to now are exact and approximations are needed in order to make them of practical use. CPT introduces two approximations:

1) $|\Psi_0^N\rangle \sim |\Phi_0^N\rangle$

2) $\sum_m |\Phi_m^{N-1}\rangle\langle\Phi_m^{N-1}| \sim \sum_{il\alpha}\hat{c}_{il\alpha}\,|\Phi_0^N\rangle\langle\Phi_0^N|\,\hat{c}^\dagger_{il\alpha} = 1$
$\sum_m |\Phi_m^{N+1}\rangle\langle\Phi_m^{N+1}| \sim \sum_{il\alpha}\hat{c}^\dagger_{il\alpha}\,|\Phi_0^N\rangle\langle\Phi_0^N|\,\hat{c}_{il\alpha} = 1$

The first one substitutes the unknown ground state $|\Psi_0^N\rangle$ of the full interacting Hamiltonian with $|\Phi_0^N\rangle$, the ground state of $\hat{H}_c$ defined in Eq. (3). As mentioned above, this choice is fairly accurate in the regime of $U/t > 1$ and less correct in the opposite limit. The second assumption corresponds to an approximate expression of the decomposition of unity in terms of a reduced basis for the Fock space of $N \pm 1$ particles.
Altogether we obtain for the total (causal) Green function

$$\begin{aligned}
\underset{ll'}{\mathcal{G}_{i\alpha i'\beta}(\omega)} &= \langle\phi_0^K|\hat{c}_{il\alpha}^\dagger\,\hat{G}^c\,\hat{c}_{i'l'\beta}|\phi_0^K\rangle\,\delta_{ll'} + \langle\phi_0^K|\hat{c}_{il\alpha}\,\hat{G}^c\,\hat{c}_{i'l'\beta}^\dagger|\phi_0^K\rangle\,\delta_{ll'} \\
&\quad + \sum_{l''l'''}\sum_{i''i'''}\sum_{\gamma\gamma'}\Big[\langle\Phi_0^N|\hat{c}_{il\alpha}^\dagger\,\hat{G}^c\,\hat{c}_{i''l''\gamma}|\Phi_0^N\rangle\,\delta_{l''l} + \langle\Phi_0^N|\hat{c}_{il\alpha}\,\hat{G}^c\,\hat{c}_{i''l''\gamma}^\dagger|\Phi_0^N\rangle\,\delta_{l''l}\Big] \\
&\qquad\qquad \times \langle\Phi_0^N|\hat{c}_{i''l''\gamma}^\dagger\,\hat{V}\,\hat{c}_{i'''l'''\gamma'}|\Phi_0^N\rangle\langle\Phi_0^N|\hat{c}_{i'''l'''\gamma'}^\dagger\,\hat{G}\,\hat{c}_{i'l'\beta}|\Phi_0^N\rangle \\
&= \mathcal{G}^c_{i\alpha i'\beta}(\omega)\,\delta_{ll'} \\
&\quad + \sum_{l''l'''}\sum_{i''i'''}\sum_{\gamma\gamma'}\mathcal{G}^c_{i\alpha i'\beta}(\omega)\,\delta_{ll'}\,\langle\Phi_0^N|\hat{c}_{i''l''\gamma}^\dagger\,\hat{V}\,\hat{c}_{i'''l'''\gamma'}|\Phi_0^N\rangle\langle\Phi_0^N|\hat{c}_{i'''l'''\gamma'}^\dagger\,\hat{G}\,\hat{c}_{i'l'\beta}|\Phi_0^N\rangle\,,
\end{aligned} \tag{10}$$

where $\mathcal{G}^c_{i\alpha i'\beta}(\omega) = \langle\Phi_0^N|\hat{c}_{il\alpha}^\dagger\,\hat{G}^c\,\hat{c}_{i'l'\beta}|\Phi_0^N\rangle + \langle\Phi_0^N|\hat{c}_{il\alpha}\,\hat{G}^c\,\hat{c}_{i'l'\beta}^\dagger|\Phi_0^N\rangle$ is the Green function of a disconnected cluster. It is calculated in the Lehmann representation in terms of the few-body states of interacting clusters containing K and $K \pm 1$ electrons

$$\mathcal{G}^c_{i\alpha i'\beta}(\omega) = \sum_n \frac{\langle\phi_0^K|\hat{c}_{i\alpha}^\dagger|\phi_n^{K-1}\rangle\langle\phi_n^{K-1}|\hat{c}_{i'\beta}|\Phi_0^K\rangle}{\omega - (E_0^K - E_n^{K-1})} + \sum_n \frac{\langle\phi_0^K|\hat{c}_{i\alpha}|\phi_n^{K+1}\rangle\langle\phi_n^{K+1}|\hat{c}_{i'\beta}^\dagger|\phi_0^K\rangle}{\omega - (E_n^{K+1} - E_0^K)}. \tag{11}$$

Eq. (10) contains the matrix elements of the inter-cluster potential that are simply calculated identifying the indices $l - l'''$, $i - i'''$, $\gamma - \gamma'$ that give a non-zero contribution.
After summation over the cluster positions in Eq. (8), one eventually reaches an explicit equation for the lattice Green function, namely

$$\mathcal{G}_{i\alpha i'\beta}(\mathbf{k}\omega) = \mathcal{G}^c_{i\alpha i'\beta}(\omega) + \sum_{i'''\gamma'} B_{i\alpha i'''\gamma'}(\mathbf{k}\omega)\,\mathcal{G}_{i'''\gamma' i'\beta}(\mathbf{k}\omega)\,, \tag{12}$$

where the $K \times K$ matrix $B_{i\alpha i'''\gamma'}(\mathbf{k}\omega)$ is the Fourier transform of $\hat{G}^c\hat{V}$ matrix elements involving neighboring sites that belong to different clusters. Eq. (12) is solved by a $K \times K$ matrix inversion at each $\mathbf{k}$ and ω.
The k- and ω-dependent lattice Green function $\mathcal{G}(\mathbf{k}n\omega)$ is obtained by a final summation over the intra-cluster site positions modulated by the single-particle band coefficients as in Eq. (7). The quasi-particle excitation energies correspond to peaks of the k and band-index dependent spectral function

$$A(k, n, \omega) = \operatorname{Im}\mathcal{G}(\mathbf{k}n\omega). \tag{13}$$

Examples of quasi-particle band structure obtained by CPT for model systems are reported in the next section where we start analyzing CPT results for a simplified model system. This analysis will allow us to identify the main features of CPT and to recognize its *pro et contra* with respect to the other many-body approaches. This analysis will constitute a benchmark for CPT and for its application to realistic systems.

3 CPT for model systems

3.1 The role of symmetry

We consider a square 2D lattice with one orbital per site and the standard orbital-independent Hubbard Hamiltonian

$$\begin{aligned} \hat{H}_c &= \sum_{il} \varepsilon_{il}\, \hat{n}_{il} + \sum_{ijl} t_{il,jl}\, \hat{c}^{\dagger}_{il}\hat{c}_{jl} + \sum_{il} U^i\, \hat{n}_{il\uparrow}\hat{n}_{il\downarrow} \\ \hat{V} &= \sum_{ijl\neq l'} t_{il,jl'}\, \hat{c}^{\dagger}_{il}\hat{c}_{jl'} \end{aligned} \tag{14}$$

For this lattice we easily identify various possible "tilings": 4-atom 2×2 square, 4-atom chain, 6-atom rectangle etc. They differ by the number of atoms and also by their symmetry, the 4-atom square being the only one that preserves the full point symmetry of the entire lattice.
The simplest way to check the quality of the main approximation of CPT, the expression of the lattice Green function in terms of Green functions of decoupled clusters, is to look for a convergence in the cluster size, comparing results obtained with larger and larger cluster sizes. This procedure has two serious restrictions that arise i) by the dimensions of Hilbert space used in the exact diagonalization, dimensions that grow exponentially with the number of sites and ii) by symmetry requirements. The second restriction, even if clearly stated in the early developments of Quantum Cluster theories [7], is often overlooked in the implementations. Independently on the various QC *flavors* such as plain CPT [10], variational CPT [13], cellular dynamical mean-field theory [9], the cluster symmetry should be as close as possible to the one of the lattice.
As we know from elementary solid state theory there is a large arbitrariness in the choice of the elementary units that describe a crystalline solid: either the primitive cell that contains the minimum number of atoms, or any larger unit that, via translation invariance, reproduces the crystalline lattice. So the band structure of non-interacting electrons in a 2D square lattice can be calculated using unit cells containing a variable number of atoms, 1, 2, 4, 6, etc., providing exactly the same result, except for a trivial "band folding" that can be easily eliminated by an "unfolding procedure", see Fig. 1.[1]
The situation is quite different for interacting electrons as described by QC theories. In this case the smallest unit must obviously contain more than one atom but its choice is now far less arbitrary since the extended system is described as a periodic repetition of units of correlated electrons and the translation periodicity is preserved only at the superlattice level. In other words, the e-e interaction affects the electronic states inside the cluster, resulting in a sort of hopping renormalization, while the inter-cluster hopping is unaffected. For this reason the cluster symmetry should be as close as possible to the one of the lattice: any significant deviation

[1] The unfolding procedure corresponds to identifying within the bands obtained with a large unit cell those that correspond to the primitive cell. The unfolding procedure is used in CPT in order to implement correctly Eq. (7) where the band index n runs over the number of unfolded bands ($n = 1$ instead of $n = 4$ or $n = 6$ in the present case) but the eigenstates are to be taken in the larger unit cell basis ($i = 1, 4$ or $i = 1, 6$)

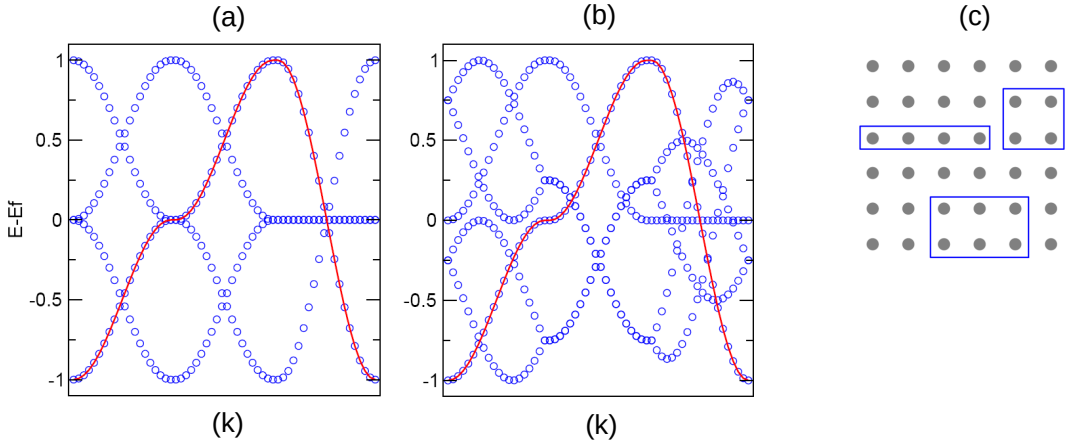

Fig. 1: *Single-particle band structure obtained assuming different unit cells for the 2D square lattice: the 4-site square (a) and the 6-site rectangle (b) (open circles). The red line is the "unfolded" band structure obtained assuming the usual 1-site unit cell. Panel (c) shows different tilings for the 2D square lattice (see text).*

from this requirement would induce a wrong behavior of the quasi-particle band dispersion: quasi-particle energies at k and Rk, R being a point group rotation, would be different, violating a very basic rule of solid state theory.

The influence of cluster symmetry on the quasi-particle band structure is illustrated in Fig. 2 for the square lattice at half occupation. It appears that clusters that are not invariant under lattice point-group rotations give rise to quasi-particle bands that violate the above mentioned rule. Quasi-particle energies should be identical at k-points K_1 and K_2 since K_1 and K_2 are connected by a point-group rotation but for the 4-site chain and the 6-site rectangle they are not, major differences occurring in the first case due to the largest symmetry discrepancies.

Fig. 3 shows a similar comparison for another 2D model system, the honeycomb lattice. In this case two tilings have been considered: the 6-site hexagon and the elongated 8-site cluster. The differences are striking and this is due to the fact that the 8-site tiling has a preferred direction. Hence the dispersions along K–K' and K'–K'' appear different. This result is particularly relevant since it explains some significant discrepancies that are present in the literature on correlated electrons in graphene [14, 15]. In fact, in the honeycomb lattice where the Dirac cones are the consequence of perfect long-range order, theories based on quantum cluster schemes, regardless of them being variational or not and independent on the details of the specific implementations, give rise to a spurious excitation gap for $U \to 0$. A strategy has been proposed that seems to overcome this shortcoming, providing for the undistorted honeycomb lattice a semimetal behavior up to some finite U [16]. The strategy consists in choosing clusters that break the lattice point C_6 symmetry (8- and 10-site clusters). The quasi-particle band dispersion that is obtained in this way presents, however, the above mentioned unphysical behavior which, by the way, is just the origin of the semimetallic behavior at finite U since the gap closes at one K but not at its rotated counterpart. For this reason breaking the rotational symmetry is not an allowed strategy to correct the erroneous insulating phase.

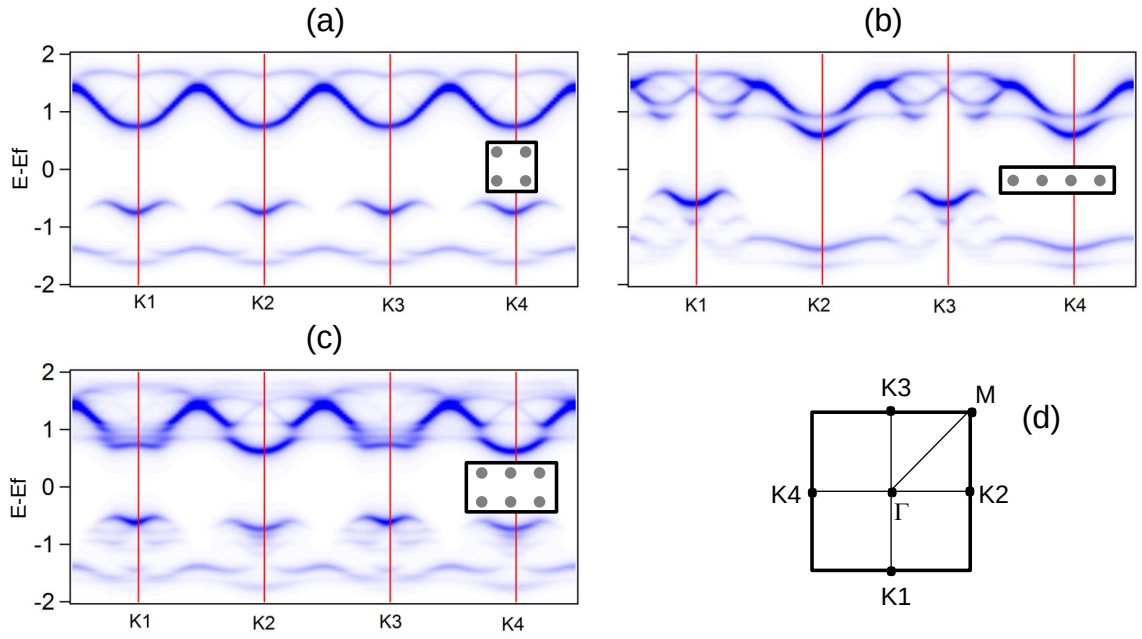

Fig. 2: *Spectral functions obtained for the square lattice at half occupation ($t = 0.25$, $U = 2$) reproduced by different tilings, 4-site square (a), 4-site chain (b) and 6-site rectangle (c). In (d) the 2D square Brillouin Zone is shown.*

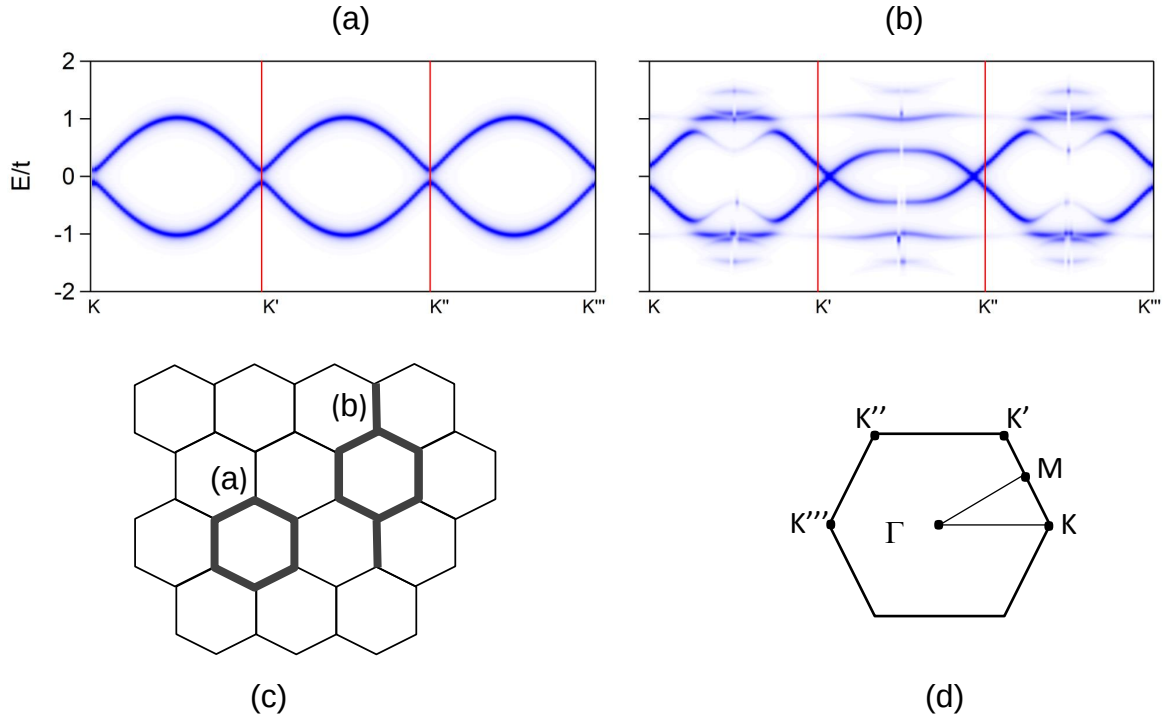

Fig. 3: *Spectral functions obtained for the honeycomb lattice ($t = 1$, $U = 2$) at half occupation using different tilings shown in (c): a 6-site hexagon(a) and an 8-site cluster (b). In (d) the honeycomb Brillouin Zone is shown.*

3.2 CPT vs. other many-body schemes

The agreement between theory and experiments is the ultimate validation of any theoretical scheme. Many-body quasi-particle band structure calculations rely, however, on drastic approximations that may work as *ad-hoc* ingredients that affect the final result: different single-particle band structures are used as a starting point, different strategies are implemented to take into account the double-counting of the e-e interaction, etc. It is then interesting to make a comparison within theory, applying different many-body schemes to the same simplified model. This provides a sort of benchmark for the various theoretical schemes. We choose again the 2D square lattice at half occupation as a paradigmatic case.

Among the non-perturbative techniques that have been proposed to augment band theory by e-e correlations we consider 3-Body Scattering (3BS) theory, a method that shares with other approaches, DMFT above all, the calculation of Green functions in terms of self-energy $\Sigma(\mathbf{k}n\omega)$

$$\mathcal{G}(\mathbf{k}n\omega) = \frac{1}{\omega - e_{\mathbf{k}n} - \Sigma(\mathbf{k}n\omega)}\,, \tag{15}$$

where $e_{\mathbf{k}n}$ are the single-particle band eigenvalues.

In the 3BS approach the interacting many-body state is expanded in the configurations obtained by adding electron-hole pairs to the ground state of the single-particle Hamiltonian. The response of the interacting system to the creation of one hole is then described in terms of interactions between configurations with one hole plus one e-h pair, giving rise to multiple h-h and h-e scattering. The advantage of 3BS with respect to other approaches is to provide a rather intuitive interpretation of the effect of electron correlation on one electron removal energies in terms of Auger-like relaxations. Interestingly, the results of DMFT and 3BS are in many cases quantitatively very similar [4, 17].

The results obtained by 3BS and CPT for the 2D square lattice with $t = 0.25$ and $U = 2, 3, 4$ are shown in Figs. 4 and 5. Both methods provide, for sufficiently large values of U, an insulating behavior but in 3BS the gap opens up only at very large U ($U \geq 2W$) while in CPT the gap is present already at much lower U-values. Indeed, in CPT, at half occupation, the gap is *always* present. It has recently been shown [18] that the existence of a gap down to $U \to 0$ is characteristic of all quantum cluster schemes with the only exception of the dynamical cluster approximation (DCA) [8]. This is due to the aforementioned violation of translational symmetry in quantum cluster methods. DCA preserves translation symmetry and has been shown to describe better the small-U regime; it becomes, however, less accurate at large U values where it overemphasizes the metallic behavior [18]. Aware of this shortcomings we are comparing here results obtained for relatively large U values where CPT limitations are not effective: For $U \gg t$ cluster perturbation theory is expected to provide reliable results.

Other remarkable differences exist between 3BS and CPT results, mainly related to the quasi-particle k-dispersion. This is essentially due to a limitation of the methods based on self-energy calculation, since the self-energy is in most cases assumed k-independent. On the contrary, CPT provides a clear k-dependent energy renormalization and single-particle eigenstates at different k-points are differently affected by e-e correlation. This is shown more clearly by extracting

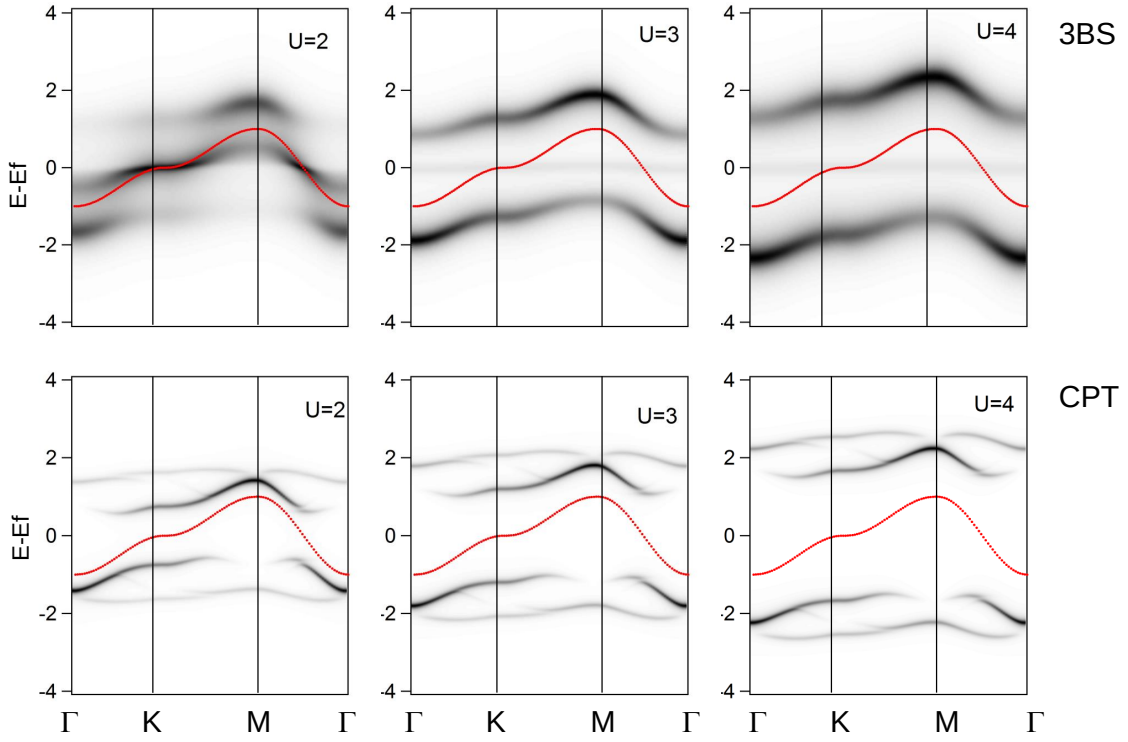

Fig. 4: *Quasi-particle band structure obtained by 3BS (upper panel) and CPT (lower panel) for the 2D square lattice with $t = 0.25$. Increasing values of Hubbard U ($U = 2, 3, 4$) are considered. The k-points are shown in Fig. 2(d).*

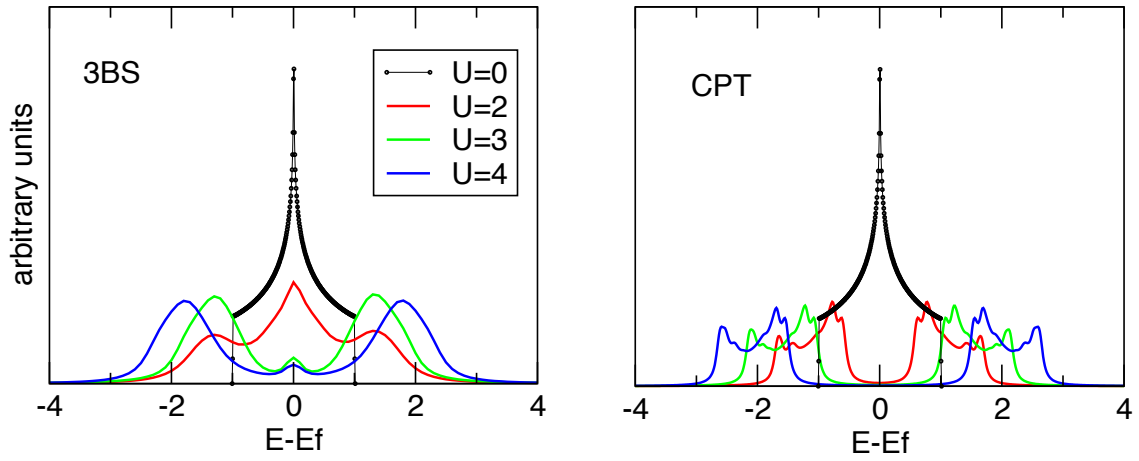

Fig. 5: *Quasi-particle density of states obtained by 3BS (left panel) and CPT (right panel) for the 2D square lattice. Parameter values are the same in Fig. 4.*

from CPT a self-energy

$$\Sigma(\mathbf{k}n\omega) = \omega - e_{\mathbf{k}n} - \mathcal{G}(\mathbf{k}n\omega)^{-1}. \tag{16}$$

CPT self-energies are shown in Fig. 6 at the high symmetry points of the 2D square lattice showing a well defined k-dependence.

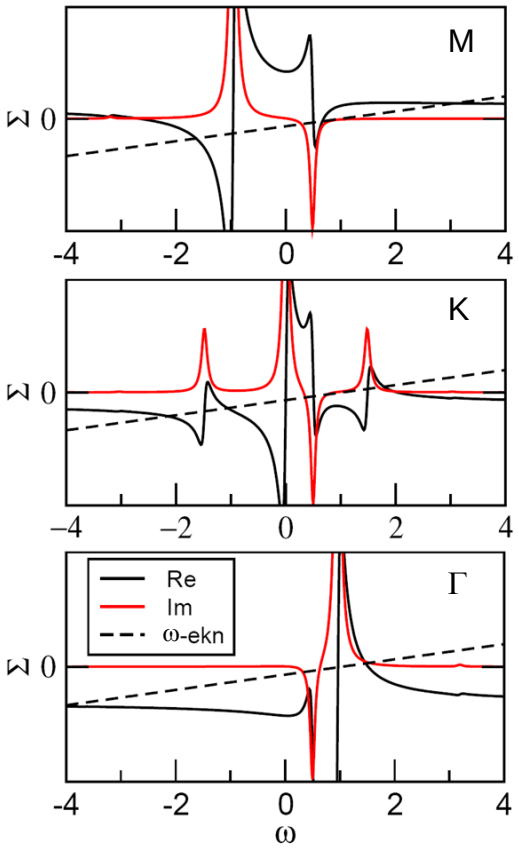

Fig. 6: *k-dependent CPT self-energy for the 2D square lattice. Parameters as in Fig. 4.*

4 Transition-metal oxides

4.1 Preliminaries

We move now to Transition Metal (TM) oxides as an example of the application of CPT to real materials.

The non interacting contribution to the Hubbard Hamiltonian is a standard Tight-Binding (TB) Hamiltonian that can be written in terms of Koster-Slater parameters obtained by fitting ab-initio band structure. Tables 1 and 2 report the Koster-Slater tight-binding parameters of the $3d$ transition-metal oxides obtained by least squares fitting of ab-initio band structures calculated in the DFT-LMTO scheme.

When using TB parameters in the Hubbard Hamiltonian we must take care of the double-counting issue: the ab-initio band structures, and the TB parameters deduced from it, contain the e-e Coulomb repulsion as a mean-field that must be removed before including U as a true many-body term. "Bare" on-site parameters are calculated by subtracting the mean filed value of the Hubbard term, namely

$$E^*_\alpha = E_\alpha - \sum_i U^i_\alpha \langle n_{i\alpha\uparrow}\rangle\langle n_{i\alpha\downarrow}\rangle \,. \tag{17}$$

This definition involves the d occupation inside the cluster that is actually used in exact diagonalization and cancels out the energy shift due to double counting within each sub-cluster. Other

Table 1: *On-site Koster-Slater parameters (in eV).*

	$E_s(TM)$	$E_p(TM)$	$E_{t2g}(TM)$	$E_{eg}(TM)$	$E_s(O)$	$E_p(O)$
MnO	7.313	11.546	-0.763	-0.010	-18.553	-4.806
FeO	8.208	12.232	-0.857	-0.132	-18.489	-4.723
CoO	8.221	12.040	-1.383	-0.734	-18.673	-4.891
NiO	8.6332	12.176	-1.767	-1.165	-18.608	-4.806

Table 2: *Inter-site Koster-Slater parameters (in eV).*

atom	atom	ss_σ	pp_σ	pp_π	dd_σ	dd_π	dd_δ	sp_σ	sd_σ	pd_σ	pd_π
Mn	Mn	-0.514	1.435	-0.137	-0.353	0.028	0.047	0.486	-0.285	-0.081	0.209
O	Mn	0.0	0.0	0.0	0.0	0.0	0.0	0.0	-1.074	-1.243	0.632
O	O	-0.124	0.519	-0.102	0.0	0.0	0.0	-0.016	0.0	0.0	0.0
Fe	Fe	-0.529	1.470	-0.128	-0.341	0.023	0.046	0.487	-0.275	-0.083	0.195
O	Fe	0.0	0.0	0.0	0.0	0.0	0.0	0.0	-1.083	-1.027	0.640
O	O	-0.140	0.578	-0.109	0.0	0.0	0.0	-0.015	0.0	0.0	0.0
Co	Co	-0.537	1.497	-0.109	-0.306	0.015	0.045	0.483	-0.283	-0.123	0.193
O	Co	0.0	0.0	0.0	0.0	0.0	0.0	0.0	-1.023	-1.235	0.616
O	O	-0.145	0.609	-0.112	0.0	0.0	0.0	-0.043	0.0	0.0	0.0
Ni	Ni	-0.549	1.527	-0.090	-0.280	0.006	0.043	0.488	-0.294	-0.113	0.189
O	Ni	0.0	0.0	0.0	0.0	0.0	0.0	0.0	-0.969	-1.209	0.608
O	O	-0.154	0.656	-0.116	0.0	0.0	0.0	-0.101	0.0	0.0	0.0

Table 3: d*-orbital occupations.*

	MnO	FeO	CoO	NiO
n_{t2g}	4.941	5.770	5.961	5.966
n_{eg}	0.599	0.672	1.614	2.556
n_d	5.540	6.441	7.575	8.522

definitions of double-counting correction have been proposed in the spirit of LDA+U [12] that involve the average d-occupation in the solid calculated by single-particle theory. Our choice should be preferred when using multiple partitions of sites/orbitals: this double-counting correction in fact amounts to readjusting the "center of mass" of the calculated few-particle states by realigning the calculated $\frac{1}{2}(E_0^{N+1} - E_0^{N-1})$ to its $U = 0$ value and to keep the distinction between filled and empty states.

Fig. 7 reports the local density of states obtained in the non-interacting scheme. We focus in particular on the TM d-orbital contribution. Crystal field symmetry induces a split of d-orbitals into t_{2g}/e_g-states and according to ab-initio band theory these states have different occupations (see Table 3). This is a crucial point that will be exploited later in applying CPT to TM oxides.

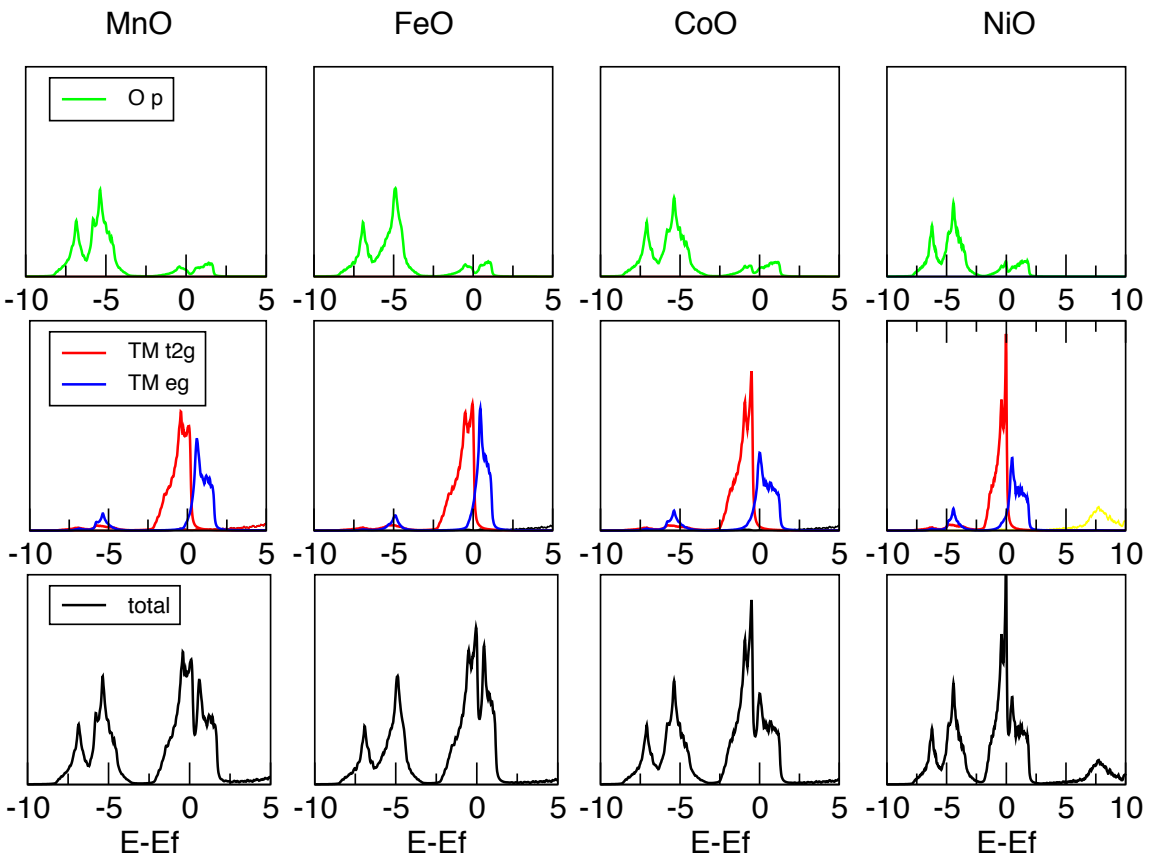

Fig. 7: *Single-particle Density of States (DOS) for TM oxides of the* $3d$ *series. The total DOS is reported (lower panel) together with the contributions of TM d-orbital (in red and blue* t_{2g} *and* e_g*, respectively) and of oxygen* sp*-orbitals in the upper panels.*

4.2 Lattice tiling: a multiple partition strategy

As outlined in the previous sections, the first step of the CPT procedure is the partitioning of the lattice into clusters. Obviously the choice in not unique but must satisfy some requirements: the clusters should be connected by inter-site hopping as schematically indicated in Fig. 8(c), namely they should not overlap; moreover they should contain enough atoms to include the relevant physics of the interacting system and finally the number of sites/orbitals per cluster should be tractable in an exact diagonalization procedure. Another relevant criterion is that, as discussed in Section 3, the cluster symmetry should be as close as possible to the lattice one.

TM oxides of the $3d$ series (MnO, NiO, CoO, FeO) crystallize in the rocksalt structure. An octahedral cluster containing one TM atom and 6 nearest-neighbor oxygens has been originally proposed as the elementary unit containing all the relevant physics of the system; atomic multiplet theory applied to this isolated cluster [19] has been used to reproduce some features of the solid state system, losing, however, the translational symmetry and all k-related quantities. The same cluster has been used as the basic unit to be embedded in an infinite medium in the spirit of variational CPT [12]. These clusters, however, do overlap in the rocksalt structure and cannot be used as elementary unit in CPT calculations. Moreover this cluster contains just one TM atom and even in variational CPT the resulting self-energy turns out to be k-independent [12].

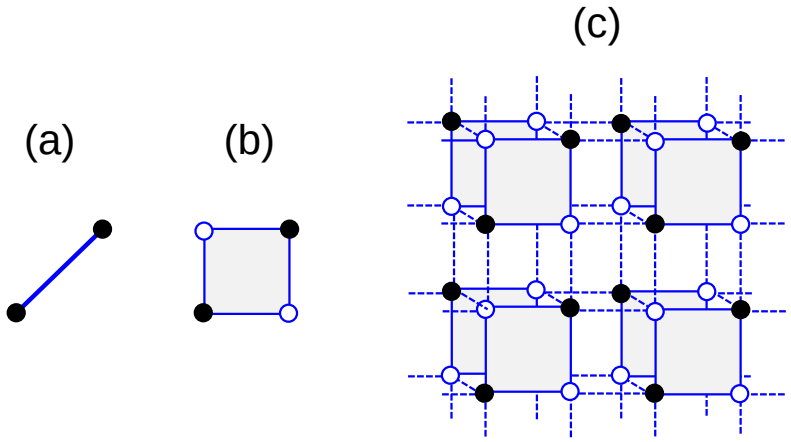

Fig. 8: *Building blocks of the 3D Rocksalt structure for a transition-metal mono-oxide: (a) a dimer of 2 TM atoms (filled black circles); (b) a* 2×2 *plaquette containing the two atomic species (oxygens as open circles); (c) stacking of plaquette layers reproducing the 3D lattice. Dotted lines indicate the inter-cluster hopping.*

The smallest cluster containing more than one TM atom and reproducing, without overlaps, the 3D rocksalt lattice is the 2×2 plaquette of Fig. 8(b) with two TM atoms and two oxygens. Since the bands of TM oxides around the Fermi energy are described by 9 spd-orbitals for each TM atom and 4 sp-orbitals for each oxygen, the dimension of the Hilbert space spanned by the Slater determinants that are obtained by populating in all possible ways the $K = 26$ orbitals with P electrons of a given spin ($P = 13 \ldots 16$ from MnO to NiO) is far too big (number of configurations $= (\frac{K!}{P!(K-P)!)})^2$) for exact diagonalization.
A reduction of the number of sites/orbitals per cluster is mandatory. To this end we may identify, within a single cluster, two classes of orbitals (centered on different sites and of different symmetry) that we call A and B; we may then write the cluster Hamiltonian as the sum of on-site and inter-site terms connecting all kinds of orbitals: A-A, B-B (diagonal terms), and A-B (off-diagonal terms):

$$\hat{H}_c \;=\; \hat{H}^{\rm diag} + \hat{V}_{AB} \tag{18}$$

with

$$\hat{H}^{\rm diag} = \hat{H}_c^{AA} + \hat{H}_c^{BB} \quad \text{and} \quad \hat{V}_{AB} = \sum_{\alpha_A \beta_B} t_{il\alpha_A, jl\beta_B}\, \hat{c}^{\dagger}_{il\alpha_A} \hat{c}_{jl'\beta_B}\,. \tag{19}$$

Here

$$\hat{H}_c^{AA} = \sum_{il\alpha_A} \varepsilon_{il\alpha_A}\, \hat{n}_{il\alpha_A} + \sum_{\alpha_A \beta_A} \sum_{ijl} t_{il\alpha_A, jl\beta_A}\, \hat{c}^{\dagger}_{il\alpha_A} \hat{c}_{jl\beta_A} + \sum_{il\alpha_A\beta_A} U^{i}_{\alpha_A\beta_A}\, \hat{n}_{il\alpha_A\uparrow} \hat{n}_{il\beta_A\downarrow} \tag{20}$$

and a similar expression for $\hat{H}_c^{BB}$.
Correspondingly we have again $\hat{G^c}^{-1} = z - \hat{H}_c = (\hat{G}^{\rm diag})^{-1} - \hat{V}_{AB}$ which results, as before, in a Dyson-like equation

$$\hat{G^c} = \hat{G}^{\rm diag} + \hat{G}^{\rm diag}\, \hat{V}_{AB}\, \hat{G^c}\,. \tag{21}$$

In the local basis $\hat{G}^{\rm diag}$ is block-diagonal and the non-zero elements $\hat{G}^{diag}_{AA}$ and $\hat{G}^{\rm diag}_{BB}$ are obtained by performing separate exact diagonalizations that include either A or B orbitals. In this basis Eq. (21) can be solved by matrix inversion.

$$\hat{G}^c = (\mathbb{I} - \hat{G}^{\rm diag}\,\hat{V}_{AB})^{-1}\,\hat{G}^{\rm diag} \tag{22}$$

with $\mathbb{I}$ the unit matrix and indices running over the $K = 26$ sites/orbitals of the plaquette (9 spd-orbitals on 2 TM atoms and 4 sp-orbitals on 2 oxygens). More explicitly

$$\begin{pmatrix} G_{AA} \\ G_{AB} \\ G_{BA} \\ G_{BB} \end{pmatrix} = \begin{pmatrix} 1 & 0 & -G^{\rm diag}_{AA}\,V_{AB} & 0 \\ 0 & 1 & 0 & -G^{\rm diag}_{AA}\,V_{AB} \\ -G^{\rm diag}_{BB}\,V_{BA} & 0 & 1 & 0 \\ 0 & -G^{\rm diag}_{BB}\,V_{BA} & 0 & 1 \end{pmatrix}^{-1} \begin{pmatrix} G^{\rm diag}_{AA} \\ 0 \\ 0 \\ G^{\rm diag}_{BB} \end{pmatrix}. \tag{23}$$

Of course this multiple partition – within the lattice and within the cluster – makes the problem numerically tractable. In this case the CPT prescriptions may be rephrased as follows: chose a partitioning of the lattice Hamiltonian into a set of non-overlapping clusters connected by inter-cluster hopping; make a further partition inside each cluster defining a suitable collection of sites/orbitals; perform separate exact diagonalizations plus matrix inversion to calculate the cluster Green function in the local basis by Eq. (23) and finally obtain the full lattice Green function in the Bloch basis by Eq. (12).

This technique can be extended to more than two subsets of sites/orbitals, and, in fact, we have applied it to a triple partition (subsets A, B and C) as we will show in more detail below. It has the advantage to replace an unmanageable exact diagonalization with two (or more) separate ones followed by a matrix inversion. It shares with CPT the assumption about the states of the *cluster* interacting electrons $\phi^K(r_1, r_2.., r_K) \sim \phi_A(r_1, r_2.., r_A)\phi_B(r_1, r_2.., r_B)...$ This is a drastic approximation whose validity must be verified performing calculations with different partitions and/or finding explicit and justified rules for the adopted choice. These rules must be based on clear and sound conjectures and will be inevitably system-dependent.

4.3 Multiple partition for TM oxides

We come now to the practical implementation appropriate for transition-metal oxides. TM oxides of the $3d$ series differ drastically in d-band occupation; according to single-particle band theory reported in Tab. 3 and Fig. 7, NiO and CoO have t_{2g}-states fully occupied ($n_{t2g} \simeq 6$ in both cases) while the e_g-states are responsible for the metallic behavior; on the contrary, in MnO and FeO both t_{2g}- and e_g-states cross the Fermi level. Since only partially occupied shells are affected by the e-e interaction this suggests different partitions for the two classes of TM oxides, NiO, CoO on one side (with only e_g-orbitals centered on the two TM atoms in the plaquette) and FeO, MnO on the other site (with both t_{2g}-e_g-orbitals).

Once we have made this assumption we are also able to predict straightaway which TM oxide will develop in CPT a Mott-Hubbard gap: in exact diagonalization, in fact, only systems at half occupation exhibit a finite energy separation between hole and particle excitations and

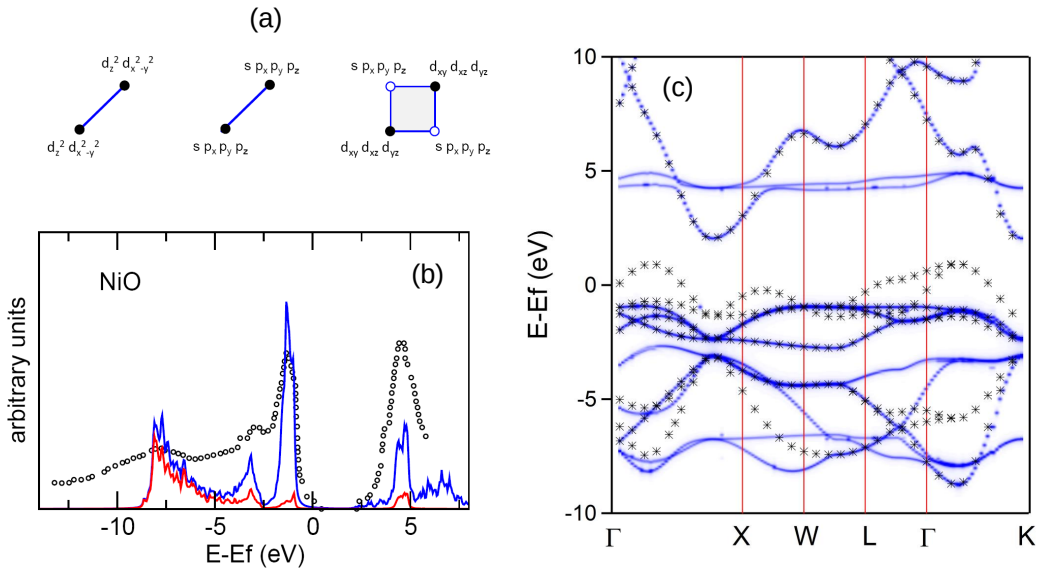

Fig. 9: *CPT results for NiO assuming the multiple partition indicated in (a) (see text). (b): orbital resolved density of quasi-particle states compared with experimental results (open circles). Blue (red) line is for TM d (Oxygen sp) orbital contribution. (c): Quasi-particle band dispersion (blue line) compared with the single-particle result (black asterisks).*

we expect NiO and MnO (having 2 e_g and 5 t_{2g}-e_g electrons respectively) to be well-defined Mott insulators, while in FeO and CoO, where both t_{2g} and e_g are not half occupied, local e-e repulsion is expected to induce a readjustment of spectral weight but not necessarily a well defined gap. In the following we will describe how CPT can be implemented to capture gap opening in MnO and NiO.

The multiple-partition–multiple-embedding procedure for NiO starts from a separation of Ni-d orbitals into t_{2g} and e_g contributions. As already mentioned, in NiO only e_g-states are partially occupied and it is reasonable to expect them to be most affected by e-e interaction. We identify the set of finite systems shown in Fig. 9(a), namely: i) a Ni dimer containing e_g orbitals, ii) a Ni dimer containing sp-orbitals, iii) a 4-atom plaquette with Ni t_{2g}- and O sp-orbitals. Three distinct exact diagonalizations are performed assuming for simplicity non-zero on-site repulsion between Ni d-orbitals only. Three cluster Green functions are calculated within the Lehmann representation: G_{AA}, G_{BB}, and G_{CC} with $A \equiv$ Ni e_g, $B \equiv$ Ni sp, and $C \equiv$ O p Ni t_{2g}. The total Green function for the plaquette is obtained by putting them together. This is the first embedding procedure and amounts to solving the matrix equation (23) extended to a triple-partition.

The second embedding procedure corresponds to going from the 2×2 plaquette to the extended lattice and requires the kind of "periodization" described in Sec. 2, where we go from the cluster Green function to the lattice Green function by solving again the Dyson-like equation involving now inter-cluster interactions. In order to implement Eq. (12) one needs first of all to define for each site $r_{i'}$ in the plaquette the position of the nearest neighbors $\mathbf{r}_{i''}$ and the corresponding lattice vectors $\mathbf{R}_{l''}$ connecting the cluster with the neighboring ones. Then the matrix $B_{i\alpha j\gamma}(\mathbf{k}\omega)$ is obtained as follows

$$B_{i\alpha j\gamma}(\mathbf{k}\omega) = \sum_{i'i''l''} t_{i'0\alpha i''l''\gamma}\, e^{-i\mathbf{k}\cdot\mathbf{R}_{l''}}\, \mathcal{G}^c{}_{i\alpha i'\gamma}(\omega)\, \delta_{i''j}\,. \tag{24}$$

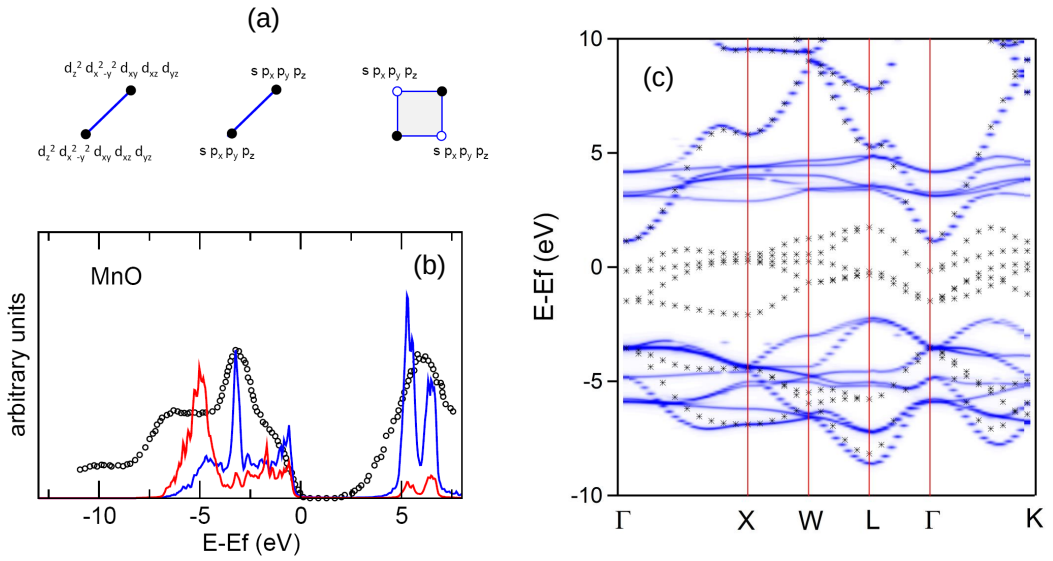

Fig. 10: *CPT results for MnO. (a): multiple partition of orbitals in dimer and* 2×2 *plaquette (see text). (b): orbital resolved density of quasi-particle states compared with the experimental data (circles). Blue (red) line is for TM* d *(Oxygen* sp*) orbital contribution. (c): quasi-particle band dispersion (blue line) compared with the single-particle result (black asterisks).*

Here $t_{i'0\alpha i''l''\gamma}$ are the inter-site hopping terms previously defined (Eq. (2)) obtained in terms of Koster-Slater parameters in the usual way.

The on-site e-e interaction involving Ni d-orbitals has the effect of opening a gap between t_{2g}-states as expected and to turn the NiO into a wide-gap insulator. The Hubbard U is used here as a tunable parameter to reproduce the experimental gap but its value ($U = 11$ eV) is within the current estimates. We notice that, in spite of the drastic approximations, the agreement between theory and experiment is quite good, not only for the correct gap that is somewhat fixed by the value of the e-e repulsion, but also for the orbital character of the valence-band edge, largely involving O $2p$-states as known from experiments.

Let us consider now MnO where, according to the previous discussion, we include in the smallest elementary unit (the dimer) all d electrons (Fig. 10(a)). Then also in this case we will be dealing with an exact diagonalization at half occupation. The dimension of the Hilbert space spanned by the Slater determinants is here $n_{\rm conf} = (\frac{K!}{P!(K-P)!})^2 = 63\,504$, so large to require the band-Lanczos algorithm to obtain ~ 1000 eigenvalues and eigenvectors $E_n^{N\pm1}$, $\Phi_n^{N\pm1}$ for the system with $N \pm 1$ electrons as well as the ground state E_n^N, Φ_0^N for the N electron system. Also in this case the dimer problem accounts for both hopping and e-e repulsion on the d-orbitals of the TM atoms and therefore includes a large part of the relevant physics of the interacting system. In particular, since also in this case the system is half occupied, we expect the ground state E_0^{N+1} to be larger than E_0^{N-1} with an energy distance growing with U. This is essential in view of a gap opening in the extended system.

We then proceed as before to *embed* first the dimer into the plaquette and finally the plaquette into the extended lattice. Results are shown in Fig. 10. In this case the e-e repulsion is responsible for a complete removal of all Mn d-states around the Fermi level as required for the gap opening.

Figure 10(b) shows a comparison between the quasi-particle density of states and the experimental results of Ref. [20]. We observe that the gap value is well reproduced as well as most of the spectroscopic structures. We do not find evidence of structures below the valence-band bottom that are observed in photoemission experiments; this might be due to the reduced number of excited states that are obtained by the Lanczos procedure. We mention however that the origin of satellite features in MnO has been somewhat controversial in the literature attributing them either to intrinsic [20] or extrinsic effects [21]. Apart from the satellite structure our results are comparable with what has been obtained by variational cluster approximation [12] in spite of a different choice of the cluster, and by a recent DMFT calculations [22]. Since these two approaches are either variationally optimized or self-consistent, we may identify in the present CPT scheme the advantage of giving comparable results by a single-shot calculation thanks, we believe, to our cluster choice.

5 Concluding remarks

In this lecture we have reviewed a possible strategy, based on a multi-orbital extension of the CPT approach, to include on-site e-e interactions in real materials and we have discussed its application to the paradigmatic case of transition-metal oxides. The CPT strategy is applied twice, first to identify a partition of the lattice into non overlapping clusters and secondly to calculate the cluster Green function in terms of two or more local ones. This procedure has the advantage of replacing an unmanageable exact diagonalization by two or more separate ones followed by a matrix inversion. This strategy may be adopted whenever dealing with exceedingly large dimensions of the configuration space, for instance in treating correlated electrons in low-dimensional systems such as surfaces and interfaces, where the translation invariance is reduced and the unit cell contains many atoms. Of course there are drastic approximations involved: in the same way as in the standard single-orbital CPT, writing the lattice Green function in terms of Green functions of decoupled subunits amounts to identifying the many-electron states of the extended lattice as the product of cluster few-electron states. In the present case in particular, choosing the TM dimer as the basic unit we have excluded from the few-electron eigenstates obtained by exact diagonalization the contribution of oxygen sp-orbitals, treating the O sp – TM d hybridization by the embedding procedure. The non-interacting part of the lattice Hamiltonian is described in terms tight-binding parameters deduced by a least-squares fitting of an ab-initio single-particle band structure, including all the relevant orbitals. To our purposes, since we do not need any real-space expression of the single-particle wavefunctions, this tight-binding parametrization is fully equivalent to a representation in terms of maximally localized Wannier functions. We have applied this method to NiO and MnO as test cases and, using a single value of the Hubbard U, we have found a reasonable agreement with experimental data and with theoretical results obtained by different methods.

References

[1] G. Kotliar, S.Y. Savrasov, K. Haule, V.S. Oudovenko, O. Parcollet, and C.A. Marianetti, Rev. Mod. Phys. **78**, 865 (2006)

[2] F. Manghi, C. Calandra, and S. Ossicini, Phys. Rev. Lett. **73**, 3129 (1994)

[3] S. Monastra, F. Manghi, C.A. Rozzi, C. Arcangeli, E. Wetli, H.-J. Neff, T. Greber, and J. Osterwalder, Phys. Rev. Lett. **88**, 236402 (2002)

[4] J. Sánchez-Barriga, J. Fink, V. Boni, I. Di Marco, J. Braun, J. Minár, A. Varykhalov, O. Rader, V. Bellini, F. Manghi, H. Ebert, M.I. Katsnelson, A.I. Lichtenstein, O. Eriksson, W. Eberhardt, and H.A. Dürr, Phys. Rev. Lett. **103**, 267203 (2009)

[5] J. Sánchez-Barriga, J. Minár, J. Braun, A. Varykhalov, V. Boni, I. Di Marco, O. Rader, V. Bellini, F. Manghi, H. Ebert, M.I. Katsnelson, A.I. Lichtenstein, O. Eriksson, W. Eberhardt, H.A. Dürr, and J. Fink, Phys. Rev. B **82**, 104414 (2010)

[6] J. Sánchez-Barriga, J. Braun, J. Minár, I. Di Marco, A. Varykhalov, O. Rader, V. Boni, V. Bellini, F. Manghi, H. Ebert, M.I. Katsnelson, A.I. Lichtenstein, O. Eriksson, W. Eberhardt, H.A. Dürr, and J. Fink, Phys. Rev. B **85**, 205109 (2012)

[7] T. Maier, M. Jarrell, T. Pruschke, and M.H. Hettler, Rev. Mod. Phys. **77**, 1027 (2005)

[8] M.H. Hettler, A.N. Tahvildar-Zadeh, M. Jarrell, T. Pruschke, and H.R. Krishnamurthy, Phys. Rev. B **58**, R7475 (1998)

[9] G. Kotliar, S.Y. Savrasov, G. Pálsson, and G. Biroli, Phys. Rev. Lett. **87**, 186401 (2001)

[10] D. Sénéchal, D. Perez, and M. Pioro-Ladrière, Phys. Rev. Lett. **84**, 522 (2000)

[11] F. Manghi, J. Phys.: Condens. Matter **26**, 015602 (2014)

[12] R. Eder, Phys. Rev. B **78**, 115111 (2008)

[13] M. Potthoff, M. Aichhorn, and C. Dahnken, Phys. Rev. Lett. **91**, 206402 (2003)

[14] F. Grandi, F. Manghi, O. Corradini, and C.M. Bertoni, Phys. Rev. B **91**, 115112 (2015)

[15] F. Grandi, F. Manghi, O. Corradini, C.M. Bertoni, and A. Bonini, New J. Phys. **17**, 023004 (2015)

[16] M. Laubach, J. Reuther, R. Thomale, and S. Rachel, Phys. Rev. B **90**, 165136 (2014)

[17] F. Manghi and V. Boni, Journal of Electron Spectroscopy and Related Phenomena **200**, 181 (2015)

[18] A. Liebsch and W. Wu, Phys. Rev. B **87**, 205127 (2013)

[19] A. Fujimori, K. Terakura, M. Taniguchi, S. Ogawa, S. Suga, M. Matoba, and S. Anzai, Phys. Rev. B **37**, 3109 (1988)

[20] J. van Elp, R.H. Potze, H. Eskes, R. Berger, and G.A. Sawatzky, Phys. Rev. B **44**, 1530 (1991)

[21] A. Fujimori, N. Kimizuka, T. Akahane, T. Chiba, S. Kimura, F. Minami, K. Siratori, M. Taniguchi, S. Ogawa, and S. Suga, Phys. Rev. B **42**, 7580 (1990)

[22] P. Thunström, I. Di Marco, and O. Eriksson, Phys. Rev. Lett. **109**, 186401 (2012)

7 Orbital Ordering

Eva Pavarini
Institute for Advanced Simulation
Forschungszentrum Jülich GmbH

Contents

E. Pavarini, E. Koch, J. van den Brink, and G. Sawatzky (eds.)
Quantum Materials: Experiments and Theory
Modeling and Simulation Vol. 6
Forschungszentrum Jülich, 2016, ISBN 978-3-95806-159-0
http://www.cond-mat.de/events/correl16

1 Introduction

The term *orbital ordering* (OO) indicates the emergence of a broken symmetry state in which localized occupied orbitals form a regular pattern, in a similar way as spins do in magnetically ordered structures. Orbital ordering phenomena typically occur in Mott insulators with *orbital degrees of freedom*; for transition-metal compounds, the main focus of this lecture, the latter stem from the partially filled d shells of the transition metal. The perhaps most representative case is the perovskites $KCuF_3$, shown in Fig. 1. In first approximation $KCuF_3$ is cubic (O_h point group) with Cu^{2+} at the center of a regular octahedron of F^- ions (anions), enclosed in a cage of K^+ (cations). Due to O_h symmetry at the Cu site, the d manifold, 5-fold degenerate for free Cu^{2+}, splits into a t_{2g} triplet (xz, yz, xy), lower in energy, and a e_g doublet (x^2-y^2 and $3z^2-r^2$); the electronic configuration of the Cu^{2+} ion is thus $t_{2g}^6 e_g^3$ (one hole). The t_{2g} states are completely filled and do not play any active role in OO; instead, electrons in the e_g^3 configuration have orbital degeneracy $d=2$. Making an analogy with spin degrees of freedom, they behave as an effective $\tau = 1/2$ *pseudospin*; in this view, one of the two e_g states, say $|x^2-y^2\rangle$, plays the role of the pseudospin up, $|\nearrow\rangle$, and the other one, $|3z^2-r^2\rangle$, of the pseudospin down, $|\searrow\rangle$. The two pseudospin states are degenerate and, by symmetry, one could expect them to be equally occupied. In reality the symmetry is broken and $KCuF_3$ is orbitally ordered with the orbital structure shown in Fig. 1; depicted are the empty (hole) e_g states at each Cu site. Furthermore, the system exhibits a *co-operative Jahn-Teller distortion*, also shown in Fig. 1, with long and short Cu-F bonds alternating in the $\boldsymbol{ab}$ plane. Indeed, the two phenomena – electronic orbital ordering and structural Jahn-Teller distortion – are concurrent; it is therefore difficult to say which one is the cause and which one is, instead, the effect. The second paradigmatic system showing OO is $LaMnO_3$ (ion Mn^{3+}, configuration $3d^4$), the mother compound of colossal magnetoresistance manganites, also a perovskite. Due to the Hund's rule coupling J, the actual electronic configuration of Mn^{3+} is $t_{2g}^3 e_g^1$. The half-filled t_{2g}^3 state has no orbital degeneracy; the only orbital degrees of freedom are, as for $KCuF_3$, those associated with e_g electrons. Again, the system is orbitally ordered and orbital ordering goes hand in hand with the co-operative Jahn-Teller distortion. Among t_{2g} systems, i.e., materials with partially filled t_{2g} shells, classical examples of orbitally-ordered crystals are the perovskites $LaTiO_3$ and $YTiO_3$ (configuration t_{2g}^1), $LaVO_3$ and YVO_3 (t_{2g}^2), and Ca_2RuO_4 (t_{2g}^4); in these cases the t_{2g} electrons behave as a orbital pseudospin $\tau = 1$. Although this is not a prerequisite for orbital ordering, as we have seen, many orbitally-ordered materials are perovskites; for this reason in the present lecture we will use the perovskite structure as representative.

The origin of orbital ordering has been investigated for decades. One of the problems in clarifying its nature is that, while magnetic order can be directly probed, e.g., via neutron scattering experiments, orbital ordering is typically only indirectly observed. Indeed, its principal hallmark is the presence of the co-operative Jahn-Teller distortion itself. Identifying the origin of orbital ordering is thus intimately related to finding the cause of the co-operative Jahn-Teller distortion. In this lecture I will illustrate the two main mechanisms [1, 2] which have been proposed as possible explanation for OO phenomena, the classical Jahn-Teller effect [1], perhaps

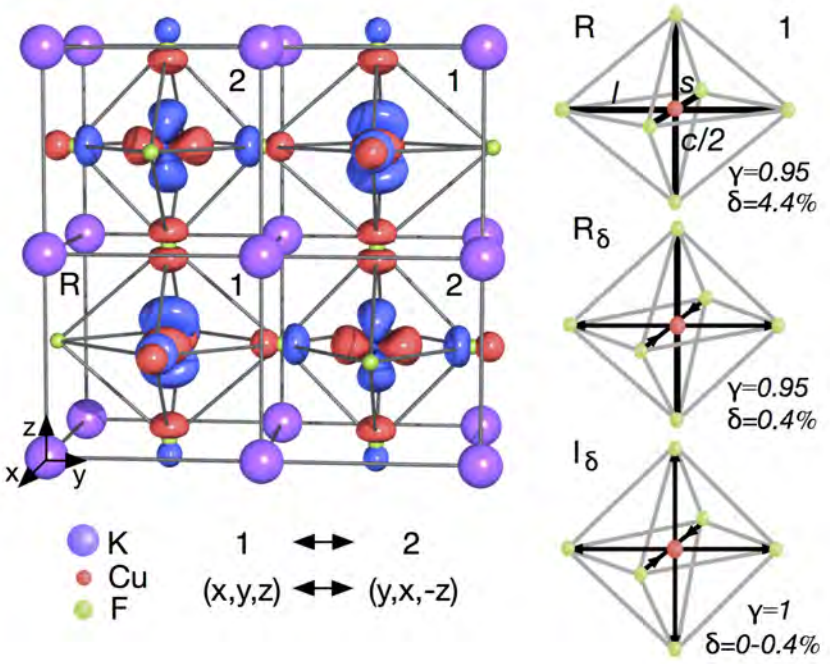

Fig. 1: *Crystal structure, distortions, and orbital order in $KCuF_3$. Cu is at the center of F octahedra enclosed in a K cage. The conventional cell is tetragonal with axes* $\mathbf{a}$, $\mathbf{b}$, $\mathbf{c}$. *The pseudocubic axes* $\mathbf{x}$, $\mathbf{y}$, $\mathbf{z}$ *pointing towards neighboring Cu are shown in the corner. Short (s) and long (l) CuF bonds alternate between* $\mathbf{x}$ *and* $\mathbf{y}$ *along all pseudocubic axes (co-operative Jahn-Teller distortion). The distortions are measured by $\delta = (l-s)/(l+s)/2$ and $\gamma = c/a\sqrt{2}$. R is the experimental structure ($\gamma = 0.95$, $\delta = 4.4\%$), R_δ ($\gamma = 0.95$) and I_δ ($\gamma = 1$) two ideal structures with reduced distortions. In the I_0 structure the cubic crystal-field at the Cu site splits the $3d$ manifold into a t_{2g} triplet and a e_g doublet. In the R structure, site symmetry is lowered further by the tetragonal compression ($\gamma < 1$) and the Jahn-Teller distortion ($\delta \neq 0$). The figure shows the highest-energy d orbital. From Ref. [3].*

enhanced by Coulomb repulsion [4], and Kugel-Khomskii superexchange [2]. Kanamori well illustrated the first mechanism in an influential work [1] in 1960; the main idea is that electron-phonon coupling yields a static Jahn-Teller distortion, which lowers the symmetry of the system and produces a crystal-field splitting. As a consequence, electrons preferably occupy the lower energy states, giving rise to a periodic pattern of occupied orbitals. This is self-evident in the limit in which the crystal-field splitting is very large, let us say, larger than the bandwidth; the lower-energy states at each site will be clearly the first ones to be occupied. If, however, the bandwidth is large in comparison with the crystal-field splitting, the hopping integrals can strongly reduce such a tendency to orbital ordering. A natural question thus arises at this point. How large should the crystal-field splitting be to give rise to a orbitally-ordered state? To answer this question we have to remind ourselves that transition-metal systems with partially filled d shells are also typical examples of strongly-correlated materials. Their low-energy properties are believed to be well described by a generalized multi-band *Hubbard model*

$$\hat{H} = \hat{H}_0 + \hat{H}_U,$$

the sum over a one-electron term $\hat{H}_0$ describing the transition-metal d bands and a Coulomb electron-electron repulsion term $\hat{H}_U$. The one-electron term is

$$\hat{H}_0 = -\sum_{ii'}\sum_{\sigma}\sum_{mm'} t^{i,i'}_{mm'}\, c^{\dagger}_{im\sigma} c_{im'\sigma}\,,$$

where $c^{\dagger}_{im\sigma}$ creates an electron at site i with spin σ and orbital quantum number m, and the parameter $t^{i,i'}_{mm'}$ are the hopping integrals ($i \neq i'$) or the crystal-field splittings ($i = i'$). The Coulomb repulsion can be written as

$$\hat{H}_U = \frac{1}{2}\sum_{i}\sum_{\sigma\sigma'}\sum_{m_\alpha m'_\alpha}\sum_{m_\beta m'_\beta} U_{m_\alpha m_\beta m'_\alpha m'_\beta}\, c^{\dagger}_{im_\alpha\sigma} c^{\dagger}_{im_\beta\sigma'} c_{im'_\beta\sigma'} c_{im'_\alpha\sigma}\,.$$

The elements the Coulomb interaction tensor, $U_{m_\alpha m_\beta m'_\alpha m'_\beta}$, can be expressed in terms of the Slater integrals[1] labeled as F_0, F_2 and F_4. Here we will restrict the discussion to the e_g or t_{2g} manifolds only. In this case, in the basis of real harmonics, the Hubbard model takes the form

$$\begin{aligned}\hat{H} = &-\sum_{ii'}\sum_{\sigma}\sum_{mm'} t^{i,i'}_{mm'}\, c^{\dagger}_{im\sigma} c_{im'\sigma} + U\sum_{i}\sum_{m}\hat{n}_{im\uparrow}\hat{n}_{im\downarrow} \\ &+\frac{1}{2}\sum_{i}\sum_{\sigma\sigma'}\sum_{m\neq m'}\left(U - 2J - J\delta_{\sigma,\sigma'}\right)\hat{n}_{im\sigma}\hat{n}_{im'\sigma'} \\ &-J\sum_{i}\sum_{m\neq m'}\left[c^{\dagger}_{im\uparrow}c^{\dagger}_{im\downarrow}c_{im'\uparrow}c_{im'\downarrow} + c^{\dagger}_{im\uparrow}c_{im\downarrow}c^{\dagger}_{im'\downarrow}c_{im'\uparrow}\right], \end{aligned} \tag{1}$$

where m, m' are here either t_{2g} or e_g states, $U_{mm'mm'} = U_{m,m'} = U - 2J(1-\delta_{m,m'})$ and, for $m \neq m'$, $U_{mm'm'm} = J_{m,m'} = J$. The last two terms describe the pair-hopping and spin-flip processes ($U_{mmm'm'} = J_{m,m'}$ if we use a basis of real harmonics, while for spherical harmonics $U_{mmm'm'} = 0$). Finally, $U = U_0$ and $J = J_1$ (t_{2g} electrons) or $J = J_2$ (e_g electrons), with

$$\begin{aligned} U_0 =& F_0 + \frac{8}{5}\mathcal{J}_{\rm avg} \\ \mathcal{J}_{\rm avg} =& \frac{5}{7}\frac{1}{14}(F_2 + F_4) \\ J_1 =& \frac{3}{49}F_2 + \frac{20}{9}\frac{1}{49}F_4 \\ J_2 =& -2\mathcal{J}_{\rm avg} + 3J_1\,. \end{aligned}$$

In strongly correlated systems described by a Hamiltonian of type (1) it turns out that a small crystal-field splitting, a fraction of the bandwidth, is sufficient to produce orbital order even at high temperature. This happens because the Coulomb repulsion effectively enhances it, while suppressing orbital fluctuations [4]. Hence, the mechanism illustrated by Kanamori becomes very efficient in the presence of strong correlations (small t/U limit, the typical limit for Mott insulators; here t is an average hopping integral). This is, however, not the end of the story:

[1] For a pedagogical introduction see, e.g, Ref. [5], or the lecture of Robert Eder in the present book.

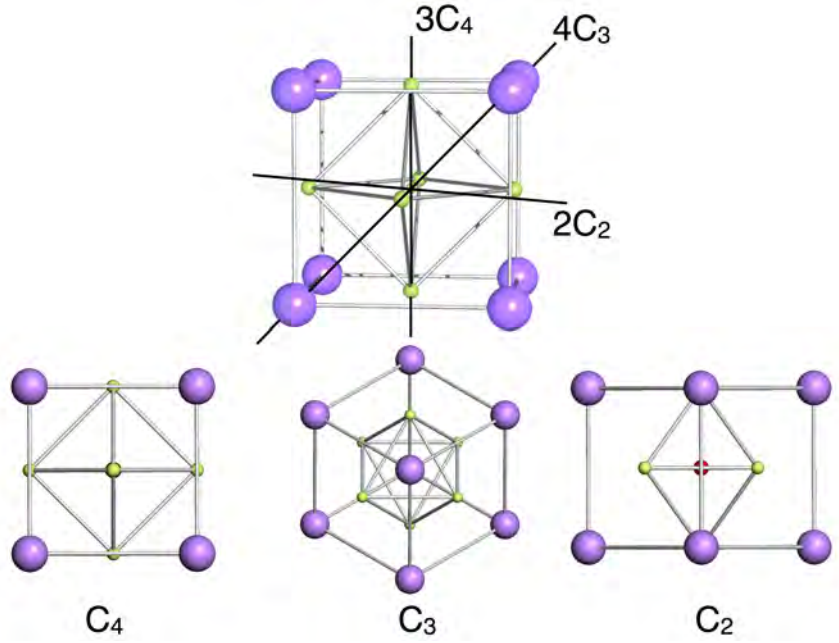

Fig. 2: *The unit cell of a cubic perovskite ABC_3 and its symmetry axes; the lattice constant is a. The transition metal B (red) is at $(0,0,0)$; the ligands C (green) are located at $(\pm a/2,0,0)$, $(0,\pm a/2,0)$,$(0,0,\pm a/2)$ and form an octahedron; the cations A are located at $(\pm a/2,\pm a/2,\pm a/2)$, $(\pm a/2,\mp a/2,\pm a/2)$, $(\mp a/2,\pm a/2,\pm a/2)$, $(\pm a/2,\pm a/2,\mp a/2)$ and form a cube. The bottom figures illustrate the rotational symmetries of the cell.*

Coulomb electron-electron interaction provides, in addition, an alternative explanation of the origin of orbital ordering. In a seminal work, Kugel and Khomskii [2] have shown in 1973 that, in the presence of orbital degeneracy, many-body effects can produce orbital ordering even in the absence of a static distortion, i.e., of a crystal-field splitting. This happens via electronic spin-orbital superexchange, the effective low-energy interaction which emerges, in the small t/U limit, from the orbitally-degenerate Hubbard model. In this picture, the co-operative Jahn-Teller distortion is rather the consequence than the cause of orbital order. The predictions of the two theories for what concerns, e.g., the final broken-symmetry structure, are basically identical; thus it is very hard to determine which of the two mechanisms, Jahn-Teller effect or Kugel-Khomskii superexchange, dominates in real systems. In the last part of the lecture we will see how the problem was recently solved [3, 6] by using a new theoretical approach based on the local-density-approximation + dynamical mean-field theory (LDA+DMFT) [7, 8] method. For the representative materials $KCuF_3$ and $LaMnO_3$, it was shown that Kugel-Khomskii superexchange alone, although strong, cannot explain the presence of the Jahn-Teller distortion above 350 K ($KCuF_3$) [3] and 650 K ($LaMnO_3$) [6]; experimentally, however, the distortion persists in both systems basically up to the melting temperature. This leads to the conclusion that a mechanism directly generating a static crystal-field splitting, such as the standard Jahn-Teller effect, is necessary to explain the experimental findings.

2 Cubic crystal-field splitting

Let us consider a system with the ideal cubic perovskite structure ABC_3, shown in Fig. 2, where B is the transition metal with partially filled d shell. The site symmetry at a B site is cubic; as we mentioned before, d states split into e_g and t_{2g} at a site with cubic symmetry. Let us understand how exactly this happens. For a free ion, the potential $v_{\rm R}(\boldsymbol{r})$ which determines the one-electron energies is rotationally invariant, i.e., it has symmetry $O(3)$. This means that all one-electron states within a given l shell are degenerate, as it happens in the case of hydrogen-like atoms. When the same ion is inside a molecule or a solid, $v_{\rm R}(\boldsymbol{r})$ has in general lower symmetry, the symmetry corresponding to a finite point group.[2] Thus one-electron states within a given shell l, degenerate for the free atom, can split. The symmetry reduction arises from the *crystal field*; the latter has two components, the Coulomb potential generated by the surrounding charged ions, dominant in ionic crystals, and the *ligand field* due to the bonding neighbors. In this section we will analyze the first contribution; the covalent contribution to the crystal-field splitting is discussed in the next section. Both effects give rise to a similar splitting of levels, and which contribution dominates depends on the system.

Let us thus assume that the crystal is perfectly ionic and that the ions can be treated as point charges q_α (point-charge model). Then, the one-electron potential can be written as

$$v_{\rm R}(\boldsymbol{r}) = \sum_\alpha \frac{q_\alpha}{|\boldsymbol{R}_\alpha - \boldsymbol{r}|} = v_0(r) + \sum_{\alpha\neq 0} \frac{q_\alpha}{|\boldsymbol{R}_\alpha - \boldsymbol{r}|} = v_0(r) + v_c(\boldsymbol{r}), \tag{2}$$

where $\boldsymbol{R}_\alpha$ are the positions of the ions and q_α their charges. The term $v_0(r)$ is the ionic central potential at site $\boldsymbol{R}_0$, and has spherical symmetry. The term $v_c(\boldsymbol{r})$ is the electric field generated at a given site $\boldsymbol{R}_0$ by all the surrounding ions in the crystal and it is called *crystal-field potential*. For the perovskite structure ABC_3 we are interested in the crystal-field potential at the site of the transition metal, B. Let us first assume that only the contribution of nearest neighbors (the negative C ions, typically oxygens or fluorines) is relevant. The six C ions are located at positions $(\pm d_C, 0, 0), (0, \pm d_C, 0), (0, 0, \pm d_C)$ and have all the same charge q_C, while the B ion is at $(0, 0, 0)$; in terms of a, the cubic lattice constant, $d_C = a/2$. Then we can write the potential around ion B as

$$v_{\rm R}(\boldsymbol{r}) = \frac{q_B}{r} + \frac{q_C}{d_C}\left[\Delta v\left(\frac{x}{d_C};\frac{r}{d_C}\right) + \Delta v\left(\frac{y}{d_C};\frac{r}{d_C}\right) + \Delta v\left(\frac{z}{d_C};\frac{r}{d_C}\right)\right]$$

where

$$\Delta v(\xi;\rho) = \frac{1}{\sqrt{1+\rho^2}}\left[\frac{1}{\sqrt{1+\frac{2\xi}{1+\rho^2}}} + \frac{1}{\sqrt{1-\frac{2\xi}{1+\rho^2}}}\right].$$

Via the Taylor expansion

$$\frac{1}{\sqrt{1+\eta}} \sim 1 - \frac{1}{2}\eta + \frac{3}{8}\eta^2 - \frac{5}{16}\eta^3 + \frac{35}{128}\eta^4 + \dots$$

[2] For a concise introduction to group theory see, e.g., Ref. [9], chapter 6.

we can find the approximate expression of $\Delta v(\xi;\rho)$ for small ξ, i.e., close to ion B; the first contribution with less than spherical symmetry is

$$v_{\rm oct}(\boldsymbol{r}) = \frac{35}{4}\frac{q_C}{d^5}\left(x^4+y^4+z^4-\frac{3}{5}r^4\right) = D\left(x^4+y^4+z^4-\frac{3}{5}r^4\right).$$

We can rewrite this potential as

$$v_{\rm oct}(\boldsymbol{r}) = \frac{7\sqrt{\pi}}{3}\frac{q_C}{d^5}r^4\left[Y_0^4(\theta,\phi)+\sqrt{\frac{5}{14}}\left(Y_4^4(\theta,\phi)+Y_{-4}^4(\theta,\phi)\right)\right], \tag{3}$$

where

$$\begin{aligned} Y_0^4(\theta,\phi) &= \frac{3}{16}\frac{1}{\sqrt{\pi}}\left(35\cos^4\theta-30\cos^2\theta+3\right) = \frac{3}{16}\frac{1}{\sqrt{\pi}}\frac{35z^4-30z^2r^2-3r^4}{r^4}, \\ Y_{\pm4}^4(\theta,\phi) &= \frac{3}{16}\sqrt{\frac{35}{2\pi}}\sin^4\theta e^{\pm4i\phi} = \frac{3}{16}\sqrt{\frac{35}{2\pi}}\frac{(x\pm iy)^4}{r^4}. \end{aligned}$$

To obtain the crystal field due to the cubic cage of cations A (with charge q_A), shown in Fig. 2 we repeat the same calculation; the main difference is that there are eight A ions, located at positions of type $(\pm d_A,\pm d_A,\pm d_A)$,$(\mp d_A,\pm d_A,\pm d_A)$, $(\pm d_A,\mp d_A,\pm d_A)$, $(\pm d_A,\pm d_A,\mp d_A)$ with $d_A = a/2$. By following the same procedure that we used for B octahedron, one can show that

$$v_{\rm cube}(\boldsymbol{r}) = -\frac{8}{9}\frac{q_A}{q_C}\left(\frac{d_A}{d_C}\right)^5 v_{\rm oct}(\boldsymbol{r}),$$

i.e., $v_{\rm cube}(\boldsymbol{r})$ has the same form as $v_{\rm oct}(\boldsymbol{r})$; this happens because a cube and an octahedron are dual polyhedra[3] and have therefore the same symmetry properties. If $q_A/q_C > 0$, $v_{\rm cube}(\boldsymbol{r})$ has opposite sign than $v_{\rm oct}(\boldsymbol{r})$; in the case of a perovskite, however, A positions are occupied by cations, i.e., positive ions; thus the crystal field due to the A cage has the same sign of the crystal field generated by the B octahedron.

The crystal-field potential $v_{\rm c}(\boldsymbol{r})$ lowers the site symmetry and can therefore split the $(2l+1)$-fold degeneracy of the atomic levels. To calculate how the l manifold splits, we use two approaches. The first is exact and based on group theory. We assume for simplicity that the symmetry is only O (group of the proper rotations which leave a cube invariant); using the full symmetry group of the cube, $O_h = O\otimes C_i$ (where C_i is the group made by the identity and the inversion) does not change the result, because the spherical harmonics are all either even or odd. The character table of group O is given by

partner	functions	O	E	$8C_3$	$3C_2$	$6C_2'$	$6C_4$
	$(x^2+y^2+z^2)$	A_1	1	1	1	1	1
		A_2	1	1	1	-1	-1
	$(x^2-y^2, 3z^2-r^2)$	E	2	-1	2	0	0
(R_x,R_y,R_z)	(x,y,z)	T_1	3	0	-1	-1	1
	(xy,xz,yz)	T_2	3	0	-1	1	-1

(4)

[3]Every polyhedron has a dual which can be obtained by exchanging the location of faces and vertices.

Let us explain this table. The first line yields the group, here O, and the symmetry operations of the group, collected in classes $\mathcal{C}_k$, here $\{E\}, \{C_3\}, \{C_2\}, \{C_2'\}, \{C_4\}$. For each class only a representative element is given and the number N_k in front of this element yields the number of operations in the class; for example $8C_3$ indicates 8 symmetry operations in class $\{C_3\}$. The symmetry operation C_n is an anticlockwise rotation of an angle $\alpha = 2\pi/n$. For a finite group with h elements, the h group operations $\{O(g)\}$ can be expressed as h matrices $\{\Gamma(g)\}$ acting on an invariant linear space; the basis of this space, $\{|m\rangle\}$, can be, for example, a finite set of linearly independent functions, such as the spherical harmonics with angular quantum number l. The collection of matrices $\{\Gamma(g)\}$ is a *representation* of the group; the dimension of the invariant linear space yields also the dimension of the matrices, i.e., the *dimensionality* of the representation. Each group has infinitely many possible representations, but some sets are special and play the role of an orthonormal basis in a space of vectors; they are called *irreducible*. If G is the group of operations which leave the Hamiltonian invariant, the irreducible representations of G can be used to classify all eigenstates of the Hamiltonian; eigenstates which build a basis for different irreducible representations are mutually orthogonal and have typically (leaving the cases of accidental degeneracy and hidden symmetry aside) different energies. The irreducible representations Γ_i of group O are listed in the first column of Table 4, below the group name; they are A_1 (trivial representation, made of 1-dimensional identity matrices), A_2, also 1-dimensional, E, two-dimensional, and T_1 and T_2, both three-dimensional. The numbers appearing in Table 4 are the characters $\chi_i(g)$, defined as

$$\chi_i(g) = \mathrm{Tr}\ \Gamma_i(g) = \sum_m \langle m|\Gamma_i(g)|m\rangle = \sum_m \Gamma_i^{mm}(g)\,.$$

For a given representation (corresponding to a line of Table 4) the character for a specific element can be found below the corresponding class label (columns of Table 4); all elements in the same class have the same character. Thus the second column of the character table, showing the character of the identity, yields also the dimensionality d_i of the representation itself. Next we calculate the characters of the matrix representation Γ^l constructed using spherical harmonics with angular quantum number l as a basis. An easy way to do this is to assume that the rotation axis is also the axis of quantization, i.e., $\hat{z}$; the characters do not depend on the actual direction of the quantization axis but only on the angle α of rotation. Thus for $O(g) = C_\alpha$ we have

$$\begin{aligned} C_\alpha\ Y_m^l(\theta,\phi) =& Y_m^l(\theta,\phi-\alpha) = e^{-im\alpha}\ Y_m^l(\theta,\phi) \\ \Gamma^l_{mm'}(C_\alpha) =& \delta_{mm'} e^{-im\alpha}. \end{aligned}$$

This yields the following expression for the character

$$\chi^l(C_\alpha) = \sum_{m=-l}^{l} e^{-im\alpha} = \frac{\sin(l+\frac{1}{2})\alpha}{\sin\frac{\alpha}{2}}\,.$$

The characters for representations Γ^l are therefore

O	E	$8C_3$	$3C_2$	$6C_2$	$6C_4$
$\Gamma^0 = \Gamma^s$	1	1	1	1	1
$\Gamma^1 = \Gamma^p$	3	0	-1	-1	1
$\Gamma^2 = \Gamma^d$	5	-1	1	1	-1
$\Gamma^3 = \Gamma^f$	7	1	-1	-1	-1

In spherical symmetry (group $O(3)$) representations Γ^l are irreducible. In cubic symmetry (group O), instead, the Γ^l can be reducible, i.e., they can be written as the tensorial sum $\oplus$ of irreducible representations of the group O. The various components can be found by using the orthogonality properties of irreducible representations, which lead to the decomposition formula

$$\Gamma^l = \bigoplus_i a_i \Gamma_i \qquad \text{with} \quad a_i = \langle \Gamma_i | \Gamma^l \rangle = \frac{1}{h} \sum_g \left[\chi_i(g)\right]^* \chi^l(g)\,, \tag{5}$$

where h, the number of elements in the group, is 24 for group O. Hereafter the symmetry representations of electronic states are written in lower case to distinguish them from capital letters which we will use later for labeling vibrational modes. We find

$$\begin{aligned} \Gamma^s &= a_1 \\ \Gamma^p &= t_1 \\ \Gamma^d &= e \oplus t_2 \\ \Gamma^f &= a_2 \oplus t_1 \oplus t_2\,. \end{aligned}$$

Thus, in cubic symmetry, the s- and the p-functions do not split, because the a_1 irreducible representation is one-dimensional and the t_1 irreducible representation is 3-dimensional. Instead, d-functions split into a doublet and a triplet, and f-functions into a singlet and two triplets. To determine which functions $\{|m\rangle_i\}$ form a basis (a so-called set of *partner functions*) for a specific irreducible representation Γ_i we can, e.g., use the projector for that representation

$$\hat{\mathcal{P}}_i = \frac{d_i}{h} \sum_g \left[\chi_i(g)\right]^* O(g). \tag{6}$$

In our case, we can read directly the partner functions $\{|m\rangle_i\}$ for a given irreducible representation of the group O in the first column of Table 4, on the left. In short, for representation e partner functions are (x^2-y^2, $3z^2-r^2$) and for representation t_2 they are (xy, xz, yz). A small step is still missing: As we already mentioned, the full symmetry of the B site is O_h, and the group O_h can be obtained as direct product, $O_h = O \otimes C_i$; with respect to O, group O_h has twice the number of elements and classes, and thus twice the number of irreducible representations. The latter split into even ($a_{1g}, a_{2g}, e_g, t_{1g}, t_{2g}$) and odd ($a_{1u}, a_{2u}, e_u, t_{1u}, t_{2u}$). All d-functions are even, and therefore x^2-y^2 and $3z^2-r^2$ are partners functions for the e_g irreducible representation, while xy, xz, yz are partner functions for the t_{2g} irreducible representation. Summarizing,

t_{2g} states (xy, xz, and yz) and e_g states (x^2-y^2 and $3z^2-r^2$) have in general (again excluding the cases of accidental degeneracy and hidden symmetry) different energy.
Group theory tells us *if* the degenerate $2l+1$ levels split at a given site in a lattice, but not of *how much* they do split, and which orbitals are higher in energy. We can, however, calculate the crystal-field splitting approximately using the potential (3) as a perturbation. This is the second approach previously mentioned; differently from group theory, it is not exact, but it gives us an estimate of the size of the effect and the sign of the splitting. For d states we can calculate the elements of the octahedral potential $v_{\rm oct}(\boldsymbol{r})$ in the basis of atomic functions $\psi_{nlm}(\rho,\theta,\phi) = R_{nl}(\rho)Y_l^m(\theta,\phi)$, where $R_{nl}(\rho)$ is the radial part, $\rho = Zr$, Z is the atomic number, $Y_l^m(\theta,\phi)$ a spherical harmonic, and n the principal quantum number (Appendix B). We obtain

$$\langle\psi_{n20}\ |\hat{v}_{\rm oct}|\psi_{n20}\ \rangle = +6Dq \qquad \langle\psi_{n2\pm1}|\hat{v}_{\rm oct}|\psi_{n2\pm1}\rangle = -4Dq$$
$$\langle\psi_{n2\pm2}|\hat{v}_{\rm oct}|\psi_{n2\pm2}\rangle = +\ Dq \qquad \langle\psi_{n2\pm2}|\hat{v}_{\rm oct}|\psi_{n2\mp2}\rangle = +5Dq$$

where $Dq = q_C\langle r^4\rangle/6d_C^5$ and $\langle r^k\rangle = \int r^2dr\ r^k\ R_{n2}^2(Zr)$. The crystal-field splitting between e_g and t_{2g}-states can be then obtained by diagonalizing the crystal-field matrix

$$H_{\rm CF} = \begin{pmatrix} Dq & 0 & 0 & 0 & 5Dq \\ 0 & -4Dq & 0 & 0 & 0 \\ 0 & 0 & 6Dq & 0 & 0 \\ 0 & 0 & 0 & -4Dq & 0 \\ 5Dq & 0 & 0 & 0 & Dq \end{pmatrix}.$$

We find two degenerate e_g eigenvectors with energy $6Dq$

$$|\psi_{n20}\rangle = |3z^2-r^2\rangle,$$
$$\frac{1}{\sqrt{2}}\left[|\psi_{n22}\rangle + |\psi_{n2-2}\rangle\right] = |x^2-y^2\rangle,$$

and three degenerate t_{2g} eigenvectors with energy $-4Dq$

$$\frac{i}{\sqrt{2}}\left[|\psi_{n22}\rangle - |\psi_{n2-2}\rangle\right] = |xy\rangle,$$
$$\frac{1}{\sqrt{2}}\left[|\psi_{n21}\rangle - |\psi_{n2-1}\rangle\right] = |xz\rangle,$$
$$\frac{i}{\sqrt{2}}\left[|\psi_{n21}\rangle + |\psi_{n2-1}\rangle\right] = |yz\rangle.$$

The total splitting is

$$\Delta_{\rm CF} = E_{e_g} - E_{t_{2g}} = 10Dq.$$

Thus the e_g-states are actually higher in energy than the t_{2g}-states. This happens because e_g electrons point towards the negative C ions (see Fig. 3), and will therefore feel a larger Coulomb repulsion than t_{2g} electrons, which have the lobes directed between the negative C ions.

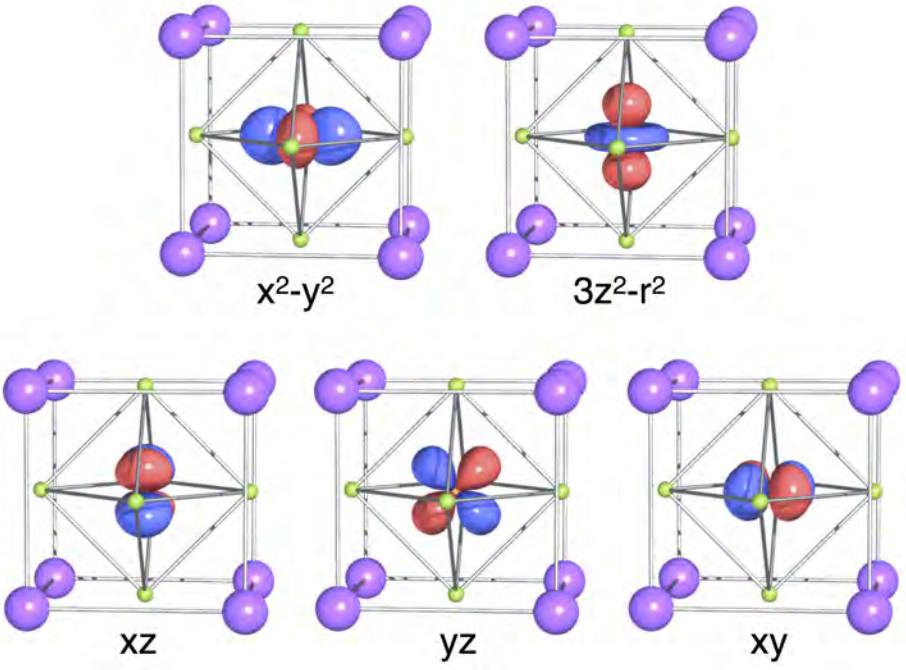

Fig. 3: *The Cu e_g and t_{2g} Wannier orbitals for the cubic perovskite $KCuF_3$, obtained from first principles calculations, using a Wannier basis that spans all bands.*

How general is, however, this result? We obtained it via a truncated Taylor expansion of the potential close to the nucleus. Does this mean that we have perhaps neglected important higher-order terms? For a generic lattice, we can expand the crystal-field potential (2) in spherical harmonics using the exact formula

$$\frac{1}{|\boldsymbol{r}_1 - \boldsymbol{r}_2|} = \sum_{k=0}^{\infty} \frac{r_<^k}{r_>^{k+1}} \frac{4\pi}{2k+1} \sum_{q=-k}^{k} Y_q^k(\theta_2, \phi_2) \overline{Y}_q^k(\theta_1, \phi_1),$$

where $r_<$ ($r_>$) is the smaller (larger) of r_1 and r_2. The crystal-field potential takes the form

$$v_c(\boldsymbol{r}) = \sum_{k=0}^{\infty} \sum_{q=-k}^{k} B_q^k Y_q^k, \tag{7}$$

where $B_q^k = (-1)^q \bar{B}_{-q}^k$. Although the series in (7) is in principle infinite, one can terminate it by specifying the wavefunctions, since

$$\langle Y_m^l | Y_q^k | Y_{m'}^l \rangle = 0 \quad \text{if} \quad k > 2l.$$

For example, for p electrons $k \leq 2$, for d-electrons, $k \leq 4$, and f electrons $k \leq 6$. Thus, for d-electrons and O_h symmetry, the terms that appear in the potential (3) are actually also the only ones to be taken into account, because all other terms yield an expectation value equal to zero. Finally, the derivation of both equations (3) and (7) presented here might let us think that the first-nearest neighbors are those that determine the crystal field. This is, however, not always the case, because Coulomb repulsion is a long-range interaction; for example, in some systems

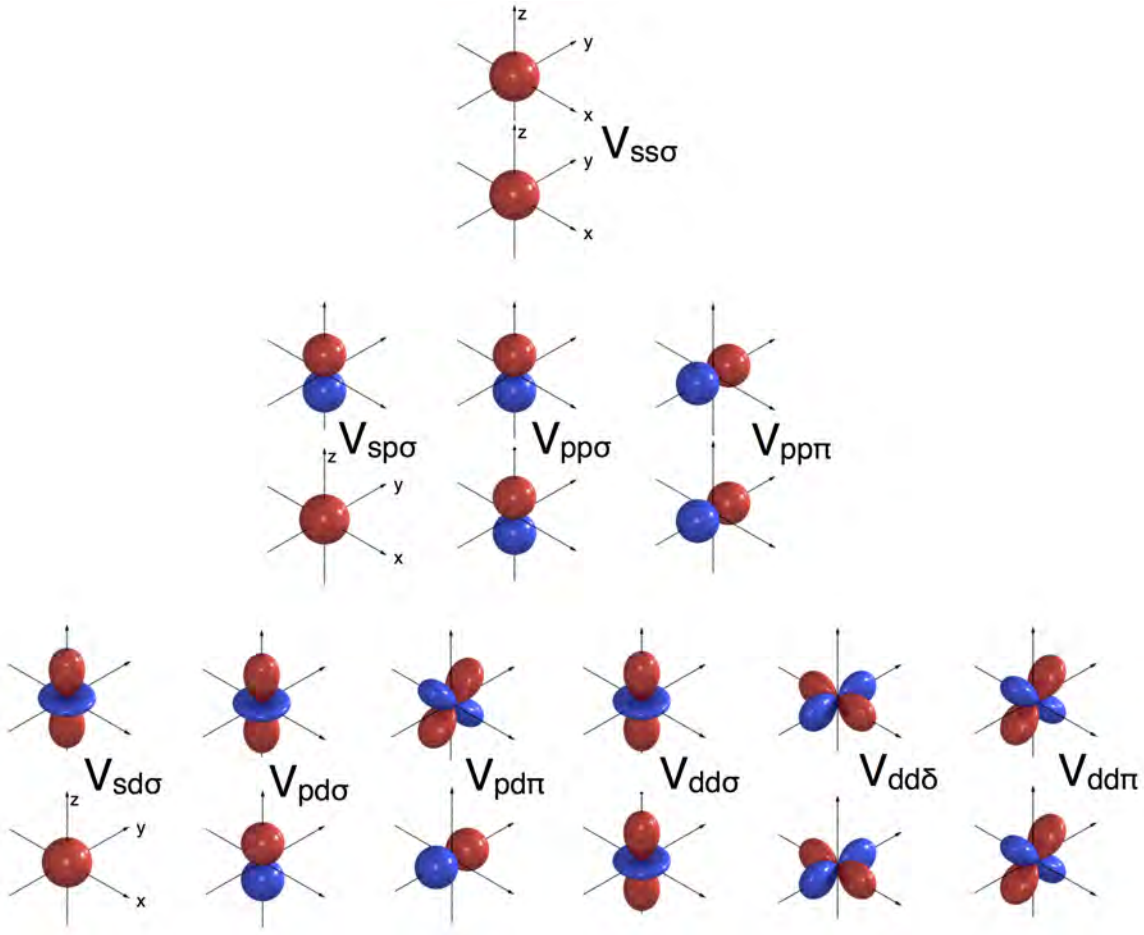

Fig. 4: *Independent Slater-Koster two-center integrals for s, p, and d atomic orbitals (Appendix B). The label σ indicates that the bonding state is symmetrical with respect to rotations about the bond axis; the label π that the bond axis lies in a nodal plane; the label δ that the bond axis lies in two nodal planes.*

the first-nearest neighbors yield cubic symmetry at a given site but further neighbors lower the symmetry.[4] Furthermore, the point-charge model discussed in this section is useful to explain the relation between crystal field and site symmetry, however yields unsatisfactory results for the crystal-field splitting in real materials. Corrections beyond the point-charge approximation turn out to be important. In addition, as we will see in the next section, in many systems the crystal field has a large, sometimes dominant, covalent contribution, the ligand field. The modern approach to calculate crystal-field splittings including the ligand-field contribution is based on material-specific potentials obtained *ab-initio* via density-functional-theory (DFT) and the associated DFT localized Wannier functions. Nevertheless, it is worth to point out the remarkable success of the point-charge model in giving qualitatively correct d crystal-field states in cubic perovskites; such a success relies on the fact that this approach, even if approximate, yields the exact symmetry of final states, i.e., the same obtained via group theory, and does not neglect any relevant (e.g., high-order) term.

[4] This means that, of course, O_h is not the actual symmetry of the site.

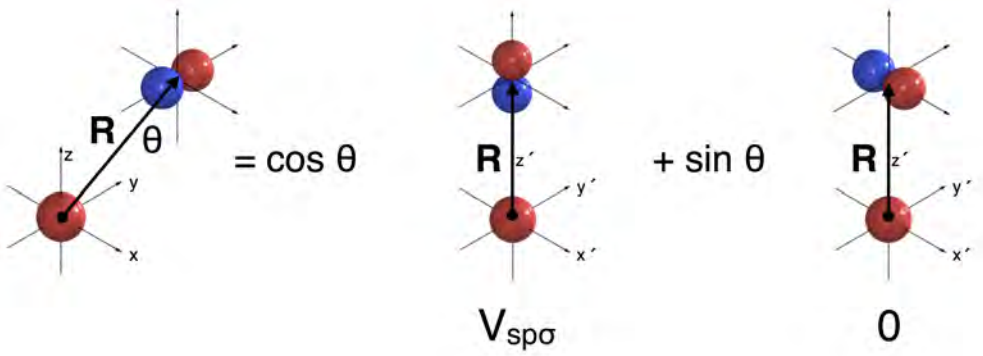

Fig. 5: *Illustration of the decomposition of a general s-p two-center integral in terms of $V_{sp\sigma}$.*

3 Tight-binding e_g and t_{2g} bands of cubic perovskites

In this section we will construct the bands of $KCuF_3$ in the cubic limit using tight-binding theory. Let us first remind ourselves of the crucial steps of this approach. The one-electron Hamiltonian can be written as

$$\hat{h}_e(\boldsymbol{r}) = -\frac{1}{2}\nabla^2 + \sum_{i\alpha} v(\boldsymbol{r} - \boldsymbol{T}_i - \boldsymbol{R}_\alpha) = -\frac{1}{2}\nabla^2 + v_R(\boldsymbol{r}),$$

where $\boldsymbol{R}_\alpha$ are the positions of the basis $\{\alpha\}$ atoms in the unit cell and $\boldsymbol{T}_i$ the lattice vectors. We take as a basis atomic orbitals with quantum numbers lm (we drop here the principal quantum number for convenience). For each atomic orbital we construct a Bloch state

$$\psi^\alpha_{lm}(\boldsymbol{k}, \boldsymbol{r}) = \frac{1}{\sqrt{N}} \sum_i e^{i\boldsymbol{T}_i\cdot\boldsymbol{k}}\, \psi_{lm}(\boldsymbol{r} - \boldsymbol{T}_i - \boldsymbol{R}_\alpha), \tag{8}$$

where N is the number of lattice sites. In the Bloch basis (8), the Hamiltonian and the overlap matrix are given by

$$H^{\alpha,\alpha'}_{lm,l'm'}(\boldsymbol{k}) = \langle \psi^\alpha_{lm}(\boldsymbol{k}) | \hat{h}_e | \psi^{\alpha'}_{l'm'}(\boldsymbol{k}) \rangle,$$
$$O^{\alpha,\alpha'}_{lm,l'm'}(\boldsymbol{k}) = \langle \psi^\alpha_{lm}(\boldsymbol{k}) | \psi^{\alpha'}_{l'm'}(\boldsymbol{k}) \rangle.$$

These matrices define a generalized eigenvalue problem, the solution of which yields the band structure. The Hamiltonian matrix is given by

$$H^{\alpha,\alpha'}_{lm,l'm'}(\boldsymbol{k}) = \varepsilon^0_{l'\alpha'}\, O^{\alpha,\alpha'}_{lm,l'm'}(\boldsymbol{k}) + \Delta\varepsilon^\alpha_{lm,l'm'}\, \delta_{\alpha,\alpha'} - \frac{1}{N} \sum_{i\alpha\neq i'\alpha'} e^{i(\boldsymbol{T}_{i'} - \boldsymbol{T}_i)\cdot\boldsymbol{k}}\, t^{i\alpha,i'\alpha'}_{lm,l'm'}\,.$$

Here $\varepsilon^0_{l\alpha}$ are the atomic levels, and $\Delta\varepsilon^\alpha_{lm,l'm'}$ the crystal-field matrix elements

$$\Delta\varepsilon^\alpha_{lm,l'm'} = \int d\boldsymbol{r}\; \overline{\psi_{lm}}(\boldsymbol{r} - \boldsymbol{R}_\alpha) \Big[v_R(\boldsymbol{r}) - v(\boldsymbol{r} - \boldsymbol{R}_\alpha) \Big] \psi_{l'm'}(\boldsymbol{r} - \boldsymbol{R}_\alpha)\,, \tag{9}$$

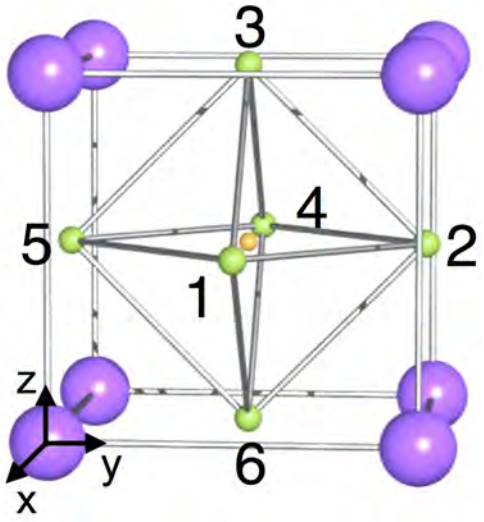

Fig. 6: *Unit cell of idealized cubic $KCuF_3$ with cubic axes in the left corner.*

which are two-center integrals. Finally,

$$t^{i\alpha,i'\alpha'}_{lm,l'm'} = -\int d\boldsymbol{r}\ \overline{\psi_{lm}}(\boldsymbol{r}-\boldsymbol{R}_\alpha-\boldsymbol{T}_i)\Big[v_R(\boldsymbol{r})-v(\boldsymbol{r}-\boldsymbol{R}_{\alpha'}-\boldsymbol{T}_{i'})\Big]\psi_{l'm'}(\boldsymbol{r}-\boldsymbol{R}_{\alpha'}-\boldsymbol{T}_{i'}). \quad (10)$$

The hopping integrals (10) contain two- and three-center terms; if the basis is sufficiently localized we can, however, neglect the three-center contributions and assume $t^{i\alpha,i'\alpha'}_{lm,l'm'} \sim -V^{i\alpha,i'\alpha'}_{lm,l'm'}$, where

$$V^{i\alpha,i'\alpha'}_{lm,l'm'} = \int d\boldsymbol{r}\ \overline{\psi_{lm}}(\boldsymbol{r}-\boldsymbol{R}_\alpha-\boldsymbol{T}_i)v(\boldsymbol{r}-\boldsymbol{R}_\alpha-\boldsymbol{T}_i)\psi_{l'm'}(\boldsymbol{r}-\boldsymbol{R}_{\alpha'}-\boldsymbol{T}_{i'})$$

is a Slater-Koster two-center integral (Appendix B). A generic Slater-Koster two-center integral can be expressed as a function of a few independent two-center integrals, shown in Fig. 4 for s, p, and d-functions. Apart from the σ bond, which is the strongest, other bonds are possible; the π bonds are made of orbitals which share a nodal plane to which the bond axis belongs, and the δ bond, for which two nodal planes intersect in the bond axis connecting the two ions. Fig. 5 shows how to obtain a generic two-center integral involving p and s orbitals.[5] Let us now consider the case of the e_g and t_{2g} bands of $KCuF_3$; here we assume for simplicity that the system is an ideal cubic perovskite, shown in Fig. 6. The primitive cell contains one formula unit (a single K cube in Fig. 1). The cubic axes are $\boldsymbol{x}$, $\boldsymbol{y}$, $\boldsymbol{z}$, and the lattice constant is a. A Cu atom at site $\boldsymbol{R}_i$ is surrounded by two apical F atoms, F_3 at $\boldsymbol{R}_i + \frac{1}{2}\boldsymbol{z}$ and F_6 at $\boldsymbol{R}_i - \frac{1}{2}\boldsymbol{z}$, and four planar F atoms, F_1 and F_4 at $\boldsymbol{R}_i \pm \frac{1}{2}\boldsymbol{x}$ and F_2 and F_5 at $\boldsymbol{R}_i \pm \frac{1}{2}\boldsymbol{y}$. In Fig. 7 one can see the effects of the cubic approximation on the e_g bands: the crystal-field splitting of the e_g states is zero, the band width slightly reduced, gaps disappear, and the dispersion relations is sizably modified. The cubic band structure in Fig. 7 was obtained with a unit cell containing two formula units, in order to compare it with the band structure of the experimental (Jahn-Teller distorted) structure of $KCuF_3$; hence we see four (instead of two) e_g bands. The band-structure of cubic $KCuF_3$ for

[5] More details on the tight-binding approach can be found either in Ref. [9] or in the lecture of Matthew Foulkes.

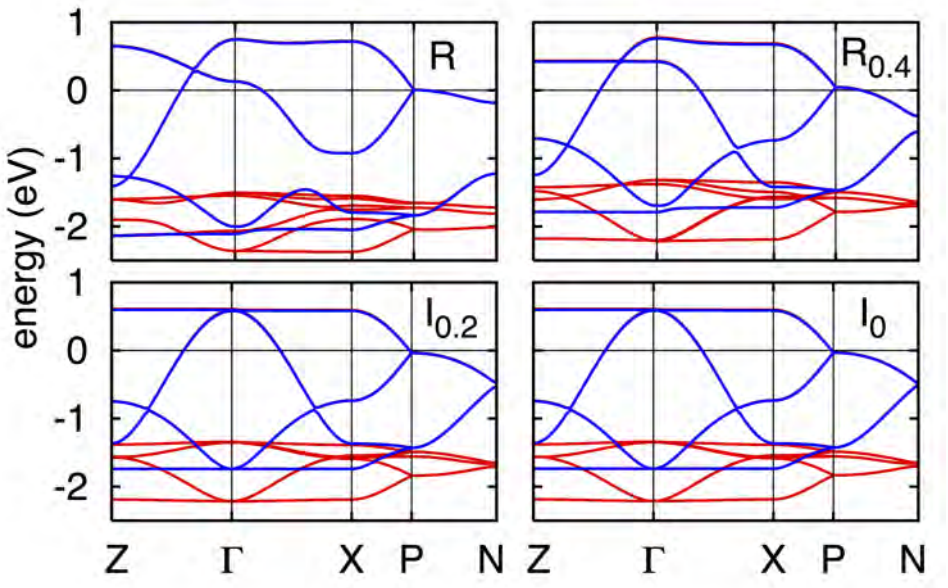

Fig. 7: *LDA e_g (blue) and t_{2g}(red) band structure of $KCuF_3$ for the experimental structure (R) and ideal structures with progressively reduced distortions (see Fig. 1). I_0: simple cubic. The unit cell used in this calculation contains two formula units. The figure is from Ref. [3].*

a cell with one formula unit is shown in Fig. 8; in the following we will refer for comparison to that figure only. Let us take as tight-binding basis the atomic $3d$ e_g orbitals for Cu and the $2p$ orbitals for F; we neglect for convenience the overlap integrals (i.e., we assume that our atomic functions are, approximately, localized *Wannier functions*). For such a tight-binding basis the only relevant Slater-Koster parameter is $V_{pd\sigma}$. The $|3z^2-r^2\rangle_i$ and $|x^2-y^2\rangle_i$ states of the Cu at $\boldsymbol{R}_i$ can couple via $V_{pd\sigma}$ to $|z^c\rangle_i$, the p_z orbitals of F_3 and F_6, to $|x^a\rangle_i$, the p_x orbitals of F_1 and F_4 and to $|y^b\rangle_i$, the p_y orbitals of F_2 and F_5. From the basis $|\alpha\rangle_i$ of localized atomic functions we construct the Bloch states $|\boldsymbol{k}\alpha\rangle = \frac{1}{\sqrt{N}}\sum_i e^{i\boldsymbol{k}\cdot\boldsymbol{R}_i}|\alpha\rangle_i$, and obtain the tight-binding Hamiltonian

$H^{\rm TB}_{e_g}$	$\lvert\boldsymbol{k}\ z^c\rangle$	$\lvert\boldsymbol{k}\ x^a\rangle$	$\lvert\boldsymbol{k}\ y^b\rangle$	$\lvert\boldsymbol{k}\ 3z^2-r^2\rangle$	$\lvert\boldsymbol{k}\ x^2-y^2\rangle$
$\lvert\boldsymbol{k}\ z^c\rangle$	ε_p	0	0	$-2V_{pd\sigma}s_z$	0
$\lvert\boldsymbol{k}\ x^a\rangle$	0	ε_p	0	$V_{pd\sigma}s_x$	$-\sqrt{3}V_{pd\sigma}s_x$
$\lvert\boldsymbol{k}\ y^b\rangle$	0	0	ε_p	$V_{pd\sigma}s_y$	$\sqrt{3}V_{pd\sigma}s_y$
$\lvert\boldsymbol{k}\ 3z^2-r^2\rangle$	$-2V_{pd\sigma}\overline{s}_z$	$V_{pd\sigma}\overline{s}_x$	$V_{pd\sigma}\overline{s}_y$	ε_d	0
$\lvert\boldsymbol{k}\ x^2-y^2\rangle$	0	$-\sqrt{3}V_{pd\sigma}\overline{s}_x$	$\sqrt{3}V_{pd\sigma}\overline{s}_y$	0	ε_d

(11)

where $s_\alpha = ie^{-ik_\alpha a/2}\sin k_\alpha a/2$, $\alpha = x,y,z$, $\varepsilon_p < \varepsilon_d = \varepsilon_p + \Delta_{pd}$, and $V_{pd\sigma} < 0$. If $|V_{pd\sigma}|/\Delta_{pd}$ is small, the occupied bands are F p-like, while the partially filled bands Cu e_g-like. We now calculate the bands along high-symmetry lines.[6] Along Γ-Z, the eigenvalues ε_i ($\varepsilon_i \le \varepsilon_{i+1}$) of

[6]Special points: $\Gamma = (0,0,0)$, Z$= (0,0,\pi/a)$, X$= (\pi/a,0,0)$, M$= (\pi/a,\pi/a,0)$, R$= (\pi/a,\pi/a,\pi/a)$.

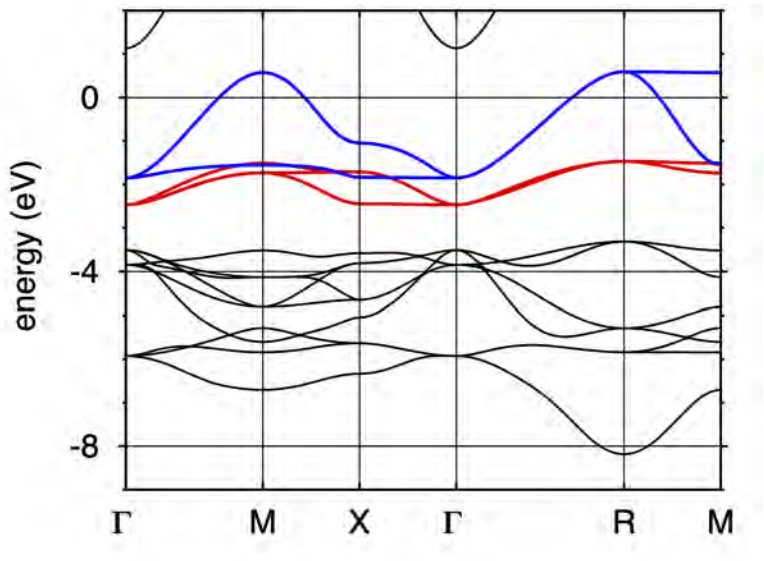

Fig. 8: *LDA band structure of cubic $KCuF_3$. The t_{2g} bands are in red and the e_g bands in blue.*

$H^{\rm TB}_{e_g}$ are

$$\begin{aligned}
\varepsilon_2 &= \varepsilon_p \\
\varepsilon_3 &= \varepsilon_p \\
\varepsilon_4 &= \varepsilon_d \\
\varepsilon_{1,5} &= \varepsilon_p + \tfrac{1}{2}\Delta_{pd} \pm \tfrac{1}{2}\sqrt{\Delta^2_{pd} + 16V^2_{pd\sigma}|s_z|^2}
\end{aligned}$$

where ε_1 (sign $-$) is bonding and F z-like, while ε_5 (sign $+$) anti-bonding and Cu $3z^2-r^2$-like. Along Γ-X, we have instead the dispersion relations

$$\begin{aligned}
\varepsilon_2 &= \varepsilon_p \\
\varepsilon_3 &= \varepsilon_p \\
\varepsilon_4 &= \varepsilon_d \\
\varepsilon_{1,5} &= \varepsilon_p + \tfrac{1}{2}\Delta_{pd} \pm \tfrac{1}{2}\sqrt{\Delta^2_{pd} + 16V^2_{pd\sigma}|s_x|^2}
\end{aligned}$$

where ε_1 is bonding and F x-like, while ε_5 anti-bonding and Cu x^2-y^2-like. To obtain the e_g-like bands, instead of diagonalizing $H^{\rm TB}_{e_g}$ as we have done above, we can also use the *down-folding* procedure, which, for non-interacting electrons, can be carried out exactly. This method works as follows. We divide the orbitals in passive (F p) and active (Cu d), and write the eigenvalues equation as

$$\begin{bmatrix} H_{pp} & H_{pd} \\ H_{dp} & H_{dd} \end{bmatrix} \begin{bmatrix} |\boldsymbol{k}\, p\rangle \\ |\boldsymbol{k}\, d\rangle \end{bmatrix} = \varepsilon \begin{bmatrix} I_{pp} & 0 \\ 0 & I_{dd} \end{bmatrix} \begin{bmatrix} |\boldsymbol{k}\, p\rangle \\ |\boldsymbol{k}\, d\rangle \end{bmatrix},$$

where H_{pp} (I_{pp}) is the Hamiltonian (identity matrix) in the p-electron space (3×3), and H_{dd} (I_{dd}) the Hamiltonian (identity matrix) in the d-electron space (2×2). By downfolding to the d sector we obtain the energy-dependent operator H^{ε}_{dd}, which acts in the d space only

$$H^{\varepsilon}_{dd} = H_{dd} - H_{dp}(H_{pp} - \varepsilon I_{pp})^{-1} H_{pd},$$

and a correspondingly transformed and energy-dependent basis set for the active space, $|\mathrm{k}\ d\rangle_\varepsilon$. The operator H^ε_{dd} has the same eigenvalues and eigenvectors as the original Hamiltonian. In the case of the e_g bands ($H^\varepsilon_{dd} = H^\varepsilon_{e_g}$) of $KCuF_3$

$$\begin{array}{c|cc} H^\varepsilon_{e_g} & |\boldsymbol{k}\ 3z^2{-}r^2\rangle_\varepsilon & |\boldsymbol{k}\ x^2{-}y^2\rangle_\varepsilon \\ \hline |\boldsymbol{k}\ 3z^2{-}r^2\rangle_\varepsilon & \varepsilon'_d{-}2t^\sigma_\varepsilon[\frac{1}{4}(\cos k_x a{+}\cos k_y a){+}\cos k_z a] & 2t^\sigma_\varepsilon[\frac{\sqrt{3}}{4}(\cos k_x a{-}\cos k_y a)] \\ |\boldsymbol{k}\ x^2{-}y^2\rangle_\varepsilon & 2t^\sigma_\varepsilon[\frac{\sqrt{3}}{4}(\cos k_x a{-}\cos k_y a)] & \varepsilon'_d{-}2t^\sigma_\varepsilon[\frac{3}{4}(\cos k_x a{+}\cos k_y a)] \end{array} \qquad (12)$$

where the effective parameters are

$$t^\sigma_\varepsilon = \frac{V^2_{pd\sigma}}{\varepsilon - \varepsilon_p}, \quad \varepsilon'_d = \varepsilon_d + 3t^\sigma_\varepsilon .$$

The downfolding procedure has *renormalized* the parameters ε_d of the original model (11), but also introduced a new interaction: inter-orbital coupling. Furthermore, H^ε_{dd} and the Bloch basis are now energy dependent. Along ΓZ, the eigenvalues of (12) are given implicitly by the equations $\varepsilon = \varepsilon_d + 2t^\sigma_\varepsilon - 2t_\varepsilon \cos k_z a$ (band ε_5) and $\varepsilon = \varepsilon_d$ (band ε_4); in second-order perturbation theory we find

$$t^\sigma_\varepsilon \sim t^\sigma_{\varepsilon_d} = \frac{V^2_{pd\sigma}}{\Delta_{pd}},$$

$$\varepsilon_5 \sim \varepsilon_d + 2t^\sigma_{\varepsilon_d} - 2t^\sigma_{\varepsilon_d} \cos k_z a\,.$$

From Hamiltonian (12) it is relatively easy to see that the e_g bands are 2-fold degenerate along direction Γ-R, to find the dispersion along Γ-M and R-M, and to obtain the e_g-like bands in Fig. 8. By Fourier transforming the Bloch states $|\boldsymbol{k}\ 3z^2 - r^2\rangle_\varepsilon$ and $|\boldsymbol{k}\ x^2 - y^2\rangle_\varepsilon$ we can build a set of Wannier functions. They have $3z^2 - r^2$ or $x^2 - y^2$ symmetry as the atomic orbitals, and, additionally, they span, to arbitrary accuracy, the e_g bands. These Wannier functions are by construction longer range than atomic orbitals, since they have p tails on the downfolded neighboring F sites.

We can now repeat the same calculation for the t_{2g} bands. The minimal tight-binding basis is of course different with respect to the case of e_g bands. The states $|xy\rangle_i$ of the Cu ion located at $\boldsymbol{R}_i$ are coupled via $V_{pd\pi}$ to the $|y^a\rangle_i$, the p_y orbitals of F_1 and F_4 and to $|x^b\rangle_i$, the p_x orbitals of F_2 and F_5; in a similar way, $|xz\rangle_i$ is coupled via $V_{pd\pi}$ to the $|z^a\rangle_i$, the p_z orbitals of F_1 and F_4, and to the $|x^c\rangle_i$, the p_x orbitals of F_3 and F_6; finally $|yz\rangle_i$ is coupled via $V_{pd\pi}$ to the $|z^b\rangle_i$, the p_z orbitals of F_2 and F_5, and to the $|y^c\rangle_i$, the p_y orbitals of F_3 and F_6. After constructing for each $|\alpha\rangle_i$ the corresponding Bloch state, we obtain the tight-binding Hamiltonian. The latter splits into three decoupled blocks,

$$\begin{array}{c|ccc} H^{\mathrm{TB}}_{t_{2g}} & |\boldsymbol{k}\ y^a\rangle & |\boldsymbol{k}\ x^b\rangle & |\boldsymbol{k}\ xy\rangle \\ \hline |\boldsymbol{k}\ y^a\rangle & \varepsilon_p & 0 & 2V_{pd\pi}s_x \\ |\boldsymbol{k}\ x^b\rangle & 0 & \varepsilon_p & 2V_{pd\pi}s_y \\ |\boldsymbol{k}\ xy\rangle & 2V_{pd\pi}\overline{s}_x & 2V_{pd\pi}\overline{s}_y & \varepsilon_d \end{array}$$

and cyclic permutations of x, y, and z (and, correspondingly, of a, b, and c). In the Γ-X direction we thus find

$$\begin{aligned}\varepsilon_{2'}(\boldsymbol{k}) =&\varepsilon_d \\ \varepsilon_5(\boldsymbol{k}) =&\varepsilon_p + \frac{\Delta_{pd}}{2} + \frac{\sqrt{\Delta_{pd}^2 + 16V_{pd\pi}^2|s_x|^2}}{2} \\ \sim&\varepsilon_d + 2t^\pi_{\varepsilon_d} - 2t^\pi_{\varepsilon_d}\cos k_x a\end{aligned}$$

where $t^\pi_{\varepsilon_d} = V^2_{pd\pi}/\Delta_{pd}$. By downfolding the oxygen states we obtain

$H^\varepsilon_{t_{2g}}$	$\|\boldsymbol{k}\ yz\rangle_\varepsilon$	$\|\boldsymbol{k}\ xz\rangle_\varepsilon$	$\|\boldsymbol{k}\ xy\rangle_\varepsilon$
$\|\boldsymbol{k}\ yz\rangle_\varepsilon$	$\varepsilon''_d - 2t^\pi_\varepsilon\,(\cos k_x a + \cos k_y a)$	0	0
$\|\boldsymbol{k}\ xz\rangle_\varepsilon$	0	$\varepsilon''_d - 2t^\pi_\varepsilon\,(\cos k_x a + \cos k_z a)$	0
$\|\boldsymbol{k}\ yz\rangle_\varepsilon$	0	0	$\varepsilon''_d - 2t^\pi_\varepsilon\,(\cos k_y a + \cos k_z a)$

where the parameters in the matrix are

$$\begin{aligned}\varepsilon''_d =&\varepsilon_d + 4t^\pi_\varepsilon, \\ t^\pi_\varepsilon =&\frac{|V_{pd\pi}|^2}{\varepsilon - \varepsilon_p}.\end{aligned}$$

As in the case of the e_g bands, we find renormalized energy levels and effective band dispersions; since different Cu t_{2g} states couple to different F p states, and we neglected hopping integral between oxygens, the xy, xz, and yz bands are totally decoupled in our model. We are now in the position of calculating the (approximate) expression of the covalent contribution to the e_g-t_{2g} crystal-field splitting, i.e., the energy difference

$$\Delta_{\rm CF} \sim \varepsilon'_d - \varepsilon''_d = 3\frac{|V_{pd\sigma}|^2}{\Delta_{pd}} - 4\frac{|V_{pd\pi}|^2}{\Delta_{pd}} > 0. \tag{13}$$

As we can see, the sign of the covalent crystal-field splitting is the same as that of the ionic contribution. This happens for two reasons. First, the so-called d bands are the anti-bonding states of the p-d Hamiltonian, hence both the energy of the e_g and t_{2g} states moves upwards due to the interaction with the p orbitals. Second, σ bonds are stronger than π bonds, hence e_g states shift to sizably higher energy than t_{2g} states.

The tight-binding model we have used so far is oversimplified, but it already qualitatively well describes the e_g and t_{2g} bands in Fig. 8. A more accurate description can be obtained including other Slater-Koster integrals, such as the hopping to apical F s states, or between neighboring F p states. With increasing number of parameters, it becomes progressively harder to estimate them, e.g., from comparison with experiments; furthermore a large number of fitting parameters makes it impossible to put a theory to a test. Modern techniques allow us, however, to calculate hopping integrals and crystal-field splittings *ab-initio*, using localized Wannier functions as basis instead of atomic orbitals, and the DFT potential $v_R(\boldsymbol{r})$ as one-electron potential; because Wannier functions are orthogonal, the corresponding overlap matrix is by construction diagonal.

4 Jahn-Teller effect

In order to introduce the Jahn-Teller effect we have to take a step backwards and start from the central equation of solid-state physics, the eigenvalue problem $\hat{H}\Psi = E\Psi$, defined (in the non-relativistic limit) by the many-body Hamiltonian

$$\hat{H} = \underbrace{-\frac{1}{2}\sum_i \nabla_i^2}_{\hat{T}_e} + \underbrace{\frac{1}{2}\sum_{i\neq i'} \frac{1}{|\boldsymbol{r}_i - \boldsymbol{r}_{i'}|}}_{\hat{V}_{ee}} \underbrace{-\sum_{i\alpha} \frac{Z_\alpha}{|\boldsymbol{r}_i - \boldsymbol{R}_\alpha|}}_{\hat{V}_{en}} \underbrace{-\sum_\alpha \frac{1}{2M_\alpha}\nabla_\alpha^2}_{\hat{T}_n} + \underbrace{\frac{1}{2}\sum_{\alpha\neq\alpha'} \frac{Z_\alpha Z_{\alpha'}}{|\boldsymbol{R}_\alpha - \boldsymbol{R}_{\alpha'}|}}_{\hat{V}_{nn}} .$$

Here $\{\boldsymbol{r}_i\}$ are the coordinates of the N_e electrons, $\{\boldsymbol{R}_\alpha\}$ those of the N_n nuclei, Z_α the atomic numbers, and M_α the nuclear masses. The Born-Oppenheimer Ansatz

$$\Psi(\{\boldsymbol{r}_i\},\{\boldsymbol{R}_\alpha\}) = \psi(\{\boldsymbol{r}_i\};\{\boldsymbol{R}_\alpha\})\, \Phi(\{\boldsymbol{R}_\alpha\}) \,, \tag{14}$$

splits the Schrödinger equation $\hat{H}\Psi = E\Psi$ into the system

$$\begin{cases} \hat{H}_e\psi(\{\boldsymbol{r}_i\};\{\boldsymbol{R}_\alpha\}) &= \varepsilon(\{\boldsymbol{R}_\alpha\})\psi(\{\boldsymbol{r}_i\};\{\boldsymbol{R}_\alpha\}), \\ \\ \hat{H}_n\Phi(\{\boldsymbol{R}_\alpha\}) &= E\Phi(\{\boldsymbol{R}_\alpha\}), \end{cases} \tag{15}$$

where the Hamilton operator for the electrons ($\hat{H}_e$) and that for the lattice ($\hat{H}_n$) are

$$\hat{H}_e = \hat{T}_e + \hat{V}_{ee} + \hat{V}_{en} + \hat{V}_{nn}, \tag{16}$$

$$\hat{H}_n = \hat{T}_n + \varepsilon(\{\boldsymbol{R}_\alpha\}) = \hat{T}_n + \hat{U}_n, \tag{17}$$

and where in (17) we neglect non-adiabatic corrections.[7] In the electronic Hamiltonian (16) the atomic positions $\{\boldsymbol{R}_\alpha\}$ are simple parameters. The electronic eigenvalue $\varepsilon(\{\boldsymbol{R}_\alpha\})$ acts as potential for the nuclei and defines a Born-Oppenheimer (BO) energy surface. While (16) describes the electronic structure, (17) yields the equilibrium crystal structure and the vibrational modes. These equations are impossible to solve in the general case. The first difficulty is that Hamiltonian (16) describes the electronic quantum many-body problem. The latter can be solved only approximately, for example the energy of the ground state can be obtained via density-functional theory using one of the known approximations to the universal functional. For strongly-correlated systems, advanced methods combine density-functional theory with many-body approaches such as the dynamical mean-field theory [7, 8]. The second issue is the very high number of atoms, and therefore of $\{\boldsymbol{R}_\alpha\}$ parameters to explore; finally, even if we solve the electronic many-body problem exactly, we still have to deal with the nuclear many-body problem, Hamiltonian (17). Despite all these obstacles, let us assume for a moment that, for a given system, we did solve the electronic problem for general values of $\{\boldsymbol{R}_\alpha\}$. Let us also assume that the set of positions $\{\boldsymbol{R}_\alpha\} = \{\boldsymbol{R}_\alpha^0\}$ defines a specific crystal structure, whose

[7] We neglect the operator $\hat{\Lambda}_n$, with elements $\langle m|\hat{\Lambda}_n|m'\rangle = -\sum_\alpha \frac{1}{M_\alpha}\left[\frac{1}{2}\langle\psi_m|\nabla_\alpha^2\psi_{m'}\rangle + \langle\psi_m|\nabla_\alpha\psi_{m'}\rangle\cdot\nabla_\alpha\right]$

electronic ground state (i.e., the lower energy BO surface) has degeneracy $d > 1$. We can at this point ask ourself the question: Is structure $\{\boldsymbol{R}^0_\alpha\}$ actually stable?
The Jahn-Teller theorem states that any electronically degenerate system can lower its energy by undergoing some structural distortions, and therefore is unstable.[8] This is due to the coupling between electrons and lattice. In order to better understand the microscopic origin of this phenomenon, let us consider a system in a high-symmetry structure, $\{\boldsymbol{R}^0_\alpha\}$, for which the electronic ground state has energy $\varepsilon(\{\boldsymbol{R}^0_\alpha\})$ with degeneracy $d > 1$. This means that there are d Born-Oppenheimer surfaces degenerate for $\{\boldsymbol{R}_\alpha\} = \{\boldsymbol{R}^0_\alpha\}$,

$$\varepsilon_m(\{\boldsymbol{R}^0_\alpha\}) = \varepsilon(\{\boldsymbol{R}^0_\alpha\}).$$

In the rest of the chapter we will take $\varepsilon(\{\boldsymbol{R}^0_\alpha\})$ as the energy zero. The corresponding degenerate electronic wavefunctions are $\psi_m(\{\boldsymbol{r}_i\};\{\boldsymbol{R}^0_\alpha\})$. Let us expand the nuclear potential $\hat{U}_n$ for one of these surfaces around the symmetric structure $\{\boldsymbol{R}^0_\alpha\}$. This leads to the Taylor series

$$\hat{H}_n = \hat{T}_n + \sum_{\alpha\mu}\left[\frac{\partial \hat{U}_n}{\partial u_{\alpha\mu}}\right]_{\{\boldsymbol{R}^0_\alpha\}} u_{\alpha\mu} + \frac{1}{2}\sum_{\alpha\mu}\sum_{\alpha'\mu'}\left[\frac{\partial^2 \hat{U}_n}{\partial_{\alpha\mu}\partial_{\alpha'\mu'}}\right]_{\{\boldsymbol{R}^0_\alpha\}} u_{\alpha\mu}\, u_{\alpha'\mu'} + \ldots,$$

where $\boldsymbol{u}_\alpha = \boldsymbol{R}_\alpha - \boldsymbol{R}^0_\alpha$ are displacement vectors with respect to the equilibrium position, and $\mu = x, y, z$. If $\{\boldsymbol{R}^0_\alpha\}$ is an equilibrium structure, the gradient is zero and

$$\hat{H}_n \sim \hat{T}_n + \frac{1}{2}\sum_{\alpha\mu}\sum_{\alpha'\mu'}\left[\frac{\partial^2 \hat{U}_n}{\partial_{\alpha\mu}\partial_{\alpha'\mu'}}\right]_{\{\boldsymbol{R}^0_\alpha\}} u_{\alpha\mu}u_{\alpha'\mu'} + \cdots = \hat{T}_n + \hat{U}^{\rm PH}_n(\{\boldsymbol{R}^0_\alpha\}) + \ldots, \qquad (18)$$

The standard procedure to diagonalize (18) consists of two steps. First we change coordinates

$$\tilde{u}_{\alpha\mu} = u_{\alpha\mu}\sqrt{M_\alpha}.$$

Second we introduce the dynamical matrix

$$D_{\alpha\mu,\alpha\mu'} = \frac{1}{\sqrt{M_\alpha}}\frac{1}{\sqrt{M_{\alpha'}}}\left[\frac{\partial^2 \hat{U}_n}{\partial_{\alpha\mu}\partial_{\alpha'\mu'}}\right]_{\{\boldsymbol{R}^0_\alpha\}},$$

and diagonalize it. Its N_m eigenvectors are the normal modes $\boldsymbol{Q}_\eta$,

$$D\boldsymbol{Q}_\eta = \omega^2_\eta \boldsymbol{Q}_\eta,$$

$$Q_{\eta\nu} = \sum_{\alpha=1}^{N_n}\sum_{\mu=x,y,z} a_{\eta\nu,\alpha\mu}u_{\alpha\mu},$$

with $\eta = 1, \ldots N_m$, and $\nu = x, y, z$. The *normal coordinates* $\{Q_{n\nu}\}$, together with the associated canonically-conjugated momenta $\{P_{n\nu}\}$, bring (18) in the form

$$\hat{H}_n \sim \frac{1}{2}\sum_{\eta\nu}\left[P^2_{\eta\nu} + \omega^2_\eta Q^2_{\eta\nu}\right]. \qquad (19)$$

[8] The only exceptions are linear molecules and Kramers degeneracy.

In a crystal, this Hamiltonian yields the phonon energy levels. Let us now determine the possible N_m normal modes for a cubic perovskite. For simplicity we consider here only a single octahedron and the modes associated with the vibrations of its atoms. Given that each atom can move in three directions, and there are 6 atoms of type C and 1 atom of type B, in principle such a system has 21 degrees of freedom; eliminating global translations (3 degrees of freedom) and global rotations (3 degrees of freedom), i.e., displacements which are not vibrations, 15 degrees of freedom are left, hence the system has 15 possible normal modes. In group theory language, assuming again for simplicity that the group is O instead of O_h, one can show that these modes can be labeled as belonging to irreducible representations A_1, E, T_1 or T_2. To obtain this result we first build a matrix representation of the group in the linear space of all possible displacements; this space is 21-dimensional, and so is the associated matrix representation $\Gamma_{\rm tot}$. The latter can be expressed as the direct product $\Gamma_{\rm tot} = \Gamma_{\rm a.s.} \otimes \Gamma_{\rm vector}$, where $\Gamma_{\rm a.s.}$ is the so-called atomic-site representation. $\Gamma_{\rm a.s.}$ has as a basis the original atomic positions (without displacements); in our case it is has therefore dimensionality 7. The character of $\Gamma_{\rm a.s.}$ for a given operation is simply the number of sites left invariant by that operation. Finally, in group O the irreducible representation for a vector is $\Gamma_{vector} = T_1$; this can be seen from the partner functions (x, y, z) in Table 4. Summarizing all this in a character table, we have

O	E	$8C_3$	$3C_2$	$6C_2$	$6C_4$
$\Gamma^{\rm a.s.}$	7	1	3	1	3
$\Gamma^{\rm tot} = \Gamma^{\rm a.s.} \otimes \Gamma_{\rm vector}$	21	0	-3	-1	3

Once we know the characters for representation $\Gamma_{\rm tot}$, we can split the latter into irreducible representations of group O via the decomposition formula Eq. (5). After subtracting (tensor subtraction $\ominus$) the representations for mere translations (T_1) and mere rotations (T_1) of the octahedron,[9] we arrive at the final decomposition of the vibrational-modes representation $\Gamma_{\rm vibrations} = \Gamma_{\rm tot} \ominus \Gamma_{\rm vector} \ominus \Gamma_{\rm rotation} = A_1 \oplus E \oplus 2T_1 \oplus 2T_2$. Normal modes which are a basis for different irreducible representations have in general different energies. Let us focus on modes A_1 and E. We can obtain mode A_1 by using the projector, Eq. (6), for irreducible representation A_1. As a matter of fact, if we assume that atom F_1 (Fig. 9) is displaced by $\boldsymbol{u}_1$, by applying the projector $\hat{P}^{A_1}$ to $\boldsymbol{u}_1$ we generate automatically the linear combination of atomic displacements (all having the same length) forming the mode of symmetry A_1. This leads to

$$\boldsymbol{Q}_0 = \boldsymbol{u}_1(q_0) + \boldsymbol{u}_2(q_0) + \boldsymbol{u}_3(q_0) + \boldsymbol{u}_4(q_0) + \boldsymbol{u}_5(q_0) + \boldsymbol{u}_6(q_0).$$

[9]The representation for an improper vector (rotation) is $\Gamma_{rotation} = T_1$, as can be seen from the corresponding partner functions (R_x, R_y, R_z) in Table 4.

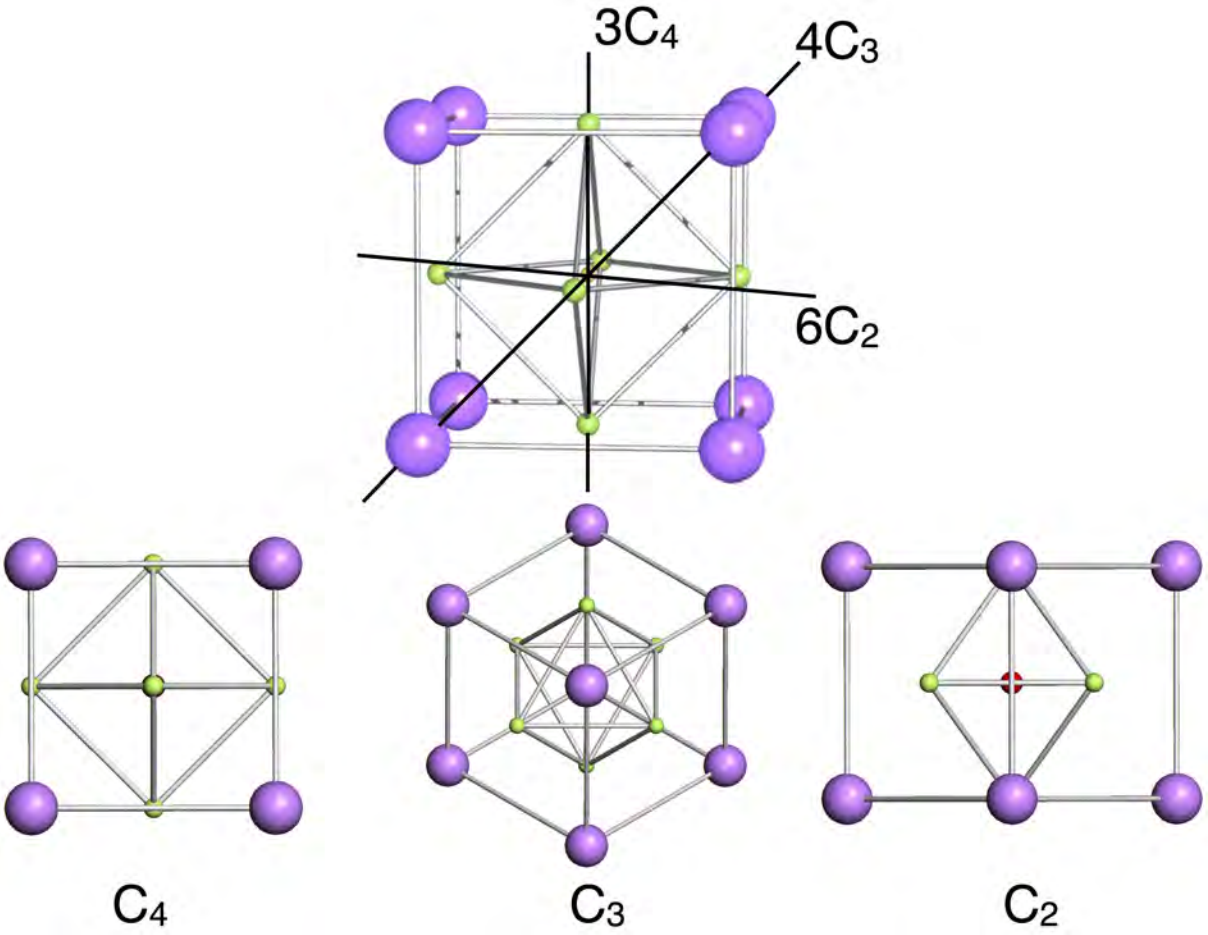

Fig. 9: *Unit cell (top) and vibrational modes Q_0, Q_1, and Q_2 of cubic $KCuF_3$.*

Here $\boldsymbol{u}_i$ are the (normalized) displacements for the C_i atom (see Fig. 9) which we rewrite as

$$\begin{aligned}
\boldsymbol{u}_1(q_0) &= \tfrac{1}{\sqrt{6}} q_0 (1,0,0) \\
\boldsymbol{u}_2(q_0) &= \tfrac{1}{\sqrt{6}} q_0 (0,1,0) \\
\boldsymbol{u}_3(q_0) &= \tfrac{1}{\sqrt{6}} q_0 (0,0,1) \\
\boldsymbol{u}_4(q_0) &= -\tfrac{1}{\sqrt{6}} q_0 (1,0,0) \\
\boldsymbol{u}_5(q_0) &= -\tfrac{1}{\sqrt{6}} q_0 (0,1,0) \\
\boldsymbol{u}_6(q_0) &= -\tfrac{1}{\sqrt{6}} q_0 (0,0,1)
\end{aligned}$$

The potential energy of such a *breathing mode* is

$$U_n^{\rm PH} = \frac{1}{2} C_{A_1} q_0^2 \,.$$

The $\boldsymbol{Q}_0$ mode expands or compresses the unit cell, but does not change its symmetry which remains cubic. Hence, this mode has no influence on the stability of the structure, at most it can affect the actual value of the lattice constant. More interesting are the two degenerate modes of type E. These modes can be obtained in a similar way as we have done for $\boldsymbol{Q}_0$, this time using the projector for irreducible representation E; within the resulting 2-dimensional space,

we choose as basis the mutually orthogonal modes that transform as the $l = 2$ partner functions of E, $x^2 - y^2$ and $3z^2 - r^2$. These are $\boldsymbol{Q}_1$ and $\boldsymbol{Q}_2$, shown in Fig. 9. They are defined as

$$\boldsymbol{Q}_1 = \boldsymbol{u}_1(q_1) + \boldsymbol{u}_2(q_1) + \boldsymbol{u}_4(q_1) + \boldsymbol{u}_5(q_1),$$
$$\boldsymbol{Q}_2 = \boldsymbol{u}_1(q_2) + \boldsymbol{u}_2(q_2) + \boldsymbol{u}_3(q_2) + \boldsymbol{u}_4(q_2) + \boldsymbol{u}_5(q_2) + \boldsymbol{u}_6(q_2),$$

where the displacements are

$$\begin{array}{rclrcl}
\boldsymbol{u}_1(q_1) &=& \frac{1}{\sqrt{4}} q_1(1,0,0) & \boldsymbol{u}_1(q_2) &=& -\frac{1}{\sqrt{12}} q_2(1,0,0) \\
\boldsymbol{u}_2(q_1) &=& -\frac{1}{\sqrt{4}} q_1(0,1,0) & \boldsymbol{u}_2(q_2) &=& -\frac{1}{\sqrt{12}} q_2(0,1,0) \\
\boldsymbol{u}_3(q_1) &=& (0,0,0) & \boldsymbol{u}_3(q_2) &=& \frac{2}{\sqrt{12}} q_2(0,0,1) \\
\boldsymbol{u}_4(q_1) &=& -\frac{1}{\sqrt{4}} q_1(1,0,0) & \boldsymbol{u}_4(q_2) &=& \frac{1}{\sqrt{12}} q_2(1,0,0) \\
\boldsymbol{u}_5(q_1) &=& \frac{1}{\sqrt{4}} q_1(0,1,0) & \boldsymbol{u}_5(q_2) &=& \frac{1}{\sqrt{12}} q_2(0,1,0) \\
\boldsymbol{u}_6(q_1) &=& (0,0,0) & \boldsymbol{u}_6(q_2) &=& -\frac{2}{\sqrt{12}} q_2(0,0,1)
\end{array}$$

The corresponding quadratic potential has the form

$$\hat{U}_n^{\mathrm{PH}} = \frac{1}{2} C_E (q_1^2 + q_2^2).$$

The normal modes T_1 and T_2 can be obtained in a similar way; since they are not relevant for structure stability in the example considered here we do not provide their form explicitly.
Up to now we have assumed that the hypothetical high-symmetry structure $\{\boldsymbol{R}_\alpha^0\}$ is a stationary point. In general, however, this might or might not be true. The behavior of the BO energy surfaces close to the point in which they are degenerate allows us to separate them into two classes, the first one in which $\{\boldsymbol{R}_\alpha^0\}$ is a stationary point for all degenerate electronic states m (Renner-Teller intersection), and the second in which the surface is not a stationary point at least for some of the surfaces (Jahn-Teller intersection). The classical Jahn-Teller systems are those for which $\nabla \hat{U}_n(\{\boldsymbol{R}_\alpha^0\}) \neq 0$ at least in some direction (see, e.g., Fig. 10). Let us now calculate the first-order correction to the m degenerate eigenvalues due to a small distortion around $\{\boldsymbol{R}_\alpha^0\}$. The electronic Hamiltonian (16) has matrix elements

$$\langle \psi_m | \hat{H}_e(\{\boldsymbol{R}_\alpha\}) | \psi_{m'} \rangle = \underbrace{\sum_{\alpha\mu} \langle \psi_m | \left[\frac{\partial \hat{H}_e}{\partial u_{\alpha\mu}} \right]_{\{\boldsymbol{R}_\alpha^0\}} | \psi_{m'} \rangle u_{\alpha\mu}}_{\hat{U}^{\mathrm{JT}}_{m,m'}} + \cdots = \hat{U}^{\mathrm{JT}}_{m,m'} + \ldots .$$

The perturbation $\hat{U}^{\mathrm{JT}}$, the Jahn-Teller potential, couples the degenerate BO energy surfaces; it also couples electrons and lattice vibrations, as we can see from the coordinates $u_{\alpha\mu}$ appearing in the expression above. Thus, if there are modes for which $\hat{U}^{\mathrm{JT}} \neq C\,\hat{I}$ where $\hat{I}$ is the identity matrix and C a constant, the system gains energy at linear order via a distortion which lowers the symmetry; the Jahn-Teller theorem states that such modes always exist for electronically degenerate systems (with the exceptions of Kramers degeneracy and linear molecules).

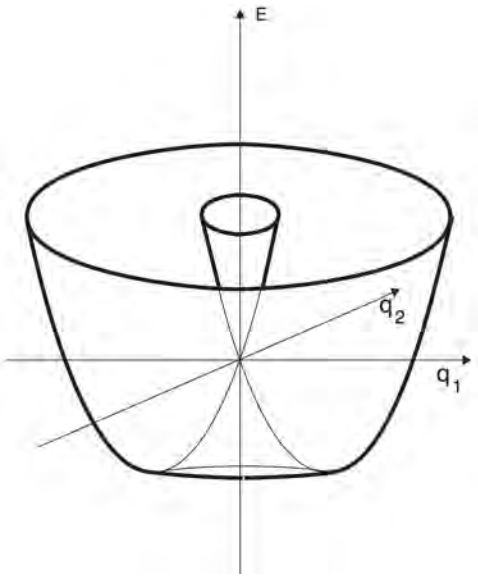

Fig. 10: *Born-Oppenheimer potential-energy surface exhibiting the form of a mexican hat. The slope of the curve at small distortions q_1, q_2 yields the Jahn-Teller coupling constant λ.*

In order to better understand the effect of the electron-lattice coupling, we generalize the Born-Oppenheimer Ansatz as follows

$$\Psi(\{\boldsymbol{r}_i\},\{\boldsymbol{R}_\alpha\}) \;=\; \sum_m \psi_m(\{\boldsymbol{r}_i\};\{\boldsymbol{R}_\alpha\})\,\Phi_m(\{\boldsymbol{R}_\alpha\}).$$

To find the equations for the functions $\{\Phi_m\}$, we write the Schrödinger equation $H\Psi = E\Psi$, multiply on the left by $\overline{\psi_m}$, and integrate over the coordinates of the electrons. We obtain

$$\hat{H}_n\Phi_m(\{\boldsymbol{R}_\alpha\}) = \left[\hat{T}_n + \hat{U}_n^{\rm PH}\right]\Phi_m(\{\boldsymbol{R}_\alpha\}) + \sum_{m'}\hat{U}^{\rm JT}_{m,m'}\Phi_{m'}(\{\boldsymbol{R}_\alpha\}) = E\Phi_m(\{\boldsymbol{R}_\alpha\}). \qquad (20)$$

The dynamics of the system close to the degeneracy point is determined by all degenerate sheets. The minimization of the new potential energy yields a new structure $\{\tilde{\boldsymbol{R}}^0_\alpha\}$ in which the electronic states are not any more degenerate. The modes that can produce such an instability should satisfy the condition

$$[\Gamma_m \otimes \Gamma_m] \cap \Gamma_{\rm vibrations} \supset A_1,$$

where Γ_m is the irreducible representation to which the electronic degenerate states belong, and $[\Gamma_m \otimes \Gamma_m]$ is the symmetric direct product. The trivial representation A_1 has to be excluded because, as already discussed, it does not lower the symmetry. In the case cubic $KCuF_3$ the relevant normal modes coupling to the degenerate e_g electronic states are the E modes; as for the electronic states, if the group $O \to O_h$, then $E \to E_g$. Thus we can say that $KCuF_3$ is an example of a $e_g \otimes E_g$ Jahn-Teller system, a system in which an electronic doublet (e_g) is coupled to a doublet of normal modes (E_g). The form of the Jahn-Teller potential $\hat{U}^{\rm JT}$ can be obtained from the effect of perturbations of type $\boldsymbol{Q}_1$ and $\boldsymbol{Q}_2$ on the crystal-field matrix. As for the crystal field, there are both a ionic and a covalent contribution. For the ionic contribution,

we can use once more perturbation theory. In this case, we have to take into account that the Cu-F distance d_C depends on the direction, i.e,

$$d_C \to d_C + \delta d_C^{\mu},$$

where $\mu = x, y, z$; the specific δd_C^{μ} values for each atom are given by the specific vibrational mode. After summing up all contribution, the first non-cubic correction due to E_g modes is

$$\Delta v_{\rm JT} = \frac{q_C}{d_C^6}\frac{25}{14\sqrt{3}}\langle r^4\rangle \begin{pmatrix} q_2 & q_1 \\ q_1 & -q_2 \end{pmatrix}.$$

It is, at this point, useful to introduce pseudo-spin operators acting on the e_g states, i.e., operators $\hat{\tau}_\mu$ with $\mu = x, y, z$ and

$$\hat{\tau}_z|\searrow\rangle = -|\searrow\rangle, \qquad \hat{\tau}_x|\searrow\rangle = +|\nearrow\rangle, \qquad \hat{\tau}_y|\searrow\rangle = -i|\nearrow\rangle$$

$$\hat{\tau}_z|\nearrow\rangle = +|\nearrow\rangle, \qquad \hat{\tau}_x|\nearrow\rangle = +|\searrow\rangle, \qquad \hat{\tau}_y|\nearrow\rangle = +i|\searrow\rangle$$

where $|\nearrow\rangle = |x^2 - y^2\rangle$ and $|\searrow\rangle = |3z^2 - r^2\rangle$. In matrix form these operators can be written as pseudo-Pauli matrices

$$\hat{\tau}_z = \begin{pmatrix} 1 & 0 \\ 0 & -1 \end{pmatrix} \quad \hat{\tau}_x = \begin{pmatrix} 0 & 1 \\ 1 & 0 \end{pmatrix} \quad \hat{\tau}_y = \begin{pmatrix} 0 & -i \\ i & 0 \end{pmatrix}. \tag{21}$$

We can then rewrite the Jahn-Teller potential as

$$\Delta v_{\rm JT} = \lambda\Big[q_1\tau_x + q_2\tau_z\Big],$$

where $\lambda = (q_C/d_C^6)\ (25/14\sqrt{3}) > 0$. This potential expresses both the essence of the Jahn-Teller theorem and its relation with orbital order; the systems gains energy at linear order by making a distortion; the latter produces a crystal-field splitting, which leads to preferential occupation of the lower energy level. For example, if $q_1 = 0$ and $q_2 < 0$ (tetragonal compression) the $3z^2 - r^2$ state is higher in energy. Let us now calculate the covalent contribution to the Jahn-Teller potential. In this case the linear-order correction is

$$\Delta\varepsilon_{lm,l'm'}(\mathbf{0}, \boldsymbol{R}_\alpha + \boldsymbol{u}) - \Delta\varepsilon_{lm,l'm'}(\mathbf{0}, \boldsymbol{R}_\alpha) \sim \nabla\Delta\varepsilon_{lm,l'm'}(\mathbf{0}, \boldsymbol{R}_\alpha)\cdot\boldsymbol{u}$$

For e_g-states we use for simplicity the following approximations[10]

$$\begin{aligned}
\Delta\varepsilon_{3z^2-r^2,3z^2-r^2} &\sim \left[n^2 - \frac{1}{2}(l^2+m^2)\right]^2 \tilde{V}_{dd\sigma}, \\
\Delta\varepsilon_{3z^2-r^2,x^2-y^2} &\sim \frac{\sqrt{3}}{2}(l^2-m^2)\left[n^2 - \frac{1}{2}(l^2+m^2)\right]\tilde{V}_{dd\sigma}, \\
\Delta\varepsilon_{x^2-y^2,x^2-y^2} &\sim \frac{3}{4}(l^2-m^2)^2\tilde{V}_{dd\sigma}.
\end{aligned}$$

[10]The crystal-field integrals are also two-center integrals; the table of Slater-Koster integrals in Appendix B is thus still valid, provided that $V_{ll'\alpha}$ are replaced by the corresponding crystal-field terms, which we indicate as $\tilde{V}_{ll'\alpha}$.

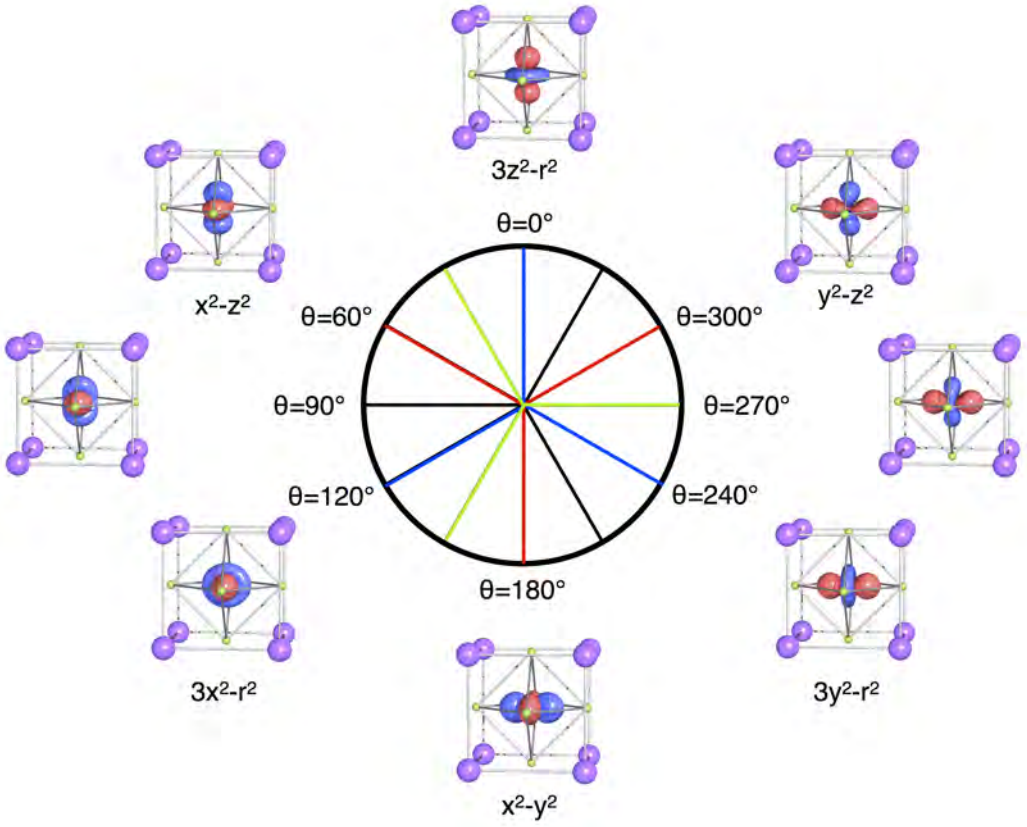

Fig. 11: *Linear combinations of e_g-states, $|\theta\rangle = -\sin\frac{\theta}{2}|x^2-y^2\rangle + \cos\frac{\theta}{2}|3z^2-r^2\rangle$. The $\theta = 0^o$ orbital is the excited state in the presence of a tetragonal compression along the z axis, while $\theta = \pm 2\pi/3$ are excited states for a tetragonal compression along x or y. This three-fold degeneracy (rotation by $\pm 2\pi/3$) is due to cubic symmetry.*

By summing up the contributions from all C ions for each mode, we obtain

$$\Delta\varepsilon_{\rm JT}(q_1,q_2) = \lambda \begin{pmatrix} q_2 & q_1 \\ q_1 & -q_2 \end{pmatrix} = \lambda\Big[q_1\hat{\tau}_x + q_2\hat{\tau}_z\Big],$$

where $\lambda \sim -\frac{\sqrt{3}}{2}\tilde{V}'_{dd\sigma} > 0$. This is the same form of potential that we have obtained for the ionic contribution. Again, if $q_1 = 0$ and $q_2 < 0$ (tetragonal compression) the $3z^2 - r^2$ is higher in energy. In conclusion, if we neglect the kinetic energy of the nuclei (limit $M_\alpha/m_e \to \infty$), the ground state of the system can be calculated by minimizing a potential energy of the form

$$\hat{U}(q_1,q_2) = \hat{U}^{\rm JT} + \hat{U}^{\rm PH}_n = \lambda \begin{pmatrix} q_2 & q_1 \\ q_1 & -q_2 \end{pmatrix} + \frac{1}{2}C_E\,(q_1^2+q_2^2)\,\hat{I}, \qquad (22)$$

where $\hat{I}$ is the 2×2 identity matrix. To find the minimum of (22), it is convenient to introduce polar coordinates, which we define as $q_2 = -q\cos\theta$, $q_1 = -q\sin\theta$, so that for $0 < \theta < \pi/2$ we have $q_1 \le 0$ (compression of $\hat{x}$ axis) and $q_2 \le 0$ (compression of $\hat{z}$ axis); this corresponds to

the distortion of the octahedron labeled with number 1 in Fig. 1. In these coordinates

$$\hat{U}^{\rm JT} = -\lambda q \begin{pmatrix} \cos\theta & \sin\theta \\ \sin\theta & -\cos\theta \end{pmatrix}.$$

The diagonalization of matrix (22) yields two eigenvalues; the lower energy branch

$$E_-(q) = -\lambda q + \frac{C_E}{2} q^2$$

takes the form of a mexican hat, shown in Fig. 10. The minimum of $E_-(q)$ is obtained for $q = q_0 = \lambda/C$ and has value

$$E_{\rm JT} = -\lambda^2/2C_E;$$

the quantity $E_{\rm JT}$ is defined as the Jahn-Teller energy of the system. The electronic ground state can be written as

$$|\theta\rangle_G = -\sin\frac{\theta-\pi}{2}|x^2-y^2\rangle + \cos\frac{\theta-\pi}{2}|3z^2-r^2\rangle.$$

The excited state (hole orbital), with energy

$$E_+(q) = \lambda q + \frac{C_E}{2} q^2,$$

is then given by

$$|\theta\rangle_E = -\sin\frac{\theta}{2}|x^2-y^2\rangle + \cos\frac{\theta}{2}|3z^2-r^2\rangle.$$

The states $|\theta\rangle_E$ with different θ are shown in Fig. 11. In the simple model discussed so far, all states $|\theta\rangle_G$ have the same Jahn-Teller energy. Cubic symmetry, however, only requires that states

$$|\theta\rangle,\ |\theta+2\pi/3\rangle,\ |\theta-2\pi/3\rangle$$

are degenerate. The additional (accidental) degeneracy is removed when we take into account anharmonic terms, the lowest order of which has the form

$$U^{\rm anh}(q_1,q_2) = A(q_2^3 - 3q_2q_1^2) = Aq^3(\cos^3\theta - 3\cos\theta\sin^2\theta) = -Aq^3\cos 3\theta$$

and yields the tetragonal distortion as a ground state, with $\theta = 0, \pm 2\pi/3$ for positive A and with $\theta = \pi, \pi \pm 2\pi/3$ for negative A. Higher-order terms can make the $\boldsymbol{Q}_1$ Jahn-Teller distortion ($\theta = \pi/2, \pi/2 \pm 2\pi/3$) more stable [1]. For a periodic lattice, mode $\boldsymbol{Q}_1$ leads to a co-operative distortion where long and short bonds alternate in the x and y direction; in such a case, the hole orbital rotates by $\pi/2$ if we move from a Cu site to its Cu first-nearest neighbors in the $\boldsymbol{ab}$ plane. Let us now analyze the different electronic configurations that can occur in perovskites. For the electronic configuration $3d^1 = 3t_{2g}^1$, the procedure is as the one illustrated above, except that t_{2g} states are 3-fold degenerate and form π bonds, which are weaker, therefore the splitting introduced by the Jahn-Teller effect is smaller than for e_g states. In the case of electronic configurations $3d^n$ with $n > 1$, to determine if the ion is Jahn-Teller active one has to consider the degeneracies of the many-body state, including Coulomb repulsion. Weak Jahn-Teller states are $3d^1$ (Ti^{3+} in $LaTiO_3$) and $3d^2$ (V^{3+} in $LaVO_3$), as also $3t_{2g}^4$, $3t_{2g}^5$, $3t_{2g}^4e_g^2$, $3t_{2g}^5e_g^2$; strong Jahn-Teller configurations are, e.g., $3d^9$ (Cu^{2+} in $KCuF_3$) and $3t_{2g}^3e_g^1$ (Mn^{3+} in $LaMnO_3$); the configurations $3t_{2g}^3$ and $3t_{2g}^3e_g^2$ are not degenerate and therefore not Jahn-Teller active.

5 Kugel-Khomskii superexchange

Let us now start from a totally different perspective, from the Hubbard model for a cubic perovskite with partially filled e_g shells. The Hamiltonian takes the form $\hat{H} = \hat{H}_0 + \hat{H}_T + \hat{H}_U$ where

$$\begin{aligned}
\hat{H}_0 =& \varepsilon_{e_g} \sum_i \sum_\sigma \sum_m \hat{n}_{im\sigma} \\
\hat{H}_T =& -\sum_{i\neq i'} \sum_\sigma \sum_{mm'} t^{i,i'}_{mm'}\, c^\dagger_{im\sigma} c_{im'\sigma} \\
\hat{H}_U =& U \sum_i \sum_m \hat{n}_{im\uparrow}\hat{n}_{im\downarrow} + \frac{1}{2}\sum_i \sum_{\sigma\sigma'} \sum_{m\neq m'} (U - 2J - J\delta_{\sigma,\sigma'})\, \hat{n}_{im\sigma}\hat{n}_{im'\sigma'} \\
& -J \sum_i \sum_{m\neq m'} \left[c^\dagger_{im\uparrow} c^\dagger_{im\downarrow} c_{im'\uparrow} c_{im'\downarrow} + c^\dagger_{im\uparrow} c_{im\downarrow} c^\dagger_{im'\downarrow} c_{im'\uparrow} \right],
\end{aligned}$$

and where $m, m' = x^2 - y^2, 3z^2 - r^2$. Kugel and Khomskii have shown that, in the large t/U limit, this Hamiltonian can be mapped onto an effective generalized superexchange Hamiltonian with an orbitally-ordered ground state. To understand this, let us simplify the problem and consider first a system with only two atoms ($i = A, B$) for which the hopping matrix is diagonal in the orbitals

$$\hat{H}_T = -t \sum_\sigma \sum_m \left[c^\dagger_{Am} c_{Bm} + c^\dagger_{Bm} c_{Am} \right].$$

Furthermore, let us simplify the Coulomb interaction and neglect the spin-flip and pair-hopping terms

$$\hat{H}_U = U \sum_{i=AB} \sum_m \hat{n}_{im\uparrow}\hat{n}_{im\downarrow} + \frac{1}{2} \sum_{i=AB} \sum_{\sigma\sigma'} \sum_{m\neq m'} (U - 2J - J\delta_{\sigma,\sigma'})\, \hat{n}_{im\sigma}\hat{n}_{im'\sigma'}.$$

Finally, we assume that the systems has one electron per atom (quarter filling, e_g^1 configuration). In the $t = 0$ or atomic limit there are two types of possible states for this system, those in which each atom is occupied by one electron, $|1,1\rangle_\alpha$, and those in which one atom has two electrons and the other zero, $|2,0\rangle_{\alpha'}$. The 16 states of type $|1,1\rangle_\alpha$, all degenerate with energy $E_\alpha(1,1) = 2\varepsilon_{e_g}$, can be written as $c^\dagger_{Am_A\sigma_A} c^\dagger_{Bm_B\sigma_B}|0\rangle$ with $\alpha = (m_A\sigma_A, m_B\sigma_B)$; here $m_i\sigma_i$ are the quantum numbers for the electron at site $i = A, B$. There are 12 states $|2,0\rangle_\alpha$ with one atom occupied by two electrons; they are listed below together with their energies

$\|2,0\rangle_{\alpha'}$			$E_{\alpha'}(2,0)$	
$\|2,0\rangle_{i1m}$	$=$	$c^\dagger_{im\uparrow} c^\dagger_{im\downarrow}\|0\rangle$	$2\varepsilon_{e_g} + U$	
$\|2,0\rangle_{i2m}$	$=$	$c^\dagger_{im\uparrow} c^\dagger_{im'\downarrow}\|0\rangle$	$2\varepsilon_{e_g} + U - 2J$	$m' \neq m$
$\|2,0\rangle_{i3\sigma}$	$=$	$c^\dagger_{im\sigma} c^\dagger_{im'\sigma}\|0\rangle$	$2\varepsilon_{e_g} + U - 3J$	$m' \neq m$

The Coulomb repulsion U is positive and J is small with respect to U; therefore the $|1,1\rangle_\alpha$ states define the ground-state manifold. If t is finite but small ($t/U \ll 1$), we can treat $\hat{H}_T$ as

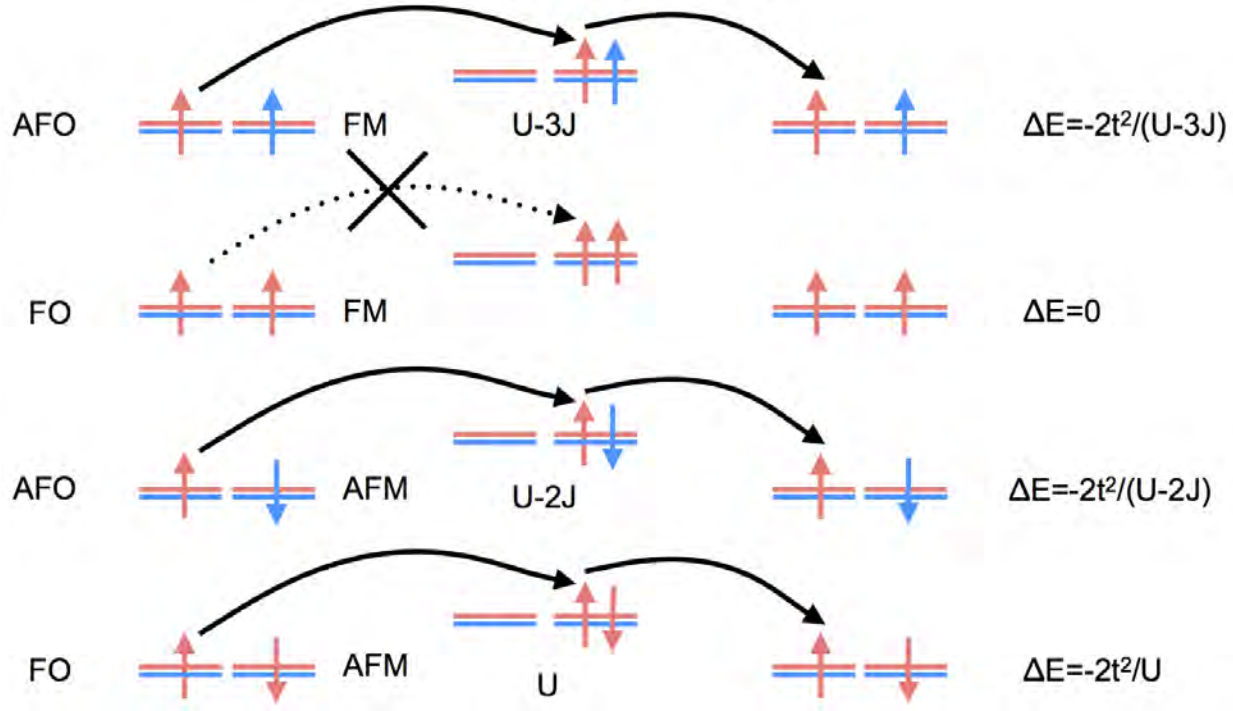

Fig. 12: *Superexchange energy gain for possible quarter-filling ground states of a two-site 2-fold degenerate Hubbard model with orbital- and spin-diagonal hopping matrices.*

a perturbation, and calculate the second-order correction to the energy of states $|1,1\rangle_\alpha$. This correction is always negative (energy gain) and it is given by the matrix

$$\Delta E_{\alpha_1,\alpha_2}(1,1) = -\sum_{\alpha'} {}_{\alpha_1}\langle 1,1|\hat{H}_T|2,0\rangle_{\alpha'} \frac{1}{E_{\alpha'}(2,0) - E_\alpha(1,1)} {}_{\alpha'}\langle 2,0|\hat{H}_T|1,1\rangle_{\alpha_2}$$

There are four interesting cases, depicted in Fig. 12. The first is the ferro-magnetic (same spin) and antiferro-orbital (different orbitals) state, first line of the figure. The corresponding second order energy gain ($\alpha_1 = \alpha_2 = m\sigma, m'\sigma$) is

$$\Delta E_{\alpha_1,\alpha_1}(1,1) = -\frac{2t^2}{U-3J}.$$

For the ferro-magnetic (same spin) and ferro-orbital (same orbital) state (second line in the figure, $\alpha_1 = \alpha_2 = m\sigma, m\sigma$) the energy gain is, instead, zero

$$\Delta E_{\alpha_1,\alpha_1}(1,1) = 0.$$

The reason is that no hopping is possible due to the Pauli principle. For the antiferro-magnetic antiferro-orbital state (third line, $\alpha_1 = \alpha_2 = m\sigma, m' - \sigma$), we have

$$\Delta E_{\alpha_1,\alpha_1}(1,1) = -\frac{2t^2}{U-2J},$$

and finally for the antiferro-magnetic ferro-orbital state ($\alpha_1 = \alpha_2 = m\sigma, m - \sigma$) we find

$$\Delta E_{\alpha_1,\alpha_1}(1,1) = -\frac{2t^2}{U}.$$

Among these four states, the ferro-magnetic antiferro-orbital state is thus the lowest in energy. The main message is that the system gains superexchange energy by occupying preferentially different orbitals with the same spin, although the orbitals are by themselves degenerate. The 16×16 matrix of the second-order energy corrections $\Delta E_{\alpha_1,\alpha_2}(1,1)$ can be rewritten as the effective superexchange Hamiltonian

$$\begin{aligned}\hat{H}_{\rm SE} =& 2\Gamma_{-+}\left[\boldsymbol{S}^A\cdot\boldsymbol{S}^B-\frac{1}{4}\right]\left[O_z^A\,O_z^B\,+\,\frac{1}{4}\right]+2\Gamma_{+-}\left[\frac{1}{4}\,+\,S_z^A\,S_z^B\right]\left[\boldsymbol{O}^A\cdot\boldsymbol{O}^B-\frac{1}{4}\right]\\ &+2\Gamma_{--}\left[\left(\boldsymbol{S}^A\cdot\boldsymbol{S}^B-S_z^A\,S_z^B\right)\left(\boldsymbol{O}^A\cdot\boldsymbol{O}^B-O_z^A\,O_z^B\right)-\left(S_z^A\,S_z^B-\frac{1}{4}\right)\left(O_z^A\,O_z^B-\frac{1}{4}\right)\right]\end{aligned}$$

where $\mathbf{O}_i=\boldsymbol{\tau}_i/2$ are operators acting only on orbital degrees of freedom and $\boldsymbol{\tau}$ are the pseudo-spin operators introduced in the previous section, Eq. (21), and

$$\Gamma_{-+}=\frac{4t^2}{U}\qquad\qquad \Gamma_{+-}=\frac{4t^2}{U-3J}\qquad\qquad \Gamma_{--}=-\frac{4t^2}{U-2J}.$$

When the second-order Hamiltonian is written in this form it is immediately clear that, among the four states we considered, the ferro-magnetic antiferro-orbital state is lower in energy. This happens because the superexchange coupling Γ_{+-} is the largest. If the orbital degeneracy is one, we can replace the terms $\boldsymbol{O}^A\cdot\boldsymbol{O}^B$ and $O_z^A\,O_z^B$ with the ferro-orbital value 1/4; then, the terms proportional to Γ_{+-} and Γ_{--} drop out and we recover the Heisenberg superexchange Hamiltonian, as expected for the one-band Hubbard model.

What about $KCuF_3$ and $LaMnO_3$? If we consider only hopping integrals between neighboring B sites in the cubic perovskite structure, the hopping integral matrices take the simple form

$$t_{mm'}^{i,i\pm\hat{z}}=t_\varepsilon\begin{pmatrix}0&0\\0&1\end{pmatrix}\qquad t_{mm'}^{i,i\pm\hat{x}}=t_\varepsilon\begin{pmatrix}\frac{3}{4}&\frac{\sqrt{3}}{4}\\\frac{\sqrt{3}}{4}&\frac{1}{4}\end{pmatrix}\qquad t_{mm'}^{i,i\pm\hat{y}}=t_\varepsilon\begin{pmatrix}\frac{3}{4}&-\frac{\sqrt{3}}{4}\\-\frac{\sqrt{3}}{4}&\frac{1}{4}\end{pmatrix}. \tag{23}$$

The structure of these matrices can be obtained by using Slater-Koster two-center integrals. The only non-zero hopping integral in the $\hat{z}$ direction is the one between $|3z^2-r^2\rangle$ states. As we have previously seen by using the downfolding approach, it is given by $t_\varepsilon=V_{pd\sigma}^2/(\varepsilon-\varepsilon_p)$.

As in the case of the two-site molecule, for integer filling (n electrons per atom) and in the large t_ε/U limit the lattice Hubbard model can be mapped onto an effective superexchange Hamiltonian by downfolding high-energy states in which some of the atoms have an electron number larger than n. Only two electronic configurations are relevant for orbital ordering, e_g^1 ($LaMnO_3$) and e_g^3 ($KCuF_3$). The remaining partially filled state, e_g^2, is magnetic with $S=1$ but, due to Hund's rule coupling J, it exhibits no orbital degeneracy ($L=0$). After excluding e_g^2 we can, for simplicity, set $J=0$. Let us now construct all atomic states $|N_e\rangle_\alpha$ with N_e electrons.

For a single atom they are

$\|N_e\rangle_\alpha$	$E_{\alpha'}(N_e)$	$d(N_e)$
$\|0\rangle$	$E(0)=0$	$d(0)=1$
$\|1\rangle = c^\dagger_{m\sigma}\|0\rangle$	$E(1)=\varepsilon_{e_g}$	$d(0)=4$
$\|2\rangle = c^\dagger_{m\sigma}c^\dagger_{m'\sigma'}\|0\rangle$	$E(2)=2\varepsilon_{e_g}+U$	$d(0)=6$
$\|3\rangle = c^\dagger_{m\sigma}c^\dagger_{m'\uparrow}c^\dagger_{m'\downarrow}\|0\rangle$	$E(3)=3\varepsilon_{e_g}+3U$	$d(0)=4$
$\|4\rangle = c^\dagger_{m\uparrow}c^\dagger_{m\downarrow}c^\dagger_{m'\uparrow}c^\dagger_{m'\downarrow}\|0\rangle$	$E(4)=4\varepsilon_{e_g}+6U$	$d(0)=1$

The total (spin and orbital) degeneracy of the n-electron sector, $d(N_e)$, is given in the third column. Let us consider two neighboring sites i and i' and their states $|N_e\rangle^i_\alpha$ and $|N'_e\rangle^{i'}_{\alpha'}$, where α and α' run over all degenerate states in the N_e-electron sector. We define the collective state of such a two-site system as $|N_e\rangle^i_\alpha|N'_e\rangle^{i'}_{\alpha'}$. Let us start from an e_g^1 configuration. In the large-U limit, at quarter filling ($n=1$) the ground state will be within the $N_e = N'_e = 1$ manifold, $|\mathrm{G}\rangle = \{|1\rangle^i_\alpha|1\rangle^{i'}_{\alpha'}\}$. The latter has a degeneracy 4^N, where N is the number of sites, here $N=2$; this degeneracy can be partially lifted via virtual excitations to the doubly occupied states $|\mathrm{E}\rangle = \{|2\rangle^i_\alpha|0\rangle^{i'}\}, \{|0\rangle^i|2\rangle^{i'}_{\alpha'}\}$, which in turn generate an effective low-energy Hamiltonian $\hat{H}_{\mathrm{SE}}$. We can again calculate $\hat{H}_{\mathrm{SE}}$ by treating $\hat{H}_T$ as a perturbation.
Let us consider at first only pairs of sites along the $\hat{z}$ axis. In second-order perturbation theory in $\hat{H}_T$, we obtain for the lattice the following effective Hamiltonian

$$\begin{aligned}
\hat{H}^{\hat{z}}_{\mathrm{SE}} &\sim -\frac{1}{U}\sum_E \hat{H}_T|E\rangle\langle E|\hat{H}^\dagger_T \\
&= -\frac{t^2}{U}\frac{1}{2}\sum_{ii'}\sum_{\sigma\sigma'}\sum_{\alpha}\left\{c^\dagger_{i\tau\sigma}|0\rangle^{i\,i}\langle 0|c_{i\tau\sigma'}\left[c_{i'\tau\sigma}|2\rangle^{i'\,i'}_{\alpha\,\alpha}\langle 2|c^\dagger_{i'\tau\sigma'}\right] + (i\longleftrightarrow i')\right\}\delta_{\tau,\searrow} \\
&= -\frac{2t^2}{U}\frac{1}{2}\sum_{ii'}\sum_{\sigma\sigma'}\left\{(-1)^{-\sigma'-\sigma}P^i_{\tau\sigma-\sigma'}P^{i'}_{\tau\sigma'-\sigma} + \frac{1}{2}\left[P^i_{\tau\sigma\sigma}P^{i'}_{-\tau\sigma'\sigma'} + P^i_{-\tau\sigma\sigma}P^{i'}_{\tau\sigma'\sigma'}\right]\right\}\delta_{\tau,\searrow},
\end{aligned}$$

where we already replaced in the denominator $\Delta E = E(2)+E(0)-2E(1)$ with its value, U, and where, once more, $|\searrow\rangle = |3z^2-r^2\rangle$, $|\nearrow\rangle = |x^2-y^2\rangle$. In Hamiltonian $\hat{H}^{\hat{z}}_{\mathrm{SE}}$ we introduced the operators $P^i_{\tau\sigma\sigma'}$, which are given by

$$P^i_{\tau\sigma\sigma'} = c^\dagger_{i\tau\sigma}|0\rangle\langle 0|c_{i\tau\sigma'} = \hat{o}^z_{\tau\tau}\left[\hat{s}^z_{\sigma\sigma'} + \hat{s}^+_{\sigma\sigma'} + \hat{s}^-_{\sigma\sigma'}\right].$$

In this expression on the right-hand side we rewrote $P^i_{\tau\sigma\sigma'}$ as product of an orbital and a spin term, defined as follows:

$$\begin{aligned}
\hat{o}^z_{\tau\tau'} &= \left[\frac{n_i}{2}\,\hat{I} + (-1)^\tau O^i_z\right]\delta_{\tau\tau'} & \hat{s}^z_{\sigma\sigma} &= \left[\frac{n_i}{2}\,\hat{I} + (-1)^\sigma S^i_z\right]\delta_{\sigma\sigma'} \\
\hat{o}^+_{\tau\tau'} &= O^i_+(1-\delta_{\tau\tau'}) & \hat{s}^+_{\sigma\sigma'} &= S^i_+(1-\delta_{\sigma\sigma'}) \\
\hat{o}^-_{\tau\tau'} &= O^i_-(1-\delta_{\tau\tau'}) & \hat{s}^-_{\sigma\sigma'} &= S^i_-(1-\delta_{\sigma\sigma'}),
\end{aligned}$$

where $(-1)^\sigma = +1$ for spin (pseudospin) up and -1 otherwise; the operator $\hat{I}$ is the identity matrix. Hence, we can express the effective Hamiltonian as

$$\hat{H}^{\hat{z}}_{\rm SE} = \frac{\Gamma}{2}\sum_{ii'}\left[\boldsymbol{S}^i\cdot\boldsymbol{S}^{i'} - \frac{n_i n_{i'}}{4}\right]\left[O^i_z - \frac{n_i}{2}\right]\left[O^{i'}_z - \frac{n_{i'}}{2}\right] + \frac{1}{2}\left[O^i_z O^{i'}_z - \frac{n_i n_{i'}}{4}\right],$$

where $\Gamma = 4t^2/U > 0$. If we drop all processes involving orbital $|\nearrow\rangle$ we recover the usual superexchange Heisenberg Hamiltonian for the one-band Hubbard model

$$\hat{H}^{\hat{z}}_{\rm SE} = \frac{\Gamma}{2}\sum_{ii'}\left[\boldsymbol{S}^i\cdot\boldsymbol{S}^{i'} - \frac{n_i n_{i'}}{4}\right].$$

Let us now consider two neighboring sites and the energy of some possible states $|{\rm G}\rangle = \{|1\rangle^i_\alpha|1\rangle^{i'}_{\alpha'}\}$. A ferro-magnetic spin configuration has energy

$$\Delta E_{\tau\uparrow,\tau'\uparrow} = -\frac{\Gamma}{4}(1-\delta_{\tau,\tau'}),$$

hence, there is an energy gain if the electrons occupy different orbitals, i.e., if the systems has antiferro-orbital arrangement. Let us consider now a antiferro-magnetic spin arrangement. The corresponding energy is

$$\Delta E_{\tau\uparrow,\tau'\downarrow} = -\frac{\Gamma}{2}\delta_{\tau,\tau'}\delta_{\tau,\searrow} - \frac{\Gamma}{4}(1-\delta_{\tau,\tau'})$$

The expression above shows that in the antiferro-magnetic case the system gains more energy if the occupied state is $|\searrow\rangle$ at both sites. Up to now we considered magnetically ordered states. In $LaMnO_3$ and $KCuF_3$, however, orbital order takes place well above the magnetic transition. Let us then assume that the system is orbitally ordered but paramagnetic, with occupied state

$$|\theta\rangle_i = -\sin\frac{\theta-\pi}{2}|x^2-y^2\rangle + \cos\frac{\theta-\pi}{2}|3z^2-r^2\rangle$$

at site i and $|\theta\rangle_{i\pm\hat{z}} = |\theta\rangle_i$ at the neighboring site $i' = i \pm \hat{z}$. This choice corresponds to ferro-orbital order along $\hat{z}$, the type of stacking realized in $LaMnO_3$ (see Fig. 13). What is the value of θ than minimizes the energy? We can calculate it using the variational method. The superexchange energy gain with respect to a paramagnetic paraorbital state is given by

$$\Delta E(\theta) = \frac{\Gamma}{16}\Big[\cos^2(\theta-\pi) + 2\cos(\theta-\pi)\Big].$$

This function is minimized for $\theta = 0$, an angle corresponding to a tetragonal compression. To determine the optimal angle for the three-dimensional system we have in addition to take into account the effective Hamiltonian stemming from virtual hoppings in the remaining directions. Due to cubic symmetry, if we rotate the quantization axis, the superexchange Hamiltonian has the same form in all directions; to sum up all terms we have merely to rotate back the quantization axis to $\hat{z}$. Hence, we have to make the replacements

$$O^i_z \underbrace{\to}_{\hat{z}\to\hat{x}} -\frac{1}{2}O^i_z - \frac{\sqrt{3}}{2}O^i_x$$

$$O^i_z \underbrace{\to}_{\hat{z}\to\hat{y}} -\frac{1}{2}O^i_z + \frac{\sqrt{3}}{2}O^i_x$$

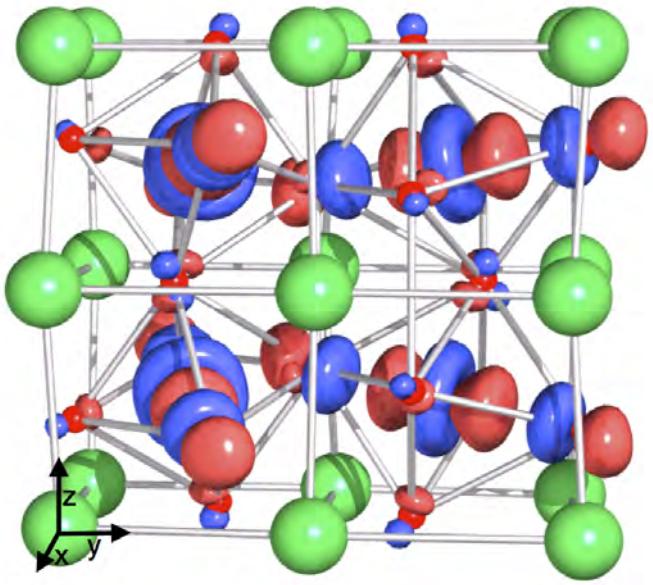

Fig. 13: *Orbital order (LDA+DMFT calculations) in the rare-earth perovskite $TbMnO_3$ with the $GdFeO_3$-type structure. From Ref. [6]. This system has the same structure of $LaMnO_3$.*

Let us assume antiferro-orbital order in the plane, again as in the case of $LaMnO_3$, shown in Fig. 13. This means that, for $i' = i \pm \hat{x}$ or $i' = i \pm \hat{y}$, the occupied state is

$$|\theta\rangle_{i'} = +\sin\frac{\theta-\pi}{2}|x^2-y^2\rangle + \cos\frac{\theta-\pi}{2}|3z^2-r^2\rangle.$$

We can easily verify that $|\theta\rangle_{i'} = |-\theta+2\pi\rangle_i$. This is state $|\theta\rangle_i$ rotated by $\pi/2$ ($x \to y$, $y \to -x$). The total superexchange energy gain with respect to a paramagnetic paraorbital state is then given by

$$\Delta E(\theta) = \frac{\Gamma}{16}\left[3\cos^2(\theta-\pi) - \frac{3}{2}\right].$$

This expression has a minimum for $\theta = \pi/2$ (Jahn-Teller-like $\boldsymbol{Q}_1$ distortion). For the e_g^3 configuration ($KCuF_3$), due to particle-hole symmetry, we obtain the same result. This can be verified by observing, first of all, that the e_g bands obtained from the hopping-integrals matrices (23) – bands which we have discussed in detail in Sec. 3 – are symmetric with respect to the Fermi level for half filling. In addition, the energy difference entering in the denominator of the superexchange Hamiltonian for an e_g^3 ground state, $\Delta E = E(4) + E(2) - 2E(3)$, has the same value ($\Delta E = U$) as in the case of an e_g^1 ground state. The main difference between $LaMnO_3$ (e_g^1) and $KCuF_3$ (e_g^3), for what concerns the results presented in this section, is that the stacking along $\hat{z}$, ferro-orbital for $LaMnO_3$, can be either antiferro- or ferro-orbital for $KCuF_3$; Fig. 1 shows the case of antiferro-orbital arrangement. Remarkably, the variational energy gain $\Delta E(\theta)$ is the same for both types of stacking along $\hat{z}$, i.e., for $|\theta\rangle_{i\pm\hat{z}} = |\theta\rangle_i$ and for $|\theta\rangle_{i\pm\hat{z}} = |-\theta+2\pi\rangle_i$. The conclusions of this section are thus identical for $LaMnO_3$ and $KCuF_3$.

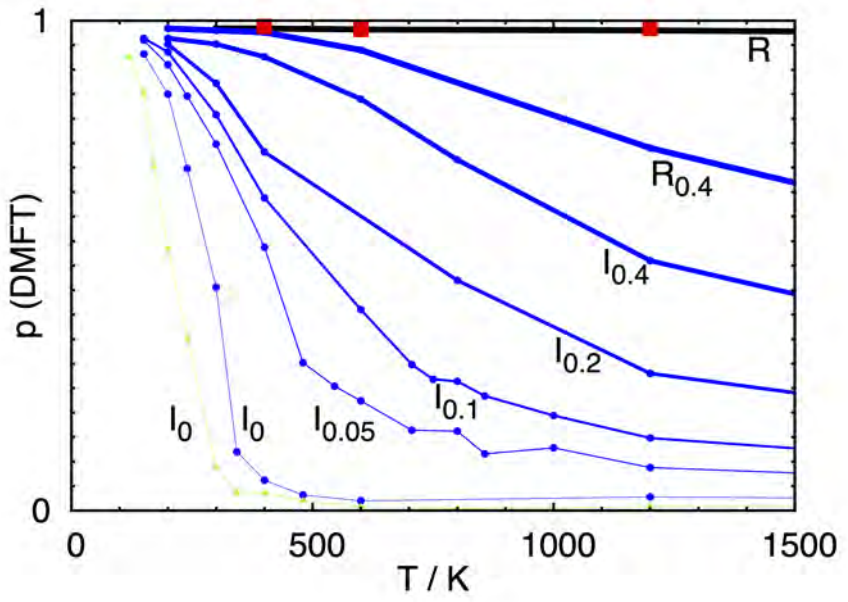

Fig. 14: *Orbital order transition in $KCuF_3$. Orbital polarization p as a function of temperature calculated in LDA+DMFT. R: experimental structure. Circles: idealized structures R_δ and I_δ with decreasing crystal-field and $U = 7$ eV. Green/Triangles: $U = 9$ eV, I_0 only. Red/Squares: two-sites CDMFT. From Ref. [3].*

6 The origin of orbital order

As we discussed in the introduction, the hallmark of orbital order is the co-operative Jahn-Teller distortion. This static distortion gives rise to a crystal field, which splits the otherwise degenerate e_g doublet. Due to Coulomb repulsion, it turns out that even a crystal-field splitting much smaller than the band width can lead to orbital order. The importance of this effect for real materials has been realized first for $LaTiO_3$ and $YTiO_3$ [4]. This reduction of orbital fluctuation is dynamical, but it can be already understood from the static Hartree-Fock contribution to the self-energy; the latter yields an effective enhancement of the crystal-field proportional to orbital polarization p. For an e_g system p is defined as the difference in occupation between the most and the least occupied orbital, $|1\rangle$ and $|2\rangle$, the so-called natural orbitals. Thus $p = n_1 - n_2$, and the Hartree-Fock self-energy correction to the crystal-field splitting is

$$\Delta\varepsilon_{\rm CF} = \Sigma_2(\omega_n \to \infty) - \Sigma_1(\omega_n \to \infty) \sim \frac{1}{2}(U - 5J)p.$$

If $p > 0$, as it happens in the presence of a crystal-field $\varepsilon_{\rm CF} = \varepsilon_2 - \varepsilon_1 > 0$, this term effectively increases the crystal-field splitting. This effect is at work not only in $LaTiO_3$ and $YTiO_3$, but also in several other systems with different electronic structure and even smaller crystal-field splittings. The case of $3d^9$ $KCuF_3$ and $3d^4$ $LaMnO_3$ is extreme: the e_g crystal-field splitting is $\sim 0.5 - 1$ eV; with such a large splitting, orbital fluctuations are suppressed up to the melting temperature. Thus, Coulomb repulsion makes the Jahn-Teller mechanism proposed by Kanamori very efficient. This result, however, does not clarify which of the two mechanisms,

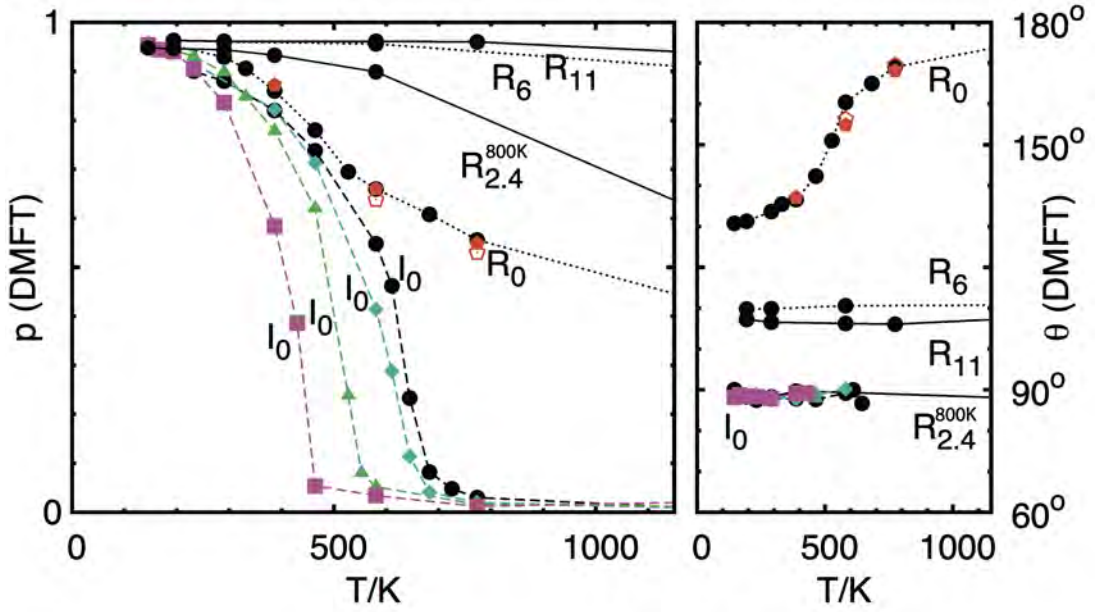

Fig. 15: *Orbital order transition in $LaMnO_3$. Orbital polarization p (left) and (right) occupied state $|\theta\rangle = \cos\frac{\theta}{2}|3z^2 - r^2\rangle + \sin\frac{\theta}{2}|x^2 - y^2\rangle$ as a function of temperature. Solid lines: 300 K experimental structure (R_{11}) and 800 K experimental structure. Dots: orthorhombic structures with half (R_6) or no (R_0) Jahn-Teller distortion. Pentagons: 2 (full) and 4 (empty) site CDMFT. Dashes: ideal cubic structure (I_0). Circles: $U = 5$ eV. Diamonds: $U = 5.5$ eV. Triangles: $U = 6$ eV. Squares: $U = 7$ eV. Crystal field splittings (meV): 840 (R_{11}), 495 (R_6), 168 ($R_{2.4}^{800\,K}$), and 0 (I_0). From Ref. [6].*

Kugel-Khomskii superexchange or Kanamori electron-phonon coupling, plays the major role in causing orbital order and stabilizing the distortion. Remarkably, Coulomb repulsion has also an important effect on structure stabilization. LDA+U total energy calculations have early on shown that the co-operative Jahn-Teller distortion is stabilized by U [10, 11], a result confirmed recently by LDA+DMFT [12]. This could be – and initially was – taken as an indication that superexchange is the driving mechanism. If this is the case, it is, however, hard to explain why the magnetic transition temperature ($T_N \sim 40$ K for $KCuF_3$ and $T_N \sim 140$ K for $LaMnO_3$), also determined by superexchange, is relatively low while the co-operative Jahn-Teller distortion persists up to the melting temperature. On the other hand, if Kugel-Khomskii superexchange is not the driving mechanism, the associated energy gain should be small with respect to the total energy gain due to the Jahn-Teller distortion.

To clarify the nature of the dominant mechanism, we disentangled electron-phonon and superexchange effects. To this end we performed LDA+DMFT (single-site and cluster) calculations for a series of hypothetical structures, in which the distortions (and thus the crystal-field splitting) are progressively reduced. In the case of $KCuF_3$, these hypothetical structures are shown in Fig. 1, and the corresponding e_g bands are shown in Fig. 7. For each structure we calculate the order parameter, the orbital polarization p. In Fig. 14 we show p as a function of temperature. For the experimental structure (R in the figure), we find that $p(T) \sim 1$ up to the melting temperature. The empty orbitals on different sites make the pattern shown in Fig. 1. For

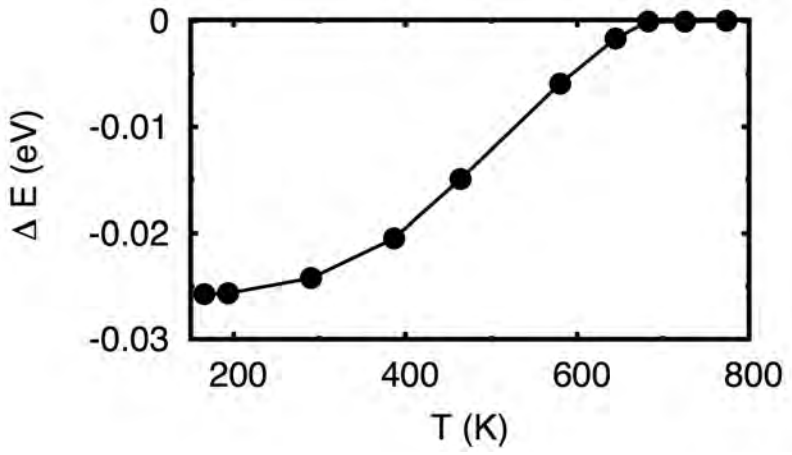

Fig. 16: *Superexchange energy gain for LaMnO$_3$, $\Delta E \sim -T_{\rm KK}/2$. From Ref. [6].*

the ideal cubic structure I_0, we find that $p(T) = 0$ at high temperature, but a transition occurs at $T_{\rm KK} \sim 350$ K. This $T_{\rm KK}$ is the critical temperature in the absence of electron-phonon coupling, i.e., the superexchange critical temperature. Our results show that around 350 K superexchange alone could indeed drive the co-operative Jahn-Teller distortion; it cannot, however, explain the presence of a co-operative Jahn-Teller distortion above 350 K. We performed a similar study fo LaMnO$_3$. For this $t_{2g}^3 e_g^1$ system we have to take into account the Hund's rule coupling between e_g electrons and t_{2g} spins, $\boldsymbol{S}_{t_{2g}}$. Thus the minimal model to understand orbital order is the modified Hubbard model [13]

$$H = -\sum_{ii'}\sum_{\sigma\sigma'}\sum_{mm'} t_{m,m'}^{i,i'}\, u_{\sigma,\sigma'}^{i,i'}\, c_{im\sigma}^{\dagger} c_{i'm'\sigma'} - h\sum_{im}(\hat{n}_{im\uparrow} - \hat{n}_{im\downarrow})$$

$$+U\sum_{im}\hat{n}_{im\uparrow}\hat{n}_{im\downarrow} + \frac{1}{2}\sum_{i}\sum_{\sigma\sigma'}\sum_{m(\neq m')}(U - 2J - J\delta_{\sigma,\sigma'})\,\hat{n}_{im\sigma}\hat{n}_{im'\sigma'}\ .$$

Here the local magnetic field $h = JS_{t_{2g}}$ describes the Hund's rule coupling to t_{2g} electrons, and $u_{i\sigma,i'\sigma'} = 2/3(1 - \delta_{i,i'})$ accounts for the disorder in orientation of the t_{2g} spins. By performing the same type of analysis as for KCuF$_3$, we find the impressively large $T_{\rm KK} \sim 700$ K (Fig. 15). There is a small point neglected so far; besides the co-operative Jahn-Teller distortion and tetragonal compression, LaMnO$_3$ exhibits a GdFeO$_3$-type distortion (Fig. 13), which tends to reduce the e_g band width [4]. To account for this we studied the orbital-order transition for the ideal structure R_0, which retains all distortions except for the Jahn-Teller one. For structure R_0 we cannot obtain $T_{\rm KK}$ from $p(T)$, because, due to the $\sim$ 200 meV crystal-field splitting, Coulomb repulsion strongly suppress orbital fluctuations even at 1500 K. We can, however, study the evolution with temperature of the occupied orbital, here defined as $|\theta\rangle = \cos\frac{\theta}{2}|3z^2 - r^2\rangle + \sin\frac{\theta}{2}|x^2 - y^2\rangle$. For the experimental structure (R_{11}) we find $\theta \sim 108^o$, in agreement with experiments, while for the I_0 structure we obtain $\theta = 90^o$. For the R_0 structure we find two regimes: At high temperature the occupied orbital is the lower-energy crystal-field orbital ($\theta = 180^o$). At $T_{\rm KK} \sim 550$ K superexchange rotates this θ towards 90^o, reaching

130^0 in the zero-temperature limit; this is the actual superexchange transition temperature for $LaMnO_3$. Such $T_{\rm KK}$ is still remarkably large, however not sufficiently to explain the persistence of the Jahn-Teller distortion in nanoclusters up to basically melting temperature [14]. Furthermore, the superexchange energy gain associated with orbital order (Fig.16) is small compared to the total energy gain due to the Jahn-Teller distortion, calculated via LDA+U [10, 11] or LDA+DMFT [12]. Thus, as in the case of $KCuF_3$, the conclusion is that a static crystal-field splitting, as the one generated by the electron-lattice coupling, is essential to explain orbital ordering at high temperature.

7 Conclusion

In this lecture we have studied two mechanisms that can lead to orbital ordering phenomena in Mott insulators. The first one is well illustrated in the influential paper of Kanamori, Ref. [1]. In this picture, a co-operative Jahn-Teller distortion generates a static crystal-field, which in turn splits orbitals otherwise degenerate. This mechanism is made more efficient by Coulomb repulsion; the latter enhances the orbital polarization, leading to a orbitally-ordered state even if the crystal-field splitting is a mere fraction of the bandwidth [4]. The second mechanism, proposed by Kugel and Khomskii [2] in 1973, predicts orbital ordering even in the absence of a static crystal field; in this picture, orbital ordering is due to the superexchange interaction, the effective interaction emerging from the orbitally-degenerate Hubbard model in the large U limit. Since both mechanism predict a similar type of order, identifying which one dominates for real materials is very difficult. Indeed, the origin of orbital order has been a matter of debate for decades. In the last section we saw how this problem was recently solved by disentangling the superexchange Kugel-Khomskii interaction from the rest. It was shown for the two most representative orbitally-ordered materials, $KCuF_3$ and $LaMnO_3$, that although Kugel-Khomskii superexchange is very efficient, it cannot alone explain the presence of a co-operative Jahn-Teller distortion up to the melting temperature. An interaction giving directly rise to a crystal-field splitting, e.g., electron-phonon coupling, is necessary to explain experimental findings.

Acknowledgment

Support of the Deutsche Forschungsgemeinschaft through FOR1346 is gratefully acknowledged.

Appendices

A Constants and units

In this lecture, formulas are given in atomic units. The unit of mass m_0 is the electron mass ($m_0 = m_e$), the unit of charge e_0 is the electron charge ($e_0 = e$), the unit of length a_0 is the Bohr radius ($a_0 = a_B \sim 0.52918$ Å), and the unit of time is $t_0 = 4\pi\varepsilon_0\hbar a_0/e^2$. In these units, m_e, a_B, e and $1/4\pi\varepsilon_0$ have the numerical value 1, the speed of light is $c = 1/\alpha \sim 137$, and the unit of energy is $1\text{Ha} = e^2/4\pi\varepsilon_0 a_0 \sim 27.211$ eV.

B Atomic orbitals

B.1 Radial functions

The nlm hydrogen-like atomic orbital is given by

$$\psi_{nlm}(\rho,\theta,\phi) = R_{nl}(\rho)Y_l^m(\theta,\phi),$$

where $R_{nl}(\rho)$ is the radial function and $Y_m^l(\theta,\phi)$ a spherical harmonic, $\rho = Zr$ and Z the atomic number. In atomic units, the radial functions are

$$R_{nl}(\rho) = \sqrt{\left(\frac{2Z}{n}\right)^3 \frac{(n-l-1)!}{2n[(n+l)!]^3}} e^{-\rho/n} \left(\frac{2\rho}{n}\right)^l L_{n-l-1}^{2l+1}\left(\frac{2\rho}{n}\right),$$

where L_{n-l-1}^{2l+1} are generalized Laguerre polynomials of degree $n-l-1$.
The radial function for $n = 1, 2, 3$ are

$$\begin{aligned}
R_{1s}(\rho) &= 2 \; Z^{3/2} && e^{-\rho} \\
R_{2s}(\rho) &= \tfrac{1}{2\sqrt{2}} \; Z^{3/2} && (2-\rho)\, e^{-\rho/2} \\
R_{2p}(\rho) &= \tfrac{1}{2\sqrt{6}} \; Z^{3/2} && \rho\, e^{-\rho/2} \\
R_{3s}(\rho) &= \tfrac{2}{3\sqrt{3}} \; Z^{3/2} && (1-2\rho/3+2\rho^2/27)\, e^{-\rho/3} \\
R_{3p}(\rho) &= \tfrac{4\sqrt{2}}{9\sqrt{3}} \; Z^{3/2} && \rho(1-\rho/6)\, e^{-\rho/3} \\
R_{3d}(\rho) &= \tfrac{2\sqrt{2}}{81\sqrt{15}} \; Z^{3/2} && \rho^2\, e^{-\rho/3}
\end{aligned}$$

where we used the standard notation s for $l = 0$, p for $l = 1$ and d for $l = 2$.

B.2 Real harmonics

To study solids, it is usually convenient to work in the basis of real harmonics. The latter are defined in terms of the spherical harmonics as follows:

$$y_{l0} = Y_0^l, \quad y_{lm} = \frac{1}{\sqrt{2}}(Y_{-m}^l + (-1)^m Y_m^l), \quad y_{l-m} = \frac{i}{\sqrt{2}}(Y_{-m}^l - (-1)^m Y_m^l), \quad m > 0.$$

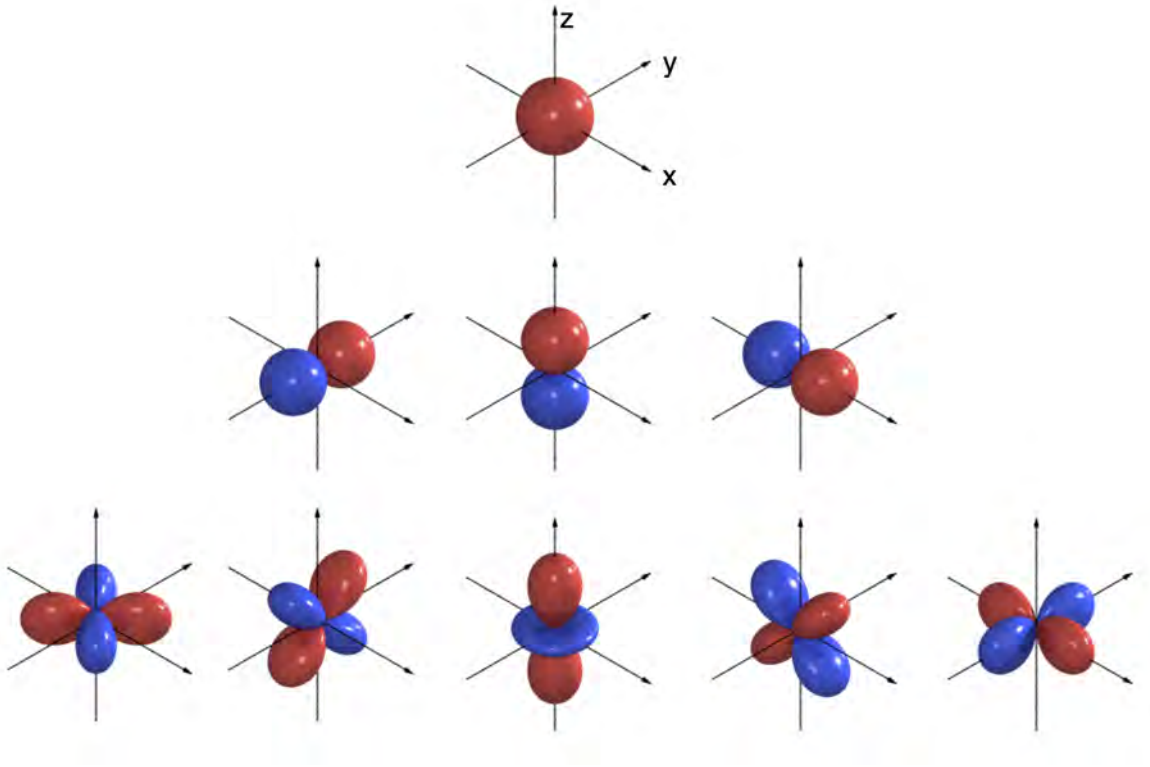

Fig. 17: *The s (first row), p_y, p_z, p_x (second row), and d_{xy}, d_{yz}, $d_{3z^2-r^2}$, d_{xz}, $d_{x^2-y^2}$ (last row) real harmonics.*

Using the definitions $x = r\sin\theta\cos\phi$, $y = r\sin\theta\sin\phi$, $z = r\cos\theta$, we can express the $l = 0, 1, 2$ real harmonics (Fig. 17) as

$$
\begin{aligned}
s &= y_{00} = Y_0^0 &&= \sqrt{\tfrac{1}{4\pi}} \\
p_y &= y_{1-1} = \tfrac{i}{\sqrt{2}}(Y_1^1 + Y_{-1}^1) &&= \sqrt{\tfrac{3}{4\pi}}\, y/r \\
p_z &= y_{10} = Y_2^0 &&= \sqrt{\tfrac{3}{4\pi}}\, z/r \\
p_x &= y_{11} = \tfrac{1}{\sqrt{2}}(Y_1^1 - Y_{-1}^1) &&= \sqrt{\tfrac{3}{4\pi}}\, x/r \\
d_{xy} &= y_{2-2} = \tfrac{i}{\sqrt{2}}(Y_2^2 - Y_{-2}^2) &&= \sqrt{\tfrac{15}{4\pi}}\, xy/r^2 \\
d_{yz} &= y_{2-1} = \tfrac{i}{\sqrt{2}}(Y_1^2 + Y_{-1}^2) &&= \sqrt{\tfrac{15}{4\pi}}\, yz/r^2 \\
d_{3z^2-r^2} &= y_{20} = Y_2^0 &&= \sqrt{\tfrac{15}{4\pi}}\tfrac{1}{2\sqrt{3}}\,(3z^2 - r^2)/r^2 \\
d_{xz} &= y_{21} = \tfrac{1}{\sqrt{2}}(Y_1^2 - Y_{-1}^2) &&= \sqrt{\tfrac{15}{4\pi}}\, xz/r^2 \\
d_{x^2-y^2} &= y_{22} = \tfrac{1}{\sqrt{2}}(Y_2^2 + Y_{-2}^2) &&= \sqrt{\tfrac{15}{4\pi}}\tfrac{1}{2}\,(x^2 - y^2)/r^2
\end{aligned}
$$

B.3 Slater-Koster integrals

The interatomic Slater-Koster two-center integrals are defined as

$$E_{lm,l'm'} = \int d\boldsymbol{r}\ \overline{\psi_{lm}}(\boldsymbol{r}-\boldsymbol{d})V(\boldsymbol{r}-\boldsymbol{d})\psi_{l'm'}(\boldsymbol{r}).$$

They can be expressed as a function of radial integrals $V_{ll'\alpha}$, which scale with the distance d roughly as $d^{-(l+l'+1)}$ [15], and direction cosines, defined as

$$l = \boldsymbol{d}\cdot\hat{x}/d, \quad m = \boldsymbol{d}\cdot\hat{y}/d, \quad n = \boldsymbol{d}\cdot\hat{z}/d.$$

The Slater-Koster integrals for s-, p-, and d-orbitals [15] are listed below.

$E_{s,s}$	=	$V_{ss\sigma}$		
$E_{s,x}$	=	$lV_{sp\sigma}$		
$E_{x,x}$	=	$l^2V_{pp\sigma}$	$+(1-l^2)V_{pp\pi}$	
$E_{x,y}$	=	$lmV_{pp\sigma}$	$-lmV_{pp\pi}$	
$E_{x,z}$	=	$lnV_{pp\sigma}$	$-lnV_{pp\pi}$	
$E_{s,xy}$	=	$\sqrt{3}lmV_{sd\sigma}$		
E_{s,x^2-y^2}	=	$\frac{1}{2}\sqrt{3}(l^2-m^2)V_{sd\sigma}$		
$E_{s,3z^2-r^2}$	=	$[n^2-\frac{1}{2}(l^2+m^2)]V_{sd\sigma}$		
$E_{x,xy}$	=	$\sqrt{3}l^2mV_{pd\sigma}$	$+m(1-2l^2)V_{pd\pi}$	
$E_{x,yz}$	=	$\sqrt{3}lmnV_{pd\sigma}$	$-2lmnV_{pd\pi}$	
$E_{x,zx}$	=	$\sqrt{3}l^2nV_{pd\sigma}$	$+n(1-2l^2)V_{pd\pi}$	
E_{x,x^2-y^2}	=	$\frac{\sqrt{3}}{2}l[(l^2-m^2)]V_{pd\sigma}$	$+l(1-l^2+m^2)V_{pd\pi}$	
E_{y,x^2-y^2}	=	$\frac{\sqrt{3}}{2}m[(l^2-m^2)]V_{pd\sigma}$	$-m(1+l^2-m^2)V_{pd\pi}$	
E_{z,x^2-y^2}	=	$\frac{\sqrt{3}}{2}n[(l^2-m^2)]V_{pd\sigma}$	$-n(l^2-m^2)V_{pd\pi}$	
$E_{x,3z^2-r^2}$	=	$l[n^2-\frac{1}{2}(l^2+m^2)]V_{pd\sigma}$	$-\sqrt{3}ln^2V_{pd\pi}$	
$E_{y,3z^2-r^2}$	=	$m[n^2-\frac{1}{2}(l^2+m^2)]V_{pd\sigma}$	$-\sqrt{3}mn^2V_{pd\pi}$	
$E_{z,3z^2-r^2}$	=	$n[n^2-\frac{1}{2}(l^2+m^2)]V_{pd\sigma}$	$+\sqrt{3}n(l^2+m^2)V_{pd\pi}$	
$E_{xy,xy}$	=	$3l^2m^2V_{dd\sigma}$	$+(l^2+m^2-4l^2m^2)V_{dd\pi}$	$+(n^2+l^2m^2)V_{dd\delta}$
$E_{xy,yz}$	=	$3lm^2nV_{dd\sigma}$	$+ln(1-4m^2)V_{dd\pi}$	$+ln(m^2-1)V_{dd\delta}$
$E_{xy,zx}$	=	$3l^2mnV_{dd\sigma}$	$+mn(1-4l^2)V_{dd\pi}$	$+mn(l^2-1)V_{dd\delta}$
E_{xy,x^2-y^2}	=	$\frac{3}{2}lm(l^2-m^2)V_{dd\sigma}$	$2lm(m^2-l^2)V_{dd\pi}$	$\frac{1}{2}lm(l^2-m^2)V_{dd\delta}$
E_{yz,x^2-y^2}	=	$\frac{3}{2}mn(l^2-m^2)V_{dd\sigma}$	$-mn[1+2(l^2-m^2)]V_{dd\pi}$	$+mn[1+\frac{1}{2}(l^2-m^2)]V_{dd\delta}$
E_{zx,x^2-y^2}	=	$\frac{3}{2}nl(l^2-m^2)V_{dd\sigma}$	$+nl[1-2(l^2-m^2)]V_{dd\pi}$	$-nl[1-\frac{1}{2}(l^2-m^2)]V_{dd\delta}$
$E_{xy,3z^2-r^2}$	=	$\sqrt{3}lm[n^2-\frac{1}{2}(l^2+m^2)]V_{dd\sigma}$	$-2\sqrt{3}lmn^2V_{dd\pi}$	$\frac{\sqrt{3}}{2}lm(1+n^2)V_{dd\delta}$
$E_{yz,3z^2-r^2}$	=	$\sqrt{3}mn[n^2-\frac{1}{2}(l^2+m^2)]V_{dd\sigma}$	$+\sqrt{3}mn(l^2+m^2-n^2)V_{dd\pi}$	$-\frac{\sqrt{3}}{2}mn(l^2+m^2)V_{dd\delta}$
$E_{zx,3z^2-r^2}$	=	$\sqrt{3}ln[n^2-\frac{1}{2}(l^2+m^2)]V_{dd\sigma}$	$+\sqrt{3}ln(l^2+m^2-n^2)V_{dd\pi}$	$-\frac{\sqrt{3}}{2}ln(l^2+m^2)V_{dd\delta}$
$E_{x^2-y^2,x^2-y^2}$	=	$\frac{3}{4}(l^2-m^2)^2V_{dd\sigma}$	$+[l^2+m^2-(l^2-m^2)^2]V_{dd\pi}$	$+[n^2+\frac{1}{4}(l^2-m^2)^2]V_{dd\delta}$
$E_{x^2-y^2,3z^2-r^2}$	=	$\frac{\sqrt{3}}{2}(l^2-m^2)[n^2-\frac{1}{2}(l^2+m^2)]V_{dd\sigma}$	$+\sqrt{3}n^2(m^2-l^2)V_{dd\pi}$	$+\frac{1}{4}\sqrt{3}(1+n^2)(l^2-m^2)V_{dd\delta}$
$E_{3z^2-r^2,3z^2-r^2}$	=	$[n^2-\frac{1}{2}(l^2+m^2)]^2V_{dd\sigma}$	$+3n^2(l^2+m^2)V_{dd\pi}$	$\frac{3}{4}(l^2+m^2)^2V_{dd\delta}$

References

[1] J. Kanamori, J. Appl. Phys. **31**, S14 (1960)

[2] K.I. Kugel and D.I. Khomskii, Zh. Eksp. Teor. Fiz. **64**, 1429 (1973)

[3] E. Pavarini, E. Koch, and A.I. Lichtenstein, Phys. Rev. Lett. **101**, 266405 (2008)

[4] E. Pavarini, S. Biermann, A. Poteryaev, A.I. Lichtenstein, A. Georges, O.K. Andersen, Phys. Rev. Lett. **92**, 176403 (2004)
E. Pavarini A. Yamasaki, J. Nuss and O.K. Andersen, New J. Phys. **7**, 188 (2005)

[5] E. Pavarini: *The LDA+DMFT Approach*, in [7]

[6] E. Pavarini and E. Koch, Phys. Rev. Lett. **104**, 086402 (2010)
A. Flesch, G. Zhang, E. Koch, and E. Pavarini, Phys. Rev. B **85**, 035124 (2012)

[7] E. Pavarini, E. Koch, A. Lichtenstein, D. Vollhardt (eds.):
The LDA+DMFT approach to strongly correlated materials,
Reihe Modeling and Simulation, Vol. 1 (Forschungszentrum Jülich, 2011)
`http://www.cond-mat.de/events/correl11`

[8] E. Pavarini, E. Koch, A. Lichtenstein, D. Vollhardt (eds.):
DMFT at 25: Infinite Dimensions,
Reihe Modeling and Simulation, Vol. 4 (Forschungszentrum Jülich, 2014)
`http://www.cond-mat.de/events/correl14`

[9] E. Pavarini, E. Koch, F. Anders, M. Jarrell (eds.):
Correlated Electrons: From Models to Materials,
Reihe Modeling and Simulation, Vol. 2 (Forschungszentrum Jülich, 2012)
`http://www.cond-mat.de/events/correl12`

[10] V.I. Anisimov, F. Aryasetiawan and A.I. Lichtenstein, J. Phys. Cond. Mat. **9**, 767 (1997)

[11] W.G. Yin, D. Volja, and W. Ku, Phys. Rev. Lett. **96**, 116405 (2006)

[12] I. Leonov, N. Binggeli, Dm. Korotin, V.I. Anisimov, and D. Vollhardt, Phys. Rev. Lett. **101**, 096405 (2008); I. Leonov, Dm. Korotin, N. Binggeli, V.I. Anisimov, and D. Vollhardt Phys. Rev. B **81**, 075109 (2010)

[13] K.H. Ahn, and A.J. Millis, Phys. Rev. B **61**, 13545 (2000)

[14] M.C. Sánchez, G. Subías, J. García, and J. Blasco, Phys. Rev. Lett. **90**, 045503 (2003)

[15] W.A. Harrison: *Electronic Structure and The Properties of Solids* (Dover, 1989)

8 Studying Continuous Symmetry Breaking with Exact Diagonalization

A.M. Läuchli, M. Schuler, and A. Wietek
Institut für Theoretische Physik
Universität Innsbruck

Contents

E. Pavarini, E. Koch, J. van den Brink, and G. Sawatzky (eds.)
Quantum Materials: Experiments and Theory
Modeling and Simulation Vol. 6
Forschungszentrum Jülich, 2016, ISBN 978-3-95806-159-0
http://www.cond-mat.de/events/correl16

1 Introduction

Spontaneous symmetry breaking is amongst the most important concepts in condensed matter physics. The fact that a ground or thermal state of a system does not obey its full symmetry explains most of the well-known phase transitions in solid state physics like crystallization of a fluid, superfluidity, magnetism, superconductivity, and many more. A standard concept for investigating spontaneous symmetry breaking is the notion of an order parameter. In the thermodynamic limit it is non-zero in the symmetry-broken phase and zero in the disordered phase.

Another concept to detect spontaneous symmetry breaking less widely known but equally powerful is the *tower of states analysis* (TOS) [1, 2]. The energy spectrum, i.e., the eigenvalues of the Hamiltonian of a *finite* system in a symmetry-broken phase, has a characteristic and systematic structure: several eigenstates are quasi-degenerate on finite systems and become degenerate in the thermodynamic limit and possess certain quantum numbers. The TOS analysis deals with understanding the spectral structure and predicting quantum numbers of the groundstate manifold. Also on finite systems spontaneous symmetry breaking manifests itself in the structure of the energy spectra which are accessible via numerical simulations. Most prominently the Exact Diagonalization method [3, 4] can exactly calculate these spectra and quantum numbers on moderate system sizes. The predictions of TOS analyses are highly nontrivial statements which can be used to unambiguously identify symmetry-broken phases. Thus TOS analysis is a powerful technique to investigate many condensed matter systems using numerical simulations. The goal of these lecture notes is to explain the specific structure of energy spectra and their quantum numbers in symmetry-broken phases. The anticipated structure is then compared to several actual numerical simulations using Exact Diagonalization.

These lecture notes have been written at the kind request of the organizers of the Jülich 2016 Autumn School on Correlated Electrons. The notes build on and complement previously available lecture notes by Claire Lhuillier [2], by Grégoire Misguich and Philippe Sindzingre [5] and by Karlo Penc and one of the authors [3].

The outline of these notes is as follows: in Section 2 we introduce the tower of states of continuous symmetry breaking and derive its scaling behavior. We investigate a toy model which shows most of the relevant features. Section 3 explains in detail how the multiplicities and quantum numbers in the TOS can be predicted by simple group theoretical methods. To apply these methods we discuss several examples in Section 4 and compare them to actual numerical data from Exact Diagonalization.

2 Tower of states

We start our discussion of spontaneous symmetry breaking of continuous symmetries by investigating the Heisenberg model on the square lattice. Its Hamiltonian is given by

$$H = J \sum_{\langle i,j \rangle} \mathbf{S}_i \cdot \mathbf{S}_j \tag{1}$$

and is invariant under global $SU(2)$ spin rotations, i.e., a rotation of every spin on each site with the same rotational $SU(2)$ matrix. Therefore the total spin

$$\mathbf{S}_{\text{tot}}^2 = \left(\sum_i \mathbf{S}_i\right)^2 = S_{\text{tot}}(S_{\text{tot}}+1) \tag{2}$$

is a conserved quantity of this model and every state in the spectrum of this Hamiltonian can be labeled via its total spin quantum number. The Heisenberg Hamiltonian on the square lattice has the property of being *bipartite*: The lattice can be divided into two sublattices A and B such that every term in Eq. (1) connects one site from sublattice A to sublattice B. It was found out early [1] that the groundstate of this model bears resemblance with the classical *Néel state*

$$|\text{Néel class.}\rangle = |\uparrow\downarrow\uparrow\downarrow\cdots\rangle \tag{3}$$

where the spin-ups live on the A sublattice and the spin-downs live on the B sublattice. This state does not have the total spin as a good quantum number. From elementary spin algebra we know that it is rather a superposition of several states with different total spin quantum numbers. For example the 2-site state

$$|\uparrow\downarrow\rangle = \frac{|\uparrow\downarrow\rangle - |\downarrow\uparrow\rangle}{2} + \frac{|\uparrow\downarrow\rangle + |\downarrow\uparrow\rangle}{2} = |S_{\text{tot}}=0, m=0\rangle + |S_{\text{tot}}=1, m=0\rangle \tag{4}$$

is the superposition of a singlet ($S_{tot}=0$) and a triplet ($S_{tot}=1$). Therefore if such a state were to be a groundstate of Eq. (1) several states with different total spin would have to be degenerate. It turns out that on finite bipartite lattices this is not the case: The total groundstate of the Heisenberg model on bipartite lattices can be proven to be a singlet state with $S_{\text{tot}}=0$. This result is known as *Marshall's Theorem* [6–8]. So how can a Néel state resemble the singlet groundstate? To understand this we drastically simplify the Heisenberg model and investigate a toy model whose spectrum we can fully understand analytically.

2.1 Toy model: the Lieb-Mattis model

By introducing the Fourier-transformed spin operators

$$\mathbf{S}_{\mathbf{k}} = \frac{1}{\sqrt{N}} \sum_{j=0}^{N} e^{i\mathbf{k}\cdot\mathbf{x}_j} \mathbf{S}_j \,, \tag{5}$$

we can rewrite the original Heisenberg Hamiltonian in terms of these operators as

$$H = J \sum_{\mathbf{k}\in\text{B.Z.}} \omega_{\mathbf{k}}\, \mathbf{S}_{\mathbf{k}} \cdot \mathbf{S}_{-\mathbf{k}} \,, \tag{6}$$

where $\omega_{\mathbf{k}} = \cos(k_x) + \cos(k_y)$ and the sum over $\mathbf{k}$ runs over the momenta within the first Brillouin zone. Let $\mathbf{k}_0 = (\pi, \pi)$ be the ordering wavevector which is the dual to the translations that leave the square Néel state invariant. We now want to look at the truncated Hamiltonian

$$H_{\text{LM}} = 2J\left(\mathbf{S}_{(0,0)}^2 - \mathbf{S}_{\mathbf{k}_0}\cdot\mathbf{S}_{-\mathbf{k}_0}\right) \tag{7}$$

where we omit all Fourier components in Eq. (6) except $\mathbf{k} = (0,0)$ and $\mathbf{k}_0$. This model is called the Lieb-Mattis model [7] and has a simple analytical solution. To see this, we notice that Eq. (7) is given by

$$H_{LM} = \frac{4J}{N} \sum_{i\in A,\, j\in B} \mathbf{S}_i \cdot \mathbf{S}_j \tag{8}$$

in real space where A and B denote the two bipartite sublattices within the square lattice and each spin is only coupled with spins in the other sublattice. The interaction strength is equal regardless of the distance between the two spins. Thus this model is not likely to be experimentally relevant. Yet it will serve as an illustrative example how breaking the spin-rotational symmetry manifests itself in the spectrum of a finite size system. We can write Eq. (8) as

$$H_{LM} = \frac{4J}{N} \left(\sum_{i,j\in A\cup B} \mathbf{S}_i \cdot \mathbf{S}_j - \sum_{i,j\in A} \mathbf{S}_i \cdot \mathbf{S}_j - \sum_{i,j\in B} \mathbf{S}_i \cdot \mathbf{S}_j \right) \tag{9}$$

$$= \frac{4J}{N} (\mathbf{S}^2_{\text{tot}} - \mathbf{S}^2_A - \mathbf{S}^2_B) \tag{10}$$

From this it is obvious that the Lieb-Mattis model can be considered as the coupling of two large spins S_A and S_B to a total spin S_{tot}.

We find that the operators $\mathbf{S}^2_{\text{tot}}$, S^z_{tot}, $\mathbf{S}^2_A$ and $\mathbf{S}^2_B$ commute with this Hamiltonian and therefore the sublattice spins S_A and S_B as well as the total spin S_{tot} and its z-component m_{tot} are good quantum numbers for this model. For a lattice with N sites (N even) the sublattice spins can be chosen in the range $S_{A,B} \in \{0, 1, \ldots, N/4\}$ and by coupling them

$$S_{\text{tot}} \in \{|S_A - S_B|, |S_A - S_B| + 1, \ldots, S_A + S_B\} \tag{11}$$

$$m_{\text{tot}} \in \{-S_{\text{tot}}, -S_{\text{tot}} + 1, \ldots, S_{\text{tot}}\} \tag{12}$$

can be chosen.[1] A state $|S_{\text{tot}}, m, S_A, S_B\rangle$ is thus an eigenstate of the systems with energy

$$E(S_{\text{tot}}, m, S_A, S_B) = \frac{4J}{N} \left[S_{\text{tot}}(S_{\text{tot}} + 1) - S_A(S_A + 1) - S_B(S_B + 1) \right] \tag{13}$$

independent of m, so each state is at least $(2S_{\text{tot}} + 1)$-fold degenerate.

Tower of states We first want to consider only the lowest energy states for each S_{tot} sector. These states build the famous *tower of states* and collapse in the thermodynamic limit to a highly degenerate groundstate manifold, as we will see now.

For a given total spin S_{tot} the lowest energy states are built by maximizing the last two terms in Eq. (13) with $S_A = S_B = N/4$ and

$$E_0(S_{\text{tot}}) = E(S_{\text{tot}}, m, N/4, N/4) = \frac{4J}{N} S_{\text{tot}}(S_{\text{tot}} + 1) - J \left(\frac{N}{4} + 1 \right). \tag{14}$$

The groundstate of a finite system will thus be the singlet state with $S_{\text{tot}} = 0$.[2] On a finite system the groundstate is, therefore, totally symmetric under global spin rotations and does not break

[1] This set of states spans the full Hilbert space of the model.

[2] The groundstate of the Heisenberg model Eq. (1) on a bipartite sublattice with equal sized sublattices is also proven to be a singlet state $S_{tot} = 0$ by Marshall's Theorem [8, 6, 7].

the $SU(2)$-symmetry. In the thermodynamic limit $N \to \infty$, however, the energy of all states scales to zero and all these states constitute the groundstate manifold.
The classical Néel state with fully polarized spins on each sublattice can be built out of these states by a linear combination of all the S_{tot} levels with $m_{tot} = 0$ [2]. All other Néel states pointing in a different direction in spin-space can be equivalently built out of this groundstate manifold by considering linear combinations with other m_{tot} quantum numbers. In the thermodynamic limit, any infinitesimal small field will force the Néel state to choose a direction and the groundstate spontaneously breaks the $SU(2)$-symmetry.
The states which constitute the groundstate manifold in the thermodynamic limit can be readily identified on finite-size systems as well, where their energy is given by Eq. (14). These states are called the *tower of states* (TOS) or also *Anderson tower*, *thin spectrum*, and *quasi-degenerate joint states* [1, 9–11].

Excitations The lowest excitations above the tower of states can be built by lowering the spin of one sublattice S_A or S_B by one, see Eq. (13). Let us set $S_A = N/4$ and $S_B = N/4 - 1$ which implies that $S_{\text{tot}} \in \{1, 2, \ldots, N/2 - 1\}$. We can directly compute the energy $E_1(S_{\text{tot}})$ of these excited states for each allowed S_{tot} and the energy gap to the tower of states is constant[3]

$$E_{\text{exc}}(S_{\text{tot}}) = E_1(S_{\text{tot}}) - E_0(S_{\text{tot}}) = J\,. \tag{15}$$

As the energy gap is constant, the lowest excitations of the Lieb-Mattis model are static spin-flips. The next lowest excitations are spin-flips on both sublattices, $S_A = S_B = N/4 - 1$ with excitation energy $E_{\text{exc}_2} = 2J$ and $S_{\text{tot}} \in \{0, 1, \ldots, N/2 - 2\}$. We see that the energy gap of no levels except for the TOS vanishes in the thermodynamic limit, so the TOS indeed solely contributes to the groundstate manifold.

Quantum Fluctuations When we introduced the Lieb-Mattis model Eq. (7) from the Heisenberg model Eq. (6) we neglected all Fourier components except of $\mathbf{k} = (0, 0)$ and $\mathbf{k} = \mathbf{k}_0$. This was a quite crude approximation and it is not guaranteed that all results for the Lieb-Mattis model will survive for the short-range Heisenberg model. To get some first results regarding this question, we can introduce small quantum fluctuations on top of the Néel groundstate of the Lieb-Mattis model and perform a perturbative spin-wave analysis in first order.[4] This approach does not affect the scaling of the tower of states levels, but it has an important effect on the excitations. They are not static particles anymore, but are spinwaves (magnons) with a dispersion, which is linear around the ordering-wave vector $\mathbf{k} = \mathbf{k}_0$ and $\mathbf{k} = (0, 0)$. On a finite-size lattice the momentum space is discrete with a distance proportional to $1/L$ between them, where L is the linear size of the system. The energy of the lowest excitation above the

[3] This is an artifact of the infinite-range interaction in the Lieb-Mattis model. In the original Heisenberg model these modes become gapless magnon excitations.

[4] A more detailed discussion can be found in [2].

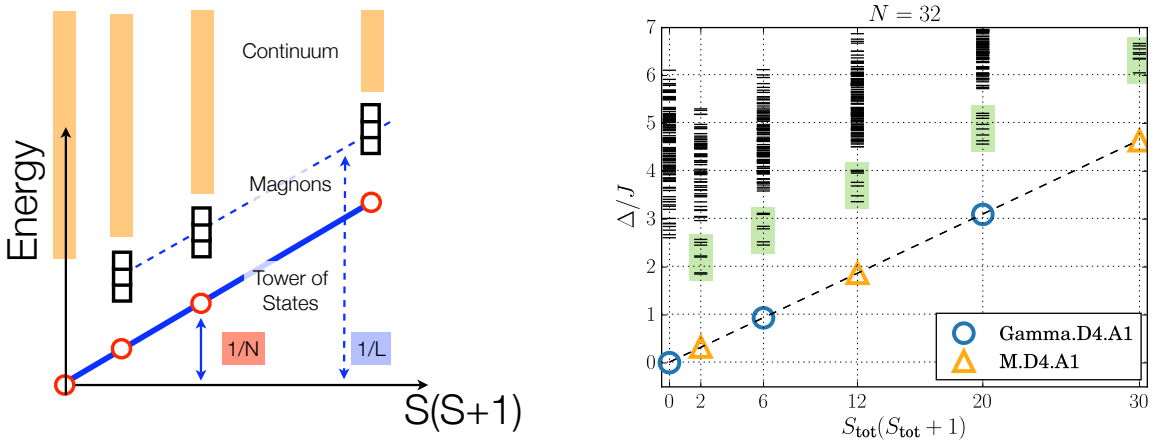

Fig. 1: *Left: Schematic finite-size energy spectrum of an antiferromagnet breaking $SU(2)$ spin-rotational symmetry. The TOS levels are the lowest energy levels for each total spin S and scale with $1/N$ to the groundstate energy. The low-energy magnon excitations are separated from the TOS and a continuum of higher energy states and scale with $1/L$. Right: Energy spectrum for the Heisenberg model on a square lattice. The TOS levels are connected by a dashed line. The single-magnon dispersion (green boxes) with $S_{tot} \in \{1, 2, \dots\}$ are well separated from the TOS and the higher multi-particle continuum. The different symbols represent quantum numbers related to space-group symmetries and agree with the expectations for a Néel state (See section 3).*

TOS, the single magnon gap, therefore scales as $E_{\text{exc}} \propto J/L$ to zero.[5] As the scaling is, however, slower for $d > 1$-dimensional systems than the TOS scaling, these levels do not influence the groundstate manifold in the thermodynamic limit. Finally, the excitation of two magnons results in a two-particle continuum above the magnon mode.

The properties of the TOS and its excitations are summarized in Fig. 1. The left figure shows the general properties of the finite-size energy spectrum which can be expected when a continuous symmetry group is spontaneously broken in the thermodynamic limit. The right figure depicts the TOS spectrum for the Heisenberg model on a square lattice with $N = 32$ sites, obtained with Exact Diagonalization. One can clearly identify the TOS, the magnon dispersion and the many-particle continuum. The existence of a Néel TOS was not only confirmed numerically for the Heisenberg model on the square lattice, but also with analytical techniques beyond the simplification to the Lieb-Mattis model [1, 10, 11]. The different symbols in Fig. 1 represent different quantum numbers related to the space-group symmetries on the lattice. In the next section we will see that the structure of these quantum numbers depends on the exact shape of the symmetry-broken state and we will learn how to compute them.

[5] In the thermodynamic limit the single magnon mode is gapless and has linear dispersion around $\mathbf{k} = \mathbf{k}_0$ and $\mathbf{k} = (0, 0)$. It corresponds to the well-known Goldstone mode which is generated when a continuous symmetry is spontaneously broken.

3 Symmetry analysis

In the analysis of excitation spectra from Exact Diagonalization on finite-size simulation clusters the *tower of states analysis* (TOS) is a powerful tool to detect spontaneous symmetry breaking. Symmetry breaking implies degenerate groundstates in the thermodynamic limit. On finite-size simulation clusters this degeneracy is in general not exact. We rather expect a certain scaling of the energy differences in the thermodynamic limit. We distinguish two cases:

- **Discrete symmetry breaking:** In this case we have a degeneracy of finitely many states in the thermodynamic limit. The groundstate splitting Δ on finite size clusters scales as $\Delta \sim \exp(N/\xi)$, where N is the number of sites in the system
- **Continuous symmetry breaking:** Here the groundstate in the thermodynamic limit is infinitely degenerate. The states belonging to this degenerate manifold collapse as $\Delta \sim 1/N$ on finite size clusters as we have seen in section 2. It is important to understand that these states are not the Goldstone modes of continuous symmetry breaking. Both the degenerate groundstate and the Goldstone modes appear as low-energy levels on finite size clusters but have different scaling behaviors.

The scaling of these low-energy states can now be investigated on finite size clusters. More importantly, also the quantum numbers of these low-energy states such as momentum, pointgroup representation, or total spin can be predicted [2,5,12]. The detection of correct scaling behavior together with correctly predicted quantum numbers yields very strong evidence that the system spontaneously breaks symmetry in the way that has been anticipated. This is the TOS method. In the following we will discuss how to predict the quantum numbers for discrete as well as continuous symmetry breaking. The main mathematical tool we use is the character-formula from basic group representation theory.
Lattice Hamiltonians like a Heisenberg model often have a discrete symmetry group arising from translational invariance, pointgroup invariance, or some discrete local symmetry, like a spin-flip symmetry. In this chapter we will first discuss the representation theory and the characters of the representations of space groups on finite lattices. We will then see how this helps us to predict the representations of the degenerate ground states in discrete as well as continuous symmetry breaking.

3.1 Representation theory for space groups

For finite discrete groups such as the space group of a finite lattice the full set of irreducible representations (irreps) can be worked out. Let us first discuss some basic groups. Let's consider an $n \times n$ square lattice with periodic boundary conditions and a translationally invariant Hamiltonian like the Heisenberg model on it. In the following we will set the lattice spacing to $a = 1$. The discrete symmetry group we consider is $\mathcal{T} = \mathbb{Z}_n \times \mathbb{Z}_n$ corresponding to the group of translations on this lattice. This is an Abelian group of order n^2. Its representations can be labeled by the momentum vectors $\mathbf{k} = (\frac{2\pi i}{n}, \frac{2\pi j}{n})$, $i, j \in \{0, \cdots, n-1\}$ which just correspond

to the reciprocal Bloch vectors defined on this lattice. Put differently, the vectors $\mathbf{k}$ are the reciprocal lattice points of the lattice spanned by the simulation torus of our $n \times n$ square lattice. The character $\chi_{\mathbf{k}}$ of the $\mathbf{k}$-representation is given by

$$\chi_{\mathbf{k}}(\mathbf{t}) = \mathrm{e}^{i\mathbf{k}\cdot\mathbf{t}} \tag{16}$$

where $\mathbf{t} \in \mathcal{T}$ is the vector of translation. This is just the usual Bloch factor for translationally invariant systems.

Let us now consider a (symmorphic) space group of the form $\mathcal{D} = \mathcal{T} \times \mathrm{PG}$ as the discrete symmetry group of the lattice where PG is the pointgroup of the lattice. For a model on an $n \times n$ square lattice this could for example be the dihedral group of order 8, D_4, consisting of four-fold rotations together with reflections. The representation theory and the character tables of these point groups are well-known. Since $\mathcal{D}$ is now a product of the translation and the point group we could think that the irreducible representations of $\mathcal{D}$ are simply given by the product representations $(\mathbf{k} \otimes \rho)$ where $\mathbf{k}$ labels a momentum representation and ρ an irrep of PG. But here is a small caveat. We have to be careful since $\mathcal{D}$ is only a semidirect product of groups since translations and pointgroup symmetries do not necessarily commute. This alters the representation theory for this product of groups and the irreps of $\mathcal{D}$ are not just simply the products of irreps of $\mathcal{T}$ and PG. Instead the full set of irreps for this group is given by $(\mathbf{k} \otimes \rho_{\mathbf{k}})$ where $\rho_{\mathbf{k}}$ is an irrep of the so called *little group* $L_{\mathbf{k}}$ of $\mathbf{k}$ defined as

$$L_{\mathbf{k}} = \{g \in \mathrm{PG};\ g(\mathbf{k}) = \mathbf{k}\} \tag{17}$$

which is just the stabilizer of $\mathbf{k}$ in PG. For example all pointgroup elements leave $\mathbf{k} = (0, 0)$ invariant, thus the little group of $\mathbf{k} = (0, 0)$ is the full pointgroup. In general this does not hold for other momenta and only a subgroup of PG will be the little group of $\mathbf{k}$. In Fig. 4 we show the $\mathbf{k}$-points of a 6×6 triangular lattice together with its little groups as an example. The K point in the Brillouin zone has a D_3 little group, the M point a D_2 little group. Having discussed the representation theory for (symmorphic) space groups we state that the characters of these representations are just given by

$$\chi_{(\mathbf{k},\rho_{\mathbf{k}})}(\mathbf{t}, p) = \mathrm{e}^{i\mathbf{k}\cdot\mathbf{t}}\chi_{\rho_{\mathbf{k}}}(p) \tag{18}$$

where $\mathbf{t} \in \mathcal{T}$, $p \in \mathrm{PG}$ and $\chi_{\rho_{\mathbf{k}}}$ is the character of the representation $\rho_{\mathbf{k}}$ of the little group $L_{\mathbf{k}}$.

3.2 Predicting irreducible representations in spontaneous symmetry breaking

Spontaneous symmetry breaking at $T = 0$ occurs when the groundstate $|\psi_{\mathrm{GS}}\rangle$ of H in the thermodynamic limit is not invariant under the full symmetry group $\mathcal{G}$ of H. We will call a specific groundstate $|\psi_{\mathrm{GS}}\rangle$ a *prototypical state* and the *groundstate manifold* is defined by

$$V_{\mathrm{GS}} = \mathrm{span}\left\{|\psi^i_{\mathrm{GS}}\rangle\right\}, \tag{19}$$

where $|\psi^i_{\text{GS}}\rangle$ is the set of degenerate groundstates in the thermodynamic limit. This groundstate manifold space can be finite or infinite dimensional depending on the situation. For breaking a discrete finite symmetry, such as in the example given in section 4.1.2, this state will be finite dimensional, for breaking continuous $SO(3)$ spin rotational symmetry[6] as in section 4.2 this groundstate manifold is infinite dimensional in the thermodynamic limit. For every symmetry $g \in \mathcal{G}$ we denote by O_g the symmetry operator acting on the Hilbert space. The groundstate manifold becomes degenerate in the thermodynamic limit and we want to calculate the quantum numbers of the eigenstates in this manifold. Another way of saying this is that we want to compute the irreducible representations of $\mathcal{G}$ to which the eigenstates belong. For this we look at the action Γ of the symmetry group $\mathcal{G}$ on V_{GS} defined by

$$\Gamma : \mathcal{G} \to \text{Aut}(V_{\text{GS}}) \tag{20}$$

$$g \mapsto \left(\langle\psi^i_{\text{GS}}|O_g|\psi^j_{\text{GS}}\rangle\right)_{i,j} . \tag{21}$$

This is a representation of $\mathcal{G}$ on V_{GS}, so every group element $g \in \mathcal{G}$ is mapped to an invertible matrix on V_{GS}. In general this representation is reducible and can be decomposed into a direct sum of irreducible representations

$$\Gamma = \bigoplus_\rho n_\rho \rho \,. \tag{22}$$

These irreducible representations ρ are now the quantum numbers of the eigenstates in the groundstate manifold and n_ρ are their respective multiplicities (or degeneracies). Therefore these irreps constitute the TOS for spontaneous symmetry breaking [2]. To compute the multiplicities we can use a central result from representation theory, the *character formula*

$$n_\rho = \frac{1}{|\mathcal{G}|} \sum_{g\in\mathcal{G}} \overline{\chi_\rho(g)}\ \text{Tr}(\Gamma(g)) \,, \tag{23}$$

where $\chi_\rho(g)$ is the character of the representation ρ and $\text{Tr}(\Gamma(g))$ denotes the trace over the representation matrix $\Gamma(g)$ as defined in Eq. (20). Often we have the case that

$$\langle\psi_{\text{GS}}|O_g|\psi'_{\text{GS}}\rangle = \begin{cases} 1 & \text{if } O_g\,|\psi'_{\text{GS}}\rangle = |\psi_{\text{GS}}\rangle \\ 0 & \text{otherwise} \end{cases} \tag{24}$$

With this we can simplify Eq. (23) to what we call the *character-stabilizer formula*

$$n_\rho = \frac{1}{|\text{Stab}(|\psi_{\text{GS}}\rangle)|} \sum_{g\in\text{Stab}(|\psi_{\text{GS}}\rangle)} \chi_\rho(g) \tag{25}$$

where

$$\text{Stab}(|\psi_{\text{GS}}\rangle) \equiv \{g \in \mathcal{G} :\ O_g\,|\psi_{\text{GS}}\rangle = |\psi_{\text{GS}}\rangle\} \tag{26}$$

is the stabilizer of a prototypical state $|\psi_{\text{GS}}\rangle$. We see that for applying the character-stabilizer formula in Eq. (25) only two ingredients are needed:

[6] The actual symmetry group of Heisenberg antiferromagnets is usually $SU(2)$. For simplicity we only consider the subgroup $SO(3)$ in these notes which yields the same predictions for the case of sublattices with even number of sites (corresponding to integer total sublattice spin).

- the stabilizer Stab($|\psi_{\text{GS}}\rangle$) of a prototypical state $|\psi_{\text{GS}}\rangle$ in the groundstate manifold
- the characters of the irreducible representations of the symmetry group $\mathcal{G}$

We want to remark that in the case of $\mathcal{G} = \mathcal{D} \times \mathcal{C}$ where $\mathcal{D}$ is a discrete symmetry group, such as the spacegroup of a lattice, and $\mathcal{C}$ is a continuous symmetry group, such as $SO(3)$ rotations for Heisenberg spins, Eqs. (23) and (25) include integrals over Lie groups additionally to the sum over the elements of the discrete symmetry group $\mathcal{D}$. Furthermore, also the characters for Lie groups like $SO(3)$ are known. For an element $R \in SO(3)$ the irreducible representations are labeled by the spin S and its characters are given by

$$\chi_s(R) = \frac{\sin\left[(S+\frac{1}{2})\varphi\right]}{\sin(\varphi/2)}\,, \tag{27}$$

where $\varphi \in [0, 2\pi]$ is the angle of rotation of the spin rotation R. We work out several examples for this case in section 4.2 and compare the results to actual numerical data from Exact Diagonalization.

4 Examples

4.1 Discrete symmetry breaking

In this section we want to apply the formalism of section 3 to systems, where only a discrete symmetry group is spontaneously broken and not a continuous one. In this case, the groundstate of the system in the thermodynamic limit is described by a superposition of a finite number of degenerate eigenstates with different quantum numbers. On finite-size systems, however, the symmetry cannot be broken spontaneously and a unique groundstate will be found. The other states constituting the degenerate eigenspace in the thermodynamic limit exhibit a finite-size energy gap which is exponentially small in the system size N, $\Delta \propto \mathrm{e}^{-N/\xi}$. The quantum numbers of these quasi-degenerate sets of eigenstates are defined by the symmetry-broken state in the thermodynamic limit.

4.1.1 Introduction to valence-bond solids

In section 2 we have seen that the classically ordered Néel state is a candidate to describe the groundstate of the antiferromagnetic Heisenberg model Eq. (1) with $J > 0$ in the thermodynamic limit on a bipartite lattice. The energy expectation value of this state on each bond is $e_{\text{Néel}} = -J/4$.
The state which minimizes the energy of a single bond is, however, a singlet state $|S = 0\rangle$ formed by the two spins on the bond with energy $e_{\text{VB}} = -3J/4$, called a valence bond (VB) or dimer. A valence bond covering of an N-site lattice can then be described by a tensor product of $N/2$ VBs, where each site belongs to exactly one VB.[7] Another possible candidate for the

[7] The set of all possible valence bond coverings with arbitrary length spans the full $S_{\text{tot}} = 0$ sector of the models Hilbert space and is overcomplete [13, 14].

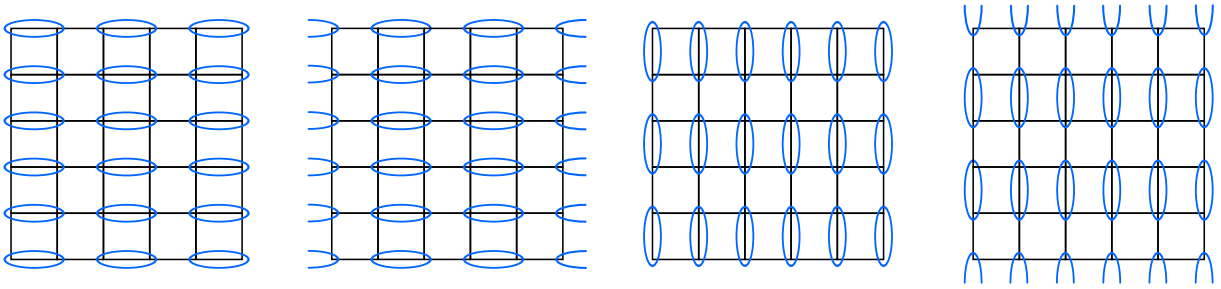

Fig. 2: *The four columnar VBS coverings of a square lattice. Valence bonds (spin singlets) are indicated by blue ellipses.*

thermodynamic groundstate of Eq. (1) is then a superposition of all possible VB coverings with nearest neighbor VBs. Such states do not break the $SU(2)$ spin-rotational symmetry as $S_{\text{tot}} = 0$ and are in general not eigenstates of the Hamiltonian: Acting with the operator $\mathbf{S}_i \cdot \mathbf{S}_j$ between sites i and j belonging to two different VBs changes the VB configuration.

This classical groundstate manifold is highly degenerate. As the VB coverings are in general not eigenstates of the Hamiltonian, they encounter quantum fluctuations. The energy corrections due to these fluctuations are usually not equivalent for different coverings, although the bare energies are identical. The VB coverings with the largest energy gain are selected by the fluctuations as the true groundstate configurations. If this *order-by-disorder* mechanism [15,16] selects regular patterns of VB coverings, the discrete lattice symmetries are spontaneously broken in the thermodynamic limit, and a *valence bond solid* (VBS) is formed. Fig. 2 and Fig. 3 show two different VBS states on the square lattice. VBSs show no long-range spin order, but long-range dimer-correlations $\langle(\mathbf{S}_a \cdot \mathbf{S}_{a'})(\mathbf{S}_b \cdot \mathbf{S}_{b'})\rangle$ where a, a' and b, b' label sites on individual dimers. In section 4.1.2 we will see how different VBS states can be identified and distinguished by the quantum numbers of the quasi-degenerate groundstate manifold on finite-size systems.

The groundstate of the Heisenberg model Eq. (1) on the square lattice is not a VBS but a Néel state, which has already on the classical level a lower variational energy. Nevertheless, several models in 1- and 2-D are known which feature VBS groundstates [17–21]. Interestingly, in [22] a model was proposed, which shows a direct continuous quantum phase transition between a Néel state and a VBS. This transition exhibits very exotic, non-classical behavior and is called *deconfined quantum critical point* [23].

4.1.2 Identification of VBSs from finite-size spectra

Columnar valence-bond solid A columnar VBS (cVBS) on a square lattice is shown in Fig. 2. Four equivalent states can be found, indicating that there will be a four-fold quasi-degenerate groundstate manifold. A cVBS obviously breaks the translational and point-group symmetries of an isotropic $SU(2)$-invariant Hamiltonian on the lattice spontaneously but not the continuous spin symmetry group.

In the following we use Eq. (25) to compute the symmetry sectors of the groundstate manifold.

C_4	1	C_4	C_2	$(C_4)^3$
A	$+1$	$+1$	$+1$	$+1$
B	$+1$	-1	$+1$	-1
E_a	$+1$	$+i$	-1	$-i$
E_b	$+1$	$-i$	-1	$+i$

Table 1: *Character table for pointgroup* C_4.

The discrete symmetry group is

$$\mathcal{G} = \mathcal{D} = \mathcal{T} \times \mathrm{PG} \tag{28}$$

where $\mathcal{T} = \mathbb{Z}_2 \times \mathbb{Z}_2 = \{1, t_x, t_y, t_x t_y\}$ are the non-trivial lattice translations with translation vectors

$$\mathbf{t}_1 = (0,0), \quad \mathbf{t}_x = (1,0), \quad \mathbf{t}_y = (0,1), \quad \mathbf{t}_{xy} = (1,1) \tag{29}$$

and $\mathrm{PG} = \mathrm{C}_4$ denotes the point-group of lattice rotations.[8] To compute the groundstate symmetry sectors we do not need to consider the full symmetry group $\mathcal{G}$ but only the stabilizer $\mathrm{Stab}(|\Psi_{cVBS}\rangle)$, leaving one of the states in Fig. 2 unchanged. Without loss of generality we choose the first covering as prototype $|\Psi_{cVBS}\rangle$. The stabilizer is given by

$$\mathrm{Stab}(|\Psi_{cVBS}\rangle) = \{1 \times 1\} \cup \{1 \times C_2\} \cup \{t_y \times 1\} \cup \{t_y \times C_2\} \tag{30}$$

where C_2 denotes the rotation about an angle π around the center of a plaquette.
The irreducible representations (irreps) of the group of lattice translations $\mathcal{T}$ can be labelled by the allowed momenta $\mathbf{k}$

$$\mathbf{k} \in \mathrm{Irreps}(\mathcal{T}) = \{(0,0), (\pi,0), (0,\pi), (\pi,\pi)\}, \tag{31}$$

and the corresponding characters for an element $t \in \mathcal{T}$ are

$$\chi_{\mathbf{k}}(t) = \mathrm{e}^{i\mathbf{k}\cdot\mathbf{t}}. \tag{32}$$

The irreps (usually called A, B and E) and characters for the point-group C_4 are given in Tab. 1. Using Eq. (25) we can now reduce the representation induced by the state $|\Psi_{cVBS}\rangle$ to irreducible representations to get the quantum numbers of the quasi-degenerate groundstate manifold. Let us explicitly consider $n_{(\pi,0)A/B}$ as an example:

$$n_{(\pi,0)A} = \frac{1}{|\mathrm{Stab}(|\Psi_{cVBS}\rangle)|} \sum_{d \in \mathrm{Stab}(|\Psi_{cVBS}\rangle)} \chi_A(d)\, \chi_{\mathbf{k}=(\pi,0)}(d) \tag{33}$$

$$= \frac{1}{4}\left[1\, e^{i\mathbf{k}\cdot(0,0)} + 1\, e^{i\mathbf{k}\cdot(0,0)} + 1\, e^{i\mathbf{k}\cdot(0,1)} + 1\, e^{i\mathbf{k}\cdot(0,1)}\right] = 1 \tag{34}$$

$$n_{(\pi,0)B} = \frac{1}{|\mathrm{Stab}(|\Psi_{cVBS}\rangle)|} \sum_{d \in \mathrm{Stab}(|\Psi_{cVBS}\rangle)} \chi_B(d)\, \chi_{\mathbf{k}=(\pi,0)}(d) \tag{35}$$

$$= \frac{1}{4}\left[1\, e^{i\mathbf{k}\cdot(0,0)} + (-1)\, e^{i\mathbf{k}\cdot(0,0)} + 1\, e^{i\mathbf{k}\cdot(0,1)} + (-1)\, e^{i\mathbf{k}\cdot(0,1)}\right] = 0 \tag{36}$$

[8] The dihedral group D_4 is also a symmetry group of the model. For the sake of simplicity we decided to only consider the subgroup C_4 in this section.

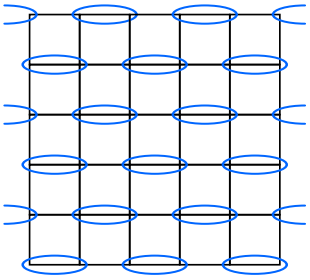

Fig. 3: *One of the four identical staggered VBS coverings on the square lattice.*

Eventually, the cVBS covering will be described by a four-fold quasi-degenerate groundstate manifold with the following quantum numbers

$$\chi(|\Psi_{cVBS}\rangle) = (0,0)\mathrm{A} \oplus (0,0)\mathrm{B} \oplus (\pi,0)\mathrm{A} \oplus (0,\pi)\mathrm{A}\,. \tag{37}$$

VBS states are a superposition of spin singlets on the lattice, therefore the spin quantum number for all levels in the groundstate manifold must be trivial, $S_{\text{tot}} = 0$.

Staggered valence-bond solid The columnar VBS is not the only regular dimer covering of the square lattice. Another possible regular covering is the staggered VBS (sVBS), where again four equivalent configurations span the groundstate manifold. One of these configurations is shown in Fig. 3.

Obviously, also the sVBS spontaneously breaks the translational and point-group symmetries of an isotropic Hamiltonian, but not the spin-rotational symmetry. Following the same steps as before we can compute the quantum numbers of the four quasi-degenerate groundstates for the sVBS. The stabilizer turns out to be different to the case of the cVBS and thus also the decomposition into irreps yields a different result:

$$\chi(|\Psi_{sVBS}\rangle) = (0,0)\mathrm{A} \oplus (0,0)\mathrm{B} \oplus (\pi,\pi)\mathrm{E}_a \oplus (\pi,\pi)\mathrm{E}_b. \tag{38}$$

Tab. 2 shows a comparison of the irreducible representations in the groundstate manifold of the cVBS and sVBS states.

By a careful analysis of the quasi-degenerate states and their quantum numbers on finite systems it is thus possible to identify and distinguish different VBS phases which spontaneously break the translational and point-group symmetries in the thermodynamic limit.

Irreps	cVBS	sVBS
$(0\,,\,0)A$	1	1
$(0\,,\,0)B$	1	1
$(\pi,\,0)A$	1	0
$(0\,,\pi)A$	1	0
$(\pi,\pi)E_a$	0	1
$(\pi,\pi)E_b$	0	1

Table 2: *Multiplicities of the irreducible representations in the four-fold degenerate groundstate manifolds of the columnar and staggered VBS on a square lattice.*

4.2 Continuous symmetry breaking

In this section we give several examples of systems breaking continuous $SO(3)$ symmetry. We discuss the introductory example of the Heisenberg antiferromagnet, calculate the irreps in the TOS and compare this to actual energy spectra from Exact Diagonalization on a finite lattice in section 4.2.1. Next we discuss three magnetic orders on the triangular lattice and a model where all of these are stabilized. We show again results from Exact Diagonalizations and compare the representations in these spectra to the predictions from TOS analysis in section 4.2.2. Finally we introduce quadrupolar order and show that also this kind of symmetry breaking can be analyzed using the TOS technique in section 4.2.3.

4.2.1 Heisenberg antiferromagnet on square lattice

We now give a first example how the TOS method can be applied to predict the structure of the tower of states for magnetically ordered phases. We look at the Néel state of the antiferromagnet on the bipartite square lattice with sublattices A and B. A prototypical state in the groundstate manifold is given by

$$|\psi\rangle = |\uparrow\downarrow\uparrow\downarrow\cdots\rangle \tag{39}$$

where all spins point up on sublattice A and down on sublattice B. The symmetry group $\mathcal{G} = \mathcal{D} \times \mathcal{C}$ of the model we consider is a product between discrete translational symmetry $\mathcal{D} = \mathbb{Z}_2 \times \mathbb{Z}_2 = \{1, t_x, t_y, t_{xy}\}$ and spin rotational symmetry $\mathcal{C} = SO(3)$. We remark that we restrict our translational symmetry group to $\mathcal{D} = \mathbb{Z}_2 \times \mathbb{Z}_2$ instead of $\mathcal{D}' = \mathbb{Z} \times \mathbb{Z}$ because the Néel state transforms trivially under two-site translations $(t_x)^2, (t_y)^2$. Thus, only the representations of $\mathcal{D}'$ trivial under two-site translations are relevant; these are exactly the representations of $\mathcal{D}$. Put differently we only have to consider the translations in the unitcell of the magnetic structure which in the present case can be chosen as a 2-by-2 cell. Furthermore, we will for now neglect pointgroup symmetries like rotations and reflections of the lattice to simplify our calculations. At the end of this section we give results where also these symmetry elements are incorporated. The groundstate manifold V_{GS} we consider are the states related to $|\psi\rangle$ by an element of the symmetry group $\mathcal{G}$, i.e.,

$$V_{\text{GS}} = \{O_g\,|\psi\rangle\,;\ g \in \mathcal{G}\}\ . \tag{40}$$

The symmetry elements in $\mathcal{G}$ that leave our prototypical state $|\psi\rangle$ invariant are given by two sets of elements:

- No translation in real space or a diagonal t_{xy} translation together with a spin rotation $R_z(\alpha)$ around the z-axis with an arbitrary angle α.
- Translation by one site, t_x or t_y, followed by a rotation $R_a(\pi)$ of 180° around an axis $a \perp z$ perpendicular to the z-axis.

So the stabilizer of our prototype state $|\psi\rangle$ is given by

$$\text{Stab}(|\psi\rangle) = \{1 \times R_z(\alpha)\} \cup \{t_{xy} \times R_z(\alpha)\} \cup \{t_x \times R_a(\pi)\} \cup \{t_y \times R_a(\pi)\}\,. \tag{41}$$

The representations of the discrete symmetry group can be simply labeled by four momenta $\mathbf{k} \in \{(0,0),\ (0,\pi),\ (\pi,0),\ (\pi,\pi)\}$ with corresponding characters

$$\chi_{\mathbf{k}}(t) = \mathrm{e}^{i\mathbf{k}\cdot\mathbf{t}}.$$

The continuous symmetry group is the Lie group $SO(3)$. Its representations are labeled by the total spin S and the character of the spin-S representation is given by

$$\chi_S(R) = \frac{\sin\left[(S+\frac{1}{2})\varphi\right]}{\sin(\varphi/2)}$$

where $\varphi \in [0, 2\pi]$ is the angle of rotation of the element $R \in SO(3)$. We see that spin rotations with different axes but same rotational angle give rise to the same character. The representations of the total symmetry group $\mathcal{G} = \mathcal{D} \times \mathcal{C}$ are now just the product representations of $\mathcal{D}$ and $\mathcal{C}$, therefore also the characters of representations of $\mathcal{G}$ are the product of characters of $\mathcal{D}$ and $\mathcal{C}$. We label these representations by $(\mathbf{k}, S)$ where $\mathbf{k}$ denotes the lattice momentum and S the total spin. We now apply the character-stabilizer formula, Eq. (25), to derive the multiplicities of the representations $(\mathbf{k}, S)$ in the groundstate manifold. In the case of the square antiferromagnet this yields

$$n_{(\mathbf{k},S)} = e^{i\mathbf{k}\cdot 0}\frac{1}{4\,|R_z(\alpha)|}\int_0^{2\pi} d\alpha\,\chi_S(R_z(\alpha)) + e^{i\mathbf{k}\cdot(\mathbf{e}_x+\mathbf{e}_y)}\frac{1}{4\,|R_z(\alpha)|}\int_0^{2\pi} d\alpha\,\chi_S(R_z(\alpha)) \tag{42}$$

$$+\, e^{i\mathbf{k}\cdot\mathbf{e}_x}\frac{1}{4\,|R_a(\pi)|}\int_0^{2\pi} d\alpha\,\chi_S(R_a(\pi)) + e^{i\mathbf{k}\cdot\mathbf{e}_y}\frac{1}{4\,|R_a(\pi)|}\int_0^{2\pi} d\alpha\,\chi_S(R_a(\pi))\,. \tag{43}$$

We compute

$$|R_z(\alpha)| = |R_a(\pi)| = \int_0^{2\pi} d\varphi = 2\pi\,,$$

$$\frac{1}{2\pi}\int_0^{2\pi} d\alpha\,\chi_S(R_z(\alpha)) = \frac{1}{2\pi}\int_0^{2\pi} d\alpha\,\frac{\sin\left[(S+\frac{1}{2})\alpha\right]}{\sin(\alpha/2)} = \frac{1}{2\pi}\int_0^{2\pi} d\varphi\sum_{l=-S}^{S} e^{il\varphi} = 1\,, \tag{44}$$

and

$$\frac{1}{2\pi}\int_0^{2\pi} d\varphi\,\chi_S(R_a(\pi)) = \frac{1}{2\pi}\int_0^{2\pi} d\varphi\,\frac{\sin\left[(S+\frac{1}{2})\pi\right]}{\sin(\pi/2)} = (-1)^S. \tag{45}$$

Putting this together gives the final result for the multiplicities of the representations in the tower

S	$\Gamma.A1$	$M.A1$
0	1	0
1	0	1
2	1	0
3	0	1

Table 3: *Multiplicities of irreducible representations in the TOS for the Néel antiferromagnet on a square lattice.*

of states

$$n_{((0,0),S)} = \frac{1}{4}\left(1\cdot 1 + 1\cdot 1 + 1\cdot(-1)^S + 1\cdot(-1)^S\right) = \begin{cases} 1 \text{ if } S \text{ even} \\ 0 \text{ if } S \text{ odd} \end{cases} \tag{46}$$

$$n_{((\pi,\pi),S)} = \frac{1}{4}\left(1\cdot 1 + 1\cdot 1 - 1\cdot(-1)^S - 1\cdot(-1)^S\right) = \begin{cases} 0 \text{ if } S \text{ even} \\ 1 \text{ if } S \text{ odd} \end{cases} \tag{47}$$

$$n_{((0,\pi),S)} = \frac{1}{4}\left(1\cdot 1 - 1\cdot 1 + 1\cdot(-1)^S - 1\cdot(-1)^S\right) = 0 \tag{48}$$

$$n_{((\pi,0),S)} = \frac{1}{4}\left(1\cdot 1 - 1\cdot 1 - 1\cdot(-1)^S + 1\cdot(-1)^S\right) = 0 \tag{49}$$

Tab. 3 lists the computed multiplicities of the irreducible representations where additionally the D_4 point group was considered in the symmetry analysis. Comparing this to Fig. 1 we observe that these are exactly the irreducible representations (momenta and point group irreps) and multiplicities observed in the tower of states for the Heisenberg model on the square lattice.

4.2.2 Magnetic order on the triangular lattice

On the triangular lattice several magnetic orders can be stabilized. The Heisenberg nearest neighbor model has been shown to have a 120° Néel ordered groundstate where spins on neighboring sites align in an angle of 120° [24, 25]. Upon adding further second nearest neighbor interactions J_2 to the Heisenberg nearest-neighbor model with interaction strength J_1 it was shown that the groundstate exhibits *stripy order* for $J_2/J_1 \gtrsim 0.18$ [26]. Here spins are aligned ferromagnetically along one direction of the triangular lattice and antiferromagnetically along the other two. Interestingly, it was shown that there is a phase between these two magnetic orders whose exact nature is unclear until today. Several articles propose that in this region an exotic *quantum spin liquid* is stabilized [27–30]. In a recent proposal two of the authors established an approximate phase diagram of an extended Heisenberg model with further scalar chirality interactions $J_\chi \mathbf{S}_i \cdot (\mathbf{S}_j \times \mathbf{S}_k)$ [31] on elementary triangles. Thus, the Hamiltonian of the system is given by

$$\mathcal{H} = J_1 \sum_{\langle i,j\rangle} \mathbf{S}_i \cdot \mathbf{S}_j + J_2 \sum_{\langle\langle i,j\rangle\rangle} \mathbf{S}_i \cdot \mathbf{S}_j + J_\chi \sum_{i,j,k\in\triangle} \mathbf{S}_i \cdot (\mathbf{S}_j \times \mathbf{S}_k). \tag{50}$$

Amongst the already known 120° Néel and stripy phases an exotic *Chiral Spin Liquid* and a magnetic *tetrahedrally ordered* phase were found. Here we will only discuss the magnetic

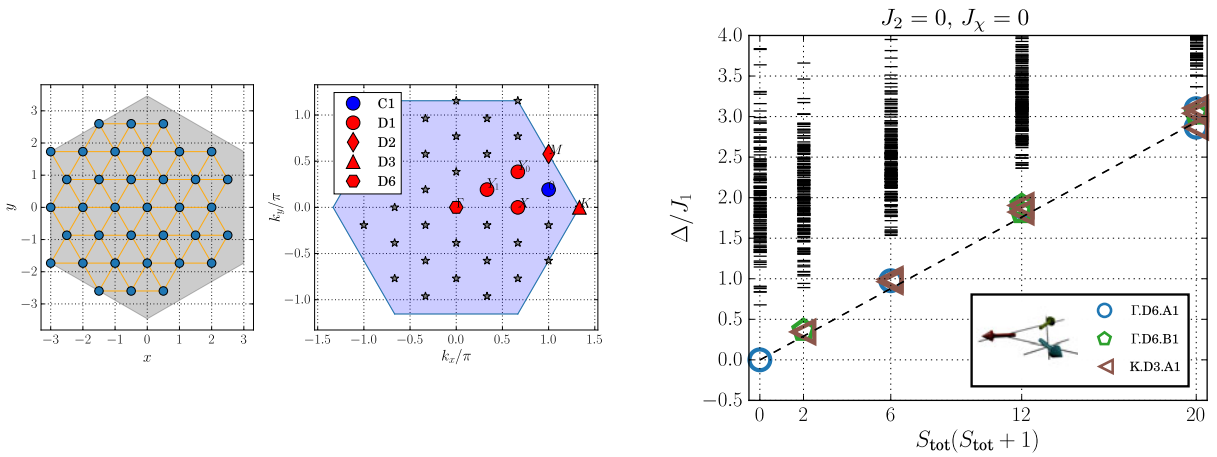

Fig. 4: *(Left): Simulation cluster for the Exact Diagonalization calculations. (Center): Brillouin zone of the triangular lattice with the momenta which can be resolved with this choice of the simulation cluster. Different symbols denote the little groups of the corresponding momentum. (Right): TOS for the* $120°$ *Néel order on the triangular lattice. The symmetry sectors and multiplicities fulfill the predictions from the symmetry analysis (See Tab. 5). One should note, that the multiplicities grow with* S_{tot} *for non-collinear states.*

orders appearing in this model. The non-coplanar tetrahedral order has a four-site unitcell where four spins align such that they span a regular tetrahedron. In this chapter we show the tower of states for the three magnetic orders in this model.

First of all, Fig. 4 shows the simulation cluster used for the Exact Diagonalization calculations in [31]. We chose a $N = 36 = 6 \times 6$ sample with periodic boundary conditions. This sample allows to resolve the momenta Γ, K and M, amongst several others in the Brillouin zone. The K and M momenta are the ordering vectors for the $120°$, stripy and tetrahedral order. Furthermore this sample features full six-fold rotational as well as reflection symmetries (the latter only in the absence of the chiral term). Its pointgroup is therefore given by the dihedral group of order 12, D_6. The little groups of the individual $\mathbf{k}$ vectors are also shown in Fig. 4. For our tower of states analysis we now want to consider the discrete symmetry group

$$\mathcal{D} = \mathcal{T} \times \mathrm{D}_6 \tag{51}$$

where $\mathcal{T}$ is the translational group of the magnetic unitcell. The full set of irreducible representations of this symmetry group is given by the set $(\mathbf{k} \otimes \rho_{\mathbf{k}})$ where $\mathbf{k}$ denotes the momentum and $\rho_{\mathbf{k}}$ is an irrep of the little group associated to $\mathbf{k}$. The points Γ, K and M give rise to the little groups D_6, D_3 and D_2 (the dihedral groups of order 12, 8, and 4), respectively. For the stripy and tetrahedral order we can choose a 2×2 magnetic unitcell, and a 3×3 unitcell for the $120°$ Néel order. The spin rotational symmetry lets us again consider the continuous symmetry group

$$\mathcal{C} = SO(3). \tag{52}$$

We can therefore label the full set of irreps as $(\mathbf{k}, \rho_{\mathbf{k}}, S)$ where S denotes the total spin S representation of $SO(3)$. Similarly to the previous chapter we now want to apply the character-stabilizer formula, Eq. (25), to determine the multiplicities of the representations forming the

D_6	1	$2C_6$	$2C_3$	C_2	$3\sigma_d$	$3\sigma_v$
A_1	1	1	1	1	1	1
A_2	1	1	1	1	-1	-1
B_1	1	-1	1	-1	1	-1
B_2	1	-1	1	-1	-1	1
E_1	2	1	-1	-2	0	0
E_2	2	-1	-1	2	0	0

Table 4: *Character table for pointgroup D_6.*

	120° Néel			stripy order			tetrahedral order			
S	Γ.A1	Γ.B1	K.A1	Γ.A1	Γ.E2	M.A	Γ.A	Γ.E2a	Γ.E2b	M.A
0	1	0	0	1	1	0	1	0	0	0
1	0	1	1	0	0	1	0	0	0	1
2	1	0	2	1	1	0	0	1	1	1
3	1	2	2	0	0	1	1	0	0	2

Table 5: *Multiplicities of irreducible representations in the Anderson tower of states for the three magnetic orders on the triangular lattice defined in the main text.*

tower of states. The characters of the irreps $(\mathbf{k}, \rho_{\mathbf{k}}, S)$ are given by

$$\chi_{(\mathbf{k},\rho_{\mathbf{k}},S)}(t,p,R) = \mathrm{e}^{i\mathbf{k}\cdot\mathbf{t}}\chi_{\rho_{\mathbf{k}}}(p)\frac{\sin\left[(S+\frac{1}{2})\varphi\right]}{\sin(\varphi/2)}\,, \tag{53}$$

where again $\varphi \in [0, 2\pi]$ is the angle of rotation of the spin rotation R. The characters of the pointgroup D_6 are given in Tab. 4. We skip the exact calculations which follow closely the calculations performed in the previous chapter, although now also pointgroup symmetries are additionally taken into account. The results are summarized in Tab. 5. We remark that the tetrahedral order is stabilized only for $J_\chi \neq 0$ where the model in Eq. (50) does not have reflection symmetry any more since the term $\mathbf{S}_i \cdot (\mathbf{S}_j \times \mathbf{S}_k)$ does not preserve this symmetry. Therefore we used only the pointgroup C_6 of six-fold rotation in the calculations of the tower of states for this order.

If we compare these results to Figs. 4 and 5 we see that these are exactly the representations appearing in the TOS from Exact Diagonalization for certain parameter values J_2 and J_χ. This is a strong evidence that indeed $SO(3)$ symmetry is broken in these models in a way described by the $120°$ Néel, stripy, and tetrahedral magnetic prototype states.

4.2.3 Quadrupolar order

All examples of continuous symmetry breaking we have discussed so far spontaneously broke $SO(3)$ symmetry but exhibited a magnetic moment. In the following we will show examples of phases that do not exhibit any magnetic moment but break spin-rotational symmetry anyway and discuss the influences on the tower of states. We will only discuss quadrupolar phases in $S = 1$ models here, a broader introduction to nematic and multipolar phases can be found in [32].

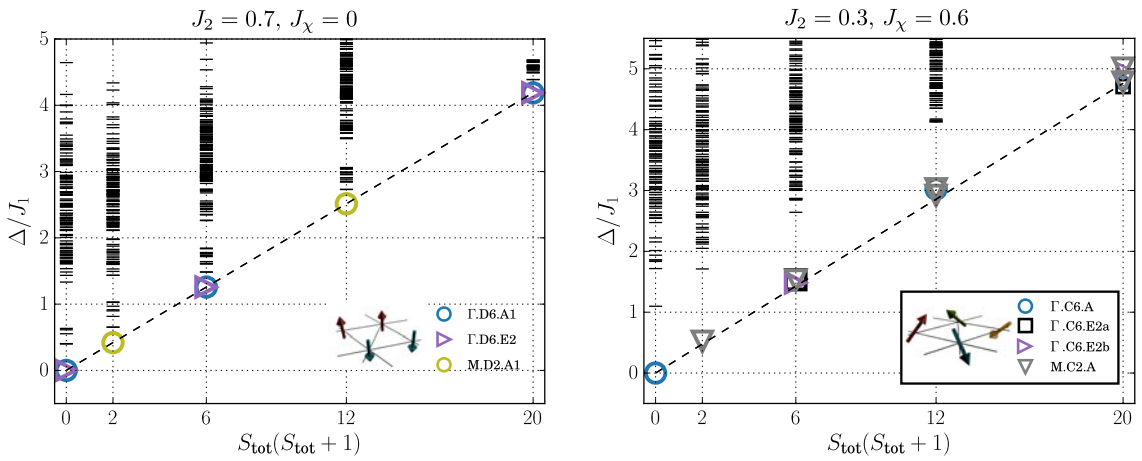

Fig. 5: *(Left): TOS for the stripy phase on the triangular lattice. The multiplicities for each even/odd S_{tot} are constant for collinear phases. (Right): TOS for the tetrahedral order on the triangular lattice.*

Quadrupolar states We denote the basis states for a single spin $S = 1$ with $S^z = 1, -1, 0$ as $|1\rangle, |\bar{1}\rangle, |0\rangle$. In contrast to the usual $S = 1/2$ case not each basis state can be obtained by a SU(2) rotation of any other basis state. The state $|0\rangle$, for example cannot be obtained by a rotation of $|1\rangle$ or $|\bar{1}\rangle$ as it has no orientation in spin-space at all, $\langle 0|S^\alpha|0\rangle = 0$ [32]. The state $|0\rangle$ can, however, be described as a spin fluctuating in the x-y plane in spin space as

$$\langle 0|(S^x)^2|0\rangle = \langle 0|(S^y)^2|0\rangle = 1, \quad \langle 0|(S^z)^2|0\rangle = 0. \tag{54}$$

We can thus assign a director along the z-axis to this state. $SU(2)$ rotations will change the director of such a state, but not its property of being non-magnetic. These states can be detected by utilizing the quadrupolar operator [32]

$$Q^{\alpha\beta} = S^\alpha S^\beta + S^\beta S^\alpha - \frac{2}{3} S(S+1)\delta_{\alpha\beta} \tag{55}$$

therefore they are identified as quadrupolar states.

To study the possible formation of an ordered quadrupolar phase on a lattice, where the directors of the quadrupoles on each lattice site follow a regular pattern, we consider the *bilinear-biquadratic* model with Hamiltonian

$$H = \sum_{\langle i,j\rangle} J\ \mathbf{S}_i \cdot \mathbf{S}_j + Q\left(\mathbf{S}_i \cdot \mathbf{S}_j\right)^2 \tag{56}$$

and $S = 1$. The second term in Eq. (56) can be rewritten in terms of the elements of $Q^{\alpha\beta}$ which can be rearranged into a 5-component vector $\mathbf{Q}$ such that

$$\mathbf{Q}_i \cdot \mathbf{Q}_j = 2(\mathbf{S}_i \cdot \mathbf{S}_j)^2 + \mathbf{S}_i \cdot \mathbf{S}_j - \frac{4}{3}. \tag{57}$$

The expectation value of Eq. (57) for quadrupolar states on sites i and j can be given in terms of their directors $\mathbf{d}_{i,j}$ [32]

$$\langle \mathbf{Q}_i \cdot \mathbf{Q}_j \rangle = 2\left(\mathbf{d}_i \cdot \mathbf{d}_j\right)^2 - \frac{2}{3}. \tag{58}$$

Therefore, the second term in Eq. (56) favors regular patterns of the directors of quadrupoles. When such states are formed, they spontaneously break the $SU(2)$ symmetry without exhibiting any kind of magnetic moment. The first term in Eq. (56), on the other hand, favors spin ordering as we have already discussed in previous sections.
The phase diagram of Eq. (56) on the triangular lattice shows extended ferromagnetic, antiferromagnetic ($120°$), ferroquadrupolar (FQ), and antiferroquadrupolar (AFQ) ordered phases. In the FQ phase quadrupoles on each lattice site are formed with all directors pointing in a single direction, whereas the directors form a $120°$ structure in the AFQ phase. In the following, we will see that the FQ and AFQ phases can be identified and distinguished from the spin ordered phases using a tower-of-states analysis on finite clusters.

TOS for quadrupolar phases The TOS for the FQ and AFQ phases can be expected to show similar behavior as the TOS for magnetically ordered states as both spontaneously break the spin-rotational symmetry. If we identify the symmetry-broken quadrupolar phases with their directors pointing in any direction in spin-space we can perform the symmetry analysis of the TOS levels in a very similar manner as for the spin-ordered systems in the previous sections. There is, however, one important thing to consider: The directors should not be considered to be described with vectors, but with axes; a quadrupole is recovered (up to a phase) by rotations about an angle π around any axis a in the x-y-plane:

$$\mathrm{e}^{i\pi S^a} \left|0\right\rangle = -\left|0\right\rangle . \tag{59}$$

Thus, the stabilizer in Eq. (25) is different for quadrupolar phases and the TOS shows a different structure. This property makes it possible to distinguish, e.g., a magnetic $120°$ phase from its quadrupolar counterpart, the AFQ phase, with a TOS analysis.
A prototype for the FQ phase is a product states of quadrupoles with directors in z-direction, $|\Psi\rangle = |0,0,0,\ldots\rangle$. This state does not break any space-group symmetries, so only the trivial irreps of the space group, $\mathbf{k} = \Gamma = (0,0).A1$, will be present in the TOS. The remaining stabilizer of the spin-rotation group is a rotation about the z-axis by an arbitrary angle and a rotation about an arbitrary axis lying in the x-y-plane,

$$\mathrm{Stab}(|\Psi\rangle) = \{R_z(\alpha), R_a(\pi)\}. \tag{60}$$

The multiplicities in the TOS can then be computed as

$$n_S = \frac{1}{2}\left(\frac{1}{|R_z(\alpha)|}\int_0^{2\pi} d\alpha\, \chi_S(R_z(\alpha)) + (-1)^N \frac{1}{|R_a(\pi)|}\int_0^{2\pi} da\, \chi_S(R_a(\pi))\right) \tag{61}$$

$$= \frac{1}{2}\left(1 + (-1)^N(-1)^S\right), \tag{62}$$

where the integrals have already been computed in Eqs. (44) and (45). The system size dependent factor $(-1)^N$ is imposed from Eq. (59). To sum up, the TOS for the FQ phase has single levels for even (odd) S with trivial space-group irreps and no levels for odd (even) S

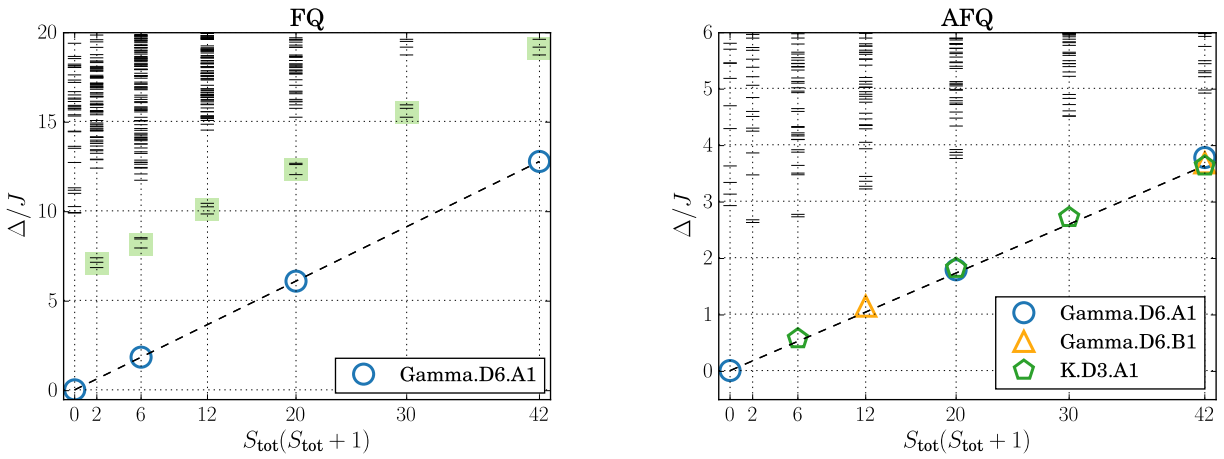

Fig. 6: *Tower of states for the ferroquadrupolar (left) and antiferroquadrupolar (right) states on a triangular lattice with $N = 12$ sites from Exact Diagonalization. The single-magnon branch for the FQ phase is highlighted with green boxes.*

sectors when N is even (odd).[9] The absence of odd (even) S levels is caused by the invariance of quadrupoles under π-rotation and distinguishes the TOS for a FQ phase from a usual ferromagnetic phase. In Fig. 6 the TOS for the model, Eq. (56), in the FQ phase is shown on the left. It shows the expected quantum numbers and multiplicities in the TOS and also an easily identifiable magnon branch below the continuum.

The symmetry analysis for the AFQ phase can be performed in a similar manner and shows a similar structure to the 120°-Néel phase, but again, levels are deleted for the AFQ. In this case, however, not all odd levels are deleted but some levels in both, odd and even, S sectors. Tab. 6 shows the multiplicities of irreps in the TOS of the AFQ model in comparison to the magnetic 120°-Néel state for even N. Fig. 6 shows the simulated TOS for the AFQ phase for the bilinear-biquadratic model Eq. (56). The symmetry sectors and multiplicities agree with the expected ones.

	AFQ			120° Néel		
S	Γ.A1	Γ.B1	K.A1	Γ.A1	Γ.B1	K.A1
0	1	0	0	1	0	0
1	0	0	0	0	1	1
2	0	0	1	1	0	2
3	0	1	0	1	2	2

Table 6: *Irreducible representations and multiplicities for the AFQ phase compared to the magnetic 120°-Néel phase.*

[9] For the simple case of the FQ phase one can also easily calculate the decomposition of a state $|S = 1, m = 0\rangle \otimes |S = 1, m = 0\rangle \otimes \dots$ into states $|S_{tot}, m = 0\rangle$ with the use of Clebsch-Gordan coefficients.

5 Outlook

In the previous sections we have discussed the features of the energy spectrum for states which spontaneously break the spin-rotational symmetry, $SU(2)$, in the thermodynamic limit. We have seen that on finite-size systems the energy spectra of such states exhibit a tower of states (TOS) structure. The tower of states scales as $S_{\text{tot}}(S_{\text{tot}}+1)/N$ and generates the groundstate manifold in the thermodynamic limit $N \to \infty$, which is indispensable to spontaneously break a symmetry. The quantum numbers of the levels in the TOS depend on the particular state which is formed after the symmetry breaking and can be predicted using representation theory.

As a generalization to the $SU(2)$-symmetric Heisenberg model, Eq. (1), one can introduce $SU(n)$ Heisenberg models with $n > 2$. Such models can experimentally be realized by ultracold multicomponent fermions in a optical lattices. When the on-site repulsion is strong enough, the Hamiltonian can be effectively described by an $SU(n)$-symmetric permutation model on the lattice [33]. When the exchange couplings are antiferromagnetic, $SU(n)$ generalized versions of the Néel state might be realized as groundstates, which then spontaneously break the $SU(n)$ symmetry of the Hamiltonian. On finite systems this becomes again manifest in the emergence of a tower of states, where the scaling is found to be proportional to $C_2(n)/N$ [34–37, 33]. $C_2(n)$ denotes the quadratic Casimir operator of $SU(n)$.[10] The symmetry analysis of the levels in the TOS can, in principle, be performed similar to the case of $SO(3)$ discussed in these notes, but the symmetry group and its characters have to be replaced with the more complicated group $SU(n)$.

On the other side, it can be also interesting to study models where the continuous symmetry group is smaller. In real magnetic materials, the isotropic Heisenberg interaction is often accompanied by other interactions which, when they are strong enough, might reduce the symmetry group of spin rotations from $SO(3)$ to $O(2)$; only spin rotations around an axis are a symmetry of the system and can be spontaneously broken in the thermodynamic limit. This symmetry group is also interesting in the field of ultracold gases, as BECs spontaneously break an $O(2)$ symmetry by choosing a phase. Tower of states can also be found in this case and the quantum numbers and multiplicities of the TOS levels can be computed similar to the $SU(2)$ case [12].

We have seen, that the energy spectrum of Hamiltonians on finite lattices may contain a lot of information about the system. One can identify groundstates which will spontaneously break discrete as well as continuous symmetries in the thermodynamic limit and by imposing a classical state as symmetry-broken state one can even predict the quantum numbers and multiplicities of the levels in the tower of states or in the quasi-degenerate groundstate manifold. When we impose an additional interaction to a system with spontaneously broken groundstate, e.g., a magnetic field, it is possible that a *continuous quantum phase transition* (cQPT) from the ordered state to a disordered state appears for some critical ratio of the couplings. Such cQPTs are interesting as they can be described by universal features which do not depend on the details of

[10] For $n = 2$ the quadratic Casimir operator $C_2 = S_{\text{tot}}(S_{\text{tot}}+1)$.

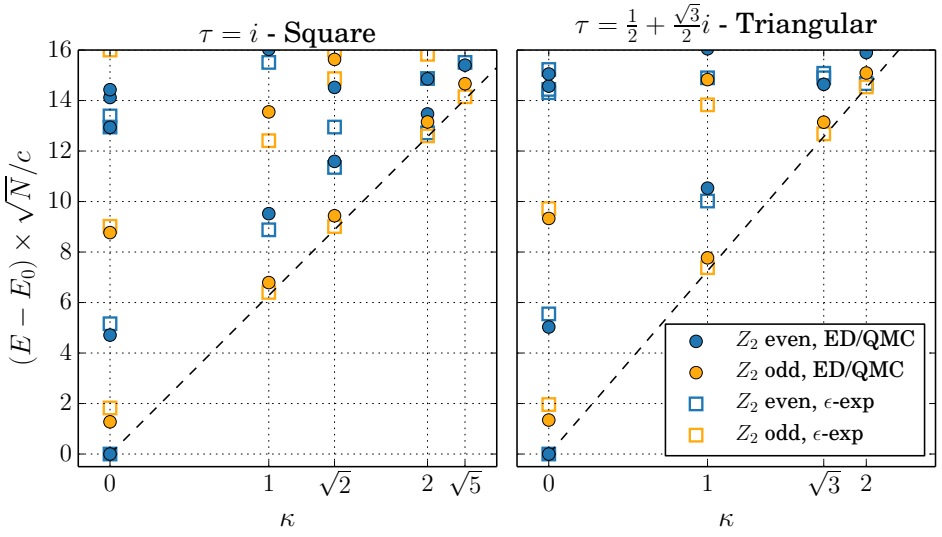

Fig. 7: *Universal torus spectrum for a continuous quantum phase transition in the 3D Ising universality class. Full symbols denote numerical results while empty symbols denote ϵ-expansion results. The dashed line shows a dispersion with the speed of light.*

the model. Interestingly, the energy spectrum on finite systems can even be used to identify and characterize cQPTs. It is given by universal numbers times $1/L$, where $L = \sqrt{N}$ is the linear size of the lattice. The quantum numbers of the energy levels show universal features and are related to the operator content of the underlying *critical field theory*, although the relation between them is not yet fully understand for non-flat geometries, like a torus [38, 39]. The critical spectrum for the transverse-field Ising model on a torus is shown in Fig. 7. It is a fingerprint for the 3D Ising cQPT.

References

[1] P.W. Anderson, Phys. Rev. **86**, 694 (1952)

[2] C. Lhuillier, arXiv:cond-mat pp. 161–190 (2005)

[3] A.M. Läuchli: *Numerical Simulations of Frustrated Systems* (Springer, Heidelberg, 2011), pp. 481–511

[4] A.W. Sandvik, A. Avella, and F. Mancini: in *AIP Conf. Proc.* (2010), Vol. 1297, pp. 135–338

[5] G. Misguich and P. Sindzingre, J. Phys. Condens. Matter **19**, 145202 (2007)

[6] W. Marshall, Proc. R. Soc. A Math. Phys. Eng. Sci. **232**, 48 (1955)

[7] E. Lieb and D. Mattis, Journal of Mathematical Physics **3**, 749 (1962)

[8] A. Auerbach: *Interacting Electrons and Quantum Magnetism* (Springer, New York, 1994)

[9] T.A. Kaplan, W. von der Linden, and P. Horsch, Phys. Rev. B **42**, 4663 (1990)

[10] P. Hasenfratz and F. Niedermayer, Zeitschrift für Phys. B Condens. Matter **92**, 91 (1993)

[11] P. Azaria, B. Delamotte, and D. Mouhanna, Phys. Rev. Lett. **70**, 2483 (1993)

[12] I. Rousochatzakis, A.M. Läuchli, and F. Mila, Phys. Rev. B **77**, 094420 (2008)

[13] S. Liang, B. Doucot, and P.W. Anderson, Phys. Rev. Lett. **61**, 365 (1988)

[14] C. Lhuillier and G. Misguich: In C. Lacroix, P. Mendels, and F. Mila (Eds.): *Introduction to Frustrated Magnetism*, *Springer Series in Solid-State Sciences*, Vol. 164 (Springer, Heidelberg, 2011), pp. 23–41

[15] E. Shender, Sov. Phys. JETP **56**, 178 (1982)

[16] C.L. Henley, Phys. Rev. Lett. **62**, 2056 (1989)

[17] J. Fouet, P. Sindzingre, and C. Lhuillier, Eur. Phys. J. B **20**, 241 (2001)

[18] A. Läuchli, S. Wessel, and M. Sigrist, Phys. Rev. B **66**, 014401 (2002)

[19] A. Läuchli, J.C. Domenge, C. Lhuillier, P. Sindzingre, and M. Troyer, Phys. Rev. Lett. **95**, 137206 (2005)

[20] M. Mambrini, A. Läuchli, D. Poilblanc, and F. Mila, Phys. Rev. B **74**, 144422 (2006)

[21] A. Gellé, A.M. Läuchli, B. Kumar, and F. Mila, Phys. Rev. B **77**, 014419 (2008)

[22] A.W. Sandvik, Phys. Rev. Lett. **98**, 227202 (2007)

[23] T. Senthil, A. Vishwanath, L. Balents, S. Sachdev, and M.P.A. Fisher, Science **303**, 1490 (2004)

[24] T. Jolicoeur, E. Dagotto, E. Gagliano, and S. Bacci, Phys. Rev. B **42**, 4800 (1990)

[25] A. V. Chubukov and T. Jolicoeur, Phys. Rev. B **46**, 11137 (1992)

[26] P. Lecheminant, B. Bernu, C. Lhuillier, and L. Pierre, Phys. Rev. B **52**, 6647 (1995)

[27] Y. Iqbal, W.-J. Hu, R. Thomale, D. Poilblanc, and F. Becca, Phys. Rev. B **93**, 144411 (2016)

[28] R. Kaneko, S. Morita, and M. Imada, J. Phys. Soc. Jpn. **83**, 093707 (2014)

[29] W.-J. Hu, S.-S. Gong, W. Zhu, and D.N. Sheng, Phys. Rev. B **92**, 140403 (2015)

[30] Z. Zhu and S.R. White, Phys. Rev. B **92**, 041105 (2015)

[31] A. Wietek and A.M. Läuchli, ArXiv e-prints (2016)

[32] K. Penc and A.M. Läuchli: *Spin Nematic Phases in Quantum Spin Systems* (Springer Berlin, Heidelberg, 2011), pp. 331–362

[33] P. Nataf and F. Mila, Phys. Rev. Lett. **113**, 127204 (2014)

[34] K. Penc, M. Mambrini, P. Fazekas, and F. Mila, Phys. Rev. B **68**, 012408 (2003)

[35] T. A. Tóth, A.M. Läuchli, F. Mila, and K. Penc, Phys. Rev. Lett. **105**, 265301 (2010)

[36] P. Corboz, A.M. Läuchli, K. Penc, M. Troyer, and F. Mila, Phys. Rev. Lett. **107**, 215301 (2011)

[37] P. Corboz, M. Lajkó, K. Penc, F. Mila, and A.M. Läuchli, Phys. Rev. B **87**, 195113 (2013)

[38] M. Schuler, S. Whitsitt, L.-P. Henry, S. Sachdev, and A.M. Läuchli, arXiv:1603.03042

[39] S. Whitsitt and S. Sachdev, arXiv:1603.05652

9 Introduction to Full Configuration Interaction Quantum Monte Carlo with Applications to the Hubbard model

Ali Alavi
Max-Planck-Institut für Festkörperforschung, Stuttgart
University Chemical Laboratory, Cambridge

Contents

E. Pavarini, E. Koch, J. van den Brink, and G. Sawatzky (eds.)
Quantum Materials: Experiments and Theory
Modeling and Simulation Vol. 6
Forschungszentrum Jülich, 2016, ISBN 978-3-95806-159-0
http://www.cond-mat.de/events/correl16

1 Introduction

The Full Configuration Interaction Quantum Monte Carlo (FCIQMC) technique is a stochastic method to compute the ground-state energy (and expectation values over two-particle operators of the ground state) of extremely large many-body Hamiltonians, usually in the context of 'Full CI' methods: that is to say electronic wavefunctions expanded in Slater determinant spaces comprising of all possible determinants constructable from a given spatial orbital basis. Introduced in 2009 [1], it has been developed in a number of ways which greatly extends the scope of the methodology: the *initiator method* [2], introduced in 2010, enables much larger Hilbert spaces to be accessed with a relatively small number of walkers, albeit at the cost of a systematically improveable bias, followed in 2012 the development of the *semi-stochastic* FCIQMC method (S-FCIQMC) [3, 4], which greatly reduces the stochastic error bars for a given amount of computer effort, resulting in $\sim$1000-fold increase in efficiency. In 2014, the *replica method* to compute reduced-density matrices (1- and 2-body) was introduced [5], which has enabled other developments, including property calculations [6], stochastic CASSCF [6, 7], and F12 corrections [8], and finally the method was extended to excited states [9–13]. FCIQMC has also led to stochastic techniques for solving other types of quantum chemical equations: the Coupled-Cluster Monte Carlo technique [14], and the density matrix QMC method [15], respectively.

The scope of this short tutorial lecture cannot possibly cover all of the above aspects. We will limit ourselves to the description of the algorithm, together with its semi-stochastic variant, as well as some illustrative examples using the Hubbard model. It should be pointed out, however, that the FCIQMC has proven most useful for quantum chemical systems, often characterized by large basis sets (i.e., a large ratio of the number of orbitals to the number of electrons), and in which the full CI eigenvector is very sparse in comparison to the size of the Hilbert space. FCIQMC manages to perform an efficient sampling of such sparse solutions without *a priori* knowledge of the wavefunction, and importantly, without encountering a severe sign problem. In other words, the signal-to-noise ratio of the simulations are perfectly stable and manageable, and does not deteriorate with time as the simulation proceeds. However, where sparsity does not exist in the wavefunction, in other words where the entire Hilbert space is relevant to the description of the wavefunction, it is inevitable that the computational effort of the FCIQMC simulation involves sampling the whole (exponentially large) space. This is found to be the case for the Hubbard model, where, depending on the strength of the Hubbard U, the exact solution can be either sparse or dense, the latter being the case for example in the Hubbard model as U/t becomes large (in a plane-wave basis). In this case, FCIQMC is not much more efficient than conventional exact diagonalization. It does raise the question of representation, though. At very large U (which by numerical experimentation is found to be around $30t$) it is more efficient to use a real-space representation to express the FCI solution, whereas at smaller U plane-waves are more efficient. However for the intermediate U regime, i.e., from 4-12, we have not found any representation to be efficient, and the FCI solution appears to be quite dense in both real and reciprocal space.

Nevertheless, the important property of the FCIQMC method rests on its intrinsic ability to locate the important parts of the wavefunction, *and to entangle them correctly*. In other words the correct linear combination of Slater determinants emerges from the simulation, without the need to perform any explicit diagonalization, or similar numerical procedure. In order to do this, the key step is the *walker-annihilation* step of the algorithm, which will be discussed later on. It turns out that this process can be done in a *local* manner, in an $\mathcal{O}(N_w)$ process, i.e., scaling linearly with the number of walkers, without the need to invoke global processes involving the entire walker population or Hilbert space, which would be intractable. Furthermore, this allows for massive parallelization, which is without doubt one of the key strengths of the technique. It gives it an exciting future perspective.

2 FCIQMC

Given a second-quantized Hamiltonian of the type

$$\hat{H} = \sum_{pq} h_{pq} c_p^\dagger c_q + \sum_{pqrs} v_{pqrs} c_p^\dagger c_q^\dagger c_s c_r \tag{1}$$

defined over a set of spin-orbitals $\{\varphi_1, ...\varphi_p, ..., \varphi_q, ..., \varphi_{2M}\}$ with

$$h_{pq} = \langle \varphi_p | h | \varphi_q \rangle \tag{2}$$

$$v_{pqrs} = \langle \varphi_p \varphi_q | r_{12}^{-1} | \varphi_r \varphi_s \rangle \,, \tag{3}$$

the object is to solve for the lowest-energy eigenstate of such an Hamiltonian for an N-electron system

$$\hat{H}|\Psi_0\rangle = E_0 |\Psi_0\rangle \,. \tag{4}$$

FCIQMC can be considered as a stochastic minimization of the energy with respect to a sampled full configuration interaction wavefunction expansion. This wavefunction is a simple linear combination of all Slater determinants that can be constructed from distributing the available electrons within the (orthonormalized) single-particle orbitals spanning the space, as

$$|\Psi_0\rangle = \sum_{\mathbf{i}} C_{\mathbf{i}} |D_{\mathbf{i}}\rangle, \tag{5}$$

where $|D_{\mathbf{i}}\rangle$ represents a Slater determinant, labeled by the orbital-occupation string $\mathbf{i}$. The linear coefficients of this expansion are the objects that are stochastically sampled using a *delta function* or *walker* representation: given an ensemble of N_w walkers distributed over the Hilbert space, each with a sign $s = \pm 1$ and Slater determinant $\mathbf{i}$

$$\{s_1 \mathbf{i}_1, s_2 \mathbf{i}_2, ..., s_{N_w} \mathbf{i}_{N_w}\} \tag{6}$$

the number of walkers on each determinant is

$$n_{\mathbf{i}} = \sum_{w}^{N_w} s_w \delta(\mathbf{i}_w - \mathbf{i}). \tag{7}$$

The FCIQMC algorithm is then a population dynamics of such an assembly of walkers with the aim that in a long-time (β) simulation, the expectation value of the $n_{\mathbf{i}}$ becomes proportional to the $C_{\mathbf{i}}$

$$\langle n_{\mathbf{i}} \rangle_\beta \propto C_{\mathbf{i}} \,. \tag{8}$$

The stochastic, iterative equations that govern this dynamics are given by

$$\Delta n_{\mathbf{i}}(\beta + \tau) = -\tau \left[\sum_{\mathbf{j} \neq \mathbf{i}} H_{\mathbf{ij}}\, n_{\mathbf{j}}(\beta) \right] - \tau (H_{\mathbf{ii}} - S)\, n_{\mathbf{i}}(\beta) \,, \tag{9}$$

where $\Delta n_{\mathbf{i}}(\beta)$ represents the change in 'walker' population/weight on determinant $|D_{\mathbf{i}}\rangle$ in the time step $\beta \rightarrow \beta + \tau$. This leads to population dynamics of a set of walkers which occupy determinants connected to each other in this many-electron Hilbert space. This dynamics can be achieved by a set of local, stochastically realized, Markov-chain processes as follows:
The first is a 'spawning' step, which is performed for each occupied determinant, and a number of times proportional to the walker weight at that determinant ($n_{\mathbf{i}}$). A single or double excitation is randomly chosen, with normalized probability $p_{\text{gen}}(\mathbf{j}|\mathbf{i})$ for the excitation from $|D_{\mathbf{i}}\rangle$ to $|D_{\mathbf{j}}\rangle$. The walker amplitude on $|D_{\mathbf{j}}\rangle$ is then augmented with a signed probability given by

$$p_{\text{spawn}} = -\frac{\tau H_{\mathbf{ij}}}{p_{\text{gen}}(\mathbf{j}|\mathbf{i})} \,. \tag{10}$$

Finally, a 'death' step is performed, by which the amplitude on each determinant, $|D_{\mathbf{i}}\rangle$, is (generally) reduced with probability $\tau(H_{\mathbf{ii}} - S)n_{\mathbf{i}}$. Taken together, these two steps simulate the dynamic in Eq. (9). However, an additional 'annihilation' step is essential in order to overcome an exponential increase in noise and other features associated with the Fermion sign problem [1]. In this step, walkers of opposite signs on the same determinant are removed from the simulation.
The energy of the QMC-sampled wavefunction can be extracted from a projected estimator, the simplest of which is

$$E_{\text{Proj}} = \frac{\langle D_{\text{HF}} | \hat{H} | \Psi \rangle}{\langle D_{\text{HF}} | \Psi \rangle} \,, \tag{11}$$

where the projection is done onto the Hartree-Fock determinant D_{HF}. This is a reasonable projection as long as D_{HF} has a non-negligible overlap with the ground-state wavefunction Ψ. In case of wavefunctions with multi-reference character, it is better to perform a projection onto a multi-determinantal trial wavefunction $\Psi_T = \sum_{\{\mathbf{i}\}} C^T_{\mathbf{i}} |D_{\mathbf{i}}\rangle$, so that

$$E_T = \frac{\langle \Psi_T | \hat{H} | \Psi \rangle}{\langle \Psi_T | \Psi \rangle} \,. \tag{12}$$

For a well-chosen Ψ_T, so that the denominator stays far from zero (which can be generated on the fly during the FCIQMC simulation), this leads to a significantly better behaved energy

estimator with smaller bias and smaller stochastic errors. In the NECI code, Ψ_T is generated by diagonalizing H is a sub-space containing a specified number of leading determinants obtained from an FCIQMC simulation.
The value of the shift S is varied throughout the simulation in order to maintain a constant, desired weight of walkers. At convergence, this value should fluctuate about the energy of the system, providing an alternative estimator for the energy based on the total growth rate of all the walkers in the system. More details on the specific implementation of these steps, and the derivation of this dynamic from the imaginary-time Schrödinger equation can be found in Refs. [1, 16, 3]. Furthermore, the systematically improvable *initiator* approximation is almost always used (sometimes denoted i-FCIQMC to distinguish it from the full method). This involves a dynamically truncated Hamiltonian operator, where spawning events to unoccupied determinants are constrained to be only allowed if they come from a determinant with a walker weight greater than n_{add}. This approximation can be systematically improved as the number of walkers increases, as increasing numbers of determinants fulfil the criteria, and the sampled Hamiltonian therefore approaches the exact Hamiltonian. More details and benchmarking of this approximation can be found in Refs. [2, 17].

3 Semi-stochastic FCIQMC

The FCIQMC wave function is represented by a collection of walkers which have a weight and a sign and reside on a particular basis state, sometimes referred to as a *site*. The total signed weight of walkers on a site is interpreted as the amplitude of that basis state in the (unnormalized) FCI wave function expansion. The FCIQMC algorithm consists of repeated application of the projection operator

$$\hat{P} = \mathbb{1} - \tau(\hat{H} - S\mathbb{1}) \tag{13}$$

to some initial state, where $\hat{H}$ is the Hamiltonian operator, τ is some small time step and S is an energy offset ('shift') applied to the Hamiltonian to control the total walker population. With sufficiently small τ, exact repeated application of $\hat{P}$ will project the initial state to the ground state of $\hat{H}$ [18]. In FCIQMC, $\hat{P}$ is applied such that the correct projection is only performed on average, thus leading to a stochastic sampling of the ground state wave function.
The projection operator can be expanded in the chosen FCI basis as

$$\hat{P} = \sum_{\mathbf{ij}} P_{\mathbf{ij}} |\mathbf{i}\rangle\langle\mathbf{j}|. \tag{14}$$

In the semi-stochastic adaptation the set of basis states is divided into two sets, D and S. We refer to the space spanned by those basis states in D as the *deterministic space*, and refer to the basis states themselves as *deterministic states*. The terms in Eq. (14) can then be divided into two separate operators,

$$\hat{P} = \hat{P}^D + \hat{P}^S, \tag{15}$$

where $\hat{P}^D$ refers to the deterministic projection operator,

$$\hat{P}^D = \sum_{\mathbf{i}\in D, \mathbf{j}\in D} P_{\mathbf{ij}} |\mathbf{i}\rangle\langle\mathbf{j}|, \tag{16}$$

and $\hat{P}^S$ is the stochastic projection operator containing all other terms. In semi-stochastic FCIQMC, $\hat{P}^D$ is applied exactly by performing an exact matrix multiplication, while $\hat{P}^S$ is applied using the stochastic FCIQMC spawning steps as usual.[1]

In order to perform an exact projection in the deterministic space, the walkers weights must be allowed to be non-integers. This differs from most previous descriptions of the FCIQMC algorithm thus far. To be clear in notation, we use $C_{\mathbf{i}}$ to refer to the *signed* amplitude on a site, and $N_{\mathbf{i}}$ to refer to the *unsigned* amplitude (and so $|C_{\mathbf{i}}| = N_{\mathbf{i}}$), which we refer to as the *weight* on the site.

A complete iteration of semi-stochastic FCIQMC is performed as follows, where we use the notation $\hat{T} = -(\hat{H} - S\mathbb{1})$:

1. **stochastic projection**: Loop over all sites. Perform $\chi_{\mathbf{i}}$ spawning attempts from site $|\mathbf{i}\rangle$, where $\chi_{\mathbf{i}}$ is specified below. For each spawning attempt, choose a random connected site $|\mathbf{j}\rangle$ with probability $p_{\mathbf{ij}}$, where connected means that $H_{\mathbf{ij}} = \langle\mathbf{i}|H|\mathbf{j}\rangle \neq 0$ and $\mathbf{i} \neq \mathbf{j}$. The attempt fails if both $|\mathbf{i}\rangle$ and $|\mathbf{j}\rangle$ belong to D, otherwise a new walker on site $|\mathbf{j}\rangle$ is created with weight $|T_{\mathbf{ji}}|\,\mathrm{sign}(C_{\mathbf{i}})\,\tau/p_{\mathbf{ij}}$.

2. **deterministic projection**: New walkers are created on sites in D with weights equal to $\tau \boldsymbol{T}^D \boldsymbol{C}^D$, where $\boldsymbol{C}^D$ is the vector of amplitudes currently on sites in D.

3. **death/cloning**: Loop over all sites in S. For each site create a spawned walker with weight and sign given by $T_{\mathbf{ii}}\, C_{\mathbf{i}}\, \tau$.

4. **annihilation**: Combine all newly spawned walkers with walkers previously in the simulation by summing together the weights of all walkers on the same site.

$\chi_{\mathbf{i}}$ is chosen probabilistically such that the expectation value $E[\chi_{\mathbf{i}}] = N_{\mathbf{i}}$. Although other approaches have been used [3], in this work we set

$$\chi_i = \lceil N_{\mathbf{i}} \rceil \text{ with probability } N_{\mathbf{i}} - \lfloor N_{\mathbf{i}} \rfloor, \tag{17}$$

$$= \lfloor N_{\mathbf{i}} \rfloor \text{ otherwise.} \tag{18}$$

If integer weights are used, then this reduces to $\chi_{\mathbf{i}} = N_{\mathbf{i}}$, as used in previous work [1].

In order to reduce the memory demands of having a large number of sites occupied with a low weight, a minimum occupation threshold, N_{occ}, is defined. After all annihilation has occurred, any walkers with a weight less than N_{occ} are rounded up to N_{occ} with probability N_i/N_{occ} or otherwise down to 0. In practice, we always choose $N_{\mathrm{occ}} = 1$. The occupation threshold is not applied to deterministic states such that the deterministic projection is applied exactly.

[1] If the deterministic space is the entire FCI space, then the algorithm reduces to the power method without explicit normalization; FCIQMC can be viewed as a stochastic version of this approach.

We further use a modification to the initiator adaptation to FCIQMC [2, 19] by allowing all spawnings both from and to the deterministic space to survive. This effectively forces all deterministic states to be initiators, which is sensible since these states should be selected by their importance (i.e. weight). We note that this is different from the more complicated adaptation made by Petruzielo *et al.* [3], where the initiator threshold is allowed to vary based on the number of steps since a walker last visited the deterministic space. We note that it is not necessary to use both the initiator and semi-stochastic adaptations together; the benefits from both extensions are largely independent of each other.

Using non-integer weights can have a significant memory impact compared to integer weights due to the large number of additional spawned walkers, which also increases time demands due to expensive extra processing and communication steps. We therefore apply an unbiased procedure to stochastically remove walkers with very small weights, similar to that above. Following the notation of Overy *et al.* [5], we use a spawning cutoff, κ, where $\kappa = 0.01$ unless stated otherwise. A spawning of weight $N_\mathbf{j} < \kappa$ is rounded up to κ with probability $N_\mathbf{j}/\kappa$ or otherwise down to 0. Spawned walkers with weights greater than κ are left unaltered.

4 Choosing the deterministic space

The key to reducing the stochastic error is to choose D such that most of the weight of the true FCI wave function is in this space. For a given number of basis states in the deterministic space, $|D|$, it is expected that the best possible deterministic space (the one which reduces noise the most) is obtained by choosing the $|D|$ most highly weighted basis states in the exact expansion of the ground-state wave function. Achieving this optimal space requires knowledge of the exact wave function and so is not feasible in general.

A sensible choice for D in many systems would be a configuration interaction (CI) or complete active space (CAS), generally regarded as being effective at describing situations where dynamical and static correlation, respectively, are important. We have found from experience that such spaces are useful and lead to a large reduction in stochastic noise. This leads to the question: can one find a better deterministic space, at least in common cases?

Petruzielo *et al.* [3] describe an iterative method for choosing the deterministic space. First the space connected to the space from the previous iteration is generated and the ground state of the Hamiltonian in this subspace is calculated. The most significant basis states in this ground-state expansion are kept (according to a criterion on the amplitude of coefficients). The initial space contains (e.g.) the Hartree–Fock determinant. This process is repeated for some number of iterations. This approach has been demonstrated to give much greater improvements than by simply using the space connected to the Hartree–Fock state, even with a reduced size for D, as it can contain the chemically-relevant basis states [3].

In the NECI code we use a different method of generating the deterministic space. Inspired by the spirit of FCIQMC, we allow the deterministic space to emerge from the calculation itself: we simply perform a fully-stochastic FCIQMC calculation (or a semi-stochastic calculation with a simple deterministic space, such as a CISD space) until the ground state is deemed to have

been reached, and then choose the most populated basis states in the FCIQMC wave function to form D. In this initial FCIQMC calculation, it is not necessary to employ a large number of walkers, as its purpose is simply to identify determinants which are likely to be important in the converged solution. The generation of the deterministic subspace is therefore extremely rapid. This approach has the benefit that it does not require performing an exact ground-state diagonalization within a (potentially large) subspace, which can be very expensive. The only parameter is the desired size of the deterministic space and it is therefore considerably more black-box like. Since the initial FCIQMC calculation need not be limited to low-order excitations (such as the double excitations of a reference determinant), but can develop significant walker population on some determinants deep in the Hilbert space (on quadruple, sextuple and higher excitation levels) our procedure can select close-to-optimal deterministic spaces in a very inexpensive and rapid manner.

Although the FCIQMC wave function is only a stochastic snapshot of the true ground state, the most significant basis states in the expansion will tend to remain highly occupied throughout the simulation with weights fluctuating about their exact values. It is therefore not surprising that our approach works well. For very large deterministic spaces, states with the minimum occupation weight, may be included in the space. In this case there is some redundancy in how D is chosen, and the choice of D will probably not be optimized fully, although we still find this approach to work very well. It is simple to include a cutoff to avoid this if desired, although we do not do so in the calculations presented here.

We emphasize that we prefer our approach to the iterative scheme of Petruzielo *et al.* because it avoids large ground-state calculations which, for large systems and values of $|D|$, can take up a significant amount of time and memory. If the size of the space at the start of an iteration in this iterative scheme is given by X, and the average number of connections to each state is n_c (which, in general, grows quadratically with system size), then one will have to perform a ground-state calculation in a space of size $\sim Xn_c$. For many cases, including those considered in this article, such a space is extremely, if not prohibitively, large. Indeed, as FCIQMC is applied to increasingly larger systems, such an approach will become less feasible. Already, FCIQMC has been applied to systems where the number of connections to the Hartree–Fock state is $\mathcal{O}[10^5 - 10^6]$ [20,6]. In these cases, it might be possible to apply the iterative scheme if only a small number of states are kept in each iteration, but in this case the final space would be unoptimized. Another approach would be to generate the final space by finding the connections to the previous (small) space but *not* performing a ground-state calculation, but again the generated space would be unoptimized. We therefore feel that our approach is an altogether more black box and scalable approach to generating an effective deterministic space.

5 An application of FCIQMC to the Hubbard model

The Hubbard model Hamiltonian is usually expressed in a real-space lattice as

$$\hat{H} = -t \sum_{\langle p,q\rangle,\sigma} \left(c^\dagger_{p\sigma} c_{q\sigma} + \text{h.c.} \right) + U \sum_p n_{p\uparrow} n_{p\downarrow} \,, \tag{19}$$

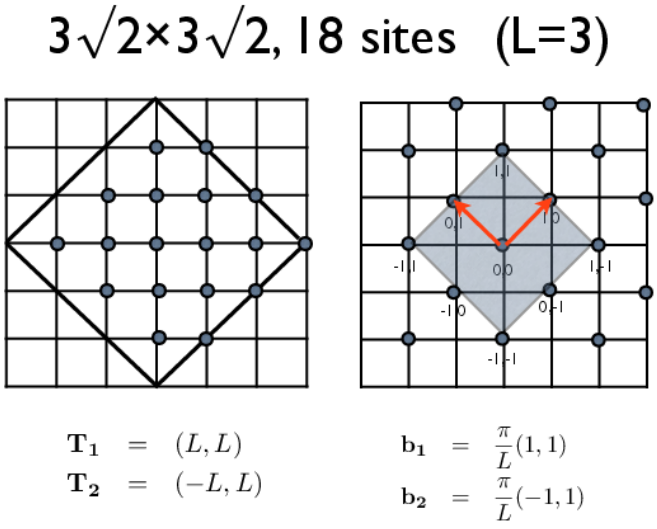

Fig. 1: *The 18-site Hubbard model on a tilted lattice. (a) Real-space lattice. (b) Reciprocal space lattice, showing the occied Fermi 'square' at half-filled occupancy*

where $n_{p\sigma} = c^\dagger_{p\sigma} c_{p\sigma}$ is the number operator on site p for σ-spin electrons. The sum $\langle p, q \rangle$ is taken over nearest-neighbor lattice sites p and q and periodic boundary conditions are applied. Twisted periodic boundary conditions can also be applied, in order to reduce finite size effects and to perform "twist-averaging", but in the numerical examples below this is not done.
For the purposes of FCIQMC, it is more convenient to work in a plane-wave, reciprocal space, representation in which the orbitals are unitarily transformed as

$$|\mathbf{k}\rangle = \frac{1}{\sqrt{\Omega}} \sum_p e^{-i\mathbf{k}.\mathbf{r}_p} |p\rangle, \tag{20}$$

where Ω is the number of sites in the lattice and $\mathbf{r}_p$ is the position of lattice site p. In this momentum basis, the Hubbard Hamiltonian takes the form

$$\hat{H} = \sum_{\mathbf{k},\sigma} \epsilon_{\mathbf{k}} c^\dagger_{\mathbf{k},\sigma} c_{\mathbf{k},\sigma} + \frac{U}{\Omega} \sum_{\mathbf{k},\mathbf{q},\mathbf{Q}} c^\dagger_{\mathbf{k}+\mathbf{Q}\uparrow} c^\dagger_{\mathbf{q}-\mathbf{Q},\downarrow} c_{\mathbf{k}\uparrow} c_{\mathbf{q}\downarrow}. \tag{21}$$

The precise form of $\epsilon_{\mathbf{k}}$ depends on the lattice vectors of the lattice being studied. For this study we shall use the tilted 2-dimensional square lattice shown in Fig. 1, with super-cell lattice vectors

$$\mathbf{T}_1 = \begin{pmatrix} L \\ L \end{pmatrix} \quad \text{and} \quad \mathbf{T}_2 = \begin{pmatrix} -L \\ L \end{pmatrix}, \tag{22}$$

where L is an odd integer. This leads to a supercell containing $\Omega = \sqrt{2}L \times \sqrt{2}L$ sites. The dispersion relation for $\epsilon_{\mathbf{k}}$ can be expressed in terms of the reciprocal lattice vectors of $\mathbf{T}_1, \mathbf{T}_2$, namely $\mathbf{b}_1, \mathbf{b}_2$

$$\mathbf{b}_1 = \frac{\pi}{L} \begin{pmatrix} 1 \\ 1 \end{pmatrix} \quad \text{and} \quad \mathbf{b}_2 = \frac{\pi}{L} \begin{pmatrix} 1 \\ -1 \end{pmatrix} \tag{23}$$

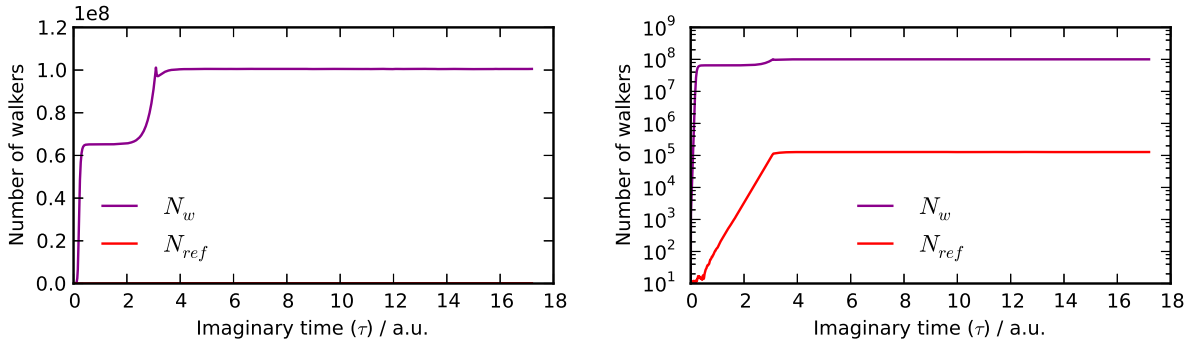

Fig. 2: *The number of walkers in a* non-initiator *FCIQMC calculation, showing a plateau for the (18,18) $U/t = 4$ system at $\approx 62 \times 10^6$ walkers. The second plateau corresponds to the onset of variable-shift mode, in which the walker population is stabilized at 10^8 walkers. The Hilbert space corresponds to $\approx 131 \times 10^6$ determinants. The number of walkers on the reference determinant is 127000, and is barely visible on this plot. The plot on the right shows the same information on a logarithmic scale.*

with allowable $\mathbf{k} = \mathbf{k}_{n,m}$ as follows:

$$\mathbf{k}_{n,m} = n\mathbf{b}_1 + m\mathbf{b}_2 \tag{24}$$

$$\epsilon_{\mathbf{k}} = -2t\left(\cos\frac{\pi(n+m)}{L} + \cos\frac{\pi(n-m)}{L}\right) \tag{25}$$

We are aware of exact diagonalization results for the half-filled 18-site $(L = 3)$ model to which we will compare the FCIQMC results [21], which we shall refer to as the $(18, 18)$ system. This system has a Hilbert space of $N_{FCI} \approx \frac{1}{18}\binom{18}{9}^2 \approx 131 \times 10^6$ Slater determinants. The calculations have been done with $\tau = 0.001$ for a range of $U/t = 1-4$. We have also performed calculations on the Hubbard model with 2 holes (maintaining zero momentum and zero total spin), i.e., the $(18, 16)$ system, to exhibit the effect of moving off half-filling on the FCIQMC method.

We first perform a non-initiator FCIQMC calculation, which exhibits a *plateau* in the walker growth when the shift is held fixed at $S = 0$ (Fig. 2). This plateau occurs when roughly 50% of the Hilbert space has been populated by walkers. For smaller values of U, the plateau height decreases linearly, vanishing when $U < 1$ (Fig. 3). This implies that for such values of U, it is possible to sample the Hilbert space with a vanishingly small number of walkers [22] even without the initiator method.

Figure 4 shows the error in the projected energy as a function of imaginary time for the (18,18) Hubbard model with $U/t = 4$ using FCIQMC without the initiator method. With the initiator method, it can be seen that a small but systematic bias is induced at small walker population, which diminishes with increasing number of walkers. Even with a small number of walkers, the simulations are stable with a constant signal to noise ratio in the long time limit. This is shown in Fig. 5 for the (18,18) and the (18,16) Hubbard model, both with $U/t = 4$. The cost of the initiator runs is however much lower. Fig. 6 shows the time per iteration for each of the runs, including the 10^8 walker non-initiator run. The time per iteration is linear in the number of walkers, and there additional overhead associated with the initiator method compared to the full method.

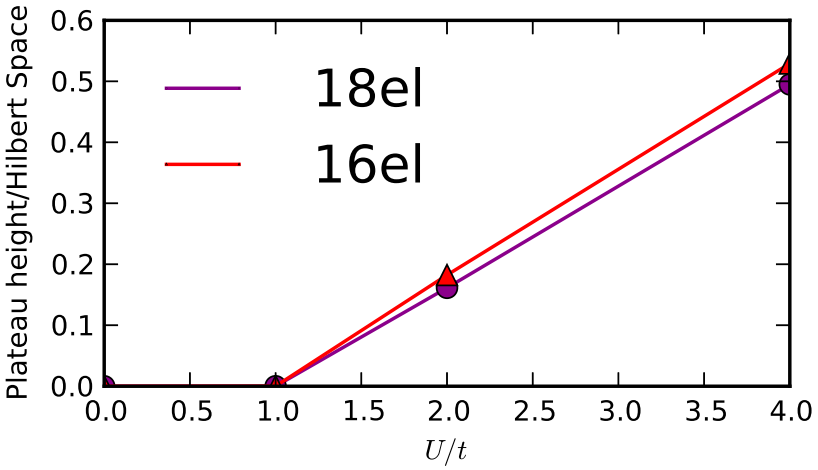

Fig. 3: *The ratio of plateau heights to the size of the Hilbert space as a function of U for the 18-electron and 16-electron (2-hole) system. As the value of U decreases, an off-set linear decrease in the plateau height is observed, vanishing at $U = 1$. The 2-hole system exhibits slightly higher values of the plateau as a ratio of the Hilbert space, presumably because of the more multi-reference nature of the ground state wavefunction.*

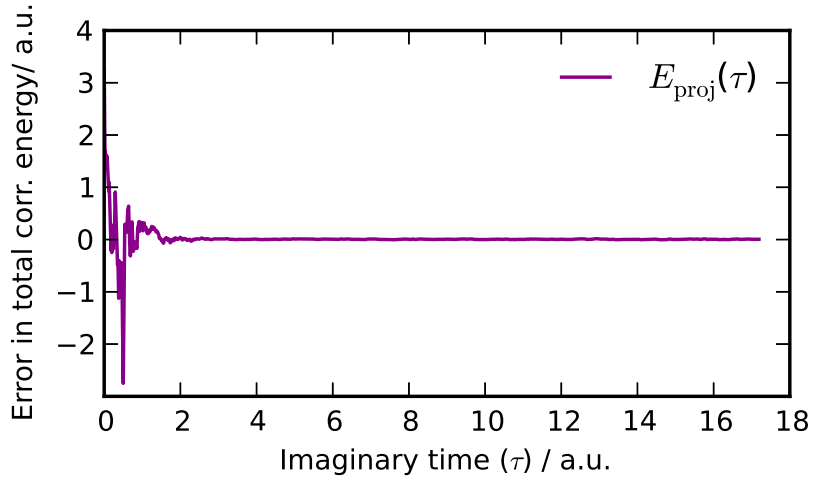

Fig. 4: *The error in the projected energy as a function of imaginary time for the (18,18) Hubbard model at $U/t = 4$. The initiator method is not used, leading to a plateau in the walker-growth of the simulation (see Fig. 2). The initial value of the energy is the Hartree-Fock energy ($-14\,t$), which is $3.25239\,t$ above the exact energy of $-17.25239\,t$. All energy plots are shown relative to this exact energy. It is evident that after propagation of ≈ 2 units of imaginary time ($\tau = 0.001\,t$), the simulation has converged, and crucially, the energy stable, i.e., there is no growth in noise as the simulation proceeds.*

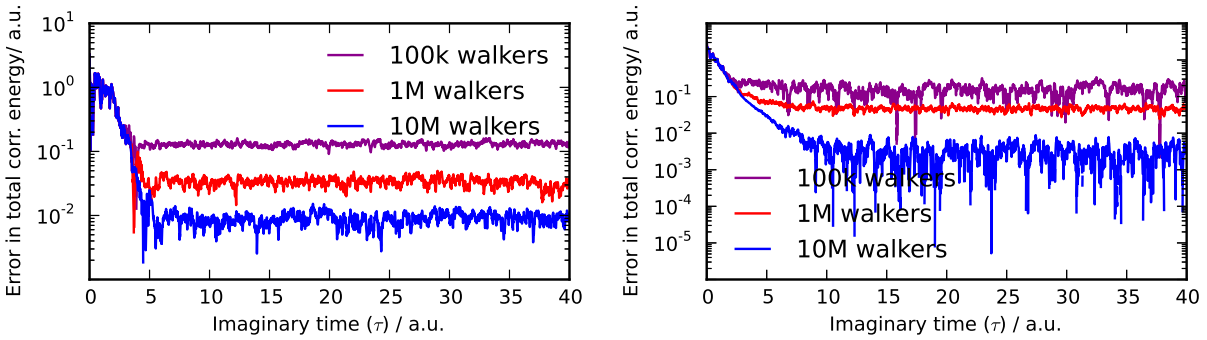

Fig. 5: *Error of different initiator runs of varying number of walkers for the Hubbard model with $U/t = 4$. Left: Half-filled (18,18) system. The initiator error is seen to decrease as the walker population is increased. The signal to noise ratio of the initiator simulations is also stable in the long time limit, even with low walker population. Right: 2-hole doped (18,16) system. The behavior is very similar to the half-filled case, indicating that the severity of the sign-problem is not increased when moving away from half-filling. Indeed the convergence of the initiator bias is faster, owing presumably to the smaller Hilbert space of the 2-h system.*

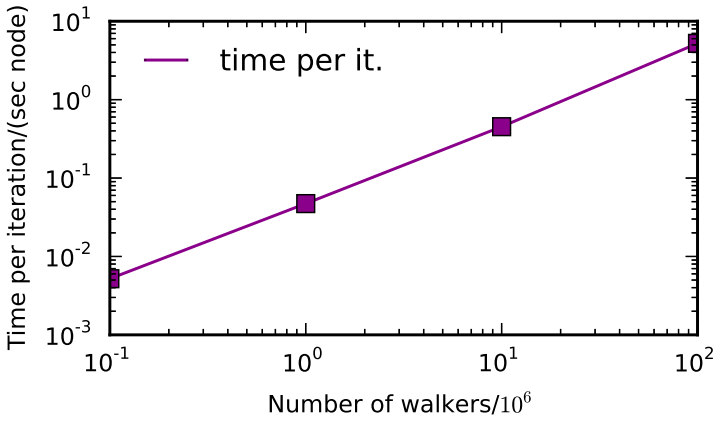

Fig. 6: *Time per iteration on one node (20 core) as a function of the number of walkers. The three runs at 100k, 1M, and 10M walkers were initiator simulations, whilst the run with 10^8 walkers is a non-initiator simulation.*

6 Future perspectives

Although the FCIQMC technique has thus far been formulated in a Slater determinant basis, its ideas can be extended to other more general types of basis functions which span the same Hilbert space. A notable example are configuration state functions (CSFs), each one of which preserves the total spin S quantum number, in addition to the spin-polarization quantum number M_S. Spaces of CSFs are typically an order of magnitude smaller than the corresponding Slater determinant basis, but the matrix element calculations between CSFs is more complex. Development of fast algorithms capable of handing CSFs would greatly help in the study of systems with small spin-gaps (which includes Hubbard models in the intermediate U range), and we believe this to be an important area of research. Another important question is to understand the factors that govern the rate of convergence of the initiator method, with the aim to

try to improve it. In the study of quantum chemical systems, and of the uniform electron gas, it is frequently found that the initiator method works extremely well, so that Hilbert spaces as large as 10^{108} have been sampled with $\sim 10^9$ walkers [23]. However for the 2D Hubbard model, particularly in the 'interesting' range of $U/t = 4-12$ one observes much larger initiator biases. Is this inevitable? In other words, is the complexity of the ground-state wavefunction such that, no matter which technique is employed, the convergence is governed by the complete Hilbert space? This is unclear. Perhaps some fusion of FCIQMC with other types of wavefunction representations, such as matrix product states or tensor networks could be envisaged. But there is at present no equivalent projector method to FCIQMC in such representations which does so – only variational methods or fixed-node approximations. These are indeed extremely important questions to be addressed in the future.

Acknowledgments

I am grateful to a large number of former and present PhD students and postdocs who have helped develop the FCIQMC method and the NECI code, in Cambridge and in Stuttgart: George Booth, Alex Thom, Diedre Cleland, Simon Smart, James Shepherd, Nick Blunt, Catherine Overy, Jennifer Kersten, Robert Thomas, Werner Dobrautz, Giovanni Li Manni, Sasha Lozovoi, Dongxia Ma, Guillaume Jeanmairet, and Michele Ruggeri. The work has been funded by the EPSRC and by the Max Planck Society.

References

[1] G.H. Booth, A.J.W. Thom, and A. Alavi, J. Chem. Phys. **131**, 054106 (2009)

[2] D.M. Cleland, G.H. Booth, and A. Alavi, J. Chem. Phys. **132**, 041103 (2010)

[3] F.R. Petruzielo, A.A. Holmes, H.J. Changlani, M.P. Nightingale, and C.J. Umrigar, Phys. Rev. Lett. **109**, 230201 (2012)

[4] N.S. Blunt, S.D. Smart, J.A.F. Kersten, J.S. Spencer, G.H. Booth, and A. Alavi, J. Chem. Phys. **142**, 184107 (2015)

[5] C. Overy, G.H. Booth, N.S. Blunt, J.J. Shepherd, D. Cleland, and A. Alavi, J. Chem. Phys. **141**, 244117 (2014)

[6] R.E. Thomas, G.H. Booth, and A. Alavi, Phys. Rev. Lett. **114**, 033001 (2015)

[7] G. Li Manni, S. Smart, and A. Alavi, J. Chem. Theor. Comput. **12**, 1245 (2016)

[8] G.H. Booth, D. Cleland, A. Alavi, and D.P. Tew, J. Chem. Phys. **137**, 164112 (2012)

[9] G.H. Booth and G.K.-L. Chan, J. Chem. Phys. **137**, 191102 (2012)

[10] S. Ten-no, J. Chem. Phys. **138**, 164126 (2013)

[11] A. Humeniuk and R. Mitrić, J. Chem. Phys. **141**, 194104 (2014)

[12] N.S. Blunt, A. Alavi, and G.H. Booth, Phys. Rev. Lett. **115**, 050603 (2015)

[13] N.S. Blunt, G.H. Booth, and A. Alavi, J. Chem. Phys. **143**, 134117 (2015)

[14] A. Thom, Phys. Rev. Lett. **105**, 263004 (2010)

[15] N.S. Blunt, T.W. Rogers, J.S. Spencer, and W.M.C. Foulkes, Phys. Rev. B **89**, 245124 (2014)

[16] G.H. Booth, S.D. Smart, and A. Alavi, Mol. Phys. **112**, 1855 (2014)

[17] G.H. Booth, A. Gruneis, G. Kresse, and A. Alavi, Nature **493**, 365 (2012)

[18] J.S. Spencer, N.S. Blunt, and W.M.C. Foulkes, J. Chem. Phys. **136**, 054110 (2012)

[19] D.M. Cleland, G.H. Booth, and A. Alavi, J. Chem. Phys. **134**, 024112 (2011)

[20] J.J. Shepherd, G.H. Booth, and A. Alavi, J. Chem. Phys. **136**, 244101 (2012)

[21] H. Lin, Phys. Rev. B **44**, 7151 (1991)

[22] J.J. Shepherd, G. Scuseria, and J.S. Spencer, Phys. Rev. B **90**, 155130 (2014)

[23] J.J. Shepherd, G.H. Booth, A. Grüneis, and A. Alavi, Phys. Rev. B **85**, 081103(R) (2012)

10 Linear Response and More: the Bethe-Salpeter Equation

Lucia Reining
Laboratoire des Solides Irradiés and
European Theoretical Spectroscopy Facility
École Polytechnique, CNRS, CEA,
Université Paris-Saclay, 91128 Palaiseau, France

Contents

E. Pavarini, E. Koch, J. van den Brink, and G. Sawatzky (eds.)
Quantum Materials: Experiments and Theory
Modeling and Simulation Vol. 6
Forschungszentrum Jülich, 2016, ISBN 978-3-95806-159-0
http://www.cond-mat.de/events/correl16

1 Introduction

In this lecture we will present the Bethe-Salpeter equation (BSE) from the point of view of its use in condensed matter physics and chemistry. In this context it is most often applied to the calculation of optical spectra. For this reason we will work in the framework of linear response theory, although, as we will see at the end, there are other uses of the BSE.
The BSE solves a many-body problem, expressed in terms of electrons, holes, and their interaction. It is convenient to formulate such a problem in terms of Green functions. Therefore, we will start by briefly recalling the necessary tools.

2 Green functions and Dyson equations

Green functions are often encountered in scattering theory. Suppose a system is described by $\hat{H}_0$, and $\hat{V}$ indicates an extra potential that acts as a center for scattering. Assuming that the energies ω form a continuum, one only has to determine the wavefunctions of the scattered states. The Lippmann-Schwinger equation [1] gives the relation between an unperturbed state $|\phi^0\rangle$ and an eigenstate of the full Hamiltonian $|\phi\rangle$ at the same energy ω:

$$|\phi\rangle = (1 - G_0\hat{V})^{-1}|\phi^0\rangle \qquad \text{with} \qquad G_0 \equiv (\omega + i\eta - \hat{H}_0)^{-1}_{|_{\eta\to 0^+}} . \tag{1}$$

The Green function G_0 depends only on the unperturbed system. Moreover, it contains a boundary condition: one imposes that the scattering contribution $|\phi\rangle - |\phi^0\rangle$ contains only outgoing contributions. This boundary condition, which guarantees that the solution is causal, is fulfilled thanks to the positive infinitesimal η. Eq. (1) is equivalent to $|\phi\rangle = GG_0^{-1}|\phi^0\rangle$ with the definition of the full Green function $G \equiv (1 - G_0\hat{V})^{-1}G_0$, which fulfills the *Dyson equation* $G = G_0 + G_0\hat{V}G$.
Like the Hamiltonian, the Green functions are non-local in space. In general they can also be non-local in a spin coordinate. Moreover, their dependence on the frequency ω (see Eq. (1)) corresponds to a dependence on a time difference (whereas G depends on two times when the Hamiltonian is time-dependent). In the following we denote a space-spin-time argument with $1 \to (x_1, t_1) \to (\mathbf{r}_1, \sigma_1, t_1)$, and we use the convention that arguments with a bar are integrated over: $f(\bar{1})g(\bar{1}) \to \int d1\, f(1)g(1)$. Then the Dyson equation can be written as

$$G(1,2) = G_0(1,2) + G_0(1,\bar{3})\,\hat{V}(\bar{3})\,G(\bar{3},2)\,. \tag{2}$$

The Dyson equation is a general way to move from the Green function of a simpler system to the Green function of a system in presence of an extra potential, which may depend on space, spin and time. In the following we do not display spin unless necessary, supposing that we are interested in spin-unpolarized systems.[1] Moreover for simplicity we assume the temperature to

[1] In the most general case the Green function depends on two spin arguments. When the interaction is spin-independent, the Green function is spin-diagonal, and in the absence of spin polarization, the two spin components are equal. We mostly suppose to be in that case, and do not display spin for simplicity. Details on the spin-dependent BSE can be found in [2].

be zero, and the system to be in its ground state. To simplify notation we also omit the hat on operators whenever it does not create confusion.

In the many-body electron system, there is scattering because of the Coulomb interaction between electrons, so the same considerations as above hold. The starting G_0 is an independent-particle Green function, describing electrons that are *not* scattered by other electrons.[2] Its retarded version G_0^R reads

$$G_0^R(\mathbf{r},t,\mathbf{r}',t') = -i\Theta(t-t')\sum_s \psi_s(\mathbf{r})\,\psi_s^*(\mathbf{r}')\,e^{-i\varepsilon_s(t-t')}\,, \tag{3}$$

where ε_s and ψ_s are the eigenvalues and eigenfunctions of the single-electron Hamiltonian h_0. The ε_s are the poles of G_0 in frequency space, where $G_0^R(\mathbf{r},\mathbf{r}';\omega) = \sum_s \frac{\psi_s(\mathbf{r})\,\psi_s^*(\mathbf{r}')}{\omega-\varepsilon_s+i\eta}$.

Often it is more convenient to work with time-ordered Green functions instead of retarded ones; we will also adopt this framework here. The time-ordered Green function G_0 of an independent-particle system reads

$$G_0(\mathbf{r},t,\mathbf{r}',t') = -i\Big[\Theta(t-t')\,\Theta(\varepsilon_s-\mu) - \Theta(t'-t)\,\Theta(\mu-\varepsilon_s)\Big]\sum_s \psi_s(\mathbf{r})\psi_s^*(\mathbf{r}')e^{-i\varepsilon_s(t-t')} \tag{4}$$

so that electrons (states above the chemical potential μ) and holes (states below μ) contribute with opposite sign.

The independent-particle Green function yields some important observables of the independent-particle system. In particular, the density is $n_0(\mathbf{r}) = \sum_s^{\text{occ}} |\psi_s(\mathbf{r})|^2 = -iG_0(\mathbf{r},t,\mathbf{r},t^+)$, where t^+ stands for $t+\eta$. The diagonal of the *spectral function* $A_{ss}(\omega) = \frac{1}{\pi}\text{Im}\,G_{0,\text{ss}}(\omega)$, which is the imaginary part of the Green function in frequency space, is $A^0_{ss}(\omega) = \delta(\omega-\epsilon_s)$: it exhibits the spectrum of electron addition and removal energies.

Suppose now that we add an extra static potential v_a to the system. The new Green function G can be obtained from the Dyson equation (2) where $\hat{V}$ is replaced by v_a. It will have the same form as Eq. (4), but the eigenvalues and eigenfunctions that appear in Eq. (4) are those of h_0+v_a. They can also be used to evaluate the density and spectral function as above. Importantly for our purpose, the independent-particle expressions are also valid when v_a is not some *external* potential, but a system-*internal* mean-field potential such as the Hartree (v_H) or Kohn-Sham (v_xc) ones. They even hold when one introduces a spatially non-local mean field, such as the Hartree-Fock potential $\Sigma_{H\text{x}}$, for which the Dyson equation reads

$$G(1,2) = G_0(1,) + G_0(1,\bar{3})\,\Sigma_{H\text{x}}(\bar{3},\bar{4})\,G(\bar{4},2)\,. \tag{5}$$

Note that like the Hartree or Kohn-Sham potentials, the Hartree-Fock potential is instantaneous, i.e., local in time, which means that $\Sigma_{H\text{x}}(3,4)$ is proportional to $\delta(t_3^+ - t_4)$.

When v_a depends explicitly on time, i.e., the system is out of equilibrium, G is no longer of the simple form of Eq. (3). Although we will implicitly apply such a potential to our system later, we do not need to consider the resulting Green functions explicitly here, since we will limit ourselves to linear response.

[2] An independent-particle system can be the non-interacting one in some external potential, or it can have also a part of the interaction included through a static mean field.

However, below we will replace the instantaneous Hartree-Fock mean field by a more general self-energy $\Sigma(3,4)$, which is *not* instantaneous, i.e., it depends on two time arguments (t_3, t_4), or one time difference $(t_3 - t_4)$ (one frequency) in equilibrium. As a consequence, G has no longer the same simple structure as G_0. Still, it can be calculated from the Dyson equation, if the self-energy is known.

There are two ways to understand why the full self-energy is not instantaneous, or equivalently, why the full Green function has a form different from Eq. (4). They are linked to the definition and meaning of G. The one-body Green function is defined such that it describes electron addition and removal from the full many-body system. In the Hartree and Hartree-Fock single-particle Schrödinger equation the eigenvalues are directly the addition and removal energies; this is Koopmans' theorem. It implies that electrons are added or removed without influencing the already present system electrons. However, in reality the system should react to the addition of a charge, which leads to *screening*. This reaction is not instantaneous, but it needs time to build up a screening cloud, and charge oscillations can be excited.[3] This explains why the total effective potential, which includes the self-energy, is not instantaneous but depends on a time difference.

The fundamental difference between a static mean-field and a fully interacting system can also be understood by looking directly at the Green function. The generalization of Eq. (4) to the fully interacting Green function at zero temperature is [3]

$$G(\mathbf{r},t,\mathbf{r}',t') = -i\langle N|\mathrm{T}\left[\hat{\psi}(\mathbf{r},t)\,\hat{\psi}^\dagger(\mathbf{r}',t')\right]|N\rangle, \tag{6}$$

where $|N\rangle$ is the N-particle many-body ground state, $\hat{\psi}$ are field operators in the Heisenberg picture, and T is the time-ordering operator defined as

$$\mathrm{T}\left[A(t_1)B(t_2)\right] \equiv \begin{cases} A(t_1)B(t_2), & t_1 > t_2 \\ B(t_2)A(t_1), & t_1 < t_2. \end{cases} \tag{7}$$

Eq. (6) shows that the Green function G is the probability amplitude to find an electron in $(\mathbf{r},t)$ if it has been inserted in $(\mathbf{r}',t')$ (and vice versa for a hole). This definition reduces to Eq. (4) in absence of interaction, where the ground state $|N\rangle$ is a Slater determinant built with the single particle orbitals $\psi_s(\mathbf{r})$. As one can see from the definition (6) of the Green function, in analogy to the non-interacting case,

$$n(\mathbf{r}) = -iG(\mathbf{r},t,\mathbf{r}t^+)\,. \tag{8}$$

The spectral function becomes

$$A_{\mathrm{ss}}(\omega) = -\frac{1}{\pi}\,\mathrm{Im}\,G_{\mathrm{ss}}(\omega) = \sum_\lambda |f_{\mathrm{s}\lambda}|^2\,\delta(\omega-\varepsilon_\lambda)\,, \tag{9}$$

[3]Note that especially in finite systems the Hartree or Hartree-Fock approximations are also used in a Δ self-consistent field (Δ-SCF) approach, where charges are explicitly added to the system, which is allowed to relax self-consistently. In this case, one implicitly includes screening, although in an adiabatic approximation that does not lead to excitations.

where ε_λ are electron addition and removal energies, and the $f_{s\lambda}$ are Dyson amplitudes projected on single particle orbitals. These projections are in general not sharp. Therefore, contrary to the non-interacting case the interacting spectral function is not just a single δ-peak, and it shows a continuous distribution of weight in an extended system, although a pronounced "quasi-particle" peak may still dominate the spectrum. Such a spectral function can only be produced if G is solution of a Dyson equation with self-energy that is not instantaneous, and which has therefore a Fourier transform that depends on frequency.

3 Linear response

In the following we will concentrate mainly on spectroscopic measurements, such as optical absorption, electron energy loss experiments, or inelastic x-ray scattering. The experimental results can often be understood in terms of linear response theory. In particular, they are related to the frequency-dependent dielectric function $\epsilon(\omega)$, or equivalently, to the linear density-density response function $\chi(\omega)$. The linear response is the first-order change of the density δn in a system due to an external perturbation v_{ext}, given as $\delta n = \chi\, v_{\text{ext}}$. The response function and the inverse dielectric function are related by

$$\epsilon^{-1}(\mathbf{r}_1, \mathbf{r}_2; \omega) = \delta(\mathbf{r}_1 - \mathbf{r}_2) + \int d\mathbf{r}_3\, v_c(|\mathbf{r}_1 - \mathbf{r}_3|)\, \chi(\mathbf{r}_3, \mathbf{r}_2; \omega)\,, \tag{10}$$

where v_c is the bare Coulomb interaction. More specifically, in a periodic system, this reads

$$\epsilon^{-1}_{\mathbf{G}\mathbf{G}'}(\mathbf{q}; \omega) = \delta_{\mathbf{G}\mathbf{G}'} + v_c(\mathbf{q} + \mathbf{G})\, \chi_{\mathbf{G}\mathbf{G}'}(\mathbf{q}; \omega)\,, \tag{11}$$

where $\mathbf{q}$ is a vector in the first Brillouin zone and $\mathbf{G}$ is a reciprocal lattice vector. Spectra are obtained from ϵ or χ. The most important quantities are:

- **The loss function** $-\operatorname{Im} \epsilon^{-1}_{\mathbf{G}\mathbf{G}}(\mathbf{q}; \omega) = -v_c(\mathbf{q} + \mathbf{G}) \operatorname{Im} \chi_{\mathbf{G}\mathbf{G}}(\mathbf{q}; \omega)$. This quantity can be measured in an electron microscope by performing a momentum-resolved electron energy loss experiment with a selected momentum transfer $\mathbf{Q} = \mathbf{q} + \mathbf{G}$.

- **The dynamic structure factor** $S(\mathbf{Q}, \omega) = -\frac{1}{\pi} \operatorname{Im} \chi_{\mathbf{G},\mathbf{G}}(\mathbf{q}, \omega)$. One can measure S as a function of energy and momentum transfer $\mathbf{Q} = \mathbf{q} + \mathbf{G}$ at a synchrotron by performing inelastic x-ray scattering (IXS).

- **The optical absorption spectrum** $\operatorname{Im} \epsilon_M(\mathbf{q}, \omega)$. Under certain conditions, it is given by the macroscopic dielectric function $\epsilon_M(\mathbf{q}, \omega) = 1/[\epsilon(\mathbf{q}, \omega)]^{-1}_{\mathbf{G}=\mathbf{G}'=0}$ in the limit of long wavelength, $\mathbf{q} \to 0$. In rather homogeneous systems, where the off-diagonal elements of the matrix $\epsilon_{\mathbf{G},\mathbf{G}'}$ are small, $\epsilon_M(\mathbf{q}, \omega) \approx \epsilon_{\mathbf{G}=\mathbf{G}'=0}(\mathbf{q}, \omega)$.

Note that ϵ^{-1} yields the screened Coulomb interaction, $W = \epsilon^{-1}\, v_c$, which is the effective interaction between classical charges in a medium. It is a key quantity in Hedin's equations and in the GW approximation to the self-energy. Both will be briefly recalled in Sec. 4.

We will now see how to calculate linear response using Green functions. Let us concentrate on the density-density response function $\chi = \delta n/\delta v_{\rm ext}$. With Eq. (8), this can be written as

$$\chi(1,2) = iG(1,\bar{3})\,\frac{\delta G^{-1}(\bar{3},\bar{4})}{\delta v_{\rm ext}(2)}\,G(\bar{4},1^+)\,, \tag{12}$$

where we have used $\delta G/\delta v = -G\,[\delta G^{-1}/\delta v]\,G$. Eq. (12) is a convenient starting point for the various approximations that we will consider in the following.
Let us first look at the case of non-interacting particles. We can apply a potential $v_{\rm ext}$ to the system and evaluate the linear response. In that case we have

$$G^{-1}[v_{\rm ext}] = G_0^{-1} - v_{\rm ext}\,, \tag{13}$$

where we have indicated explicitly that now G is a functional of $v_{\rm ext}$. Using Eq. (12) we obtain the independent-particle response function

$$\chi_0(1,2) = -iG_0(1,2)G_0(2,1^+)\,. \tag{14}$$

Because of the opposite time-ordering of the two Green functions, one of the two G_0 contributes only with a sum over occupied states v in Eq. (4), and the other one with a sum over empty states c. Altogether, using Eq. (4) for G_0, one finds the usual expression for the linear response function χ_0 of a non-interacting system, consisting of a sum over all possible transitions from occupied to empty states (the *resonant* part) and vice versa (the *anti-resonant* part):

$$\chi_0(\mathbf{r},\mathbf{r}',\omega) = \sum_{vc}\left[\frac{\psi_v^*(\mathbf{r})\,\psi_c(\mathbf{r})\;\psi_c^*(\mathbf{r}')\,\psi_v(\mathbf{r}')}{\omega-(\varepsilon_c-\varepsilon_v)-i\eta} - \frac{\psi_v(\mathbf{r})\,\psi_c^*(\mathbf{r})\;\psi_c(\mathbf{r}')\,\psi_v^*(\mathbf{r}')}{\omega+(\varepsilon_c-\varepsilon_v)+i\eta}\right]. \tag{15}$$

This *independent-particle approximation* is frequently used to describe absorption spectra. Instead, it is not at all appropriate to directly access loss spectra. The difference between absorption and loss is illustrated in Fig. 1: The left panel shows the absorption spectrum of bulk silicon, the right panel shows the imaginary part of the full density-density response function χ, as measured in electron energy loss spectroscopy at vanishing momentum transfer. The absorption spectrum rises steeply above 3 eV, which corresponds to the direct band gap. Instead, the loss spectrum has its main feature at much higher energy, around 17 eV. In order to understand how this difference comes about, let us move on and put some interaction in our system.
Suppose that we do this first on a mean-field level, by adding a potential $v_{\rm mf}$. Since this potential is supposed to stem from the interaction between all electrons, in the spirit of DFT it is reasonable to assume that it is a functional of the density, $v_{\rm mf} = v_{\rm mf}[n]$. Now we have

$$G^{-1} = G_0^{-1} - v_{\rm ext} - v_{\rm mf}[n]\,, \tag{16}$$

which leads to

$$\chi(1,2) = \chi_0(1,2) - iG(1,\bar{3})\,\frac{\delta v_{\rm mf}[n](\bar{3})}{\delta v_{\rm ext}(2)}\,G(\bar{3},1^+)\,, \tag{17}$$

where $\chi_0 = -iG\,G_{|v_{\rm ext}\to 0}$ is now built with a pair of equilibrium mean-field Green functions.

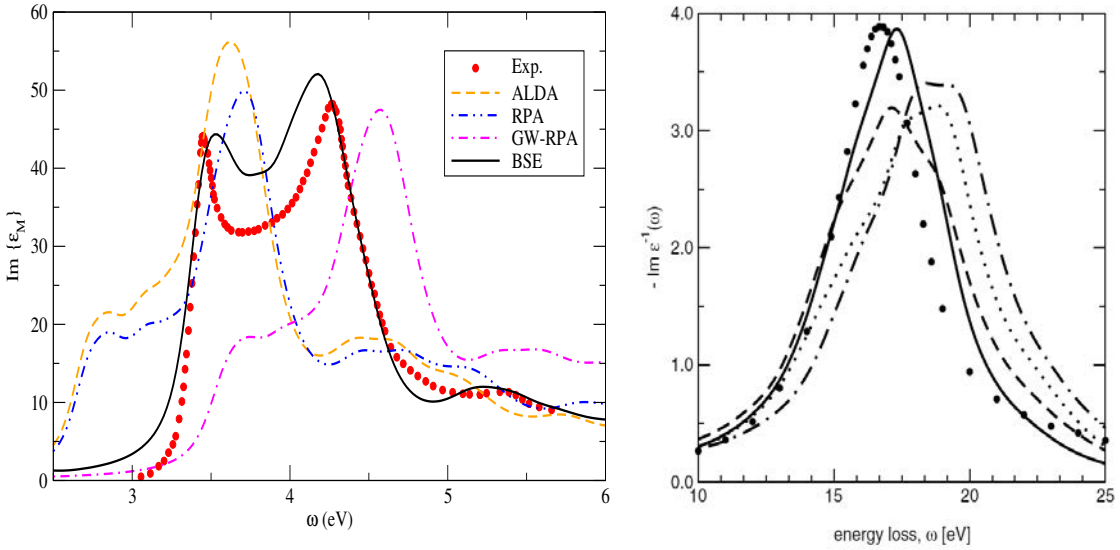

Fig. 1: *Electronic spectra of bulk silicon. Left panel: absorption spectrum* $\mathrm{Im}\,\epsilon_M(\omega)$ *(figure by Francesco Sottile; experiment from [4]). Right panel: loss spectrum for vanishing momentum transfer, from [5]. The important curves are experiment (dots), RPA (dashed), and BSE (continuous).*

Since v_{mf} is a density functional, and the density itself depends on the external potential v_{ext}, we can use a chain rule in the functional derivative, which leads to a Dyson equation for χ

$$\begin{aligned}\chi(1,2) &= \chi_0(1,2) - iG(1,\bar{3})\,\frac{\delta v_{\mathrm{mf}}[n](\bar{3})}{\delta n(\bar{5})}\,\frac{\delta n(\bar{5})}{\delta v_{\mathrm{ext}}(2)}\,G(\bar{3},1^+)\\ &= \chi_0(1,2) + \quad \chi_0(1,\bar{3})\,\frac{\delta v_{\mathrm{mf}}[n](\bar{3})}{\delta n(\bar{5})}\,\chi(\bar{5},2)\,. \end{aligned} \tag{18}$$

One important example for such a mean-field response is the time-dependent Hartree approximation, where $v_{\mathrm{mf}}[n](\mathbf{r},t) = v_H[n](\mathbf{r},t) = \int d\mathbf{r}'\, v_c(\mathbf{r}-\mathbf{r}')\,n(\mathbf{r}',t)$. In that case the functional derivative, the *kernel* of the Dyson equation, equals simply v_c, and χ_0 is built with Hartree Green functions. More generally, an approximation of the form $\chi = \chi_0 + \chi_0 v_c \chi$ for any $\chi_0 = iGG$, where G is some mean-field Green function, is called *Random Phase Approximation* (RPA). The RPA has been proposed for the homogeneous electron gas by Pines and Bohm [6–8], and it is today used in many contexts and for many materials.

The natural way to go beyond the time-dependent Hartree approximation is Time-Dependent Density-Functional Theory (TDDFT). We can do this by adding a Kohn-Sham exchange-correlation potential v_{xc} such that $v_{\mathrm{mf}} = v_H + v_{\mathrm{ext}} + v_{\mathrm{xc}}$. This potential should be a functional of the density in the whole space, and at all past times.[4] Following the same path that has led to Eq. (18) this yields

$$\chi(1,2) = \chi_0(1,2) + \chi_0(1,\bar{3})\left[\delta(t_{\bar{3}} - t_{\bar{5}})v_c(\mathbf{r}_{\bar{3}} - \mathbf{r}_{\bar{5}}) + f_{\mathrm{xc}}(\bar{3},\bar{5})\right]\chi(\bar{5},2)\,, \tag{19}$$

[4]This is a requirement of causality. TDDFT is usually formulated in a causal framework. We use mostly a time-ordered formulation in these lecture notes, because this facilitates many-body perturbation theory which is the main topic here. However, it is easy to move from one to the other, as one can see for example by comparing Eqs. (3) and (4). One only has to be careful to be consistent.

where we have defined the exchange-correlation kernel $f_{\rm xc}(3,5) = \delta v_{\rm xc}(3)/\delta n(5)$. Note that, contrary to the Hartree part, it is not instantaneous.

If the exact $v_{\rm xc}$ were known, χ from Eq. (19) would be the exact density-density response function, because the potential would yield the exact time-dependent density. However, this is not the case. Most often very simple approximations are used, such as the adiabatic local density approximation (ALDA), where $v_{\rm xc}(\mathbf{r},t)$ depends only on the density at point $\mathbf{r}$ and time t and $f_{\rm xc}(3,5)$ is therefore proportional to $\delta(t_3-t_5)\,\delta(\mathbf{r}_3-\mathbf{r}_5)$. In extended systems, the ALDA often yields results close to the RPA ones, when the same χ_0 is used. This is illustrated in the left panel of Fig. 1. The curves labeled RPA and ALDA have been obtained using LDA Green functions for G. The ALDA shows only minor modifications with respect to the RPA. Both are not very good: the Kohn-Sham gap in χ_0 underestimates the experimental gap by about 50%. This is not recovered by the RPA or ALDA kernels, so the onset of absorption is underestimated with respect to experiment. Also the lineshape differs from the measured one, since there is not enough oscillator-strength on the low-energy side, although one can still recognize a correspondence between calculated and measured spectra. The loss spectrum in the right panel, instead, is reasonably well described by the RPA.

In order to understand the difference between absorption and loss spectra, it is enough to look at the RPA, and to neglect off-diagonal elements of the matrices in reciprocal space. Then, as outlined in the beginning of this section, absorption is given approximately by

$$\mathrm{Im}\,\epsilon_{\mathbf{G}=\mathbf{G}'=0}(\mathbf{q},\omega) = -v_c(\mathbf{q})\,\mathrm{Im}\,\chi_{0,\mathbf{G}=\mathbf{G}'=0}(\mathbf{q},\omega) \quad \text{for} \quad \mathbf{q}\to 0\,,$$

whereas the loss function at vanishing momentum transfer is

$$-\mathrm{Im}\,[1/(1-v_c(\mathbf{q})\chi_{0,\mathbf{G}=\mathbf{G}'=0}(\mathbf{q},\omega))] \quad \text{for} \quad \mathbf{q}\to 0\,.$$

To first order in the Coulomb interaction the two expressions are equal. However, the Coulomb interaction is strong, and the difference is very obvious for bulk silicon in Fig. 1. As anticipated, comparison of the two panels shows that the loss function in the right panel has its main structures at much higher energies than the absorption spectrum, which is shown in the left panel. In the RPA the difference between the two only stems from the long-range Coulomb interaction v_c. This interaction causes a correlated motion of all particles as response to an external perturbation. These are long-range charge oscillations, called plasmons. They give rise to the strong peak in the loss function in Fig. 1. With $v_c(q) = 4\pi/q^2$, the Coulomb kernel is particularly important for small momentum transfer q in extended systems. It is the dominant effect in loss spectra.

At larger momentum transfer $4\pi/q^2$ is smaller, and the two kinds of spectra are more similar. The energy of the plasmon changes as a function of momentum transfer. With this plasmon dispersion, the sharp peak moves into the continuum of electron-hole transitions and decays into a broad structure. Plasmons are a broad topic, and more can be found for example in [9]. Here the important lesson to take away is that the RPA contains the physics of plasmons, because it includes the long-range variation of the Hartree potential.

The neglect of off-diagonal elements is an approximation. As Eq. (11) shows, because of scattering at the periodic crystal potential, $\epsilon_{\mathbf{G}\mathbf{G}'}$ is not diagonal, so its inversion (or, equivalently, the solution of the Dyson equation) mixes different momentum transfers. Therefore, even when one is interested in the response to a macroscopic, long-range, perturbation the system can respond with charge fluctuations on a microscopic scale. These are included in a calculation through the $\mathbf{G} \neq 0$ components of $v_c(\mathbf{q} + \mathbf{G})$. The effects of the microscopic components of v_c are called *crystal local-field effects* (LFE) [10–12]. Microscopic components of the induced Hartree potential gain in importance when the system is inhomogeneous, and when one probes shorter distances, with increased momentum transfer. In absorption spectra, only the microscopic components contribute, since the macroscopic component of v_c is eliminated by the double inversion $\epsilon_M = 1/\epsilon^{-1}$. The effect of the microscopic components (the LFE) is usually moderate in extended systems, with variations of spectra of the order of 10% or less for simple semiconductors, but they can have more important effects in systems with localized electrons, or in layered systems, which are more inhomogeneous.

The fact that the RPA contains plasmons and crystal local-field effects explains its generally good performance in describing loss spectra, the dynamic structure factor, and therefore also the screened Coulomb interaction W. The limitations of the RPA, instead, can be best detected when one looks at optical absorption in the first few eV spectral range. We have seen the example of silicon in Fig. 1 above. It is typical for simple semiconductors.

The situation is even worse for insulators, where strongly bound *excitons* can occur. Roughly speaking, excitons are due to an effective interaction between the excited electron and the hole left behind. Since these are a positive and a negative charge, similar to a hydrogen atom, the interaction can lead to bound states that are clearly detected in experimental absorption spectra. However, neither in the RPA nor in the ALDA bound excitons can be described. To date, a few exchange-correlation kernels exist that can produce bound excitons, but their reliability and/or computational efficiency are not yet satisfactory. Moreover, none of them can overcome the problem that the Kohn-Sham band gap is usually smaller than the threshold of optical absorption. This means that the kernel should shift the spectrum to higher energies, which turns out to be a very difficult task. These problems suggest to move away from density functional theory, towards Green function functional theory, using self-energies and many-body perturbation theory.

4 Self-energies and generalized response: the Bethe-Salpeter equation

In order to understand how moving to the framework of Green functions and self-energies can cure the problems of approximate density functionals, we can look at the simplest approximation to the self-energy, the Fock exchange operator Σ_{x}.

Let us start with the band gap. In Hartree-Fock (HF) we have Koopmans' theorem, which states that HF eigenvalues equal electron removal and addition energies, expressed as Hartree-Fock

total energy differences. Since relaxation is not included in this framework, the HF band gap is in general much too large compared to experiment. For example, in silicon the direct HF gap is almost 9 eV, whereas the experimental value is about 3 eV (see Fig. 2).
Let us now try to calculate the HF response function using, again, Eq. (12). From Eq. (5) the equivalent to Eq. (16) is

$$G^{-1} = G_0^{-1} - v_{\rm ext} - v_H - \Sigma_{\rm x}\,. \tag{20}$$

Strictly speaking, like v_H also the exchange self-energy $\Sigma_{\rm x}$ is a functional of the density. However, its explicit form is not known, maybe not existent or at best non-analytic. Instead, we know $\Sigma_{\rm x}(1,2)$ as a functional of the one-body spin-resolved density *matrix* $\rho(1,2) = -iG(x_1.t_1;x_2,t_1^+)$; it is $\Sigma_{\rm x}(1,2) = -\delta(t_1^+ - t_2)\,v_c(\mathbf{r}_1-\mathbf{r}_2)\,\rho(1,2)$. Let us now try to follow the lines of Eq. (18) while using ρ instead of the density n in the chain rule for $\Sigma_{\rm x}$. This yields

$$\chi(1,2) = \chi_0(1,2) + \chi_0(1,\bar{3})\delta(t_{\bar{3}}-t_{\bar{5}})v_c(\mathbf{r}_{\bar{3}}-\mathbf{r}_{\bar{5}})\chi(\bar{5},2) + \chi_0^{\rm nl}(1;\bar{4},\bar{3})\frac{\delta\Sigma_{\rm x}[\rho](\bar{3},\bar{4})}{\delta\rho(\bar{6},\bar{5})}\chi_{\rm nl}(\bar{6},2,\bar{5}), \tag{21}$$

where we have defined the three-point response functions

$$\chi_0^{\rm nl}(1;4,3) \equiv -iG(1,3)G(4,1^+) \qquad \text{and} \qquad \chi_{\rm nl}(6,2,5) \equiv \frac{\delta\rho(6,5)}{\delta v_{\rm ext}(2)}\,. \tag{22}$$

The additional non-locality in $\chi_0^{\rm nl}$ stems from the non-locality of $\Sigma_{\rm x}$ and is not problematic. Instead, the functional derivative with respect to the non-local density matrix creates a problem: Eq. (21) is not a closed equation for the desired $\chi(1,2)$. In order to obtain a closed equation, we have to generalize the equation to make it fully three-point, by looking from the very start at $\delta\rho(1,1')/\delta v_{\rm ext}(2)$. With $\delta\Sigma_{\rm x}[\rho](3,4)/\delta\rho(6,5) = -\delta(t_3^+ - t_4)\,\delta(3,6)\,\delta(4,5)\,v_c(\mathbf{r}_3-\mathbf{r}_4)$ and carrying out the same steps as before, this leads to

$$i\chi_{\rm nl}(1,2,1') = G(1,2)\,G(2,1') + G(1,\bar{3})\,G(\bar{4},1')\,i\Xi_{H{\rm x}}(3,5,4,6)\,\chi_{\rm nl}(\bar{6},2,\bar{5})\,, \tag{23}$$

where the kernel of this Dyson equation reads

$$i\Xi_{H{\rm x}}(3,5,4,6) \;\equiv\; i\,\frac{\delta\Sigma_{H{\rm x}}(3,4)}{\delta G(6,5)} \;=\; \delta(3,4)\,\delta(5,6)\,v_c(3,5) - \delta(3,6)\,\delta(4,5)\,v_c(3,4)\,, \tag{24}$$

and $v_c(1,2)$ includes the δ-function in time. This is now a closed equation for the response of the spin-resolved density *matrix*. In order to obtain the desired density response, one has *first to solve* for the density matrix response, and *then* use the fact that by definition $\chi(1,2) = \chi_{\rm nl}(1,2,1)$.[5] Note that G are now HF Green functions at $v_{\rm ext}=0$. Indeed, Eq. (23) is the linear response in the time-dependent Hartree Fock (TDHF) approximation.
Fig. 2 shows the result for bulk silicon, taken from [13]. The dots are the experimental spectrum, the same as in Fig. 1. At the far right of the figure, the dot-dashed curve represents $\mathrm{Im}\,\chi_0$ built with HF Green functions. Since the HF gap is almost 9 eV, the result is far off experiment.

[5] For the response of the total density one also has to sum over spin.

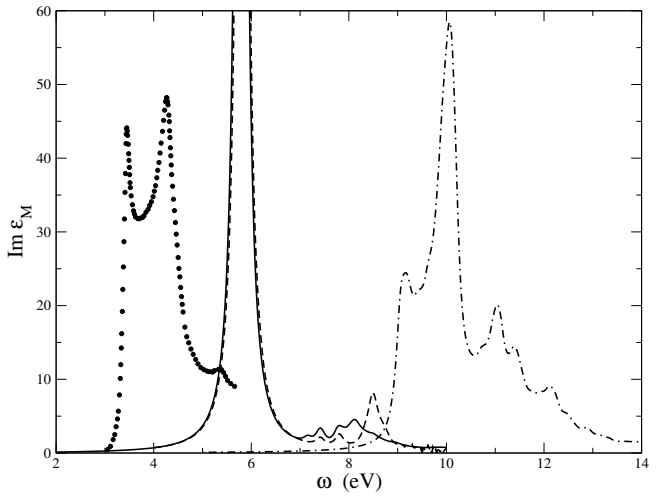

Fig. 2: *Absorption spectrum of bulk silicon in the TDHF approximation, from [13]. Dots: experiment. Dot-dashed curve: independent-particle spectrum using Hartree-Fock ingredients. Continuous curve: TDHF result.*

Instead, the kernel Ξ_{Hx} used in Eq. (23) has a dramatic effect: the spectrum becomes sharper and moves to lower energies, recovering more than half of the discrepancy to experiment. This very important effect is due to the second part of Ξ_{Hx}, the derivative of Σ_x. The effect of the first part is a shift of spectral weight to higher energies, but it is very small since, as explained earlier, only the microscopic part of the variation of the Hartree potential contributes to the final absorption spectrum.
The TDHF case contains almost everything we need to understand the Bethe-Salpeter equation:

- A Dyson equation for the density-matrix response has to be solved in order to obtain the density response.
- The starting χ_0 has a gap that can be interpreted as a difference between electron addition and removal energies. This is called the quasi-particle gap, and it is the gap that would be measured for example in direct and inverse photoemission.
- The variation of the Hartree potential is the same as in the RPA. Its effect on absorption spectra is moderate (whereas it is responsible for plasmons that are seen in loss spectra).
- The variation of the Fock exchange moves the spectrum to lower energies. Its effect is strong. We find now spectral weight within the quasi-particle gap: this means that we have a bound exciton. In other words, the variation of the exchange is responsible for the electron-hole attraction.

All this might seem to be meaningless, since what judges a theory at the end is agreement with experiment – and TDHF visibly does less well than the simple RPA based on an LDA G shown in Fig. 1! However, the problem of HF is clear: it is the absence of screening (or more generally formulated, of correlation), which makes band gaps too large, and interactions too strong. The

introduction of screening, even in relatively simple ways, brings remarkable improvement. For example, hybrid functionals include screening in a effective way by adding a fraction of Fock exchange to local Kohn-Sham potentials. Moving from time-dependent HF to time-dependent hybrid-functional calculations leads to very decent absorption spectra in semiconductors, as has been shown for example in [14].

A more systematic way to introduce screening is to get better self-energies $\Sigma_{\rm xc}$ instead of $\Sigma_{\rm x}$ from many-body perturbation theory. We will do this in the next section; here we will conclude by generalizing Eq. (23) to a form that is usually called the *Bethe-Salpeter equation* (BSE).

The BSE describes a generalized response, where a non-local (in space, spin and time) "potential" is applied to the system, and the variation of the Green function, instead of its equal-time limit (the density matrix) is determined. Moreover, since now we are heading for a more general self-energy, we can no longer suppose that it is known as functional of the density matrix; instead, we will have approximations that are explicit functionals of the Green function. With this is mind, all steps can be carried out in close analogy to the derivation of the TDHF equations. With the definition

$$L(1,2,1',2') \equiv \frac{\delta G(1,1')}{\delta v_{\rm ext}(2',2)} \tag{25}$$

we find the Bethe-Salpeter equation [15]

$$L(1,2,1',2') = L_0(1,2,1',2') + L_0(1,\bar{3}',1',\bar{3})\,\Xi(\bar{3},\bar{2},\bar{3}',\bar{2}')\,L(\bar{2}',2,\bar{2},2')\,, \tag{26}$$

with

$$\Xi(\bar{3},\bar{2},\bar{3}',\bar{2}') \equiv -i\delta(\bar{3},\bar{3}')\,\delta(\bar{2}',\bar{2})\,v_c(\bar{3},\bar{2}) + \frac{\delta\Sigma_{\rm xc}(\bar{3},\bar{3}')}{\delta G(\bar{2}',\bar{2})}\,. \tag{27}$$

The uncorrelated $L_0(1,2,1',2') = G(1,2')\,G(2,1')$ contains the Green function G, solution of the Dyson equation

$$G(1,2) = G_0(1,2) + G_0(1,\bar{3})\,\Sigma(\bar{3},\bar{4})\,G(\bar{4},2)\,. \tag{28}$$

This is analogous to Eq. (5), with $\Sigma_{H\rm x}$ replaced by the full self-energy $\Sigma = v_H + \Sigma_{\rm xc}$.

From the definition of L in Eq. (25) it follows that

$$\chi(1,2) = -iL(1,2;1^+,2^+)\,; \tag{29}$$

as in the case of TDHF, χ can only be obtained after solving the full BSE for L.

The four-point function L is a two-particle correlation function. One can calculate it formally from Eq. (25), starting from a one-body Green function G in the presence of an external potential. The derivation is delicate since the potential can be non-local in time [16], but the result is qualitatively intuitive: the applied potential contributes $v_{\rm ext}\,\psi^\dagger\,\psi$ to the time evolution in the Heisenberg picture. The derivative of $G = -i\langle N|{\rm T}\left[\hat{\psi}\,\hat{\psi}^\dagger\right]|N\rangle$ with respect to $v_{\rm ext}$ leads therefore to an expression with four field operators. It is closely linked to the two-particle Green function

$$G_2(1,2,1',2') = (-i)^2\,\langle T\left[\hat{\psi}(1)\,\hat{\psi}(2)\,\hat{\psi}^\dagger(2')\,\hat{\psi}^\dagger(1')\right]\rangle\,, \tag{30}$$

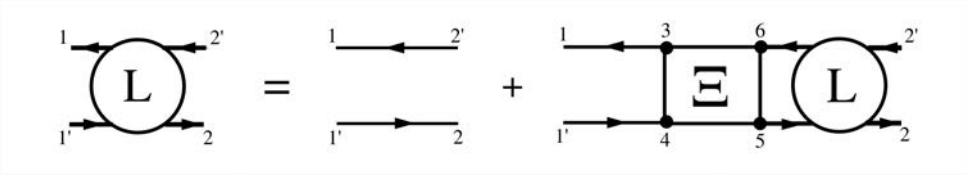

Fig. 3: *The Bethe Salpeter equation for the propagation of an electron-hole pair.*

via

$$L(1,2,1',2') = -G_2(1,2,1',2') + G(1,1')\,G(2,2')\,. \tag{31}$$

The two-particle correlation function, and therefore the BSE, contain much more than just the density-density response function, which is the small part given by Eq. (29). In particular, the order of times is crucial to select different pieces of physics, since it determines the order of the four field operators. In the density-density response this order alternates ψ and $\psi^\dagger$, which means that electron-hole pairs are described. Alternatively, the order can be for example $\psi^\dagger\psi^\dagger\psi\psi$: this describes the propagation of two holes. Also various combinations of spin-resolved response can be described. We will not delve into these subjects, but it should be clear that, given the general Bethe-Salpeter equation, these problems can be treated in strict analogy to the electron-hole case. The BSE for the propagation of an electron-hole pair is expressed graphically by the diagrams in Fig. 3.

The time structure of the BSE is a particular complication. The quantities that appear in the BSE depend on four time arguments, which corresponds in equilibrium to three time differences, or three frequencies in the Fourier transform. With the definition of the time differences [17]

$$\tau_2 = t_1 - t_{1'}, \quad \tau_3 = t_2 - t_{2'}, \quad \tau_1 = \frac{1}{2}\left[(t_1 + t_{1'}) - (t_2 + t_{2'})\right] \tag{32}$$

and of the Fourier transform

$$C(t_1,t_2,t_{1'},t_{2'}) = \frac{1}{(2\pi)^3}\int d\bar\omega_1\, d\bar\omega_2\, d\bar\omega_3\; C(\bar\omega_1,\bar\omega_2,\bar\omega_3)\, e^{-i\bar\omega_1\tau_1}\, e^{-i\bar\omega_2\tau_2}\, e^{-i\bar\omega_3\tau_3}, \tag{33}$$

the frequency structure of the BSE (26) is [18]

$$L(\omega_1,\omega_2,\omega_3) = L_0(\omega_1,\omega_2,\omega_3) + \frac{L_0(\omega_1,\omega_2,\bar\omega_4)}{(2\pi)^2}\,\Xi(\omega_1,\bar\omega_4,\bar\omega_5)\,L(\omega_1,\bar\omega_5,\omega_3)\,. \tag{34}$$

The definitions are not unique, and the only requirement is to be consistent. With the present choice, τ_2 and τ_3 are differences in the time where the electron and the hole are considered, and τ_1 is the average time of propagation. In frequency space the density-density response from Eq. (29) reads

$$\chi(\omega) = \frac{1}{(2\pi)}\int d\omega_2\; L(\omega,\omega_2) = \frac{1}{(2\pi)^2}\int d\omega_2\, d\omega_3\; L(\omega,\omega_2,\omega_3)\,, \tag{35}$$

where we have used the same symbol L for the integrated function that depends only on two frequencies.

Since ω_3 appears as a dummy index in Eq. (34), it can be integrated before the equation is solved. The new equation reads

$$L(\omega_1,\omega_2) = L_0(\omega_1,\omega_2) + \int d\omega_4\, d\omega_5\ \frac{L_0(\omega_1,\omega_2,\omega_4)}{(2\pi)^2}\, \Xi(\omega_1,\omega_4,\omega_5)\, L(\omega_1,\omega_5)\,, \tag{36}$$

with

$$L_0(\omega_1,\omega_2) = -iG(\omega_2+\frac{\omega_1}{2})\, G(\omega_2-\frac{\omega_1}{2})\,. \tag{37}$$

If one performs also the integration over ω_2 in Eq. (36), one runs into a problem similar to the density response in HF, namely, the equation is no longer of closed form. Therefore, one has to solve Eq. (36) and only subsequently perform the integration.

5 The Bethe-Salpeter equation from the GW approximation

At this stage, we have everything in hand to calculate the response function starting from an arbitrarily complicated self-energy. The task is hence to find a good approximation for Σ, beyond $\Sigma_{H\mathrm{x}}$. We have already anticipated that the most important missing ingredient for our purpose is screening. The task of the present section is to put this hand-waving argument on a more rigorous basis. A widely used approach is diagrammatic expansions in the framework of many-body perturbation theory. Here we take another (though strictly analogous) way, which is closer to the spirit of this lecture about linear response. There is no space for a detailed derivation; more can be found in the book [19], which we closely follow here.
From the definition (6) of the Green function one can derive its equation of motion

$$G(1,1') = G_0(1,1') + G_0(1,\bar{2})\, v_H(\bar{2})\, G(\bar{2},1') + iG_0(1,\bar{2})\, v_c(\bar{2},\bar{3})\, L(\bar{2},\bar{3}^+,1',\bar{3}^{++})\,. \tag{38}$$

It expresses the fact that the propagation of a particle in a system of many electrons equals the propagation of a single particle, modified by the classical electrostatic (Hartree) potential of all electrons, the Fock exchange that is contained in the last term (and that can be obtained with the approximation $L \approx L_0$), and correlation effects such as the reaction of the other electrons, which is expressed by the fact that L is related to a variation of G via Eq. (25).
We can now transform Eq. (38) into a Dyson equation by using Eq. (25) and the trick $\delta G/\delta v = -G\,[\delta G^{-1}/\delta v]\,G$. This defines a self-energy $\Sigma = v_H - iv_cG\,[\delta G^{-1}/\delta v_{\mathrm{ext}}]$. Moreover, we can introduce screening by using the chain rule $\delta/\delta v_{\mathrm{ext}} = [\delta/\delta v_{\mathrm{cl}}][\delta v_{\mathrm{cl}}/\delta v_{\mathrm{ext}}]$, where $v_{\mathrm{cl}} \equiv v_{\mathrm{ext}} + v_H$. With this choice, $\delta v_{\mathrm{cl}}/\delta v_{\mathrm{ext}} = \epsilon^{-1}$, which makes the screened Coulomb interaction $W = \epsilon^{-1}\, v_c$ appear. Altogether, these manipulations lead to a set of equations known as *Hedin's equations*:

$$\begin{aligned}
\Sigma_{\mathrm{xc}}(1,2) &= iG(1,\bar{4})\, W(1^+,\bar{3})\, \tilde{\Gamma}(\bar{4},2;\bar{3}) && (39)\\
W(1,2) &= v_c(1,2) + v_c(1,\bar{3})\, P(\bar{3},\bar{4})\, W(\bar{4},2) && (40)\\
P(1,2) &= -iG(1,\bar{3})\, G(\bar{4},1)\, \tilde{\Gamma}(\bar{3},\bar{4};2) && (41)\\
\tilde{\Gamma}(1,2;3) &= \delta(1,2)\,\delta(1,3) + \frac{\delta\Sigma_{\mathrm{xc}}(1,2)}{\delta G(\bar{4},\bar{5})}\, G(\bar{4},\bar{6})\, G(\bar{7},\bar{5})\, \tilde{\Gamma}(\bar{6},\bar{7};3) && (42)\\
G(1,2) &= G_0(1,2) + G_0(1,\bar{3})\, \Sigma(\bar{3},\bar{4})\, G(\bar{4},2)\,. && (43)
\end{aligned}$$

These equations contain

- the *irreducible polarizability* P, Eq. (41). It is the response of the density to the total classical perturbation $v_{\rm cl}$. It is linked to χ via $\chi = P + P\, v_c\, \chi$. When the *vertex function* $\tilde{\Gamma}$ is set to 1, P describes non-interacting electron-hole pairs: this is the RPA. Otherwise, $\tilde{\Gamma}$ contains the information that the two particles interact. The equation for $\tilde{\Gamma}$ can be transformed into a BSE for the irreducible part $\tilde{L}$ (the generalization to four points of P) of L by integrating with two Green functions, or into the BSE (26) for L by including the Hartree potential.

- The *screened interaction* W is different from the bare v_c when the system is polarizable, i.e., P is not zero. It is dynamical, which means, frequency-dependent, because of the frequency-dependence of P.

- The *vertex function* $\tilde{\Gamma}$ also appears in the self-energy: it corrects for the fact that W is the screened interaction between classical charges, whereas the system particles are fermions. Moreover, P is the polarizability of all electrons, including the one that should be screened. This self-screening error is removed by the $\tilde{\Gamma}$ in the self-energy.

- Variations of the self-energy, in turn, determine the vertex function. Similarly to the bare Coulomb interaction, which is a first derivative of the Hartree potential, $\delta\Sigma_{\rm xc}/\delta G$ plays the role of an effective exchange-correlation interaction.

The GW approximation consists in setting $\tilde{\Gamma}$ to 1 everywhere. This means that W is calculated in the RPA, and $\Sigma = iGW$. This approximation is exactly what we have been heading for: it is a sort of dynamically screened Hartree-Fock. Contrary to Hartree-Fock, the GW self-energy is not instantaneous, because W depends on a time difference.
The Dyson equation for G in Hedin's equations is the only equation that exhibits the external potential via the non-interacting G_0. The other equations are universal, and can be used to create expressions for the quantity of interest with increasing accuracy. Typically one starts with a guess, like $\Sigma_{\rm xc} = 0$, and from this calculates $\tilde{\Gamma}$, P, W, and then again $\Sigma_{\rm xc}$ as functional of G. This yields expressions with terms of higher orders in W. The formulae become increasingly complex, and one cannot go too far. However, at least one update of W has become a standard ingredient in the toolbox of condensed matter calculations: in a first step $\tilde{\Gamma} = 1$, which yields the RPA for P and W and the GW approximation for $\Sigma_{\rm xc}$. Then $\tilde{\Gamma}$ is recalculated. This can be transformed into a BSE (26) for L, with $\Xi_{\rm xc} = \delta\Sigma_{\rm xc}^{GW}/\delta G$. The resulting kernel reads

$$\Xi_{xc}^{GWA}(1,2,3,4) = i\delta(1,4)\,\delta(2,3)\,W(1,2) + iG(1,3)\,\frac{\delta W(1,3)}{\delta G(4,2)}\,. \tag{44}$$

The first term is very similar to $\Xi_{\rm x}$ of time-dependent Hartree-Fock, but now it is screened. The diagrams for the contribution to $\Xi_{H{\rm xc}}$ that contains only the variation of the Hartree potential and this first term are shown in Fig. 4.
The second term is of higher order in W [20], and it goes beyond the linear response of the electrons to an added charge: the screened interaction itself changes when the system is perturbed.

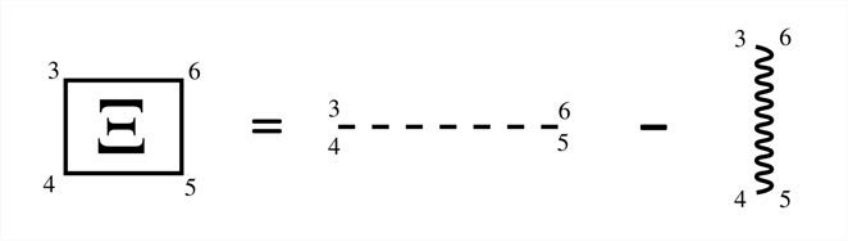

Fig. 4: *Kernel of the GW-BSE, as explained in the text. The dashed line is the electron-hole exchange interaction that stems from the variation of the Hartree potential. The wiggly line represents the direct electron-hole attraction. It is depicted with a minus sign in order to stress the fact that it is attractive.*

Usually this term is neglected, both because it is of higher order, and, very pragmatically, because it would be much more cumbersome to calculate. It has not been investigated very much, but there has been no strong evidence to date that it would be crucial to include it. Therefore, one usually sets

$$\Xi_{\rm xc}^{GW}(\omega_1,\omega_2,\omega_3) \approx iW(\omega_2-\omega_3)\,. \tag{45}$$

Here we can see a major difference to TDHF: since the GW self-energy is not instantaneous, the BSE cannot be solved frequency by frequency. From Eq. (36), the coupling of frequencies reads

$$L(\omega_1,\omega_2) = L_0(\omega_1,\omega_2) + \frac{1}{2\pi}L_0(\omega_1,\omega_2)\int d\bar{\omega}_3\,[v_c - W(\omega_2-\bar{\omega}_3)]\,L(\omega_1,\bar{\omega}_3)\,. \tag{46}$$

This looks very annoying. However, it should be noted that also L_0 has acquired a non-trivial frequency dependence: the Green functions that yield $L_0 = GG$ are now GW ones, which means, they are no longer of an independent-particle type but have a complicated spectral function, where weight is transferred from the quasi-particle to satellites. If the remaining quasi-particle weight is $Z < 1$ (let us say, 0.7), a transition between quasi-particle peaks would show up in the spectrum of L_0 with weight Z^2 [21] (which would yield a weight reduction by a factor of 1/2). This, however, is not what is observed. The reason is that these *dynamical effects* in L_0 cancel to a large extent with the dynamical effects in $\Xi_{\rm xc}^{GW}$ [22]. Therefore, in realistic calculations most often the Green functions G in L_0 are replaced by quasi-particle ones with weight $Z = 1$, and the frequency dependence of W in $\Xi_{\rm xc}^{GW}$ is neglected. Besides the fact that the quasi-particle G's are usually derived as an approximation from the fully frequency dependent GW self-energy, one might call the resulting method "linear-response time-dependent screened Hartree-Fock".

Now one can integrate ω_2 in Eq. (46), and the GW-BSE becomes

$$\begin{aligned} L(x_1,x_2,x_{1'},x_{2'};\omega) \;=\;& L_0(x_1,x_2,x_{1'},x_{2'};\omega) \\ & - iL_0(x_1,\bar{x}_3,x_{1'},\bar{x}_3;\omega)\,v_c(\bar{x}_3,\bar{x}_4)\,L(\bar{x}_4,x_2,\bar{x}_4,x_{2'};\omega) \\ & + iL_0(x_1,\bar{x}_4,x_{1'},\bar{x}_3;\omega)\,W(\bar{x}_3,\bar{x}_4)\,L(\bar{x}_3,x_2,\bar{x}_4,x_{2'};\omega)\,. \end{aligned} \tag{47}$$

This equation still exhibits all spin arguments. The spin structure of $\Xi^{GW}_{H\mathrm{xc}}$ is

$$\Xi^{GW}_{\sigma_3\sigma_2\sigma_{3'}\sigma_{2'}} = -i\delta_{\sigma_3\sigma_{3'}}\,\delta_{\sigma_{2'}\sigma_2}\,v_c + i\delta_{\sigma_3\sigma_{2'}}\,\delta_{\sigma_{3'}\sigma_2}\,W. \tag{48}$$

In spin space, the equation can be decoupled into singlet and triplet contributions [2]. In a spin-unpolarized material and without a spin-dependent interaction the result is

$$\begin{aligned} L^{singlet} &= L_0 + iL_0\,[W - 2v_c]\,L^{singlet} \\ L^{triplet} &= L_0 + iL_0\;W L^{triplet}. \end{aligned} \tag{49}$$

As we can see, the variation of the Hartree potential enters with a factor of two in the singlet, whereas it is absent in the triplet. This difference causes the so-called singlet-triplet splitting. In the following we concentrate on singlets, which can be optically allowed.

6 A two-body Schrödinger equation

There are various ways to solve the BSE (47), for example, by iterative inversion. For small (less than 100 electrons) systems sometimes the equation is transformed into the form of an effective two-particle Hamiltonian that is then diagonalized. This is interesting, because it suggests a simple physical interpretation. To obtain this form, we first write the equation in the basis of the orthonormal orbitals $\psi_n(\mathbf{r})$ that diagonalize G_0, and therefore L_0, which reads

$$L_{0n_1n_3}^{n_4n_2}(z) = 2i\frac{(f_{n_1} - f_{n_2})\,\delta_{n_1n_4}\delta_{n_2n_3}}{z - (\varepsilon_{n_1} - \varepsilon_{n_2})}\,, \tag{50}$$

where z is a complex frequency containing the appropriate infinitesimal imaginary part, f are occupation numbers, and spin has been summed. We also define interaction matrix elements as

$$v_{n_1n_3}^{n_4n_2} = \int d\mathbf{r}_1\,d\mathbf{r}_2\;\psi^*_{n_1}(\mathbf{r}_1)\,\psi_{n_4}(\mathbf{r}_1)\;v(\mathbf{r}_1,\mathbf{r}_2)\;\psi_{n_3}(\mathbf{r}_2)\,\psi^*_{n_2}(\mathbf{r}_2)\,, \tag{51}$$

for both v_c and W. This transforms the BSE into

$$L_{n_1n_3}^{n_4n_2}(z) = [L_0^{-1} + \frac{i}{2}\Xi]^{-1}{}_{n_1n_3}^{n_4n_2} = 2i\,[H^{2p} - \mathbb{I}\,z]^{-1}{}_{n_1n_3}^{n_4n_2}(f_{n_2} - f_{n_4}) \tag{52}$$

with $\mathbb{I}$ the identity matrix. Here we have defined the *effective two-particle Hamiltonian* H^{2p}

$$H^{2p}{}_{n_1n_3}^{n_4n_2} \equiv (\varepsilon_{n_2} - \varepsilon_{n_1})\,\delta_{n_1n_4}\delta_{n_2n_3} + (f_{n_1} - f_{n_3})\,\Xi_{n_1n_3}^{n_4n_2}\,, \tag{53}$$

where

$$\Xi_{n_1n_3}^{n_4n_2} \equiv 2v_c{}_{n_1n_4}^{n_3n_2} - W_{n_1n_3}^{n_4n_2}\,. \tag{54}$$

Optical transitions happen between occupied and empty states. Therefore the only combination of indices that is needed in a non-metal at $T = 0$ is couples of occupied and empty states, which means, we only need terms of the form

$$\Xi_{v\,c}^{v'c'} = 2v_c{}_{vv'}^{cc'} - W_{v\,c}^{v'c'}\,. \tag{55}$$

As we can see, the variation of the Hartree potential gives rise to a dipole-dipole interaction, called *electron-hole exchange*. The variation of the GW self-energy, instead, is called *direct electron-hole interaction*, since it contains the interaction between the charge densities of electrons and holes.

The full two-particle Hamiltonian is only pseudo-hermitian [23], because of the coupling between resonant ($v \to c$) and anti-resonant ($c \to v$) transitions. In the Tamm–Dancoff approximation (TDA) [24, 25, 3], this coupling is neglected. This is often a very good approximation for optical spectra of bulk materials [26]. It is more critical for finite systems [23]. One also has to be careful when calculating loss spectra [5], because they are influenced by the long-range part of v_c, which gives rise to strong coupling. For simplicity, in the following we give expressions in the TDA; the appropriate formula for the pseudo-hermitian full case can be found for example in [27, 19].

To perform BSE calculations in practice, one first determines W and the quasi-particle band structure, typically from a GW calculation. With this, the two-particle Hamiltonian H^{2p} is built using the expressions above. The next step is its diagonalization,

$$\sum_{n_3 n_4} H^{2p\, n_3 n_4}_{\quad n_1 n_2} A^{n_3 n_4}_\lambda = E_\lambda A^{n_1 n_2}_\lambda . \tag{56}$$

In the TDA, the retarded L is then built from

$$L^{n_3 n_4}_{n_1 n_2}(\omega) = 2i \sum_\lambda \frac{A^{n_1 n_2}_\lambda A^{* n_3 n_4}_\lambda}{\omega - E_\lambda \ + i\eta} (f_{n_4} - f_{n_3}) \, . \tag{57}$$

Each couple (nn') corresponds to a pair (vc) of an occupied and an empty state. In the absence of electron-hole interaction, each eigenstate $A^{*n_1 n_2}_\lambda$ would correspond to a given electron-hole pair, $A^{vc}_\lambda = \delta_{v v_\lambda} \delta_{c c_\lambda}$, and the transition energy would be $\varepsilon_c - \varepsilon_v$. Instead, when the electron-hole interaction is switched on, one can no longer associate a transition λ with one independent-quasiparticle transition (vc): transitions are mixed by the interaction. Note that this already occurs when only the variation v_c of the Hartree potential is considered, i.e., in the RPA: the self-consistent response of the electron system, even on a classical electrostatic level, has non-trivial effects. Of course, the interaction also affects the transition energies, which are now E_λ instead of $\varepsilon_c - \varepsilon_v$.

In a solid and for vanishing momentum transfer $\mathbf{q} \to 0$, the resonant part of the independent-particle retarded response function reads

$$\chi^0_{00}(\mathbf{q} \to 0, \omega) = 2 \sum_{vc\mathbf{k}} \frac{|\tilde{\rho}_{v\mathbf{k}c}|^2}{\omega - (\varepsilon_{c\mathbf{k}} - \varepsilon_{v\mathbf{k}}) + i\eta} \, , \tag{58}$$

where the $\tilde{\rho}$ are dipole transition matrix elements between quasi-particle states. Instead, with all the above approximations the result obtained from the BSE is

$$\chi_{00}(\mathbf{q}, \omega) = 2 \sum_\lambda \frac{|\sum_{vc\mathbf{k}} A^{v\mathbf{k}c}_\lambda \tilde{\rho}_{v\mathbf{k}c}|^2}{\omega - E_\lambda + i\eta} \, . \tag{59}$$

Again we can see the mixing of transitions induced by the eigenstates A_λ of the BSE two-particle Hamiltonian, and the modification of transition energies. Note that this expression yields directly the optical spectra, if the long-range ($\mathbf{G} = 0$) contribution to v_c is omitted in the BSE.

Let us now illustrate and analyze the BSE with two examples. We will concentrate on the effect of the direct electron-hole interaction W, since the contribution v_c has been discussed earlier in the framework of the RPA.

The first example is the optical absorption of bulk silicon. The modest performance of the RPA and the ALDA has been shown in the left panel of Fig. 1, and the crucial need for screening was illustrated by the TDHF results in Fig. 2. The pink dot-dashed curve in the left panel of Fig. 1 is GW-RPA, which means, the GW-BSE is solved by neglecting W in the kernel. Since now the starting band structure is the GW one, the spectrum is at higher energies than the RPA or ALDA ones. However, it is now too much displaced to higher energies. On the other hand, since screening is included, the overshooting is not as drastic as in HF in Fig. 2. The GW-BSE results including W in the kernel are given by the continuous black curve: it shows very good agreement with experiment, both concerning position and spectral shape.

One might wonder why there is any effect of W at all in bulk silicon, since its dielectric constant is about $\epsilon_M \approx 12$, so screening is very strong, and W should be small. Indeed, a closer analysis shows that the transition *energies* are almost unchanged with respect to the GW-RPA ones. It should be noted that in infinite systems transition energies do not change to first order in W, because the first order is given by the diagonal of the matrix, which tends to zero for an infinitely dense $\mathbf{k}$-point sampling, so for small W no effect on energies should be expected. The coefficients A_λ, instead, can change already to first order, since matrix elements are summed in the first order correction to eigenstates. Moreover, in the first-order perturbation correction to states, matrix elements appear in the numerator, and differences between zero-order transition energies in the denominator. The bandstructure of silicon shows almost parallel bands in large portions of the Brillouin zone, and has therefore many independent-particle transitions at similar energies. This makes the denominator small and creates a strong effect of the electron-hole interaction, even though the numerator is small because W is so strongly screened. The shift to lower energies of spectral weight in the optical spectrum of silicon is hence a pure interference effect.

On the opposite side, we find large gap insulators or low-dimensional systems with weak screening. In this case even the transition energies can be strongly affected. In particular, W is an attractive interaction, because here W is the interaction between an electron and a hole. This leads to new transition energies within the quasi-particle gap: these are the energies of bound excitons. The difference between the transition energy and the quasi-particle gap is called *exciton binding energy*. It can be as large as several eV.

Indeed, when one approximates the band structure by two parabolic bands, calculates the matrix element of W using plane waves for the orbitals, and replaces sums over $\mathbf{k}$-points in the Brillouin zone by integrals over the whole $\mathbf{k}$-space, the GW-BSE takes the form of a Schrödinger equation for the hydrogen atom, with a modified electron and proton mass and a screened

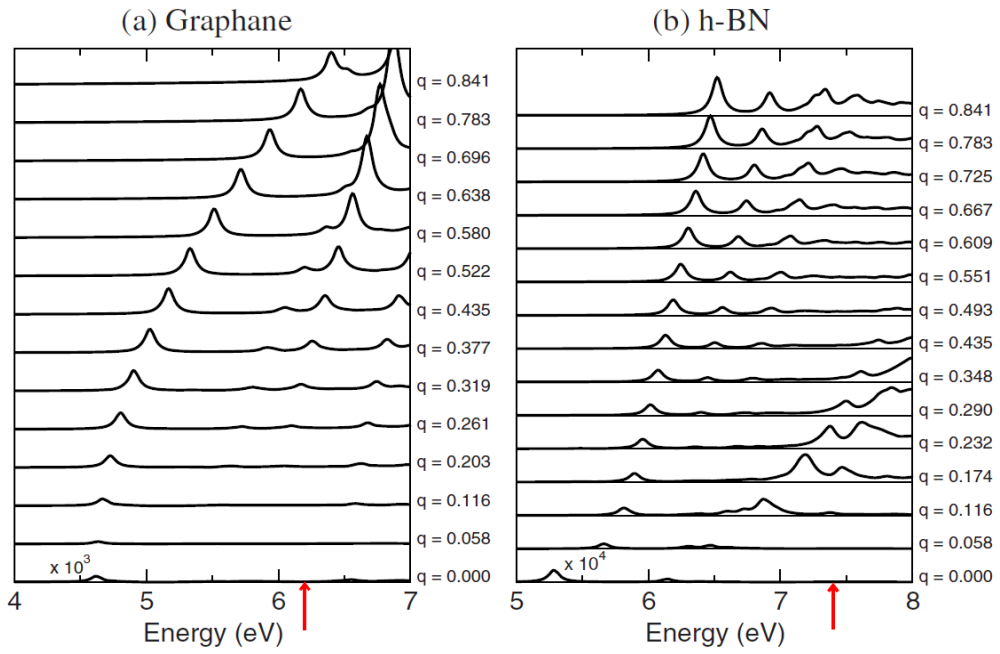

Fig. 5: *Excitonic spectra* $q^2 \,\mathrm{Im}\,\epsilon_M(\mathbf{q},\omega)$ *in graphane (left) and a hexagonal BN sheet (right), for various momentum transfers* $\mathbf{q}$ *along the* Γ-M *direction, indicated on the right side in* $\mathring{A}^{-1}$. *The quasi-particle band gap is shown by the red arrow. From [28].*

Coulomb interaction. This is the Wannier model for excitons, which predicts Rydberg series of bound electron-hole states for three-dimensional solids. It works surprisingly well for not too strongly bound excitons, and can yield reasonable results even for binding energies in the eV range. For even stronger bound excitons, where the onsite interaction dominates, the Frenkel model is more appropriate; it can also be derived from the GW-BSE (see [19]).
As an example for bound excitons, Fig. 5 shows $q^2 \,\mathrm{Im}\,\epsilon_M(\mathbf{q},\omega)$ for graphane (a hydrogenated graphene sheet, left panel) and one layer of hexagonal boron nitride (right panel). In both cases, important structures are found within the quasi-particle band gap, which is indicated by the red arrow. Binding energies are larger than one eV in both cases. The different nature of the excitons in these two materials can be inferred from their dispersion: the bound exciton in graphane changes its position in a parabolic way, whereas in h-BN the dispersion is rather linear, after a first, more rapid, rise. This is discussed in [28].

7 Excitons and correlation

In the context of these lecture notes, it is interesting to comment about various aspects of correlation concerning excitons. Here we would like to concentrate on two points:

- Excitons are strongly correlated electron-hole pairs.
- The BSE contains cancellation effects between self-energy corrections and electron-hole interaction. These can be particularly important in correlated materials with localized electrons.

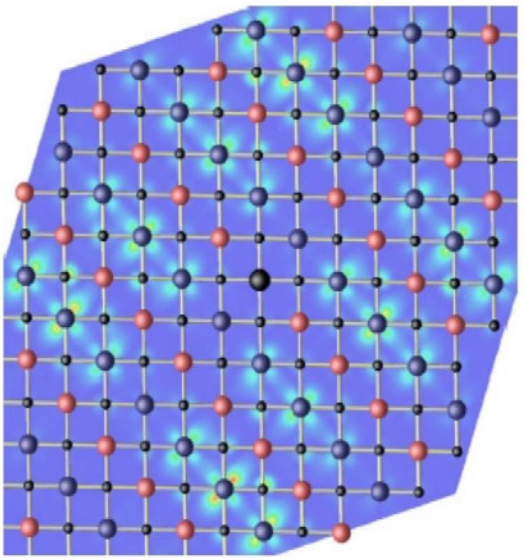

Fig. 6: *Excitonic effects in MnO, from [29]. Distribution of spin-up density in the (001) plane for an excitation at 5.2 eV. The position of the hole is indicated by the large black ball in the center. Light red balls represent Mn atoms with occupied $3d$ spin-up orbitals and dark blue balls are Mn atoms with occupied $3d$ spin-down orbitals. Oxygen atoms are indicated by small black balls.*

To illustrate the first point, it is enough to look at the exciton wavefunction. It is a superposition of products of the wavefunctions of the single electrons and holes, determined by the coefficients A_λ

$$\Psi_\lambda(\mathbf{r}_e, \mathbf{r}_h) = \sum_{v\mathbf{k}c} A_\lambda^{v\mathbf{k}c}\, \psi^*_{v\mathbf{k}}(\mathbf{r}_e)\psi_{c\mathbf{k}}(\mathbf{r}_h)\,. \tag{60}$$

This is a correlated two-particle wavefunction: in order to know the probability distribution of the electron, one has to fix the position of the hole, and vice versa.

Let us look at such a wavefunction, for the example of the magnetic material MnO [29]. Its antiferromagnetic ordering consists of alternating planes of occupied spin-up and spin-down Mn $3d$ orbitals. In order to visualize the charge density of an excited electron, one has to chose the excitation energy, and the position of the hole. In Fig. 6, which is taken from [29], the excitation energy corresponds to a peak in the absorption spectrum at 5.2 eV. For the hole position one usually chooses an occupied orbital; here the hole is fixed on an Mn atom where the spin-up orbital is occupied. Because of the dipole transition rules, a spin-up electron is excited from an occupied to an empty spin-up orbital. This determines the distribution that is observed in Fig. 6.

Surprisingly, the picture in Fig. 6 breaks translational invariance, since the exciton extends over several unit cells. How is this possible? The reason is that we had to fix the position of the hole, because of the electron-hole correlation. However, the probability to find the hole in a given unit cell is periodic, so overall translational invariance is respected.

Let us now come to the second point anticipated above, cancellations. To get an idea, think of a single electron. Even if you excite it, there should be no interaction effects – there is no other electron to interact with. However, the BSE starts with L_0, in other words, with a difference of electron addition and removal. In the addition process the system gets two electrons: now there *is* interaction! This spurious effect has to be removed by the electron-hole interaction. In a solid with delocalized electrons some cancellation is seen (look for example at silicon in the left panel of Fig. 1), but it is far from complete; otherwise, we would never need the BSE. However, when electrons are localized, and especially at low density, in a certain sense one comes closer to the regime of single electrons, and cancellations are more important. Therefore in these materials sometimes the RPA evaluated with Kohn-Sham wavefunctions gives surprisingly decent excitation spectra, for example in transition metal oxides like V_2O_3 [30].

There are many more aspects of optical or loss spectra in the BSE that one might want to address; more can be found for example in [19]. However, one should not forget that the BSE yields in principle the full two-particle correlation function, and more information can be gained from it. Applications such as the calculation of correlated two-hole states [31, 32], or total energies [33], promise an increasingly broad horizon for people interested in the Bethe-Salpeter equation.

References

[1] B. A. Lippmann and J. Schwinger, Phys. Rev. **79**, 469 (1950)

[2] F. Bechstedt: *Many-Body Approach to Electronic Excitations, Concepts and Applications* Springer Series in Solid-State Sciences, Vol. 181 (Springer, Heidelberg, 2015)

[3] A. L. Fetter and J. D. Walecka: *Quantum Theory of Many-particle Systems* (McGraw-Hill, New York, 1971)

[4] P. Lautenschlager, M. Garriga, L. Vina, and M. Cardona, Phys. Rev. B **36**, 4821 (1987)

[5] V. Olevano and L. Reining, Phys. Rev. Lett. **86**, 5962 (2001)

[6] D. Bohm and D. Pines, Phys. Rev. **82**, 625 (1951)

[7] D. Pines and D. Bohm, Phys. Rev. **85**, 338 (1952)

[8] D. Bohm and D. Pines, Phys. Rev. **92**, 609 (1953)

[9] G. Giuliani and G. Vignale: *Quantum Theory of the Electron Liquid* (Cambridge University Press, Cambridge, U.K., 2005)

[10] V. Ambegaokar and W. Kohn, Phys. Rev. **117**, 423 (1960)

[11] S.L. Adler, Phys. Rev. **126**, 413 (1962)

[12] N. Wiser, Phys. Rev. **129**, 62 (1963)

[13] F. Bruneval, F. Sottile, V. Olevano, and L. Reining, J. Chem. Phys. **124** (2006)

[14] J. Paier, M. Marsman, and G. Kresse, Phys. Rev. B **78**, 121201 (2008)

[15] E.E. Salpeter and H.A. Bethe, Phys. Rev. **84**, 1232 (1951)

[16] R. van Leeuwen, N.E. Dahlen, and A. Stan, Phys. Rev. B **74**, 195105 (2006)

[17] G. Strinati, Rivista del Nuovo Cimento **11**, 1 (1988)

[18] P. Romaniello, D. Sangalli, J.A. Berger, F. Sottile, L.G. Molinari, L. Reining, and G. Onida, J. Chem. Phys. **130** (2009)

[19] R.M. Martin, L. Reining, and D.M. Ceperley: *Interacting Electrons: Theory and Computational Approaches* (Cambridge University Press, 2016)

[20] A. Schindlmayr and R.W. Godby, Phys. Rev. Lett. **80**, 1702 (1998)

[21] R. Del Sole and R. Girlanda, Phys. Rev. B **54**, 14376 (1996)

[22] F. Bechstedt, K. Tenelsen, B. Adolph, and R. Del Sole, Phys. Rev. Lett. **78**, 1528 (1997)

[23] M. Gruning, A. Marini, and X. Gonze, Nano Lett. **9**, 2820 (2009)

[24] I. Tamm, J. Phys. (USSR) **9**, 449 (1945)

[25] S.M. Dancoff, Phys. Rev. **78**, 382 (1950)

[26] S. Albrecht, L. Reining, R. Del Sole, and G. Onida, Phys. Rev. Lett. **80**, 4510 (1998)

[27] G. Onida, L. Reining, and A. Rubio, Rev. Mod. Phys. **74**, 601 (2002)

[28] P. Cudazzo, L. Sponza, C. Giorgetti, L. Reining, F. Sottile, and M. Gatti, Phys. Rev. Lett. **116**, 066803 (2016)

[29] C. Rödl, F. Fuchs, J. Furthmüller, and F. Bechstedt, Phys. Rev. B **77**, 184408 (2008)

[30] F. Iori, F. Rodolakis, M. Gatti, L. Reining, M. Upton, Y. Shvyd'ko, J.-P. Rueff, and M. Marsi, Phys. Rev. B **86**, 205132 (2012)

[31] Y. Noguchi, S. Ishii, K. Ohno, I. Solovyev, and T. Sasaki, Phys. Rev. B **77**, 035132 (2008)

[32] Y. Noguchi, S. Ishii, and K. Ohno, J. Chem. Phys. **125** (2006)

[33] E. Maggio and G. Kresse, Phys. Rev. B **93**, 235113 (2016)

11 Optical Properties of Correlated Electrons

Dirk van der Marel
Department of Quantum Matter Physics
Université de Genève
Quai Ernest-Ansermet 24, CH-1211 Genève 4

Contents

E. Pavarini, E. Koch, J. van den Brink, and G. Sawatzky (eds.)
Quantum Materials: Experiments and Theory
Modeling and Simulation Vol. 6
Forschungszentrum Jülich, 2016, ISBN 978-3-95806-159-0
http://www.cond-mat.de/events/correl16

1 Introduction

Optical spectroscopy is one of the most versatile spectroscopic techniques of condensed matter physics [1]. It can be used to study lattice vibrations, electronic excitations, electronic collective modes of materials and can be readily applied in the presence of magnetic fields, high pressure, low or high temperatures. Optical spectrometers exist for almost any wavelength band of the electromagnetic spectrum and span from radio-waves through THz, visible, UV to X-rays. By virtue of a high control and reproducibility various different kinds of calibration techniques permit to obtain precise absolute numbers for the constants characterizing the optical spectra of a material. This state of affairs is further improved by advances in the past decade permitting the direct measurement of the amplitude and phase of reflected signals in the THz band of the spectrum.

Many possible experimental configurations giving access to the intrinsic optical constants of materials are nowadays routinely used, including transmission, absorption, reflection, ellipsometry, and combinations thereof. We will not dwell on all these different techniques here, but give two simple examples and continue with a short summary of how from measured optical data one obtains the fundamental properties such as optical conductivity and dielectric function. If a ray of light is reflected from the surface of a material with an angle θ relative to the surface normal, the two orthogonal types of polarization of the electric field (see Fig. 1) are (i) perpendicular to the plane of reflection ("senkrecht" in German) indicated as s-polarization, and (ii) perpendicular to the plane of reflection indicated as p-polarization. For an isotropic material the reflection coefficients for these two geometries are provided by Fresnel's laws

$$r_s = \frac{\cos\theta - \sqrt{\epsilon - \sin^2\theta}}{\cos\theta + \sqrt{\epsilon - \sin^2\theta}} \quad \text{and} \quad r_p = \frac{\epsilon\cos\theta - \sqrt{\epsilon - \sin^2\theta}}{\epsilon\cos\theta + \sqrt{\epsilon - \sin^2\theta}}\,. \tag{1}$$

Note that these reflection coefficients are complex numbers. Experimentally one can measure the intensity $R = |r|^2$ of a reflected signal quite easily, but obtaining the phase is often much more difficult. One of the solutions consists of doing a so-called "ellipsometry" experiment, whereby the state of elliptical polarization of a light-ray is measured after reflection, where the incident ray is linearly polarized with a polarization being a linear superposition of s- and p-polarization. We will not dwell on the details here, but the important thing is, that this provides the ratio r_p/r_s which now *is* a complex number. An alternative method is to take advantage of the fact that $\ln r = \ln\sqrt{R} + i\phi$ where $\phi = \mathrm{Arg}(r)$, and that $\ln\sqrt{R(\omega)}$ and $\phi(\omega)$ satisfy

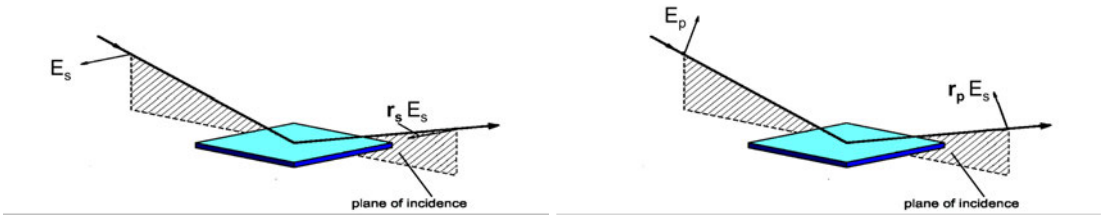

Fig. 1: *Left (right): Geometry for the reflection of s (p) polarized light.*

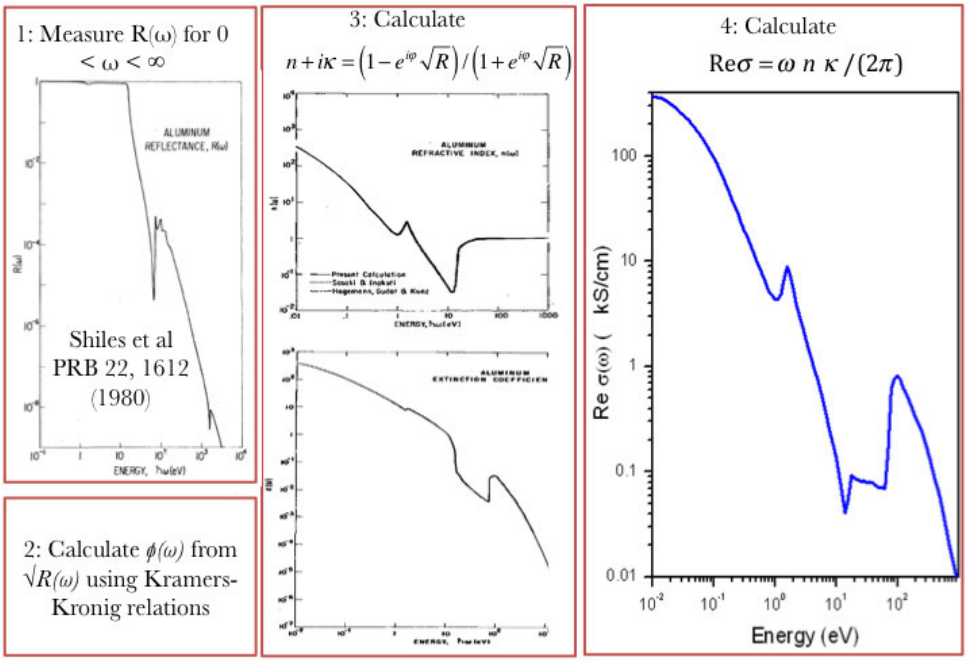

Fig. 2: *The four steps of calculating the optical conductivity from a reflectivity spectrum using the example of aluminum (after Ref. [2]).*

Kramers-Kronig relations. It is then sufficient to measure $R(\omega)$ in a sufficiently broad spectral range, in order to calculate also $\phi(\omega)$, and from these two together obtain the real and imaginary part of ϵ. This constitutes the first of the four steps providing the optical conductivity function indicated in Fig. 2 for the example of aluminum. The second is to invert the Fresnel expression for the reflection coefficient at the given angle of incidence and polarization of the light, giving as a first step the index of refraction, $n = \mathrm{Re}\,\sqrt{\epsilon}$ and the extinction coefficient $\kappa = \mathrm{Im}\,\sqrt{\epsilon}$, and from there the optical conductivity

$$\sigma(\omega) = \frac{\omega}{4\pi i}\,[\,\epsilon(\omega) - 1\,]\,. \tag{2}$$

The optical conductivity is one of the most commonly used parameters to describe the electromagnetic response. Macroscopically, the frequency dependent conductivity tensor $\sigma(\omega)$ constitutes a natural extension to the DC electrical conductivity relating electric field and current density: $\vec{j} = \sigma\vec{E}$, where $\vec{j}$ and $\vec{E}$ are the macroscopic current density and electric field components. In what follows we will assume that $\vec{j}$ and $\vec{E}$ are parallel to one of the axes of the conductivity tensor $\sigma(\omega)$, and drop explicit tensor and vector notation to keep the notation as light as possible. On the microscopic level $\sigma(\omega)$ is proportional to the current-current correlation function

$$\sigma(\omega) = \frac{e^2}{\omega V}\left\{\frac{iN}{m} + \int_0^\infty dt e^{i\omega t}\langle\psi|\,[\hat{\jmath}(t), \hat{\jmath}(0)]\,|\psi\rangle\right\}, \tag{3}$$

where N is the number of electrons, V the volume, m and e the electron mass and charge, and $\hat{\jmath}(t) = e^{iHt/\hbar}\,\hat{\jmath}\,e^{-iHt/\hbar}$ is the velocity operator. The time integral can be carried out explicitly,

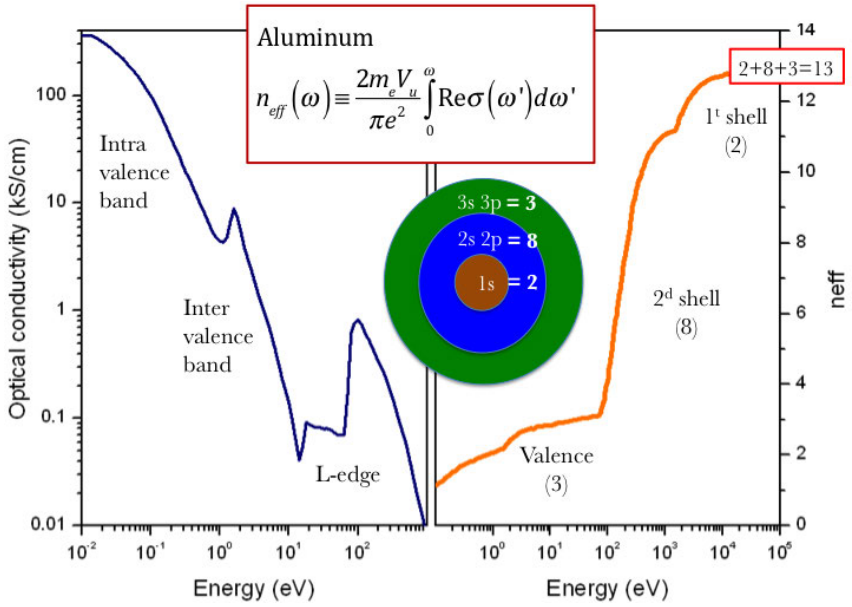

Fig. 3: *Illustration of the f-sum rule for the case of aluminum (after Ref. [2]).*

providing for the real part of the conductivity of a system in thermal equilibrium

$$\mathrm{Re}\,\sigma(\omega) = \frac{\pi e^2}{V} \sum_{\mu\nu} (Z_\nu - Z_\mu) \frac{\langle\nu|\hat{\jmath}|\mu\rangle\langle\mu|\hat{\jmath}|\nu\rangle}{E_\mu - E_\nu} \delta(\hbar\omega + E_\nu - E_\mu)\,, \tag{4}$$

where $|\eta\rangle$ is a many-body eigenstate with energy E_η and Z_η is the statistical probability to find the system in this state (the "partition function"). Integration of both sides over ω yields

$$\int_{-\infty}^{\infty} \mathrm{Re}\,\sigma(\omega)d\omega = \frac{2\pi e^2}{V} \sum_{\mu,\nu} Z_\nu \frac{\langle\nu|\hat{\jmath}|\mu\rangle\langle\mu|\hat{\jmath}|\nu\rangle}{E_\mu - E_\nu}\,. \tag{5}$$

Using $\hat{H}|\nu\rangle = E_\nu|\nu\rangle$ and $\hat{\jmath} = i\hbar^{-1}[\hat{H}, \hat{x}]$ one can show in a few steps that

$$\int_{-\infty}^{\infty} \mathrm{Re}\,\sigma(\omega)\,d\omega = \frac{\pi e^2}{i\hbar V} \langle[\hat{\jmath}, \hat{x}]\rangle\,. \tag{6}$$

At this point we can substitute on the right hand side the following useful property of the many-body current and position operators: $[\hat{\jmath}, \hat{x}] = i\hbar N/m$. We take advantage of the fact that for a time-reversal symmetric situation $\mathrm{Re}\,\sigma(\omega) = \mathrm{Re}\,\sigma(-\omega)$, so we can restrict to positive frequencies and arrive at the so-called f-sum rule

$$\int_0^{\infty} \mathrm{Re}\,\sigma(\omega)\,d\omega = \frac{\pi e^2 n}{2m}. \tag{7}$$

This f-sum rule, or Thomas Reich Kuhn (TRK) rule, is one of the most powerful tools in optical studies of materials. It relates the integrated optical conductivity directly to the density of charged objects, and the absolute value of their charge and mass.

In Fig. 3 the f-sum rule is illustrated by the earlier example of the aluminum: The right hand panel shows the partial integral

$$n_{\mathrm{eff}}(\omega) = \frac{2m_e V_u}{\pi e^2} \int_0^{\omega} \mathrm{Re}\,\sigma(\omega')\,d\omega'. \tag{8}$$

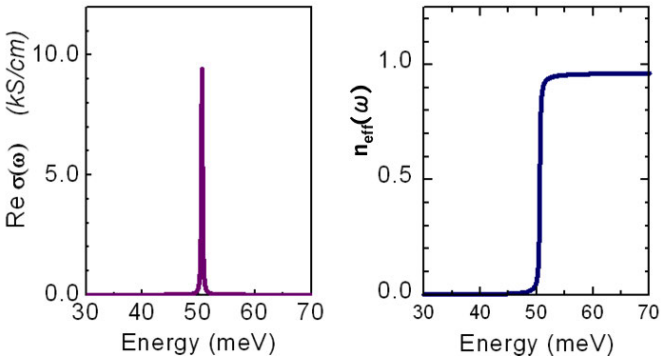

Fig. 4: *Optical conductivity and partial sumrule for the optical phonon spectrum of MgO.*

First of all it demonstrates that in the limit $\omega \to \infty$ the number $n_{\rm eff}$ approaches 13, which is exactly the number of electrons (core and valence together) per aluminum atom. Moreover, the function $n_{\rm eff}(\omega)$ rises in a number of steps: The first step from 0 to 2 eV gives approximately two electrons, from 2 to 100 eV yields an additional one, from 100 to 1000 eV adds 8 more, and above 1000 eV a final pair of electrons is added. We see, that the number of electrons in a given shell is recovered in the optical transitions from the corresponding shell to the empty states above the Fermi energy, revealing in the present example the configuration $1s^2 2s^2 2p^6 3s^1 3p^2$ (where the labels $3s$ and $3p$ are not to be taken literally in view of the lattice surrounding each Al atom). The plot also gives an impression of the scale over which one has to integrate in order to detect the spectral weight of the valence electrons: The full spectral weight corresponding to the three valence electrons is retrieved only at $\hbar\omega \approx 50$ eV.

Of course the nuclei also contribute to the f-sum rule. We left this point out of consideration until now since it usually plays a minor role, but it becomes important when analyzing the vibrational spectra of insulating materials. The f-sum rule accounting for all types of particles j with charge e_j, mass m_j and density n_j in the sample reads

$$\mathrm{Re}\int_0^\infty \sigma(\omega)\,d\omega = \sum_j \frac{\pi e_j^2 n_j}{2m_j}\,. \tag{9}$$

In Fig. 4 we show the infrared optical conductivity of the insulator MgO together with the partial sum-rule integral

$$n_{\rm eff}(\omega) = \frac{2V_u}{\pi(2e)^2(m_O^{-1}+m_{Mg}^{-1})}\int_0^\omega \mathrm{Re}\,\sigma(\omega')\,d\omega' \tag{10}$$

to illustrate that masses and charges of the Mg^{2+} and O^{2-} ions account for the spectral weight of the optical phonons. Note, however, that the spectral weight having to do with the nuclear masses is tiny as compared to the electrons. The electronic part contains some 5 orders of magnitude more spectral weight, but is not visible on this scale since the spectral range shown here is far below the band gap of this insulating material.

To provide some representative examples of the optical spectra of strongly correlated metals and insulators, we close this section with the optical spectra of the rare-earth nickelates $RNiO_3$, where R is a trivalent rare-earth ion. These transition metal compounds display a phase tran-

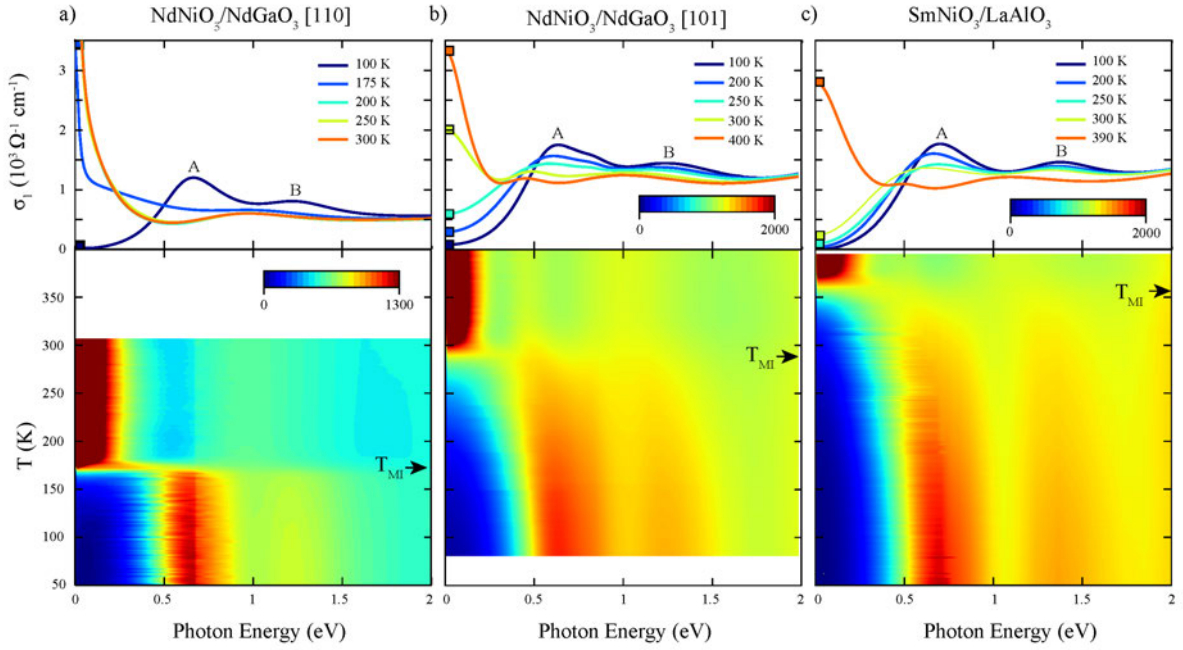

Fig. 5: *Real part of the optical conductivity for selected temperatures and energy/temperature color maps of samples (a) $NdNiO_3$/$NdGaO_3$-110, (b) $NdNiO_3$/$NdGaO_3$-101, and (c) $SmNiO_3$/$LaAlO_3$-001. Metal-insulator phase transitions are indicated by arrows on the color maps. A and B designate two peaks in the insulating phase (reproduced from Ref. [3]).*

sition between a high-temperature metallic phase and low-temperature insulating phases (paramagnetic or magnetic). This transition is highly sensitive to changing the rare-earth ion R, as well as structural constraints and strain. This could find applications to switches or to the recently proposed piezoelectric transistors. Furthermore strain-control can be used in order to 'orbital engineer' the nickelates, stabilizing the $d_{x^2-y^2}$ component of the e_g doublet at the expense of the d_{z^2} one. If full orbital polarization could be reached, this would lead to a 'single-band' material, with an electronic structure very similar to that of a cuprate, and hence possibly to high-temperature superconductivity. A single active band is favorable because of: (i) the absence of competing orbital fluctuations and (ii) importantly, the large antiferromagnetic superexchange expected in this case. Fig. 5 shows the energy dependence (upper panels) and energy/temperature color maps (lower panels) of the real part of the optical conductivity for three differently strain- and composition-tuned samples. In the insulating state, at low temperatures, the dominant features of the optical conductivity are two peaks at 0.6 (A) and 1.4 eV (B) for all three samples. Upon increasing the temperature and passing through the insulator-metal transition, the peaks vanish and a broad 1 eV peak along with a weak feature at 0.5 eV for samples (b) and (c) appear instead. Formation of free carriers is clearly visible with the growth of a zero energy mode in the optical conductivity for $\hbar\omega = 1$ eV (Fig. 5) as well as a sign change in the real part of the dielectric function.

The physics as to why this transition takes place is quite interesting and has been discussed in a number of recent papers. Here we quote the discussion in Ref. [3]: "Dynamical mean-field

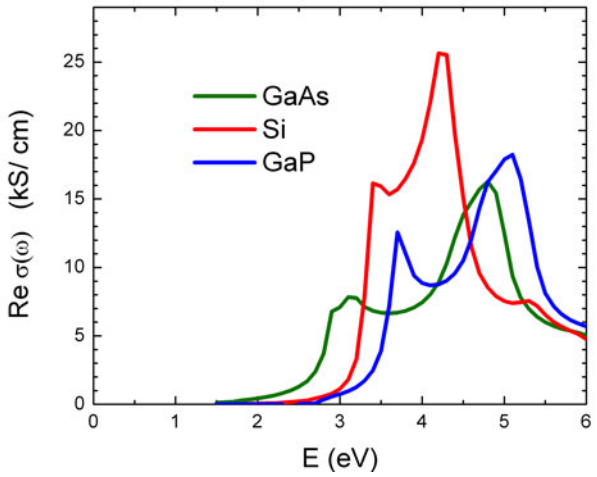

Fig. 6: *Optical conductivity of the semiconductors GaAs, Si, and GaP (after Ref. [4])*

theory calculations confirm aforementioned two-peak structure and allow us to identify these spectral changes and the associated changes in the electronic structure. We demonstrate that the insulating phase in these compounds and the associated characteristic two-peak structure are due to the combined effect of bond disproportionation and Mott physics associated with half of the disproportionated sites. We also provide insights into the structure of excited states above the gap."

2 Insulators and excitons

The example of $RNiO_3$ of the previous chapter is perhaps somewhat untypical in that the material owes its insulating gap, at least in part, to a many-body effect. In a standard semiconducting material such as GaAs the optical absorption is understood to arise from the optical excitation of individual electrons across the band gap, resulting in optical spectra such as displayed in Fig. 6. However, in many insulating materials additional absorption is observed for energies smaller than the gap, for reasons having nothing to do with impurities. The reason why this happens has to do with a fundamental issue related to the interactions between the electrons, and this shows up already when one is trying to excite a single electron. Naively one may be tempted to assume that, left by itself, a single electron should not suffer much influence of many-body effects, but this is nonetheless not justified. The problem is, that in an optical process one always creates an electron along with a hole, and these two particles interact, in fact, quite strongly. As a result, provided the electron and hole are not too far apart from each other, can (and do) form bound states, better known as excitons. The physics of excitons has much in common with that of the hydrogen atom, or rather of positronium, since both the electron and the hole have about the same mass. The fact that their masses are different coming from the fact that the electron is in the band above the gap, and the hole in the band below the gap, and the dynamical masses in these bands are usually different. The theory of exciton bound states is rather well developed. We provide a few key elements here.

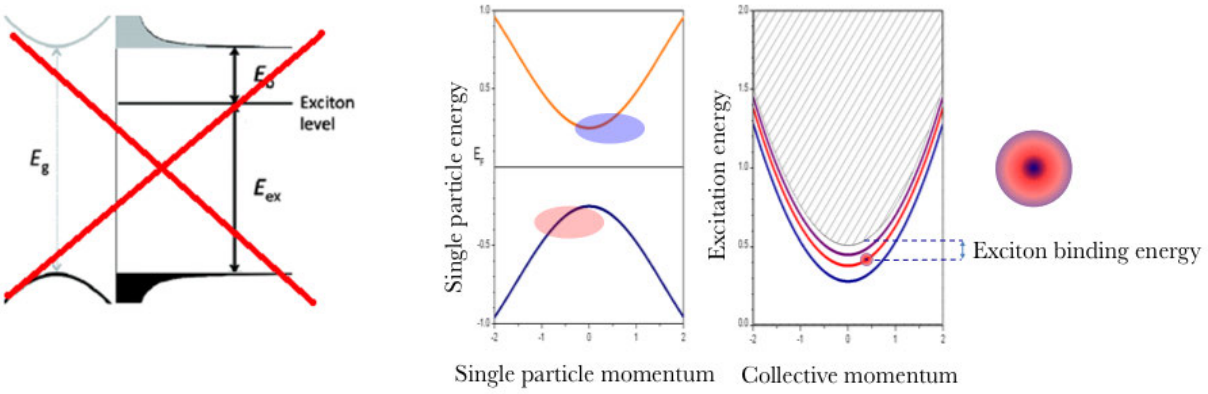

Fig. 7: *Left: incorrect way to plot the energy of an exciton. Middle panel: Sketch of the single electron dispersion curves of a direct gap insulator. Right-hand panel: Electron-hole excitation continuum corresponding to the bandstructure of the middle panel (shaded) and sketch over several "flavors" of excitons in the gap. The red and blue blobs in the middle panel indicate roughly the envelope of momentum-values involved in creating an exciton bound state with finite momentum of the collective center-of-mass coordinate.*

Quite frequently excitons are plotted in the band structure, in the way shown in the left-hand panel of Fig. 7. The difficulty is, that excitons are neutral excitations, they are bosonic, carry spin $S = 0$ or $S = 1$. Since the band-structure graph shows the energies and momenta of single-electron states, there is no unambiguous way to draw an exciton in such a diagram, and if one thinks a bit longer about the problem one realizes that by doing so one misses some important aspects of the excitonic states related to the many-body nature of these excitations, having far-reaching consequences. The middle and right-hand graphs illustrate how, as a first step, one associates electron-hole continua with a given momentum-transfer (note that only one dimension of momentum space is shown, the additional dimensions extend the number of electron-hole states for a given value of their collective momentum q shown in the right-hand panel). The electron-hole attractive Coulomb interaction can pull one or several excitonic bound states out of the continuum for any given value of q.
In the simplest description the excitons are described by the two-particle Hamiltonian

$$\begin{aligned} H &= \frac{P_{coll}^2}{2M} + \frac{p_{rel}^2}{2\mu} - \frac{e^2}{\epsilon r_{rel}} \\ M &= m_e + m_h \qquad (11) \\ \mu^{-1} &= m_e^{-1} + m_h^{-1} \qquad (12) \end{aligned}$$

so that the energies of the combined electron-hole states are described by

$$\begin{aligned} \text{Continuum states:} \quad & E_{cnt} = E_{gap} + \frac{\hbar^2 q^2}{2M} + \frac{\hbar^2 k^2}{2\mu} \\ \text{Bound states:} \quad & E_{bnd} = E_{gap} + \frac{\hbar^2 q^2}{2M} - \frac{Ry^*}{n^2} \qquad (13) \\ \text{Effective Rydberg:} \quad & Ry^* = \frac{\mu e^4}{2\epsilon^2 \hbar^2} \; . \qquad (14) \end{aligned}$$

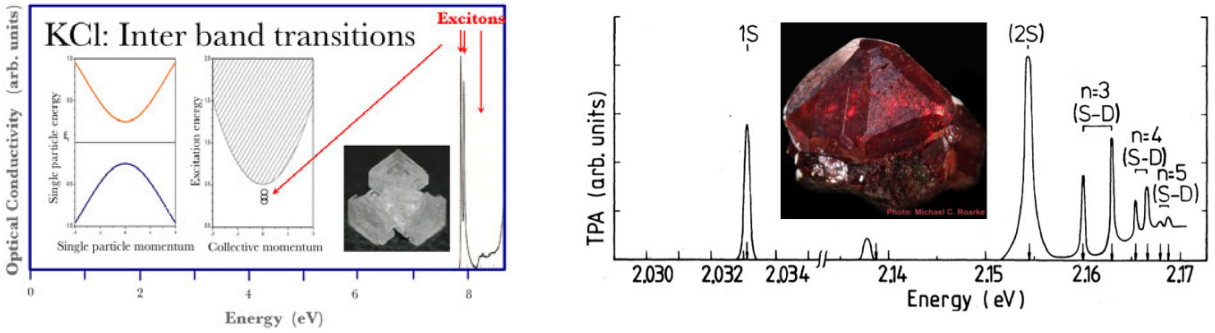

Fig. 8: *Electron-hole gap and excitonic bound states of KCl [5] and Cu_2O [6] .*

In Fig. 8 two examples are shown of simple insulating materials, with clear excitonic spectra. The left-hand graph is of KCl, having a gap of 8.5 eV, the right one of Cu_2O with a gap of and 2.17 eV. However, the single-particle bandstructure of these materials is not really described by free electron and hole parabolas, and moreover ϵ has non-trivial momentum dependence, hence the predictions of Eq. (14) can not be expected to be overly accurate, but they can provide a ballpark estimate. Indeed, the observed deepest ($n = 1$) exciton binding energies of about 0.3 eV for KCl and 0.1 eV for Cu_2O are in the right ballpark estimated from the $q = 0$ dielectric constants $\epsilon \sim 5$ for KCl, and $\epsilon \sim 7$ for Cu_2O.

Even more extreme cases of deeply bound excitons occur in Mott-Hubbard insulators, provided there is some orbital degeneracy. This is the case in, for example, $CuGeO_3$ [7] and in NiO [8,9]. In both these materials the on-site Coulomb repulsion splits apart the one-electron-removal- and one-electron-addition-states close to the Fermi-energy, with an energy separation of about 8 eV. This, in fact, pushes the one-electron removal states below the occupied oxygen band, so that the observed correlation-induced gap corresponds to the charge transfer from oxygen to Cu in the former and oxygen to Ni in the latter example. These gaps are several eV large (see Fig. 9), but a much less energy-costly excitation is possible whereby the electron-hole pair stays on the same copper or nickel site! This happens by exciting the electron from its ground state orbital

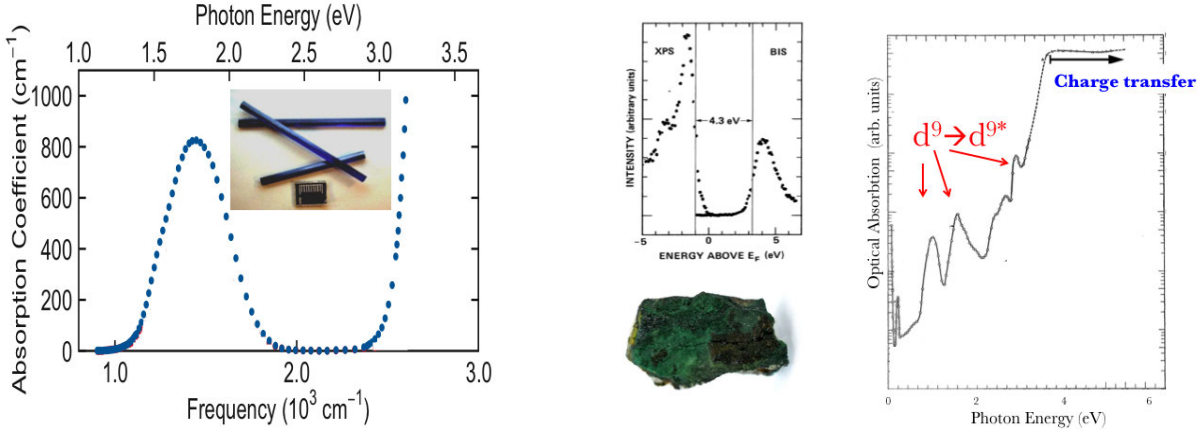

Fig. 9: *Optical spectra of the charge-transfer insulators $CuGeO_3$ [7] and NiO [8, 9], demonstrating bound neutral excitations deep inside the correlation gap.*

in the $3d$ shell to an unoccupied one. Since the electron-hole attractive interaction is of the same order as the Hubbard U, this kind of excitations (which go under the name crystal-field excitation or orbital excitation) lives deep inside the Hubbard gap. In the case of $CuGeO_3$ it gives rise to a single peak at 1.8 eV, while the charge transfer gap is about 3.1 eV. In NiO the orbital degeneracy is larger, so that a series of several peaks is observed at 1, 1.5, and 2 eV, deep inside the charge transfer gap of 4 eV.

3 Superconductors and plasmons

According to BCS theory the superconducting ground state can be described by the wavefunction

$$\begin{aligned} |\Psi_{BCS}\rangle &= \prod_k \left(u_k + v_k c^\dagger_{k,\uparrow} c^\dagger_{-k,\downarrow}\right)|0\rangle \\ |u_k|^2 + |v_k|^2 &= 1 \\ 2u_k v_k &= \frac{\Delta_k}{\sqrt{\xi_k^2 + |\Delta_k|^2}} \end{aligned} \tag{15}$$

where Δ_k is the superconducting gap. One of the most obvious and widely reported optical phenomena in a superconductor is the BCS gap. An example is shown in Fig. 10 for the conventional s-wave superconductor NbN [10].

However, in the context of superconductivity in the cuprates a number of additional effects related to superconductivity has been discovered. Here we will discuss some of these: c-axis kinetic-energy driven superconductivity has been proposed within the context of inter-layer tunneling, and has been extensively discussed in a large number of papers [11–15]. One of the main reasons to suspect that superconductivity was c-axis kinetic driven, was the observation of 'incoherent' c-axis transport of quasi-particles in the normal state [16] and, rather surprisingly, *also* in the superconducting state [17–19], thus providing a channel for kinetic energy lowering for charge carriers as soon as pairing sets in. A very useful tool in the discussion of kinetic

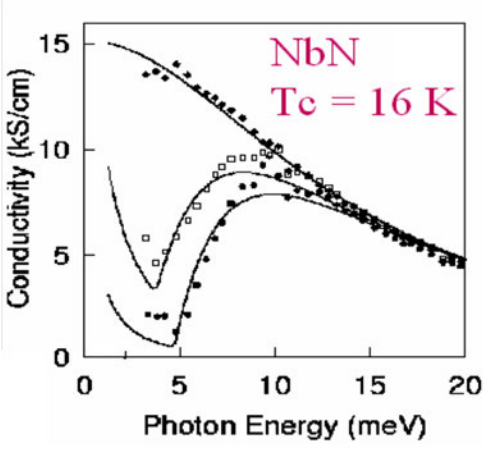

Fig. 10: *Optically detected superconducting gap of NbN*

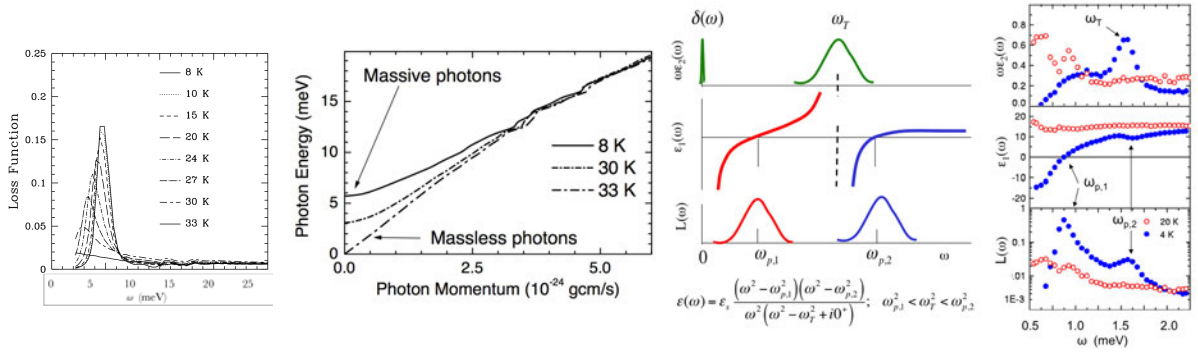

Fig. 11: *Leftmost panel: Loss-function of $La_{2-x}Sr_xCuO_4$ for field and current oriented perpendicular to the superconducting planes. The plasmon shows up in the superconducting state and is associated to the Josephson coupling between the planes. Second panel: Energy-momentum dispersion of photons polarized along the c-direction in $La_{1.85}Sr_{0.15}CuO_{4+\delta}$ for different temperatures. T_c of this sample is 33 K. The photons travelling inside the superconductor become massive, when the U(1) gauge symmetry is broken in the superconductor to which the photons are coupled. (Figure and caption copied from Ref. [20]) Third panel: Simulation of the dielectric function in a material with two types of Josephson coupling alternating [21]. Fourth (rightmost) panel: The c-axis optical conductivity and loss-function, of $SmLa_{0.8}Sr_{0.2}CuO_{4-\delta}$ for 4 K (closed symbols), and 20 K (open symbols). T_c of this sample is 16 K. When the sample enters the superconducting state, two longitudinal collective modes appear (7 and 12.8 cm^{-1}) and one with transverse polarization (12.1 cm^{-1}). The two modes near 12 cm^{-1} correspond to relative phase fluctuations of the two copper-oxygen layers within the unit cell [22]. (Figure and caption copied from Ref. [20])*

energy is the low frequency spectral weight associated with the charge carriers. In infrared spectra this spectral weight is contained within a the 'Drude' conductivity peak centered at $\omega = 0$. Within the context of the tight-binding model a simple relation exists between the kinetic energy per site, with volume per site V_u, and the low frequency spectral weight [23, 24]

$$E_{\rm kin} = \frac{\hbar^2 V_u}{4\pi e^2 a^2}\,\omega_p^2\,. \tag{16}$$

Here the plasma frequency, ω_p, is used to quantify the low frequency spectral weight

$$\frac{\omega_{p,s}^2}{8} + \int_{0^+}^{\omega_m} \mathrm{Re}\,\sigma(\omega)\,d\omega = \frac{1}{8}\,\omega_p^2\,, \tag{17}$$

where the integration should be carried out over all transitions within the band, *including* the δ-function at $\omega = 0$ in the superconducting state.

The $\delta(\omega)$ peak in $\mathrm{Re}\,\sigma(\omega)$ is of course not visible in the spectra directly. However, the presence of the superfluid is manifested prominently in the London term of $\mathrm{Re}\,\epsilon(\omega)$ (proportional to $\mathrm{Im}\,\sigma(\omega)$): $\epsilon_L(\omega) = -\omega_{p,s}^2\omega^{-2}$. In $La_{2-x}Sr_xCuO_4$ the London term is manifested in a spectacular way as a prominent plasma resonance perpendicular to the superconducting planes [25]. To illustrate this, the left-hand panel of Fig. 11 shows the so-called Loss-function

$$L(\omega) = -\,\mathrm{Im}\,\frac{1}{\epsilon(\omega)}\,, \tag{18}$$

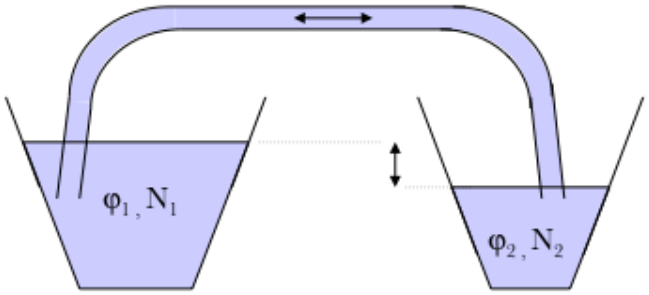

Fig. 12: *Sketch of the forces governing a Leggett mode.*

which shows its peak at the frequency where $\epsilon(\omega)$ crosses zero, which corresponds to the screened plasma-frequency. The right-hand panel shows the corresponding dispersion of the transverse polarized "polariton" waves inside the material (always with electric field perpendicular to the planes, hence the wave propagates along the planes)

$$p = \hbar\omega c^{-1}\sqrt{\epsilon(\omega)}\,. \tag{19}$$

The right-hand graph is, by the way, a nice demonstration of the Anderson-Higgs mechanism: The electromagnetic waves inside the superconductor acquire a mass $mc^2 = \hbar\omega_{p,s}$ due to the spontaneous breaking of $U(1)$ gauge symmetry associated with the superconducting order. Coupling of the superconducting order parameter to the fluctuations of charge and phase introduces a mass-gap both in the longitudinal plasmons and in the transverse polariton modes.

To return to the Josephson plasmons, a further effect was discovered when two Josephson junctions alternate along the c-direction. In this case one will observe two longitudinal Josephson plasmons, and an additional one in-between, which shows up as a peak in the optical conductivity and has transverse polarization (but always with electric field perpendicular to the planes). This was predicted theoretically and indeed observed experimentally by a number of groups. Interestingly this mode has many properties in common with the so-called Leggett mode. When in a two-band system the charge distribution is brought out of equilibrium the electronic compressibility constitutes a restoring force, whereas the inertia is given by the Josephson coupling between the two reservoirs (see sketch in Fig. 12). For a Fermi-liquid the compressibility $Kn^2 = \partial n/\partial\mu$ corresponds to density of states at the Fermi level. In the context of 'excitons' in two-band superconductors, the compressibility term has been first considered in 1966 by Leggett [26]. In neutral fluids the compressibility causes propagation of sound, whereas for electrons it causes the dispersion of plasmons.

The peak in the loss-function can be used to estimate the superfluid spectral weight, $\omega_{p,s}^2$, from the experimental spectra. Apart from universal prefactors, the amount of spectral weight of the $\delta(\omega)$ conductivity peak corresponds to the Josephson coupling energy, which in turn is the inter-layer *pair*hopping amplitude. It therefore provides an upper limit to the change of kinetic energy between the normal and the superconducting state [11], because the spectral weight transferred from higher frequencies to the $\delta(\omega)$-peak cannot exceed this amount. This allowed

a simple experimental way to test the idea of c-axis kinetic energy driven superconductivity by comparing the experimentally measured values of the condensation energy ($E_{\rm cond}$) and E$_J$. The inter-layer tunneling hypothesis required, that $E_J \approx E_{\rm cond}$. Measurements of λ_c [13] (approximately 17 μm) and the Josephson plasma resonance (JPR) [12] at 28 cm^{-1}, allowed a definite determination of the Josephson coupling energy of this compound, indicating that $E_J \approx 0.3$ μeV in Tl2201 with $T_c = 80$ K. This is a factor 400 lower than $E_{cond} \approx 100$ μeV per copper, based either on c_V experimental data [27], or on the formula $E_{cond} = 0.5N(0)\Delta^2$ with $N(0) = 1eV^{-1}$ per copper and $\Delta \simeq 15meV$. A direct determination of $E_{{\rm kin},s} - E_{{\rm kin},n}$ is obtained by measuring experimentally the amount of spectral weight transferred to the $\delta(\omega)$ peak due to the passage from the normal to the superconducting state, as was done by Basov *et al.* [14, 28]. These data indicated that for under-doped materials about 60% comes from the sub-gap region in the far infrared, while about 40% originates from frequencies much higher than the gap, whereas for optimally doped cuprates at least 90% originates from the gap-region, while less than 10% comes from higher energy.

In summary $\Delta E_{{\rm kin},c} < 0.1E_J$ in most cases. For several of the single-layer cuprates it has become clear now, that $\Delta E_{\rm kin}$ significantly undershoots the condensation energy, sometimes by two orders of magnitude or worse.

3.1 The internal energy of superconductors

The case of electrons moving in a central potential deserves our special attention: As a result of the virial theorem particles moving in a central potential of the form $V(r) = ar^n$ satisfy the relation $\langle H_{\rm kin}\rangle = \frac{n}{2}\langle V\rangle$. For an ensemble of non-interacting electrons moving in a central potential (e.g. an ensemble of hydrogen atoms) the only terms in the Hamiltonian are the kinetic energy and $V(r)$, so that the average kinetic energy is therefore a constant fraction of the average total energy, $\langle H_{\rm kin}\rangle = \frac{n}{2+n}\langle H_{\rm tot}\rangle$. The thermally induced changes of $\langle H_{\rm tot}\rangle$ are always smaller that $3k_BT$ per particle. For electrons moving in an e^2/r potential this sets an upper limit of k_BT to the change of kinetic energy, and an upper limit $4k_BT/3$ on the photon energy range over which spectral weight can be transferred as a function of temperature. From the example of a harmonic oscillator, discussed below, we will see that transfer of spectral weight as a function of temperature can even be completely absent.

A necessary condition for the existence of superconductivity is, that the free energy of the superconducting state is lower than that of the non-superconducting state. At sufficiently high temperature important contributions to the free energy are due to the entropy. These contributions depend strongly on the nature of the low-energy excitations, first and foremost of all their nature, be it fermionic, bosonic or of a more complex character due to electron correlation effects. At $T = 0$ the free energy and internal energy are equal, and are given by the quantum expectation value of the Hamiltonian, which can be separated into an interaction energy and a kinetic energy.

3.2 The Coulomb interaction energy

In a series of papers Leggett has discussed the change of Coulomb correlation energy for a system which becomes superconducting [29], and has argued, that this energy would actually decrease in the superconducting state. Experimentally the changes of Coulomb energy can be measured directly in the sector of q-space of vanishing q. The best, and most stable, experimental technique is to measure the dielectric function using spectroscopic ellipsometry, and to follow the changes as a function of temperature carefully as a function of temperature. Because the cuprates are strongly anisotropic materials, it is crucial to measure both the in-plane and out-of-plane pseudo-dielectric functions, from which the full dielectric tensor elements along the optical axes of the crystal then have to be calculated. In a recent study the evolution of the Coulomb energy was measured as a function of temperature and doping of the loss function spectra in the infrared-visible spectral range of double- and triple-layer bismuth cuprates [30]. Our experiments indicate that for the overdoped samples the superconducting phase transition is accompanied by a saving of the Coulomb interaction energy, on the underdoped side there is an increase of the Coulomb energy below T_c, and the change of Coulomb energy for $q < 0.31$ Å^{-1} is about the same size as the condensation energy. This state of affairs calls for studies with other experimental techniques, in particular electron energy loss spectroscopy, to explore the momentum dependent structure of these phenomena. Departure of a T^2 dependence of the measured loss-function data indicates a corresponding temperature dependence of the density-density correlations. Unambiguous assignment to a precursor of superconducting pairing, to another type of correlation, or neither of these two, is not possible at this stage. The S–N difference of the Coulomb energy has similar doping dependence as the total condensation energy. While the latter is in the range of 0 to 2 K per CuO_2 unit, the Coulomb energy varies between –1 and 1 K. Consequently, while it cannot be the whole cause of superconductivity, the Coulomb energy is a major factor in the total energy balance stabilizing the superconducting state. The experiments presented here demonstrate that it is in principle possible to determine the subtle changes of Coulomb correlation energy associated with a superconducting phase transition, and constitute a promising first step in the experimental exploration of the Coulomb correlation energy as a function of momentum and energy.

3.3 The kinetic energy

Based on the tight-binding approximation, a partial sum rule is sometimes employed, where the integral is limited to the valence band, excluding all other bands. Although the theoretical expressions based on the tight-binding formula are well defined, experimentalists face a problem here, due to the fact that experimentally the valence electron band overlaps with other bands, thus hindering an unambiguous separation of the various contribution in the experimental spectra. Nevertheless, relatively clear-cut cases have been reported in the literature, thus motivating us to address also the tight-binding approximation in our discussion. For a square lattice with

nearest-neighbor coupling the Hamiltonian is

$$H_{t,\alpha} = t \sum_{\vec{R},\sigma} \left(c^{\dagger}_{\vec{R}+\vec{\delta}_\alpha,\sigma} c_{\vec{R},\sigma} + c^{\dagger}_{\vec{R},\sigma} c_{\vec{R}+\vec{\delta}_\alpha,\sigma} \right) \tag{20}$$

and $H = \sum_\alpha H_{t,\alpha} - \mu N$. The commutators in Eq. (6) can be easily calculated, resulting in the f-sum

$$\int_0^\omega \mathrm{Re}\,\sigma(\infty)\, d\omega' = -\frac{\pi e^2 a^2}{2\hbar^2 V} \langle H_{t,\alpha} \rangle \,. \tag{21}$$

Note, that the chemical potential term commutes with x and drops out of the expression for the f-sum. Hence the tight-binding f-sum provides only the *kinetic energy* contribution, which depends both on the number of particles and the hopping parameter t. It is easy to see, that for a small filling fraction of the band we return to the continuum result: The occupied electron states are now all located just above the bottom of the valence band, with an energy $-t$. Hence in leading orders of the filling fraction $-\langle \psi_g | H_t | \psi_g \rangle = Nt$. Identifying $a^2 \hbar^{-2} t^{-1}$ as the effective mass m^* we recognize the familiar f-sum rule, Eq. (6), with the free electron mass replaced by the effective mass. In BCS theory the lowering of the pair-interaction energy is partly compensated by a change of kinetic energy of opposite sign. This can be understood qualitatively in the following way: The correlated motion in pairs causes a localization of the relative coordinates of electrons, thereby increasing the relative momentum and the kinetic energy of the electrons. Another way to see this, is that in the superconducting state the step of n_k at the Fermi momentum is smoothed, causing E_{kin} to become larger [31].

A pedagogical example where the kinetic energy of a pair is higher in the superconducting state, is provided by the negative-U Hubbard model [32]: Without interactions, the kinetic energy is provided by the expression

$$E_{\mathrm{kin}} = -t \sum_{\langle i,j \rangle,\sigma} \left\langle \Psi | c^{\dagger}_{i\sigma} c_{j\sigma} + H.c. | \Psi \right\rangle . \tag{22}$$

Let us consider a 2D square lattice. If the band contains two electrons, the kinetic energy of each electron is $-2t$, the bottom of the band, hence $E_{\mathrm{kin}} = -4t$. (In a tight-binding picture the reference energy is the center of the band irrespective of E_F, causing E_{kin} to be always negative). Let us now consider the kinetic energy of a pair in the extreme pairing limit, i.e. $U \gg t$, causing both electrons to occupy the same site, with an interaction energy $-U$. The occupation function n_k in this case becomes

$$n_k \approx \frac{1}{N_k} \frac{t}{U} \frac{1}{(1 + 4\epsilon_k/U)^2} \,. \tag{23}$$

This implies that the kinetic energy approaches $E_{\mathrm{kin}} \to -8t^2/U$. Hence the kinetic energy increases from $E^n_{\mathrm{kin}} = -4t$ to $E^s_{\mathrm{kin}} = -\frac{8t^2}{U}$ when the local pairs are formed. The paired electrons behave like bosons of charge $2e$. A second order perturbation calculation yields an effective boson hopping parameter [33] $t' = t^2/U$. In experiments probing the charge dynamics, this hopping parameter determines the inertia of the charges in an accelerating field. As a result

the plasma frequency of such a model would be

$$\omega_{p,s}^2 = 4\pi \frac{n}{2} (2e)^2 \frac{a^2 t^2}{\hbar^2 U} , \tag{24}$$

whereas if these pair correlations are muted

$$\omega_{p,n}^2 = 4\pi n e^2 \frac{a^2 t}{\hbar^2} . \tag{25}$$

Because the plasma frequency is just the low-frequency spectral weight associated with the charge carriers, this demonstrates, that for conventional pairs, i.e., those which are formed due to interaction energy lowering, the expected trend is, that in the superconducting state the spectral weight *de*creases. Note, that this argument can only demonstrate the direction in which the plasma frequency changes when the pair correlations become reduced, but it does not correctly provide the quantitative size of the change, since the strong coupling regime of Eq. (24) implies the presence of a finite fraction of uncondensed 'preformed' pairs in the normal state. The same effect exists in the limit of weak pairing correlations. In Ref. [34] (Eq. 29, ignoring particle-hole asymmetric terms) the following expression was derived for the plasma resonance

$$\omega_{p,s}^2 = \frac{4\pi e^2}{V} \sum_k \frac{\Delta_k^2}{\hbar^2 E_k^3} \left[\frac{\partial \epsilon_k}{\partial k} \right]^2 , \tag{26}$$

where V is the volume of the system, and $E_k^2 = \epsilon_k^2 + |\Delta_k|^2$. Integrating in parts, using that $\Delta_k^2 E_k^{-3} \partial_k \epsilon_k = \partial_k \left(\epsilon_k / E_k \right)$, and that $\partial_k \epsilon_k = 0$ at the zone-boundary, we obtain

$$\omega_{p,s}^2 = \frac{4\pi e^2}{V} \sum_k \frac{n_k}{m_k} \tag{27}$$

where $m_k^{-1} = \hbar^{-2} \partial^2 \epsilon_k / \partial k^2$, and $n_k = 1 - \epsilon_k / E_k$. For a monotonous band dispersion the plasma frequency of the superconductor is always *smaller* than that of the unpaired system: Because the sign of the band-mass changes from positive near the bottom of the band to negative near the top, the effect of the broadened occupation factors n_k is to give a slightly smaller average over m_k^{-1}, hence ω_p^2 is smaller. Note that the mass of free electrons does not depend on momentum, hence in free space ω_p^2 is unaffected by the pairing.

To obtain an estimate of the order of magnitude of the change of spectral weight, we consider a square band of width W with a Fermi energy $E_F = N_e/(2W)$, where N_e is the number of electrons per unit cell. To simplify matters we assume that $1/m_k$ varies linearly as a function of band energy: $1/m(\epsilon) = (W - 2E_F - 2\epsilon)/(W m_0)$. We consider the limit where $\Delta \ll W, E_F$. Let us assume that the bandwidth ~ 1 eV, and $\Delta \sim 14$ meV corresponding to T_c =90 K. The reduction of the spectral weight is then 0.28%. If we assume that the bandwidth is 0.1 eV, the spectral weight reduction would typically be 11.4%.

If the state above T_c is *not* a Fermi liquid, the situation could be reversed. Indeed even for the 1D Luttinger liquid $n(k)$ has an infinite slope at k_F. If indeed the normal state would have a broad momentum distribution like the one indicated, the total kinetic energy becomes lower once pairs

are formed, provided that the slope of $n(k)$ at k_F is steeper in the superconducting state. This is not necessarily in contradiction with the virial theorem, even though ultimately all relevant interactions (including electron-phonon interactions) are derived from the Coulomb interaction: The superconducting correlations involve the low energy scale quasi-particle excitations and their interactions. These *effective* interactions usually have characteristics quite different from the original Coulomb interaction, resulting in $E_c/E_{\rm kin} \neq -2$ for the low-energy quasi-particles. Various models have been recently proposed involving pairing due to a *reduction* of kinetic energy. In strongly anisotropic materials such as the cuprates, two possible types of kinetic energy should be distinguished: Perpendicular to the planes [11, 35] (along the c-direction) and along the planar directions [36–41]. Interestingly, it turns out that in underdoped samples of the cuprates the "kinetic" energy behaves oppositely to the BCS prediction (i.e. it is decreased by the N–S transition), while on the overdoped side it behaves consistently with BCS (i.e. it is increased) [42–44], which is in fact consistent with numerical calculations based on the Hubbard model and the t-J model [45, 46].

4 Conclusions

The optical conductivity is a fundamental property of solids that contains the contributions of vibrational and electronic character. Among the electronic type of excitations the intra-band and inter-band transitions, excitons, and plasmons of different types correspond to the most prominent features in the spectra. In addition multi-magnon excitations or more exotic collective modes can often be detected. The careful study of the optical properties of solids can provide valuable microscopic information about the electronic structure of solids. In contrast to many other spectroscopic techniques, it is relatively easy to obtain reliable absolute values of the optical conductivity. As a result sum rules and sum rule related integral expressions can often be applied to the optical spectra.

References

[1] D.N. Basov, R.D. Averitt, D. van der Marel, M. Dressel, and K. Haule Rev. Mod. Phys., **83**, 471 (2011)

[2] E. Shiles, T. Sasaki, M. Inokuti, and D.Y. Smith, Phys. Rev. B **22**, 1612 (1980)

[3] J. Ruppen, J. Teyssier, O.E. Peil, S. Catalano, M. Gibert, J. Mravlje, J.-M. Triscone, A. Georges, and D. van der Marel, Phys. Rev. B **92**, 155145 (2015)

[4] D.E. Aspnes and A.A. Studna, Phys. Rev. B **27**, 985 (1983)

[5] T. Tomiki, J. Phys. Soc. Jpn. **26**, 738 (1969)

[6] Ch. Uihlein, D. Fröhlich, and R. Kenklies Phys. Rev. B **23**, 2731 (1981)

[7] M. Bassi, P. Camagni, R. Rolli, G. Samoggia, F. Parmigiani, G. Dhalenne and A. Revcolevschi, Phys. Rev. B **54**, R11030 (1996)

[8] G.A. Sawatzky, and J.W. Allen, Phys. Rev. Lett. **53**, 2339 (1984)

[9] R. Newman and R.M. Chrenko, Phys. Rev. **114**, 1507(1959)

[10] H.S. Somal, B.J. Feenstra, J. Schuetzmann, D. van der Marel, J.H. Kim, Z.H. Barber, V.H.M. Duijn, N.T. Hien, A.A. Menovsky, M. Palumbo, Phys. Rev. Lett. **76**, 1525 (1996)

[11] P.W. Anderson, Science **268**, 1154 (1995)

[12] A. Tsvetkov, D. van der Marel, K.A. Morel, J.R. Kirtley, J.L. de Boer, A. Meetsma, Z.F. Ren, N. Koleshnikov, D. Dulic, A. Damascelli, M. Grüninger, J. Schützmann, J.W. van der Eb, H.S. Somal, and J.H. Wang, Nature **395**, 360 (1998)

[13] K.A. Moler, J.R. Kirtley, D.G. Hinks, T.W. Li, and Ming Xu, Science **279**, 1193 (1998)

[14] D.N. Basov, S.I. Woods, A.S. Katz, E.J. Singley, R.C. Dynes, M. Xu, D.G. Hinks, C.C. Homes, M. Strongin, Science **283**, 49 (1999)

[15] J.R. Kirtley, K.A. Moler, G. Villard, A. Maignan, Phys. Rev. Lett. **81**, 2140 (1998)

[16] S.L. Cooper, and K.E. Gray, in D.M. Ginsberg (ed.): *Physical Properties of High Temperature Superconductors IV* (World Scientific, Singapore 1994)

[17] J.H. Kim, H.S. Somal, D. van der Marel, A.M. Gerrits, A. Wittlin, V.H.M. Duijn, N.T. Hien and A.A. Menovsky, Physica C **247**, 297 (1995)

[18] D. Dulic, D. van der Marel, A.A. Tsvetkov, W.N. Hardy, Z.F. Ren, J.H. Wang, and B.A. Willemsen, Phys. Rev. B **60**, R15051 (1999)

[19] A. Hosseini, S. Kamal, D.A. Bonn, Ruixing Liang, and W.N. Hardy, Phys. Rev. Lett. **81**, 1298 (1998)

[20] D. van der Marel, Journal of Superconductivity **17**, 559 (2004)

[21] D. van der Marel, and A.A. Tsvetkov, Phys. Rev. B **64**, 024530 (2001)

[22] D. Dulic, A. Pimenov, D. van der Marel, D.M. Broun, S. Kamal, W.N. Hardy, A.A. Tsvetkov, I.M. Sutjaha, Ruixing Liang, A.A. Menovsky, A. Loidl and S.S. Saxena, Phys. Rev. Lett. **86**, 4144 (2001)

[23] P.F. Maldague, Phys. Rev. **16**, 2437 (1977)

[24] D. Baeriswyl, J. Carmelo, and A. Luther, Phys. Rev. B **33**, 7247 (1986)

[25] K. Tamasaku, Y. Nakamura, and S. Uchida, Phys. Rev. Lett. **69**, 1455 (1992)

[26] A.J. Leggett, Prog. Theor. Phys. **36**, 901 (1966)

[27] J.W. Loram, K.A. Mirza, J.M. Wade, J.R. Cooper, and W.Y. Liang, Physica C **235-240**, 134 (1994)

[28] D.N. Basov, C.C. Homes, E.J. Singley, M. Strongin, T. Timusk, G. Blumberg, and D. van der Marel, Phys. Rev. B **63**, 134514 (2001)

[29] A.J. Leggett, Proc. Natl. Acad. Sci. USA Vol. **96**, 8365 (1999)

[30] J. Levallois, M.K. Tran, D. Pouliot, C.N. Presura, L.H. Greene, J.N. Eckstein, J. Uccelli, E. Giannini, G.D. Gu, A.J. Leggett, and D. van der Marel, arXiv:1512.00672

[31] M.R. Norman, M. Randeria, B. Janko, J.C. Campuzano, Phys. Rev. B **61**, 14724 (2000)

[32] R. Micnas, J. Ranninger, and S. Robaszkiewicz, Rev. Mod. Phys. **62**, 113 (1990)

[33] P. Nozières, and S. Schmitt-Rink, J. Low Temp. Phys **59**, 195 (1985)

[34] D. van der Marel, Phys. Rev. B. **51**, 1147 (1995)

[35] S. Chakravarty, Eur. Phys. J. B **5**, 337 (1998)

[36] J.E. Hirsch, Physica C **199**, 305 (1992)

[37] S. Alexandrov and N.F. Mott: *High Temperature Superconductors and Other Superfluids* (Taylor and Francis, 1994)

[38] V. Emery and S.A. Kivelson, Nature **374**, 4347 (1995)

[39] F.F. Assaad, M. Imada, and D.J. Scalapino, Phys. Rev. Lett. **77**, 4592 (1996)

[40] P.A. Lee, Physica C **317**, 194 (1999)

[41] P.W. Anderson, Physica C **341-348**, 9 (2000)

[42] H.J.A. Molegraaf, C. Presura, D. van der Marel, P.H. Kes, M. Li, Science **295**, 2239 (2002)

[43] G. Deutscher, A.F. Santander-Syro, and N. Bontemps, Phys. Rev. B **72**, 092504 (2005)

[44] F. Carbone, A.B. Kuzmenko, H.J.A. Molegraaf, E. van Heumen, V. Lukovac, F. Marsiglio, D. van der Marel, K. Haule, G. Kotliar, H. Berger, S. Courjault, P.H. Kes, and M. Li, Phys. Rev. B **74**, 064510 (2006)

[45] E. Gull and A.J. Millis, Phys. Rev. B **86**, 241106 (2012)

[46] K. Haule and G. Kotliar, Europhys. Lett. **77**, 27007 (2007)

12 Resonant Inelastic X-ray Scattering on Elementary Excitations

Jeroen van den Brink
Institute for Theoretical Solid State Physics
IFW Dresden

Contents

E. Pavarini, E. Koch, J. van den Brink, and G. Sawatzky (eds.)
Quantum Materials: Experiments and Theory
Modeling and Simulation Vol. 6
Forschungszentrum Jülich, 2016, ISBN 978-3-95806-159-0
http://www.cond-mat.de/events/correl16

1 Introduction

In the past decade, Resonant Inelastic X-ray Scattering (RIXS) has made remarkable progress as a spectroscopic technique. This is a direct result of the availability of high-brilliance synchrotron X-ray radiation sources and of advanced photon detection instrumentation. The technique's unique capability to probe elementary excitations in complex materials by measuring their energy-, momentum-, and polarization-dependence has brought RIXS to the forefront of experimental photon science. In these lecture notes we discuss both the theoretical background of RIXS, focusing on those determining the low-energy charge, spin, orbital and lattice excitations of solids. These lecture notes are based on and to a large extend an excerpt from a recent review article [1].

Resonant Inelastic X-ray Scattering is a fast-developing experimental technique in which one scatters X-ray photons inelastically off matter. It is a *photon-in − photon-out* spectroscopy for which one can, in principle, measure the energy, momentum, and polarization change of the scattered photon. The change in energy, momentum, and polarization of the photon are transferred to intrinsic excitations of the material under study and thus RIXS provides information about those excitations. RIXS is a resonant technique in which the energy of the incident photon is chosen such that it coincides with, and hence resonates with, one of the atomic X-ray transitions of the system. The resonance can greatly enhance the inelastic scattering cross-section, sometimes by many orders of magnitude, and offers a unique way to probe charge, magnetic, and orbital degrees of freedom on selective atomic sites in a crystal. Early experimental work, and some more recent reviews include [2–9].

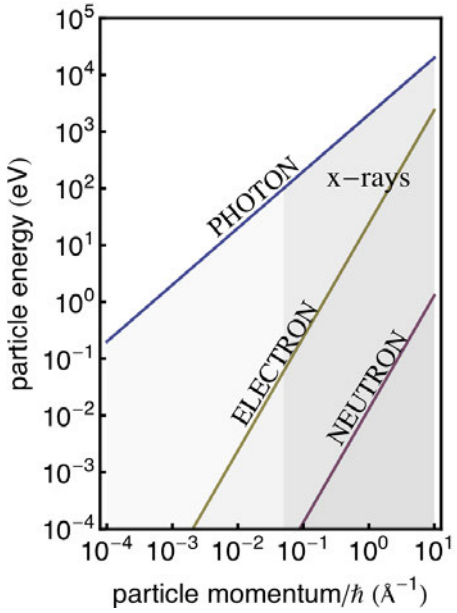

Fig. 1: *(Kinetic) energy and momentum carried by the different elementary particles that are often used for inelastic scattering experiments. The scattering phase-space (the range of energies and momenta that can be transferred in a scattering event) of X-rays is indicated in blue, electrons in brown and neutrons in red.*

1.1 Features of RIXS as an experimental method

Compared to other scattering techniques, RIXS has a number of unique features: it covers a huge scattering phase-space, is polarization dependent, element and orbital specific, bulk sensitive, and requires only small sample volumes. We briefly illustrate these features below and discuss them more extensively in the sections to follow.

1. RIXS exploits both the *energy and momentum* dependence of the photon scattering cross-section. Comparing the energies of a neutron, electron, and photon, each with a wavelength on the order of the relevant length scale in a solid, i.e., the interatomic lattice spacing, which is on the order of a few Angstroms, it is obvious that an X-ray photon has much more energy than an equivalent neutron or electron, see Fig. 1. The scattering phase space (the range of energies and momenta that can be transferred in a scattering event) available to X-rays is therefore correspondingly larger and is in fact without equal. For instance, unlike photon scattering experiments with visible or infrared light, RIXS can probe the full dispersion of low energy excitations in solids.

2. RIXS is *element and orbital specific*: Chemical sensitivity arises by tuning the incident photon energy to specific atomic transitions of the different types of atoms in a material. Such transitions are called absorption edges. RIXS can even differentiate between the same chemical element at sites with inequivalent chemical bondings, with different valencies or at inequivalent crystallographic positions if the absorption edges in these cases are distinguishable. In addition, the type of information that may be gleaned about the electronic excitations can be varied by tuning to different X-ray edges of the same chemical element (e.g., K-edge for exciting $1s$ electrons, L-edge for electrons in the $n = 2$ shell, or M-edge for $n = 3$ electrons), since the photon excites different core-electrons into different valence orbitals at each edge. The energies of these edges are shown in Fig. 2.

3. RIXS is *bulk sensitive*: the penetration depth of resonant X-ray photons is material and scattering-geometry specific, but typically it is on the order of a few μm for photons of 10 keV in the hard X-ray regime, and on the order of 0.1 μm for photons of 1 keV in the soft X-ray regime.

4. RIXS needs only *small sample volumes*: the photon-matter interaction is relatively strong, compared to, for instance, the neutron-matter interaction strength. In addition, photon sources deliver many orders of magnitude more particles per second, in a much smaller spot, than do neutron sources. These facts make RIXS possible on very small volume samples, thin films, surfaces, and nano-objects, in addition to bulk single crystal or powder samples.

5. RIXS can utilize the *polarization* of the photon: the nature of the excitations created in the material can be disentangled through polarization analysis of the incident and scattered

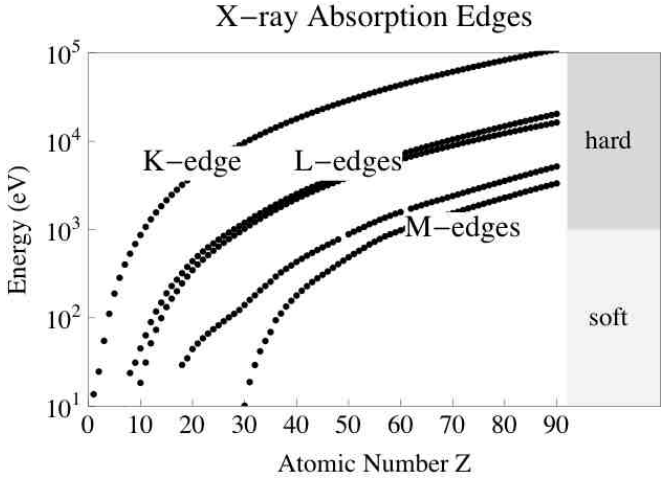

Fig. 2: *Energy of the K, L_1, L_3, M_1, and M_5 X-ray absorption edges as a function of atomic number Z. X-ray energies below 1 keV are referred to as soft, above as hard.*

photons, which allows one, through the use of various selection rules, to characterize the symmetry and nature of the excitations. To date, very few experimental facilities allow the polarization of the scattered photon to be measured [10, 11], though the incident photon polarization is frequently varied. It is important to note that a polarization change of a photon is necessarily related to an angular momentum change. Conservation of angular momentum means that any angular momentum lost by the scattered photons has been transferred to elementary excitations in the solid.

In principle RIXS can probe a very broad class of intrinsic excitations of the system under study, as long as these excitations are overall charge-neutral. This constraint arises from the fact that in RIXS the scattered photons do not add or remove charge from the system under study. In principle then, RIXS has a finite cross-section for probing the energy, momentum and polarization dependence of, for instance, the electron-hole continuum and excitons in band metals and semiconductors, charge transfer and d-d-excitations in strongly correlated materials, lattice excitations and so on. In addition magnetic excitations are also symmetry-allowed in RIXS, because the orbital angular momentum that the photons carry can in principle be transferred to the electron's spin angular moment. This versatility of RIXS is an advantage and at the same time a complicating factor, because different types of excitations will generally be present in a single RIXS spectrum.

The generic advantages of the RIXS technique listed above perhaps raise the question as to why this spectroscopic technique is not as widely used as, say, angle-resolved photoemission (ARPES) or neutron scattering. The main limitation is that the RIXS process is photon-hungry, i.e., it requires a substantial incident photon flux to obtain enough scattered photons to collect spectra with a high enough resolution in energy and momentum in a reasonable time. With a required resolving power (defined as the incident photon energy divided by the energy resolution) of four orders of magnitude, RIXS has been a real challenge. Up until a few years ago this has limited RIXS experiments to measuring energy losses on the order of half an electron

volt or greater. Thus neutron scattering and ARPES offered a more direct examination of the low energy excitations near the Fermi level. However, recent progress in RIXS instrumentation has been dramatic and this situation is now changing. One of the purposes of these notes is to summarize this progress which is beginning to elevate RIXS into an important condensed matter physics tool for probing elementary excitations in solids.

1.2 Progress of RIXS in the last decades

As discussed above, the generic features of RIXS make it, in principle, an attractive technique to study the intrinsic momentum dependent, low-energy response of a material. However there are of course practical limitations. The most critical of these is the energy resolution, which is determined both by the availability of the instrumentation necessary to energy-resolve the photons, and by the availability of tunable photon sources of sufficient intensity.

In order to tune the incident photon energy to a particular edge, a tunable X-ray photon source is essential. This can be achieved with synchrotron radiation sources and their increase in brilliance over the past decades has been many orders of magnitudes in the 10^3-10^4 eV X-ray regime. The next generation photon sources include X-ray free electron lasers (FELs), which are coming on line at the time of writing. The peak brilliance of these sources is again orders of magnitude larger than that of the third generation synchrotrons and it is likely that these sources will provide further advances, particularly for time-resolved experiments.

This vast increase in photon flux has been matched by advances in the RIXS instrumentation: the monochromators, analyzers, and spectrometers. The resulting increase in resolution of RIXS experiments over time, as measured for instance at the hard X-ray Cu K- and soft X-ray Cu L_3-edges, has greatly improved in the past decade. In concert with the great progress in the RIXS experiments, there has been a similarly rapid advance in the theoretical understanding of the scattering process and of the dynamic correlation functions that the technique probes. Taken together, the theoretical and experimental advances have driven an enormous increase in the number of RIXS-related publications.

It seems likely that this strong growth will continue. First, because of the ongoing push to better energy resolutions. Second, and perhaps more importantly, because there are a multitude of different X-ray absorption edges, in particular for the heavier elements in the periodic table, and each one of these can, in principle, be exploited for RIXS measurements. The bulk of RIXS data so far has been collected at $3d$ transition metal and oxygen edges. This is motivated by the intense scientific interest in strongly correlated transition-metal oxides such as the high-T_c cuprate superconductors and the colossal magnetoresistance manganites. This focus on transition-metal oxides is an accident of history. It has been very beneficial to the field, driving advances in instrumentation and theory at the relevant edges, but there is clearly a huge potential for growth as interest moves on to other materials and other fields.

1.3 Probing elementary excitations with RIXS

The elementary excitations of a material determine many of its important physical properties, including transport properties and its response to external perturbations. Understanding the excitation spectrum of a system is key to understanding the system.

In this respect strongly correlated electron materials, e.g. transition-metal oxides, are of special interest because the low-energy electronic properties are determined by high-energy electron-electron interactions (energies on the order of eV's). From these strong interactions and correlations a set of quantum many-body problems emerge, the understanding of which lies at the heart of present day condensed matter physics. Most often this many-body physics is captured in model Hamiltonians, the exact parameters of which must be determined experimentally. RIXS, along with other spectroscopic techniques, can play an important role there, though we note that it is a spectroscopic technique applicable to many other materials and is, of course, not limited to correlated systems.

In the following, we discuss the relevant excitation energy and momentum scale on which RIXS can probe the excitation spectrum of a solid. We then briefly introduce the kinds of elementary excitations that are accessible to RIXS.

Excitation Energy and Momentum Scale As is shown in Fig. 3, the elementary excitation spectrum in solids spans the range from plasmons and charge transfer excitations at a few eV, determining for instance optical properties, through excitons, d-d excitations and magnons down to phonons at the meV scale. In principle, RIXS can measure the momentum-dependence of the excitation energy of all these modes, i.e. their dispersion, because the photon transfers momentum as well as energy to the material under study.

This is unusual if one is accustomed to optical light scattering, such as Raman scattering [12]. Photons in the visible range of the spectrum with an energy of a few eV carry negligible momentum compared to the quasi-momentum of the elementary excitations of a solid (Fig. 1). A photon of 2 eV has a momentum of roughly $\hbar q = 10^{-27}$ kg m/s, or a wavevector $q = 10^{-3}$ Å^{-1} whereas elementary excitations in a crystal with a lattice constant of say 3 Å have wavevectors up to $q = 2\pi/3 \approx 2$ Å^{-1}. On this scale optical light scattering is in essence a zero momentum probe. To measure the dispersion of elementary excitations for momenta in a sizable portion of a typical Brillouin zone, X-rays with energy on the order of 1 keV or more are needed, corresponding to, for instance, the Cu L-edge.

Overview of elementary excitations In this paragraph we briefly discuss the different elementary excitations accessible to RIXS.

Plasmons. Collective density oscillations of an electron gas are referred to as plasmons. They can be observed by inelastic X-ray scattering (IXS) or by optical probes since they occur at finite energy for q=0. Plasmon-like excitations were also observed early on in RIXS [13], but their resonant enhancement with respect to IXS is weak, and little work has been done since.

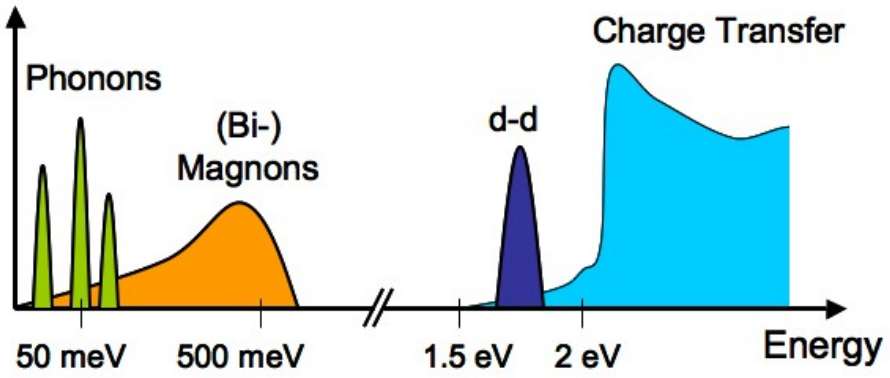

Fig. 3: *Different elementary excitations in condensed matter systems and their approximate energy scales in strongly correlated electron materials such as transition-metal oxides.*

Charge-transfer excitations. Charge transport in a condensed matter system is determined by the energetics of moving electrons from one site to another. In a transition-metal oxide, there are two relevant energy scales for this process. The first is the energy associated with an electron hopping from a ligand site to a metal site. This is known as the charge transfer energy, Δ, where $\Delta = E(d^{n+1}\underline{L}) - E(d^n)$, and $\underline{L}$ represents a hole on the ligand site. The second energy scale is the energy, U, associated with moving a d-electron from one metal site to another where $U = E(d^{n+1}) + E(d^{n-1}) - 2E(d^n)$. Strongly correlated insulators may be classified by which of these two energies is the larger [14]. If $U > \Delta$, then the gap is of the charge transfer type and the system is said to be a charge-transfer insulator. Conversely, if $U < \Delta$, then the gap is controlled by the d-d Coulomb energy and the system is said to be a Mott-Hubbard insulator.

The bulk of the interesting transition metal oxide compounds, including the cuprates, nickelates and manganites are all in the charge transfer limit. This means the lowest lying excitations across the optical gap are charge transfer excitations and therefore these are of central importance in these materials. Key questions include the size of the gap (typically on the order of a few eV) and the nature of the excitations: Do they form bound exciton states? Are these localized or can they propagate through the lattice? What are their lifetimes, symmetries, and temperature dependence, etc. While some studies have been performed using other techniques, notably EELS and optical conductivity measurements, RIXS offers a powerful probe for many of these questions and has been applied extensively.

Crystal-field and orbital excitations. Many strongly correlated systems exhibit an orbital degree of freedom, that is, the valence electrons can occupy different sets of orbitals. Orbitally active ions are also magnetic: they have a partially filled outer shell. This orbital degree of freedom determines many physical properties of the solid, both directly, and also indirectly because the orbitals couple to other degrees of freedom. For instance, the orbital's charge distribution couples to the lattice, and according to the Goodenough-Kanamori rules for superexchange the orbital order also determines the spin-spin interactions. The nature of the orbital degree of freedom, i.e., the orbital ground state and its excitations, are an important aspect of strongly correlated systems.

In many Mott insulators this orbital physics is governed by the crystal field: the levels of the orbitally active ion are split and the orbital ground state is uniquely determined by local, single-ion considerations. The orbital excitations from this ground state are transitions between the crystal field levels. Crystal field transitions between different d-orbitals are called d-d excitations. Such excitations are currently routinely seen by RIXS and are now well understood.
In other cases the crystal field does not split the levels of the outer shell very much, leaving an orbital (quasi-)degeneracy in the ground state. This local low-energy degree of freedom can couple to orbital degrees of freedom on neighboring sites by superexchange processes, and in this way collective orbital excitations can emerge. The quanta of these collective modes are called orbitons, in analogy to spin waves and magnons. Definitive proof of the existence of orbitons remains elusive. RIXS is contributing significantly to the search for orbitons.
Magnetic excitations. Magnetism and long-range magnetic ordering are arguably the best known and most studied consequences of the electron-electron interactions in solids. When usual magnetic order sets in, be it either of ferro-, ferri-, or antiferromagnetic type, the global spin rotation symmetry in the material is broken. As a result characteristic collective magnetic excitations emerge. The resulting low-energy quasiparticles, the magnons, and the interactions between them determine all low temperature magnetic properties. Magnon energies can extend up to ~ 0.3 eV (e.g. in cuprates) and their momenta up to ~ 1 Å^{-1}. Recently magnon dispersions have been measured for the first time at the Cu L-edge on thin films of La_2CuO_4 [15]. In K-edge RIXS bi-magnon excitations and their dispersions have also been observed [16].
A melting of the long-range ordering, for instance through an increase in quantum fluctuations as a result of the introduction of mobile charge carriers in a localized spin system, or by the frustration of magnetic interactions between the spins, can result in the formation of spin-liquid ground states. Spin liquids potentially have elusive properties such as high-temperature superconductivity or topological order, which one is only beginning to explore and understand. Some of the more exotic magnetic excitations that emerge from these ground states, such as spinons and triplons can also be observed by RIXS [17].
Phonons. Phonons are the quantized lattice vibration modes of a periodic solid. These are bosonic modes with energies typically below 0.1 eV, so that the detection of single phonon excitations is only just possible with present day RIXS resolution. Therefore phonon loss features were resolved for the first time with RIXS only very recently, at the Cu L- [15] and K-edge [18]. In addition anomalous features in CuB_2O_4 have been qualitatively described by extending the electron-only considerations to include the lattice degrees of freedom [19]. Theoretically, the study of phonons in RIXS promises quantitative investigations of the electron-phonon coupling [20].

2 The RIXS process

The microscopic picture of the resonant inelastic X-ray scattering process is most easily explained in terms of an example. We will choose a copper-oxide material as a typical example, but it should be stressed once more that the focus of RIXS on transition-metal oxides is

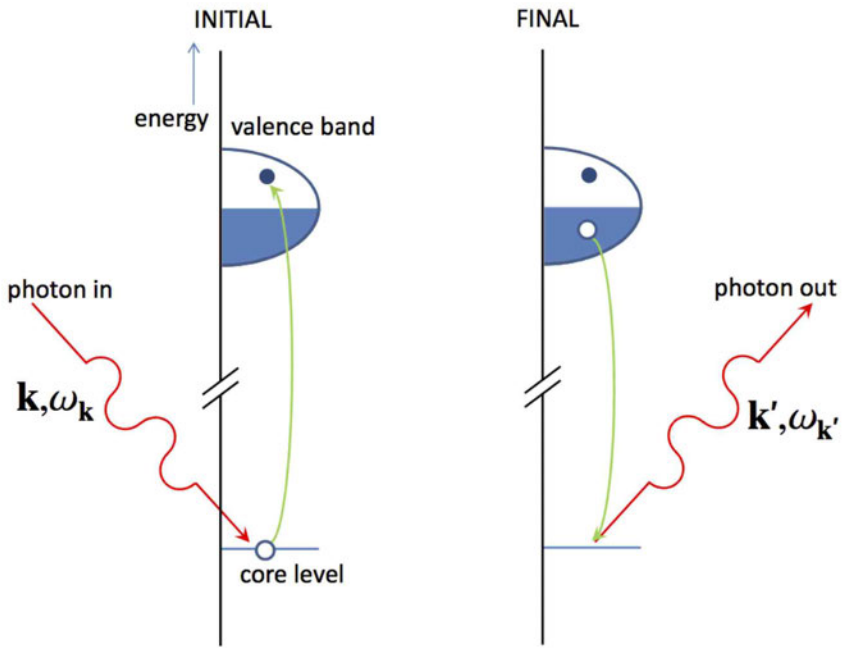

Fig. 4: *In a direct RIXS process the incoming X-rays excite an electron from a deep-lying core level into the empty valence. The empty core state is then filled by an electron from the occupied states under the emission of an X-ray. This RIXS process creates a valence excitation with momentum* $\hbar\mathbf{k}' - \hbar\mathbf{k}$ *and energy* $\hbar\omega_{\mathbf{k}} - \hbar\omega_{\mathbf{k}'}$.

something of an accident of history and is not a fundamental limitation of the technique. In a copper-oxide material, one can tune the incoming photon energy to resonate with the copper K, L, or M absorption edges, where in each case the incident photon promotes a different type of core electron into an empty valence shell, see Figs. 4 and 5. The electronic configuration of Cu^{2+} is $1s^2 2s^2 2p^6 3s^2 3p^6 3d^9$, with the partially filled $3d$ valence shell characteristic of transition metal ions. The copper K-edge transition $1s \rightarrow 4p$, is around 9000 eV and in the *hard X-ray* regime. The $L_{2,3}$-edge $2p \rightarrow 3d$ ($\sim$ 900 eV) and $M_{2,3}$-edge $3p \rightarrow 3d$ ($\sim$ 80 eV) are *soft X-ray* transitions. Alternatively, by tuning to the Oxygen K-edge, one can choose to promote an O $1s$ to an empty $2p$ valence state, which takes $\sim$ 500 eV.

After absorbing a soft or hard X-ray photon, the system is in a highly energetic, unstable state: a hole deep in the electronic core is present. The system quickly decays from this intermediate state, typically within 1–2 femtoseconds. Decay is possible in a number of ways, for instance via an Auger process, where an electron fills the core hole while simultaneously emitting another electron. This non-radiative decay channel is not relevant for RIXS, which instead is governed by fluorescent decay, in which the empty core-state is filled by an electron and at the same time a photon is emitted.

There are two different scattering mechanisms by which the energy and momentum of the emitted photon can change from the incident one. These are known as *direct* and *indirect* RIXS. The distinction between these two is discussed below.

2.1 Direct and indirect RIXS

Resonant inelastic X-ray scattering processes are classified as either direct or indirect [21, 22]. This distinction is useful because the cross-sections for each are quite different. When direct scattering is allowed, it is the dominant inelastic scattering channel, with indirect processes contributing only in higher order. In contrast, for the large class of experiments for which direct scattering is forbidden, RIXS relies exclusively on indirect scattering channels.

Direct RIXS For direct RIXS, the incoming photon promotes a core-electron to an empty valence band state, see Fig. 4. Subsequently an electron from a *different* state in the valence band decays and annihilates the core hole.
The net result is a final state with an electron-hole excitation, since an electron was created in an empty valence band state and a hole in the filled valence band. The electron-hole excitation can propagate through the material, carrying momentum $\hbar\mathbf{q}$ and energy $\hbar\omega$. Momentum and energy conservation require that $\mathbf{q} = \mathbf{k}' - \mathbf{k}$ and $\omega = \omega_{\mathbf{k}'} - \omega_{\mathbf{k}}$, where $\hbar\mathbf{k}$ ($\hbar\mathbf{k}'$) and $\hbar\omega_{\mathbf{k}}$ ($\hbar\omega_{\mathbf{k}'}$) are the momentum and energy of the incoming (outgoing) photon, respectively.
For direct RIXS to occur, both photoelectric transitions, the initial one from core to valence state and succeeding one from conduction state to fill the core hole, must be allowed. These transitions can for instance be an initial dipolar transition of $1s \rightarrow 2p$ followed by the decay of another electron in the $2p$ band from $2p \rightarrow 1s$, in for example wide-band gap insulators. This happens for instance at the K-edge of oxygen, carbon, and silicon. At transition-metal L-edges, dipole transitions give rise to direct RIXS via $2p \rightarrow 3d$ absorption and subsequent $3d \rightarrow 2p$ decay. In all these cases, RIXS probes the valence and conduction states directly. Although the direct transitions into the valence shell dominate the spectral line shape, the spectral weight can be affected by interactions in the intermediate-state driven by, for example, the strong core-hole potential.

Indirect RIXS The indirect RIXS process is slightly more complicated. For pure indirect RIXS to occur, photoelectric transitions from the core-state to conduction-band states must be weak. Instead, the incoming photon promotes a core-electron into an empty state several electron volts above the Fermi level. Subsequently the electron from this same state decays to fill the core hole, see Fig. 5. The most studied example is RIXS at the transition-metal K-edges ($1s \rightarrow 4p$). Obviously, in the absence of any additional interaction, no inelastic scattering would be observed. But in the intermediate state a core hole is present, which exerts a strong potential on the $3d$ valence electrons, that therefore tend to screen the core hole. The core-hole potential scatters these valence electrons, thereby creating electron-hole excitations in the valence band. After the $4p \rightarrow 1s$ decay, the electron-hole excitations are then left behind in the system.
Indirect RIXS is thus due to shakeup excitations created by the intermediate state core hole. The fact that close to the absorption edge the $1s$ core hole and $4p$ electron bind together to form an exciton does not change this picture conceptually. In this case, one may think of the valence electrons as scattering off this exciton.

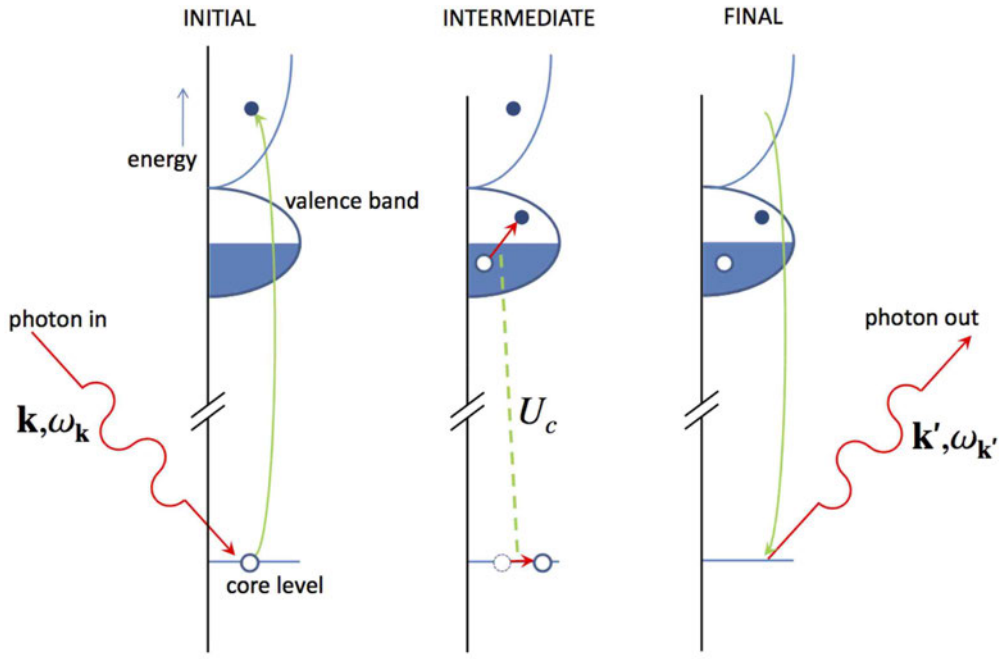

Fig. 5: *In an indirect RIXS process, an electron is excited from a deep-lying core level into the valence shell. Excitations are created through the Coulomb interaction U_c between the core hole (and in some cases the excited electron) and the valence electrons.*

In RIXS, the solid is taken from a ground state with energy E_g, to a final-state with excitations and an energy E_f. The energy and momentum of the excitation is determined by the difference in photon energy $\hbar\omega_{\mathbf{k}} - \hbar\omega_{\mathbf{k}'}$ and momentum $\hbar\mathbf{k}' - \hbar\mathbf{k}$, respectively. The RIXS intensity can in general be written in terms of a scattering amplitude as

$$I(\omega, \mathbf{k}, \mathbf{k}', \boldsymbol{\epsilon}, \boldsymbol{\epsilon}') = \sum_f \left|\mathcal{F}_{fg}(\mathbf{k}, \mathbf{k}', \boldsymbol{\epsilon}, \boldsymbol{\epsilon}', \omega_{\mathbf{k}})\right|^2 \delta(E_f + \hbar\omega_{\mathbf{k}'} - E_g - \hbar\omega_{\mathbf{k}}) \,,$$

where the delta function enforces energy conservation and the amplitude $\mathcal{F}_{fg}(\mathbf{k}, \mathbf{k}', \boldsymbol{\epsilon}, \boldsymbol{\epsilon}', \omega_{\mathbf{k}})$ reflects which excitations are probed and how, for instance, the spectral weights of final-state excitations depend on the polarization vectors, $\boldsymbol{\epsilon}$ and $\boldsymbol{\epsilon}'$ of the incoming and outgoing X-rays, respectively. The following sections derive the RIXS scattering amplitude and demonstrate how it can be broken down into separate pieces.

First, we need to derive a general expression for the RIXS scattering amplitude. Section 3 looks at the interaction between photons and matter. RIXS refers to the process where the material first absorbs a photon. The system is then in a short-lived intermediate state, from which it relaxes radiatively. In an experiment, one studies the X-rays emitted in this decay process. This two-step process cannot be described simply by using Fermi's Golden Rule, but requires a higher-order treatment, known as the Kramers-Heisenberg equation [23]. Since the absorption and emission are single-photon processes, the interactions between the X-rays and the material are dominated by the terms in the cross-section proportional to $\mathbf{p} \cdot \mathbf{A}$, where $\mathbf{p}$ is the momentum of the electrons in the material and $\mathbf{A}$ is the vector potential of the photon. The interaction

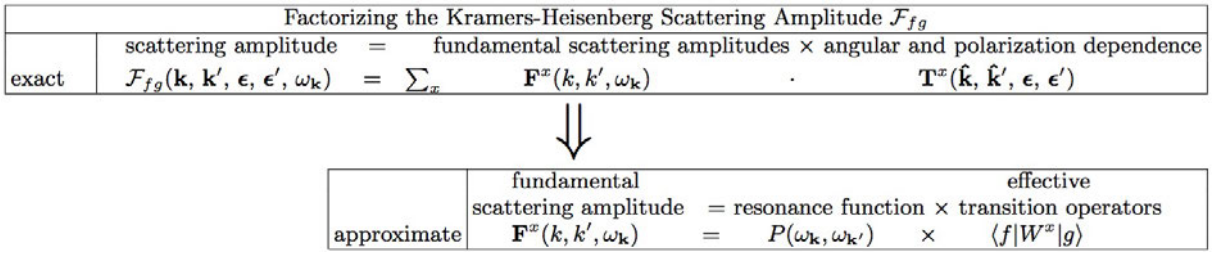

Fig. 6: *In the theory of RIXS, the scattering amplitude $\mathcal{F}_{fg}$ occurring in the Kramers-Heisenberg equation is separated into several pieces. One can split off the angular and polarization dependence $\mathbf{T}^x$, leaving fundamental scattering amplitudes $\mathbf{F}^x$. Several approximation schemes then break down these scattering amplitudes into a resonance function P and effective transition operators W^x.*

between the X-rays and the material depends on external quantities, such as wavevector $\mathbf{k}$ and polarization vectors $\boldsymbol{\epsilon}$ of the X-rays, and operators, such as $\mathbf{p}$ and $\mathbf{r}$. As a result the electronic transitions are intermingled. The scattering amplitude can be split into an angular and polarization dependence $\mathbf{T}^x(\hat{\mathbf{k}}, \hat{\mathbf{k}}', \boldsymbol{\epsilon}, \boldsymbol{\epsilon}')$ related to the experimental geometry and spectral functions $\mathbf{F}^x(k, k', \omega_{\mathbf{k}})$ that measure the properties of the material, see Fig. 6. This separation can be done exactly. It is important to note that there are only a finite number of fundamental scattering amplitudes $\mathbf{F}^x(k, k', \omega_{\mathbf{k}})$ and that the RIXS scattering amplitude is a linear combination of these fundamental scattering amplitudes weighted by the angular functions $\mathbf{T}^x(\hat{\mathbf{k}}, \hat{\mathbf{k}}', \boldsymbol{\epsilon}, \boldsymbol{\epsilon}')$.
The next step is to understand the fundamental scattering amplitudes. This can be done numerically but, in addition, several authors have used approximation schemes in order to provide more insight into the scattering amplitude. Generally, the approximations involve the propagation of the system in the time between the absorption and emission processes. The schemes generally allow the separation of the fundamental scattering amplitudes into a resonance function $P(\omega_{\mathbf{k}}, \omega_{\mathbf{k}'})$ and an effective transition between ground and final states $\langle f|W^x|g\rangle$, see Fig. 6. The resonance function gives the strength of the fundamental scattering amplitude, which is a combination of radial matrix elements of the transition operators and energy denominators that describe the resonant effect as a function of $\omega_{\mathbf{k}}$. The effective transition operators create excitations in the valence shell similar to an optical excitation. In certain cases, these operators can also be related to correlation functions such as the dynamic structure factor. The approximations depend on the RIXS process. Direct RIXS is approximated by using a fast-collision approximation and indirect RIXS can be approached via perturbative methods or an ultra-short core-hole lifetime expansion, see Section 4.1.

3 Interaction of light and matter

To develop the theory of RIXS, we first need to derive the Hamiltonian that describes the interaction of the incident X-ray beam with the electrons in the sample. The interaction terms in this Hamiltonian are small, controlled by the dimensionless fine structure constant $\alpha =$

$e^2/4\pi\epsilon_0\hbar c \approx 1/137$, with $e = |e|$ the magnitude of the elementary charge and ϵ_0 the permittivity of free space. Therefore they can be treated as a perturbation to the terms in the Hamiltonian that describe the system under study. To second order in such a perturbation theory, we obtain the Kramers-Heisenberg formula, which describes RIXS very well. We need to go to second order because two interactions are needed: one to create the core hole, and one for the subsequent radiative de-excitation.

3.1 Kramers-Heisenberg cross-section

The incident X-rays are described by an electromagnetic field with vector potential $\mathbf{A}(\mathbf{r}, t)$. The coupling between such a field and electrons is given by the theory of quantum electrodynamics. It is common to start from the exactly solvable case of a single electron without potentials ($\mathbf{A}$ and electric potential $\phi(\mathbf{r}, t)$). Then, the potentials are (perturbatively) introduced and one takes two limits. The first of these is that the electrons travel at speeds, v, small compared to the speed of light. This is a good approximation even for, e.g., copper $1s$ core electrons, where we estimate $v \sim \hbar Z/ma_0 \approx 0.21c$ with Z the atomic number for copper and a_0 the Bohr radius. At first glance, v/c might not appear small in this case, but $\gamma = 1/\sqrt{1 - v^2/c^2} \approx 1.02$ and relativistic effects are still small. The second limit is that the potentials related to both the electrons and the photons in the system are small compared to twice the mass of the electron: $e\phi/2mc^2,\ e|\mathbf{A}|/2mc \ll 1$ (m is the electron mass). Although the intrinsic potentials of materials diverge close to the nuclei, they may be treated consistently within the whole procedure for $Z \ll 137$ (see page 948 in [24]). Photon potentials at existing X-ray sources satisfy these limits. However, in the future at very strongly focussed X-ray Free Electron Lasers, the electric field of the photon is projected to exceed 10^{16} V/m, which gives $e|\mathbf{A}| \sim 2mc$ at a photon energy of ~ 8 keV so that these approximations are no longer valid. However, such effects are neglected here and the formalism is developed for non-relativistic electrons in small potentials.
In these limits, one obtains for a system with N electrons, in SI units (see pages 944–947 in [24] or pages 85–88 in [25]),

$$\begin{aligned} H = \sum_{i=1}^{N} \Bigg[& \frac{\left(\mathbf{p}_i + e\mathbf{A}(\mathbf{r}_i)\right)^2}{2m} + \frac{e\hbar}{2m}\boldsymbol{\sigma}_i \cdot \mathbf{B}(\mathbf{r}_i) \\ & + \frac{e\hbar}{2(2mc)^2}\,\boldsymbol{\sigma}_i \cdot \Big(\mathbf{E}(\mathbf{r}_i) \times \left(\mathbf{p}_i + e\mathbf{A}(\mathbf{r}_i)\right) - \left(\mathbf{p}_i + e\mathbf{A}(\mathbf{r}_i)\right) \times \mathbf{E}(\mathbf{r}_i) \Big) \Bigg] \\ & + \frac{e\hbar^2 \rho(\mathbf{r}_i)}{8(mc)^2\epsilon_0} + H_{\text{Coulomb}} + \sum_{\boldsymbol{\kappa},\boldsymbol{\varepsilon}} \hbar\omega_{\boldsymbol{\kappa}} \left(a^\dagger_{\boldsymbol{\kappa}\boldsymbol{\varepsilon}} a_{\boldsymbol{\kappa}\boldsymbol{\varepsilon}} + \frac{1}{2} \right), \end{aligned} \tag{1}$$

where $\mathbf{p}_i$, $\mathbf{r}_i$ and $\boldsymbol{\sigma}_i$ are, respectively, the momentum and position operators and the Pauli matrices acting on electron i. $\mathbf{A}(\mathbf{r})$ is the vector potential, $\mathbf{E}(\mathbf{r}) = -\nabla\phi - \partial\mathbf{A}/\partial t$, the electric field, and $\mathbf{B}(\mathbf{r}) = \nabla \times \mathbf{A}$, the magnetic field. $a^{(\dagger)}_{\boldsymbol{\kappa}\boldsymbol{\epsilon}}$ annihilates (creates) a photon in the mode with wave vector $\boldsymbol{\kappa}$ and polarization vector $\boldsymbol{\varepsilon}$. The second term yields the Zeeman splitting, and the third includes spin-orbit coupling. The interaction of electrons with an external electric

potential and with other electrons and nuclei in the sample (including the Darwin term) are all described by $H_{\rm Coulomb}$. The vector potential can be expanded in plane waves as

$$\mathbf{A}(\mathbf{r}) = \sum_{\boldsymbol{\kappa},\boldsymbol{\varepsilon}} \sqrt{\frac{\hbar}{2\mathcal{V}\epsilon_0\omega_{\boldsymbol{\kappa}}}} \left(\boldsymbol{\varepsilon}\, a_{\boldsymbol{\kappa}\boldsymbol{\varepsilon}} e^{i\boldsymbol{\kappa}\cdot\mathbf{r}} + \boldsymbol{\varepsilon}^* a^\dagger_{\boldsymbol{\kappa}\boldsymbol{\varepsilon}} e^{-i\boldsymbol{\kappa}\cdot\mathbf{r}}\right), \tag{2}$$

where $\mathcal{V}$ is the volume of the system.

In order to derive the photon scattering cross-section one splits the Hamiltonian H into an electron-photon interaction part, H', and the remaining terms, H_0, which describe the electron and photon dynamics in the absence of electron-photon interactions. H' is then treated as a perturbation to H_0. To calculate the RIXS cross-section in this perturbation scheme, it is assumed that there is a single photon in the initial state with momentum $\hbar\mathbf{k}$, energy $\hbar\omega_{\mathbf{k}}$ and polarization $\boldsymbol{\epsilon}$ that is scattered to $(\hbar\mathbf{k}', \hbar\omega_{\mathbf{k}'}, \boldsymbol{\epsilon}')$ in the final state. Photon scattering then induces a change in the material from ground state $|g\rangle$ to final state $|f\rangle$, with energies E_g and E_f respectively. In the process, the photon loses momentum $\hbar\mathbf{q} = \hbar\mathbf{k} - \hbar\mathbf{k}'$ and energy $\hbar\omega = \hbar\omega_{\mathbf{k}} - \hbar\omega_{\mathbf{k}'}$ to the sample. Fermi's Golden Rule to second order gives the transition rate for this process :

$$w \;=\; \frac{2\pi}{\hbar} \sum_{\mathtt{f}} \left| \langle \mathtt{f}|\, H' \,|\mathtt{g}\rangle + \sum_n \frac{\langle \mathtt{f}|\, H' \,|n\rangle \langle n|\, H' \,|\mathtt{g}\rangle}{E_{\mathtt{g}} - E_n} \right|^2 \delta(E_{\mathtt{f}} - E_{\mathtt{g}}), \tag{3}$$

where the initial state $|\mathtt{g}\rangle = |g; \mathbf{k}\boldsymbol{\epsilon}\rangle$, the intermediate state $|n\rangle$ and the final state $|\mathtt{f}\rangle = |f; \mathbf{k}'\boldsymbol{\epsilon}'\rangle$ are eigenstates of H_0 with energies $E_{\mathtt{g}} = E_g + \hbar\omega_{\mathbf{k}}$, E_n, and $E_{\mathtt{f}} = E_f + \hbar\omega_{\mathbf{k}'}$, respectively. The first order amplitude in general dominates the second order, but when the incoming X-rays are in resonance with a specific transition in the material ($E_{\mathtt{g}} \approx E_n$), then the second order terms become large. The second order amplitude causes resonant scattering, while the first order yields non-resonant scattering.

In order to derive H' it is useful to classify the terms of Eq. (1) by powers of $\mathbf{A}$. Terms of H that are quadratic in $\mathbf{A}$ are the only ones to contribute to the first order amplitude, because they contain terms proportional to $a^\dagger_{\mathbf{k}'\boldsymbol{\epsilon}'} a_{\mathbf{k}\boldsymbol{\epsilon}}$ and $a_{\mathbf{k}\boldsymbol{\epsilon}} a^\dagger_{\mathbf{k}'\boldsymbol{\epsilon}'}$. To be specific, the quadratic contribution from the first term of H gives rise to non-resonant scattering, while the third term of H yields magnetic non-resonant scattering. Although both appear in the first order scattering amplitude, they in principle also contribute to the second order, but we neglect these processes because they are of order $\alpha^{3/2}$.

The interaction terms linear in $\mathbf{A}$ do not contribute to the first order amplitude, but do contribute to the second order. They thus give rise to resonant processes. In the following, we neglect such contributions that come from the third term of Eq. (1), because they are of second order in two separate expansions. Firstly, this term of H is of second order in the limits discussed above, and secondly, it appears in the second order of the scattering amplitude. Finally, all terms in Eq. (1) that are independent of $\mathbf{A}$ are included in H_0. The relevant remaining terms are

$$H' = \sum_{i=1}^{N} \left[\frac{e}{m}\mathbf{A}(\mathbf{r}_i)\cdot\mathbf{p}_i + \frac{e^2}{2m}\mathbf{A}^2(\mathbf{r}_i) + \frac{e\hbar}{2m}\boldsymbol{\sigma}_i\cdot\nabla\times\mathbf{A}(\mathbf{r}_i) - \frac{e^2\hbar}{(2mc)^2}\boldsymbol{\sigma}_i\cdot\frac{\partial\mathbf{A}(\mathbf{r}_i)}{\partial t}\times\mathbf{A}(\mathbf{r}_i)\right], \tag{4}$$

where the gauge was fixed by choosing $\nabla\cdot\mathbf{A}(\mathbf{r}) = 0$ so that $\mathbf{A}\cdot\mathbf{p} = \mathbf{p}\cdot\mathbf{A}$.

The two terms of H' that contribute to the first order amplitude are the one proportional to $\mathbf{A}^2$ and the $\boldsymbol{\sigma}\cdot(\partial\mathbf{A}/\partial t)\times\mathbf{A}$ term. The latter is smaller than the former by a factor $\hbar\omega_{\mathbf{k}^{(\prime)}}/mc^2 \ll 1$, and is therefore neglected. The first order term in Eq. (3) then becomes

$$\frac{e^2}{2m}\langle \mathtt{f}|\sum_i \mathbf{A}^2(\mathbf{r}_i)\,|\mathrm{g}\rangle = \frac{\hbar e^2}{2m\mathcal{V}\epsilon_0}\frac{\boldsymbol{\epsilon}'^*\cdot\boldsymbol{\epsilon}}{\sqrt{\omega_{\mathbf{k}}\omega_{\mathbf{k}'}}}\langle f|\sum_i e^{i\mathbf{q}\cdot\mathbf{r}_i}\,|g\rangle\,. \tag{5}$$

When the incident energy $\hbar\omega_{\mathbf{k}}$ is much larger than any resonance of the material, the scattering amplitude is dominated by this channel, which is called Thompson scattering. In scattering from a crystal at zero energy transfer, this term contributes amongst others to the Bragg peaks. It also gives rise to non-resonant inelastic scattering. In practice, RIXS spectra show a strong resonance behavior, demonstrating that for these processes, it is the second order term that dominates the scattering. We therefore omit the $\mathbf{A}^2$ contribution in the following. More details on non-resonant inelastic X-ray scattering can be found in, for instance, [8, 26].

The second order amplitude in Eq. (3) becomes large when $\hbar\omega_{\mathbf{k}}$ matches a resonance energy of the system, and the incoming photon is absorbed first in the intermediate state, creating a core hole. The denominator $E_g+\hbar\omega_{\mathbf{k}}-E_n$ is then small, greatly enhancing the second order scattering amplitude. We neglect the other, off-resonant processes here, though they do give an important contribution to non-resonant scattering [6]. The resonant part of the second order amplitude is

$$\frac{e^2\hbar}{2m^2\mathcal{V}\epsilon_0\sqrt{\omega_{\mathbf{k}}\omega_{\mathbf{k}'}}}\sum_n\sum_{i,j=1}^{N}\frac{\langle f|\,e^{-i\mathbf{k}'\cdot\mathbf{r}_i}\left(\boldsymbol{\epsilon}'^*\cdot\mathbf{p}_i-\frac{i\hbar}{2}\boldsymbol{\sigma}_i\cdot\mathbf{k}'\times\boldsymbol{\epsilon}'^*\right)|n\rangle}{E_g+\hbar\omega_{\mathbf{k}}-E_n+i\Gamma_n}\langle n|\,e^{i\mathbf{k}\cdot\mathbf{r}_j}\left(\boldsymbol{\epsilon}\cdot\mathbf{p}_j+\frac{i\hbar}{2}\boldsymbol{\sigma}_j\cdot\mathbf{k}\times\boldsymbol{\epsilon}\right)|g\rangle \tag{6}$$

where a lifetime broadening Γ_n is introduced for the intermediate states. This accounts for the many non-radiative interaction terms that are not included in H' (for example Auger decay), which make the intermediate states very short lived.

Resonant scattering can thus occur via a magnetic and a non-magnetic term. An estimate shows that the latter dominates. The size of localized $1s$ copper core orbitals is $a_0/Z \approx 0.018$ Å so that for 10 keV photons the exponential $e^{i\mathbf{k}\cdot\mathbf{r}}$ is close to unity and can be expanded. The non-magnetic term can induce a dipole transition of order $|\mathbf{p}| \sim \hbar Z/a_0 \sim 5.9\cdot10^{-23}$ kg m/s, whereas the magnetic term gives a dipole transition of order $(\mathbf{k}\cdot\mathbf{r})\hbar|\mathbf{k}|/2 \sim 2.5\cdot10^{-25}$ kg m/s. We thus ignore the magnetic term here, and the relevant transition operator for the RIXS cross-section is

$$\mathcal{D} = \frac{1}{im\omega_{\mathbf{k}}}\sum_{i=1}^{N} e^{i\mathbf{k}\cdot\mathbf{r}_i}\,\boldsymbol{\epsilon}\cdot\mathbf{p}_i\,, \tag{7}$$

where a prefactor has been introduced for convenience in the following expressions.

The double-differential cross-section $I(\omega,\mathbf{k},\mathbf{k}',\boldsymbol{\epsilon},\boldsymbol{\epsilon}')$ is now obtained by multiplying by the density of photon states in the solid angle $d\Omega$ $(=\mathcal{V}\mathbf{k}'^2\,d|\mathbf{k}'|\,d\Omega/(2\pi)^3)$ and dividing by the incident flux $c/\mathcal{V}$ [25, 6, 8]

$$I(\omega,\mathbf{k},\mathbf{k}',\boldsymbol{\epsilon},\boldsymbol{\epsilon}') = r_e^2m^2\omega_{\mathbf{k}'}^3\omega_{\mathbf{k}}\sum_{\mathtt{f}}|\mathcal{F}_{fg}(\mathbf{k},\mathbf{k}',\boldsymbol{\epsilon},\boldsymbol{\epsilon}',\omega_{\mathbf{k}},\omega_{\mathbf{k}'})|^2\,\delta(E_g-E_f+\hbar\omega)\,, \tag{8}$$

where the classical electron radius $r_e = \frac{1}{4\pi\epsilon_0}\frac{e^2}{mc^2}$. The scattering amplitude at zero temperature is given by

$$\mathcal{F}_{fg}(\mathbf{k},\mathbf{k}',\boldsymbol{\epsilon},\boldsymbol{\epsilon}',\omega_{\mathbf{k}},\omega_{\mathbf{k}'}) = \sum_n \frac{\langle f|\,\mathcal{D}'^{\dagger}\,|n\rangle\,\langle n|\,\mathcal{D}\,|g\rangle}{E_g+\hbar\omega_{\mathbf{k}}-E_n+i\Gamma_n}, \tag{9}$$

where the prime in $\mathcal{D}'$ indicates it refers to transitions related to the outgoing X-rays. Eqs. (8) and (9) are referred to as the Kramers-Heisenberg equations, which are generally used to calculate the RIXS cross-section.

Alternatively, we can rewrite the denominator for the intermediate-states in terms of a Green function, which is also referred to as the intermediate-state propagator, which describes the system in the presence of a core hole:

$$G(z_{\mathbf{k}}) = \frac{1}{z_{\mathbf{k}}-H} = \sum_n \frac{|n\rangle\langle n|}{z_{\mathbf{k}}-E_n}, \tag{10}$$

where $|n\rangle$ forms a complete basis set and

$$z_{\mathbf{k}} = E_g + \hbar\omega_{\mathbf{k}} + i\Gamma, \tag{11}$$

where Γ is taken to be independent of the intermediate states. The quantity $z_{\mathbf{k}}$ is the energy of the initial state combined with the finite lifetime of the core hole. In the following we will often suppress the explicit label $\mathbf{k}$ of $z_{\mathbf{k}}$ and denote it simply by z, with an implicit incident energy dependence. With the core-hole propagator G and transition operators $\mathcal{D}$ in place, the RIXS scattering amplitude $\mathcal{F}_{fg}$ finally reduces to the elegant expression

$$\mathcal{F}_{fg} = \langle f|\,\mathcal{D}'^{\dagger}\,G(z_{\mathbf{k}})\,\mathcal{D}\,|g\rangle\,. \tag{12}$$

3.2 Scattering amplitude in dipole approximation

In the previous section, Eqs. (8) and (9) give the Kramers-Heisenberg expression for RIXS. The next step is to separate the part pertaining to the geometry of the experiment from the fundamental scattering amplitudes that relate to the physical properties of the system, see Fig. 6. In addition, better-defined transition operators will be obtained. Due to the complexity of the multipole expansion, we first give a derivation in the dipole limit allowing the reader to better follow the arguments. In the next section, we present the higher order transitions.

In the dipole limit, one assumes that $e^{i\mathbf{k}\cdot\mathbf{r}_i} \cong e^{i\mathbf{k}\cdot\mathbf{R}_i}$ where $\mathbf{R}_i$ indicates the position of the ion to which electron i is bound. Note that $\mathbf{R}_i$ is not an operator. This has as a result that the electronic transitions are due to the momentum operator $\mathbf{p}$ and Eq. (7) becomes

$$\mathcal{D} = \boldsymbol{\epsilon}\cdot\mathbf{D} \quad \text{with} \quad \mathbf{D} = \frac{1}{im\omega_{\mathbf{k}}}\sum_{i=1}^{N} e^{i\mathbf{k}\cdot\mathbf{R}_i}\mathbf{p}_i\,. \tag{13}$$

Generally, the matrix elements are expressed in terms of the position operator $\mathbf{r}$. For example, in the absorption step, one can write

$$\begin{aligned}\langle n|\,\mathbf{D}\,|g\rangle &= \sum_{i=1}^{N}\frac{e^{i\mathbf{k}\cdot\mathbf{R}_i}}{im\omega_{\mathbf{k}}}\langle n|\,\mathbf{p}_i\,|g\rangle \;=\; \sum_{i=1}^{N}\frac{e^{i\mathbf{k}\cdot\mathbf{R}_i}}{\hbar\omega_{\mathbf{k}}}\langle n|\,[\frac{\mathbf{p}_i^2}{2m},\mathbf{r}_i]\,|g\rangle \\ &\cong \sum_{i=1}^{N}\frac{e^{i\mathbf{k}\cdot\mathbf{R}_i}}{\hbar\omega_{\mathbf{k}}}(E_n-E_g)\langle n|\,\mathbf{r}_i\,|g\rangle \;\cong\; \sum_{i=1}^{N}e^{i\mathbf{k}\cdot\mathbf{R}_i}\langle n|\,\mathbf{r}_i\,|g\rangle\ ,\end{aligned}$$

where $\hbar\omega_{\mathbf{k}} \cong E_n - E_g$. The operator thus reduces to the dipole operator $\mathbf{D} = \sum_{i=1}^{N} e^{i\mathbf{k}\cdot\mathbf{R}_i}\mathbf{r}_i$ that causes electronic transitions.

The next step is to separate the part that pertains to the geometry of the experiment (the polarization vectors $\boldsymbol{\epsilon}'$ and $\boldsymbol{\epsilon}$) from the physical properties of the system. Ultimately, our interest lies in the spectral functions of a material. The geometry is chosen in an optimal way to measure them. Using spherical-tensor algebra, we can rewrite the scattering amplitude, Eq. (12), remaining in the dipole limit, Eq. (13), as

$$\mathcal{F}_{fg} = \sum_{x=0}^{2}[x]\,n_{11x}^2\,\langle f|\,[\boldsymbol{\epsilon}'^{*},\,\boldsymbol{\epsilon}]^x\cdot[\mathbf{D}^\dagger,\,G(z_{\mathbf{k}})\mathbf{D}]^x\,|g\rangle\,,$$

using the shorthand $[l_1\cdots l_n] = (2l_1+1)\cdots(2l_n+1)$; n_{11x} is a normalization constant, and $[\ ,\ ]^x$ is a tensor product. Since the tensor product couples tensors of rank 1 (the polarization vectors and the position vector $\mathbf{r}$), the rank x of the tensor products can assume the values 0, 1, and 2. The fundamental scattering amplitudes are given by

$$\mathbf{F}^x(z_{\mathbf{k}}) = \langle f|\,[\mathbf{D}^\dagger,\,G(z_{\mathbf{k}})\mathbf{D}]^x\,|g\rangle\,. \tag{14}$$

For each value of x, there are $2x+1$ components F_q^x with $q = -x, -x+1, \ldots, x$. Note that, whereas there is an infinite number of different scattering amplitudes, for dipole transitions, there are only nine fundamental ones ($3\times 3 = 1+3+5 = 9$). All the other possible scattering amplitudes are combinations of these fundamental scattering amplitudes with a weighting determined by the angular dependence

$$\mathbf{T}^x(\boldsymbol{\epsilon},\boldsymbol{\epsilon}') = [x]n_{11x}^2[\boldsymbol{\epsilon}'^{*},\boldsymbol{\epsilon}]^x, \tag{15}$$

which again has nine components $T_q^x(\boldsymbol{\epsilon},\boldsymbol{\epsilon}')$. For $x = 0, 1$, the angular dependence is given by the inner product, $T_0^0(\boldsymbol{\epsilon},\boldsymbol{\epsilon}') = \frac{1}{3}\boldsymbol{\epsilon}'^{*}\cdot\boldsymbol{\epsilon}$, and the outer product, $T_\alpha^1(\boldsymbol{\epsilon},\boldsymbol{\epsilon}') = \frac{1}{2}(\boldsymbol{\epsilon}'^{*}\times\boldsymbol{\epsilon})_\alpha$ of the polarization vectors, respectively. The total scattering amplitude in the dipole limit can now be written as

$$\mathcal{F}_{fg}(\boldsymbol{\epsilon},\boldsymbol{\epsilon}',\omega_{\mathbf{k}}) = \sum_{x=0}^{2}\mathbf{T}^x(\boldsymbol{\epsilon},\boldsymbol{\epsilon}')\cdot\mathbf{F}^x(z_{\mathbf{k}})\,. \tag{16}$$

The spectra for different x and q are combinations of the spectra for different polarizations. Usually, the scattering amplitudes are calculated in terms of the components D_α of the dipole operator, where $\alpha = 1, 0, -1$ in spherical symmetry or $\alpha = x, y, z$ in Cartesian coordinates.

The spectra for different polarizations are then combined to form the fundamental scattering amplitudes. This can be compared with X-ray absorption. The circular dichroic spectrum (the $x = 1$ fundamental spectrum for X-ray absorption) is usually calculated by subtracting the spectra for left and right circularly polarized light ($\alpha = \pm 1$). The scattering amplitudes in terms of the components of the dipole operator are given by

$$F_{\alpha'\alpha} = \langle f | D^\dagger_{\alpha'} G(z_{\mathbf{k}}) D_\alpha | g \rangle = \sum_n \frac{\langle f | D^\dagger_{\alpha'} | n \rangle \langle n | D_\alpha | g \rangle}{\hbar\omega_{\mathbf{k}} + E_g - E_n + i\Gamma} . \tag{17}$$

Note that again there are only nine spectra and this is just a representation of the nine fundamental spectra in a different basis. The simplest scattering amplitude is the isotropic one given by $x = 0$. The tensor containing the isotropic scattering amplitudes $\mathbf{F}^0$ has only one component F^0_0,

$$F^0_0 = F_{00} + F_{11} + F_{-1,-1} = F_{xx} + F_{yy} + F_{zz}, \tag{18}$$

which is just a sum of all the different polarization components. For the expressions in spherical symmetry, note that, since $r^\dagger_{i\alpha'} = (-1)^{\alpha'} r_{i,-\alpha'}$, there is no net transfer of angular momentum to the system for the isotropic scattering amplitude. Since the angular dependence is given by $\mathbf{T}^0 = \boldsymbol{\epsilon}'^* \cdot \boldsymbol{\epsilon}$, the isotropic contribution to the spectral line shape is removed in many experiments by the use of a 90° scattering condition with the incoming polarization vector in the scattering plane (π-polarized). This makes the incoming polarization vector perpendicular to both possible outgoing polarization vectors and therefore $\boldsymbol{\epsilon}'^* \cdot \boldsymbol{\epsilon} = 0$. In addition, this has the advantage that it strongly reduces the non-resonant $\mathbf{A}^2$ term from the experimental RIXS data (which has the same polarization dependence). This contributes mostly to the elastic line and is frequently the major experimental impediment to measuring low-energy excitations.

Tensors of rank $x = 1$ have three components. For example, the $q = 0$ component is given by

$$F^1_0 = F_{11} - F_{-1,-1} = F_{xy} - F_{yx}. \tag{19}$$

For resonant elastic X-ray scattering, the F^1_0 scattering amplitude is the one that gives rise to, amongst others, magnetic scattering. The angular dependence for $x = 1$, is given by an outer product $\mathbf{T}^1 = \boldsymbol{\epsilon}'^* \times \boldsymbol{\epsilon}$.

At this point it is useful to make a comparison with X-ray absorption (XAS) and resonant X-ray (elastic) scattering (RXS), which are determined by the scattering amplitude $\mathcal{F}_{gg}$

$$I_{\mathrm{XAS}}(\boldsymbol{\epsilon}, \omega_{\mathbf{k}}) = -\frac{1}{\pi} \mathrm{Im}\left[\mathcal{F}_{gg}(\boldsymbol{\epsilon}, \boldsymbol{\epsilon}, \omega_{\mathbf{k}})\right] \tag{20}$$

$$I_{\mathrm{RXS}}(\boldsymbol{\epsilon}, \boldsymbol{\epsilon}', \omega_{\mathbf{k}}) = |\mathcal{F}_{gg}(\boldsymbol{\epsilon}, \boldsymbol{\epsilon}', \omega_{\mathbf{k}})|^2, \tag{21}$$

where for X-ray absorption, there is only a polarization vector for the incident X-rays, and $\boldsymbol{\epsilon}' \equiv \boldsymbol{\epsilon}$. Since for XAS and RXS the "final" state is equivalent to the ground state in the scattering amplitude ($|f\rangle = |g\rangle$) an additional restriction is imposed on the scattering. In many symmetries, this means that only the $q = 0$ component contributes, reducing the scattering amplitude determining XAS and RXS to

$$\mathcal{F}_{gg}(\omega_{\mathbf{k}}) = \sum_{x=0}^{2} T^x_0(\boldsymbol{\epsilon}, \boldsymbol{\epsilon}')\, F^x_0(z_{\mathbf{k}}) . \tag{22}$$

This implies that of the $3 \times 3 = 9$ components in the full scattering amplitude, only 3 components, corresponding to $x = 0, 1, 2$ and $q = 0$, remain. For X-ray absorption, these correspond to the well-known isotropic, circular dichroic, and linear dichroic spectra, respectively.

3.3 Scattering amplitude for a multipole expansion

We next generalize the ideas from the previous section to include the different types of multipoles arising from the $\mathbf{p} \cdot \mathbf{A}$ interaction in Eq. (4). Since the dipolar and quadrupolar transitions in RIXS are predominantly excitations from a localized core hole into the valence states, the common approach is to expand the plane wave in the vector potential, see Eq. (2), around the site where the absorption takes place. Essentially, one is using an approximation of the type $e^{i\mathbf{k}\cdot\mathbf{r}_i} \cong 1 + i\mathbf{k} \cdot \mathbf{r}_i$ but in spherical harmonics. In the previous section, we treated the case that $e^{i\mathbf{k}\cdot\mathbf{r}_i} \cong 1$. The plane wave can be expanded in terms of spherical harmonics $Y_{lm}(\theta, \varphi)$ and spherical Bessel functions j_l [27]

$$e^{i\mathbf{k}\cdot\mathbf{r}_i} = 4\pi \sum_{l=0}^{\infty} \sum_{m=-l}^{l} i^l j_l(kr_i)\, Y^*_{lm}(\theta_{\hat{\mathbf{k}}}, \varphi_{\hat{\mathbf{k}}})\, Y_{lm}(\theta_{\hat{\mathbf{r}}_i}, \varphi_{\hat{\mathbf{r}}_i}).$$

In order to arrive at the standard transition operators, it makes sense, at this point, to rewrite the above equation in terms of spherical tensors. A common set of tensors are the normalized spherical harmonics, which we write as the tensor $\hat{\mathbf{r}}^{(l)}$ with components $\hat{r}^{(l)}_m = \sqrt{4\pi/[l]}\, Y_{lm}(\theta_{\hat{\mathbf{r}}}, \varphi_{\hat{\mathbf{r}}})$. In addition, $\mathbf{r}^{(l)} = r^l \hat{\mathbf{r}}^{(l)}$. Note that $\mathbf{r}^{(0)} = 1$. For spherical harmonic tensors of order $l = 1$, the superscript is dropped $\mathbf{r} = \mathbf{r}^{(l)}$. This allows us to rewrite the expansion as

$$e^{i\mathbf{k}\cdot\mathbf{r}_i} = \sum_{l=0}^{\infty} [l]\, i^l j_l(kr)\, \hat{\mathbf{k}}^{(l)} \cdot \hat{\mathbf{r}}^{(l)}_i. \tag{23}$$

As in the previous section, we want to separate the momentum and polarization vectors of the X-rays (the geometry of the experiment) from the transitions in the material under consideration (the fundamental spectra). This can be done by recoupling the different tensors. Recoupling of the tensors [27–29] leads to

$$\mathcal{D} \;=\; \frac{1}{im\omega} \sum_{i=1}^{N} e^{i\mathbf{k}\cdot\mathbf{r}_i}\, \boldsymbol{\epsilon} \cdot \mathbf{p}_i = \frac{1}{im\omega} \sum_{i=1}^{N} \sum_{lL} \frac{[lL]\, i^l}{[l]!!} n^2_{1lL}\, k^l [\mathbf{p}_i, \mathbf{r}^{(l)}_i]^L \cdot [\boldsymbol{\epsilon},\, \hat{\mathbf{k}}^{(l)}]^L, \tag{24}$$

where the approximation $j_l(kr) \cong (kr)^l/[l]!!$ for $kr \ll 1$ has been used, with the double factorial $l!! = l(l-2)\cdots$. Note that the operators acting on the electrons, namely the momentum $\mathbf{p}_i$ and position $\mathbf{r}_i$, are coupled together to form an effective operator $\mathbf{D}^{lL}$ of rank $L = l-1, l, l+1$. The quantities related to the photons, namely, the wavevector $\mathbf{k}$ and polarization $\boldsymbol{\epsilon}$ also form a tensor of rank L. Let us first consider the transition operators in Eq. (24) by introducing the transition operators [30]

$$\mathbf{D}^{lL} = \frac{p_{lL}(k)}{im\omega} \sum_{i=1}^{N} [\mathbf{p}_i,\, \mathbf{r}^{(l)}_i]^L, \tag{25}$$

with $p_{lL}(k) = [lL]\, n_{1lL}^2\, k^l/[l]!! = 1,\ k/2,\ k/6$ for $lL = 01, 11, 12$, respectively. The values of l and L give rise to the usual dipolar ($lL = 01$), magnetic dipolar (11), and quadrupolar (12) transition operators. For $l = 0$, one has $\mathbf{r}_i^{(0)} = 1$ and the operator simplifies to $\mathbf{D}^{01} = \sum_i \mathbf{p}_i/im\omega$, which is equivalent to the dipole operator in Eq. (13) of the previous Section. In cartesian coordinates, the operator $[\mathbf{r}_i, \mathbf{p}_i]^1 = \mathbf{L}_i$ and $\mathbf{D}^{11} = \frac{\alpha a_0}{2} \sum_i \mathbf{L}_i$, with a_0 the Bohr radius and the angular momentum given in $\hbar$. The orbital moment forms, together with the Zeeman term in Eq. (1), the magnetic dipole transition. Since magnetic dipole transitions are of the order of $\alpha^2 = 1/137^2$, i.e., about five orders of magnitude, smaller than the electric dipole transitions of the same wavelength, they will be neglected in the remainder of this paper. The next operator is $\mathbf{D}^{12} = \frac{k}{6} \sum_{i=1}^N \mathbf{r}_i^{(2)}$ which is the electric quadrupole operator.

In the remainder, we limit ourselves to the electric L-pole transitions, and we can drop the $l = L - 1$ from the expressions, i.e., $\mathbf{D}^{L-1,L} \rightarrow \mathbf{D}^L$. The transition operators are then $\mathcal{D} \sim [\boldsymbol{\epsilon}, \mathbf{k}^{(L-1)}]^L \cdot \mathbf{D}^L$ with $\mathbf{D}^L = p_L(k) \sum_{i=1}^N \mathbf{r}_i^{(L)}$ with $L = 1, 2$ for dipolar and quadrupolar transitions, respectively. The relative strengths of the components of the multipole transition operators $r_M^{(L)}$ depend on the direction of polarization and wavevector through $[\boldsymbol{\epsilon}, \mathbf{k}^{(L-1)}]^L$. These reduce to $\boldsymbol{\epsilon}$ and $[\boldsymbol{\epsilon}, \mathbf{k}]^2$, for the electric dipolar and quadrupolar transitions, respectively. As discussed in the previous section, the part that depends on the geometry of the experiment and the fundamental spectra (9 and 25 for dipolar and quadrupolar transitions, respectively) that describe the physical properties of the system can be separated exactly. This can again be achieved by applying a recoupling on the scattering amplitude, which can then be rewritten as

$$F_{fg}(\mathbf{k}, \mathbf{k}', \boldsymbol{\epsilon}, \boldsymbol{\epsilon}', \omega_{\mathbf{k}}) = \sum_{x=0}^{2L} \mathbf{T}^{Lx}(\hat{\mathbf{k}}, \hat{\mathbf{k}}', \boldsymbol{\epsilon}, \boldsymbol{\epsilon}') \cdot \mathbf{F}^{Lx}(k, k', \omega_{\mathbf{k}})\,.$$

Neglecting interference effects between different multipoles, the scattering amplitude for a particular multipole is given by [30]

$$\mathbf{F}^{Lx}(k, k', \omega_{\mathbf{k}}) = \sum_n \frac{[\langle f|\,(\mathbf{D}^L)^\dagger\,|n\rangle\,, \langle n|\,\mathbf{D}^L\,|g\rangle]^x}{\hbar\omega_{\mathbf{k}} + E_g - E_n + i\Gamma},$$

which has angular dependence

$$\mathbf{T}^{Lx}(\hat{\mathbf{k}}, \hat{\mathbf{k}}', \boldsymbol{\epsilon}, \boldsymbol{\epsilon}') = [x]\, n_{LLx}^2\, [[\boldsymbol{\epsilon}'^*, \hat{\mathbf{k}}'^{(L-1)}]^L,\ [\boldsymbol{\epsilon}, \hat{\mathbf{k}}^{(L-1)}]^L]^x.$$

The above equations give an exact separation of the Kramers-Heisenberg expression for RIXS into an angular dependence and a fundamental scattering amplitude, achieving the first step shown in Fig. 6.

In the previous section the Kramers-Heisenberg expression for the RIXS scattering amplitude $\mathcal{F}_{\mathtt{fg}}$, Eq. (9), was derived and re-expressed as a product of a photon absorption operator $\mathcal{D}$, the intermediate state propagator G and a photon emission operator $\mathcal{D}^\dagger$, sandwiched between the RIXS final and ground state

$$\mathcal{F}_{\mathtt{fg}} = \langle \mathtt{f}|\mathcal{D}^\dagger\, G\, \mathcal{D}|\mathtt{g}\rangle\,. \tag{26}$$

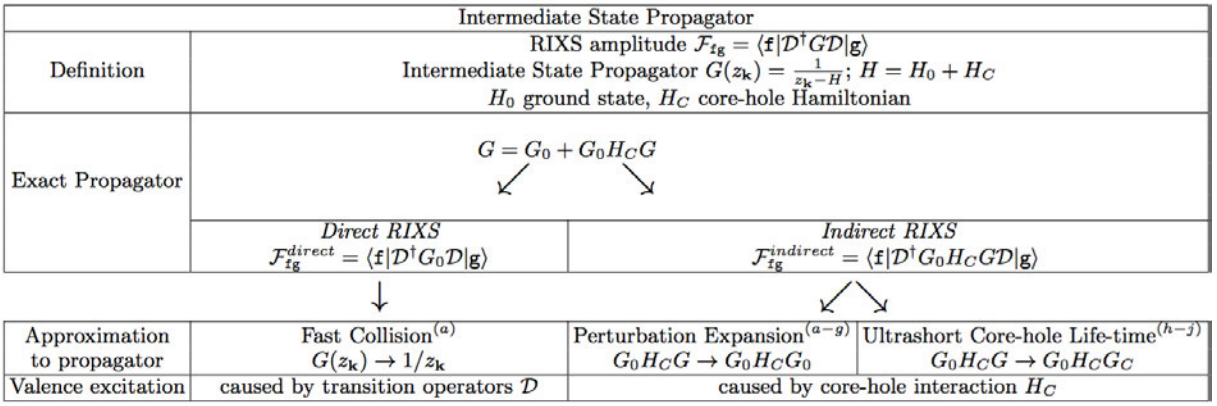

Fig. 7: *Theoretical approach to the intermediate state propagator, classifying direct and indirect RIXS processes and common approximations to the propagator:* [a] *[31],* [b] *[32],* [c] *[33],* [d] *[34],* [e] *[35],* [f] *[36],* [g] *[37],* [h] *[21],* [i] *[22],* [j] *[38].*

The presence of the intermediate state propagator is what makes the theory of RIXS complicated – and interesting. The propagator G is defined in terms of the inverse of the total Hamiltonian H of the system, $G(z_\mathtt{k}) = (z_\mathtt{k} - H)^{-1}$, where the operator H naturally divides into the ground state Hamiltonian H_0 (governing the quantum system without a core hole) and the core-hole Hamiltonian H_C perturbing the system after photon absorption: $H = H_0 + H_C$. It should be noted that even if one commonly refers to H_C as the core-hole Hamiltonian, it also includes the interaction between the electron excited into the conduction band and the rest of the material. As core hole and excited electron together form an exciton, their separate effects on the system cannot, in principle, be disentangled.

4 Definition of direct/indirect RIXS

At this point it is useful to separate the full propagator G into the unperturbed propagator $G_0 = (z_\mathtt{k} - H_0)^{-1}$ and a term that contains the core-hole Hamiltonian H_C, using the identity $G = G_0 + G_0 H_C G$. This also separates the RIXS amplitude into two parts, which define *direct* and *indirect* RIXS [22]:

$$\mathcal{F}^{\text{direct}}_{\mathtt{fg}} = \langle \mathtt{f}|\mathcal{D}^\dagger\, G_0\, \mathcal{D}|\mathtt{g}\rangle \tag{27}$$

and

$$\mathcal{F}^{\text{indirect}}_{\mathtt{fg}} = \langle \mathtt{f}|\mathcal{D}^\dagger\, G_0 H_C G\, \mathcal{D}|\mathtt{g}\rangle\,. \tag{28}$$

Note that this definition of direct/indirect RIXS, based on the Kramers-Heisenberg expression, is exact.

For the direct RIXS amplitude, the core hole does not play a role – the photon absorption and emission matrix elements determine which electronic transitions are allowed. The physical picture that arises for direct RIXS is that an incoming photon promotes a core-electron to an

empty valence state and subsequently an electron from a different state in the valence band decays, annihilating the core hole, see Fig. 4. Thus for direct RIXS to occur, both photoelectric transitions, the initial one from core to valence state and the succeeding one from valence state to fill the core hole, must be allowed. These transitions can, for example, be an initial dipolar transition of $1s \rightarrow 2p$ followed by the decay of another electron in the $2p$ band from $2p \rightarrow 1s$. This happens at the K-edge of oxygen, carbon and silicon. In addition, at transition-metal (TM) L-edges, dipole transitions causing direct RIXS are possible via $2p \rightarrow 3d$ and $3d \rightarrow 2p$ dipolar transitions. In all these cases RIXS probes the valence and conduction states directly.
For indirect RIXS, the scattering amplitude depends critically on the perturbing core-hole Hamiltonian; without it the indirect scattering amplitude vanishes. In general the scattering, $\mathcal{F}_{\mathtt{fg}}^{\mathrm{indirect}}$, arises from the combined influence of H_C and transition matrix elements $\mathcal{D}$. Most often for indirect RIXS, $\mathcal{D}$/$\mathcal{D}^\dagger$ create/annihilate an electron in the same state, far above the Fermi level. For instance at the TM K-edge, the $1s \leftrightarrow 4p$ process creates/annihilates an electron in $4p$ states electonvolts above the TM $3d$ valence shell. The delocalized $4p$ electron can then be approximated as being a *spectator* because (Coulomb) interactions involving the localized core hole are usually much stronger and dominate the scattering cross-section.
It should be noted that if scattering is direct, as for instance at TM L-edges, indirect processes can also contribute to the total scattering amplitude. However, as indirect scattering arises in this case as a higher order process, it is normally weaker than the leading order direct scattering amplitude. Conversely, in case of indirect RIXS, direct processes are absent by definition.

4.1 Effective theory for indirect RIXS

In the previous section, we have seen that the direct RIXS process can be written in terms of effective transition operators (see Eq. (27)) that do not involve the core-hole Hamiltonian H_C. When higher-order contribution are neglected, this approach corresponds to the fast-collision approximation, or the lowest order in the ultrashort core-hole lifetime (UCL) expansion, see Sec. 4.3. Indirect RIXS is different, as these lowest order terms do not contribute to its RIXS cross-section and the scattering process critically depends on the higher-order terms. For example, K-edge RIXS is dominated by excitations into the transition-metal $4p$ states. Since the $4p$ states are usually almost completely empty, the effective operators for direct RIXS only contribute to the elastic line, where the effective transition operator creates an electron in the valence shell in the excitation step and annihilates it again in the emission process.
Experimentally, however, RIXS is observed at the K-edge. Particularly prominent are the charge-transfer type excitations. Also the excitation of d-d transitions and magnons have been observed. The general consensus is that these excitations are created through the interaction between the valence shell and the $1s$-$4p$ excitation created in the absorption process. Most work has focused on the interaction with the potential of the $1s$ core hole, which is known to be of the order of 6–8 eV. This potential can be written as

$$H_C = \sum_{\mathbf{k}\mathbf{k}'\mathbf{q}\mu\sigma\sigma'} U_{1s,3d}\, d^\dagger_{\mathbf{k}+\mathbf{q},\mu\sigma} s^\dagger_{\mathbf{k}'-\mathbf{q},\sigma'} s_{\mathbf{k}'\sigma'} d_{\mathbf{k}\mu\sigma}\,, \tag{29}$$

where μ sums over the different orbitals. The potential can in principle contain exchange terms, but these are negligible at the K-edge. The transient presence of this potential in the intermediate state leads to strong screening dynamics in the valence shell giving rise to the final-state excitations. This Section discusses some of the methods used to describe the excitations created by interactions in the intermediate state.

4.1.1 Momentum dependence for indirect RIXS

Recognizing that for indirect RIXS the core hole dominates the scattering process has an important consequence for the momentum dependence. In the hard X-ray regime photons have a momentum $\mathbf{q}$ that can span several Brillouin zones because it is larger than the reciprocal lattice vectors $\mathbf{G}$. The photon momentum reduced to the first Brillouin zone is, by definition, $\boldsymbol{\kappa} = \mathbf{q} - n\mathbf{G}$. The translational invariance and localized nature of the core potential in Eq. (29) imply that the momentum dependence of RIXS is determined by the *reduced* momentum $\boldsymbol{\kappa}$. It will only weakly depend on $n\mathbf{G}$ as in reality a finite, but small, length-scale is associated with the core potential. RIXS spectra will therefore appear practically identical in different Brillouin zones. This is confirmed experimentally by [39]. The weak variations found in [40], are attributed by the authors to polarization effects.

This is remarkable because in IXS the *total* momentum $\mathbf{q}$ determines the scattering amplitude. The reason for this is that in IXS $\mathbf{q}$ enters directly into the transition matrix elements, which in RIXS are dominated by dipolar transitions for which $e^{i\mathbf{q}\cdot\mathbf{r}} \cong 1$ and that are therefore independent of $\mathbf{q}$. In the following, we will see how in certain limits the indirect RIXS amplitude can be related to the dynamic electronic structure factor $S_{\mathbf{k}}(\omega)$, which is directly measured by IXS. The important difference is thus that IXS measures $S_{\mathbf{q}}(\omega)$ and RIXS is, in these cases, related to $S_{\boldsymbol{\kappa}}(\omega)$.

4.2 Perturbative approach

The most straight-forward approach to include effects of the interaction H_C between the core hole and the valence shell is the use of perturbation theory. This amounts to replacing G by G_0 in Eq. (28) [32, 34, 33, 36, 35, 41], so that

$$\mathcal{F}_{fg}^{\text{indirect}} \quad = \quad \langle f|\mathcal{D}^\dagger\, G_0 H_C G_0\, \mathcal{D}|g\rangle, \tag{30}$$

which is also referred to as the Born approximation and shown in terms of a Feynman diagram expansion in Fig. 8. For dipolar $1s \rightarrow 4p$ transitions at the K-edge, we have $\mathcal{D} = \sqrt{3}P^1_{1s,4p}\sum_{\boldsymbol{\kappa}\mathbf{k}\alpha}\varepsilon_\alpha p^\dagger_{\boldsymbol{\kappa}+\mathbf{k},\alpha\sigma}s_{\boldsymbol{\kappa}\alpha\sigma}$ with $\alpha = x, y, z$, and $P^1_{1s,4p}$ the reduced matrix element containing the integral over the radial parts of the wavefunction.

In indirect RIXS, one considers the case where the $1s$-$4p$ exciton created in the absorption step is annihilated in the emission process. Since there is a momentum transfer $\mathbf{q}$ from the photons to the system, this implies that the momentum of the $1s$-$4p$ exciton must have changed in the intermediate state. This can only be a result of interactions of the $1s$-$4p$ exciton with the valence

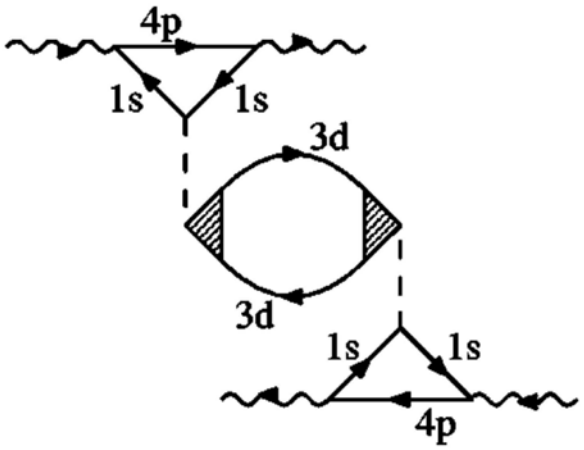

Fig. 8: *Feynman diagram for the transition probability in an indirect RIXS process in the Born approximation. Green functions for Cu* $1s$*,* $4p$*, and* $3d$ *electrons correspond to the solid lines labeled* $1s$*,* $4p$*, and* $3d$*, respectively. The wavy and broken lines represent the photon propagator and core hole potential* $U_{1s,3d}$*, respectively. The shaded triangle is the effective scattering vertex of the renormalized interaction between the valence electrons in the* $3d$*-shell [36].*

shell. If the dominant interaction is the Coulomb interaction of the core hole with the valence shell, then the isotropic scattering amplitude can be rewritten as [33, 8]

$$\mathcal{F}_{fg}^{\text{indirect}}(\mathbf{q},\omega) = P(\omega_{\mathbf{k}},\omega_{\mathbf{k}'})\, T(\boldsymbol{\epsilon},\boldsymbol{\epsilon}')\, \langle f|\rho_{\mathbf{q}}|g\rangle\,. \tag{31}$$

Note that all the operators involving the $1s$ and $4p$ states have been removed from the expression. The density operator is

$$\rho_{\mathbf{q}} = \sum_{\mathbf{k}\sigma} d^{\dagger}_{\mathbf{k}+\mathbf{q},\sigma} d_{\mathbf{k}\sigma}\,. \tag{32}$$

The resonance behavior is determined by the resonant function

$$P(\omega_{\mathbf{k}},\omega_{\mathbf{k}'}) = 3(P^{1}_{1s,4p})^2 \frac{U_{1s,3d}}{(z_{\mathbf{k}} - \hbar\omega) z_{\mathbf{k}}}, \tag{33}$$

using the fact that $\hbar\omega = \hbar\omega_{\mathbf{k}} - \hbar\omega_{\mathbf{k}'} = E_f$. The resonant function is more complex than for direct RIXS reflecting the fact that this is a higher-order excitation. The polarization dependence requires some careful consideration. In the situation where the $4p$ electron is a spectator an electron is excited into the $4p$ band with momentum $\mathbf{k}$ and band index n and subsequently removed from the same state

$$T(\boldsymbol{\epsilon},\boldsymbol{\epsilon}') = \frac{1}{N}\sum_{\mathbf{k}\alpha\alpha'} \epsilon'^{*}_{\alpha'}\epsilon_{\alpha}\, \langle 0|p_{\mathbf{k}\alpha'}|E^{4p}_{\mathbf{k}n}\rangle\langle E^{4p}_{\mathbf{k}n}|p^{\dagger}_{\mathbf{k}\alpha}|0\rangle\,, \tag{34}$$

with $\alpha = x, y, z$. In the atomic limit, this expression reduces to $\boldsymbol{\epsilon}'^{*}\cdot\boldsymbol{\epsilon}$, since the orbital of the $4p$ electron is unchanged in the intermediate state. In the absence of band effects, a change in the polarization therefore implies that the angular momentum of the valence electrons has changed. However, the $4p$ states form wide bands that are mixtures of the different $4p$ orbitals, and these

local-symmetry arguments only apply at the Γ-point. Therefore, the use of a scattering condition where the incoming polarization vector is perpendicular to the outgoing polarization vectors does not necessarily imply that a symmetry change has to occur for the valence electrons.
The essential physics of the material is contained in the fundamental scattering amplitude

$$F_{fg}(\mathbf{q}) = \langle f|\rho_{\mathbf{q}}|g\rangle. \tag{35}$$

This quantity is directly related to the dynamic structure factor, through

$$S_{\mathbf{q}}(\omega) = \sum_f |F_{fg}|^2\,\delta(E_f - \hbar\omega) = -\frac{1}{\pi}\,\mathrm{Im}\,\langle g|\rho_{-\mathbf{q}}\,\frac{1}{\hbar\omega - H + i0^+}\,\rho_{\mathbf{q}}|g\rangle\,, \tag{36}$$

which corresponds to the bubble in the Feynman diagram in Fig. 8. It should be noted that RIXS measures a projected $S_{\mathbf{q}}(\omega)$, meaning that $\rho_{\mathbf{q}}$ contains only $d^\dagger_{\mathbf{k}+\mathbf{q},\sigma}d_{\mathbf{k}\sigma}$ terms. This is a direct result of the fact that the core-hole Coulomb interaction does not scatter between different orbitals. This is different from IXS, where in principle the photon can induce a direct transition from the d states to the ligands. This does not imply that RIXS does not create charge-transfer excitations, since the charge-transfer states also have d character. In [42] multiple scattering corrections to the Born approximation are also considered on the basis of a Keldysh Green function formalism. It was found that multiple scattering effects lead to small modifications in the shape of the RIXS spectrum, which partly justifies the Born approximation for wide gap insulators such as La_2CuO_4 and NiO [43].
For direct RIXS, the detailed dependence on the polarization is given in the fundamental scattering amplitude $F^x_{fg,q}$. When including the polarization dependence for indirect RIXS, one obtains a similar fundamental scattering amplitude. The quantity F_{fg} in Eq. (35) then reduces to $F^0_{fg,0}$ and corresponds to the isotropic term. In the absence of interactions causing a transfer of angular momentum between the $4p$ and the valence shell, the indirect RIXS amplitude is simply proportional to $\rho_{\mathbf{q}}$. In terms of tensors, $\rho_{\mathbf{q}} = w_0^{dd0}(\mathbf{q})$.
A significant difference between the two processes is that when direct excitations are made into the valence shell (e.g. $2p/3p \rightarrow 3d$), the effect of the operator $\underline{w}_0^{dd0} = n_h$ is relatively small, since the excited electron screens the $2p/3p$ core-hole potential very well. The isotropic contribution then mainly contributes to the elastic line. For indirect RIXS, the excited delocalized $4p$ electron does not screen the $1s$ core-hole potential very well. This produces appreciable screening dynamics of the valence electrons in the intermediate state. This is the reason why the $\rho_{\mathbf{q}}$ response generates significant inelastic scattering intensity for indirect RIXS.

4.3 Ultrashort core-hole lifetime expansion

The potential that the core hole exerts on the valence electrons is strong, the attraction $U_{1s,3d}$ between a $1s$ core hole and $3d$ electron is typically $\sim$ 6–8 eV, which is of the same order as the d-d Coulomb interaction $U_{3d,3d}$ that appears in Hubbard-like models. Treating such a strong interaction as a weak perturbation renders a perturbation expansion uncontrolled. To deal with the strong core-hole interaction, the Ultrashort Core-hole Lifetime (UCL) expansion

was developed in [21, 22, 38], which treats the core-hole potential as the dominating energy scale.

The UCL relies on three observations. First for most RIXS intermediate states, the core hole lifetime broadening is quite large: typically Γ is of the order of 1 eV. This yields a time scale $\tau = 1/2\Gamma = 4$ fs. Only during this ultrashort time is the system perturbed by the core hole. Many elementary excitations have an intrinsic time scale that is much larger than 4 fs. *This intrinsic timescale is the fundamental oscillation period, related to the inverse frequency ω of an excitation with energy $\hbar\omega$.* For example, phonons have a typical energy scale of up to 100 meV, and magnons of up to 250 meV, thus corresponding to timescales almost an order of magnitude larger than the core hole lifetime. Even low energy electronic valence band excitations can be within this range.

The resulting physical picture of a RIXS process involving low-energy excitations is therefore that the dynamics in the intermediate state are limited because of this lack of time, provided that the excitation time scale is not decreased significantly by the core hole. The second observation is that the core-hole potential can, to good approximation, be treated as a local potential, i.e., its dominating effect is to perturb electrons on the same atom on which the core hole resides. Finally, the core hole is considered to be immobile, which is a reliable assumption for the deep core-states such as Cu $1s$.

The calculation of the indirect RIXS amplitude within the UCL expansion by [21, 22, 38] is based on a series expansion of the Kramers-Heisenberg equation, (Eq. 9). But a Green function approach is equally viable, which then starts by inserting in Eq. (28) the identity $G = G_C + G_C H_0 G$

$$\mathcal{F}_{\mathtt{fg}}^{\mathrm{indirect}} \;=\; \langle \mathtt{f}|\mathcal{D}^\dagger\, G_0 H_C G_C (1 + H_0 G)\, \mathcal{D}|\mathtt{g}\rangle, \tag{37}$$

where the Green functions, $G_0 = (z_{\mathbf{k}} - H_0)^{-1}$, $G_C = (z_{\mathbf{k}} - H_C)^{-1}$, $G = (z_{\mathbf{k}} - H)^{-1}$, correspond to the Hamiltonian of the unperturbed system H_0, the valence-electron core-hole interaction H_C, and the total Hamiltonian $H = H_0 + H_C$. The UCL is best illustrated by considering the core-hole Hamiltonian $H_C = U_C \sum_i \rho_i^s \rho_i^d$, where $U_C = U_{1s,3d}$ and ρ_i^{1s} (ρ_i^{3d}) are the density operators counting the number of $1s$ core holes ($3d$ electrons) at site i. The simplest system one can consider is one in which the $3d$ states are only occupied by either 0 or by 1 electron, for instance due to strong correlation effects in the $3d$ shell. As there is only one localized core hole present in the intermediate state, H_C then has the interesting property $H_C^l = U_C^{l-1} H_C$ for any integer $l > 0$ [21, 22], which implies that H_C is either 0 or U_C. This directly implies the relation $H_C G_C = H_C (z_{\mathbf{k}} - U_C)^{-1}$. One now obtains for the indirect RIXS amplitude

$$\mathcal{F}_{\mathtt{fg}}^{\mathrm{indirect}} \;=\; \langle \mathtt{f}|\, \mathcal{D}^\dagger\, G_0 \frac{H_C}{z_{\mathbf{k}} - U_C} (1 + H_0 G)\, \mathcal{D}\, |\mathtt{g}\rangle\ . \tag{38}$$

Note that this expression is exact, but of course specific for the present form of the core-hole potential; generalized forms are given in [21,22,38], which include the spin and possible orbital degrees of freedom of the $3d$ electrons.

In the leading order of the UCL expansion one retains in Eq. (38) the first order term in H_C so that

$$\mathcal{F}_{\mathtt{fg}}^{\text{indirect}} = \frac{\langle \mathtt{f}| \mathcal{D}^\dagger H_C \mathcal{D} |\mathtt{g}\rangle}{(z_{\mathbf{k}} - \omega)(z_{\mathbf{k}} - U_C)} = P(\omega_{\mathbf{k}}, \omega_{\mathbf{k}'}) \langle \mathtt{f}| \rho_{\mathbf{q}}^d |\mathtt{g}\rangle , \tag{39}$$

where the resonance function

$$P(\omega_{\mathbf{k}}, \omega_{\mathbf{k}'}) = (P_{1s,4p}^1)^2 U_C((z_{\mathbf{k}} - \omega)(z_{\mathbf{k}} - U_C))^{-1} \tag{40}$$

is introduced, and $P_{1s,4p}^1$ is the $1s \rightarrow 4p$ dipole transition amplitude. The generic shape of the resonance function depends on the form of the core-hole potential. It is remarkable that the RIXS amplitude found in leading order of the strong coupling UCL is directly related to the dynamic structure factor $S_{\mathbf{q}}(\omega)$ of Eq. (36), which is a situation very similar to the weak coupling perturbative approach, see Eq. (35). In fact for $U_C \rightarrow 0$ the strong coupling UCL resonance function reduces to the perturbative one. This result has important implications for the interpretation of RIXS spectra since this approach then suggests that with proper handling of the prefactor, RIXS can be considered as a weak probe that measures $S_{\mathbf{q}}(\omega)$.

The sub-leading contributions to the indirect UCL scattering amplitude of Eq. (38) are of the type $H_C H_0 H_C$. Such terms *a priori* cannot be reduced to a response of $\rho_{\mathbf{q}}$ because H_0 and H_C do not commute. Physically this term corresponds to an electron (or hole) hopping onto the core-hole site in the intermediate state. Denoting the hopping amplitude as t, these contributions to the scattering amplitude are down by a factor $t/(z_{\mathbf{k}} - U_C)$ with respect to the leading term. When tuning off-resonance, corrections to the UCL expansion thus become progressively smaller. On resonance these terms constitute contributions to the RIXS intensity of the order of $(t/\Gamma)^2$, which are thus governed by U_C and the inverse core-hole lifetime Γ. Corrections to the UCL are thus smaller for shorter-lived core holes. In cuprates, for instance the effective $3d$ valence bandwidth $t \approx 0.4$ eV and such corrections are expected to be moderate. For a specific system, the commutation relation for H_0 and H_C is known, and such a higher order term can be calculated explicitly and again be cast in the form of a product of a resonance function and a generalized charge response function.

The observation that within the UCL the RIXS cross-section can be factored into a resonant prefactor and the dynamic structure factor, $S_{\mathbf{q}}(\omega)$ was tested experimentally [44]. There an empirical comparison of Cu K-edge indirect RIXS spectra was reported, taken at the Brillouin-zone center, with optical dielectric loss functions measured in a number of copper oxides: Bi_2CuO_4, $CuGeO_3$, $Sr_2Cu_3O_4Cl_2$, La_2CuO_4, and $Sr_2CuO_2Cl_2$. Analyzing both incident and scattered-photon resonances [44] extracted an incident-energy-independent response function. The overall spectral features of the indirect resonant inelastic X-ray scattering response function were found to be in a reasonable agreement with the optical dielectric loss function over a wide energy range. In the case of Bi_2CuO_4 and $CuGeO_3$ [44] observed that the incident-energy-independent response function, $S_{\mathbf{q}=0}(\omega)$, matches very well with the dielectric loss function, $-\mathrm{Im}(1/\epsilon(\omega))$ measured with spectroscopic ellipsometry, suggesting that the local core-hole approximation treatment of the UCL works well in these more localized electron systems. Corner-sharing two-

dimensional copper oxides exhibit more complex excitation features than those observed in the dielectric loss functions, likely related to non-local core-hole screening effects.
The UCL expansion describes the RIXS cross-section in the limits of small and large core-hole potential. In the intermediate region, one has to resort to numerical calculations [45]. In the dynamic structure factor, excitations are created via $\rho_{\mathbf{q}}$, implying that electrons and holes are excited in an equivalent fashion. When dynamical effects are strong in the intermediate state, this can change and an asymmetry in the excitation of electron and holes can occur [45]. Since the screening electron is strongly bound to the core hole in the intermediate state, it is more likely to be scattered to higher lying states. The hole excitations on the other hand can delocalize and have a tendency to be closer to the Fermi level.
Besides charge excitations also magnetic and orbital excitations were studied with the UCL. Theoretically the two-magnon response of antiferromagnetic La_2CuO_4 was calculated within the UCL [46, 47], agreeing nicely with experiment [16]. Collective orbital excitations were investigated theoretically for $LaMnO_3$ [48] and for $YTiO_3$ [49] and compared to experiments on titanates [50].

Acknowledgments

These lecture notes are based on the review article [1], written by Luuk Ament, Michel van Veenendaal, Thomas P. Devereaux, John P. Hill, and the present lecturer. A far more complete review of the recent theoretical and in particular the experimental advances in RIXS can be found there. An excellent book that includes the theory of RIXS has been published very recently [9]. The lecturer acknowledges support from the Deutsche Forschungsgemeinschaft via SFB 1143.

References

[1] L.J.P. Ament, M. van Veenendaal, T.P. Devereaux, J.P. Hill, and J. van den Brink, Rev. Mod. Phys. **83**, 705 (2011)

[2] C.J. Sparks, Phys. Rev. Lett. **33**, 262 (1974)

[3] Y.B. Bannett and I. Freund, Phys. Rev. Lett. **34**, 372 (1975)

[4] P. Eisenberger, P.M. Platzman, and H. Winick, Phys. Rev. Lett. **36**, 623 (1976)

[5] P. Eisenberger, P.M. Platzman, and H. Winick, Phys. Rev. B **13**, 2377 (1976)

[6] M. Blume, J. Appl. Phys. **57**, 3615 (1985)

[7] A. Kotani and S. Shin, Rev. Mod. Phys. **73**, 203 (2001)

[8] W. Schülke: *Electron Dynamics by Inelastic X-Ray Scattering* (Oxford University Press, 2007)

[9] M. van Veenendaal: *Theory of Inelastic Scattering and Absorption of X-rays* (Cambridge University Press, 2015)

[10] L. Braicovich, A. Tagliaferri, E. Annese, G. Ghiringhelli, C. Dallera, F. Fracassi, A. Palenzona, and N.B. Brookes, Phys. Rev. B **75**, 073104 (2007)

[11] K. Ishii, S. Ishihara, Y. Murakami, K. Ikeuchi, K. Kuzushita, T. Inami, K. Ohwada, M. Yoshida, I. Jarrige, N. Tatami, S. Niioka, D. Bizen, Y. Ando, J. Mizuki, S. Maekawa, and Y. Endoh, Phys. Rev. B **83**, 241101 (2011)

[12] T.P. Devereaux and R. Hackl, Rev. Mod. Phys. **79**, 175 (2007)

[13] E.D. Isaacs, P.M. Platzman, P. Metcalf, and J.M. Honig, Phys. Rev. Lett. **76**, 4211 (1996)

[14] J. Zaanen, G.A. Sawatzky, and J.W. Allen, Phys. Rev. Lett. **55**, 418 (1985)

[15] L. Braicovich, J. van den Brink, V. Bisogni, M. Moretti Sala, L.J.P. Ament, N.B. Brookes, G.M. De Luca, M. Salluzzo, T. Schmitt, V.N. Strocov, and G. Ghiringhelli, Phys. Rev. Lett. **104**, 077002 (2010)

[16] J.P. Hill, G. Blumberg, Y.-J. Kim, D.S. Ellis, S. Wakimoto, R.J. Birgeneau, S. Komiya, Y. Ando, B. Liang, R.L. Greene, D. Casa, and T. Gog, Phys. Rev. Lett. **100**, 097001 (2008)

[17] J. Schlappa, T. Schmitt, F. Vernay, V.N. Strocov, V. Ilakovac, B. Thielemann, H.M. Rønnow, S. Vanishri, A. Piazzalunga, X. Wang, L. Braicovich, G. Ghiringhelli, C. Marin, J. Mesot, B. Delley, and L. Patthey, Phys. Rev. Lett. **103**, 047401 (2009)

[18] H. Yavaş, M. van Veenendaal, J. van den Brink, L.J.P. Ament, A. Alatas, B.M. Leu, M.-O. Apostu, N. Wizent, G. Behr, W. Sturhahn, H. Sinn, and E.E. Alp, J. Phys.: Condens. Matter **22**, 485601 (2010)

[19] J.N. Hancock, G. Chabot-Couture, and M. Greven, New J. Phys. **12**, 033001 (2010)

[20] L.J.P. Ament, M. van Veenendaal, and J. van den Brink, Europhys. Lett. **95**, 27008 (2011)

[21] J. Van den Brink and M. van Veenendaal, J. Phys. Chem. Solids **66**, 2145 (2005)

[22] J. Van den Brink and M. van Veenendaal, Europhys. Lett. **73**, 121 (2006)

[23] H.A. Kramers and W. Heisenberg, Z. Phys. **48**, 15 (1925)

[24] A. Messiah: *Quantum Mechanics, Vol. 2* (North Holland Publishing Company, Amsterdam, 1962)

[25] J.J. Sakurai: *Advanced Quantum Mechanics* (Addison-Wesley, 1967)

[26] J.-P. Rueff and A. Shukla, Rev. Mod. Phys. **82**, 847 (2010)

[27] D.A. Varshalovich, A.N. Moskalev, and V.K. Khersonskii: *Quantum Theory of Angular Momentum* (World Scientific, 1988)

[28] D.M. Brink and G.R. Satchler: *Angular Momentum* (Oxford University Press, 1962)

[29] A.P. Yutsis, I.B. Levinson, and V.V. Vanagas: *Quantum Theory of Angular Momentum* (World Scientific, 1988)

[30] M. Van Veenendaal and R. Benoist, Phys. Rev. B **58**, 3741 (1998)

[31] J. Luo, G.T. Trammell, and J.P. Hannon, Phys. Rev. Lett. **71**, 287 (1993)

[32] P.M. Platzman and E.D. Isaacs, Phys. Rev. B **57**, 11107 (1998)

[33] G. Döring, C. Sternemann, A. Kaprolat, A. Mattila, K. Hämäläinen, and W. Schülke, Phys. Rev. B **70**, 085115 (2004)

[34] P. Abbamonte, C.A. Burns, E.D. Isaacs, P.M. Platzman, L.L. Miller, S.W. Cheong, and M.V. Klein, Phys. Rev. Lett. **83**, 860 (1999)

[35] T. Nomura and J.-I. Igarashi, J. Phys. Soc. Jpn. **73**, 1677 (2004)

[36] T. Nomura and J.-I. Igarashi, Phys. Rev. B **71**, 035110 (2005)

[37] R.S. Markiewicz and A. Bansil, Phys. Rev. Lett. **96**, 107005 (2006)

[38] L.J.P. Ament, F. Forte, and J. van den Brink, Phys. Rev. B **75**, 115118 (2007)

[39] Y.-J. Kim, J.P. Hill, S. Wakimoto, R.J. Birgeneau, F.C. Chou, N. Motoyama, K.M. Kojima, S. Uchida, D. Casa, and T. Gog, Phys. Rev. B **76**, 155116 (2007)

[40] G. Chabot-Couture, J.N. Hancock, P.K. Mang, D.M. Casa, T. Gog, and M. Greven, Phys. Rev. B **82**, 035113 (2010)

[41] T. Semba, M. Takahashi, and J.-I. Igarashi, Phys. Rev. B **78**, 155111 (2008)

[42] J.-I. Igarashi, T. Nomura, and M. Takahashi, Phys. Rev. B **74**, 245122 (2006)

[43] M. Takahashi, J.-I. Igarashi, and T. Nomura, Phys. Rev. B **75**, 235113 (2007)

[44] J. Kim, D.S. Ellis, H. Zhang, Y.-J. Kim, J.P. Hill, F.C. Chou, T. Gog, and D. Casa, Phys. Rev. B **79**, 094525 (2009)

[45] K.H. Ahn, A.J. Fedro, and M. van Veenendaal, Phys. Rev. B **79**, 045103 (2009)

[46] J. Van den Brink, Europhys. Lett. **80**, 47003 (2007)

[47] F. Forte, L.J.P. Ament, and J. van den Brink, Phys. Rev. B **77**, 134428 (2008)

[48] F. Forte, L.J.P. Ament, and J. van den Brink, Phys. Rev. Lett. **101**, 106406 (2008)

[49] L.J.P. Ament and G. Khaliullin, Phys. Rev. B **81**, 125118 (2010)

[50] C. Ulrich, L.J.P. Ament, G. Ghiringhelli, L. Braicovich, M. Moretti Sala, N. Pezzotta, T. Schmitt, G. Khaliullin, J. van den Brink, H. Roth, T. Lorenz, and B. Keimer, Phys. Rev. Lett. **103**, 107205 (2009)

13 NMR in Correlated Electron Systems: Illustration on the Cuprates

Henri Alloul
Laboratoire de Physique des Solides - CNRS
Université Paris-Sud and Université Paris-Saclay

Contents

E. Pavarini, E. Koch, J. van den Brink, and G. Sawatzky (eds.)
Quantum Materials: Experiments and Theory
Modeling and Simulation Vol. 6
Forschungszentrum Jülich, 2016, ISBN 978-3-95806-159-0
http://www.cond-mat.de/events/correl16

1 Introduction: NMR basics

The electronic properties of solids were, in the first half of the twentieth century, considered mostly in the framework of an independent electron approximation with spin degeneracy. Their resulting electronic band structure is such that each electronic level could be doubly occupied. In such an approach one expects metals or insulators with no significant magnetic properties [1]. The traditional experimental studies of the electronic states in such solids usually require a determination of their electronic band structure and an investigation of its effects on the physical properties. Those are usually experimentally obtained by measurements taken at the macroscopic scale such as optical, transport, and magnetic data. To go beyond these approaches Nuclear Magnetic Resonance is thoroughly used. This technique, discovered in the mid of the 20th century is essential as it permits to perform atomic-scale measurements in the materials, differentiating the properties which can be attributed to specific phases or sites in the structure. The aim of this lecture is to present the main physical parameters accessible to NMR experiments, and to illustrate how they do reflect many aspects which are specific to the occurrence of electronic correlations in materials.

Correlations are at the origin of many exotic electronic properties of a series of compounds which have emerged from recent experimental observations. The most important phenomena discovered are related with electronic magnetic properties, which have been quite accessible to Nuclear Magnetic Resonance techniques. They specifically permit to distinguish the orbitals or electronic bands responsible for magnetism, metallic, and superconducting behaviors. They revealed quite often the physical properties which are distinct what is expected within an independent electron scheme.

In non-interacting electronic systems, one considers energy levels with spin degeneracy and fills them with two electrons per level, without any consideration of U, the local Coulomb repulsion on the atomic orbitals. But, as soon as one considers a solid which displays magnetic properties, the latter has to be considered, as U is responsible for atomic and solid-state magnetism. This is fully described in various other lectures in the present series of books.

If one starts with a completely free electron gas, the first incidence of weak correlations can be expressed in a Fermi liquid approach, that is, the electronic states at the Fermi level are not single-particle but rather quasiparticle states in which the electron is dressed by an electronic cloud which involves the electronic correlations. Those quasiparticles are populated in a same way as free-electron states, except that the population jump at the Fermi level is smaller than unity. Correspondingly these quasiparticles have effective masses $m^\star$ which differ from the electron mass. This is seen for instance in the magnitude of the specific heat and the Pauli-like spin susceptibility.

With increasing electron correlations one reaches situations where electron states are in an intermediate regime between independent extended electronic states and local states. Those intermediate electronic states are at the basis of the correlated electron physics which gives exotic properties to the materials and various competing low T states which are often far from being understood at this time.

As the NMR technique is described at length in various books and articles (see Wikipedia and Scholarpedia) for its applications in chemistry, biology, and medical sciences, we shall only recall very briefly the technical principles of NMR in the next section. However we shall recall in more detail the couplings between nuclear spins and electron spins in section 1.2. Those are essential to allow one to probe by NMR the electronic and magnetic properties of solids.

1.1 The magnetic resonance phenomenon: basic applications

Let us recall that the physical properties of solids, and in particular their magnetic properties, are of course determined by the electronic states. On the other hand, the nuclear spin moments, which do not affect these properties, provide an extremely useful probe for the electronic properties. Atomic nuclei are made up of neutrons and protons, which are spin 1/2 particles. They are assembled into quantum states in which the nuclear ground state has a total spin $\boldsymbol{I}$ that may be integer or half-integer. The associated magnetic moment $\boldsymbol{\mu}_{\rm n}$ is proportional to the magnetic moment of the proton $\mu_{\rm p}$, where the multiplicative factor is analogous to the Landé factor for an atomic electronic moment. Each atomic nucleus thus has a specific magnetic moment $\boldsymbol{\mu}_{\rm n} = \hbar\gamma_{\rm n}\boldsymbol{I}$. The gyromagnetic ratio $\gamma_{\rm n}$ is known to great accuracy for each of the stable isotopes in the periodic table. Since $\mu_{\rm p} \simeq 10^{-3}\mu_{\rm B}$, the nuclear moments are extremely small, as are their mutual interactions. As a consequence, they are almost always in a paramagnetic state with a Curie magnetization $\mu_z = N(\hbar\gamma_{\rm n})^2 I(I+1)B_0/3k_BT$. We see immediately that, in a given applied field, the nuclear magnetization is about 10^6 times smaller than the electronic magnetization. The nuclear magnetism is practically impossible to detect using just macroscopic magnetization measurements taken on bulk samples. But, although the nuclear magnetic susceptibilities are weak, they can be detected by magnetic resonance which is a spectroscopy that permits a selective detection of the nuclear spin response.

Discovered at the outset of the second world war by F. Bloch and E.M. Purcell, the nuclear magnetic resonance technique has rapidly become a unique method to investigate the chemical and physical properties of condensed matter [2, 3]. Its success results from the fact that it resolves spectroscopically the properties of the nuclear spins of the distinct atomic species present in a material. A homogeneous applied external magnetic field B_0 induces a splitting of the nuclear-spin energy level $h\nu_L = \hbar\gamma_{\rm n}B_0$ which usually falls in the radio-frequency range of the order of 10 MHz per Tesla. The absorption of a radio-frequency field at the adequate frequency ν_L permits to detect the presence of the corresponding nuclei.

One highlight of NMR is the acquired possibility to provide images of the spatial distribution of ^{1}H nuclei in-vivo in biological matter, which is the basis of medical Magnetic Resonance Imaging (MRI). Though this is the most popular application of NMR known by a large audience, NMR is an even more powerful technique when one uses the interactions of given nuclear spins in a material with their neighboring atomic states. This results in rich spectroscopic splittings of the NMR lines, which permit to locate the atoms in molecular states and therefore to determine the molecular structures in chemistry or in the solid state. Such spectroscopic techniques have been revealed since the 1960s but their impact has been tremendously highlighted by the

improvement of the superconducting-magnet industry which has allowed to produce extremely homogeneous magnetic fields B_0 as large as 21 Tesla with negligible drift in time. In the corresponding range of frequencies ν_L, exceptionally stable coherent sources are available, with narrower spectral widths than the transitions to be observed. These are obtained by electronic oscillators with frequency stabilized on the resonant mode of a piezoelectric quartz crystal. Moreover, for such frequencies, very powerful amplifiers are also available. High intensity radio-frequency pulses are used to significantly modify the populations of the spin quantum states. This approach is essential for nuclear spin relaxation studies. Therefore on the electronics side, NMR has highly benefited from all the developments of the fast semiconductor and computing capabilities associated with the expansion of information technologies.

1.2 Electronic hyperfine couplings

It is clear that changes in the magnetic induction in a material can be detected directly by a change in the nuclear Larmor frequency. In weakly magnetic materials, for which the magnetization is negligible, $B_0 = \mu_0 H_a$ and the nuclear Larmor frequency ν_L should be determined solely by the applied external field H_a. It would be difficult to obtain information about the physical properties of materials in such a limit. But we have to recall that the nucleus is a kind of atomic scale microscopic probe, coupled to the electrons. Interactions like the dipole interactions between nuclear and electronic spins are such that the nuclear spin feels a magnetic field associated with the polarization of the electronic magnetic moments. This means that the magnetic field felt by the nuclear spins is modified with respect to the applied field. It is the spectroscopy of these fields that provides atomic scale information about the immediate vicinity of the nuclei in the material. Let us examine the different on-site interactions between the nuclear spins and the magnetic moments of electronic origins, known collectively as hyperfine interactions [2, 3].

The dipole interaction between the moments associated with a nuclear spin $\boldsymbol{I}$ and an electron spin $\boldsymbol{S}$ separated by a displacement $\boldsymbol{r}$ is

$$H_{dd} = -\frac{\mu_0}{4\pi}\frac{\gamma_e\gamma_n\,\hbar^2}{r^3}\left[\boldsymbol{I}\cdot\boldsymbol{S} - \frac{3(\boldsymbol{I}\cdot\boldsymbol{r})(\boldsymbol{S}\cdot\boldsymbol{r})}{r^2}\right], \tag{1}$$

where γ_n and γ_e are the nuclear and electronic gyromagnetic moments, respectively, and $\boldsymbol{S}$ and $\boldsymbol{I}$ are here dimensionless quantities. This dipole interaction diverges when r tends to zero, and is therefore only valid for electrons with zero probability of being at the site of the nucleus. This is the case for electrons in the p, d, or f shells. On the other hand, the s electrons have nonzero probability of being at the site of the nucleus. The Dirac Hamiltonian can be used to show that the corresponding interaction, called the contact interaction H_c is scalar, and is given in this case by

$$H_c = \frac{\mu_0}{4\pi}\frac{8\pi}{3}\,\gamma_e\gamma_n\,\hbar^2\;\;\boldsymbol{I}\cdot\boldsymbol{S}\,\delta(\boldsymbol{r})\,. \tag{2}$$

Finally, the interaction with the magnetic field associated with the orbital angular momentum

of the electron is

$$H_{\rm orb} = -\frac{\mu_0}{4\pi}\gamma_e\gamma_n\,\hbar^2\;\frac{\boldsymbol{I}\cdot\boldsymbol{\ell}}{r^3}. \tag{3}$$

These Hamiltonians can all be written in the form

$$H_{\rm eff} = -\gamma_n\,\hbar\,\boldsymbol{I}\cdot\boldsymbol{B}_{\rm eff} \tag{4}$$

and we may consider that each electron induces a magnetic field $\boldsymbol{B}_{\rm eff}$ at the nuclear site. As the temporal fluctuations of the electronic moments are very fast compared with the nuclear Larmor frequency, the static component of $\boldsymbol{B}_{\rm eff}$ is its time average. The position of the NMR for a given nucleus is thus determined by the time average $\boldsymbol{B}_{\rm eff}$ of the resultant of the fields due to the different electrons in the material. It is easy to see that the hyperfine interaction will vanish for filled electronic shells, because they have zero total spin and total orbital angular momentum. When there is no applied field, $\boldsymbol{B}_{\rm eff}$ can only be nonzero for materials in which there is a static spin or orbital magnetic moment. This will be the case for magnetically ordered materials. The weakness of the interaction between electronic and nuclear spins permits to consider the nuclear spins as somewhat ideal probes of the electronic properties of materials. Those are essentially obtained from measurements of the NMR shifts or spin-lattice relaxation parameters that we shall describe in some details in these lecture notes, which are organized as follows:

It will be shown first (section 2) that in metals the Pauli paramagnetism, that is the electronic density of states is accessible through NMR-shift data. Then, in section 3, we shall demonstrate that NMR spectra do give clear evidence of the local effects induced by impurities. Such experiments permit as well (Sec. 3.1) to understand that the nuclear spins are not limited to the detection of on-site magnetic responses, but do sample as well the behavior of nearby sites through transferred hyperfine couplings.

The good knowledge of the NMR characteristics in solids for which non-interacting electron theories apply quite well, naturally permitted in the initial experiments on correlated electron systems to detect the unexpected modifications of electronic properties that occurred in such materials. This appears as an advantage of the NMR technique, with respect to most recent experimental probes which have been developed specifically to study strongly correlated electron systems. This will be illustrated in section (section 4) on two cases highlighted by NMR-shift data on important correlated physics cases. First in Sec. 4.1, we discuss the relatively simple case of the NMR studies on the magnetic properties of $3d$ impurities in metallic sp metals, well known as the "Kondo effect". This has been the earliest correlated-electron physics case which has been understood. It has opened the way to the studies of heavy fermions and Kondo lattices which are touched on in Ref. [4]. The second case is that of the high-T_c cuprates, which is of course the family of compounds that has attracted a large interest on correlated-electron physics. NMR hyperfine-coupling studies in the cuprates permitted to understand the actual electronic structure. Furthermore the NMR-shift data in the low doping part of the phase diagram were the first experimental evidence for the occurrence of a pseudogap as will be detailed in Sec. 4.3. NMR spectra taken on cuprates with substituted impurities permitted as well to reveal the magnetic properties of the pure correlated electron system, as detailed in Sec. 4.4.

Other important parameters accessible to NMR experiments are the longitudinal and transverse nuclear spin-lattice relaxations. Those processes will be recalled in section 5. They quite generally permit to use the dynamics of the nuclear magnetization to probe the excited electronic states in condensed matter. In correlated electron systems the comparison with NMR-shift data using eventually data taken on different sites of the atomic structure do give important indications on the strength of the electronic correlations (Sec. 5.3). Such measurements give access to determinations of electronic gaps in some electronic structures.
Such gaps are important in the case of superconductors as they do reflect the pairing of electrons in the superconducting state. Their existence can be probed by the large incidence on NMR-shift and spin-lattice relaxation NMR data (Sec. 6). The study of exotic superconductivities and the capability of NMR to give some hints on the symmetry of the superconducting order-parameter are illustrated in Sec. 6.3.

2 NMR shifts

In a material, each of the distinct hyperfine couplings listed above induces a specific contribution to the NMR shift. Those are of course quite dependent on the magnitude of the corresponding hyperfine coupling and of the electronic state of the considered material.

2.1 Chemical shifts

In substances where the electrons are paired in atomic or molecular orbitals, the static part of the hyperfine coupling is only nonzero in the presence of an applied field $\boldsymbol{B}_0$, and is proportional to $\boldsymbol{B}_0$ as is the magnetization. The resonance is shifted with respect to that of the free atom in a gas. The relative shift $\boldsymbol{B}_{\rm eff}/\boldsymbol{B}_0$ may be due to the orbital part of the hyperfine coupling. This is the case, for example, for the displacement due to the orbital currents induced by the external magnetic field in electronic or molecular shells close to the nucleus. Since this shift depends on the electronic charge distributions, it is highly sensitive to the chemical environment of the given atom, hence the name chemical shift. These effects are generally small, and expressed in parts per million (ppm) but can be used to distinguish the nuclear spin resonances of the different atoms depending on their environment. This has become a very powerful tool, used universally in chemistry and biology. Routine chemical analyses are carried out by NMR. It also helps one to determine the 3D structures of biological molecules, using multidimensional methods, which have reached an exceedingly high level of refinement.

2.2 Knight shifts in metals

When the electron states are not paired in molecular states or in bonds, the spin degeneracy of the electronic states might be lifted by the applied field, as for electron states at the Fermi level in a metallic band. In that case a $\boldsymbol{B}_{\rm eff}$ component due to the electronic atomic moment may arise via the contact hyperfine term. In a metal the corresponding frequency shift K of the Larmor

frequency is called Knight shift [5] and is directly proportional to the Pauli spin susceptibility χ_{P0} of the metallic band. In usual metallic systems such as alkali metals the early-day studies by NMR permitted to demonstrate that this technique gives indeed the best evaluation of the electronic spin susceptibility. Assuming that the main hyperfine coupling is the direct on-site contact interaction of Eq. (2), which can be written $H_c = A_0\ \boldsymbol{I} \cdot \boldsymbol{S}\ \delta(\boldsymbol{r})$ this yields an NMR Knight shift

$$K = A_0 \chi_{P0} / (g \mu_B \hbar \gamma_{\rm n})\,. \tag{5}$$

In such simple metals the spin susceptibility $\chi_{P0} = (g\mu_B)^2 \rho(E_F)/2$ measures the actual density of states $\rho(E_F)$ taken per spin direction at the Fermi level, which is typically T-independent as the conduction-electron bandwidth is usually quite large and the Fermi level much higher than $k_B T$. The Knight shift is usually a large quantity which is measured in %. This comes about because the contact coupling A_0 is usually much larger than the corresponding dipole or orbital couplings, which permits to sense very effectively the Pauli susceptibility.

2.3 NMR in magnetic materials

In magnetic materials, the electronic moments are static at low temperatures, as compared with their behavior at the Curie or Néel temperatures. It follows that the static effective fields are nonzero even in the absence of any applied field. For atomic nuclei carrying an electronic moment, this field will be very large (several Tesla in general), and will give rise to a resonance at the Larmor frequency $h\nu_L = \hbar \gamma_{\rm n} B_{\rm eff}$, which can be detected in the absence of an applied external field. One speaks then of Zero Field Nuclear Magnetic Resonance (ZFNMR). The fields induced on the nuclear spins of non magnetic atomic sites are generally weaker but can still give valuable information on the properties of the magnetic state.

3 Impurities: example of transferred hyperfine couplings

All real crystalline materials contain structural defects. Those are often impurity atoms substituting some atoms in the ideal structure, or disorder induced by vacancies on some sites of the atomic structure or by deviations to the ideal structural arrangement of atoms. The incidence of specific substituted impurities on the physical properties of the material is sometimes well understood. The essence of the observed phenomena is that an impurity is a local screened Coulomb potential, which ideally is a uniform perturbation in $\boldsymbol{q}$ space inducing a response, which is inhomogeneous in real space but which reflects the response to all $\boldsymbol{q}$ values. In a classical metallic system, since the response is homogeneous up to $|\boldsymbol{q}| = k_F$, the main detected feature comes from this truncation of the response at k_F, which yields the well known Friedel oscillations in the local density of states for a charge defect, and the RKKY oscillation for a spin defect. Such effects differentiate the electronic response on sites in the vicinity of the defect and can be detected by NMR experiments. We shall first illustrate this in the case of magnetic defects in sp metals and show that NMR spectra permit to probe directly the RKKY oscillations.

3.1 Local RKKY spin-density oscillations induced by magnetic impurities in metals

If one substitutes a magnetic impurity on a lattice site of a metal such as Cu, the neighboring sites are differentiated and the magnetic response depends on the distance to the impurity. For local moment impurities, Yosida [6] calculated explicitly the spin-density oscillations assuming that the free electron spin s and local moment S interact by an exchange interaction

$$H = -J\ \boldsymbol{S}\cdot\boldsymbol{s}\ \delta(\boldsymbol{r}). \tag{6}$$

The resulting local spin density, calculated in perturbation theory at a position R_n with respect to the impurity is given by

$$n(R_n) = -\frac{1}{4\pi} J\rho(E_F)\ \frac{\cos(2k_F R_n)}{R_n^3}\ \langle S_z\rangle \tag{7}$$

for a field applied in the z direction. For local-moment impurities such as Mn in Cu the NMR Knight shift of a Cu nuclear spin at position R_n with respect to the impurity acquires an extra shift ΔK given in an applied field H by

$$H\Delta K(R_n) = A_{\rm hf}\ n(R_n) = A(R_n)\langle S_z\rangle, \tag{8}$$

where $A_{\rm hf}$ is the on-site Cu hyperfine coupling. In most dilute alloys of transition elements only a few near-neighbor shells of the impurity could be resolved. However in Cu-Mn, the impurity magnetization $\langle S_z\rangle$ becomes so large at low T and high fields that $n(R_n)$ becomes sizable on many neighboring sites of the impurity. Up to 17 distinct shells of neighbors could be detected in that case, as can be seen in the spectra of Fig. 1, which gives a straightforward illustration of the occurrence of spin-density oscillations. One can see that there are about as many extra lines (we call them satellite lines) on the right and on the left of the central line. The technical details about the assignment of the different lines to specific shells of neighbors, and the analysis of the spatial dependence of the spin polarization which can be deduced from those data are summarized in Ref. [7]. One could push the analysis to a stage permitting to confirm the overall R_n^{-3} dependence, but also to evidence deviations from the asymptotic limit at short distances. Such deviations with respect to the spatial dependence of Eq. (7) could be analyzed by using a more reliable model than an exchange coupling between the impurity and electron spins.

3.2 Transferred hyperfine couplings

So far we have only considered hyperfine couplings between nuclear spins and the electrons involved in the atomic orbitals of the corresponding site. However the above illustration of the RKKY interaction did allow us to demonstrate that electrons on a given atomic site interact as well with the neighboring sites. Indeed, if we consider Eq. (8) we see that it permits to define a transferred hyperfine coupling $A(R_n)$ between the local moment at the origin and the nuclear spin at R_n.

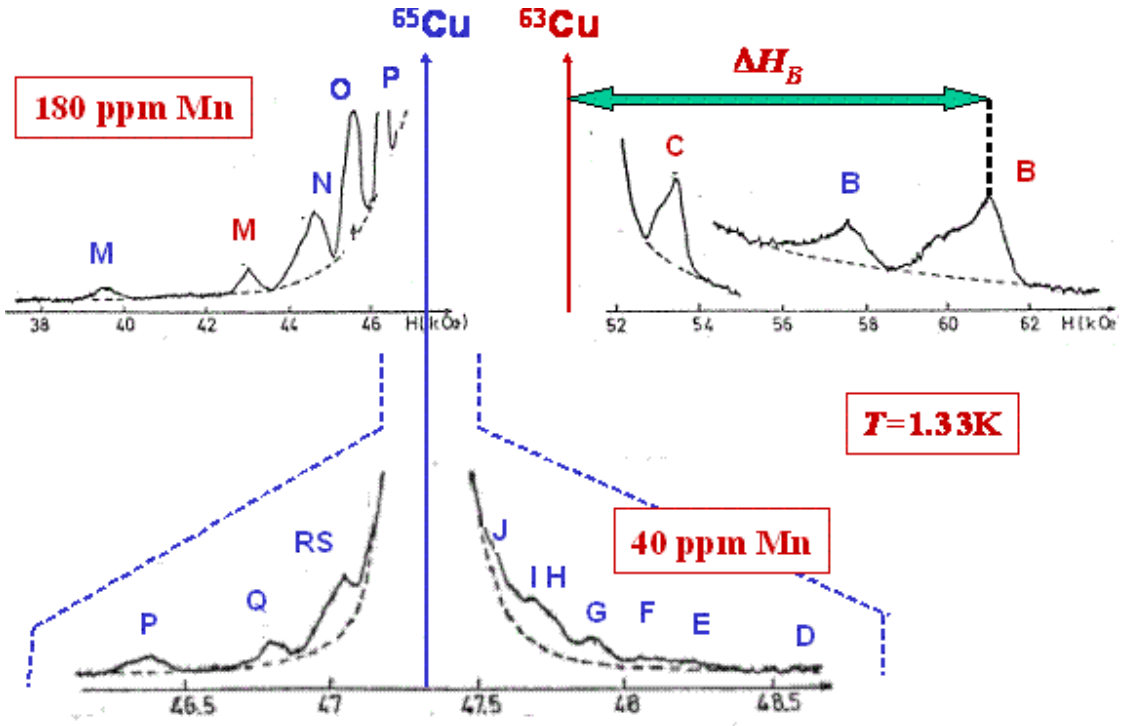

Fig. 1: *NMR spectra of the ^{63}Cu and ^{65}Cu nuclear spins in dilute Cu-Mn alloys obtained by sweeping the applied external field, at 1.3 K. The spectra have been expanded vertically to exhibit the satellite lines by cutting the large intensity central lines at the pure copper NMR positions, which are pointed by arrows. On both sides of the central lines one can see the weak NMR signals of the diverse copper shells of neighbors. The sites far from the impurities are better resolved by reducing the impurity concentration, as shown in the expanded bottom spectrum. (adapted from Ref. [7])*

Therefore, in systems where different atomic sites with distinct electronic properties are involved in a unit cell, such transferred hyperfine couplings do play an important role. In particular, if one considers atomic sites which are not displaying the most important magnetic response they will still sense the response of the magnetic sites through such transferred hyperfine couplings. In the case of Cu-Mn the transferred hyperfine coupling with the Mn magnetism extends over a large number of Cu sites. But, as the transferred hyperfine coupling decreases strongly with distance, it is often sufficient to consider solely transferred hyperfine couplings with the first nearest neighbors. For instance in a square lattice such as that of the CuO_2 planes of cuprate superconductors, for which the electronic magnetic response is located on the Cu sites, the ^{63}Cu nuclei will be coupled to the on-site magnetic response and with that of the near neighbors. This can be cast in a combined wave-vector $\boldsymbol{q}$-dependence of the hyperfine coupling $A(\boldsymbol{q}) = A_0 + \sum A_i \, e^{i\boldsymbol{q}\cdot\boldsymbol{r}_i}$ in which A_0 is the on-site local hyperfine interaction between the observed nuclear and electron spins and A_i is the hyperfine interaction with electron spins at neighboring sites at $\boldsymbol{r}_i$. We shall see later that these transferred hyperfine couplings are important for the nuclear spin-lattice relaxation induced on the various atomic sites of the structure.

4 Correlation effects: some incidences on hyperfine couplings and NMR shifts

In this section we shall consider how correlation effects can influence the electronic structure and spin susceptibilities. One of the initially most studied cases is that of the Kondo effect, which was expected to induce a modification of the spin susceptibility of a Kondo impurity and of the induced spin polarization in the host metal. Another important effect is the pseudogap which appears in the underdoped cuprates and has been discovered by NMR-shift experiments.

4.1 Magnetic impurities and Kondo effect

One of the first correlated-electron physics problem which has been fully solved has been revealed by studies of $3d$ impurities substituted on the atomic sites of regular sp metals. One usually assumed that a local moment S resides on the $3d$ sites and interacts with the free electron spin s by the exchange interaction of Eq. (6).

The Kondo problem arose with the discovery by J. Kondo that perturbation theory of the Hamiltonian of Eq. (6) resulted in a $-\ln T$ term in the resistivity of the alloys, which was indeed observed experimentally. It was understood that the conduction-electron interaction with the local moment induced a crossover of the impurity electronic state towards a low-T ground state quite different from the quasi-free local moment and that the crossover temperature defines an energy scale

$$k_B T_K = E_F \, \exp\left[\frac{1}{J\,\rho(E_F)}\right]. \tag{9}$$

This expression for the Kondo temperature T_K bears some analogy with that of T_c and the energy-gap variation with electron-phonon coupling for superconductivity. It has been harder to qualify the actual properties of the Kondo ground state, but from the observed transport and thermodynamic properties associated with the impurity degrees of freedom, it has been accepted rather soon that the impurity properties experimentally appear to evolve from a high-T magnetic state to a non-magnetic like behavior below T_K. In other words, the weak coupling regime where the impurity moment can be treated in a perturbation scheme evolves at low-T into a strong coupling regime, where the impurity and conduction electrons are bound into the ground state. The basic picture which was initially accepted is that the conduction electrons might form a singlet state with the impurity and compensate its magnetization. If such a spatially extended state occurs, one would expect to see its experimental signature on local magnetic measurements in the corresponding spatial range around the impurity, so that NMR experiments appeared as the ideal probe to view such effects. From the study of the macroscopic properties of impurities in noble metal hosts, it was established that the crossover temperature T_K was highly dependent on the impurity. This was, of course, quite compatible with the exponential expression of Eq. (9). Values of T_K could be estimated from the maximum in the impurity contribution to the specific heat or from the Weiss contribution to the spin susceptibility measured at high enough temperature, etc. This permitted to establish that T_K was below 10 mK for Cu-Mn, ~ 1 K for

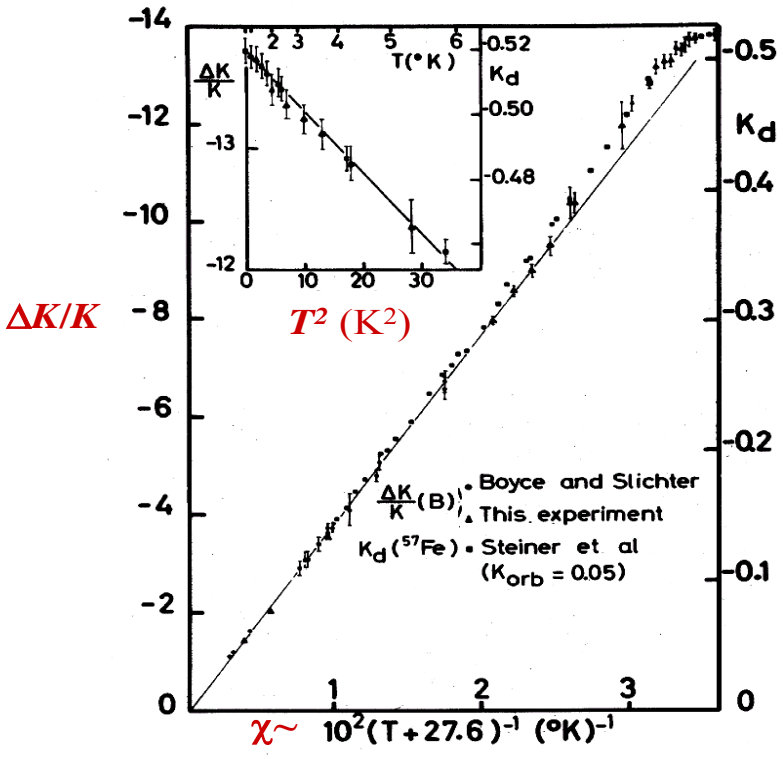

Fig. 2: *The variations of the normalized NMR shift $\Delta K/K$ induced by Fe impurities in Cu for three satellite resonances, and of the impurity susceptibility obtained by Mössbauer data (K_d) scale perfectly with each-other. This gives a good experimental determination of the variation of the local spin susceptibility through $T_K \sim 30$ K, which crosses over from a high-T Curie-Weiss dependence above T_K toward a quadratic T^2 variation below T_K (see inset) from Ref. [9].*

Cu-Cr, ~ 30 K for Cu-Fe, ~ 300 K for Au-V, etc. [8]. It was harder to consider Al-Mn along the same lines as all temperature variations were very weak in this case, so that this crossover could only occur above 1000 K, for which the alloy would have molten. Anyway, if one wanted to study experimentally the change from the magnetic state to the non-magnetic state, one needed to consider a system in which one can explore both regimes $T \gg T_K$ and $T \ll T_K$. Therefore Cu-Fe appeared immediately as the most suitable case if one wanted to avoid extremely low temperature experiments, while Cu-Mn and Al-Mn appeared as the two extreme opposite cases.

4.2 T-dependence of the susceptibility and spatial extent of the Kondo singlet

This idea of a Kondo singlet has led to some attempts to detect modifications of the host ^{63}Cu NMR width when T is decreased through T_K. Those early experiments were initially taken as a signature of the development of a static polarized cloud anti-parallel to the local impurity magnetization. But the situation was only fully clarified when NMR resonances of ^{63}Cu near neighbors to the Fe were detected (see section 3). The shifts of the various lines had T variations which scaled with each-other and displayed the same Curie-Weiss dependence as the magnetic susceptibility data taken in very dilute samples, as displayed in Fig. 2. So, on a small number

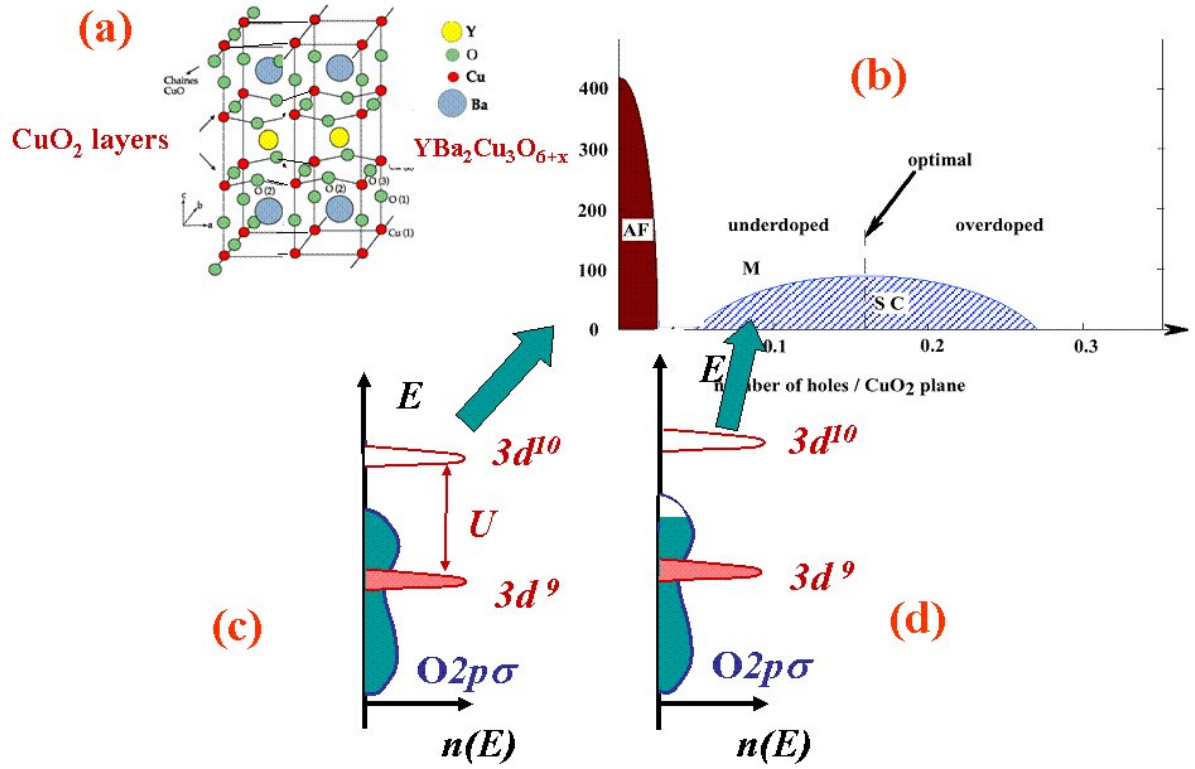

Fig. 3: **(a)** *Atomic structure of $YBa_2Cu_3O_{6+x}$. The O filling of the lower and upper CuO_x planes is responsible for hole doping.* **(b)** *Phase diagram versus hole doping of the CuO_2 planes in cuprates showing the fast decrease of the AF Néel temperature, and the SC dome.***(c)** *Band structure of the undoped parent compound.* **(d)** *possible two-band electronic structure in the absence of interaction between Cu and O holes. (Reproduced from [7])*

of sites near the impurity, the magnetic behavior does display a smooth T variation through T_K, which allowed one to deny the existence of a static compensating cloud. This result confirmed that the susceptibility reaches a low-T behavior similar to that achieved in the non-magnetic case, as has been also found by the numerical solutions of the Kondo model established by Wilson [10]. However, these results do not give any answer about the spatial extension of the correlated Kondo state (this matter is discussed in Ref. [7]).

4.3 The cuprate pseudogap

The cuprates contain as common elements CuO_2 planes (Fig. 3(a)) which are considered to contain all the important physics. Their structure is a stacking of such planes separated by other oxide layers, which maintain charge neutrality and the cohesion of the structure essentially through ionic interactions. They display the highest known superconducting temperature T_c obtained after chemical doping a parent state which is a Mott insulator. Indeed in the undoped cuprates the Cu are in a $3d^9$ state in which the Cu hole bears a $S = 1/2$ local moment (Fig. 3(c)). Those have been of course the physical properties which have driven the interest

for these systems initially both for their fundamental aspects and their potential applications. Another aspect responsible for their appeal has certainly been the fact that the carrier concentration can be easily changed by chemical heterovalent substitutions or oxygen insertion in the layers separating the CuO_2 planes, which play the important role of charge reservoirs. Electron or hole doping can then be fairly continuously controlled from zero to about 0.3 charges per unit cell, which allows one to study the evolution of the physical properties of these materials with doping and to map out their rich phase diagram (Fig. 3(b)). One important question raised concerning these doped compounds was that of the electronic structure of the band responsible for the metallic behavior. At a time when no ARPES experiments were available to map out the electronic structure, one expected that the doping holes would be located in an independent oxygen band, as exhibited in Fig. 3(d). As recalled hereafter in Sec. 4.4, the analysis of the ^{17}O,^{89}Y, and ^{63}Cu NMR shifts in $YBa_2Cu_3O_{6+x}$ cuprates has permitted to demonstrate unambiguously that the holes responsible for the measured macroscopic spin susceptibility are located on the Cu sites as expected for the undoped compound. The study of the evolution of the NMR shifts with hole doping (Sec. 4.5) allowed then to reveal the occurrence of a pseudogap in the samples with lower than optimal doping. The latter was found quite generic of the clean cuprate families (Sec. 4.6). The analysis of the NMR spin-lattice relaxation suggested a $\boldsymbol{k}$-space differentiation of the spin excitations which has been studied later in great detail by ARPES experiments (Sec. 5.3).

4.4 Carriers and hyperfine couplings

Let us assume that the Cu holes responsible for the local moments yielding the AF state of the parent compounds and the doped holes expected to be located on the oxygen orbitals are uncorrelated. In that case the macroscopic magnetic susceptibility should sum up the contributions of these two bands, while the ^{63}Cu nuclear spins would probe the spin contribution on the copper sites. Similarly the ^{89}Y and ^{17}O nuclear spins would be more likely coupled to the oxygen holes. The determination of the hyperfine fields which couple the nuclear spins with the susceptibility has been essential in the understanding of the electronic structure. The anisotropies of orbital contributions to the ^{63}Cu NMR shifts and of the ^{63}Cu spin hyperfine couplings permitted to establish that the Cu holes are located in the Cu $3d_{x^2-y^2}$ orbitals [11]. The evidence for a *negative* hyperfine coupling of ^{89}Y with the spin susceptibility allowed to demonstrate that ^{89}Y also probes the susceptibility localized on the Cu $3d_{x^2-y^2}$ orbitals through a transferred hyperfine coupling via O $2p_\sigma$ orbitals [12], which was found identical for the insulating and doped compounds. This suggested that the spin susceptibility resides in a *single spin fluid* [13], involving Cu $3d_{x^2-y^2}$ – O $2p_\sigma$ hybridized orbitals, so that the two types of holes are correlated and not independent as would be suggested by Fig. 3(d). This is fully confirmed below by the analysis of the T variations of the NMR shifts.

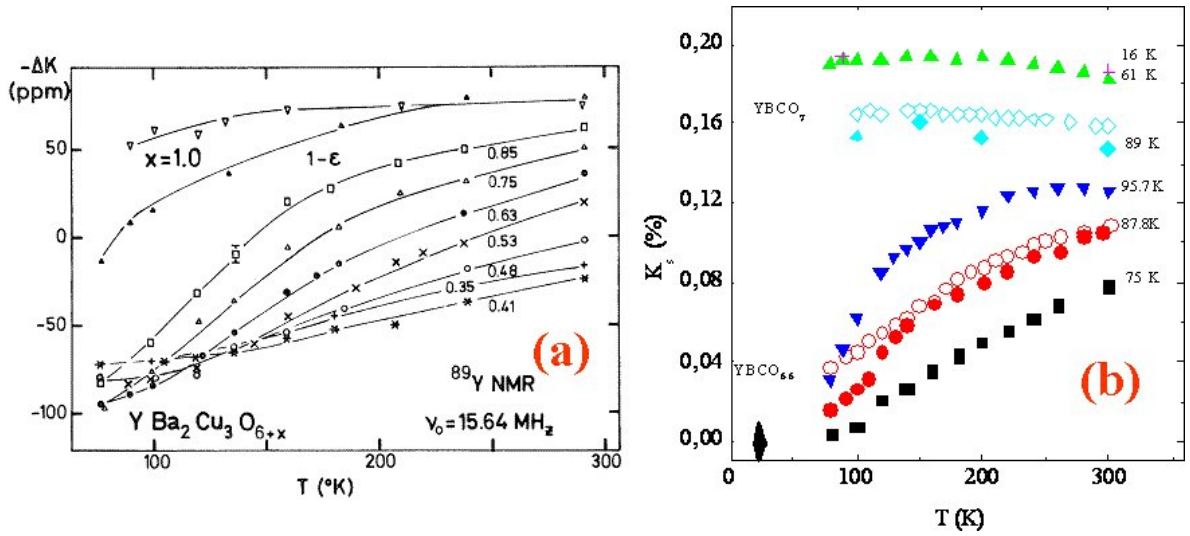

Fig. 4: **(a)** *Temperature variation of the ^{89}Y NMR shift $-\Delta K_s$ for $YBa_2Cu_3O_{6+x}$ powder samples from optimal doping to a non-superconducting sample with $x = 0.41$. The progressive increase of the pseudogap magnitude is apparent (from ref. [14]).* **(b)** *The comparison of the ^{17}O NMR-shift data in YBCO and Hg1201 permits to demonstrate that the pseudogap temperatures T^* are identical for these two compounds (from [15]).*

4.5 Evidence for a pseudogap from NMR-shift data

The optimally doped highest-T_c compounds exhibited a rather regular T-independent susceptibility together with a strange linear T variation of the resistivity above T_c. The possibility to control the hole doping in the $YBa_2Cu_3O_{6+x}$ cuprate by decreasing the oxygen content which is inserted in the intermediate planes between the CuO_2 planes permitted controlled NMR experiments in the underdoped regime for which T_c drops with decreasing hole doping. Those experiments revealed a quite distinct behavior of the NMR shifts with a dramatic drop of the spin component K_s that is of the spin susceptibility with decreasing T. Such an observation made initially by ^{89}Y NMR measurements (see Fig. 4(a)) remarkably revealed that for a composition with $T_c = 60$ K, the spin susceptibility drops by more than a factor three between room T and T_c [14]. As the spin susceptibility remains still sizable at T_c, this appeared as the signature of the opening of an imperfect gap which was qualified as a *pseudogap* already in 1989. This is remarkable inasmuch as it was not experimentally possible to detect any further sharp decrease of the spin susceptibility below T_c. The other aspect which was revealed by these experiments is that the onset-temperature T^* of the drop in K_s increases with decreasing doping. This had led to the indication that the magnitude of the pseudogap increases with decreasing doping, that is, with decreasing T_c. Most other experiments measuring uniform macroscopic responses, such as specific heat, planar resistivity ρ_{ab}, do detect an onset at similar temperatures as that of T^* [16], which is undoubtedly the highest temperature below which a detectable deviation with respect to the high-T Pauli like behavior occurs. Signatures for the pseudogap have been seen as well in optical absorption, photoemission (ARPES), or tunnel-effect experiments.

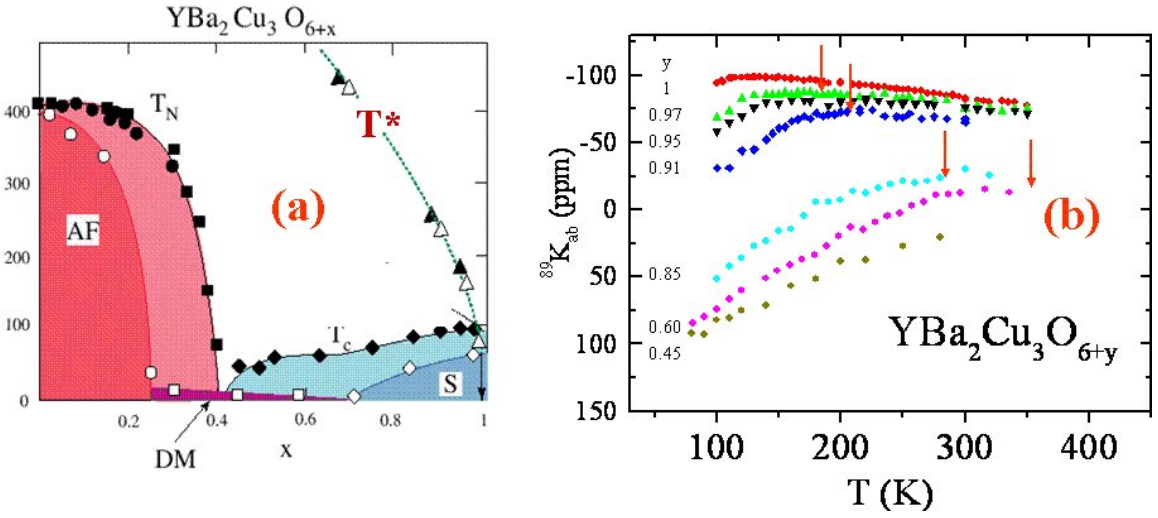

Fig. 5: **(a)** *Cuprate phase diagram obtained for $YBa_2Cu_3O_{6+x}$ by changing the oxygen content x of the Cu intermediate planes. There the phase diagram obtained for 4% Zn substitution on the Cu sites (open symbols) demonstrates that T_c is highly affected while T^* values are insensitive to disorder.* **(b)** *The determination of the T^* values from the departure of the ^{89}Y NMR shift from its high-T constant value is illustrated here by arrows. Figure composed from experimental results reported in Ref. [18].*

4.6 Universality of the pseudogap phase diagram

Data taken for the spin components of the NMR shifts for ^{63}Cu or ^{17}O in $YBa_2Cu_3O_{6+x}$ have evidenced a perfect scaling of the T variations with that of ^{89}Y, which confirmed the idea of a single spin-fluid contribution to the spin susceptibility. That was in line with the Zhang and Rice suggestion [17] that oxygen holes just form singlets with Cu and only modify the Cu susceptibility, so that the Cu and O holes are highly correlated. This identical T variation found by NMR on the various nuclear spin sites has given a universality to the pseudogap T^* deduced by NMR. Comparison between ^{17}O NMR shifts in the $YBa_2Cu_3O_{6+x}$ two-layer compound and the single layer compound $Hg_1Ba_2CuO_4$ evidenced that T^* is generic within the clean cuprate families [15] (see Fig. 4(b)). This has been confirmed by nearly all experimental determinations done by macroscopic measurements of T^*. This pseudogap T^* line introduced in the phase diagram of YBCO is displayed in Fig. 5 for pure samples but also when T_c and T_N have been decreased by 4% Zn substitution on the Cu sites, as will be discussed in Sec. 6.3.

4.7 Local magnetism induced by in-plane impurities in cuprates

An impurity is a local screened Coulomb potential, which ideally is a uniform perturbation in $\boldsymbol{q}$-space, inducing a response which is inhomogeneous in real space but which reflects the response to all $\boldsymbol{q}$ values. So quite generally, an impurity potential is a fundamental tool to probe the specific response of a pure system. For instance, the RKKY oscillations induced by a local moment impurity in a classical metal are due to the singularity associated with the truncation of the response at $|\boldsymbol{q}| = k_F$. In correlated electron systems, if some singularity occurs at a specific

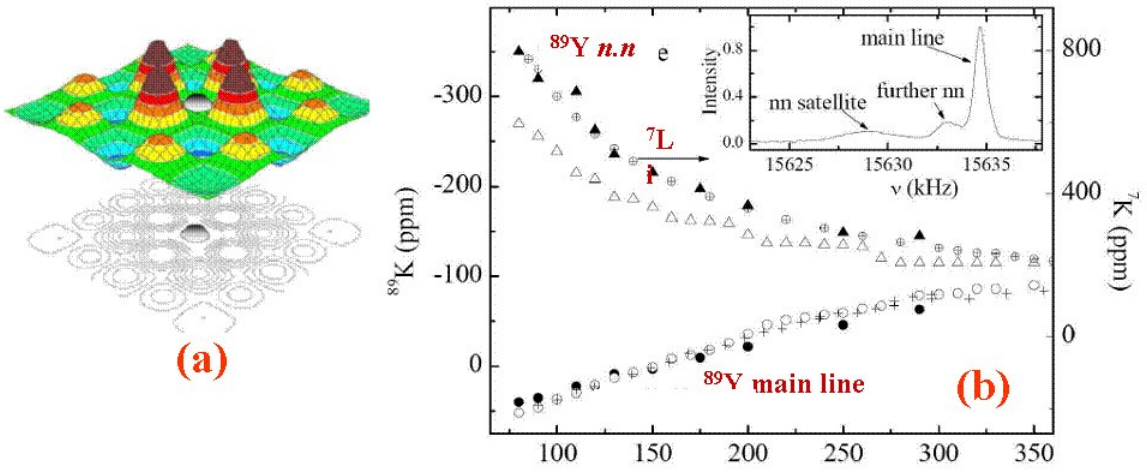

Fig. 6: **(a)** *Non magnetic impurities such as Zn or Li substituted on the Cu site in the CuO_2 plane in cuprates induce a 2D staggered magnetic response.* **(b) Inset**: *The ^{89}Y NMR spectrum exhibits a central line and satellite lines.* **Main**: *the T dependence of the satellite or ^{7}Li NMR shift permits to monitor that of the induced paramagnetism. (Figures from ref. [18]).*

"$\boldsymbol{q}$" value for a pure system, this singular response will dominate the modifications introduced by the impurity. For instance, in magnetic materials for which AF correlations can be important at a wave vector $\boldsymbol{q} = \boldsymbol{q}_{AF}$, a staggered magnetic response at this wave vector is expected. So quite generally, an impurity potential is a fundamental tool to probe the specific response of a pure system, which is all the more interesting when some physical properties might be hardly measurable directly in the pure system, or when some of the hidden physical properties can be revealed by the impurity potential. NMR experiments ideally permit to map out the spatial changes occurring around extrinsic defects. Those cannot be accessed through macroscopic non-local techniques. For instance we give evidence in Ref. [18] that the staggered magnetism induced by defects in spin chains allows to determine by NMR the correlation functions of the *pure* state. Similarly we underline hereafter that Zn or Li non-magnetic atoms substituted on the Cu sites in the cuprates induce an extended paramagnetic state in their vicinity. Such studies have been important to qualify the incidence of disorder in the various doping ranges of the cuprate phase diagram (see Ref. [18]).

As shown above, the underdoped regime of cuprates, for which a pseudogap is detected, is the interesting range, where the system is a metal with magnetic correlations, for which the use of impurities to probe the physical properties was expected to be the most fruitful. The first basic qualitative information were obtained by an approach, started in the early 1990's, using Zn and Ni impurities substituted for Cu in the $YBaCuO_{6+x}$ system specifically for $x \simeq 0.6$ for which the pseudogap occurs at $T^* \gg T_c$. The question which arose was whether a non-magnetic site induces a free paramagnetic moment in a *metallic* correlated system, as was seen later in the case of undoped spin chains and ladders. An indirect but unambiguous evidence that Zn induces a paramagnetic moment in an underdoped cuprate was obtained by monitoring the ^{89}Y NMR linewidth in $YBCO_{6.6}$:Zn_y [19]. The significant low-T increase of the linewidth that was

detected revealed the increase of the static staggered spin polarization around the impurity. This was clearly confirmed later by resolving in dilute samples the satellite NMR signals of the ^{89}Y near neighbor (*n.n.*) sites of the substituted Zn [20] (see Fig. 6(b)). This provided the first local detection of the field induced paramagnetism near the Zn, well before the equivalent information could be monitored in the case of spin chains. These data implied that the spin polarization of the Cu "n.n." to Zn is already at 100 K more than ten times larger than that of the pure host, so this was not a mere minor modification of the host density of states, but a strong effect of the electronic correlations of the system. Quite analogous ^{89}Y *n.n.* NMR data were obtained later (see Fig. 6(b)) for non magnetic Li impurities, which provided the possibility to use in the same sample the ^{7}Li, ^{89}Y, ^{17}O and ^{63}Cu nuclear spin probes. The ^{7}Li NMR permitted accurate measurements of $\chi(T)$ of the four Cu *n.n.* of the Li non-magnetic impurity. In the underdoped samples, this variation was found to display a Curie variation at low doping, which confirmed the observation made from the ^{89}Y NMR that the impurity-induced state behaves as a nearly free paramagnetic moment [21]. For increasing doping the Curie law is found to transform into a Curie-Weiss law with a Weiss temperature Θ which increases abruptly with doping. One could conclude that the low-T reduction of the susceptibility in the optimally doped case is due to the onset of the energy scale $k_B\Theta$ in analogy with the Kondo reduction of local moments in classical metallic systems. The data taken on the other nuclei has enabled the quantitative determination of the spatial structure of the induced polarization, that is, its magnitude and magnetic correlation length $\xi_{\rm imp}(T)$ which increases significantly at low T. Although $\xi_{\rm imp}$ has been found of similar magnitude at room temperature for optimal doping, it displays much weaker variations at low T than in the underdoped case. The energy scale Θ may control the T variations of both quantities, however. Since overdoping corresponds to an increase of Θ well beyond the value found for optimal doping, such a scheme would allow a smooth crossover towards the Fermi-liquid limit for large overdoping.

5 Spin-lattice relaxation

The local susceptibility measurements are giving pertinent information on the electronic properties of the material in its ground state. But NMR also permits to probe the excited electronic states through the fluctuations of the local field $\boldsymbol{B}_{\rm eff}$. This occurs through the nuclear spin-lattice relaxation (NSLR) processes which drive back the nuclear spins towards their thermodynamic equilibrium once the latter has been disturbed intentionally.

Indeed the nuclear spin magnetization is not established immediately if an external magnetic field is applied instantaneously to the material. The very interactions between the nuclear spins and the electronic degrees of freedom govern the spin-lattice relaxation time T_1 which is required to establish thermodynamic equilibrium. One typically needs transverse local field components at the Larmor frequency $h\nu_L$ to induce the difference of population of the nuclear spin levels. Therefore T_1 is directly linked with the transverse field Fourier component at ν_L of $\boldsymbol{B}_{\rm eff}(t)$. One can see that, for the hyperfine couplings considered above, this results in a measurement of the electronic dynamic susceptibility of the electron spin system.

So, in systems with unpaired spins the dominant T_1 process is due to local field fluctuations induced by the dynamics of the local electronic magnetization. Theoretically, the spin contributions to $(T_1T)^{-1}$ may be written using the imaginary part of the dynamical electron spin-susceptibility $\chi''(\mathbf{q},\nu_n)$ as

$$(T_1T)^{-1} = \frac{2\gamma_n^2 k_B}{g^2\mu_B^2} \sum_{\mathbf{q}} |A_0|^2 \, \frac{\chi''(\mathbf{q},\nu_n)}{\nu_n} \, . \tag{10}$$

Here, as for the Knight shift, we assumed that the dominant hyperfine coupling is the contact term. We shall see later many examples, which give evidence that T_1 measurements permit one to monitor the occurrence of phase transitions and to give relevant information on energy gaps between the ground state and excited states in many electronic systems. In cases where some ionic species are mobile in a material, as for instance in ionic conductors, the atomic diffusion processes can govern the local field fluctuations sensed on some nuclear spin sites, and the T_1 measurements may permit to monitor these ionic diffusion motions.

5.1 Spin-lattice relaxation in standard 3D metals

For a simple metallic band, the dynamic electronic susceptibility response is simple enough and one writes

$$\chi_0(\omega) = \sum\nolimits_{\mathbf{q}} \chi_0(\mathbf{q},\omega) = \chi_{P0} \left[1 + i\pi\hbar\omega \; \rho(E_F)\right] . \tag{11}$$

One can immediately see that this yields a simple expression for the spin-lattice relaxation from Eq. (10)

$$(T_1T)^{-1} = \pi k_B \; A_0^2 \; \rho^2(E_F)/\hbar \tag{12}$$

so that a universal relation holds between the Knight shift and T_1.

$$K^2 \, T_1T = \mathcal{S} = (\hbar/4\pi k_B) \, (g\mu_B/\hbar\gamma_{\rm n})^2 \, . \tag{13}$$

As K is T independent, this so called "Korringa" relation applies rather well in the absence of electronic correlations. As an example (see [22]) one could see that T_1T of ^{27}Al is constant in pure aluminium metal on a T range which extends over more than three orders of magnitude. The T_1 value in a metal is quite often used to define an empirical temperature scale especially in the very low T regime below 1 K.

5.2 Incidence of weak electron correlations

So far we did not consider any influence of electronic correlations though even in simple alkali metals electron-electron interactions play a role in the electronic scattering processes. We also do know that some electronic systems are on the verge of becoming magnetic. Those quasi AF or quasi ferromagnetic metals can be identified by the very fact that the Korringa relation does not apply straightforwardly as the spin susceptibility does not behave as described above for free electron Fermi liquid systems. In such cases the dynamic spin susceptibility is not uniform

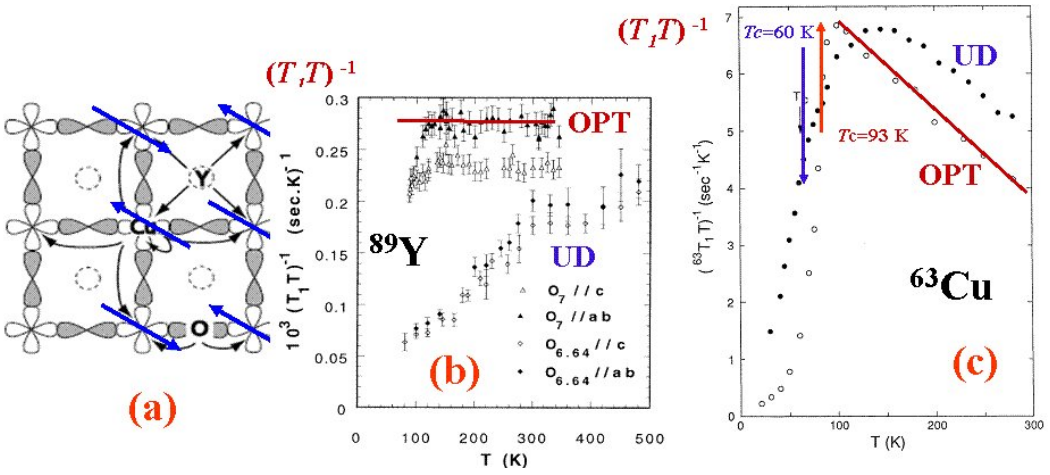

Fig. 7: **(a)** *Schematics of the Cu $3d_{x^2-y^2}$ and O $2p_\sigma$ orbitals in the CuO_2 plane showing why the AF fluctuations are filtered at the ^{17}O and ^{89}Y nuclei. This explains why the T variations of $(T_1T)^{-1}$ taken for oriented powder samples of $YBCO_7$ ($T_c = 90$ K) and $YBCO_{6.6}$ ($T_c = 60$ K) are quite different for ^{63}Cu and ^{89}Y.* **(b)** *^{89}Y data taken from Ref. [26]* **(c)** *^{63}Cu data taken from Ref. [11]. While the data for $T_c = 90$ K are T independent for ^{89}Y, as is the Knight shift, they increase at low T for ^{63}Cu. Similarly for the underdoped samples both $(T_1T)^{-1}$ and ^{89} K increase regularly up to $T^* \sim 350$ K, while those for ^{63}Cu display a maximum at $T \sim 150$ K, assigned to a spin gap.*

in q space as was shown initially by Moriya [23], and exhibits enhanced values either for $\mathrm{q} = 0$ for nearly ferromagnetic metals or for an AF wave vector $\boldsymbol{q}_{AF}$ for nearly AF materials.
In the former case the $\boldsymbol{q} = 0$ spin susceptibility is enhanced by a factor $S = 1/(1 - I\chi_{P0})$, usually called the Stoner factor, and $\chi_P = S\chi_{P0}$ exhibits a large increase with decreasing T and only saturates at very low T, as has been illustrated in the nearly ferromagnetic metals like $TiBe_2$ or in elemental Pd metal. In those cases, the enhancement of the dynamic spin susceptibility $\chi_0(\boldsymbol{q}, \omega)$ is not uniform in $\boldsymbol{q}$ space and is weaker for $\boldsymbol{q} \neq 0$, therefore the Knight shift is more enhanced than $(T_1T)^{-1}$. The Korringa relation does only apply when χ_P saturates [24], with a $T = 0$ Korringa constant $K^2T_1T = \mathit{\Delta}\, \mathcal{S}$ increased by an S-dependent factor $\mathit{\Delta}(S)$. On the contrary in nearly AF metals $\chi_0(\boldsymbol{q}, \omega)$ is peaked for $\boldsymbol{q} = \boldsymbol{q}_{AF}$ which means that the static spin susceptibility and the Knight shift K are less enhanced than $\chi_0(\boldsymbol{q}_{AF}, \omega)$. Correspondingly $K^2T_1T = \mathit{\Delta}\, \mathcal{S}$ corresponds in that case to $\mathit{\Delta} < 1$, that is a decreased Korringa constant, as has been seen for instance in the compound MnSi [25].

5.3 Dynamic spin susceptibility and electronic correlations

We shall discuss below the actual information on the AF correlations given by the measurements of the spin-lattice T_1 and transverse T_2 nuclear spin relaxation in the cuprates. As shown in the previous section, the T_1 give determinations of $\chi''(\boldsymbol{q}, \omega)$ while we shall show here that the transverse T_2 is related to $\chi'(\boldsymbol{q}, 0)$.
The feature which had been clearly evidenced was that for ^{89}Y nuclear spins $(T_1T)^{-1}$ and ^{89}K have very similar T variations (with T and doping). This is illustrated in Fig. 7(b) on data

taken on field-aligned YBCO samples realized for two compositions, O_7 for which $(T_1T)^{-1}$ is T independent as is ^{89}K, while for $O_{6.6}$ both quantities exhibit large T increases. Similar results on the ^{17}O NMR have been obtained, which established that the dynamic susceptibility viewed by these nuclei appeared quite correlated with the static susceptibility. It has been established that T_1TK_s is nearly T independent, which has been taken as an evidence for the presence of a Fermi-liquid like component in the magnetic response.

However, as was seen by many authors, the $(T_1T)^{-1}$ of ^{63}Cu behaves quite differently (for references, see Ref. [27]). In the optimally doped compound $(T_1T)^{-1}$ increases at low T while it goes through a maximum at a temperature much lower than T^* in the underdoped sample (see Fig. 7(c)). This difference between ^{63}Cu and ^{17}O (or ^{89}Y) NMR is understood as the two latter nuclear spins being coupled to two (or four) Cu moments do not detect AF fluctuations at the AF wave vector $\boldsymbol{q}_{AF} = (\pi, \pi)$, as sketched in Fig. 7(a). In other words, the ^{63}Cu data uniquely reveals the occurrence of a peaked response of $\chi''(\boldsymbol{q}, \omega)$ at $\boldsymbol{q}_{AF}$. This has been confirmed directly by inelastic neutron scattering experiments taken on underdoped samples. The maximum in $(T_1T)^{-1}$ for ^{63}Cu has been assigned to a spin gap which is quite distinct from the pseudogap T^*. It would increase much less rapidly than T^* for decreasing doping. Both the pseudogap T^* and the spin gap are detected only in underdoped samples, which suggests that they are connected.

Let us point out now that this strong magnetic response in cuprates induces a contribution to the nuclear spin transverse T_2 relaxation, which has been found to be quite important on the Cu sites. In weakly correlated solids T_2, which is measured with spin-echo experiments (see NMR wikipedia) is usually fully determined by the direct dipole-dipole interactions between nuclear spins. In cuprates and more generally in correlated systems, a nuclear spin at $\boldsymbol{R}_i$ can be viewed as a moment which induces, through the $\boldsymbol{q}$-dependent susceptibility $\chi'(\boldsymbol{q}, 0)$, a polarization of the electronic spins which extends on the sites nearby $\boldsymbol{R}_i$. This polarization does in turn couple to the nuclear spins on these sites. This indirect (RKKY-like) dipolar interaction between the nuclear spins induces a contribution to the spin echo decay. After summation of the interaction of a nuclear spin with all its neighbors, the spin echo is found to get a Gaussian decay with a time constant T_{2g} given by

$$\left(1/T_{2g}\right)^2 \propto A_{\mathbf{0}}^4 \sum_{\boldsymbol{q}} [\chi'(\boldsymbol{q}, 0)]^2 - A_{\mathbf{0}}^4 \left[\sum_{\boldsymbol{q}} \chi'(\boldsymbol{q}, 0)\right]^2 .$$

In the cuprates, $\chi'(\boldsymbol{q}, 0)$ is expected to be peaked at $\boldsymbol{q}_{AF}$ and the width of the peak defines a correlation length ξ for the AF response, which might be estimated from the T_{2g} data. Even in the underdoped pseudogapped regime ξ is found to increase steadily with decreasing T as has been seen as well from impurity studies described in Sec. 4.7.

Coming back to the pseudogap, more recently ARPES or STM experiments have given evidence that a gap in the charge excitations only occurs for the antinodal directions $(0, \pi)$ in $\boldsymbol{k}$-space. So the closed Fermi surface which occurs at high T in underdoped cuprates loses weight in the antinodal directions when T decreases, and the Fermi surface then reduces to Fermi arcs, which shrink with decreasing T (see [28]). The experimental results on $(T_1T)^{-1}$ of

^{63}Cu are certainly precursor indications of this $\boldsymbol{k}$-space differentiation which has been found by $\boldsymbol{k}$-dependent spectroscopies.

Phenomenological attempts have been done to describe the shape functions of the spin susceptibilities $\chi''(\boldsymbol{q},\omega)$ and $\chi'(\boldsymbol{q},0)$, in order to fit the NMR data [29]. Satisfactory qualitative descriptions could be achieved, with ξ values of about two lattice constants at room T in both the optimal and underdoped samples, with much larger low-T increases of ξ in the latter. However, these approaches required to introduce by hand the Fermi liquid like metallic component and did not include explicitly the occurrence of the pseudogap. A complete theory of the physical phenomena at play would require a model which generates altogether the pseudogap, the AF correlation length and its T variation.

To conclude, the pseudogap is most probably intimately linked with the correlated nature of these systems, and its actual physical origin is intensely debated. One interpretation, proposed quite early on, is that it represents a precursor pairing state, the superconducting phase being only established at T_c when the pairs achieve long-range phase-coherence [30]. Such an interpretation would imply that the SC gap increases with decreasing T_c. This is so far contradicted by direct or indirect determinations of the SC gap. Another class of interpretations could be the establishment of a hidden order disconnected from superconductivity, such as a spin ordering, for instance a Resonant Valence Bond (RVB) state (see [31]), a d density wave (ddW), a charge segregation into stripe order or an ordering involving orbital currents. Such possibilities have been recently underlined by experimental discoveries of such type of orders, which appear system dependent, and often occur at temperatures below T^*. These experiments are so novel that they have initiated vivid debates on the pseudogap, but did not permit so far to resolve the issues they raised. The pseudogap remains still today the central point debated on the cuprates and at the present writing the understanding of the pseudogap state remains controversial. The author believes that magnetic short-range correlations explain the pseudogap crossover at T^* and the Fermi surface differentiation, while the orders detected at lower T than T^* are rather consequences of the pseudogap formation than direct manifestations of the pseudogap itself.

6 NMR in superconductors

Obviously, the establishment of a SC state yields profound transformations of the electronic properties which will be seen in the NMR response. NMR experiments do not only evidence the occurrence of SC. They also permit to characterize the properties of the SC electronic state [32].

6.1 Knight shift, relaxation, and gap in the SC state

One of the major effects which occur for phonon mediated SC in usual metals is the pairing of electrons in a singlet state. Such a pairing suppresses totally the normal state spin susceptibility at $T = 0$. This is seen quite simply as a full suppression of the spin contribution K_s to the Knight shift in NMR. In type I superconductors, the magnetic induction vanishes in the Meiss-

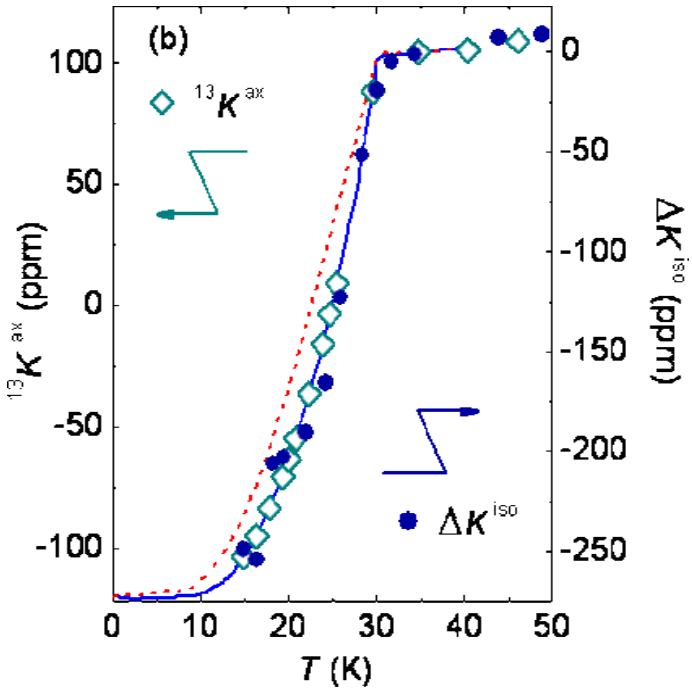

Fig. 8: *The ^{155}Cs and ^{13}C NMR shifts measured in the Cs_3C_{60} phase are plotted versus T below the superconducting temperature $T_c = 30$ K. The NMR shifts follow the standard Yosida type decrease expected for singlet superconductivity [33].*

ner state which by itself forbids observation of the NMR signal in the SC state. But in type II superconductors the field penetrates as an array of vortices, which becomes so dense near the upper critical field H_{c2} that it becomes possible to detect the NMR signal in that regime, and to see the suppression of the Knight shift. Taking into account the variation of the SC gap and the thermal population at temperatures near T_c, yields a specific T dependence of the spin susceptibility, that is of $K_s(T)$, which has been computed by Yosida [6], and which is given by

$$K_s(T)/K_n = \int_{\Delta}^{\infty} \frac{N(0)|E|}{\sqrt{E^2 - \Delta^2}} \frac{df}{dE} dE \,. \tag{14}$$

Here f is the Fermi function. The actual variation of the Knight shift with decreasing temperature can be measured and displays an agreement with this Yosida function as can be seen in Fig. 8 in the particular case of Cs_3C_{60}. As for spin-lattice relaxation data, it can be taken in type I SC using ingenious tricks such as experiments in which the external field is cycled from a field exceeding the critical field H_c down to a field $H < H_c$ in which the nuclear spin magnetization is let free to evolve under the influence of the electronic system.

The opening of the SC gap yields an activated exponential increase of the NMR spin-lattice relaxation rate as T approaches 0, which permits a determination of the SC gap magnitude from the corresponding low T variation of T_1^{-1} (Fig. 9). However the great advance of BCS theory has been its ability to describe the excited states in the SC state up to T_c. Indeed in such a BCS SC state subtle effects are revealed by T_1T data taken near T_c. An increase of the spin-lattice relaxation rate above the normal state Korringa value takes place below T_c. This

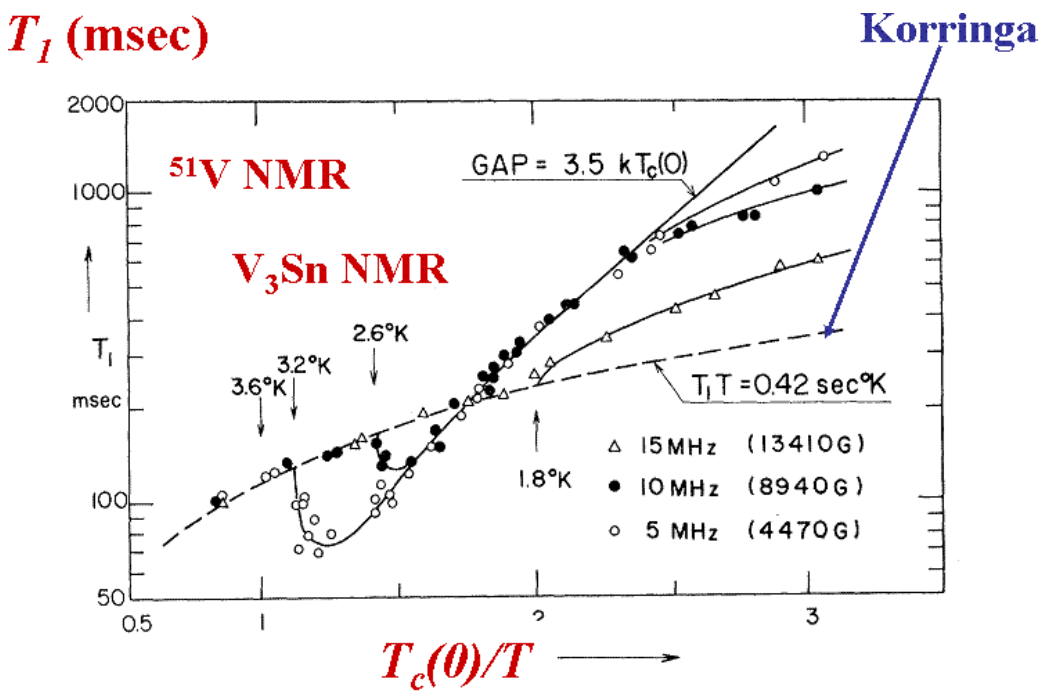

Fig. 9: *The $\log(1/T_1)$ of ^{51}V in V_3Sn is plotted versus $1/T$ for three distinct applied fields, which induce changes of T_c. In the normal state above T_c the relaxation rate is field independent with T_1T=0.42 sec°K. Below T_c the reduction of T_1 represents the Hebel Slichter coherence peak. At low T all curves point towards an activated behavior associated with the full opening of the superconducting gap (adapted from Ref. [32]).*

so called coherence peak evidenced by Hebel and Slichter [34] results partly from the thermal population of the increased density of electronic states which piles up above the SC gap. The T_1 only lengthens at somewhat lower temperatures than T_c (see Fig. 9).
Both these discoveries of the decrease of the spin susceptibility and of the occurrence of a Hebel-Slichter coherence peak have given the early evidences for the applicability of BCS theory of superconductivity in usual metallic systems.

6.2 Field distribution in the mixed state of type II superconductors

In type II superconductors the magnetic induction varies significantly in space in the mixed state. This leads to a distribution of Larmor frequencies for the nuclear spins in the material. The shape of the NMR spectrum reconstitutes the histogram of the magnetic fields. Close to H_{c2}, singularities appear in the spectrum for values of the magnetic field corresponding to the extrema of the field distribution. The shape and width of the observed resonance can be used to deduce λ, the magnetic field penetration depth. However, for experimental reasons, NMR is not the best method for studying the superconducting state. A related technique uses elementary particles called muons. These behave like heavy electrons (or light protons), and have the property of decaying by emission of positrons in the direction of their spin. A muon whose spin is initially polarized perpendicularly to the field B_0 is implanted in the sample at

time zero. One then observes the direction of the emitted positrons when it decays. By repeating this experiment for a large number of events, the free precession signal of the muon spin can be reconstructed statistically. This experiment is equivalent to an NMR experiment, and can be used to determine λ. Since muons can be implanted in almost any sample, it has been possible to make comparative measurements of λ in a wide range of superconducting materials.

6.3 Exotic superconductivities

The importance of the cuprates in the physics of correlated systems has resulted from the discovery that, when the AF is suppressed by hole doping, the doped metallic state which results has a SC ground state and displays strange metallic and magnetic properties. The most surprising feature has been the fact that the superconductivity discovered in these materials has the highest critical temperatures T_c found so far in any superconducting material, and exceeds any T_c which could be expected within the BCS approach known to apply in classical metallic states. An important observation in the cuprates has been the fact that the phase diagram with increasing hole doping displays a dome-shaped SC regime, that is, SC disappears for dopings beyond about 0.3. These non-expected features have immediately led to the idea that SC in the cuprates has an exotic origin linked with electron-electron interactions rather than the classical electron-phonon driven superconductivity which prevails in classical metals.

Obviously, the establishment of any SC state yields profound transformations of the electronic properties which are reflected in the NMR response. In BCS Superconductors the formation of singlet Cooper pairs is directly seen as a loss of the normal state spin susceptibility, that is, a drop of the NMR shift, as evidenced hereabove. NMR studies appeared then quite important in the early days after the discovery of HTSC. One indeed was interested to see whether BCS like observations would be made. For HTSC samples with high T_c around the optimal doping, the NMR data appear quite similar to those obtained in standard BCS materials inasmuch as the NMR shift of most nuclear species in the material ^{63}Cu, ^{17}O, ^{89}Y were found T independent down to T_c, and dropped abruptly at T_c in accord with spin-singlet superconductivity Fig. 10(a) [35]. In many cases for which SC is probably also more exotic than for phonon mediated SC the pairing state remains a singlet, which has been confirmed by similar NMR-shift studies.

In some exotic SC states the pair wave function can be in a spin-triplet state, a situation which has been found first for superfluidity of ^{3}He which are fermions which bind to form spin-triplet Cooper pairs [36]. As a spin triplet can be in three distinct states either $|\uparrow\uparrow\rangle, |\downarrow\downarrow\rangle, |\uparrow\downarrow\rangle + |\downarrow\uparrow\rangle$ or quantum superpositions of these components, the magnetic response to an applied field depends on the actual state of the bound pairs. This explains why ^{3}He has two different triplet superfluid phases. Phase A with equal spin states formed by $|\uparrow\uparrow\rangle$ and $|\downarrow\downarrow\rangle$ pairs displays no change of the nuclear spin susceptibility though the superfluid transition, while phase B is an equal superposition of the three states which leads to a marked decrease of the spin susceptibility which, however, does not vanish completely at $T = 0$.

In correlated electron systems one similarly expects that with spin-triplet SC the behavior of the NMR shift below T_c should permit to establish the spin-triplet pairing and to determine the

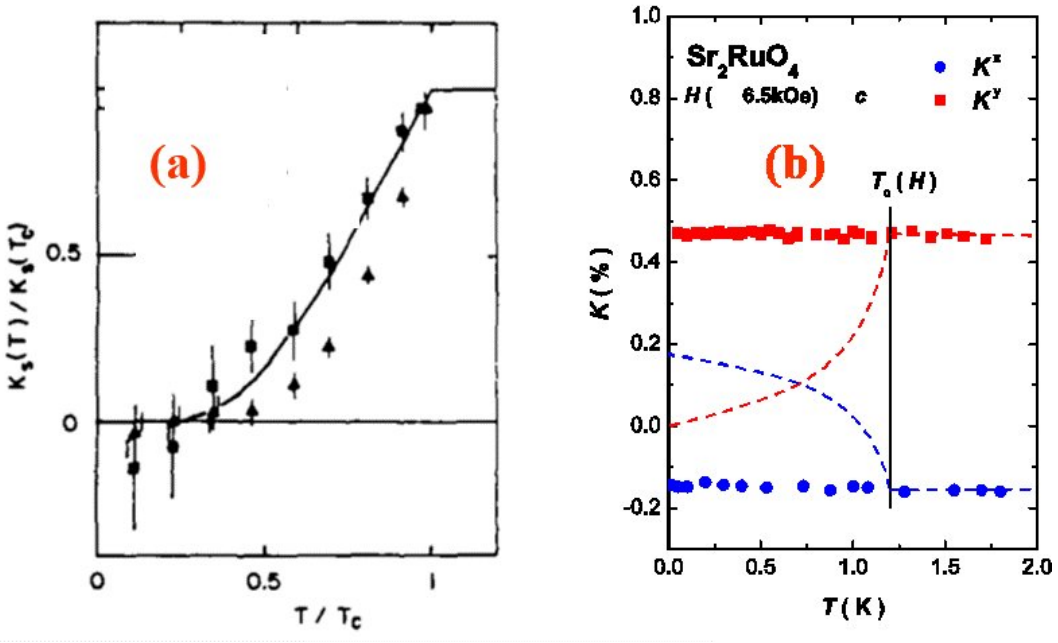

Fig. 10: *^{17}O NMR-shift data taken below T_c in the two planar directions* **(a)** *in $YBaCuO_7$ it drops below T_c and vanishes for $T \ll T_c$ [35].* **(b)** *in Sr_2RuO_4 it remains constant through T_c, which supports spin-triplet superconductivity. Here the reported lines would correspond to expectations for a singlet SC case (from ref. [37]).*

superposition of spin states. A system which has been thoroughly studied is Sr_2RuO_4, in which the RuO_2 form a square lattice which is similar to that of the cuprate La_2CuO_4. Indeed it has been shown in that compound that both ^{17}O and ^{99}Ru NMR shifts exhibit absolutely no change though T_c, Fig. 10(b), which is a strong case for spin-triplet SC with equal spin states [37]. Once the spin properties of the pairs has been established, their orbital state has a symmetry which is imposed by the total antisymmetry of the wave function. So that an antisymmetric spin-singlet state implies an even orbital state, that is an s- or d-wave symmetry of the wave function. Similarly for a symmetric triplet state, the orbital wave function should be antisymmetric that is p-wave or higher order. In most of these exotic pairing states the SC gap is not uniform over the Fermi surface as is the case for most phonon mediated cases. In these exotic superconductors the gap depends of the wave vector $(\boldsymbol{k}, -\boldsymbol{k})$ of the pairs and might exhibit gap nodes for some $\boldsymbol{k}$ values or some wave vector directions. For instance for a 2D system, if the gap has a d-wave order-parameter symmetry, the gap changes sign and therefore vanishes along two axes of the unit cell. This implies that the gapless states will be filled much faster with increasing T than in a pure s-wave BCS superconductor.

In such spin singlet states the functional form of the increase of the spin susceptibility (that is of the NMR shift) with increasing temperature from $T = 0$ permits, in principle, to determine whether nodes occur in the gap function. Experimentally this is somewhat difficult to establish from NMR shift measurements which have limited accuracy at low T due to the inhomogeneous field penetration in the vortex lattice. This is however much more accessible from $1/T_1$ data

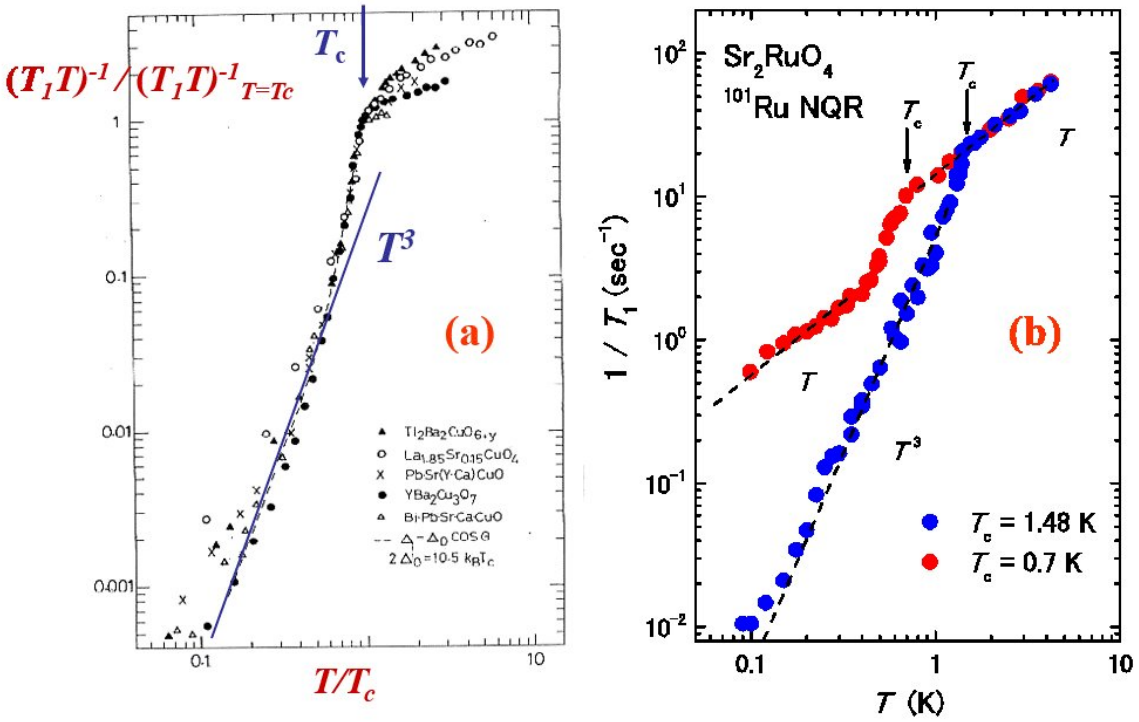

Fig. 11: **(a)** *In $YBaCuO_7$ the ^{63}Cu $1/T_1$ data has a T^3 dependence, which agrees with d-wave SC [38].* **(b)** *In Sr_2RuO_4 the sample-dependence of the Ru NQR $1/T_1$ data is illustrated. The use of a clean sample permits to evidence a T^3 variation which establishes the existence of nodes in the gap function [39].*

which display then a power law increase with an exponent that depends of the wave vector dependence of the gap. A T^3 variation of $1/T_1$ has been best evidenced by zero-field NQR experiments in cuprates, which is in accord with the d-symmetry of the SC order-parameter, Fig. 11(a) and [38]. Though these NMR data were rather conclusive, this d-wave symmetry has such an implication for the understanding of the pairing mechanism that it has only been fully accepted within the community when ARPES and phase-sensitive tunneling experiments established it independently. One has however to recall that low-T NMR measurements can be contaminated by extra contributions of impurities to the relaxation. So to conclude about the symmetry of the SC order-parameter in a given compound, great care has to be taken to avoid the presence of impurities in the actual materials. This is for instance illustrated in Fig. 11(b) for the spin-triplet SC of Sr_2RuO_4, for which a T^3 variation of $1/T_1$ has also been found once clean samples could be produced [39]. Here again this result points out the existence of lines of gap nodes, though their spatial location on the Fermi surface is not yet clarified. The spatial structure of the p-wave state symmetry which governs SC in this compound is therefore not yet fully characterized. A p-wave spin-triplet state has been proposed as well from NMR experiments in some Heavy Fermion compounds such as UPt_3 or in low-dimensional organic conductors, although more experimental confirmations would be required to fully establish the validity of these proposals.

7 Summary

Most, if not all, the discoveries which have been done since the 1980's on correlated-electron systems resulted from extensive experimental investigations. In this lecture I have shown that the NMR technique has been quite successful in this process. This has been exemplified here by revealing some important problems highly debated nowadays in correlated-electron physics. The main impact of NMR comes about as preliminary experiments can be done on powder materials which are not perfect. The second aspect which highlights this technique is that NMR results, which are not surface sensitive, are quite reproducible so that most results presented here have usually been confirmed by independent investigations done in different laboratories on distinct sample materials. All this is eased by the fact that NMR experiments allow one to detect the incidence of defects and disorder effects on the very samples on which the data are taken. We have shown here that the introduction of specific defects, associated with the capability to detect locally their incidence is a powerful tool to unravel the properties of the pure material. This altogether has induced large efforts to clarify the incidence of disorder on the properties of correlated-electron systems. A similar advantage has been highlighted as well for the STM techniques, which however require samples with sufficient surface quality and do not probe the magnetism induced by defects.

As emphasized in many instances in this article, NMR permits to probe on the local scale a large set of relevant physical quantities ranging from magnetic susceptibility, the spin fluctuations, the superconducting properties etc.. In metallic correlated electron systems, an important aspect is the ability to identify by NMR the electronic band(s) which are involved in the metallic state and to establish whether magnetism is associated with different degrees of freedom or due to the same bands. Coming to SC, one of the points which has attracted most attention is its interference (destructive or constructive) with metallic magnetism. The cuprates are in that respect certainly exotic superconductors, in which the incidence of electron correlations and AF short range interactions can be essential to drive superconductivity, or at least enhance the SC transition temperatures. Many other materials have been shown to display situations where magnetism and SC are proximate to each-other in phase diagrams. In Fe superconductors (pnictides or chalcogenides) the phase diagrams are sometimes spanned by doping as in the cuprates, but in other families of compounds the phase diagrams are spanned by pressure control of the overlap integrals as for organic, heavy fermions, or Cs_3C_{60} compounds.

In most of these cases a thorough experimental characterization of the SC order-parameter symmetry is needed prior to any determination of the pairing glue, and NMR data can be helpful in that respect. The d-wave symmetry of the order-parameter for cuprates is considered as the strongest indication that electronic correlations could be responsible for the pairing in these compounds. Even for materials less correlated than the cuprates the incidence of electronic correlations is definitely less detrimental to SC than initially expected and the existence of AF correlations in the material could as well be the boson field mediating the SC state. Many possible glues between electrons such as phonons, AF fluctuations, or charge correlations near a Quantum Critical Point, have been considered and may be at work in distinct materials. But all

this is far from being settled and requires thorough investigations specific to the various families of correlated-electron materials.

We did address here only a limited number of correlated-electron families of compounds which have been investigated using NMR techniques. One might find in Ref. [4] many other striking examples, such as 1D organic compounds, nanotubes, heavy fermions, Na cobaltates, or Kagome compounds with magnetic frustration leading to spin-liquid ground states, on which successful NMR experiments have been undertaken. Other examples are compounds on which NMR techniques permitted to study recently the insulator to metal transition induced by pressure in undoped half-filled systems, that is the actual Mott transition. This has been made possible by the recent discovery of quasi 2D organic and 3D alkali fulleride compounds, which display quasi ideal 2D or 3D Mott transitions.

Finally I should mention at this stage that I did not address here one important aspect of the NMR technique which takes advantage of nuclear quadrupole effects detected in NMR for nuclear spins with $I > 1/2$. Those quadrupole splittings of the NMR spectra usually permit to distinguish the charge environment of these nuclei. In correlated electronic solids this gives an access to charge differentiation on atomic sites or to charge density waves due to Fermi surface reconstruction when they do occur. This is also illustrated in Ref. [4] in the case of layered Na cobaltates or for the CDW which occurs well below the pseudogap T^* in underdoped cuprates [40]. The latter experiments have triggered new ideas about the origin of the pseudogap in the cuprates, but while the pseudogap T^* is generic, the CDW order and its symmetry appear somewhat dependent of the cuprate family. Therefore the charge order appears as a consequence of the pseudogap rather than its actual origin. An important tendency towards charge ordering situations has been proposed to dominate the ground state properties of correlated electron systems. Quadrupolar effects in NMR ideally permit to unravel such situations in great detail.

I shall conclude here that the description of some selected experimental cases given in this lecture permitted us to underline the importance of the NMR technique and to reveal altogether to the reader a wide range of novel phenomena specific to correlated-electron physics.

References

[1] H. Alloul: *Introduction to the physics of Electrons in Solids* (Graduate Texts in Physics, Springer, Heidelberg, 2011)

[2] A. Abragam: *The Principles of nuclear magnetism* (Clarendon Press, London, 1961)

[3] C.P. Slichter, *Principles of Magnetic Resonance* (Harper and Row, 1963 and Springer-Verlag, New York, 1989 (3rd ed.))

[4] H. Alloul: *NMR in strongly correlated materials*, Scholarpedia, 10(1):30632 (2015)

[5] W.D. Knight: *Magnetic Resonance and relaxation*, in Ed. R. Blinc, North Holland 311 (1967)

[6] K. Yosida, Phys. Rev. **110**, 769 (1956)

[7] H. Alloul, J. Supercond. Nov. Mag. **25**, 385 (2012)

[8] M.D. Daybell and W.A. Steyert, Rev. Mod. Phys. **40**, 380 (1968)

[9] H. Alloul, Phys. Rev. Lett. **35**, 460 (1975)

[10] K.G. Wilson, Rev. Mod. Phys. **47**, 773 (1975)

[11] M. Takigawa, A.P. Reyes, P.C. Hammel, J.D. Thompson, R.H. Heffner, Z. Fisk, and K.C. Ott, Phys. Rev. B **43**, 247 (1991)

[12] H. Alloul, P. Mendels, G. Collin and P. Monod, Phys. Rev. Lett. **61**, 746 (1988)

[13] F. Mila and M. Rice, Physica C **157**, 561 (1989)

[14] H. Alloul, T. Ohno and P. Mendels, Phys. Rev. Lett. **63**, 1700 (1989)

[15] J. Bobroff, H. Alloul, P. Mendels, V. Viallet, J.F. Marucco, and D. Colson, Phys. Rev. Lett. **78**, 3757 (1997)

[16] T. Timusk, and B. Statt, Rep. Prog. Phys. **62**, 61 (1999)

[17] F.C. Zhang and T.M. Rice, Phys. Rev. B **37**, 3759 (1988)

[18] H. Alloul, J. Bobroff, M. Gabay and P. Hirschfeld, Rev. Mod. Phys. **81**, 45 (2009)

[19] H. Alloul, P. Mendels, H. Casalta H., J.F. Marucco and J. Arabski, Phys. Rev. Lett. **67**, 3140 (1991)

[20] A.V. Mahajan, H. Alloul, G. Collin, and J.F. Marucco, Phys. Rev. Lett. **72**, 3100 (1994)

[21] J. Bobroff, A. Mac Farlane, H. Alloul, P. Mendels, N. Blanchard, G. Collin, and J.F. Marucco Phys. Rev. Lett. **83**, 4381 (1999)

[22] H. Alloul, *NMR studies of electronic properties of solids*, Scholarpedia, 9(9):32069 (2014)

[23] T. Moriya, Prog. Theor. Phys. **16**, 23 (1956)

[24] H. Alloul and L. Mihaly, Phys. Rev. Lett. **48**, 1420 (1982)

[25] M. Corti, F. Carbone, M. Filibian, Th. Jarlborg, A.A. Nugroho, and P. Carretta, Phys. Rev. B **75**, 115111 (2007)

[26] H. Alloul, A. Mahajan, H. Casalta and O. Klein, Phys. Rev. Lett. **70**, 1171 (1993)

[27] R.E. Walstedt: *The NMR probe of High Tc materials* Springer Tracts in Modern Physics, Vol. 228 (2008)

[28] A. Kaminski, T. Kondo, T. Takeuchi, and G. Gu, Phil. Mag., (2014)

[29] A.J. Millis, H. Monien, and D. Pines, Phys. Rev. B **42**, 167 (1990)

[30] V.J. Emery and S.A. Kivelson, Nature **374**, 434 (1995)

[31] P.W. Anderson, Science **235**, 1196–1198 (1987)

[32] D.E. Mac Laughlin: *Magnetic Resonance in the Superconducting state* Solid State Physics **31**, 1 (1976)

[33] P. Wzietek, T. Mito, H. Alloul, D. Pontiroli, M. Aramini and M. Riccò, Phys. Rev. Lett. **112**, 066401 (2014)

[34] L.C. Hebel and C.P. Slichter, Phys. Rev. **113**, 1504 (1957)

[35] M. Takigawa, P.C. Hammel, R.H. Heffner, Z. Fisk, K.C. Ott, and J.D. Thompson, Physica C **162-164**, 853 (1989)

[36] A.J. Leggett, Rev. Mod. Phys. **47**, 331 (1975)

[37] K. Ishida, H. Mukuda, Y. Kitaoka, K. Asayama, Z.Q. Mao, Y. Mori, and Y. Maeno, Nature **396**, 658 (1998)

[38] K. Asayama, G.-Q. Zheng, Y. Kitaoka, K. Ishida, and K. Fujiwara, Physica C **178**, 281 (1991)

[39] K. Ishida, H. Mukuda, Y. Kitaoka, Z.Q. Mao, Y. Mori, and Y. Maeno, Phys. Rev. Lett. **84**, 5387 (2000)

[40] T. Wu, H. Mayaffre, S. Kramer, M. Horvatic, C. Berthier, W.N. Hardy, R. Liang, D.A. Bonn, and M.-H. Julien, Nature **477**, 191 (2011)

14 Introduction to Scanning Tunneling Spectroscopy of Correlated Materials

Christian Hess
IFW Dresden
Helmholtzstraße 20, 01069 Dresden, Germany

Contents

E. Pavarini, E. Koch, J. van den Brink, and G. Sawatzky (eds.)
Quantum Materials: Experiments and Theory
Modeling and Simulation Vol. 6
Forschungszentrum Jülich, 2016, ISBN 978-3-95806-159-0
http://www.cond-mat.de/events/correl16

1 Introduction

During the last 15–20 years, scanning tunneling microscopy and spectroscopy (STM/STS) has developed into an indispensable experimental tool of modern condensed matter physics. This method provides real-space dependent spectroscopic information of a solid's surface at the atomic scale. It is thus capable to directly observe quantum mechanical effects, which in turn provide new insight into the properties of a solid, which includes, remarkably, even momentum-resolved information on electronic states.
The purpose of this lecture is to convey the main experimental concepts of STM/STS for the research on correlated materials. Thereby, it cannot and does not aim at comprehensively covering STM/STS work on all kinds of different material classes of correlated systems. The focus will be specifically on unconventional superconductors, which are, among the electronically correlated materials, the most prominent ones where STM/STS has been successfully used, providing new ground-breaking insights. After a more general introduction to the experiment itself, the lecture will first specifically address the unconventional superconductor LiFeAs, for which comprehensive STM/STS data of high quality exist and which is still a matter of ongoing research. This will be complemented by briefly summarizing fundamental work on cuprate superconductors. It can be expected readers who digest the thereby introduced techniques and concepts will be able to easily access other existing and future work on correlated materials with STM/STS.

2 Basics

2.1 Methods

We consider an atomically sharp metallic tip that is brought into close distance (a few Ångstroms) to the surface of a solid, i.e. the sample which we would like to investigate. In this situation, electrons tunnel from the tip to the sample and vice versa. If both are at the same electrochemical potential the net current will be zero. A finite net tunneling current will, however, arise when we apply an electrical bias voltage U_{bias} between the tip and the sample [1–3]

$$I = A|M|^2 N_0 \int_{-\infty}^{\infty} \rho_s(E)[f(E) - f(E - eU_{\mathrm{bias}})]\, dE\,, \tag{1}$$

with A a constant of proportionality, M the tunneling matrix element, and f the Fermi distribution function. N_0 and ρ_s are the density of states (DOS) of the tip and the local density of states (LDOS) of the sample at the position of the tip, respectively. Note that already in Eq. (1) significant approximations have been made which we will assume to be valid throughout this chapter unless stated otherwise: Both N_0 and $|M|^2$ are assumed to be energy independent, and thus can be written in front of the integral. Approximate energy independence can be achieved for the former by using an appropriate tip material. For the latter it is reasonably valid at small U_{bias} and for sufficiently simple electronic structure (see e.g. [4] for a more elaborate discussion).

It has been shown further – and this is crucial for the exploitation of the tunneling current for microscopy – that the tunneling matrix element decays exponentially with increasing distance d between the tip and the sample [2, 3], viz. $I \propto e^{-2\kappa d}$, where κ depends on the work functions of the sample and the tip. This means the well known exponentially decaying tunneling probability for one-dimensional electron tunneling depending on the width of the vacuum barrier is recovered. The other crucial finding from Eq. (1) is that, at temperature $T = 0$, the tunneling current I is proportional to the LDOS of the sample integrated between the Fermi level ϵ_F and $\epsilon_F + eU_{\rm bias}$. At finite temperature, this energy interval is, of course, broadened through the Fermi functions.

2.1.1 Scanning tunneling microscopy (STM)

In a scanning tunneling microscope, the relative position of the tunneling tip to the sample can be controlled in the three spatial dimensions x, y parallel and z perpendicular to the sample's surface, where nowadays a precision in the picometer range can be achieved (see e.g. [4, 5] for details on the technical realization). This opens up a plethora of possibilities for probing the surface of a sample. A fundamentally important measurement mode is scanning tunneling microscopy (STM), i.e., a high-resolution measurement of the surface topography. A very important way to do this (among others) is the so-called constant-current topography mode: The actuator for tip motion along the z-direction is connected to a feed-back loop that measures the tunneling current I and maintains it constant during scanning the tip in the (x, y)-plane by appropriately adjusting the z-position of the tip which regulates the distance d between tip and sample. Inspection of Eq. (1) tells us that the resulting data set $z(x, y)$ describes a plane of constant integrated LDOS of the sample (within ϵ_F and $\epsilon_F + eU_{\rm bias}$). Due to the very high lateral and vertical resolution in STM, it is possible to resolve even the atomic corrugation of a surface. Fig. 1 depicts representative data taken from 2H-$NbSe_2$. This compound exhibits a charge density wave (CDW) at low temperature, yielding a 3×3 superlattice [6]. The topographic STM data in Fig. 1 very clearly reveal this superstructure [8], which highlights that the STM is susceptible to the spatial modulations of the electronic LDOS (which in the present example is generated by the CDW). Further below, we shall see more examples of spatial modulations in the LDOS which can be detected in STM.

2.1.2 Scanning tunneling spectroscopy (STS)

Eq. (1) implies that through measuring the tunneling current as a function of $U_{\rm bias}$, the LDOS of the sample at a fixed position of the tip, i.e. $\rho_s(E)$ with $E = eU_{\rm bias}$, can be accessed. In the experiments, the differential conductance

$$\left.\frac{dI}{dU}\right|_{U=U_{\rm bias}} \propto \int_{-\infty}^{\infty} \rho_s(E) \left.\frac{\partial f(E-eU)}{\partial(eU)}\right|_{U=U_{\rm bias}} dE, \tag{2}$$

is evaluated, either by numerical derivation or by directly measuring it using a lock-in amplifier (see [4, 5] for details). Eq. (2) describes the convolution of ρ_s with the voltage derivative of the

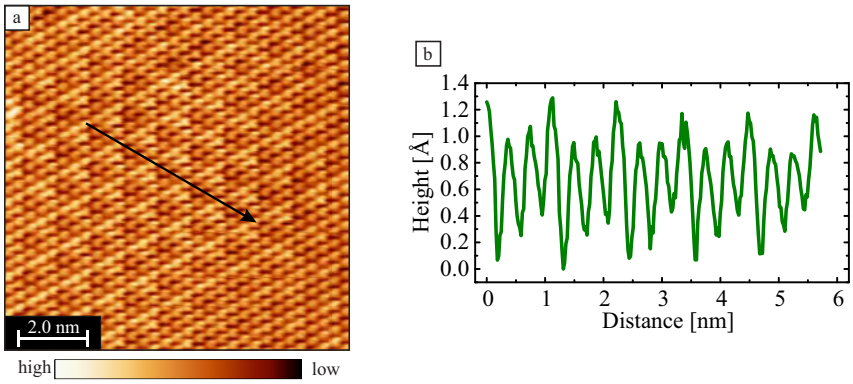

Fig. 1: *(a) Constant current topographic image of 2H-$NbSe_2$ in a field of view of* $10\ nm \times 10\ nm$*,* $U_{\rm bias} = -200$ *mV,* $I = 0.7$ *nA,* $T = 10$ *K. The topography shows the atomic corrugation of the topmost layer of Se atoms, and reveals the CDW with a periodicity of* $3a \times 3a$ *with the lattice constant* $a = 0.0345$ *nm [7]. (b) Line section taken along the arrow. Image and graph taken from [8].*

Fermi distribution function which is a bell-shaped curve centered around $U_{\rm bias}$ with a FWHM of about $3.5\, k_B T$. Thus, the spectroscopic resolution in energy ΔE is inevitably thermally broadened. Scanning tunneling spectroscopy (STS) with high energy resolution therefore requires measurements at very low temperatures. Typical values for ΔE at the cryogenically relevant temperatures 300 mK and 4.2 K are 90 μeV and 1.3 meV, respectively.

In a scanning tunneling microscope, spectroscopic measurements of the differential conductance dI/dU can be performed as a function of the spatial tip position, which provides the unique possibility to map out the energy dependent LDOS as a function of the (x, y) position. The resulting data for $\rho_s(E, x, y)$ are often false-color plotted in a two-dimensional fashion as a function of (x, y) at a fixed $E = eU_{\rm bias}$, a technique often called *Spectroscopic Imaging (SI-STM).* The resulting images provide valuable information about the energy dependence of the spatial modulations of the LDOS. Fig. 2 shows an example for the spatially dependent LDOS due to the CDW in 2H-$NbSe_2$ at two selected energies. The data reveal a much stronger impact of the CDW on the LDOS at $U_{\rm bias} = -100$ mV than at $U_{\rm bias} = +100$ mV [8].

One way to acquire the data is to measure dI/dU at a fixed $U_{\rm bias}$, while scanning a surface of interest as a function of (x, y). Here, a small modulation voltage $U_{\rm mod}$ is added to $U_{\rm bias}$, and $dI/dU|_{U_{\rm bias}}$ is measured directly with a lock-in amplifier. This method (sometimes called dI/dU*-imaging*) has the advantage that a spatially highly resolved dI/dU-map can be relatively quickly recorded together with a topographic map (in the order of minutes to a few hours), thus posing only moderate constraints on the stability of the used microscope. However, the data contain dI/dU information only for one specific energy E. Therefore, in order to acquire a much more comprehensive data set of $\rho_s(E, x, y)$ at a larger set of energy values, a different measurement protocol is used: The surface of interest is scanned topographically where the position of the tip is kept fixed (with feed-back loop switched off) at a grid of (x, y) positions, and at each of these positions the differential conductance is measured as a function of $U_{\rm bias}$. This technique typically yields a large and comprehensive data set which allows to visualize,

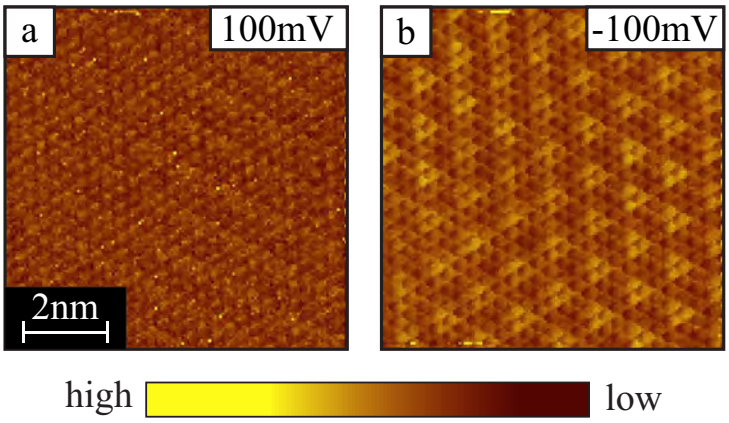

Fig. 2: 128×128 *spectroscopic* dI/dU *maps in a field of view of* $8\ nm \times 8\ nm$ *of 2H-NbSe*$_2$ *at stabilization conditions* $U_{\mathrm{bias}} = 200$ *mV,* $I = 0.7$ *nA,* $T = 10$ *K, RMS lock-in excitation* $U_{\mathrm{mod}} = 6$ *mV,* $t_{\mathrm{map}} = 16.5$ *h, spectra measured from 100 mV to* -100 *mV; (a)* dI/dU *spectroscopic map at 100 mV; (b)* dI/dU *spectroscopic map for* -100 *mV. The CDW pattern is hardly visible at 100 mV but clearly observable at* -100 *mV. The atomic structure is prominent at both voltages. Images taken from [8].*

e.g., the spatial dependence of $\rho_s(E, x, y)$ at deliberate E values. This is particularly important if the details of the energy dependence of the phenomenon under scrutiny are unknown, as is often the case for the case of correlated materials as well. The only drawback with respect to the dI/dU-imaging is the relatively long measurement duration of several days[1] for this often called *full-spectroscopy* mapping. Such long measurement times require perfect stability of the microscope with atomic fidelity during the whole measurement.

2.2 Quasiparticle interference

The screening of a point-like impurity in a metal results in an oscillating charge density as a function of distance from the impurity, known as Friedel oscillation [9]. The observation of such oscillations emerging from impurity atoms or atomic step edges [10, 11] has been one of the early groundbreaking discoveries of STM. Fig. 3 shows corresponding data for the Cu(111) surface, which possesses a two-dimensional surface state with a band minimum at about -0.44 meV [10] (see also Fig. 4c for the Fermi surface). The topography measurement in Fig. 3a very clearly reveals wave-like modulations of the integrated LDOS at the step edges, and in addition the signatures of point-like impurities on the terraces with radially emerging wave-like patterns. The latter can be observed even better in Fig. 4a. For modeling the energy-dependent modulation of the LDOS, typically a scattering scenario is invoked, where an electron is back-scattered at the step edge or the point-impurity, resulting in the wave interference of the incoming and the outgoing electrons, and thus a standing electronic wave pattern. For the step edges one finds [12, 10]

$$\rho_s(E, x) \propto \{1 - J_0[2q(E)x]\}, \tag{3}$$

[1] Simple math tells us that if a single full-spectroscopy dI/dU curve requires about 10 s measurement time, a spatially highly resolved data set at e.g. 256×256 pixels requires about 7.5 days of total measurement time.

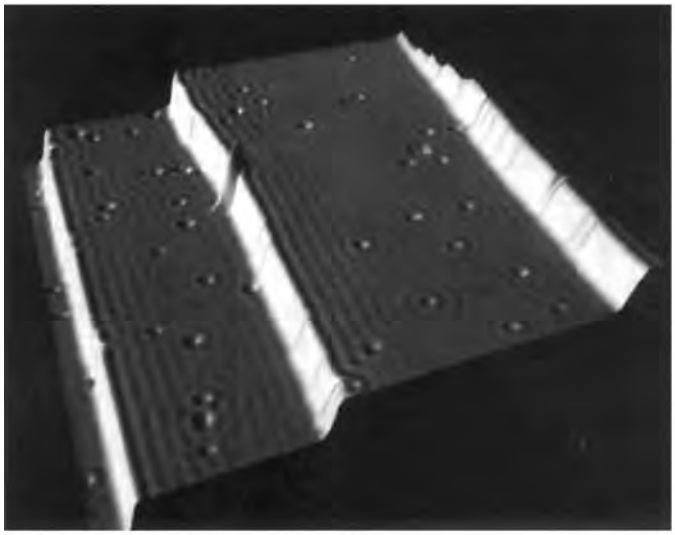

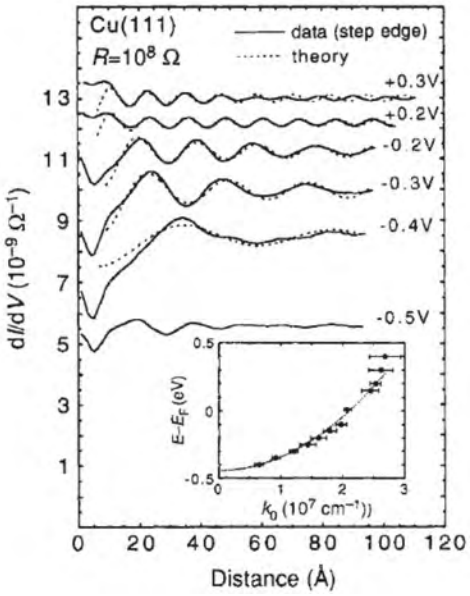

Fig. 3: *Left: constant-current* $500\ \text{Å} \times 500\ \text{Å}$ *image of the Cu(111) surface (*$U_{\text{bias}} = 0.1$ *V,* $I = 1.0$ *nA). Three monatomic steps and about 50 point defects are visible. Spatial oscillations with a periodicity of* ~ 15 *Å are clearly evident. The vertical scale has been greatly exaggerated to display the spatial oscillations more clearly. Right: Solid lines: spatial dependence of* dI/dU*, measured as a function of distance from step edge at different* U_{bias}*. Zero distance corresponds to the lower edge of the step. Dashed lines: theoretical fits of Eq.* (3) *to the data. Curves have been shifted vertically for viewing. Inset: experimental surface state dispersion, obtained from fits of Eq.* (3) *to the* dI/dU *linescan data. The dashed line is a parabolic fit used to extract the surface state effective mass and band edge. Figures taken from [10].*

with the energy E, the distance from the step edge x, and q the length of energy dependent wave vector of the modulation. J_0 is the zeroth-order Bessel function. For the point-like impurities the result is [12, 10]

$$\rho_s(E, r) \propto 1 + \frac{2}{\pi q r}\left[\cos^2\left(qr - \frac{\pi}{4} + \eta_0\right) - \cos^2\left(qr - \frac{\pi}{4}\right)\right], \tag{4}$$

where r is the radial distance from the impurity and η_0 a phase shift.
Fig. 3b shows $dI/dU|_{U_{\text{bias}}}$ measurements as a function of the distance x from the step edge at various energies $E = eU_{\text{bias}}$, which clearly reveals the energy dependence, i.e., the dispersion of the modulation, and very good fits according to Eq. (3). Since the length of the electron scattering wave vector q can therefore be related to the energy E, the 'band' dispersion $E'(q) = E(q) + \epsilon_F$ of the modulation can be determined (see inset of Fig. 3b). This dispersion has a close connection to the band structure of the surface state because q, as mentioned above, is the (elastic) scattering wave vector between two electronic states with opposite momenta $\pm k$, i.e. $q = 2k$. Petersen *et al.* [13] pointed out that a very natural way for determining the scattering wave vector from real-space data such as shown in Fig. 4a is to investigate the data's Fourier transform, shown in Fig. 4b. These data show a ring with a radius that equals twice the Fermi wave vector, i.e. $2k_F$. This reflects that the real-space data have been recorded at

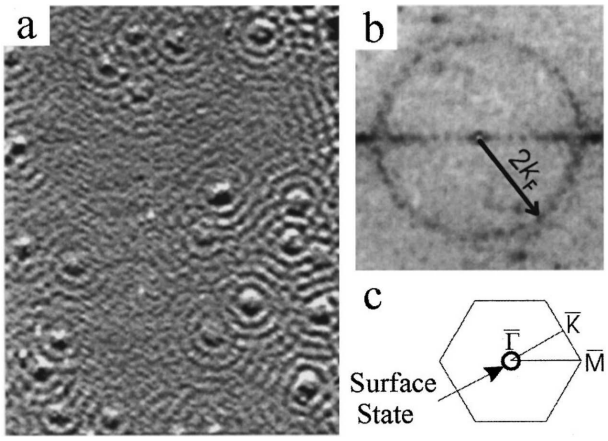

Fig. 4: *(a) Constant current STM image (425×550 Å^2) of Cu(111) obtained at $U_{\rm bias} = -5$ mV, $T = 150$ K, showing a complex pattern of circular waves extending out from point defects. (b) 2D Fourier transform of the image in (a). (c) Sketch of the surface Brillouin zone of Cu(111) with the Fermi contour.*

an energy $E = eU_{\rm bias}$ very close to the Fermi level. Of course, the spatial mapping of Friedel oscillations is in principle viable at other $U_{\rm bias}$. Furthermore, the Fourier analysis allows to extract not only the length but also the direction of the scattering wave vector $\mathbf{q}$, which becomes important when the Fermi surface, or more generally, the electronic constant energy contours (CEC) are not two-dimensional isotropic, in contrast to the case of the Cu(111) surface state. Thus, the investigation of the Friedel oscillations by means of STM/STS, which in connection to superconducting materials has been dubbed *Quasiparticle Interference* (QPI) [14], emerges as a viable route to experimentally obtain fundamental information about the electronic band structure, viz. the band dispersion of electronic states $\xi(\mathbf{k}) = E'(\mathbf{q})$ (with $\mathbf{q} = 2\mathbf{k}$), very much complementary to angular resolved photoemission spectroscopy (ARPES). The advantage of QPI measurements with respect to ARPES is that it allows to access also unoccupied electronic states. Its disadvantage is, however, that $\xi(\mathbf{k}) = E'(\mathbf{q})$ not necessarily holds if the scattering connects different CECs. We shall see examples for this complication further below.

3 Iron-based superconductors

In 2008, superconductivity has been discovered in a compound of the so-called iron pnictide family, viz. the materials $LaFeAsO_{1-x}F_x$ [15]. This has initiated a tremendous research effort which soon yielded a large variety of new superconducting iron pnictide compounds with T_c up to 55 K [16]. All compounds feature Fe_2As_2-layers as the common structural unit, with typical examples being RFeAsO (R=La or Rare Earth), AFe_2As_2 (A=alkaline earth or Eu), LiFeAs and FeSe, which commonly are referred to as '1111', '122', '111' and '11' compounds, respectively (note that Se replaces As in the last example). While the latter two compounds exhibit superconductivity already in their stoichiometric form, the parent materials RFeAsO and AFe_2As_2 are poor metals which exhibit an antiferromagnetic spin density wave (SDW) ground state. Chemical doping destabilizes this state in favor of superconductivity. The obvious proximity of

superconductivity and antiferromagnetism has lead to the conjecture that superconductivity is unconventional in these materials in the sense that spin fluctuations are the driving mechanism of superconductivity with a so-called $s_{\pm}$-wave order parameter [17].
STM/STS has been applied to the iron-based superconductors very rapidly after the discovery of superconductivity. In an initial phase, the experimental work focused on the '122'-, '1111'-, and '11'-phases, where these pioneering studies revealed very valuable information, including topographic investigations of the surfaces, the superconducting gap, vortices, and in few cases even QPI. An essential finding of that period is that for '122' and '1111' reliable STM/STS measurements are complicated by either the presence of surface states, as in '1111' [18, 19], or due to a non-trivial cleaving behavior and surface reconstruction in '122' [20]. A comprehensive review of all these works is given in Ref. [21]. The focus will be instead on one particular material, viz. LiFeAs, for which many of the mentioned difficulties are not an issue, rendering this compound paradigmatic.
Single crystals of LiFeAs exhibit clean, charge neutral cleaved surfaces [22–26] as we shall see below, with a bulk-like electronic structure at the surface [27]. LiFeAs is a *stoichiometric* superconductor, i.e., superconductivity occurs without any doping, at a relatively high critical temperature $T_c \approx 18$ K [28]. This renders it very different from the canonical '1111' and '122' iron-arsenide superconductors where the SDW instability is believed to be related to strong Fermi surface nesting. In the next sections we will discuss how STM/STS can contribute to revealing more details about the compound's electronic structure and the superconducting state.

3.1 Gap spectroscopy

Already long time before the invention of the scanning tunneling microscope [29], the pioneering work of Giaever [30, 31] and Rowell *et al.* [32] on electron tunneling through planar tunneling junctions with one or two superconducting electrodes provided fundamental insights into the nature of superconductivity. This concerns the revelation of both the gap in the quasiparticle tunneling spectrum [30, 31] as well as the signatures of the phonon density in the quasiparticle DOS of a conventional strong-coupling superconductor [32, 33], which have been understood as basic supporting evidence of the theories of Bardeen, Cooper and Schrieffer (BCS) [34] and Eliashberg [35], respectively, showing that the electron-phonon interaction is responsible for the Cooper pairing in conventional superconductors.
We give a brief reminder of some basic considerations of the superconducting state: According to BCS theory, the Bogoliubov quasiparticle bands E_k are connected to the normal state electronic bands ξ_k through $E_k^2 = \xi_k^2 + \Delta_k^2$, where Δ_k generally is a momentum dependent energy gap (see Fig. 5a for illustration). For simplicity, we neglect this momentum dependence, a situation which occurs in purely isotropic s-wave superconductors. If one performs tunneling spectroscopy on such a superconductor in the normal state (here always with a normal-state tip) one finds a linear dependence of the tunneling current I of the bias voltage $U_{\rm bias}$ (see Fig. 5b) if an idealized energy independent DOS as measured by dI/dU (see Fig. 5c) is present. In the superconducting state, however, the gap Δ opens. Hence, the quasiparticle DOS becomes zero

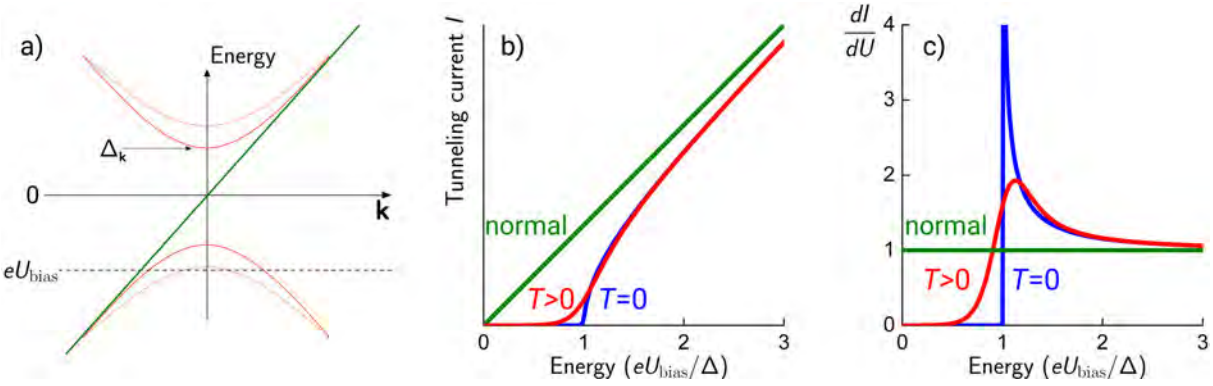

Fig. 5: *(a) Sketch of an electronic band ξ_k (green) and of Bogoliubov quasiparticle bands E_k (red). The dashed curve indicates Bogoliubov states at different momenta for the case of a momentum dependent gap. (b) and (c): Idealized tunneling current I and differential conductance dI/dU for the superconducting state at $T = 0$ (blue) and $T > 0$ (red) and in the normal state (green).*

at $eU_{\rm bias} < \Delta$ and is strongly enhanced at higher energy with a divergence towards $eU_{\rm bias} = \Delta$. In the tunneling experiment, this drastically changes I and dI/dU in the vicinity of Δ: since essentially no current flows up to Δ, it remains largely suppressed with respect to the normal state. Even more interesting is dI/dU, as it directly reflects the quasiparticle DOS, convoluted with the thermal broadening according to Eq. (2) (see Fig. 5c). This means that the differential conductance would reproduce the quasiparticle DOS only a $T \to 0$. In reality, there is of course always some inevitable finite thermal broadening, which enhances dI/dU at energies below the gap and broadens the divergence at Δ into a peak. The latter is usually referred to as *quasiparticle coherence peak*. Note, that the Bogoliubov quasiparticle states are particle-hole symmetric (as is indicated in Fig. 5a), i.e. one expects $dI/dU = -dI/dU$. Thus, the distance between the two coherence peaks in a tunneling spectrum provides convenient means to determine 2Δ.

In unconventional superconductors the situation is typically more complicated than sketched above. The superconducting order parameter could possess nodes as is the case for d-wave superconductors. Since the STS averages over all momenta, this results in a 'V'-shaped dI/dU spectrum as compared to the 'U'-shaped one of s-wave superconductors. This situation is, e.g., realized in cuprate superconductors. In iron-based superconductors, the Fermi surface is characterized by multiple pockets which are expected to possess differently sized and even anisotropic gaps. The tunneling spectrum should provide respective information, ideally by exhibiting multiple coherence peaks. Thus, STS on a superconductor with unknown order parameter structure can already provide crucial information on the order parameter symmetry.

The currently available data on LiFeAs [23, 24, 36] nicely illustrate the capabilities of STS. Fig. 6a shows an overview dI/dU spectrum [23] for $U_{\rm bias} = [-100\ {\rm mV}, 100\ {\rm mV}]$. The data immediately tell, that, apart from the superconducting gap near zero sample bias, the normal state DOS is far from being constant in energy as is assumed in the simplified conditions discussed above. The origin of the strong variation is not yet clarified for this compound. It is however reasonable to understand it as a consequence of the complicated band structure of the

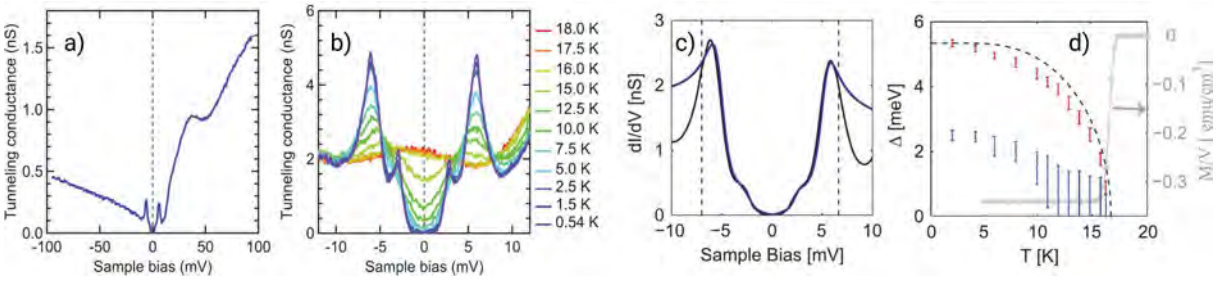

Fig. 6: *(a) Tunneling dI/dU spectrum of LiFeAs at 1.5 K in a large energy window. (b) Low-energy tunneling spectra at different temperatures. Two gaps are visible in the spectra and both gaps disappear above 18 K. Figures (a) and (b) are taken from [23]. (c) Two isotropic gaps fit (blue line) on top of measured dI/dU spectrum (black line, 2 K). The dashed lines indicate the fitting bias range from -6.8 to 6.8 mV. (d) The large gap determined by isotropic s-wave fits (red error bars) generally follows the temperature dependence predicted by the BCS weak coupling limit (dashed black line). The development of the smaller gap (blue error bars) is obscured by thermal broadening at elevated temperatures. The bulk T_c can be inferred from SQUID magnetometry data with a 1 G magnetic field (gray dots and right y axis). Figures (c) and (d) are taken from [24].*

material. Despite the strong apparent asymmetry, the tunneling data in the superconducting state (Fig. 6b) [23] is practically particle-hole symmetric at the lowest investigated temperature, as expected for the density of states of Bogoliubov quasiparticles. Interestingly, the data reveal two peaks on either polarity, one approximately at ± 6 mV, the other at about ± 3 mV. In view of the above considerations, these findings directly imply that at least two different predominant gap sizes are present in this material. Both gaps have no nodes, as revealed by the completely suppressed tunneling conductance dI/dU in a finite energy interval around zero bias voltage. This very clearly excludes d-wave type gaps to be relevant in this compound. STS can not reveal where in momentum space these gaps are located at. Further, complementary information from momentum sensitive techniques such as ARPES is indispensable to elucidate this question.

Before we come back to this point further below, it is interesting to investigate the temperature evolution of the dI/dU spectra. Upon increasing the temperature, the data in Fig. 6b show that the thermal broadening rapidly smears out the detailed gap features as already at $T \gtrsim 5$ K the signatures of the smaller gap have practically vanished. Chi *et al.* [24] nevertheless undertook the attempt to determine the temperature dependence of both gap features through fitting the spectra with an appropriate two-gap formula (Fig. 6c). The result shown in Fig. 6d suggests that the large gap follows a BCS-type temperature dependence with a gap closing at $T_c \approx 17$ K. However, such a statement is not possible for the smaller gap, obviously due to the thermal smearing.

Nag *et al.* have addressed the evolution of the differential conductance in the vicinity of T_c in more detail, by carefully studying spatially averaged dI/dU-spectra within a well-defined area as a function of temperature [36]. Fig. 7a depicts the averaged spectra for all temperatures which reveal an interesting and unexpected temperature evolution of superconductivity. At first glance, the data suggest the onset of superconductivity at $T_c = 16$ K, signalled by a clear depletion of the

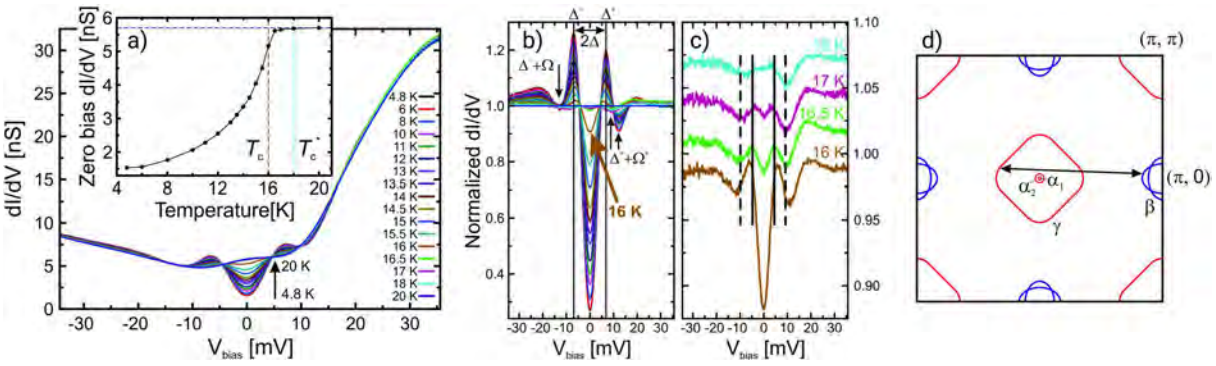

Fig. 7: *a) Temperature dependent tunneling spectra of LiFeAs measured between 6 K and 20 K. The up-arrow indicates the order of the curves at $U_{\rm bias}$ = 0 with increasing temperature. Inset: Zero bias differential conductance as a function of temperature. The horizontal dashed line is a guide to the eye. Vertical dashed lines indicate T_c and T_c^*, see text. b) Waterfall representation of the differential conductance dI/dU for various temperatures. The spectrum at 16 K is highlighted in bold. Black up-arrows indicate the shift of the position of the positive energy dip at $\Delta^+ + \Omega^+$ towards lower energy upon raising the temperature through $T_c = 16$ K. The down-arrow indicates the coarse position of the negative energy dip at $-\Delta^- - \Omega^-$. c) Waterfall representation of normalized spectra in c) at 16 K to 18 K. Superconducting coherence peaks and dip positions at 17 K are indicated by solid and dashed vertical lines, respectively. d) Schematic diagram of the first Brillouin zone (one-Fe unit cell) in LiFeAs based on ARPES data [37]. The indicated γ- and β- pockets possess only a weak k_z-dispersion while the α_1- and α_2-pockets are located only close to $k_z = \pi$. The back arrow indicates the incommensurate spin fluctuation between the γ- and the β-bands observed by Qureshi et al. [38–40]. Figures taken from [36].*

LDOS near zero bias voltage. However, closer inspection of dI/dU at zero bias voltage (inset of Fig. 7a), and in particular after normalizing the data with respect to the normal state (Fig. 7b and c) yields that even at higher temperature clear spectral features of superconductivity are present already at $T \lesssim 18$ K, i.e., a slightly reduced zero-bias dI/dU and particle-hole symmetric coherence peaks at $\Delta^{\pm}$ together with a pronounced dip at $eU_{\rm bias} = \Delta^{\pm} \pm \Omega^{\pm}$ followed by a hump. These features are clearly present at all temperatures $T \lesssim T_c^* = 18$ K, but concern at $T > 16$ K only a tiny portion of the LDOS. Nag *et al.* concluded from this observation that two distinct superconducting phases exist in this material: upon cooling one sets first in at $T_c^* = 18$ K, however being supported only by a very small portion of the Fermi surface, whereas full superconductivity, i.e., supported by all Fermi surface pockets, sets in at $T_c = 16$.

We have seen up to here that STS is capable to provide very comprehensive information about the superconducting gap even for a complicated material like LiFeAs which possesses multiple Fermi surface pockets. However, since STM/STS is (unless QPI is invoked) not momentum resolving, the further interpretation of the data requires the combination with, e.g., ARPES data. For LiFeAs, several high-resolution ARPES studies [41–43] consistently suggest a Fermi surface as sketched in Fig. 7d. It consists of quasi two-dimensional hole-like (labeled γ) and electron-like pockets (labeled β) centered around $\Gamma = (0,0)$ and $M = (\pm\pi, 0)$ or $(0, \pm\pi)$, respectively. Two further hole-like Fermi surface pockets (labeled α_1 and α_2) are centered

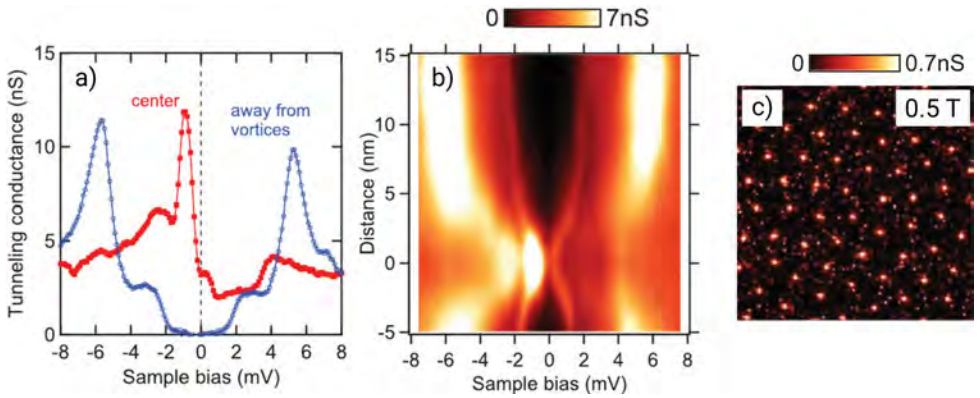

Fig. 8: *a) Tunneling spectra of LiFeAs taken at the center of vortex (red) and away from vortices (blue). b) Line profile of tunneling conductance across the vortex center along the nearest Fe-Fe direction. c) Image of vortices at 1.5 K obtained by mapping the tunneling conductance at* ϵ_F*. The tip was stabilized at* $U_{\rm bias} = +20$ *mV and* $I = 100$ *pA.* $U_{\rm mod} = 0.7$ $mV_{\rm rms}$*. Images taken from [23].*

around the Z-point. Since the latter are tiny, Nag *et al.* [36] concluded these to be natural candidates for supporting the faint superconductivity at $16\ {\rm K} < T < 18$ K. Interestingly, these pockets have been observed in ARPES to possess the largest superconducting gap $\Delta_\alpha \approx 6$ meV as compared to $\Delta_{\gamma,\beta} = 3.5$ to 4 meV at the γ- and β-pockets [42,43]. With this information the larger superconducting gap discussed for Fig. 6 can now be assigned to exactly the α-pockets, whereas the smaller gap is connected to either the γ- or the β-pockets, or both.

There is even more information provided by the dI/dU-spectra, viz. through the dip-hump structures at $eU_{\rm bias} = \Delta^{\pm} \pm \Omega^{\pm}$ in Fig. 7, the signatures of which are already apparent in the unnormalized spectra shown in Fig. 6b and c. These details have been much debated in terms of a bosonic mode of energy Ω that couples to the electrons and which should give rise to clear anomalies in the quasiparticle DOS [35,33]. Chi *et al.* suggested [24] an antiferromagnetic spin resonance as the nature of the bosonic mode. In contrast, Nag *et al.* pointed out [36] that this is not supported by the temperature independence of Ω, which in case of the dip being connected to an antiferromagnetic resonance should track the temperature dependence of order parameter, and the de facto absence of an antiferromagnetic resonance in inelastic neutron scattering results on LiFeAs [38,39]. It is interesting to note that recent theoretical work [44] suggested inelastic tunneling processes to play a very important role in the interpretation of the dip-hump feature.

3.1.1 Vortex spectroscopy

In the above considerations, the spatial dependence of the superconducting state did not play a role, i.e., the particular strength of STM/STS to spatially resolve electronic structure has not been exploited. This is in order as long as the material exhibits a spatially homogeneous superconducting state, which is often the case. A very obvious situation where the superconducting state is spatially inhomogeneous is the Shubnikov phase of a type-II superconductor, where magnetic flux lines (vortices) enter the superconducting volume. Each flux line holds one mag-

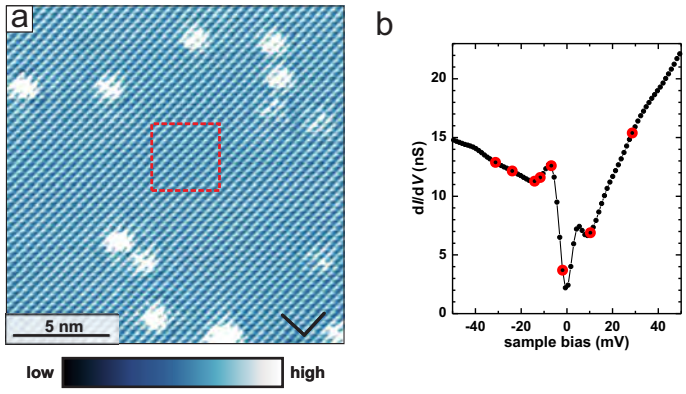

Fig. 9: *(a) Surface topography of LiFeAs measured in constant current mode ($I = 600$ pA, $V_{\mathrm{bias}} = -50$ mV) taken at $T \approx 5.8$ K. Black arrows indicate the direction of the lattice constants [28] with $a = 3.7914$ Å. (b) Spatially averaged tunneling spectrum taken in the square area (dashed lines) in (a). The spectrum exhibits a gap with $2\Delta \sim 10$ mV, which (taking thermal broadening into account) is consistent with low-temperature (~ 500 mK) tunneling data in Fig. 6 of the superconducting gap of LiFeAs. Representative energy values for further QPI analysis in Fig. 10 are marked by red circles. Figure taken from [22].*

netic flux quantum $\phi_0 = h/(2e)$. The magnetic field is maximum inside the vortex core and then radially decays on a length scale given by the London penetration depth λ_L. At the same time, the superconducting wave function decays from outside towards zero at the vortex core with the Ginzburg-Landau coherence length ξ_{GL} as the determining length scale. This has a strong impact on the LDOS measured at the vortex core, because it should be enhanced at energy values inside the superconducting gap with respect to the superconducting LDOS. This is indeed the case also for LiFeAs as is shown in Figure 8. Hanaguri *et al.* [23] report a complete suppression of the both sets of coherence peaks in favor of pronounced and asymmetric vortex core states inside the gap (Fig. 8a). Fig. 8b shows the spatial evolution of the spectrum along the Fe-Fe direction. In principle, one can expect interesting information about the nature of the superconducting order parameter from such spatial studies. However, it has been pointed out by Wang *et al.* [45] that it is *a priori* difficult to disentangle the effect of order parameter symmetry from anisotropy effects of the Fermi surface.

The enhanced LDOS at the vortex core leads to an enhanced value of the differential conductance dI/dU and thus can be used to visualize the structure of the vortex lattice as is exemplified in Fig. 8c. The investigation of such vortex matter is a separate field as such. The interested reader is referred to the original literature [23, 45] and references therein.

3.2 Quasiparticle interference

In the following we begin by largely following the first experimental paper on the QPI of LiFeAs [22]. Afterwards, we compare and discuss the earlier findings with more recent publications [26, 46, 47]. Prior to performing QPI measurements it is important to have a good account on the surface to be investigated which can be achieved by topographic STM mea-

surements. Fig. 9a shows a representative topography of the presumably Li-terminated surface taken at low-temperature (~ 5.8 K) after cleaving a crystal [22]. The data reveals a highly periodic atomically resolved surface layer and several impurity sites. A spatially averaged dI/dU spectrum, taken on a defect-free area clearly reveals a superconducting gap (Fig. 9b). Subsequently, a full-spectroscopic map was recorded on this surface as described before in section 2.1.2: STS was measured at each of the 256×256 pixel by stabilizing the tip with feedback loop engaged at a setpoint of $U_{\mathrm{bias}} = -50$ mV and $I = 600$ pA followed by subsequently ramping U_{bias} to $+50$ mV with the feedback loop switched off. During ramping the voltage $I(U_{\mathrm{bias}})$ and $dI/dU(U_{\mathrm{bias}})$ were recorded where a lock-in amplifier with a modulation voltage $U_{\mathrm{mod}} = 1.2$ mV (RMS) and a modulation frequency $f_{\mathrm{mod}} = 3.333$ kHz was used.

dI/dU maps at representative energies (Fig. 10a-h) show very clear QPI patterns which are most pronounced at energies in the vicinity of the coherence peaks at negative energy ($U_{\mathrm{bias}} \gtrsim -20$ mV). In this energy range, the QPI is clearly not only visible in real space as relatively strong modulations close to the defects but also appears as clear wave-like modulations (with a wavelength of a few lattice spacings) in the relatively large defect-free area in the center of the field of view. QPI patterns are also discernible at positive energy, but compared to the pronounced modulations at negative values, the amplitude of the modulations decay more rapidly when moving away from a defect.

In analogy to the previous example on the Cu(111) surface the real space data were Fourier-transformed in order to extract the wave vectors of the QPI at each of the measured energies. Figures 10i-p reveal a very rich structure which we discuss now in detail: The least interesting features of the data show at all energies bright spots at $(\pm\pi, \pm\pi)$ and at higher $\mathbf{q}$ (the choice of reciprocal coordinates refers to a one-iron unit cell). These result from the atomic corrugation in the real space images. The most salient feature is, however, a bright structure distributed around $\mathbf{q} = (0, 0)$. In similarity to the observed real-space modulations this feature is particularly pronounced at energies $U_{\mathrm{bias}} \approx [-20\ \mathrm{mV}, 0]$ where it attains a squarish shape with the corners pointing along the $(q_x, 0)$ and $(0, q_y)$ directions. Upon increasing U_{bias} to positive values, the intensity at the square corners increasingly fades and for $U_{\mathrm{bias}} > 10$ mV the squarish shape changes to an almost round structure which remains in that shape up to 50 mV. The Fourier transformed images also reveal further well resolved structures with significantly lower intensity centered around $(\pi/2, \pi/2)$, $(\pi, 0)$ and (π, π) which again are most pronounced between -20 mV and the Fermi level. At more negative bias, these finer structures fade, while at positive bias voltage they develop into a rather featureless diffuse background.

These rather complicated Fourier-transformed images directly account for the relevant scattering wave vectors in the QPI, and thus allow to deduce important qualitative information about the electronic structure of LiFeAs. However, one should stay extremely cautious when seeking the extraction of quasiparticle bands from the scattering image, as this is not straightforward, in contrast to one-band systems, such as the Cu(111) surface state. In order to illustrate this difficulty, we will now first show how the observed scattering vectors can clearly be assigned to particular scattering processes if other experimental data for the electronic band structure deduced from ARPES experiments [41] are taken into account. Afterwards, we will point out

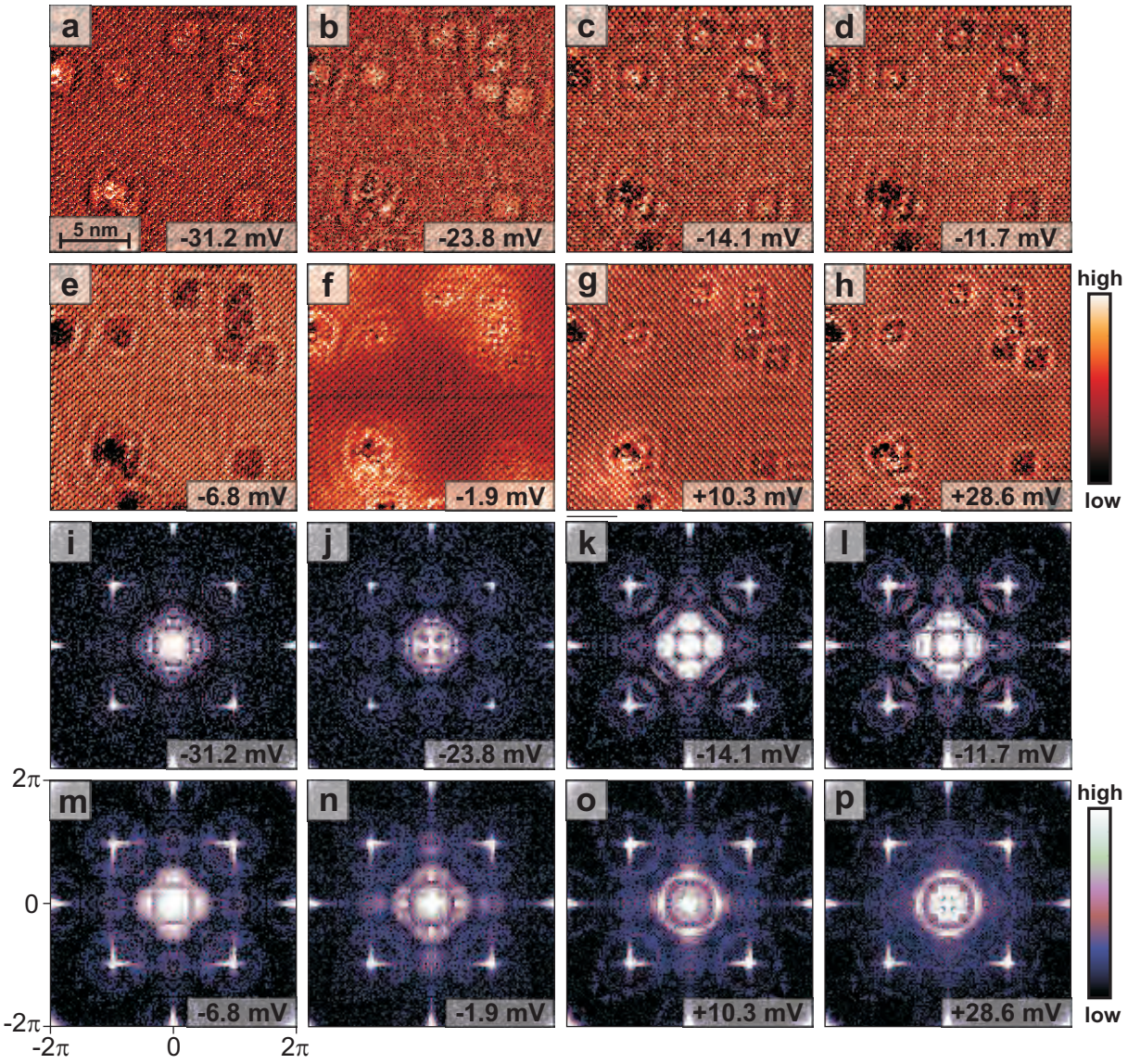

Fig. 10: *(a-h) SI-STM maps of the region shown in Fig. 9 at selected representative bias voltages. (i-p) Fourier transformed images of the maps shown in a-h. Bright spots at* $(\pm\pi, \pm\pi)$ *and at higher* $\mathbf{q}$ *result from the atomic corrugation in the real space images. Figure taken from [22].*

an alternative interpretation of the data [26], which, however, is not compatible with the compound's electronic structure.

Fig. 11a and b compare the CEC of LiFeAs at $E = -11.7$ mV derived from ARPES data [41] with the observed QPI intensities in the Fourier transformed image. Most prominent is that the observed central squarish structure in Figure 11b appears like a somewhat enlarged smeared replica of the large, hole-like CEC of the γ-band around $(0, 0)$. This observation can directly be understood as stemming from interband scattering processes ($\mathbf{q}_1$) connecting the very small CEC of the α-bands[2] and the larger squarish-shaped γ-CEC around $(0, 0)$. Furthermore, the much weaker structure at $\mathbf{q} = (\pi, 0)$ in Fig. 11b apparently can be rationalized as stemming

[2]For simplicity we do not distinguish between the α_1 and α_2-bands.

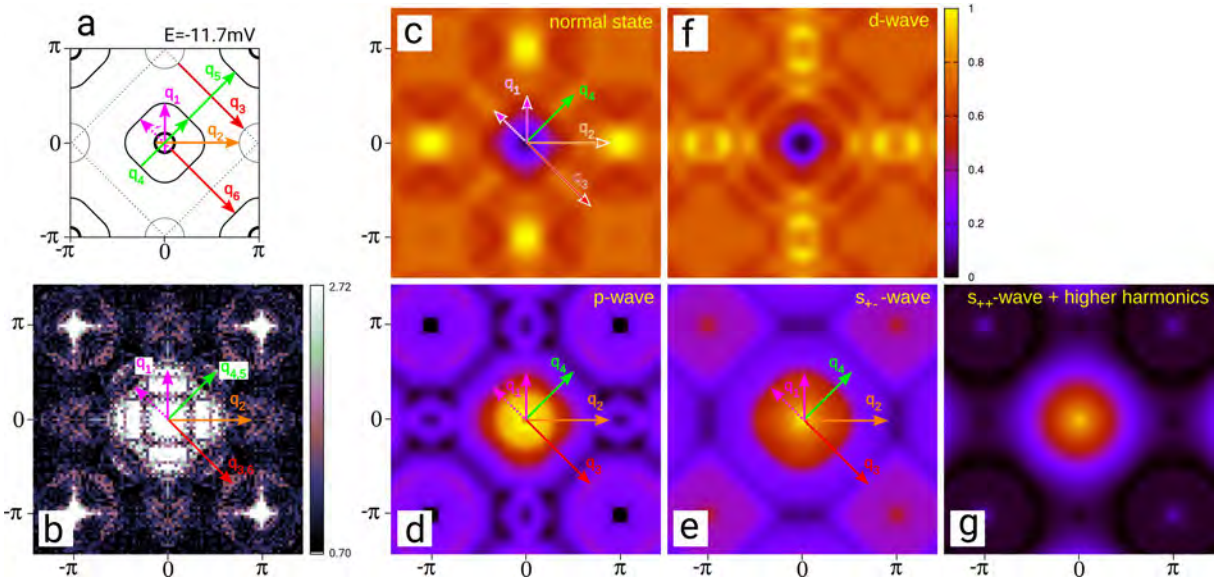

Fig. 11: *(a) Simplified CEC [41] at $E = -11.7$ meV in the periodic-zone scheme of the Brillouin Zone (BZ), where the first BZ (referring to the unit cell with two Fe atoms) is indicated by the dashed lines. However, the used coordinates in reciprocal space refer to the unit cell with one Fe atom, in order stay consistent with the theoretical work in Ref. [48]. This choice of reciprocal coordinates leads to Bragg-intensity at $(\pm\pi, \pm\pi)$ instead of $(\pm 2\pi, 0)$ (and $(0, \pm 2\pi)$) as one would expect for a two-Fe unit cell. The two pockets around $(0, 0)$ represent hole-like CEC while the pockets at the zone boundary are electron-like. $\mathbf{q}_{1,2}$ represent scattering processes which connect states on the small hole-like CEC and on other CEC, $\mathbf{q}_3$ and $\mathbf{q}_4$ represent scattering between the electron-like and within the large hole-like CEC, respectively. $\mathbf{q}_{5,6}$ represent umklapp processes. Note that each scattering process $\mathbf{q}_{1,\ldots,6}$ is described by a set of scattering vectors as is illustrated for $\mathbf{q}_1$ (dashed and solid arrows). (b) Measured Fourier transformed image at the same energy (the same as in Fig. 10l) with $\mathbf{q}_{1,\ldots,6}$ superimposed. The most salient QPI features around $(0, 0)$ and $(\pi, 0)$ match well with $\mathbf{q}_1$ and $\mathbf{q}_2$ (see text). The further observed but less prominent QPI intensities around (π, π) and at $(\pi/2, \pi/2)$ are well described by $\mathbf{q}_3$ and $\mathbf{q}_4$, respectively. The umklapp scattering vectors $\mathbf{q}_5$ and $\mathbf{q}_6$ might also be of relevance here. (c-g) Calculated QPI in $\mathbf{q}$ space assuming the normal state and a superconducting order parameter with $s_{\pm}$-, d-, p-, and s_{++} symmetry. Figure taken from [22].*

from interband scattering processes ($\mathbf{q}_2$) connecting the electron-like CEC of the β-bands with again the small α-CEC. The further observed but less prominent QPI intensities around (π, π) and at $(\pi/2, \pi/2)$ are well described by $\mathbf{q}_3$ and $\mathbf{q}_4$, respectively, which represent scattering between the electron-like β-CEC and within the large hole-like γ-CEC, respectively. $\mathbf{q}_{5,6}$ represent umklapp processes, which might also be of relevance here.

An analogous analysis can be performed at other energies. Fig. 12a and b show QPI data and a corresponding assignment to scattering processes for $E = -6.8$ meV [46], where the focus is just on small scattering vectors. Here, the contour of $\mathbf{q}_1$ in the QPI image is particularly sharp. The comparison between the QPI scattering image and the band structure can of course be undertaken on a much deeper level through comparing the experimental QPI image with calculations of the QPI pattern based on the electronic band structure of the compound. For

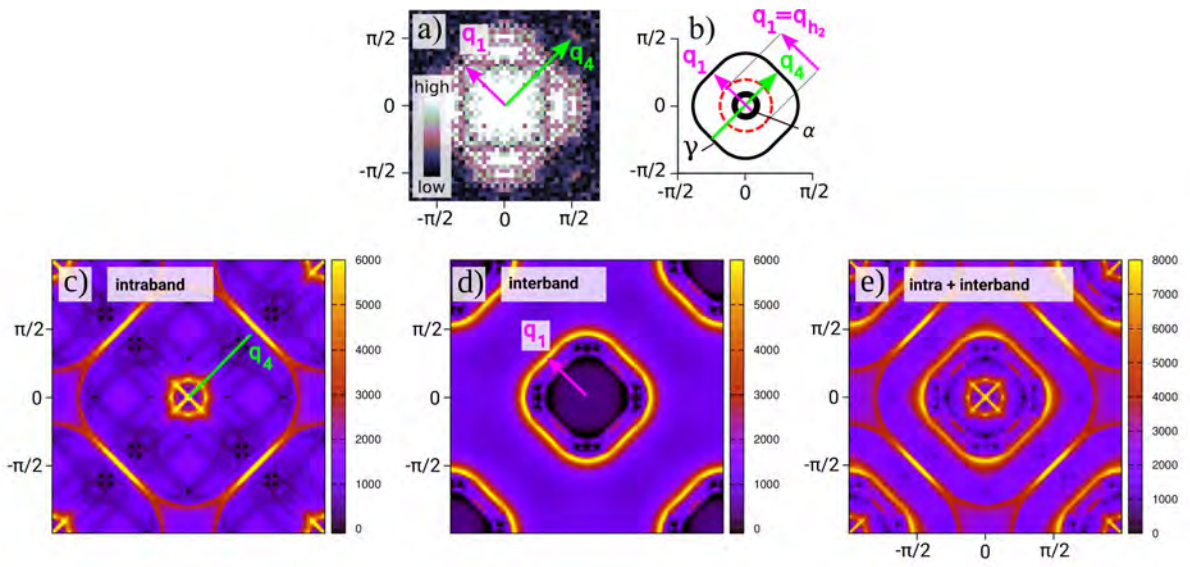

Fig. 12: *(a) Fourier transformed QPI data of LiFeAs at $E = -6.8$ meV ((the same as in Fig. 10m). (b) Simplified constant energy contours (CEC) of the hole-like α and γ bands at $E = -6.8$ meV. $\mathbf{q}_1$ represents interband scattering processes which connect states on both bands. It has the same length as $\mathbf{q}_{h_2}$ (i.e., the diameter of the dashed h_2-CEC) reported in Ref. [26]. $\mathbf{q}_4$ represents intraband scattering within the γ band. (c-e) Numerical simulation of the QPI patterns applied to a tight-binding model of the ARPES results [41, 43]. (c) Only intraband scattering within the small, hole-like band α and the large, hole-like band γ is considered. All scattering processes between α and γ and those processes involving the electron bands are suppressed in the calculation. (d) Only interband scattering between α and γ is considered. (e) Contributions displayed in panels (c) and (d) are summed up in order to enable the comparison of the intensities. The scattering vectors $\mathbf{q}_1$, $\mathbf{q}_4$ (see a, b) are indicated. Figures taken from [46].*

LiFeAs, high-precision band structure data exist. The corresponding theoretical results for the QPI are depicted in Fig. 12c to e, where intraband scattering processes within the γ-CEC (c) and interband scattering processes between the α-CEC and the γ-CEC (d) have been considered separately. Only when summed up (e), these account for the experimentally determined scattering image.

A different conclusion concerning the compatibility with ARPES is, however, reached by another QPI study on LiFeAs [26], despite geometrically very similar QPI data of excellent quality. The authors of this work attempted the very difficult task to reconstruct the band structure of LiFeAs solely based on QPI data. In order to circumvent the problem that QPI provides only access to elastic scattering vectors, i.e., the relative momentum difference of two different states at a given energy, they suggested that the QPI emerges solely from *intraband* scattering within the separate hole-like bands. Based on this assumption, the extracted scattering vectors have been used to construct three hole-band dispersions along high-symmetry directions. One of the resulting bands (labeled h_3 in Ref. [26]) is in good agreement with the size of the larger hole-like Fermi surface observed in ARPES [41,43,42], and another (h_1) matches quite well the α-bands. However, the third of the suggested bands (h_2) lacks such a correspondence since its

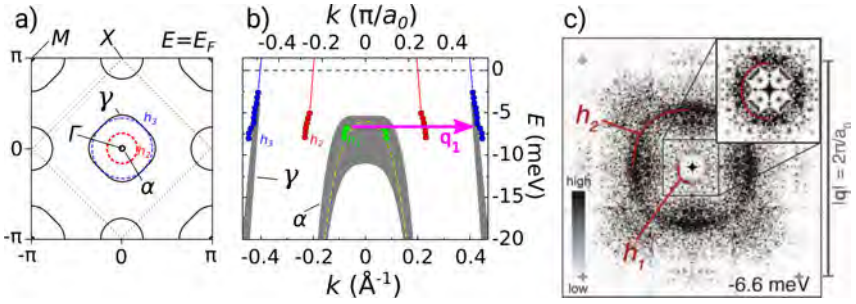

Fig. 13: *a) Schematic illustration of the Fermi surface (FS) sheets of LiFeAs. Solid lines illustrate the approximate size of the FS sheets as observed by ARPES [41, 49, 42, 43], dashed lines correspond to the hole-like FS resulting from the hole-like bands h_2 and h_3 as obtained from QPI by Allan et al. [26]. Note that Allan et al. extract the Fermi wave vectors along high-symmetry directions and that the shown FS sheets are respective isotropic two-dimensional extrapolations. The shown unfolded Brillouin zone (BZ) refers to the one-Fe unit cell. The BZ related to the two-Fe unit cell is indicated by dotted lines. b) LiFeAs band structure at negative energies. Circles represent the extracted quasiparticle dispersions E_k of the hole-like bands h_1, h_2, h_3 obtained in [26], where k is given by half of the length of the observed scattering vectors* $\mathbf{q}$*. Grey shaded contours represent α and γ bands as observed by ARPES [41, 49, 42, 43]. The extended width of the α band indicates k_z dependence obtained from different photon energies [43]. The indicated dispersion shown as a dashed line corresponds to data obtained at a photon energy $h\nu = 20$ eV. Figure taken from [46]. c) Fourier transformed QPI data of LiFeAs at $E = -6.6$ meV, taken from [26]. Note that the data refer to the two-Fe unit cell, in contrast to the data in Figures 10, 11, and 12 which causes a rotation of the coordinate system by 45°.*

Fermi wave vector $k_F \approx 0.2$ Å^{-1} [26] neither matches that of the large γ nor the small hole-like α Fermi surfaces observed in ARPES, see Fig. 13a.

Fig. 13b depicts the dispersion of all three bands h_1, h_2, and h_3. In fact, the QPI structure which has been used to extract the h_2 is geometrically very similar to the $\mathbf{q}_1$-contour in Figures 10 and 12, see the corresponding data in Figures 12 and 13. This means that the QPI intensity in Fig. 13, which has been interpreted to stem from *intraband* scattering of a hypothetical h_2 band which is unsupported by other methods like ARPES or de-Haas-van-Alphen measurements [50], can be well reinterpreted as *interband* scattering as described by $\mathbf{q}_1$ [46].

The latter example illustrates that QPI measurements can provide very valuable insights into a compound's electronic structure, in particular the electronic band structure. The caveat is, however, that QPI is not capable to provide direct information about quasiparticle states because it is only sensitive to the scattering states. Thus, one is advised to always complement QPI data with results from other techniques: ARPES and also de-Haas-van Alphen data are well suited for double checking the QPI results. On the other hand, the sensitivity to scattering events potentially brings about access to qualitatively new information which remains inaccessible by other means. We shall introduce some ideas in this respect in the following section.

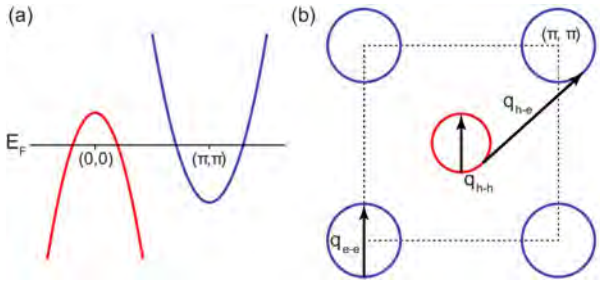

Scenario	$\mathbf{q}$ Suppressed Intensity	$\mathbf{q}$ Enhanced Intensity
nonmag. imp., s_{++}	$\mathbf{q}_{h-h}$, $\mathbf{q}_{e-e}$, $\mathbf{q}_{h-e}$	-
mag. imp., s_{++}	-	$\mathbf{q}_{h-h}$, $\mathbf{q}_{e-e}$, $\mathbf{q}_{h-e}$
nonmag. imp., $s_{\pm}$	$\mathbf{q}_{h-h}$, $\mathbf{q}_{e-e}$	$\mathbf{q}_{h-e}$
mag. imp., $s_{\pm}$	$\mathbf{q}_{h-e}$	$\mathbf{q}_{h-h}$, $\mathbf{q}_{e-e}$

Fig. 14: *(a) A simplified two-band model for the pnictides with a hole-like band centered at* $\mathbf{k} = (0,0)$ *and an electron-like band centered at* $\mathbf{k} = (\pi/a, \pi/a)$*. (b) The Fermi surfaces of the bands in (a). The vectors* $\mathbf{q}_{h\text{-}h}$ *and* $\mathbf{q}_{e\text{-}e}$ *show intraband scattering within the hole and electron pockets, respectively, while* $\mathbf{q}_{h\text{-}e}$ *shows interband scattering between the two. In the* $s_{\pm}$ *scenario* $\Delta_{\mathbf{k}}$ *switches sign between the initial and final states of the* $\mathbf{q}_{h\text{-}e}$ *scattering process, while it remains the same in the* s_{++} *scenario. Image taken from [47]. (c) A summary of the QPI selection rules expected for a pnictide superconductor with* s_{++} *or* $s_{\pm}$*. The QPI intensity of a scattering vector is either suppressed or enhanced inside the superconducting gap relative to the intensity outside the gap. The intensity variations stem from the energy dependence of the coherence factors. The four combinations of two pairing symmetries and two kinds of impurities result in four distinct sets of selection rules. Table taken from [47].*

3.2.1 Accessing the structure of the superconducting order parameter

In the superconducting state the DOS is redistributed by the opening of the superconducting gap. More specifically, in the superconducting state the DOS at energy-values close to the gap value is further boosted in comparison to the normal state since the quasiparticle dispersion $E_{\mathbf{k}} = \pm(\xi_{\mathbf{k}}^2 + |\Delta_{\mathbf{k}}|^2)^{1/2}$ is rather flat (see Fig. 5a). Furthermore, depending on the gap function $\Delta_{\mathbf{k}}$, particular scattering channels are suppressed while others are enhanced according to the coherence factors of the superconducting state. Consequently, the QPI measured at energies $|E|$ close to the averaged gap value will be redistributed, thereby containing detailed information about the structure of the superconducting order parameter. More specifically, the scattering rate between quasiparticle states with momenta $\mathbf{k}$ and $\mathbf{k}'$ is proportional to coherence factors $(u_{\mathbf{k}} u^*_{\mathbf{k}'} \mp v_{\mathbf{k}} v^*_{\mathbf{k}'})$, where the $\mp$ sign is determined by the magnetic/non-magnetic nature of the underlying scattering mechanism. The coherence factors are sensitive to the phase of the superconducting order parameter via the Bogoliubov coefficients $u_{\mathbf{k}}$ and $v_{\mathbf{k}}$ which fulfil the relation $v_{\mathbf{k}}/u_{\mathbf{k}} = (E_{\mathbf{k}} - \xi_{\mathbf{k}})/\Delta^*_{\mathbf{k}}$ with the quasiparticle energy $E_{\mathbf{k}} = \pm(\xi_{\mathbf{k}}^2 + |\Delta_{\mathbf{k}}|^2)^{1/2}$ [34, 51]. Thus, through the coherence factors, the QPI pattern is in principle decisively influenced by the nature of superconductivity, in particular the symmetry of the superconducting gap. Pioneering studies which involve the analysis of QPI data along these lines have been performed on cuprate high-temperature superconductors [52] and, more recently, also for iron-based superconductors [53]. Here, we summarize briefly the currently available results for LiFeAs.

In order to exploit the phase sensitivity of the QPI, Hänke *et al.* [22] calculated the QPI in the superconducting state using an appropriate BCS model for LiFeAs which can describe three cases of elementary singlet pairing (s_{++}, $s_{\pm}$, and d-wave) as well as a p-wave triplet pairing scenario. These calculations were based on a band structure model matching the ARPES results [41] (see

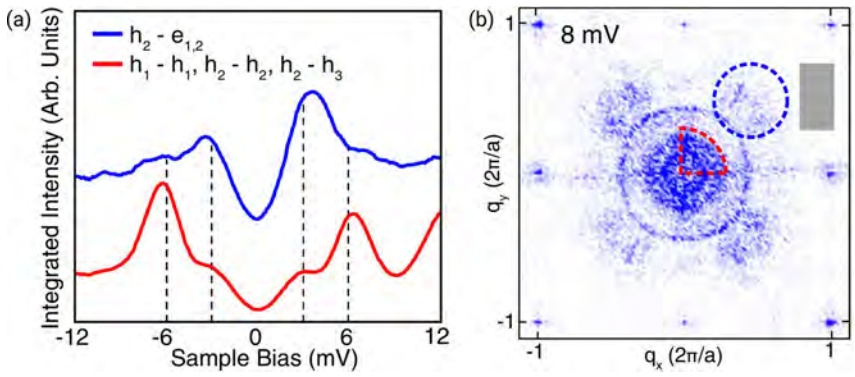

Fig. 15: *(a) The integrated intensity of the QPI signal for the intraband h-h (red) and interband h-e (blue) scattering vectors. The curves are normalized to the value at 12 meV and the interband intensity has been offset for clarity. The dashed lines indicate the values of the superconducting gaps. (b) The red sector and blue circle are the integration windows for intraband h-h and interband h-e scattering intensities in (a), respectively. A noise background signal is integrated in the grey rectangular area and subtracted. Here the windows are shown in one quarter for simplicity but the integration is performed over the equivalent areas in all four quadrants of the image. Image taken from [47].*

Fig. 11c-g for results at $E = -11.7$ mV).[3] One firm qualitative outcome of these calculations was, from the location of the high intensity region around $(0, 0)$, that in the superconducting state the dominating scattering processes are those which connect states on the hole-like bands as it was afore inferred from the mere geometrical analysis shown in Fig. 11(a), (b). The closer examination of the individual QPI patterns revealed a very strong dependence of the pattern on the assumed pairing symmetry. Interestingly, a direct comparison with the experimental result yielded a striking agreement between the experimentally observed QPI and the calculated image of Fig. 11(f), which is the result for a triplet paired state. The agreement is obviously much less pronounced for $s_{\pm}$, s_{++}, and d-wave singlet pairing cases. These qualitative statements also hold at other energies (see [22] for details).

Chi *et al.* come to a different result based on their data [47]. Based on the coherence factor analysis, they derive a set of selection rules which describe the expected enhancement and the suppression of particular scattering vectors upon tuning the energy from values outside to inside the superconducting gap depending on the type of scattering impurity and on the symmetry of the superconducting order parameter, see Fig. 14.

For the analysis, Chi *et al.* introduced to integrate with the scattering data the QPI intensity which belongs to a specific scattering process, i.e., either to intraband scattering h-h within the hole-like CEC or to interband scattering between hole and electron-like CEC h-e. From the very different energy dependence of the integrated QPI intensity for the two regions and the selection rules they conclude a support of a $s_{\pm}$-wave order parameter, see Fig. 15 and [47] for details.

[3] The experimentally observed strong intensity at $\mathbf{q} \sim (0, 0)$ reflects a constant background in the SI-STM maps which is not taken into account in the calculations. Thus there is no enhanced intensity in the calculated Fourier transformed images at $(0, 0)$.

It is worth pointing out that these unsatisfactory conflicting results [22, 47] provide the motivation for ongoing research. Hirschfeld *et al.* have theoretically addressed this problem [54] and suggested to use the temperature dependence of momentum-integrated QPI data in order to give a firm statement on the superconducting gap structure. Experimentally, this is, however, still open.

4 Cuprate superconductors

There exists vast literature which provides excellent introduction to the physics of the cuprate superconductors, see e.g. [55]. What we need to know here is that the electronic phase diagram of hole-doped cuprates has much resemblance to that of the canonical 122 or 1111 iron-based superconductors. One important difference is that the undoped parent state is an antiferromagnetic (charge transfer) insulator. Charge-doping causes its destruction and the emergence of superconductivity with the highest critical temperature T_c known so far (up to $\sim$ 135 K) for ambient pressure conditions [55]. The hole-like Fermi surface consists only of one band (which renders the situation in QPI investigations much simpler as compared to the iron-based superconductors), with a d-wave order parameter in the superconducting state with nodes on the Fermi surface along the $(\pm\pi, \pm\pi)$ directions.

4.1 Quasiparticle interference and the octet-model

In fact, the modern investigation of QPI analysis has first been introduced in pioneering work on the cuprate superconductors [14, 56, 57]. Fig. 16 shows representative experimental data for the material $Bi_2Sr_2CaCu_2O_{8+\delta}$ [56]. The topographic data in Fig. 16a reveal the characteristic BiO-terminated surface of $Bi_2Sr_2CaCu_2O_{8+\delta}$ which exhibits a stripe-like periodic superstructure. Full dI/dU spectroscopic mapping of the same field of view reveals pronounced QPI signatures; representative real space and Fourier transformed data are shown in Figures 16b and (c-f), respectively. The latter reveal multiple high-intensity spots which possess a clear energy dispersion. It has been proposed by McElroy *et al.* [56] that these spots result from quasiparticle scattering between eight specific points in momentum space which emerge in the superconducting state. The situation is illustrated in Fig. 16g which shows 'banana'-shaped quasiparticle CEC which emerge at energies smaller than the maximum $|\Delta_{\mathbf{k}}|$ in the superconducting d-wave state. McElroy *et al.* argued [56] that since the quasiparticle DOS ρ_s at a given energy $E_{\mathbf{k}} = \omega$ is proportional to

$$\int_{E_{\mathbf{k}}=\omega} |\nabla_k E_{\mathbf{k}}|^{-1} \, dk, \tag{5}$$

the primary contributions to $\rho_s(\omega)$ stem from the two tips of the 'banana' where $|\nabla_k E_{\mathbf{k}}|^{-1}$ is largest, and thus the QPI should be dominated by the seven scattering vectors $\mathbf{q}_{1...7}$ which connect the eight 'banana' tips (see Fig. 16g and h). This model has proven to describe the

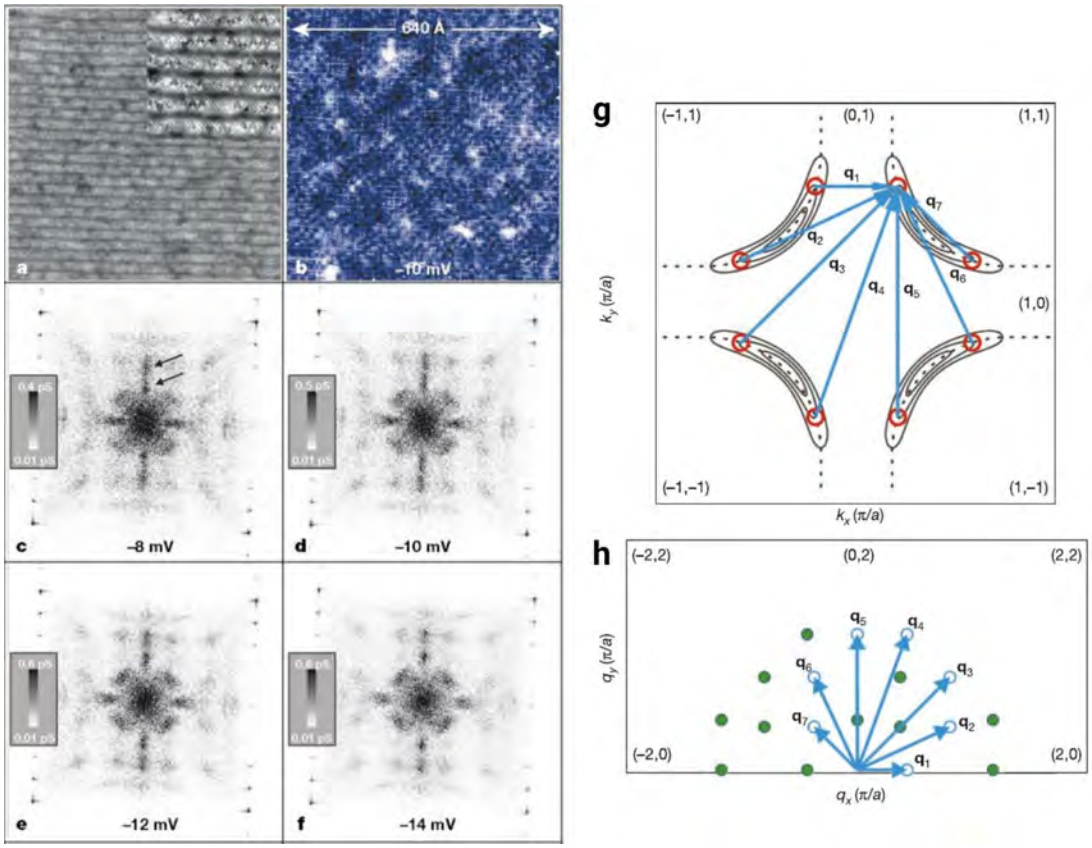

Fig. 16: *Atomic resolution images of the LDOS of $Bi_2Sr_2CaCu_2O_{8+\delta}$ and the resulting Fourier-space images of the wave vectors making up the LDOS modulations. (a) A topographic image of the BiO surface used, with location and resolution identical to the LDOS maps. The $\times 2$ magnification inset (from part of the same image) demonstrates the atomic resolution achieved. (b) Representative example of the real space $g(\mathbf{r}, E) = dI/dU|_{E=eU_{\rm bias}}$ in this field of view. All $g(\mathbf{r}, E)$ were acquired using the same atomic resolution and register. (c-f) Examples of the Fourier transformed $g(\mathbf{q}, E)$. The only non-dispersive signals (which are due to the supermodulation) are marked by arrows in (c). The reciprocal atomic lattice is located at the square of intense points near the corners of each panel. One can readily see 12 of the 16 LDOS modulations of the quasiparticle interference model. The dispersion and evolution of all the wave vectors of these modulations is evident in the differences between frames. (g, h) The expected wave vectors of quasiparticle interference patterns in a cuprate superconductor with d-wave order parameter. (g) Solid lines indicate the $\mathbf{k}$-space locations of several banana-shaped quasiparticle CEC as they increase in size with increasing energy. As an example, at a specific energy, the octet of regions of high $|\nabla_{\mathbf{k}} E_{\mathbf{k}}|^{-1}$ are shown as red circles. The seven primary scattering $\mathbf{q}$-vectors interconnecting elements of the octet are shown in blue. (h) Each individual scattering $\mathbf{q}$-vector from this set of seven is shown as a blue arrow originating from the origin in $\mathbf{q}$-space, and ending at a point given by a blue circle. The end points of all other inequivalent $\mathbf{q}$-vectors of the octet model (as determined by mirroring each of the original seven in the symmetry planes of the Brillouin zone) are shown as solid green circles. Thus, if the quasiparticle interference model is correct, there would be sixteen inequivalent local maxima in the inequivalent half of $\mathbf{q}$-space detectable by Fourier transformed STS. Images taken from [56].*

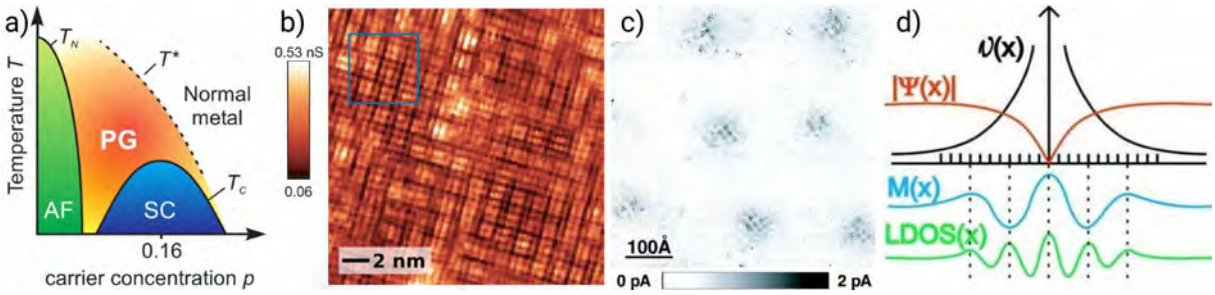

Fig. 17: *a) Schematic electronic phase diagram of the cuprates showing the antiferromagnetic parent phase (AF), the superconducting phase (SC) and the pseudogap-phase (PG). Image taken from [58]. b) Spectroscopic map of $Ca_{1.9}Na_{0.1}CuO_2Cl_2$ at $E = 24$ meV in the superconducting state. Image taken from [59]. c) Magnetic-field induced additional LDOS at magnetic vortex cores of $Bi_2Sr_2CaCu_2O_{8+\delta}$. d) A schematic model of the electronic/magnetic structure of the vortex core showing the superfluid velocity v, the superconducting order parameter $|\Psi|$, LDOS, and the anticipated periodicity of the spin density modulation M. Images taken from [60].*

QPI in a compelling way and referring to the eight momentum space points has been dubbed 'octet-model'.
Hanaguri *et al.* [52] extended the octet model by adding, for the first time, a coherence factor analysis which has been ground-breaking for all later experimental and theoretical work in this direction.

4.2 Nanoscale electronic order

In the cuprates, the emergence of superconductivity from the antiferromagnetic parent state is accompanied by the so-called pseudogap phase (see Fig. 17a). Evidence is growing that electronic order within the pseudogap phase is a crucial bit for understanding the electronic phase diagram of the cuprates and eventually the nature of superconductivity in these compounds [61, 62]. The correlation lengths of the electronic order often are relatively short which renders it challenging to be detected by neutron or X-ray diffraction techniques. Spectroscopic imaging STM, as local probe, therefore played an important role to reveal the electronic ordering states in the cuprates. In the experiments the electronic order manifests as CDW-like electronic superstructures, see, e.g., data by Hanaguri *et al.* [59] in Fig. 17b. These states seem to compete with superconductivity, as their amplitude is enhanced when superconductivity is suppressed, e.g., in the core of a magnetic vortex [60] (see Fig. 17c and d.)

5 Conclusion

In this lecture we have seen which possibilities a low-temperature scanning tunneling microscope offers to investigate the physics of correlated electron systems. This included an introduction to the most important measurement modes for microscopy and spectroscopy and the concept of studying the quasiparticle interference for achieving even momentum space information from real space data. The system which we focused on, LiFeAs, offers the advantage

that clean experimental data exist that allow to discuss many different aspects of scanning tunneling spectroscopy and the different types of information that can be gained. Further aspects of scanning tunneling spectroscopy of correlated materials were introduced through briefly discussing important work on cuprate superconductors. Thus, this lecture, together with the given literature, should provide the necessary basis for understanding the work on different systems such as the heavy fermion systems or non-superconducting transition-metal compounds.
It should be noted that the electronic ordering states which are ubiquitous in correlated electron systems in principle are expected to be accompanied by a spin density wave, as is indicated in Fig. 17d. This magnetic superstructure has not yet been observed by STM/STS because this techniques *a priori* is not sensitive to magnetism. This changes, however, if a magnetic tunneling tip is used, a technique which has been explored and brought into maturity for non- or weakly correlated systems [63]. The experimental efforts to apply this spin-polarized scanning tunneling microscopy (SP-STM) to correlated electron systems have just started, yielding first exciting results [64]. One may stay tuned.

References

[1] J. Bardeen, Phys. Rev. Lett. **6**, 57 (1961)

[2] J. Tersoff and D.R. Hamann, Phys. Rev. Lett. **50**, 1998 (1983)

[3] J. Tersoff and D.R. Hamann, Phys. Rev. B **31**, 805 (1985)

[4] J.A. Strocio and W.J. Kaiser (Eds.): *Scanning Tunneling Microscopy* (Academic Press, Inc., 1993)

[5] R. Wiesendanger: *Scanning Probe Microscopy and Spectroscopy Methods and Applications* (Cambridge University Press, 1994)

[6] D.E. Moncton, J.D. Axe, and F.J. DiSalvo, Phys. Rev. Lett. **34**, 734 (1975)

[7] B.E. Brown and D.J. Beerntsen, Acta Crystallographica **18**, 31 (1965)

[8] R. Schlegel, T. Hänke, D. Baumann, M. Kaiser, P.K. Nag, R. Voigtländer, D. Lindackers, B. Büchner, and C. Hess, Review of Scientific Instruments **85**, 013706 (2014)

[9] J. Ziman: *Principles of the Theory of Solids* (Cambridge University Press, 1972)

[10] M.F. Crommie, C.P. Lutz, and D.M. Eigler, Nature **363**, 524 (1993)

[11] Y. Hasegawa and P. Avouris, Phys. Rev. Lett. **71**, 1071 (1993)

[12] P. Avouris, I. Lyo, R.E. Walkup, and Y. Hasegawa, Journal of Vacuum Science & Technology B **12**, 1447 (1994)

[13] L. Petersen, P.T. Sprunger, P. Hofmann, E. Lægsgaard, B.G. Briner, M. Doering, H.-P. Rust, A.M. Bradshaw, F. Besenbacher, and E.W. Plummer, Phys. Rev. B **57**, R6858 (1998)

[14] J.E. Hoffman, K. McElroy, D.-H. Lee, K.M. Lang, H. Eisaki, S. Uchida, and J.C. Davis, Science **297**, 1148 (2002)

[15] Y. Kamihara, T. Watanabe, M. Hirano, and H. Hosono, J. Am. Chem. Soc. **130**, 3296 (2008)

[16] D.C. Johnston, Advances in Physics **59**, 803 (2010)

[17] I.I. Mazin, D.J. Singh, M.D. Johannes, and M.H. Du, Phys. Rev. Lett. **101**, 057003 (2008)

[18] H. Eschrig, A. Lankau, and K. Koepernik, Phys. Rev. B **81**, 155447 (2010)

[19] X. Zhou, C. Ye, P. Cai, X. Wang, X. Chen, and Y. Wang, Phys. Rev. Lett. **106**, 087001 (2011)

[20] F. Massee, S. de Jong, Y. Huang, J. Kaas, E. van Heumen, J.B. Goedkoop, and M.S. Golden, Phys. Rev. B **80**, 140507 (2009)

[21] J.E. Hoffman, Reports on Progress in Physics **74**, 124513 (2011)

[22] T. Hänke, S. Sykora, R. Schlegel, D. Baumann, L. Harnagea, S. Wurmehl, M. Daghofer, B. Büchner, J. van den Brink, and C. Hess, Phys. Rev. Lett. **108**, 127001 (2012)

[23] T. Hanaguri, K. Kitagawa, K. Matsubayashi, Y. Mazaki, Y. Uwatoko, and H. Takagi, Phys. Rev. B **85**, 214505 (2012)

[24] S. Chi, S. Grothe, R. Liang, P. Dosanjh, W.N. Hardy, S.A. Burke, D.A. Bonn, and Y. Pennec, Phys. Rev. Lett. **109**, 087002 (2012)

[25] S. Grothe, S. Chi, P. Dosanjh, R. Liang, W.N. Hardy, S.A. Burke, D.A. Bonn, and Y. Pennec, Phys. Rev. B **86**, 174503 (2012)

[26] M.P. Allan, A.W. Rost, A.P. Mackenzie, Y. Xie, J.C. Davis, K. Kihou, C.H. Lee, A. Iyo, H. Eisaki, and T.-M. Chuang, Science **336**, 563 (2012)

[27] A. Lankau, K. Koepernik, S. Borisenko, V. Zabolotnyy, B. Büchner, J. van den Brink, and H. Eschrig, Phys. Rev. B **82**, 184518 (2010)

[28] J.H. Tapp, Z. Tang, B. Lv, K. Sasmal, B. Lorenz, P.C.W. Chu, and A.M. Guloy, Phys. Rev. B **78**, 060505 (2008)

[29] G. Binnig, H. Rohrer, C. Gerber, and E. Weibel, Phys. Rev. Lett. **49**, 57 (1982)

[30] I. Giaever, Phys. Rev. Lett. **5**, 147 (1960)

[31] I. Giaever, Phys. Rev. Lett. **5**, 464 (1960)

[32] J.M. Rowell, P.W. Anderson, and D.E. Thomas, Phys. Rev. Lett. **10**, 334 (1963)

[33] D.J. Scalapino, J.R. Schrieffer, and J.W. Wilkins, Phys. Rev. **148**, 263 (1966)

[34] J. Bardeen, L.N. Cooper, and J.R. Schrieffer, Phys. Rev. **108**, 1175 (1957)

[35] G.M. Eliashberg, JETP **11** (1960)

[36] P.K. Nag, R. Schlegel, D. Baumann, H.-J. Grafe, R. Beck, S. Wurmehl, B. Büchner, and C. Hess, Scientific Reports **6**, 27926 (2016)

[37] Y. Wang, A. Kreisel, V.B. Zabolotnyy, S.V. Borisenko, B. Büchner, T.A. Maier, P.J. Hirschfeld, and D.J. Scalapino, Phys. Rev. B **88**, 174516 (2013)

[38] N. Qureshi, P. Steffens, Y. Drees, A.C. Komarek, D. Lamago, Y. Sidis, L. Harnagea, H.-J. Grafe, S. Wurmehl, B. Büchner, and M. Braden, Phys. Rev. Lett. **108**, 117001 (2012)

[39] N. Qureshi, P. Steffens, D. Lamago, Y. Sidis, O. Sobolev, R.A. Ewings, L. Harnagea, S. Wurmehl, B. Büchner, and M. Braden, Phys. Rev. B **90**, 144503 (2014)

[40] J. Knolle, V.B. Zabolotnyy, I. Eremin, S.V. Borisenko, N. Qureshi, M. Braden, D.V. Evtushinsky, T.K. Kim, A.A. Kordyuk, S. Sykora, C. Hess, I.V. Morozov, S. Wurmehl, R. Moessner, and B. Büchner, Phys. Rev. B **86**, 174519 (2012)

[41] S.V. Borisenko, V.B. Zabolotnyy, D.V. Evtushinsky, T.K. Kim, I.V. Morozov, A.N. Yaresko, A.A. Kordyuk, G. Behr, A. Vasiliev, R. Follath, and B. Büchner, Phys. Rev. Lett. **105**, 067002 (2010)

[42] K. Umezawa, Y. Li, H. Miao, K. Nakayama, Z.-H. Liu, P. Richard, T. Sato, J.B. He, D.-M. Wang, G.F. Chen, H. Ding, T. Takahashi, and S.-C. Wang, Phys. Rev. Lett. **108**, 037002 (2012)

[43] S.V. Borisenko, V.B. Zabolotnyy, A.A. Kordyuk, D.V. Evtushinsky, T.K. Kim, I.V. Morozov, R. Follath, and B. Büchner, Symmetry **4**, 251 (2012)

[44] P. Hlobil, J. Jandke, W. Wulfhekel, and J. Schmalian, arXiv:1603.05288 (2016)

[45] Y. Wang, P.J. Hirschfeld, and I. Vekhter, Phys. Rev. B **85**, 020506 (2012)

[46] C. Hess, S. Sykora, T. Hänke, R. Schlegel, D. Baumann, V.B. Zabolotnyy, L. Harnagea, S. Wurmehl, J. van den Brink, and B. Büchner, Phys. Rev. Lett. **110**, 017006 (2013)

[47] S. Chi, S. Johnston, G. Levy, S. Grothe, R. Szedlak, B. Ludbrook, R. Liang, P. Dosanjh, S.A. Burke, A. Damascelli, D.A. Bonn, W.N. Hardy, and Y. Pennec, Phys. Rev. B **89**, 104522 (2014)

[48] P.M.R. Brydon, M. Daghofer, C. Timm, and J. van den Brink, Phys. Rev. B **83**, 060501 (2011)

[49] A.A. Kordyuk, V.B. Zabolotnyy, D.V. Evtushinsky, T.K. Kim, I.V. Morozov, M.L. Kulic, R. Follath, G. Behr, B. Büchner, and S.V. Borisenko, Phys. Rev. B **83**, 134513 (2011)

[50] B. Zeng, D. Watanabe, Q.R. Zhang, G. Li, T. Besara, T. Siegrist, L.Y. Xing, X.C. Wang, C.Q. Jin, P. Goswami, M.D. Johannes, and L. Balicas, Phys. Rev. B **88**, 144518 (2013)

[51] M. Tinkham: *Introduction to Superconductivity* (McGraw-Hill, 1996)

[52] T. Hanaguri, Y. Kohsaka, M. Ono, M. Maltseva, P. Coleman, I. Yamada, M. Azuma, M. Takano, K. Ohishi, and H. Takagi, Science **323**, 923 (2009)

[53] T. Hanaguri, S. Niitaka, K. Kuroki, and H. Takagi, Science **328**, 474 (2010)

[54] P.J. Hirschfeld, D. Altenfeld, I. Eremin, and I.I. Mazin, Phys. Rev. B **92**, 184513 (2015)

[55] P.A. Lee, N. Nagaosa, and X.-G. Wen, Rev. Mod. Phys. **78**, 17 (2006)

[56] K. McElroy, R.W. Simmonds, J.E. Hoffman, D.-H. Lee, J. Orenstein, H. Eisaki, S. Uchida, and J.C. Davis, Nature **422**, 592 (2003)

[57] Q.-H. Wang and D.-H. Lee, Phys. Rev. B **67**, 020511 (2003)

[58] O. Fischer, M. Kugler, I. Maggio-Aprile, C. Berthod, and C. Renner, Rev. Mod. Phys. **79**, 353 (2007)

[59] T. Hanaguri, C. Lupien, Y. Kohsaka, D.-H. Lee, M. Azuma, M. Takano, H. Takagi, and J.C. Davis, Nature **430**, 1001 (2004)

[60] J.E. Hoffman, E.W. Hudson, K.M. Lang, V. Madhavan, H. Eisaki, S. Uchida, and J.C. Davis, Science **295**, 466 (2002)

[61] J.C.S. Davis and D.-H. Lee, Proceedings of the National Academy of Sciences **110**, 17623 (2013)

[62] E. Fradkin and S.A. Kivelson, Nat Phys **8**, 864 (2012)

[63] R. Wiesendanger, Rev. Mod. Phys. **81**, 1495 (2009)

[64] M. Enayat, Z. Sun, U.R. Singh, R. Aluru, S. Schmaus, A. Yaresko, Y. Liu, C. Lin, V. Tsurkan, A. Loidl, J. Deisenhofer, and P. Wahl, Science **345**, 653 (2014)

Index

Schriften des Forschungszentrums Jülich
Modeling and Simulation

1. **The LDA+DMFT approach to strongly correlated materials**
   Lecture Notes of the Autumn School 2011 Hands-on LDA+DMFT
   edited by E. Pavarini, E. Koch, D. Vollhardt, and A. Lichtenstein (2011), 420 pages
   ISBN: 978-3-89336-734-4

2. **Correlated Electrons: From Models to Materials**
   Lecture Notes of the Autumn School on Correlated Electrons 2012
   edited by E. Pavarini, E. Koch, F. Anders, and M. Jarrell (2012), 450 pages
   ISBN: 978-3-89336-796-

3. **Emergent Phenomena in Correlated Matter**
   Lecture Notes of the Autumn School on Correlated Electrons 2013
   edited by E. Pavarini, E. Koch, and U. Schollwöck (2013), 520 pages
   ISBN: 978-3-89336-884-6

4. **DMFT at 25: Infinite Dimensions**
   Lecture Notes of the Autumn School on Correlated Electrons 2014
   edited by E. Pavarini, E. Koch, D. Vollhardt, and A. Lichtenstein (2014), 450 pages
   ISBN: 978-3-89336-953-9

5. **Many-Body Physics: From Kondo to Hubbard**
   Lecture Notes of the Autumn School on Correlated Electrons 2015
   edited by E. Pavarini, E. Koch, and P. Coleman (2015), 500 pages
   ISBN: 978-3-95806-074-6

6. **Quantum Materials: Experiments and Theory**
   Lecture Notes of the Autumn School on Correlated Electrons 2016
   edited by E. Pavarini, E. Koch, J. van den Brink, G. Sawatzky (2016), 420 pages
   ISBN: 978-3-95806-159-0